

Computational Study of T Cell Repolarization During Target Elimination

Dissertation

zur Erlangung des Grades
des Doktors der Naturwissenschaften
der Naturwissenschaftlich-Technischen Fakultät
der Universität des Saarlandes

von

Ivan Horňák

Saarbrücken

2022

Tag des Kolloquiums:

1. Juni

Dekan:

Prof. Dr. Ludger Santen

Vorsitz:

Prof. Dr. Romanus Dyczij-Edlinger

Berichterstatter/innen:

Prof. Dr. Dr. h.c. Heiko Rieger

Prof. Dr. Ludger Santen

Akad. Beisitzer:

Dr. Martin Brinkmann

"Biology is the study of complicated things that have the appearance of having been designed with a purpose."

- quoted from Richard Dawkins

Abstract

T Cells are one of the most important players of the immune system. They are responsible for the elimination of the pathogen-infected or tumorigenic cells (target cells). When a target cell is recognized, the T Cell establishes a contact zone called the immunological synapse (IS). Subsequently, the cytoskeleton rotates and the MTOC relocates to the IS. The cytoskeleton rotation is correlated with a movement of organelles attached to microtubules (MT). The MTOC repositioning results from an interplay between MTs and dyneins in the IS pulling MTs via two mechanisms: cortical sliding and capture-shrinkage. Since many aspects of the process remain unknown, we designed a theoretical model for the molecular-motor-driven motion of the MT cytoskeleton in the cell with one or two IS. The model offers explanations of several experimental results including the biphasic nature of the MTOC movement. We also compared the two mechanisms in different cell configurations and found that the T Cell performs one of the most important immune reactions with stunning efficiency by the advantageous placement of dyneins and by employing two mechanisms acting in synergy. We also analyzed Ca^{2+} diffusion in the T Cell following the MTOC repositioning. We provided the evidence that mitochondria relocate towards the IS with the MTOC and their placement together with their ability of absorption and redistribution significantly increase the Ca^{2+} concentration.

Zusammenfassung

T Zellen sind einer der wichtigsten Spieler des Immunsystems. Sie sind verantwortlich für die Beseitigung von infizierten-oder tumorösen Zellen (Zielzellen). Wenn eine Zielzelle erkannt ist, schafft die T-Zelle eine Immunologische Synapse (IS) genannte Kontaktzone. Dann rotiert das Zytoskelett und das MTOC zieht zur IS. Die Rotation ist mit einer Bewegung von an Mikrotubuli (MT) angehefteten Organellen korreliert. Die MTOC Umpositionierung ergibt sich aus dem Zusammenspiel zwischen MT und Dyneinen in der IS wobei MTs über zwei Mechanismen gezogen werden: "cortical sliding und "capture-shrinkage". Da viele Aspekte des Prozesses unbekannt bleiben entwarfen wir ein theoretisches Modell für die durch molekulare Dyneinen Bewegung des MT Zytoskeletts in der Zelle mit einer oder zwei IS. Das Modell bietet Erklärungen mehrerer experimenteller Ergebnisse einschließlich der biphasischen Natur der MTOC Bewegung. Ebenso verglichen wir die beiden Mechanismen unter verschiedenen Konfigurationen und fanden, dass die T-Zelle eine der wichtigsten Immunreaktionen durch nutzbar Anordnung von Dyneinen und Einsatzes zweier in Synergie arbeitenden Mechanismen mit erstaunlicher Effizienz durchführt. Wir analysierten auch folgenden Ca^{2+} Diffusion in der T-Zelle. Wir liefern den Nachweis, dass Mitochondrien mit das MTOC zu der IS ziehen und ihre Platzierung, zusammen mit der Fähigkeit der Absorption und Umverteilung, die global Ca^{2+} Konzentration signifikant steigert.

Publications

Results of my work were published in the peer-reviewed publications:

- [Hornak2020] I. Hornak and H. Rieger.
Stochastic Model of T Cell Repolarization during Target Elimination (I).
Biophysical Journal, 118(7), 1733–1748, 2020.
<https://doi.org/10.1016/j.bpj.2020.01.045>.
- [Hornak2022] I. Hornak and H. Rieger.
Stochastic Model of T Cell Repolarization during Target Elimination (II).
Biophysical Journal, 121(7), 1246-1265, 2022.
<https://doi.org/10.1016/j.bpj.2022.02.029>.
- [Hornak2016] I. Maccari, R. Zhao, M. Peglow, K. Schwarz, I. Hornak, M. Pasche, A. Quintana,
M. Hoth, B. Qu, H. Rieger.
Cytoskeleton rotation relocates mitochondria to the immunological synapse and increases
calcium signals.
Cell Calcium, 60, 309-321, 2016.
<https://doi.org/10.1016/j.ceca.2016.06.007>.

Conferences

The results were also presented at the following conferences:

March 2021

Conference "DPG Spring Meeting" 2021
Virtual Conference

October 2019

Conference "Cell Physics 2019"
Saarland University
Saarbrücken, Germany

March 2019

Conference "DPG Spring Meeting" 2019
Regensburg University
Regensburg, Germany

March 2019

Conference Physical Biology Circle Meeting 2019
Saarland University
Saarbrücken, Germany

October 2017

Conference "Cell Physics 2017"
Saarland University
Saarbrücken, Germany

September 2017

Summer Camp SFB1027 "SummerCamp 2017"
Hohenwart Forum
Pforzheim, Germany

March 2017

Physical Biology Circle Meeting
EMBL Advanced Training Centre
Heidelberg, Germany

July 2016

Conference "StatPhys 26"
Centre de Congres de Lyon
Lyon, France

June 2016

Conference "Cell Physics 2016"
Saarland University
Saarbrücken, Germany

Contents

List of Figures	v
Nomenclature	vii
1. Introduction	1
1.1. Human body and threats	1
1.2. Immune system	2
1.3. Adaptive immunity	2
1.4. Cytotoxic T Cell	3
1.5. Cellular signaling	6
1.6. Ca ²⁺ signaling	8
1.7. The goals of the thesis	9
1.7.1. MTOC repositioning	9
1.7.2. Mitochondria relocation and calcium diffusion	10
1.8. Outline	11
2. State of the art	13
2.1. Cell	13
2.2. Cytoskeleton	15
2.3. Microtubules	16
2.3.1. Experiments	17
2.3.2. Models	21
2.4. MTOC	24
2.5. Molecular Motors	25
2.5.1. Myosin and kinesin	26
2.6. Dynein	26
2.6.1. Experiments	28
2.6.2. Models	30
2.7. Types of T Cell	31
2.8. Life and immune response of the cytotoxic T Cell	32
2.8.1. Bone marrow progenitors naive cells, and their activation	32
2.8.2. Recognition of the antigen-presenting cell by the effector T Cell	33
2.8.3. IS formation and structure	34
2.9. MTOC repositioning during targeted killing	36
2.9.1. Experiments	36
2.9.2. Models	38
2.10. Secretion of lytic granules	40
2.11. Memory cells	41
2.12. Roles of T Cells in different stages of life	42
2.13. MTOC repositioning during various cellular processes	42
3. Computational model	47
3.1. Model of the cell with one immunological synapse	47
3.2. Model of the cell with two immunological synapses	48
3.3. Model of the microtubule	50
3.4. Model of the MTOC	51
3.5. Model of the dynein	52
3.6. Constrained Langevin dynamics	54
3.7. Projection with the constraints	55
3.8. Code and calculations	56

4. Summary	57
4.1. Stochastic Model of T Cell Repolarization during Target Elimination (I)	57
4.2. Stochastic Model of T Cell Repolarization during Target Elimination (II)	59
4.3. Cytoskeleton rotation relocates mitochondria to the immunological synapse and increases calcium signals	62
5. Summarizing discussions	65
5.1. What did we achieve?	65
5.2. "...things that have the appearance of having been designed with a purpose."	68
6. Original publications	69
6.1. Stochastic Model of T Cell Repolarization during Target Elimination (I)	69
6.1.1. Main Manuscript	69
6.1.2. Supplemental Material	86
6.2. Stochastic Model of T Cell Repolarization during Target Elimination (II)	100
6.2.1. Main Manuscript	100
6.2.2. Supplemental Material	121
6.3. Cytoskeleton rotation relocates mitochondria to the immunological synapse and increases calcium signals	129
6.3.1. Main Manuscript	129
Bibliography: own works	I
Bibliography: references	III
A. Demarcation from the work of the co-authors	XXXIX
B. Permissions to reprint articles	XLIII
C. Permission to reprint figures	XLV
D. Requirements for the cumulative dissertation	LI
E. Curriculum vitae	LV
Acknowledgments	LIX

List of Figures

1.1. Sketch of the T Cell killing the antigen-presenting cell	4
1.2. Experimental images of the MTOC repositioning	5
1.3. Sketch of the cortical sliding and the capture-shrinkage mechanisms	6
1.4. Time-lapse images from the experiments depicting microtubules pulled by capture-shrinkage mechanism	7
1.5. Sketch of Ca^{2+} signaling and the polarization of the T Cell	9
1.6. Biphasic nature of the MTOC repositioning	10
2.1. Sketch of the eukaryotic cell	14
2.2. Sketch and the fluorescence microscope image of the cytoskeleton	15
2.3. Cytoskeletal filaments	16
2.4. Microtubule structure	17
2.5. Microtubule cross section	18
2.6. Dynamic instability	20
2.7. Microtubule depolymerization	21
2.8. Coarse-grained representation of a polymer chain	22
2.9. Sketches of basic coarse-grained models	23
2.10. Sketch of the MTOC	24
2.11. Cross section of the centriole	25
2.12. Representative structure of the cytoplasmic dynein	27
2.13. Cryo-electron microscopy of dyneins walking on the microtubule	30
2.14. Sketch of the T Cell receptor	32
2.15. Sketch of the activation of the naïve cell	33
2.16. Sketch of the immunological synapse	34
2.17. Actin filaments and the MTOC at the immunological synapse	35
2.18. Combination of capture-shrinkage and cortical sliding mechanisms	36
2.19. Modulated polarization microscopy of the MTOC repositioning during the targeted killing	37
2.20. Sketch of the deterministic mechanical model of the T Cell polarization	38
2.21. Model with mobile dyneins	39
2.22. Centrosome polarization brings lytic granules to the synapse	40
2.23. Secretion of lytic granules to the antigen-presenting cell	41
2.24. Different roles of T Cells during aging	42
2.25. MTOC repositioning in polarized cells	43
2.26. MTOC repositioning in the cell with two immunological synapses	44
3.1. Sketch of the model of the cell with one immunological synapse	48
3.2. Sketch of the model of the cell with two immunological synapses	49
3.3. Two-dimensional sketch of the microtubule discretization	51
3.4. Model of the MTOC	52
3.5. Dynein's stepping and forces	53
4.1. Repositioning of the MTOC in the cell with one IS under the effects of cortical sliding mechanism	59
4.2. Repositioning of the MTOC in the cell with two IS under the effects of capture-shrinkage mechanism	61
4.3. Model for the analysis of Ca^{2+} diffusion in the T Cell	64
5.1. Two phases of the MTOC repositioning	66
5.2. Morphological changes of the microtubule cytoskeleton	67

Nomenclature

Abbreviations

APC	Antigen presenting cell
ATP	Adenosine tri-phosphate
ADAP	Adhesion and degranulation-promoting adapter protein
BSM	Bead-spring model
CG	Coarse-grained model
CRAC	Calcium release-activated channel
CTL	Cytotoxic T lymphocyte
cSMAC	Central supramolecular activation cluster
DI	Dynamic instability
dSMAC	Distant supramolecular activation cluster
ER	Endoplasmic reticulum
FJC	Freely-jointed chain
IS	Immunological synapse
GDP	Guanosine diphosphate
GTP	Guanosine triphosphate
MHC	Major histocompatibility complex
MT	Microtubule
MTOC	Microtubule organizing center
NK	Natural killer Cell
NKT	Natural killer T Cell
PCM	Pericentriolar material
PMCA	Plasma membrane Ca^{2+} ATPase
pMHC	Peptide-major histocompatibility complex molecules
pSMAC	Peripheral supramolecular activation cluster
RER	Rough endoplasmic reticulum
SER	Smooth endoplasmic reticulum
SERCA	Sarcoendoplasmic Reticulum Calcium ATPase
SMAC	Supramolecular activation cluster
SHC	Semiflexible harmonic chain
TCR	T Cell receptor
WLC	Worm-like chain

Model parameters used in Chapter 3

Cell

k_B	Boltzmann constant
R_{Cell}	Cell radius
R_{IS}	IS radius
R_{CIS}	IS center radius
R_{nuc}	Nucleus radius
T	Temperature

Microtubule

κ	Bending rigidity
l_p	Persistence length
L	Length of the microtubule
k	Length of the segment
N	Number of microtubule beads
c_r	Catastrophe rate
v_s	Depolymerization speed
v_g	Polymerization speed
r_r	Rescue rate

MTOC

b_{MTOC}	Bending rigidity
k_{MTOC}	Elastic modulus
Q^{MTOC}	Number of MTOC points
R_{MTOC}	Radius of the MTOC

Dynein

p_a	Attachment rate
k_d	Elastic modulus of the stalk
L_0	Length of the relaxed stalk
d_{step}	Length of the step
V_F	Forward speed
V_B	Backward speed
p_+	Stepping rate to the plus end
p_-	Stepping rate to the minus end
F_D	Detachment force
F_S	Stall force

Chapter 1.

Introduction

Contents

1.1. Human body and threats	1
1.2. Immune system	2
1.3. Adaptive immunity	2
1.4. Cytotoxic T Cell	3
1.5. Cellular signaling	6
1.6. Ca ²⁺ signaling	8
1.7. The goals of the thesis	9
1.7.1. MTOC repositioning	9
1.7.2. Mitochondria relocation and calcium diffusion	10
1.8. Outline	11

1.1. Human body and threats

What keeps us alive? Many philosophers and thinkers tried to provide an answer to this overwhelmingly profound question. A biologist might answer that we are alive thanks to our immune system defending us against threats that we encounter every day of our lives. The defense of our organism is an enormous, fascinating task due to the complexity of the human body and an incredible amount of challenges present in our everyday reality. We live our lives entrapped in our bodies, relying on their functions, and perceiving the world by its senses, often without realizing its complexity. A human body, like every living system, is composed of cells that are frequently termed "the building blocks of life". The astonishing complexity of a human body is illustrated by the fact that it is composed of tens of trillions of cells [1], exceeding the number of stars in the Milky Way galaxy by an order of magnitude.

All cells are enclosed by a plasma membrane protecting the internal from the environment. Cells share many basic properties. They carry and can reproduce genetic information, perform hundreds of complex chemical processes, respond to outer stimuli, and utilize energy to carry out their function. Moreover, they evolve, which is the ability that since the dawn of history of species led to the evolution of the astonishing variety of complex living forms from single-cell organisms [2–4]. Despite their similarities, cells exhibit different shapes, sizes, and mechanical properties enabling them to perform various functions. Typical diameter of T lymphocytes of adaptive immune systems is in tens of micrometers and they search and eliminate the threats to our organisms [5–13]. The neuron cells are of elongated shape with the length greatly exceeding the width and are specialized to carry electrical impulses [14–16]. White fat cells store the energy that can be released and fuel the body during the fasting [17], brown fat cells defend mammals against hypothermia by dissipating chemical energy to create heat [18]. Hundreds of various types of cells coexist and cowork together and form the complex machinery of a human body. This great system of coworking cells never stays the same. Every day, billions of cells die in the body of an adult human and they are replaced by new ones, born from cell division or fusion in continuous, never-ending reconstruction [19, 20].

There are tens of thousands of known diseases that can endanger a human body [21]. Some of them are the most trivial ones like a common cold, but the spectrum also contains serious threats like cancer [22]. Unfortunately, a new day can bring another unexpected challenge as was recently demonstrated by the COVID-19 pandemic. We are able to survive in this potentially hostile environment only due to the

immune system, which fights new challenges as long as we live. The damage of the immune system often results in death, which we can illustrate by observing untreated HIV patients [23–26]. It is clear that our immune system has an enormous, fascinating task: to defend a constantly evolving body composed of tens of trillions of cells against thousands of existing diseases and also respond to all possible new threats. Despite the challenges of various pathogens, like viruses or bacteria that we encounter through contact, ingestion, and inhalation, we are able to function properly and most of the time in a good health. It is due to the multiple layers of the immune system that can mount a great variety of responses to diverse threats.

1.2. Immune system

The immune system of mammals can be broadly divided into innate and adaptive immunity. The two branches have many things in common and share some basic properties. For example, some agents of both systems use similar mechanisms to carry out immune responses, which can be demonstrated by the release of cytotoxic granules during target elimination by cytotoxic T lymphocytes and natural killer (NK) cells belonging to the adaptive and innate immune system, respectively [12, 27, 28]. Moreover, both must possess the fascinating ability to distinguish self from non-self, which enables the destruction of pathogens without harming the host [29]. One can only wonder about the difficulties of such a task when considering the complexity of the human organism and the variety of threats.

Despite many similarities, the principle of protection of our organism by innate immunity differs from the one by adaptive immunity. The main difference between the two branches of immunity is that innate immunity generates a non-specific response against the threats, whereas adaptive immunity responds specifically to a particular pathogen [30]. They also differ in the manner of recognizing the threats to the organism and in the speed of reaction [31]. Moreover, although both systems have a memory, the one of the adaptive immune system is more advanced, remembers previous encounters with the pathogen, and can mount a specific response [32–35]. They also differ by age. The innate immunity is evolutionary older since some of its parts appear to be very ancient, perhaps predating the division between animals and plants more than a billion years ago [29]. The elements of the innate immune system can be found in all multicellular organisms [36]. The adaptive immune system is relatively new since it arose in evolution five hundred million years ago and its complex protection provided great advantages to vertebrates [29]. While innate immunity is already present in a body, adaptive immunity is created gradually as a response of the body when exposed to specific foreign substances. But in spite of all the differences, the two branches of the immune system do not work independently. Their cooperation is demonstrated by the fact that the innate immunity shapes the differentiation and expansion of the cell of adaptive immunity [31, 37].

The innate immunity is an evolutionarily conserved defense system and some of its features are shared among a large variety of organisms, like plants, invertebrates, and mammals. The innate system consists of physical barriers, chemical barriers, and cellular defenses. The physical barriers, including the skin and the gastrointestinal tract, prevent the threats from entering a human body [36]. The chemical barriers, like stomach acid, are hostile to a large number of microorganisms and prevent the viruses from gaining a foothold [38]. When a threat overcomes barriers, the innate immune system stimulates cellular defenses [29]. Its cells and receptors quickly recognize and respond to infectious agents shared by a variety of microbes that are not present in an uninfected host [39]. Consequently, they quickly recognize the threat and react. The speed of the reaction is critical. The agents of the adaptive immunity have to be activated and expand to mount an adequate reaction. This may take days, which is arguably too slow considering that the doubling times of some bacteria are around one hour. Consequently, their number can multiply one thousand times during ten hours [31]. It is the innate immune system that defends our organisms during the first hours after encountering a new threat [40–42]. For example, when a bacteria enters a body by a wound, the innate system is the first line of defense [38].

1.3. Adaptive immunity

Contrarily to the innate system, the response of the adaptive immune system is more sophisticated and highly specific to a threat [38, 39, 43], which makes it usually substantially more powerful. The adaptive immune response has two main tasks: to create an immune response that targets specifically the invading

pathogen and to form an array of memory cells that can last for years. A substance capable of provoking adaptive immune response is called an antigen (antibody generator) [31, 38]. The agents of the adaptive immune system circulate through the organism looking for threats. The recognition of an antigen by the agents of the adaptive immune system initiates an immune reaction. The adaptive immunity consists of a relatively small number of different types of cells with a specificity for a pathogen. The particular agents must therefore proliferate massively to gain a sufficient number to fight the threat [39]. When the antigen is eliminated, the majority of the defending cells dies. The adaptive immune system then produces long-lived so-called memory cells, which remain in the organism even decades after the initial exposure in an apparently dormant state but keep their effector functions. When they encounter the specific antigen for the second time, they re-express the effector functions, which enables fast and efficient response to an already known threat [39, 44, 45]. Therefore, the memory cells provide long-lasting protection after the recovery. They also greatly increase the effectiveness of the adaptive immune system, since its reaction depends on the host's prior exposure.

The responses to pathogens are carried out by white blood cells referred to as lymphocytes, these can be divided into two different classes, the B and T lymphocytes, also known as the B and T Cells [39, 46]. These classes share some features. They both express highly antigen-specific receptors unique to them, B Cell receptor and T Cell receptor (TCR), created during somatic gene recombination [32, 47, 48]. They are both relatively small, being of approximately $10\mu\text{m}$ in diameter [5, 9, 46]. Although T Cells travel to thymus for later development, they both originate in the bone marrow [49–51]. However, despite the similarities, they carry out different functions, these can be broadly divided into two classes: the antibody responses and the cell-mediated immune responses.

During the antibody responses, the B cells fight the infection by secreting antibodies called immunoglobulins. These circulate through body fluids in search of the antigen that stimulated their production [39, 52, 53]. Antibodies have billions of forms and mediate various biological responses. They bind to the viruses and microbial toxins, thus inactivating their ability to bind to receptors on host cells [31, 54]. Moreover, the binding also marks the pathogens for the destruction by the cell of the innate immune system.

During the cell-mediated responses, the T Cells react directly against the antigen on the surface of the cell [31, 46, 55]. They direct multiple aspects of adaptive immunity responses towards the pathogens and tumors. The T Cells have a simple, although not easy objective: to control the cells of the organism and eliminate the threats. There are several types of T Cells with different functions. A helper T Cell might for example secrete signal molecules to activate macrophages destroying the invading microbes [31, 56, 57]. By contrast, a cytotoxic T lymphocyte controls the cells of the organisms and directly eliminate the infected cell posing the threat to the organism [58]. They are the line of defense against viral infections, infections caused by other intracellular pathogens replicating in the cytoplasm, and the tumors. The T Cells have a fascinating ability to react to the pathogens by massive expansion and migration to every part of the body in order to fight the infection [59–61]. Different classes of T Cells and their functions are described in Section 2.7.

The population of both the B Cells and the T Cells can be subdivided into several classes performing different functions in variable circumstances depending on the threats. Nevertheless, it would be a misconception to consider their actions separate. Similarly to the immune system having two collaborating branches, the adaptive immune system employs multiple types of cells often acting in synergy. The classes of the T and the B Cells cooperate, complete, and navigate each other in various immune responses across our organism. For example helper T Cells, a subclass of the T Cells, help to activate the B Cells to secrete antibodies and promote several aspects of immune action of T lymphocytes directly attacking the threats [57, 62–64].

1.4. Cytotoxic T Cell

A cytotoxic T Cell, a cytotoxic T lymphocyte (CTL), or a killer cell, is a representative of T Cells. The CTLs have a crucial role in our organism since they search for and destroy virus-infected and tumor cells, parasites, and foreign invaders. They are a "foot soldiers" of our immune system, capable

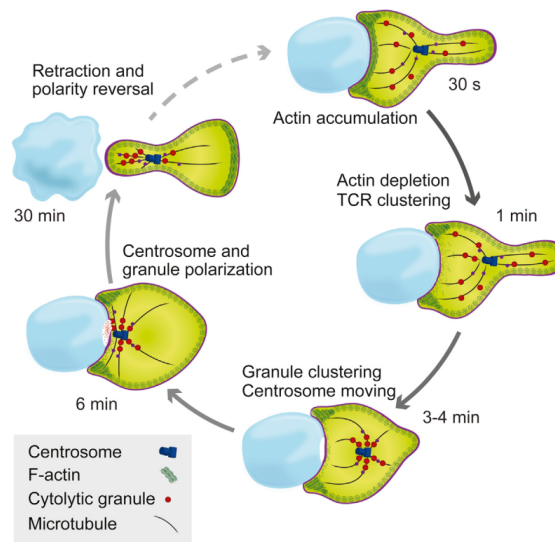


Figure 1.1.: Sketch of the CTL killing the antigen-presenting cell (APC). First, the CTL makes contact with the APC and actin filaments accumulate at the immunological synapse. Consequently, actin density in the center of the immunological synapse rapidly decreases and actin forms a ring around the immunological synapse. Then, the microtubule organizing center (MTOC) and the cytolitic granules transition towards the immunological synapse. After the secretion of granules, the CTL detaches from the APC. The figure was taken from [74] with the permissions stated in the Appendix C.

of a fast recruitment, speedy movement, quick reaction, and merciless action [59–61, 65, 66]. They are one of the several cells that have the “license to kill” other cells of the body [67–69]. They destroy an antigen-presenting cell (APC) by polarized secretion of lytic granules containing perforin and granzymes. The life and immune reaction of the CTL is thoroughly described in Chapter 2. Here, I briefly outline the CTL immune response to present the main topic and goals of my work.

Before the description of the process, it should be mentioned that the CTLs are not the only ones using the polarized secretion to kill the threats. The process is also employed by the NK cells of the innate immune system. Both the NK and the CTL cells are fundamental to host defense against threats. However, in spite of using the same mechanism, the role of the NK cells and the CTLs in the immune system differs substantially. The differences are given mainly by the fact that they belong to different branches of the immune system. The NK cells lack the antigen-specific cell surface receptors that recognize specific threats. Moreover, they participate in the early defense against the infections [70]. Contrarily to the NK cells, the CTLs have a highly specific TCR located on their surface. TCRs are immensely diverse heterodimers consisting of α and β chains. They recognize specific peptides bound to a major histocompatibility complex (MHC) on the APC and initiate an inflammatory response [71, 72]. After recognizing the antigen, the CTL proliferate to obtain sufficient numbers to fight a threat, which delays their effective response [73]. To summarize, the response of the NK cells is fast and non-specific and the response of the CTLs is specific but delayed.

Cytotoxic killing of a target cell, sketched in Fig. 1.1, is completed in a sequence of steps. First, the CTL establishes contact with the APC with the help of the TCR [75–80] that binds to the antigens on the surface of the target cell. A tight contact zone, called immunological synapse (IS), is composed of multiple supramolecular activation clusters [81–83], see Section 2.8.3. Actin filaments, one of the major components of the cytoskeleton forming complex networks under the plasma membrane, play a crucial role in the IS formation. Motile CTLs have a shape of a stereotypical tadpole and the leading edge is enriched by actin. When the CTL forms a conjugate with the APC, one observes the actin is accumulated across the synapse. Within the next minute, the actin density in the center of the IS rapidly decreases. One also observes a high actin density at the periphery of the IS [74]. Consequently, the actin forms a ring-like shape around the IS. Second, the CTL polarizes by rotating the entire microtubule (MT) cytoskeleton and repositioning the microtubule-organizing center (MTOC) towards the IS due to the forces acting on MTs,

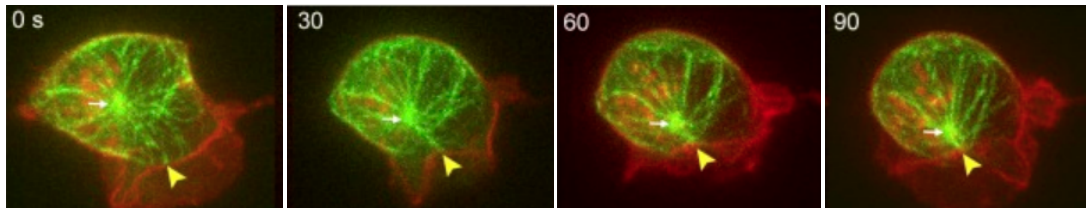


Figure 1.2.: Experimental images of the MTOC repositioning [5]. MTs and the plasma membrane of the APC are labeled green and red, respectively. The white and yellow arrows mark the MTOC and the center of the IS, respectively. In the cell configuration when the IS and the MTOC are initially diametrically opposed, the MTOC transitions to the IS during approximately ninety seconds. The figure was taken from [5] with permissions stated in the Appendix C.

see Fig. 1.2 [5–10, 84]. The mechanisms pulling MTs are described in Section 2.9. Multiple organelles, mitochondria, the Golgi apparatus, and the endoplasmic reticulum (ER) are attached to the MTs and are dragged with them. Therefore, the polarization is a complex process involving a massive rearrangement of the internal structure of the CTL. In the third and the final step, the CTL secretes the lytic granules containing cytotoxic material to the target cell, thus delivering the “kiss of death”, see Section 2.10. The lytic granules contain the pore-forming protein perforin and the apoptosis-inducing granzyme, so the APC is destroyed via apoptosis or necrosis [11–13, 85–88]. Subsequently, the CTL detaches from the APC.

This thesis focuses on the second step: the MTOC repositioning, see Fig. 1.2 [Hornak2020, Hornak2022]. As already mentioned, it is a complex process changing the entire internal structure of the cell. However, the movement originates mainly from the interplay of only two players, the MTs and the dynein motor proteins located in the IS. Due to their importance, I will briefly introduce the two players and the place where they interact.

The MTs are stiff biopolymers anchored in the MTOC from which they sprout to the cell periphery [89–91], see Section 2.3. The end of the MT anchored in the MTOC and the free end are termed the minus and the plus end, respectively. They provide a shape and a structure to the cell and play a role in a variety of cellular processes, including the movement of the cell in the environment. The MT cytoskeleton undergoes a constant reconstruction since the periods of polymerization alternate with the periods of depolymerization in a constant process termed dynamic instability (DI) [92–102], see Section 2.3.1. Due to this constant rebuilding, the cytoskeleton adapts itself to various functions of the cell and performs significant morphological changes during the cell cycle [95, 103–105]. The DI plays a key role in repositioning since the constant growing and shrinking enables the tips of polymers to find the IS where they can be captured by dyneins. A dynein, a minus end directed motor protein (towards the MTOC), is indispensable for the polarization, as was convincingly demonstrated by knock-out experiments [106–110]. It is a homodimer composed of two identical massive heavy chains ending with an MT-binding stalk, see Section 2.6. The dyneins actively walk on the MT and generate the force that pulls the filament and the MTOC towards the IS [111–113]. The IS is divided into several supramolecular activation clusters (SMACs), see Section 2.8.3. The TCRs and adhesion molecules are organized in the central supramolecular activation cluster (cSMAC) [81, 83, 114–116]. Secretion of the lytic granules takes place in a specialized secretory domain located next to the cSMAC and within the peripheral supramolecular activation cluster (pSMAC) surrounding the cSMAC. The distal cluster (dSMAC) encircling the pSMAC is the place of actin accumulation [74, 117]. It was reported that the dyneins colocalize with the adhesion and degranulation-promoting adapter protein (ADAP) forming a ring at the IS periphery [118–120]. The structure of the IS and the location of pulling forces are described in Section 2.8.3

It was suggested that the MTs are pulled by the cortical sliding mechanism, sketched in Figs. 1.3a and b, in which the dynein steps to the minus end of the MT while being anchored at the cell cortex and therefore pulls the MTOC towards the IS [9, 118, 121]. The MT tip remains free and the MT slides on the cell membrane. It was suggested that the periphery of the IS is the region where a dynein attaches and pulls MTs [9, 118]. The observations in [5] provided evidence of a second mechanism driving the repositioning: the capture-shrinkage mechanism [122], sketched in Fig. 1.3c. An optical trap was used in [5] to place a target cell in such a way that the MTOC and the IS were diametrically opposed at the

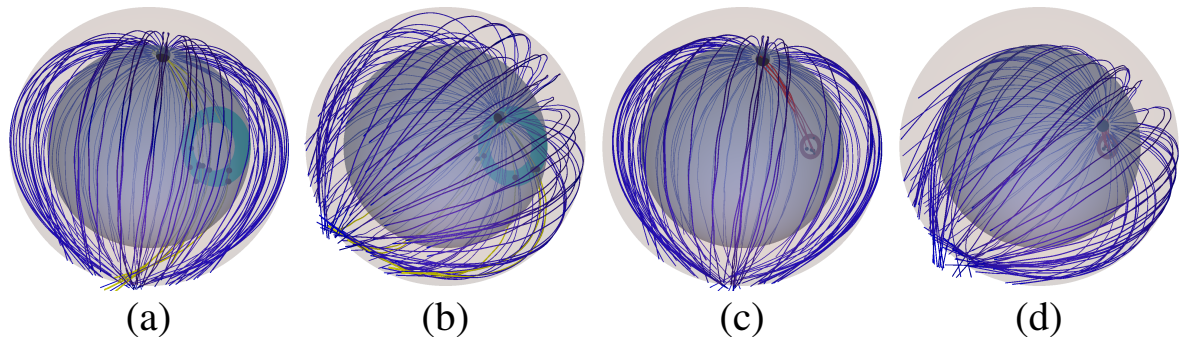


Figure 1.3.: Sketch of the cortical sliding and the capture-shrinkage mechanisms. The outer transparent and inner spheres stand for the cell membrane and the nucleus of the cell, respectively. The big and the small black spheres depict the MTOC and dynein motors, respectively. The blue lines represent unattached MT sprouting from the MTOC. They can attach to capture-shrinkage dyneins (red) or can be pulled by cortical sliding mechanism (yellow). (a-b) The cyan circle represents the periphery of the IS where cortical sliding dyneins are located. (a) MTs pulled by cortical sliding attach to the dynein at the periphery of the IS. (b) MTs slide on the cell membrane and the MTOC approaches the IS. (c-d) The brown circle denotes the center of the IS, where the capture-shrinkage dyneins are located. (c) The MTs pulled by capture-shrinkage form a stalk connecting the MTOC and the IS. (d) The MTOC approaches the IS and MTs depolymerize. The figure was made using the simulation software [Hornak2022B].

beginning of the repositioning. Such configuration allowed dynamical imaging in a quantitative fashion and observations of the morphological changes of the MT cytoskeleton, which enabled the identification of the mechanism. The capture-shrinkage mechanism acts in end-on fashion with the plus ends of the MT. The tip of the filament is fixated on the cell membrane, where it depolymerizes probably due to the forces of dyneins pulling it against the cortex [122]. The MTs, whose plus ends are captured in the center of the IS, straighten and form a stalk connecting the IS with the MTOC, see Fig. 1.4, sketched in Fig. 1.3. Subsequently, the MTs in the stalk depolymerize, visualized in Fig. 1.3d, and the MTOC approaches the IS. Simultaneously, the center of the IS invaginates to the cell proving the location of the pulling force. To summarize, the polarization is a complex process, an interplay between the MTs and the dynein motor proteins acting via two functionally and spatially different mechanisms.

The process of a CTL repositioning becomes more complicated when the T Cell attacks two targets at once. More precisely, the T Cell can attack a second target cell creating the second IS before severing the contact with the first cell [9]. In such a case, several scenarios can take place: the MTOC transitions stochastically between the two IS, it wiggles between the IS without moving to any of them, or is pulled to one and stays there [Hornak2022]. Similarly to the case of one IS, the MT cytoskeleton dynamic is the result of the interplay between the MTs and the dyneins. Contrarily, the MTs are pulled to two places simultaneously and the dyneins from different IS are in a constant tug-of-war. The MTOC movement to one of the IS is caused by the stronger forces resulting from higher number of attached dyneins. The process is influenced by the DI, since the number of the attached dynein motors must increase with the number of the intersecting MTs. At the end of the transition, dyneins detach, which is caused by several factors including the depolymerization of the capture-shrinkage MTs. Simultaneously, the MTs intersect the distant IS and attach to the dyneins that can initiate a new transition.

1.5. Cellular signaling

Although the modeling of the MTOC repositioning is the main part of the thesis, it is not the only one. The increase and the diffusion of the Ca^{2+} ions in a T Cell following the IS formation was the second subject of my work. The topics of the Ca^{2+} diffusion and the MTOC repositioning in T Cells are closely connected since multiple signaling steps governing T Cell targeted killing depend on Ca^{2+} concentration. It can be exemplified by the processes of the MTOC and the mitochondria relocation to the IS or by the secretion of the lytic granules [5, 8, 123, 124].

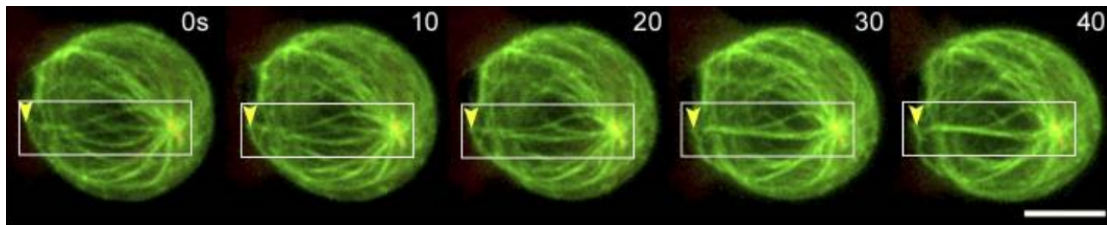


Figure 1.4.: Time-lapse images from the experiments [5] depicting MTs pulled by the capture-shrinkage mechanism. MTs sprouting from the MTOC terminate in end-on fashion in the center of the IS. Over the next forty seconds MTs straighten (white rectangle) and form a stalk connecting the MTOC and the IS. The figure was taken from [5] with permissions stated in the Appendix C.

I have already demonstrated that the human body composed of trillions of cells is a fascinating but incredibly complex system. But complex organisms need more than just protection to survive. There is one thing that is just as important as protection: good and efficient communication. Despite all the dangers the life was able to evolve in various environments and adapt to them. The key to the survival of the cells is the ability to sense their natural surroundings and to react to changing environmental conditions [125]. At the same time, the cells must be able to communicate with one another, respond to cues, and also send a message to the surrounding cells if necessary. Possibly, the prokaryotic chemotaxis system was the first, relatively simple form of a cellular signaling system [126]. However, multicellular organisms emerged and they had more than two billion years to evolve [127, 128]. As they were evolving, taking new forms, and adapting to various conditions, new signaling pathways were developed. At the end of this development, there are complex organisms composed of cells communicating with a large array of signals and carrying out thousands of functions [129–131].

The communication between the cells, also called the cellular signaling, is the fundamental ability to accept, process, and transmit signals from the environment and with itself. Cellular signaling carries information crucial for survival, like information about the availability of nutrients, variations of the light level, or changes in the temperature. Cells can also change their working based on the signals from other cells. Without this ability, multicellular life could not exist. For example the creation and maintenance of the specialized tissues of multicellular organisms, like muscles or brain tissue, relies on the tightly coordinated regulation of cell number, location, and morphology.

Signals can be divided based on the range of the communication. Paracrine (short-ranged) cell synthesized proteins affect only the neighboring cells [132]. In endocrine (long-ranged) signaling hormones travel to act on target cells at distant body sites [133]. Juxtacrine signals depend on the contact between two cells and autocrine signals act on the cell emitting the signals [134]. Signals can be physical or chemical in nature. The physical signals include the signals transmitted by pressure, temperature, voltage, light, or electromagnetic field [135–137]. Despite the large variety of physical signals, the majority of those in cells is chemical [134]. The chemical signaling is astonishingly diverse, it is carried by small molecules, such as lipids, or complex polymers of sugars. The signal molecules include growth factors, neurotransmitters, ions, gases, hormones, and extracellular matrix components [138]. Signaling molecules also differ in their action. Some cross the membrane and subsequently bind to intracellular receptors in the cytoplasm or nucleus. However, the vast majority binds to receptors on the target cell plasma membrane [133].

Cells receive and respond to the chemical messenger (ligand) through receptors located both on the surface and inside the cell [139]. The binding to the ligand results in conformational changes of the receptor. They activate complex signaling networks performed by second messengers or signaling intermediates. They relay exterior cues to the cell and lead to the reprogramming of diverse genetic, structural, and biochemical processes [134, 140]. I deal with only one messenger: Ca^{2+} . In a human body, less than ten grams of the total approximately 1400 grams of calcium escapes from being trapped in bones or teeth [141]. However, this small amount is extraordinarily significant qualitatively since it regulates a manifold of crucial biological processes.

1.6. Ca^{2+} signaling

From all the messengers carrying signals, Ca^{2+} stands out as by far the most versatile one [142]. It has a toolkit consisting of various components that can be combined to create a broad spectrum of spatial and temporal signals. Contrarily to other messengers controlling only a limited amount of functions, Ca^{2+} regulates a large number of key cellular processes, from the fertilization and the beginning of the cell life, to its end during the programmed cell death. The Ca^{2+} signals can influence both short and long-term functions of the cell. However, the functions are typically not separate, they are often in synergy and cooperate in the same biological process. When we consider the example of targeted T Cell killing, the contact with the APC induces a sudden increase in cytoplasmic Ca^{2+} leading to a short-term reduction of the motility allowing the formation of the IS [143–145]. The long-term functions include the production of cytokines and chemokines. To illustrate the versatility of Ca^{2+} signaling, one can mention the control of the fundamental cellular processes, including motility functions, muscle contractions, neuro/enzyme secretion and exocytosis, development and maintenance of neural circuits, learning, and memory [146, 147, 147–149]. The importance of Ca^{2+} signaling might also be demonstrated by the fact that its disturbance may lead to several serious illnesses, like Alzheimer’s disease and Diabetes [149]. In the cells of the immune system, calcium signaling plays a key role in various functions, including gene transcription, T Cell activation, effector function, and a variety of transcriptional programs [143, 150].

Due to its importance, Ca^{2+} concentration requires careful and efficient control. For this reason, the majority of eukaryotic cells export Ca^{2+} or close it into membrane-enclosed stores maintaining cytosolic concentration in the resting T Cell at $\sim 100\text{nM}$, which results in a 10^4 gradient between the extracellular spaces and the cytosol [148, 151, 152]. However, the intracellular concentration can increase dramatically. For example, after the contact with the APC, the Ca^{2+} concentration increases up to $\sim 1\mu\text{M}$ [153]. It is not just the global Ca^{2+} concentration in the cell that matters. Specific outcomes and various biological functions are encoded and modified by the magnitude of various spatio-temporal patterns, presence of microdomains of low or high concentration, kinetics, and frequency of Ca^{2+} waves. The high specificity of the signals in the cell is the result of a complex interplay between the channels and the pumps transferring Ca^{2+} between various organelles and driving the exchange with the exterior. The transfer takes place due to the simple diffusion along concentration gradients (channels) or by active processes (active transporters and pumps) powered by adenosine tri-phosphate (ATP). The capacities of some channels and pumps depend on the Ca^{2+} concentration and their interplay leads to complex feedback loops creating various Ca^{2+} oscillations and microdomains. The importance of the patterns can be demonstrated by the role that the Ca^{2+} microdomains play in the control of neuronal function and gene expression [154, 155]. Another process depending on the Ca^{2+} is T Cell repositioning during the target elimination.

A robust Ca^{2+} signal is necessary for the T Cell activation after the IS formation. The main entry pathway of Ca^{2+} in the cell are the Calcium release-activated calcium (CRAC) channels, which are store-operated channels activated by the depletion of the ER [157, 158]. The regulation of the Ca^{2+} concentration in the microdomain around the IS appears to be crucial since it influences the influx through the CRAC channels. The MTOC repositioning is paralleled with the relocation of several organelles, channels, and pumps to the IS, sketched in Fig. 1.5, resulting in a specific control of Ca^{2+} signals. Ca^{2+} is exported from the cell via plasma membrane Ca^{2+} ATPase (PMCA) pumps [159]. The PMCA pumps are redistributed during the polarization and accumulated in the IS proximity [160]. Since the PMCA pumps are located close to the CRAC channels, Ca^{2+} can be taken out from the cell before diffusing deeper into the cytosol. Ca^{2+} signaling is also substantially influenced by the ER, which is the main intracellular Ca^{2+} store crucial for maintaining the Ca^{2+} concentration [161, 162]. Its depletion, stimulating the influx through the CRAC channels, is triggered by an external stimulus after which Ca^{2+} is released from ER by IP_3 receptors [163–165]. The influx of CRAC channels can be stopped by the refillment of the ER, which happens when the cytosolic Ca^{2+} rises. In such a case, Sarcoendoplasmic Reticulum Calcium ATPase (SERCA) pumps on the ER membrane are activated and they transport Ca^{2+} from the cytosol back to the ER [166, 167]. The CRAC channels can be also deactivated by the high Ca^{2+} concentration in the surrounding microdomain [156, 168]. Mitochondria play a key role in diffusing Ca^{2+} in the T Cell. They relocate to the IS, where they act as sinks reducing the local Ca^{2+} concentration. In this way, they control the activity of CRAC channels dependent on the Ca^{2+} concentration in the microdomain. Absorbed Ca^{2+} is then redistributed to the rest of the cell increasing the global cytosolic concentration [160, 169, 170].

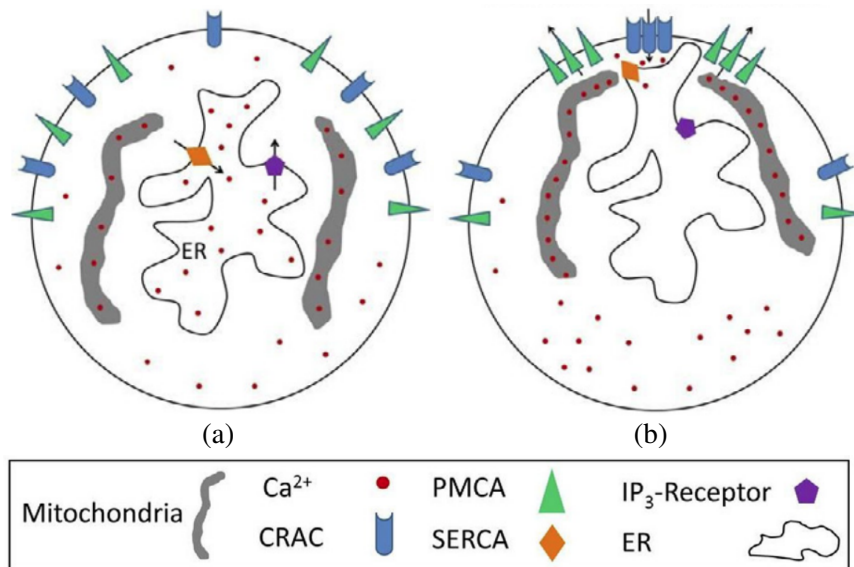


Figure 1.5.: Sketch of Ca^{2+} signaling and the polarization of the T Cell [156]. (a) The T Cell at rest. (b) Activated and polarized T Cell after the relocation of the channels, pumps, mitochondria, and the ER. The figure was taken from [156] with the permissions stated in the Appendix C.

1.7. The goals of the thesis

1.7.1. MTOC repositioning

Although the repositioning was observed in multiple experiments [5, 8, 9, 118, 121], many aspects remain poorly understood. The capture-shrinkage mechanism was identified as the main pulling force in the configuration where the MTOC and the IS are initially diametrically opposed. When the CTL was treated with taxol, an inhibitor of microtubule depolymerization, the capture-shrinkage mechanism was effectively "turned off" and the cortical sliding mechanism was the only one pulling the MTs. In such cells, one observes significantly slowed repositioning [5]. Additionally, Yi et al. [5] demonstrated that the process can be divided into two phases, see Fig. 1.6a. In the first so-called "polarization phase", the MTOC travels quickly in a circular motion around the nucleus. In the second "docking phase", the MTOC slows down and moves straight from the nucleus to the IS, see Fig. 1.6b. What causes the transition between the two phases and the decrease in the MTOC speed? Is it an emergence of a resistive force when the MTOC-IS distance is around $2\mu\text{m}$? Or is slowing caused by the detachment of dynein motors? The experiments proving the dominance of the capture-shrinkage mechanism were performed in one initial configuration where the MTOC and the IS were initially diametrically opposed. Is the capture-shrinkage mechanism dominant in other naturally occurring situations? If the capture-shrinkage indeed is dominant, what is the role of the cortical sliding mechanism? More importantly, how does the interplay of two mechanisms influence the T Cell polarization and killing? Why is the cortical sliding dynein located just on the periphery of the IS? Is it to facilitate the interaction with MTs, as was hypothesized in [9]? We analyze these questions in the framework of a quantitative theoretical model of the MTOC repositioning [Hornak2020,Hornak2022].

The MTOC repositioning was previously analyzed with computational models, as discussed in Section 2.9.2. However, our model incorporates a 3D model of the cytoskeleton and a stochastic model of dynein motor proteins firmly anchored on the cell membrane. Moreover, we perform detailed studies of the process in different initial configurations of the cell defined by the angle between the MTOC and the IS. Furthermore, we analyze the MTOC repositioning in the cell with two IS.

The model is a challenging task due to its complexity. The process of MTOC repositioning is in essence stochastic. The MT cytoskeleton is not stable but constantly changing since MTs randomly switch between the growing and shrinking state. The dynein's attachment to the filaments, the speed and the direction of stepping, and its detachment from the MT are also stochastic. One can choose from a large variety of modeling methods [171] to model polymers, see Section 2.3.2. Atomistic models offer the most accurate

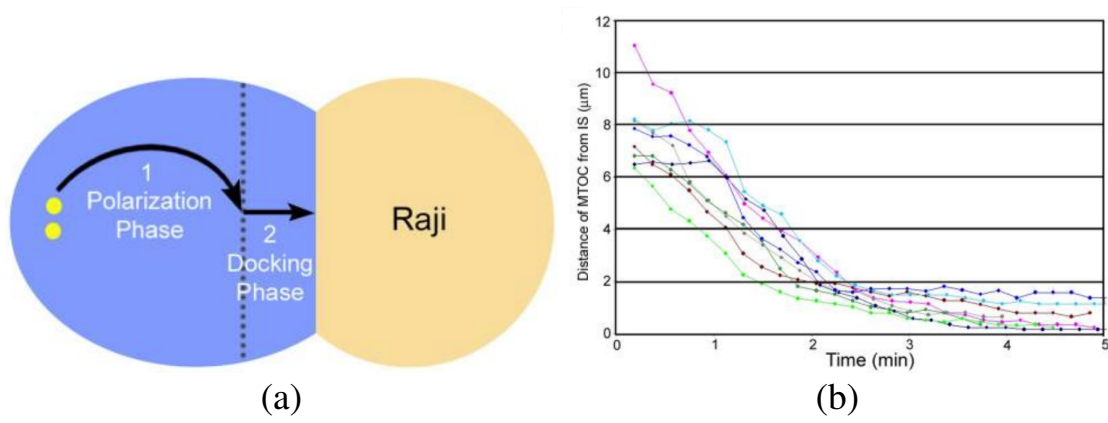


Figure 1.6.: The biphasic nature of the MTOC repositioning [5]. (a) Sketch of the two phases in the T Cell in contact with the Raji B cell (APC). In the polarization phase, the MTOC travels in a circular motion around the nucleus. In the docking phase, the MTOC moves directly from the nucleus to the center of the IS. (b) Compilation of eight MTOC repositioning events plotted as dependence of the MTOC-IS distance one time. The speed substantially decreases at the MTOC-IS distance $\sim 2\mu\text{m}$ corresponding to the change of the orientation of the MTOC motion. The figure was taken from [5] with permissions stated in the Appendix C.

descriptions of the polymer structure interactions. However, they are not suitable for the modeling of long polymers for several reasons including the computational cost. Since repositioning is a collective process of tens of MTs that takes several minutes to complete, coarse-grained models are logical choice. The MTs are modeled as inextensible polymers connected to the MTOC represented by planar, rigid structure, see Section 3.3. One filament is represented by a bead-rod model and divided into approximately twenty beads connected by segments whose length was kept constant. The IS in our model is a circular area with diameter of $2\mu\text{m}$ on the surface of the cell. If we consider the maximum density of one thousand dyneins per micrometer square, the model contains more than twelve thousands dyneins. If one adds the number of MT beads, one realizes that the model consists of more than fourteen thousand elements. The motion, probability densities, and forces have to be computed in every time step. To keep the lengths of the MT segments constant, one has to use constrained dynamics, see Section 3.6, which is computationally demanding due to the necessity to calculate projection matrices. To summarize, the simulation is computationally challenging due to a high number of elements composing the model and the need to satisfy constraints.

1.7.2. Mitochondria relocation and calcium diffusion

The publication [Hornak2016] presents results from both experiments and modeling. We analyze the geometrical paths of the mitochondria and prove that the mitochondria relocation towards the IS is correlated with the rotation of the MTOC. Subsequently, we test the hypothesis that the movement of the mitochondria combined with their ability of Ca^{2+} absorption and redistribution is sufficient to significantly increase the cytosolic concentration.

We develop a model of the cell with the specific geometries of mitochondria and ER and use it to calculate the dependence of the cytosolic concentration on the rotation angle of mitochondria. The cell and the nucleus are represented by two spheres and mitochondria by elongated rod-like structures arranged into a spindle. Two geometries of the ER are implemented, one also spindle-like, the other in a shape of a truncated cone. Compartments can exchange Ca^{2+} via channels and pumps with various spatial distributions. Mitochondria can take and release Ca^{2+} over the entire surface. CRAC channels accumulate in a narrow, circular region in the middle of the IS. PMCA pumps in the model are unequally distributed on the plasma membrane and a defined fraction accumulates around the IS. The ER exchanges the Ca^{2+} with the cytosol via SERCA pumps and IP_3 receptor channels. The Ca^{2+} currents through the plasma membrane and the compartment membranes are implemented as flux/boundary conditions on the 2D surfaces.

1.8. Outline

In Chapter 2, I will discuss the biological background of the CTL polarization. I will present organelles that play a role during the MTOC repositioning. As was stated previously, the MTOC repositioning mainly results from the interplay of MTs and dyneins. Therefore, I will focus on presenting the structure of the MT and the experiments measuring the key physical properties, see Section 2.3. Moreover, I will outline the main methods for the modeling of MTs and other biopolymers. The same attention will be given to the dynein motor protein, see Section 2.6.

CTLs go through complex development and their life consists of several phases. Their story begins long before the targeted killing and sometimes continues long after it. Moreover, they do not act alone but belong to a team of various agents of the immune system. It is my ambition to present the immune response of the CTL in a larger biological context. Therefore, I will briefly describe other types of T Cells, see Section 2.7. Then, I will also present several stages of the life of the CTL, see Section 2.8, and focus on the MTOC repositioning during the targeted killing, see Section 2.9.

The targeted killing is one of many biological functions that require large restructuring of the cytoskeleton and the repositioning of the MTOC. During these processes, the changes are often facilitated by the same agents: dyneins and MTs. I will present the MTOC repositioning during the cell migration and mitotic spindle oscillations and highlight the similarities with the MTOC dynamics in the CTL with one, or two IS, see Section 2.13.

In Chapter 3, I will introduce the computational model of the CT with one or two IS. The model consists of two main elements: the MT cytoskeleton composed from a variable number of MTs connected to a rigid MTOC, and the dynein motor proteins located in the IS pulling the MTs via two mechanisms.

In Chapter 4, I will review my manuscripts and summarize my work. In Chapter 5.1, I will briefly comment on our achievements and put them into a scientific context.

Chapter 2.

State of the art

Contents

2.1. Cell	13
2.2. Cytoskeleton	15
2.3. Microtubules	16
2.3.1. Experiments	17
2.3.2. Models	21
2.4. MTOC	24
2.5. Molecular Motors	25
2.5.1. Myosin and kinesin	26
2.6. Dynein	26
2.6.1. Experiments	28
2.6.2. Models	30
2.7. Types of T Cell	31
2.8. Life and immune response of the cytotoxic T Cell	32
2.8.1. Bone marrow progenitors naive cells, and their activation	32
2.8.2. Recognition of the antigen-presenting cell by the effector T Cell	33
2.8.3. IS formation and structure	34
2.9. MTOC repositioning during targeted killing	36
2.9.1. Experiments	36
2.9.2. Models	38
2.10. Secretion of lytic granules	40
2.11. Memory cells	41
2.12. Roles of T Cells in different stages of life	42
2.13. MTOC repositioning during various cellular processes	42

2.1. Cell

All living organisms, whether simple unicellular organisms or complex multicellular organisms, are composed of cells. The cells are incredibly diverse and their structure, complexity, and shape depend on the organism or cell's specific functions. Despite their fascinating variety, all cells share basic characteristics: they emerge by the fusion of two cells or the division of the mother cell into two daughter cells. They react to external stimuli, obtain and consume energy, and a vast majority contain DNA governing the cellular functions [172, 173].

Based on the presence of the nucleus, cells are divided into prokaryotes (Greek: “before nucleus”) and eukaryotes (“well nucleus”) [105]. The prokaryotic cells of the single cell organisms have a simpler structure than eucariotic cells composing not only unicellular but also complex multicellular organisms like animals or plants. The procaryotes are also much smaller, their diameter is typically around $1 - 2\mu\text{m}$, compared to the $5 - 100\mu\text{m}$ of eucariotic cells. The plasma membrane encloses the cells and separates the outside environment from the cell interior called cytoplasm. Both prokaryotes and eukaryotes contain the liquid component of the cytoplasm called cytosol containing salts, sugars, and soluble proteins. The main difference between the two types of the cells is compartmentalization, since the eucariotic cell contains membrane bound organelles designed for specific functions [174, 175]. The organelles important for this work are described below:

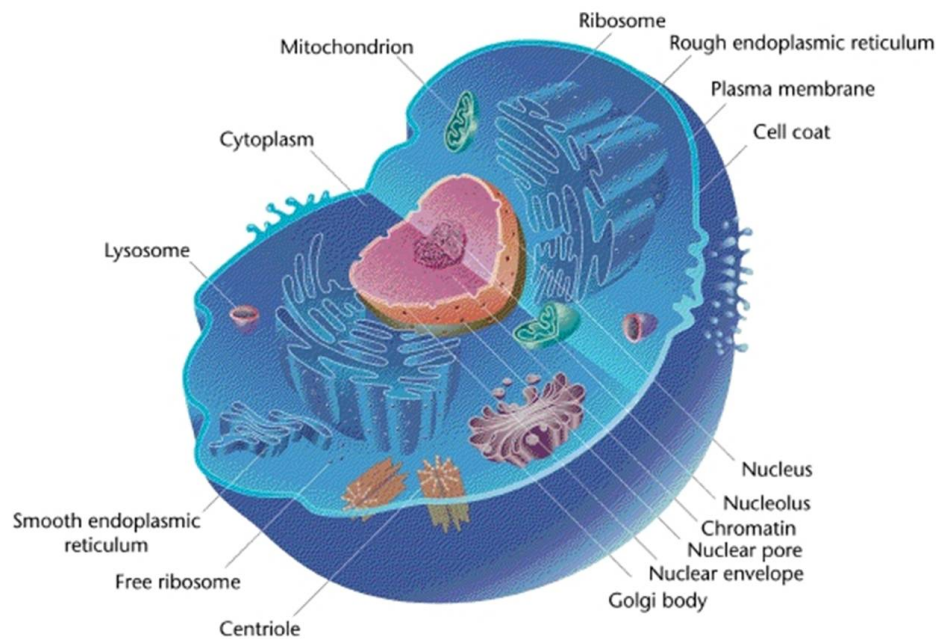


Figure 2.1.: Sketch of the Eukaryotic cell. Plasma membrane envelops the cell. The cell's nucleus has the central position. The organelles are confined between the plasma membrane and the nucleus. The two centrioles forming the MTOC are located underneath the plasma membrane. The Golgi apparatus is located close to the rough endoplasmic reticulum attached to the nucleus. The figure was reused with the permissions stated in the Appendix C.

The **nucleus** is usually the largest organelle in the cell enclosed by the nuclear envelope isolating it from the cytoplasm. It can have many shapes including spherical or ovoid. It is a specialized organelle serving as an administrative center of the cell containing the genetic material in the form of DNA [176].

Mitochondria are membrane bound organelles often having a prolonged shape. However, their shape, size, and number can change because they grow, shrink, and go through fission and fusion. They perform a wide array of functions, from which we can mention the production of the energy by the synthesis of ATP. They are often termed the "powerhouse of the cell". As the second example, one can mention the ability to absorb and redistribute calcium [156,177]. The number of mitochondria varies in different type of cells due to the different need of the energy. In the case of CTL the number was measured as 44 [Hornak2016].

The **endoplasmic reticulum** (ER) is a membrane system forming a three-dimensional network of flattened sacs and tubules enveloping the nucleus of the cell. The organelle involves with the production, processing, and transport of proteins and lipids. Based on the amount of associated ribosomes, the ER can be divided into rough (higher number of ribosomes) and smooth (smaller number of ribosomes) [178] ER.

The **smooth endoplasmic reticulum** (SER) is composed of three-dimensional polygonal networks called cisternae. The SER has a complex structure, since the cisternae have a high curvature, new tubules are budding of the sides of old ones and their branches can fuse. They are bound to the cytoskeleton, since the cisternae can slide alongside the cytoskeletal filaments or grow alongside it. The function of the SER differs in various cells. They include the synthesis of lipids and steroid hormones, storage of calcium in the cell or the detoxification of dangerous byproducts of the metabolism.

The **rough endoplasmic reticulum** (RER) is a series of flattened sacs extending across the cytoplasm. The RER is defined by the presence of ribosomes bound to the membrane. Due to the low curvature, the RER has a sheet-like appearance. It plays multiple roles including the protein synthesis and folding. RER is attached to the nucleus and located close to the Golgi apparatus [179, 180].

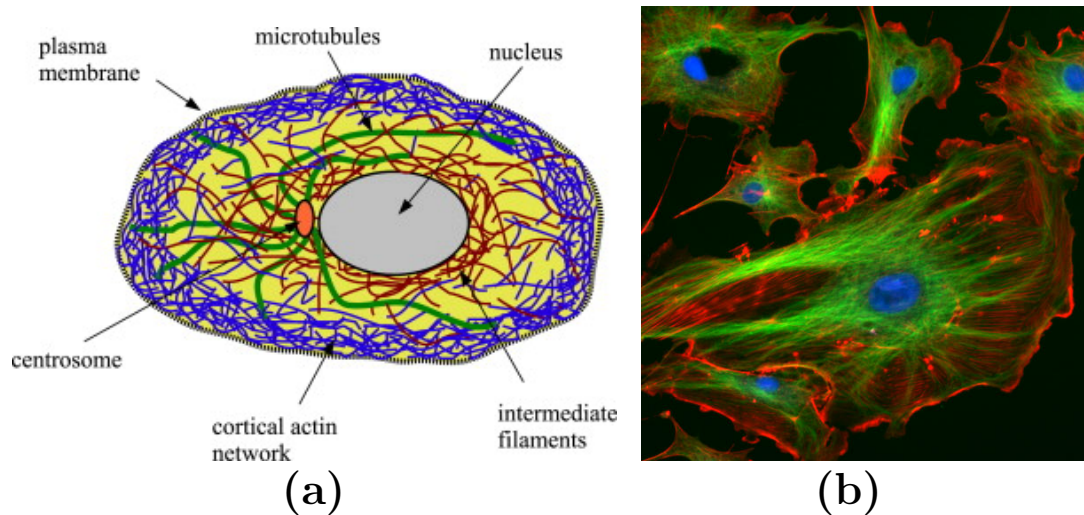


Figure 2.2.: Sketch and the fluorescence microscope image of the cytoskeleton. (a) The sketch of the typical organization of the cytoskeletal filaments in the cell is shown. The filaments are between the cell membrane and the nucleus. The actin filament network is located under the plasma membrane. MTs are connected to the centrosome (MTOC). The figure was taken from [181] with the permission stated in the Appendix C. (b) Endothelial cells under the fluorescence microscope. Nuclei, MTs, and actin filaments are marked blue, green, and red, respectively. The figure was reused with the permissions stated in the Appendix C.

Ribosomes are complex macromolecular machines composed of two subunits carrying out different functions. They can be spatially divided into two groups. Membrane-bound ribosomes are attached to the ER membrane and perform synthesis of proteins simultaneously translocated into the ER. Free ribosomes synthesize other proteins and are not attached to any membrane [173].

Golgi apparatus is a very complex, irregular structure composed of different classes of cisternae varying in shape and form stacked close to the nucleus [174]. Its function is to sort and transport vesicles to a proper location. As the products from the ER reach the Golgi apparatus, they are tagged by proteins and sugar molecules serving as identifiers. Subsequently, they are transported to the final location based on those identifiers.

Plasma membrane composed of both lipids and proteins encloses the cell [174]. The most important structure of the cell membrane is the semipermeable phospholipid bilayer forming the barrier between two aqueous domains. It provides basic protection and structural support of the cell and stabilizes the internal environment. It transports nutrient substances to the cell and toxic substances out of the cell. The proteins embedded in the bilayer perform a number of specific functions including recognition of other cells.

Since the cytoskeleton plays a key role during the repositioning, I will describe it in its own section and then focus on MTs.

2.2. Cytoskeleton

The cytoskeleton is a complex network consisting of growing and shrinking filaments crossing through the cytosol maintaining the cell's shape and providing mechanical resistance to deformation and giving structural support to organelles. The cytoskeleton also enables key functions like cell signaling, the transport of intercellular cargo, and provides mechanical support for cell division and motility. The eukaryotic cytoskeleton comprises three types of filaments: actin filaments, MTs, and intermediate filaments, see Fig. 2.2. The filaments undergo a constant reconstruction, they either shrink or prolong, which enables them to adapt to the cell shape in different conditions and various tasks.

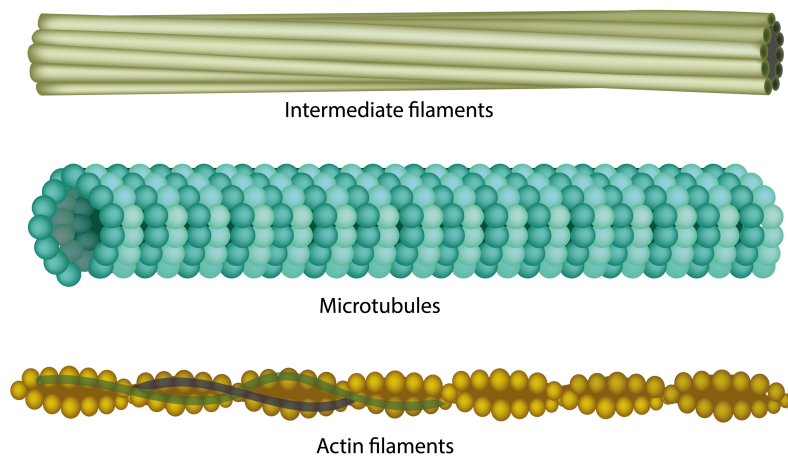


Figure 2.3.: Sketch of cytoskeletal filaments. The figure was used with the permissions stated in the Appendix C.

Actin and Intermediate filaments

Actin filaments play a crucial role in the MTOC repositioning. The network provides structural support to the cell and is one of the factors determining its shape. Consequently, the MT cytoskeleton rotates in the envelope given partially by the actin network. Moreover, the actin clearance in the IS is crucial for the recruitment of dynein and the MTOC repositioning [182].

In most eukaryotic cells, actin is the most abundant protein [183]. Actins connect in a head-to-tail fashion and create one polarized protofilament. Two protofilament intertwine in a helical fashion and form one actin filament, sketched in Fig. 2.3. They are the thinnest of all the filaments with the diameter of 4 to 7nm and the length up to several μm [184]. Compared to MTs, actin filaments are highly flexible, their persistence length is around $17.7\mu\text{m}$, three orders of magnitude smaller than the one of the MT. They are very dynamic, undergoing constant reconstruction mainly by the process of treadmilling, during which they grow at one end and depolymerize at the other. They form highly complex three-dimensional networks and bundles located mainly under the plasma membrane, see Fig. 2.2, regulated by a variety of actin-binding proteins. Actin filaments have multiple mechanical functions: They provide mechanical integrity, they are responsible for muscle contraction, and they play a key role in cell motility and intercellular transport. The recent experimental work suggests that the changes in the actin network form the IS and enable the dynein recruitment [182].

Intermediate filaments are diverse components of the cytoskeleton composed of a variety of proteins expressed in different cell types [185, 186]. They are assembled from a broad class of intermediate filament proteins [187], sketched in Fig. 2.3. They have an average diameter of 10nm, which is intermediate between the diameters of actin and MTs. They are the most flexible of all three main types of cytoskeleton filaments. The main task of intermediate filaments appears to be structural support by providing mechanical strength to cells and tissues [185, 187].

2.3. Microtubules

The tubulin subunit, a heterodimer of α - and β -tubulin, is the basic building block of MTs [188]. The length of the tubulin is approximately 8nm. Tubulin subunits are linked in a head-to-tail fashion, β -subunits of one tubulin dimer contacting the α -subunits of the next dimer. Such longitudinal contact between the subunits leads to the formation of protofilaments. Protofilaments associate side-by-side due to the lateral interactions of the tubulin subunits forming a hollow cylindrical MT, see Figs. 2.4 and 2.5. The outer and inner diameters are approximately 25nm and 13nm, respectively. The number of filaments forming MT can differ, see Fig. 2.5, but the usual number is thirteen. The asymmetry of the subunits causes the intrinsic polarity of the filament that is crucial for many biological functions.

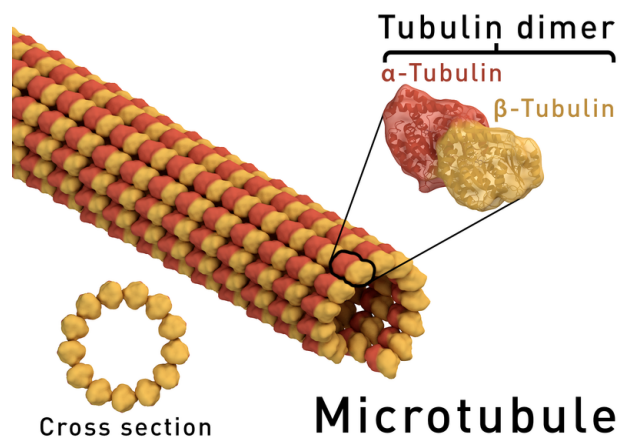


Figure 2.4.: Sketch of the MT structure. Tubulin dimers are composed of α - and β -tubulin. They form one protofilament by linking in a head-to-tail fashion, where the β -tubulin of one subunit links to the α -tubulin of the next. Thirteen protofilaments associate laterally and form a hollow MT. The figure was reused with the permissions stated in the Appendix C.

One end of the protofilament has the α -subunits exposed (minus end) while the other end terminates with the exposed β -subunits (plus end). MT is always composed of the protofilaments of the same polarity. Consequently, the plus end and minus end of the MT have only the β -subunits and α -subunits exposed, respectively. Currently, there are multiple models of the arrangements of the neighboring protofilaments. In the model sketched in Fig. 2.4 heterodimers in the adjacent protofilaments are slightly shifted forming spiraling rows of α - and β -tubulin monomers in the wall of the MT. In an alternative model, the subunits are shifted to give the MT wall a checkboard pattern [188]. Due to their tubelike construction, MTs are substantially stiffer than other components of the cytoskeleton, which is manifested by their persistence length of about 5mm [189] exceeding the diameter of the cell by two orders of magnitude. MTs are formed into various spatial arrangements to execute diverse cellular function. Filaments play a key role in maintaining cell morphology and providing mechanical stiffness to cells. They are involved in intercellular transport, cell division, moving of secretory vesicles, and the repositioning of the MTOC. MT never stays the same but constantly grows or shrinks.

In the next section, I will focus on the methods measuring the key mechanical properties. I will provide a brief historical perspective on the experimental work and then focus on recent experiments and models.

2.3.1. Experiments

MTs were observed in several experiments in early 1950s. Robertis et al. reported that the axons of amphibian sciatic nerves consists of “large bundle[s] of parallel, tightly packed fibrils” [190, 191]. The same filaments were similarly described by Palay in 1956 as “numerous, long, tubular elements of the endoplasmic reticulum, about 180Å wide and remarkably straight” [192]. Various groups reported similar filaments in early sixties in different types of cells [193–195]. Finally Slautterback, and Ledbetter and Porter described the MTs, recognized their presence in various types of cells and, perhaps the most importantly, named them. Ledbetter and Porter analyzed plant cells and reported the evidence of “slender tubules, 230 to 270Å in diameter and of indeterminate length, in plant cells of this type” [195] Slautterback observed similar tubules in protozoa. Moreover, based on the extensive research of other works in the field he compared various sightings of tubule-like structures and created a unified concept of “microtubules” [196]. Year later, Ledbetter and Porter observed the 13-fold radial symmetry of MTs and proposed that they arrange to form a hollow tubes [197]. Soon after, Mohri discovered the amino-acid composition of the protein forming MTs and coined the name tubulin [198]. Protein subunit of MTs were also isolated in by Shelanski et al. [199]. In 1970 Stephens et al. discovered the two types of MT proteins: α and β tubulins [190, 200]. Finally, basic understanding of the MT structure was established during 1970s.

Due to the key role of MTs in the intracellular processes many experiments have been carried out to

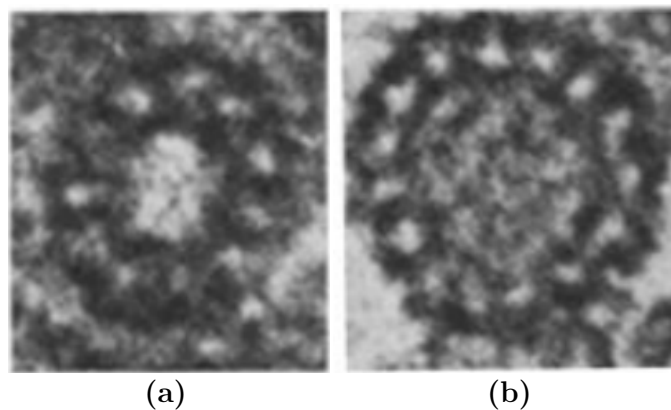


Figure 2.5.: Cross section of MTs with eleven (a), fifteen (b) protofilaments. Protofilaments form a hollow MT. The figure was taken from [201] and reused with the permissions stated in the Appendix C.

analyze their biomechanical properties in the years following their discovery [193,195,197]. More recently, a large array of techniques was used to measure their mechanical properties. Three MT parameters were crucial for my work: flexural rigidity, persistence length, and Young's modulus. The rigidity and persistence length determine the stiffness against bending and Young's modulus gives the extensibility of the MT. The review focusing on mechanical properties of MTs listing the experimental techniques and measured values can be found in [202].

The flexural rigidity

In 1993, Gittes et al. used thermal fluctuations and reported the rigidity of MTs stabilized by taxol as $2.2 \times 10^{-23} \text{Nm}^2$, which is in a range given by later measurements [91]. They also demonstrated that the MT is rigid over the typical dimensions of the cell [91]. In the same year, Dye et al. [203] reported that the taxol increases the flexibility of MTs. A year later, thermal fluctuations were used together with hydrodynamic flow to measure the rigidity by Vernier et al. [204]. Similar techniques were used to study the effects of MT-associated proteins and ligand binding on rigidity [205]. The combination of direct buckling and optical trapping techniques was used by Kurachi et al. [206]. Unexpectedly, they found that the rigidity depends on the length. Moreover, comparing the MTs with similar lengths they found that MTs assembled from brain-derived associated proteins were considerably more rigid than the MTs assembled from purified tubulin and then stabilized with taxol ($4 \times 10^{-23} \text{Nm}^2$ and $1 \times 10^{-23} \text{Nm}^2$). Felgner et al. used optical tweezers to investigate the rigidity ($3.7 \times 10^{-24} \text{Nm}^2$) and the influence of MT-associated proteins [207,208]. In 2002 by Takasone et al. used calibrated optical tweezers and confirmed that the rigidity is length dependent [209]. Janson et al. [210] demonstrated that the rigidity depends on the speed since fast growing MTs are more flexible. The elastic response was also investigated by indentation with atomic force microscopy [211,212]. The effect of various MT stabilizers, including taxol, were analyzed by Hawkins et al. in [213]. The stabilizers were also used in the experiments investigating the dependence of the rigidity on the temperature. It appears that the rigidity decreases with the rising temperature but only at the presence of certain stabilizers [214]. In vitro severing experiments were used in combination with molecular dynamics to analyze the seam interface in [215]. The results of recent work suggest that the MT adjust its conformation, stiffness, and dynamics based on multiple mechanochemical inputs [216]. One can find other experiments measuring mechanical properties of the MTs [210,217–219]. In 2021, Zhou et al. reported that in vivo the rigidity is dynamically regulated during various intracellular functions [217]. They provided plausible explanations for the discrepancies between the results of the previous studies. Their study revealed that the rigidity of the MT decreases through three phases with the increasing growth rate. This finding offers a way how to manipulate MT rigidity by altering the growth rate.

To summarize, one can see that the measured values of the flexural rigidity vary over several order of magnitudes and are usually between $1 \times 10^{-25} \text{Nm}^2$ and $4 \times 10^{-23} \text{Nm}^2$ [206,209]. The flexural rigidity depends on the presence of stabilizers, temperature, length of the MT, the speed of its growing, and the presence of MT-associated proteins. However, one fact is clear: MTs are very stiff and their persistence

length always exceeds the dimensions of the cell. Consequently, MTs can always provide the structural support to the cell regardless of the circumstances.

The persistence length

The persistence length can be in principle computed from the flexural rigidity and it was measured in some of the experiments stated above. The first experiments in 1983 used dark-field microscopic images and statistical analysis of the contour lengths and end-to-end distances [220]. The first precise measurements were performed almost a decade later. The flexural rigidity was reported as 2.0 – 6.3mm by Gittes et al., Venier et al., Kurachi et al., and Janson et al. [91, 204, 206, 210]. During the next twenty years, the persistence length was measured by various techniques and the usually accepted range of persistence length in current literature is 1 – 10mm [202]. Optical trapping was used in [206, 208, 221, 222]. The analysis of MT trajectories were used in [189, 223]. One of the most widely used techniques was thermal fluctuation [91, 204, 205, 224–229]. Thermal fluctuations were also used by Pampaloni et al., who reported that the dependence of the persistence length on the length of the filament was caused by the anisotropic association of heterodimeric α and β tubulins [230]. More recently, tangent correlations were used to determine the persistence length [231, 232]. The latest advances in the field can be illustrated by the work of Wisanpitayakorn et al. in 2022 [233]. Similarly, in 2022, Sweet et al. addressed the discrepancies between the path persistence length and filament persistence length [234]. Kabir et al. demonstrated that the rigidity of the microtubule can be manipulated by using the natural osmolyte trimethylamine N-oxide [235]. To summarize, the measuring of the persistence lengths and other properties of MTs is still vivid today after almost fifty years from the discovery of the MT.

Young's modulus

The modulus measures the tensile or compressive stiffness of a material when the force is applied longitudinally. The measured values of the Young's modulus vary over three orders of magnitude. The smallest values (1MPa) were measured in the experiments performed by Vinckier et al. [236]. Contrarily, Kurachi et al. measured values around 7GPa [206]. The measurement of the modulus was performed in many experiments [91, 206, 211, 212, 236–238] and it is usually found between 0.31–1.2GPa. The differences of the results may be caused by many factors including the length of MTs or presence of MT-associated proteins influencing their spatial organization and dynamics [239, 240].

Dynamic instability of microtubules

In the life of MT the periods of the growing exchange with the periods of rapid shrinking in a process called dynamic instability (DI). The MT can rapidly switch between the two states and both the shrinking and prolonging MTs coexist in the cytoskeleton. Some of the filaments shrink to nonexistence while others achieve great lengths. DI enables the formation of filaments of various lengths in a timescale of minutes. DI is the reason for the dynamic nature of the MT cytoskeleton allowing it to alter and adapts itself to the needs and the functions of the cell and undergo dynamic changes through the cell cycle.

DI of the MT can be empirically described by the following parameters: frequencies of catastrophe and rescue and the rates of growing and shrinking. MTs are polar filaments that grow and shrink at both ends. However, the minus ends are usually anchored in the MTOC and only the plus ends are left exposed. Since our work focuses only on MTs connected to the MTOC, we only consider the parameters concerning the plus end of the MT.

It was said previously that the MT is a polymer consisting of α - and β -tubulin dimers assembling in a head-to-tail manner. The growing and shrinking of MTs take place due to the addition and release of subunits from the ends, respectively. The addition takes place when the end of the MT collides with the free subunit. Since the frequency of the collisions increases with the amount of available tubulin around the plus end, the growth rate increases with the tubulin concentration [92, 96]. However, the DI of the MTs cannot be fully explained by the number of available subunits [95].

It appears that the guanosine triphosphate (GTP) plays a key role in switching between the two states. It bounds to the β -tubulin close to the head-to-tail interface between subunits. Its subsequent hydrolysis

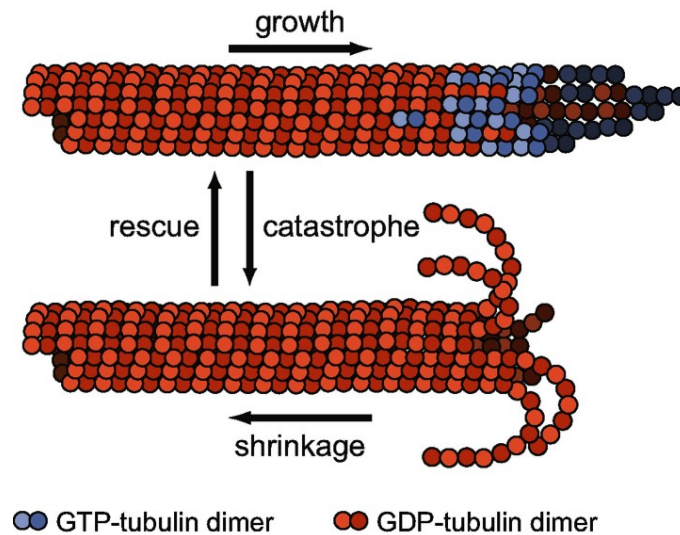


Figure 2.6.: Sketch of the DI. The MT grows by the addition of GTP-tubulin dimers at the plus end. They form a protective cap preventing the disassembly of the MT. When the protective cap is lost, the MT undergoes a catastrophe and shrinks. The MT can switch back from the period of shrinking to growing by the event called rescue. Reprinted from [241]. The figure was reused with the permissions stated in the Appendix C.

to guanosine diphosphate (GDP) deeply affects the arrangements of the polymer. The protofilament composed of GTP-tubulin is nearly straight. The GDP protofilaments curve outward from the wall of the MT probably due to the intrinsic curvature of GTP-tubulin [242–244]. MT polymer is held together by lateral forces between the subunits in protofilaments resisting the tendency of GDP filaments to bend from the MT wall. The slight change in MT structure can break bonds between the filaments. Since the tubulin subunits at the end of the protofilament are more likely to be bound to GTP, they form a protective structure against the MT disassembly known as GTP-cap. Once this structure is lost, for instance due to the depletion of available subunits around the end of the filament, the MT disassembles, see Fig. 2.7. It was suggested that the cap can be lost due to the stochastic nature of the tubulin addition. The GTP hydrolyzes in the added subunits, but the lag of hydrolysis results in GTP cap. The mean size of the cap is still disputed [98, 245] and the length fluctuates due to the addition of subunits. Eventually, the cap disappears, the GDP subunits at the end are exposed and the MT disassembles [246].

The transition from polarization to shrinking is known as a catastrophe. Contrarily to the grow rate, the speed of depolymerization is mostly insensitive to the tubulin concentration [92]. The opposite transition back to the polymerization is called rescue and its mechanisms are poorly understood. One possible explanation suggests that the GTP domains in the middle of MTs can contribute to the rescue event [247]. Another possibility is that the addition of the dimer to shrinking ends of several protofilaments can revert depolymerization [95].

Polymerization and depolymerization speeds, catastrophe and rescue rates are the four parameters defining the DI. The parameters depend on the cell phase [248, 249], distance from the cell membrane [250–253] and measured values differ substantially [93, 246, 254–262]. In general, the speed of the depolymerization is substantially faster than the growing speed and both are typically in order of tenths of micrometer per second [96, 101, 246, 246, 251, 254, 256, 256, 262–264, 264–266]. The catastrophe rate is length dependent and the number of catastrophes is higher at the periphery of the cell [103, 250, 254, 256, 264, 266, 267].

So far, I described the growing and shrinking only at the ends of filaments since the densely packed structure of the dimers distant from the ends was generally considered stable. However, Schaedel et al. reported that the MT structure can be remodeled. They suggested that dimers can spontaneously leave and be added into the lattice at the sites of structural defects [268]. This result would not have any influence on our coarse-grained modeling of the MT. However, the results show that the concept of MT dynamics

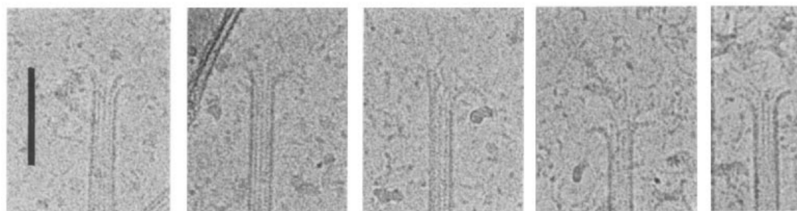


Figure 2.7.: MT depolymerization. Shrinking MTs visualized by a time-resolved cryo-electron microscopy, Bar 100nm. Reprinted from [97]. The figure was reused with the permissions stated in the Appendix C .

may need to be extended to the entire body of MT previously considered to be a stable material.

2.3.2. Models

MTs belong to one of the large array of biopolymers that living organisms synthesize. The other examples may be RNA and DNA cellulose, lipids, collagen or carbohydrates. Polymers are usually long molecules consisting of repeated subunits (monomers, dimers) that are relatively small and connected by covalent bonds.

From a point of view of computational scientist, polymers present many challenges, since they exhibit interesting behavior over a broad range of length scales from a single subunit (nm) to the length of the filaments several orders of magnitude longer. Moreover, polymers may be intertwined in a complex network displaying fascinating properties. Similarly, the time scale of the simulation can differ by several orders of magnitude ranging from femtoseconds to minutes or in some special cases to years (glasses). Models of polymers can be broadly divided into two classes: atomistic or coarse-grained [171].

Atomistic models

Atomistic models are used to analyze length scales significantly shorter than the typical length of polymer. They present a valuable tool in theoretical and computer simulations allowing an elaborate examination of the mechanics of materials. The models using the right approach allow to capture subtle structural properties and reactions of molecules. Atomistic models are the right choice to study the local, monomer-level rearrangements, interactions, fluctuations or monomer–monomer contacts at interfaces of domains [269–272]. Atomistic models can be also used to analyze how monomers and segments of polymers arrange near a nanoparticle surface [273–275], the solubility, absorption or diffusion of small gas molecules within pores of a polymer membrane affected by the specific chemistry and size of the small molecules [276], or the interactions of charged polymer [277, 278].

Atomistic models were used to simulate MTs and to validate experimental results. Two popular molecular dynamic simulation systems, Amber and Charmm, were used in molecular dynamics simulations of MTs [279–281]. Tuszynski et al. [282, 283] carried out molecular dynamic simulations of electrostatic and structural behaviors of tubulin dimers like the binding strength and lattice formations of the MT. Wells et al. created all-atom simulation of a relatively small segment of the MT to analyze its structural performance under various loads [284]. Moreover, several molecular dynamics simulations were used to analyze details of the interaction between α and β monomers [218]. Deriu et al. used the models to evaluate the elastic constants of the two monomers. Additionally, they used finite element method to examine properties of the $1\mu\text{m}$ long cylindrical MT [285]. Sept et al. combined all-atom molecular dynamics simulations with continuum mechanics to investigate mechanical properties of the MT. Structural analysis of microtubule vibration were performed by Havelka et al. [286]. The atomistic models provided a valuable insight into the mechanical properties and assembly of the MTs. However, the length scale of the MT is limited even in the recent simulations [287].

Alongside its advantages, atomistic models have several limitations. First of all, they do not necessarily provide the accurate results. The precision of the results depends heavily on the force fields, initial configuration, and even simulation protocol. Both the forces and initial configuration are often hard to

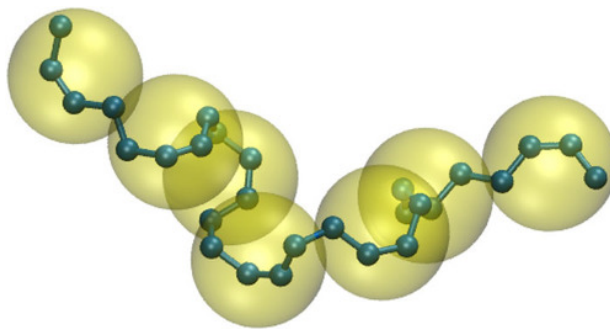


Figure 2.8.: Coarse-grained representation of a polymer chain. The small spheres depict atoms, and the big spheres represent coarse-grained beads and repeating monomeric units. Reprinted from [289]. The figure was reused with the permissions stated in the Appendix C.

optimize for some specific systems. Most importantly, they are computationally very expensive. Although the models are usually limited to the lengths scales of Å and the time scales of ns, the simulations take a large amount of time even with modern computers with hundreds of high-performance CPUs running in parallel. Due to the computational cost they cannot be used for the polymer chain-level rearrangements occurring over larger length and time scales or the slow dynamics of large molecules [288]. To simulate longer time scales and length scales, one needs to reduce computational cost while maintaining a high degree of realism.

Coarse-grained models

CG models extensively reduce the degrees of freedom by representing the segment of the filament by a single polymer "bead" [290, 291], sketched in Fig. 2.9. Such modeling approach is enabled by the fact that the dynamics and the shapes of polymer structures at the length scales approaching the chain size are not influenced by the movement of individual atoms or by changes in the local monomer structures. CG models also allow the larger time steps by removing the fast movement of individual molecules. The reduction of degrees of freedom improves the computational efficiency and prolongs time step enabling the simulation of complex polymer ensembles for substantially larger time-scales. Here, I briefly review several CG models used to model biopolymers.

Basic coarse-grained models

Freely-jointed chain (FJC) is the simplest model of the polymer [292]. The polymer has no elasticity and no resistance to bending. It is divided into the segments with constant lengths whose orientation is completely independent from the orientations of neighboring segments and positions of the beads, sketched in Fig. 2.9a. Despite its simplicity, the model is surprisingly useful and finds new applications [293].

Worm-like-chain (WLC) developed by Kratky and Porod in 1949 results from adding the resistance to bending to the FJC. WLC is used to describe the dynamics of the semi-flexible polymer that is fairly stiff, has a finite resistance to bending and the successive segments have approximately the same orientation [294]. The persistence length of such polymer exceeds its lengths by several orders of magnitude. The energy of the model is given by the angles between the neighboring segments, see Fig 2.9b. The Hamiltonian of the discretized case is expressed by the Eq. 3.6. WLC model is still relatively simple since it has only two parameters: the length and the bending rigidity that can be determined by fitting experimental data [293]. The model is suitable to describe stiffer polymers whose nearby segments are roughly aligned and therefore it is a good candidate for the model of MT and other biopolymers [295, 296].

Bead-spring model (BSM) is one of the most widely used models. As its name suggests, the beads in this model are connected by the harmonic springs, sketched in Fig. 2.9c. Usually, a simple harmonic potential is assumed and the springs follow Hooke's law of elasticity: they are infinitely extendable and their force

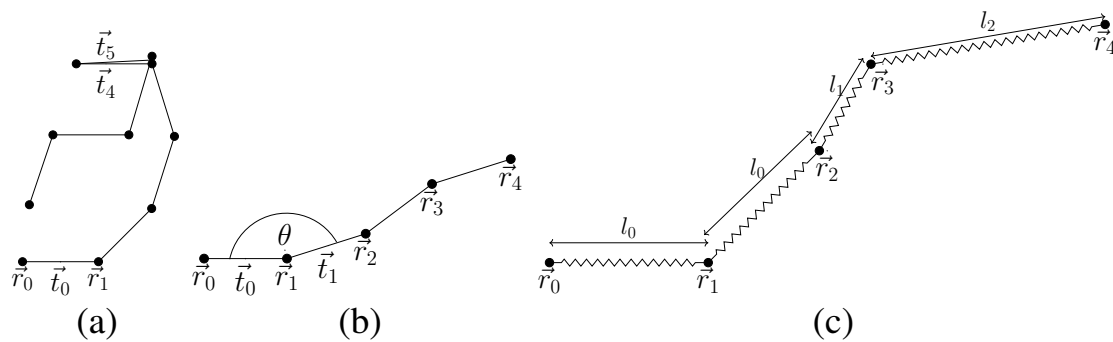


Figure 2.9.: Sketches of basic coarse-grained models. The position of the beads and the segments between them are given by the vectors \vec{r}_i and \vec{t}_i , respectively. (a) Freely jointed chain. The polymer can assume any configuration due to no interaction between the neighboring segments. Two neighboring segments \vec{t}_4 and \vec{t}_5 have almost antiparallel orientation and overlay. (b) Worm-like chain model. The bending force acting on the beads is given by the angle θ between two neighboring segments (here \vec{t}_0 and \vec{t}_1). (c) Bead-spring model. The lengths of the segments can change. The distances $\vec{r}_0-\vec{r}_1$ and $\vec{r}_1-\vec{r}_2$ correspond to the length of the relaxed stalk l_0 . Distances l_1 and l_2 are the lengths of the shorter and prolonged spring, respectively.

increases linearly with their length [297]. The Hamiltonian of such a chain is:

$$H_{\text{BSM}} = \frac{c_h}{2} \sum_0^{N-1} (|\vec{r}_{i+1} - \vec{r}_i| - l_0), \quad (2.1)$$

where \vec{r}_i are the coordinates of the beads, l_0 is the length of the relaxed stalk, N is the number of the beads, and c_h is a positive real number giving the elastic modulus. BSM with Hookean spring was widely used. However, it was well known that finite-extensibility has a key role in determining polymer's rheological properties [298, 299]. A large array of models with finite fully extended length differing by the interactions between the beads were developed to overcome the shortcomings of the model. For example in the multi-bead finitely extensible nonlinear elastic (FENE) model, the spring force acting on a bead rises non-linearly with the distance between the beads. As another example, we can name FENE-Fraenkel (FF) model that bears similarities to the FENE model, but the spring has a non-zero length [300].

Semiflexible harmonic chain (SHC) model combines bending force of the WLC and extensibility of the BSM. The Hamiltonian of the SHC with N beads divided by the segments of the same equilibrium length can be expressed as:

$$H_{\text{SHC}} = \frac{c_h}{2} \sum_0^{N-1} (|\vec{r}_{i+1} - \vec{r}_i| - l_0) + \kappa \sum_0^{N-2} (1 - \vec{q}_{i+1} \cdot \vec{q}_i), \quad (2.2)$$

where κ is the bending rigidity for the discretized case and $\vec{q}_i = \frac{\vec{r}_{i+1} - \vec{r}_i}{|\vec{r}_{i+1} - \vec{r}_i|}$ is the unit tangent vector between the two beads. The SHC model enables the study of the effects of bending rigidity, bond extension, the structure of the discrete chain, and the force-extension behaviour [301].

The models in this section are not the most recent. However, they are not outdated since they still find new applications. For example despite its simplicity, the WLC model can simulate the MT bending and due to its simplicity, it may be the right choice when simulating complex MT networks.

Recent coarse-grained models

Dima et al. analyzed microscopic origins of the mechanical response of MTs [302] with a self-organized polymer model, which is a topology-based model for tubulin. The model enabled force-induced simulations at rates and time scales similar to those used in single-molecule experiments. A complex coarse-grained model was developed by Deriu et al. to investigate the elastic networks [303]. The model was able

to simulate a system consisting of hundreds of interacting tubulin monomers enabling to simulate the entire MTs with the length up to 350nm. Theisen et al. analyzed the mechanical behavior of MTs under the influence of bending forces in order to investigate the mechanisms of MT severing [304]. A combination of severing experiments and CG models was used by Szatkowski et al. to investigate the mechanics of the MT seam interface [215]. Models were also used to study the behavior of multiple MTs. This can be exemplified by the analysis of the torsional behavior of MT bundles [305, 306]. Stevens used modeling to calculate the persistence length and Young's elastic modulus [307]. Coarse-grained models are not used only to investigate purely mechanical or dynamical properties. This can be demonstrated by the mechanochemical model created by Ji et al. used to investigate mechanical–chemical coupling of MTs [308]. The authors also used mechanochemical modeling to study the growing of MTs and the GTP cap [309]. Modeling of a contiguous microtubule fragment enabled to study the correlations of biomechanical properties with dynamic structural transitions at the nanoscale [310].

In recent years we saw the development of a new kind of model called ultra-coarse-grained (UCG) models that should address some of the weaker points of CG models. CG models assume that the details below the resolution of CG beads are averaged out. This approach however sets a limit on the resolution of practical coarse-grainings. UCG allows the construction of models with any resolution comprising discrete conformational or chemical changes within the CG beads [311, 312]. UCG models were recently used to model various functions of biomolecular complexes like mechanical properties of F-actin or conformational changes of proteins [313, 314]. UCG approach was recently used to simulate the mechanical properties of MTs including the length-dependent persistence length [218].

Closing remarks on modeling

The thesis does not intend to substitute many outstanding textbooks about modeling techniques [315–318]. Similarly, it is not and cannot be the comprehensive review of the modeling approaches that can be found in other sources [171]. I will briefly provide sources for the different modeling approaches. Lattice models can be found in [319]. Glotzer et al. provide a review of the molecular and mesoscale simulation [320]. Models for the polymeric fluids and nonequilibrium simulation methods used to study effects of mechanical shear or external field effects can be found in [321–324]. Continuum models for polymer fluid dynamics are review in [325]. The topic of polymer modeling is very vivid and new methods are developed every year. They differ in the approach, resolution, or requirements for the computational resources. At the end of this section, I will repeat what was stated at the beginning: the method must always be chosen concerning the problem and aims.

2.4. MTOC

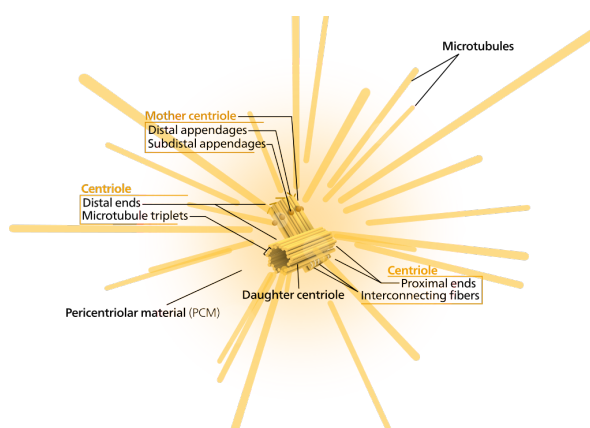


Figure 2.10.: The sketch of the MTOC. Mother and daughter centrioles are composed of nine triplets consisting of three MTs. Centrioles are arranged perpendicularly and embedded in pericentriolar material. Mother centriole carries the appendages serving as the anchoring centers MTs sprouting from the pericentriolar material. The figure was reused with the permissions stated in the Appendix C.

The MTOC nucleates and organizes the spatial arrangements of MTs. It can be found in all eukaryotic cells [326], but its morphological characteristics can differ [327]. The centrosome, a non-membrane-bound organelle of approximately $1\mu\text{m}$ in size, plays the function of the MTOC in animal somatic cells [328]. The centrosome consists of a pair of centrioles encapsulated in a matrix of proteins called pericentriolar material (PCM) [329], sketch in Fig. 2.10.

Centrioles are cylindrical structures from nine MT triplets, see Fig. 2.11a, comprising a complete A-MT oriented to the center of the centriole, and two incomplete B- and C-MTs [330]. The B-MT is attached to the wall of the A-MT and the C-MT is attached to B-MT. A-MT is connected to the C-MT of the neighboring triplet by the A-C linker, see Fig. 2.11b. The A-MTs are connected to the central hub of the centriole by radial spokes, see Fig. 2.11b. At the proximal and distal ends of the centrioles are minus and plus ends of the MTs, respectively. The centrioles are bound by interconnecting fibres [331]. The structure displays ninefold symmetry, its diameter is about 250nm and the length ranges from 150nm to 500nm. The two centrioles are not identical, since they differ by age, functions, and additional structures presented on their surface. Post-mitotic centrosome contains a fully mature mother centriole and an immature shorter daughter centriole created in the previous cell cycle [332]. The mother centriole carries characteristic distant and subdistal appendages differing quantitatively, morphologically, and functionally. The subdistal appendages are the centers of MT nucleation, since the γ -tubulin, a protein directly participating in the nucleation of MT, is localized at the head of appendages [326, 333].

PCM embedding the centrioles is a collection of hundreds proteins and acids [334]. Although the order of the PCM is still discussed, it appears that it is highly organized [335, 336]. One of its primary functions is the regulation of MTs [337]. It contains γ -tubulin and organizes MT arrays by the control of nucleation and release of MTs [338, 339].

The MTOC appears to be the major organizing center of the cell, since it determines not just the configuration of the cytoskeleton, but also the organization of the structures and organelles connected to MTs, like mitochondria, or ER. The MTOC represents a coordination center in eukaryotic cells at which hundreds of cytoplasmic proteins concentrate and react during various regulatory functions including cell cycle transitions [333, 340]. The MTOC is responsible for many key biological functions like the organization of the mitotic and meiotic spindle apparatus separating the chromosomes during the cell division and monitoring DNA damage [326, 328]. Moreover, the MTOC has many functions connected to targeted cytotoxicity like directional transport of granules, and polarization of subcellular structures [326].

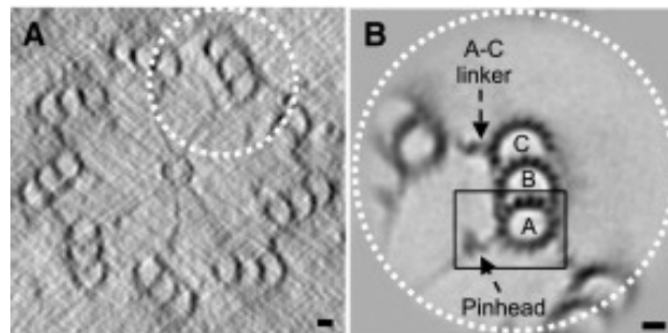


Figure 2.11.: Cross section of the centriole. (a) Transverse section of centriole tomogram. Nine MT triplets are connected to the radial linker. The dashed circle indicates the region displayed in figure b. The scale bar, 10 nm. (b) Reconstructed centriole triplet. The radial spoke is connected to the A-MT and A-MT and the C-MT of neighboring triplets are connected by the linker. Scale bar 10nm. The figure was taken from [330] and reused with the permissions stated in the Appendix C.

2.5. Molecular Motors

The cell is highly organized into many compartments having various biological functions. They can also act as factories producing various sets of products that are later needed in other compartments or consumed in

the cell [341]. The transport and distribution in such a complex environment is of utmost importance and it is a task of cytoskeleton filaments molecular motors [111,173,174,342]. Molecular motors are specialized proteins associated with cytoskeleton that can transform chemical energy into mechanical work. They have nanoscale dimensions and work in the viscous environment of the cytoplasm [173,174]. Under the overdamped conditions they cannot rely on inertia to continue the movement and they are continuously influenced by the Brownian motion. In every eukaryotic cell one can find tens of various motor proteins differing in the type of filament on which they walk, in the direction in which they walk, and in the cargo they transport [174]. Some operate as single molecules while others work in large collections as in our skeletal muscle. Some of them walk on actin filaments, while others step on MTs [111,341,343].

Three classes of motor proteins walking on the cytoskeletal filaments are known: myosin, which interacts just with actin filaments, and two proteins interacting with MTs: dynein and kinesin. Motor proteins consists of a motor domain, head region, and tail region connected by a stalk. They associate with the filament by their head region whose structure is similar among three types. Each head of the motor has a binding site for the filament and for the ATP [111,341,344]. Despite their diversity, molecular motors have one thing in common: they go through energy-dependent conformational changes resulting in unidirectional movement. They use the energy gained from repeated cycles of APT hydrolysis to walk and also carry cargo along the cytoskeletal filament [173,174,341,343]. The hydrolysis of ATP powers a mechanochemical cycle of the stepping consisting of the binding of the motor head to the filament, conformational change depending on the motor type, the release of the filament with subsequent relaxation, and the reattachment on the filament [174,341,343].

The motor proteins are involved in key biological functions. Besides their role in active intracellular transport, they carry membrane-enclosed organelles such as secretory vesicles, mitochondria, or Golgi apparatus to their destinations in the cell. Motor proteins also provide the force causing the filaments to slide against each other driving such phenomena as cell locomotion and division, muscle contraction, or ciliary beating, see Sections 2.5.1 and 2.6.

I will briefly outline the classes and functions of kinesin and myosin. Due to its importance in the MTOC repositioning, dynein will be presented in its own section.

2.5.1. Myosin and kinesin

Today, at least two dozen classes of myosin can be differentiated [345]. They differ in various characteristics like processivity and speed of the movement. Furthermore, they are involved in different functions [341,343]. Almost all of them walk on actin filament towards its plus end [346]. The speed of the movement vary for the different classes and it ranges from about 0.2 to 60 μms^{-1} [343]. Myosin is responsible for the active intercellular transport alongside the actin filaments. The interplay between the actin and myosin plays a key role in a variety of cell movements and functions with central roles in biology, like cell division, metabolism, reproduction, communication, and muscle contraction [174,347,348].

The superfamily of kinesin can be differentiated into 14 classes [349–351]. All groups except one walk on the MT towards the plus end with steps of the length of 8nm [349,352,353]. Many types of kinesin are processive motors that can walk hundreds of steps before their detachment from the filament and their run lengths can be over 2 μm . The speed of the motors depends on the type and they range from 0.02 to around 3 μms^{-1} [350]. Kinesins play an important role during the cell division since several of the kinesin superfamily members contribute to the formation of mitotic and meiotic spindle and chromosome separation [349,354].

2.6. Dynein

Dynein can be found in a variety of cells and can be divided into two main categories: axonemal and cytoplasmic dyneins [355–357]. Axonemal dyneins are mainly known to be responsible for propagating bending motions of cilia and flagella [113,358–360]. They also play a key role in neuron function and hearing [361]. A morphologically similar cytoplasmic dynein drives a large variety of fundamental cellular processes. It includes the transport of organelles towards the minus ends of MTs, neural

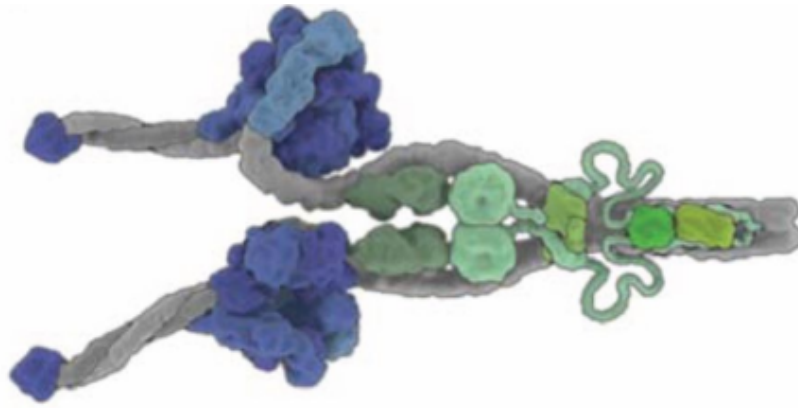


Figure 2.12.: A representative structure of the cytoplasmic dynein. "The dynein motor binds microtubules through a microtubule-binding domain (MTBD) at the end of a coiled-coil stalk (grey). The motor domain consists of a ring of AAA+ domains (dark blue) with between one and three active sites of ATP hydrolysis. The motile element is the linker (light blue), which reaches across the face of the AAA+ ring. The N-terminal tail of dynein (grey) is involved in dimerisation and binding to dimers of intermediate chains, light intermediate chains and three light chains (different shades of green). Cargo binding is mediated by these accessory chains ... The rest of the model, including the heavy chain tail (grey), intermediate chain and light intermediate chain (green), is an artist's impression." The figure was created by Janet Iwasa (Department of Biochemistry, University of Utah, UT). The figure and the caption were taken from [344]. The text of the caption is delimited by quotation marks. The permissions are stated in the Appendix C.

transport, nuclear migration, organization of the mitotic spindle, transport of a wide variety of intracellular cargoes, chromosome movement during mitosis, or maintenance of the Golgi apparatus [341,362–371].

The structure of dynein is fundamentally distinct from that of myosin or kinesin [341,372,373] since it differs in complexity and the number of ATP binding sites. Moreover, its mass is almost ten times bigger than the mass weight of kinesin. Dynein is a homodimer composed of two identical massive heavy chains comprising three functionally distinct domains: a cargo-binding tail, a large motor domain, and an MT-binding stalk, sketched in Fig. 2.12. The tail binds to dimers of intermediate chains, light intermediate chains, and three light chains that mediate binding to the cargo [344,374]. The large motor domain comprises six or seven AAA+ domains arranged in a ring around the central cavity. The domains have distinct properties; several can bind ATP with varying binding affinities. The tail is connected to the motor domains by a motile linker that can shift the position relative to the ring and play a role in the dynein motility [344,355,375,376]. The coiled-coil connects the motor domain and the small globular domain mediating the attachment to MTs. The cargo binding tail and the MT binding coil appear to extend from opposite sides of the motor domain [372,374,377–380].

Dynein steps to the minus-end of the MT powered by ATP hydrolysis and is responsible for the majority of the minus-end-directed transports in eukaryotes [341,344,355]. The complex repetitive machinery of ATP binding, hydrolysis into ADP, and subsequent release of ADP and phosphate produces the powerstroke and structural changes of dynein stepping [344,375,381]. Dynein closely interacts with the protein dynactin, which plays a general regulatory role. The disruption of dynactin interferes with the minus-end transport mediated by cytoplasmic dynein. Moreover, the presence of dynactin almost doubles the processivity of a single dynein [111,341,382]. The dynein functions as a gear and can alternate between steps of different sizes (8, 16, 24, 32nm). At high loads, the length of the step is predominantly 8nm, corresponding to the length of the tubulin heterodimer subunits of one MT protofilament. The step size at zero loads is usually 24nm or less probably 32nm [383–388]. The measured values of the speed differ. Some of them are relatively large, over $10\mu\text{ms}^{-1}$ while some are substantially under $1\mu\text{ms}^{-1}$ [174,382,383,385,386,389–391]. The dynein can move backwards with a much slower force-dependent speed [384,386,392,393].

2.6.1. Experiments

This section reviews only the most commonly used experimental methods. The review of experimental techniques can be found in [394, 395].

Biochemical experiments focus on measuring the rates of the chemical reactions associated with the activity of motor proteins. They include isotope exchange, stopped flow, fluorescent labeling, and temperature quenching. They revealed that the protein activities involve a complex network of biochemical states and structural conformations [396–400]. However, their fundamental problem is that they measure and average the properties of many active and inactive molecular motors, which makes the determination of the mechanisms of motility of a single molecule very difficult.

X-ray crystallography and cryomicroscopy methods can be used to determine structural information by providing images of biochemical states of single motors with atomic-scale resolutions [401, 402]. However, the experimental conditions may substantially differ from the conditions in the cell. The second drawback is that the methods provide just static properties and therefore cannot answer the questions related to the dynamics of motor proteins.

Single-Molecule Experimental Methods

Single-molecule experimental techniques provide most of the information about the mechanisms of motor proteins. They can observe and modify the activity of motor protein molecules with a high and unprecedented spatial and temporal resolution providing substantial insight into the dynamics of molecular motors. The single-molecule methods are described in several reviews [403–407]. Here, I want to briefly outline the most important methods.

Light microscopy usually uses fluorescent dyes to directly attach to enzyme molecules, allowing high precision localization and tracking of single molecular motors. The method is used for the clarification of the structural and dynamic properties of motor proteins [400, 408]. Video-enhanced differential interference contrast light microscopy was instrumental in the discovery of kinesin-based motility in living cells [409]. The same method was used for the investigation of the dynein's processivity in 2000 [382] and to analyze the collective behavior of multiple dyneins in 2005 [386]. Another version of light microscopy, the immunofluorescence microscopy was used already at the beginning of the 1990s to localize dynein [410]. More than a decade later, Reck-Peterson et al. used fluorescence microscopy to measure the stepping behavior and processivity of dynein [388]. In 2006, Jennifer Ross et al. measured the processive bidirectional motion of dynein–dynactin complexes by total internal reflection fluorescence microscopy [411]. Dark-field microscopy was used to study the axonemal dynein-driven motility or to investigate the functions of the dynein arm [412, 413]. Dynein's motility in the cell was also studied with fluorescence microscopy by Mitchell Ross et al. [414]. Despite its advantages, the method also has several drawbacks. The fundamental limitation is the spatial resolution due to diffraction. Usually, light microscopy cannot accurately observe structures smaller than $\sim 100\text{nm}$, which is substantially larger than the size of some motor proteins [415, 416]. This problem motivated the development of new successful experimental methods called super-resolution spectroscopy [415–417].

There are several **super-resolution** techniques currently used to analyze biological systems [400, 416, 418, 419]. Structured illumination microscopy uses varying patterns of stripes to obtain a high-resolution view of the object. Stimulated emission depletion uses a doughnut-shaped laser beam to stimulate the deactivation of the excited fluorophores to the ground state without affecting objects in the central hole area. It was developed by Stefan W. Hell in the 1990s and awarded the Nobel prize for chemistry in 2014 [420]. The method substantially improved the spatial resolution (up to 10–20nm). Recently, the method was used to investigate the interplay between MTs and dynein [421]. Photoactivated localization microscopy and stochastic optical reconstruction microscopy localize the center of mass of the image by the increasing amount of photons that are emitted from the source. The last two methods were applied to tract different motor proteins both in vivo and in vitro [400, 407, 422, 423]. The latter method was also recently used for the investigation of motor assemblies and protein stoichiometry [424].

Optical-trap spectroscopy was used for the analysis of the dynamic properties of different molecular

motors [425, 426]. It uses a laser beam to observe the movements of a bead chemically attached to a single motor protein molecule [408, 427]. The molecular motor drags the bead as it walks along the cellular track while a trapping force pushes it to the focus region of the non-uniform laser field. The optical tweezers setup can be calibrated with a very high precision and it can approach a harmonic potential. The accurate monitoring of the attached bead enables quantifying the dynamic properties of motor proteins. The method can measure nanometer displacements and forces in the range of pN, which is suitable for the analysis of couplings in motor protein systems [407]. The advantage of this method is that it can be coupled with other experimental approaches like fluorescent labeling. Unfortunately, the method can hardly be applied to analyze processes in a heterogeneous environment of living cells in a complex experimental setup. The method was used by Mallik et al. to investigate dynein stepping [387] and by Liedel et al. to measure the detachment rate and forces [428]. A year later, it was used to estimate the stall force of kinesin during intracellular transport [429]. The technique has recently been used to measure the displacement of dynein or the machinery of the dynein–dynactin [430, 431].

Magnetic tweezers utilize a magnetic field to manipulate of single molecules [408, 432]. Motor protein is chemically bound to the surface and the magnetic bead at the same time. One then tracks the position of the bead and its fluctuations parallel to the surface and the distance from it. Using the equipartition theorem, fluctuations enable to calibrate the force acting on the bead. The great advantage of the method is the capability to apply relatively large torques [408, 433], which makes it suitable for the investigation of molecules with critically important rotational degrees of freedom like nucleic acid motor proteins [434, 435]. Such molecules must perform many functions like unzipping or untangling, which is hardly possible without rotation. The drawback of the method is the low temporal resolution limiting its applications to slow dynamic processes [408]. Magnetic tweezers were used to measure kinesin stall force [436–438]. Tweezers have recently been used to investigate machinery that maintains the spindle at the center of the cell during metaphase and anaphase [439]. In 2022, Xie et al. used magnetic tweezers to investigate how the viscoelastic properties of the cytoplasm medium can hold and move spindles [440].

Atomic force microscopy is a high-resolution non-optical imaging technique developed in the middle of the 1980s by Binnig et al. [441]. The sample interacts with a microcantilever, whose deflection is measured via a reflected laser, allowing the calculation of the force on the cantilever. Moreover, time-lapse measurements can provide information on the sample’s motion. The authors reported that the method can measure forces as small as 10^{-18} N and that it has a spatial resolution of tens of Å. During the last four decades, the method has emerged as one of the most powerful and versatile single-molecule techniques due to its ability to analyze the three-dimensional morphology of biological specimens with subnanometer resolution in both air and liquid environments [442]. Conventional atomic force microscopy provides an insight into the structure and morphological changes of heterogeneous biological samples. Single-molecule force spectroscopy can investigate the nanomechanical biological properties of proteins. Moreover, it can provide the physical properties like Young’s modulus, mass-per-length values, and flexibility of specific species [442, 443]. The method is widely used to investigate biological structures. For example, it was used to investigate the substructure of the MT protofilament [212, 444, 445]. The method was used to study the cytoskeletal filaments and their associated proteins [446] and to make videos of myosin walking along an actin filament [447, 448]. Several groups used the method to investigate dynein directly. Wagner et al. investigate the interaction between the dynein motors and neurofilaments [449]. The applications of the method for the analysis of dynein and its interaction with filaments can be exemplified by two recent works from 2022 [450, 451].

As the last method, I would like to mention cryogenic electron microscopy (cryo-EM) due to the recent exciting development. Cryo-EM enables the determination of the 3D shape or structure at cryogenic temperatures. The sample is frozen and then examined by electrons. Although the method has been known for several decades, it has been substantially improved during the last few years [453, 454]. In the year 2017, Jacques Dubochet, Richard Henderson, and Joachim Frank were awarded the Nobel Prize in Chemistry for “developing cryo-EM for the high-resolution structure determination of biomolecules in solution” [455–457]. The method is increasingly used to analyze biological samples. During the last few years, several groups have investigated the dynein motor proteins, see Fig. 2.13 [452, 458, 459].

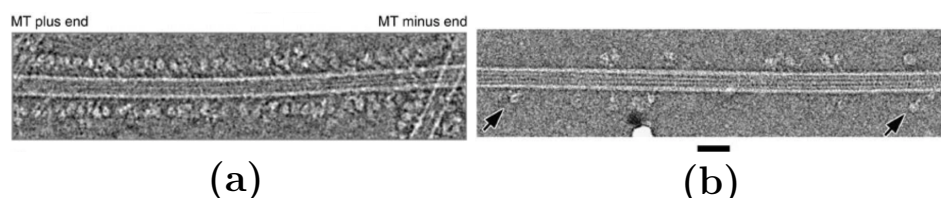


Figure 2.13.: Cryo-electron microscopy of dyneins walking on the microtubule. Scale bars, 40nm; (a) Dyneins are densely packed along the sides of the MT. (b) Dyneins are sparse on the MT. The figure was taken from [452] and reused with the permissions stated in the Appendix C.

2.6.2. Models

The modeling of the individual molecular motors can have many goals. For example, the models are used to explain the coupling between biochemical reactions and motions on the track to understand the energy conversion. However, this clearly stated task may become very challenging. In general, it is known that chemical processes may be reversible, although the exact experimental evidence can be missing [400]. Nevertheless, the reversibility of the processes cannot be neglected since it may lead to the wrong physical results. The reversibility of the motors can be exemplified by the case of ATP hydrolysis since the motors can, under certain conditions, synthesize the ATP [460]. Another challenge lies in the reversibility of the motor motion, exemplified by the case of dynein that may revert the motion and walk to the plus end of the MT under higher loads [384]. Moreover, the step length of the motor can change in different conditions. Here, I will describe three modeling approaches used to model molecular motors.

Continuum ratchet potential methods model the molecular motor as a particle moving along multiple parallel, periodic, and, in general, asymmetric free-energy potentials. Various potentials result from the interactions between motor proteins and the cellular tracks. Moreover, they interact with molecules fueling the motion, like the ATP and the products of the chemical reactions. Released chemical energy allows the motor to switch stochastically between various states. The molecular motors work in non-equilibrium and the energy from the chemical reactions is necessary for the motion. At the equilibrium conditions, no movement can be observed without its constant supply. The temporal evolution of the system can be described by the set of Fokker-Planck equations incorporating potential functions and the probability densities of the motor to be found at specific locations [400, 461, 462]. The advantage of the models is that they are solvable by using well-known analytical and numerical tools. Moreover, similar chemically-driven ratchet models can be also used to analyze non-equilibrium phenomena [463, 464]. Their disadvantage lies in the fact that to solve the equations, the potential may need to be simplified. Additionally, the realistic potentials are very hard to obtain from the experimental data, which limits the ability of models to estimate the real properties of motors. However, both the knowledge of experimental details and computational resources are increasing, which may provide new and exciting applications of the models [400].

Discrete-state stochastic models use traditional chemical kinetics to describe the movement of molecular motors as a network of chemical transitions between several biochemical states with variable positions. They approach the modeling of the movement by analyzing the probability density function relating the kinetics of motor proteins to biochemical transitions. The advantage of the model is that the transition rates can be directly measured in bulk chemical kinetic experiments and the dynamic properties can be obtained in single-molecule experiments. Consequently, when using discrete stochastic methods, one can get analytical expressions for dynamic properties of motor proteins [400, 462, 465]. The models have many merits. They were used, for example, to investigate interactions between various domains of motor proteins and how they influence the motility, and to analyze the energy landscape [465–467]. The disadvantage of discrete-state stochastic models is their weak description of connections to molecular structures. Moreover, they insufficiently describe the potential resulting from the intermolecular interactions with other molecules.

Mechanochemical and structural models can incorporate the structural properties of motor proteins [400, 468]. The models describe the mechanical changes of the motor protein using known

information about the structure. The models have been successfully used to analyze the dynamic behavior of myosins and to show how their different parts transmit forces and synchronize the movement [469,470]. They were also used to analyze the mechanochemical aspects of processive dynein motion [468]. The disadvantage of the methods is that they use simplified models of structures and coarse-grained potentials. Moreover, the structural information about the motors and cellular tracks is still incomplete. However, the progress in experimental work will provide a better understanding and the improvement of the models.

The modeling of molecular motors is a lively field and it would be impossible to review all the models here. Recent models of the dynein and reviews of modeling methods can be found in [400,465,468,471–476].

2.7. Types of T Cell

I want to remind that during cell-mediated immune responses, activated T Cells act directly against APCs by killing them or by the production of the signal molecules activating macrophages for the destruction of the virus [31,56,57,67–69]. I will briefly review other types of T Cells to put the CTL into a biological context.

Helper T Cells

Helper T Cells play a key role in adaptive immunity as they are necessary for almost all adaptive immune responses [57,477,478]. The importance of helper cells is demonstrated by AIDS resulting in the decrease in their numbers [479]. They function for the most part in peripheral tissues and various lymphoid organs [50]. As the name suggests, their role mainly consists in helping other agents of the immune system. During the activation by the APC, the naïve T Cell can evolve into one of the many subsets [480] performing different functions. For example T_H1 cells produce cytokines stimulating other immune cells. They activate CTL to kill infected cells and B Cells to secrete antibodies. They mainly defend the organism against intracellular pathogens. T_H2 cells stimulate B Cells to secrete various classes of antibodies and defend the organism against large extracellular pathogens. Regulatory T Cells (T_{Reg}) play a key role in maintaining peripheral tolerance, preventing autoimmunity and limiting chronic inflammatory diseases [481,482]. Helper T Cells can generate memory cells that can quickly react to a threat in a case of reinfection.

Natural killer T Cells

Natural killer T Cells (NKT) have the characteristics of both branches of the immune system [483]. NKT Cells exhibit a manifold of surface receptors characteristic of the NK cell lineage. Similar to other types of T lymphocytes, NKT Cells also express a TCR. However, TCR is semi-invariant with a relatively restricted repertoire [484,485]. Consequently, the functions of TCR resemble more conserved pattern-recognition receptors of innate immunity than the diverse antigen-specific receptors of the adaptive branch of the immune system. TCR engagement results in the evocation of effector functions like cytokine secretion and cytotoxicity [483,486,487]. They interact with agents from both branches of the immune system, they can activate NK cells of the innate immune system as well as B and T Cells from the adaptive branch [488,489]. NKT differentiate into multiple subsets carrying out different functions in different tissues. They are high in numbers in liver, spleen, and bone marrow [490,491]. NKT Cells contribute to the defense mechanisms against various pathogens, including bacteria, viruses, fungi, protozoa, or parasites, play an important role in autoimmune conditions, and stimulate tumor-specific T Cells and effector NK [492–494].

$\gamma\delta$ T Cells

Several properties distinguish $\gamma\delta$ T Cells from the rest of T Cells. First and foremost, they have a distinct TCR composed from glycoprotein γ and δ chains [495,496]. Second, they also have a different development, since they obtain several functions already in the thymus. When they leave, they are ready to action and do not require additional peripheral maturation to initiate effector function. Since they reside in special tissues, they can respond to tissue-specific ligands. The combination of the last two properties makes them the the first line of defense in many tissues. They are rare in the secondary lymphoid organs, but more numerous in many peripheral tissues, like the skin, intestines, or lungs [497,498]. The third property distinguishing them from other T Cells is their capacity to recognize wide range of antigen without MHC molecules [499–501]. $\gamma\delta$ T Cells recognize different constellations of antigens resulting in widening the

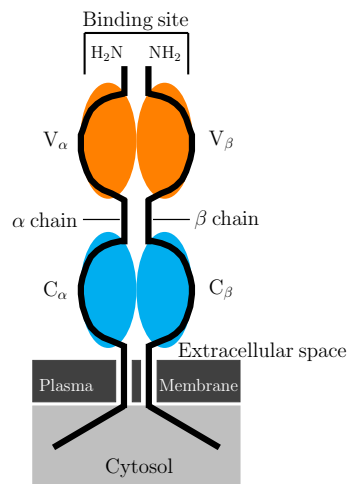


Figure 2.14.: Sketch of the TCR. TCR consists of an α and a β polypeptide chains. They are about 280 amino acids long and have a large extracellular part folded into two Ig-like domains. One domain is variable (V, shaded orange) and the second is constant (C, shaded blue). The antigen-binding site is formed by the two variable V_α and a V_β domain. Contrarily to antibodies having two antigen binding domains, TCR exhibits only one. The TCR heterodimer is associated with a large array of invariant membrane-bound proteins (not shown) playing a role in the T Cell activation after the binding of the TCR to antigen. Typically, T Cells have around 30,000 TCRs on their surface [508].

scope of immune responses. They can eliminate the APC directly by the release of cytotoxic molecules like perforin and granzymes or indirectly by activating other immune cells [502–504]. Although they are accounting for a small fraction of all T lymphocytes, they are included in a large array of immune responses. They quickly proliferate as the response to tumor, inflammation, and invading pathogens such as malaria [501, 505–507].

2.8. Life and immune response of the cytotoxic T Cell

Since the life of the CTL begins long before the immune response and continues after it the description of the APC elimination without the events leading to it would be limited. Therefore, I will describe the life of the CTL to provide a context to one of the key immune reactions of the human body. I will go through the several stages of the life of the CTL from bone marrow progenitors to naive cells, effector cells, and memory cells, and focus on the targeted killing.

2.8.1. Bone marrow progenitors naive cells, and their activation

Bone marrow is a source of different stem and progenitor cells [509]. T cells originate from bone marrow progenitors that later travel to the thymus (hence the name "T Cell") for the maturation, selection, and subsequent export to the periphery [50]. During their maturation in the thymus, T Cells rearrange gene segments, leading to the creation of a unique antigen-binding molecule, the TCR, which is responsible for the specificity of each cell [50, 510, 511]. This antigen-binding receptor was first identified by several research groups in 1980s [512]. The TCR is later responsible for the recognition of APCs. The antigen-binding heterodimer is predominantly composed of two disulfide-linked polypeptide chains called α and β [47, 508, 513], sketched in Fig. 2.14. The chains are about 280 amino acids long and have a substantial extracellular part folded into two immunoglobulin-like domains. Unlike the antibodies that have two antigen-binding sites, TCR has only one that is located in the extracellular part. Both α and β chains are connected to a large array of invariant membrane-bound proteins helping to activate the CTL following the TCR binding to the antigen. In the thymus, every TCR is associated with a coreceptor. T Cells expressing CD8 coreceptor will be later activated into CTL. The coreceptor has an additional role in the targeted killing since it binds to molecules on the surface of the APC further stabilizing the connection

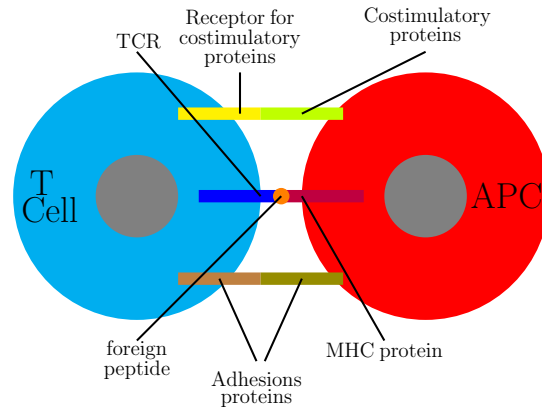


Figure 2.15.: Sketch of the activation of the naïve cell. Several types of proteins activating the T Cell are shown.

between the two cells [514].

T Cells leaving the thymus for the periphery are called naïve (resting) cells [515–517]. However, the thymus is not solely responsible for the maintenance of their numbers, since majority of naïve cells in humans derive from turnover. They are surprisingly long-lived and have expected lifespans of several years. They migrate through the secondary lymphoid tissues and peripheral circulation but are unable to mount any kind of response against a threat since they lack the necessary tools. Specifically, they lack the lytic granules that serve as CTL’s primary weapons. Before the T Cell can kill, it must turn itself into the effector T Cell capable of an immune response.

The naïve cell turns it self into an effector cell by a complex process known as activation mediated by the TCR [508, 518–520]. The process is initiated in peripheral lymphoid organs when the naïve cell encounters APC. There are three main types of APC able to activate T Cells: dendritic cells, macrophages, and B cells. It appears that dendritic cells are the most potent since their function is to present the antigen to the agents of the immune system [521]. Immature dendritic cells can be found in tissues of the body including the skin, gut, and respiratory tract. They encounter a pathogen that induces their maturation from an antigen-capturing cell to an antigen-presenting cell able to activate naïve cells. Three types of protein located on the surface of the APC play a role in naïve cell activation: major histocompatibility complex (MHC) proteins presenting foreign antigen to the TCR, costimulatory proteins binding to complementary receptors on the surface of the T Cell, and adhesion molecules enabling a T Cell to bind to APC, sketched in Fig. 2.15. The interaction between the TCR and MHC proteins is described in Section 2.8.2.

Two things take place when the APC is recognized: the CTLs prepare the weapons and expand in numbers. Following the activation, the CTL begins to synthesize cytotoxic materials and the compartments for their storage [59, 522]. However, the immune system could not mount an effective immune reaction with an insufficient number of T Cells. For this reason, activated T Cells undergo a massive proliferation that can increase their numbers by several orders of magnitude [515, 516, 523]. The new effector cells migrate through the organism in search of pathogens that stimulated their activation [508].

2.8.2. Recognition of the antigen-presenting cell by the effector T Cell

Effector CTL stroll through our organisms looking for the threats. However, before the CTL can engage the threat, it has one extremely difficult task: to recognize it. CTL can recognize intracellular threats by the detection of the foreign peptides, which are fragments of the pathogen’s proteins. Peptides are located on the cell’s surface and presented and accumulated in the large clusters of the genes termed the major histocompatibility complex (MHC). CTL (and other types of T Cells) can recognize the peptide only when they are presented by the MHC molecules [75]. Consequently, the CTL does not recognize

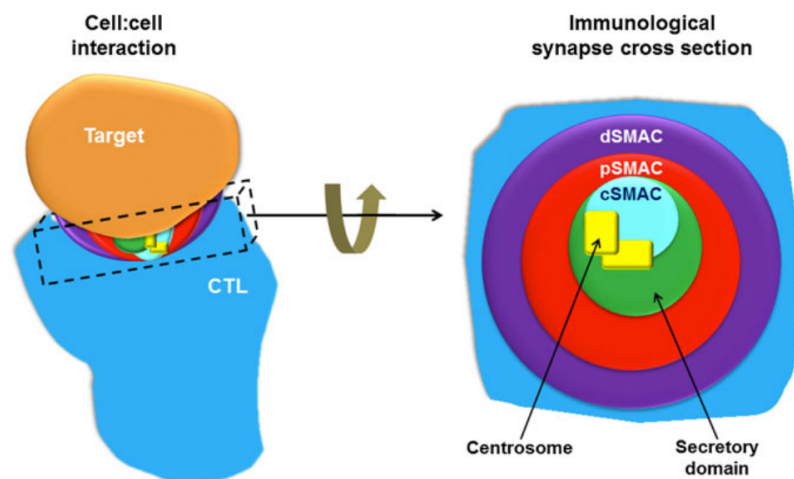


Figure 2.16.: Sketch of the IS. "The immunological synapse consists of a series of supramolecular activation clusters (SMACs) forming a bull's-eye-like ring when observed in cross section. The central SMAC (cSMAC) consists of the T-cell receptor (TCR) and associated kinases, the peripheral SMAC (pSMAC) of integrins, and the distal (dSMAC) of excluded phosphatases, such as CD45, as well as actin and actin-interacting proteins, e.g. IQGAP-1. The centrosome docks by the cSMAC and determines the point of secretory granule exocytosis in cytotoxic T lymphocytes (CTLs)." The figure and the caption was taken from [534], the text of the caption is delimited by quotation marks. The permissions are stated in the Appendix C.

the peptide, but the peptide-MHC molecules (pMHC). Surprisingly, there are over 10^{15} possible pMHCs produced from 20 proteogenic amino acids [524]. The T Cells have to recognize and react against an astonishingly large array of indicators of a danger to the organism. The recognition of the pMHC and the following initiation of the immune reaction is one of the main tasks of TCR [47,58]. The recognition of the pMHC is mediated by the variable complementarity-determining regions of the TCR [75,525]. However, the pool of TCR is still relatively limited ($< 10^8$). It is unclear how such a limited pool can provide an immune response to an enormous, several orders of magnitude higher number of peptides [524,526]. One possibility is the large degeneracy of TCR giving it the ability to respond to manifolds of pMHC.

MHC molecules have two properties that make it difficult for the pathogen to escape the detection of the immune system. First, MHC is polygenic. It contains several different MHC classes of genes possessing a set of MHC molecules with different peptide-binding specificities. Second, the MHC is highly polymorphic. There are several variants of every gene in the population. Interestingly, MHC genes are the most polymorphic genes currently known [527]. Two major MHC classes differ in their structure, their expression pattern on tissues of the body, and functions. This can be exemplified by the two main structurally and functionally distinct classes: class I and class II MHC proteins that present peptides to CTL and helper T Cell, respectively [508, 525, 528, 529]. Despite of all the effort, some of it very recent [530], many aspects of the TCR-pMHC binding remain unclear.

The engagement of the TCR results in the suppression of T Cell locomotion and the creation of the IS [531,532].

2.8.3. IS formation and structure

The IS is a complex contact zone between the two cells. The processes taking place or initiated in the IS play a key role in many basic cellular functions. It can be exemplified by the influx of the Ca^{2+} through the CRAC channels [Hornak2016] or by the TCR signaling [533]. It is impossible to review here all of its functions. I will outline the organization, shape, and the location of the pulling forces.

The IS was first described by the Kupfer's group in 1998 as a highly organized contact zone with radially symmetric compartments termed supramolecular activation clusters (SMAC) [81], sketched in

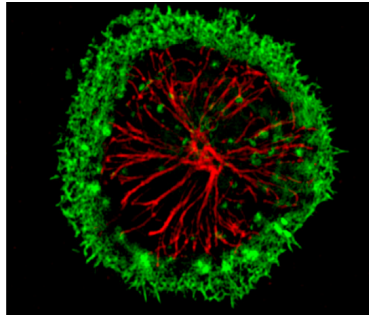


Figure 2.17.: Actin filaments and the MTOC at the IS. Cortical actin is reduced at the synapse when the MTOC is docked. Green and red represent actin and tubulin, respectively. The MTs connect to the MTOC located in the middle of the actin ring. The figure was taken from [74] with the permissions stated in the Appendix C.

Fig. 2.16. The early experiments describe the mature IS as a bull's eye arrangement of SMACs formed within the first few minutes of T Cell-APC contact [535, 536]. The center of the bull's eye (cSMAC), accumulates TCR, pMHC complexes, and various signaling molecules, like protein kinase C θ , which seems to be a marker for achieving the stable IS. The peripheral SMAC (pSMAC) forms an adhesive ring around the cSMAC. It contains integrins and integrin-associated cytoskeletal proteins. The pSMAC is also the region where dyneins accumulate, which will be discussed later. It is encircled by the distant SMAC (dSMAC) playing many important roles. Most notably, the actin filaments accumulate in the dSMAC at the beginning of the IS formation [74, 537]. When the MTOC translocates towards the IS, it contacts the plasma membrane close to the center of the IS, behind the central cSMAC. The place for the secretion of lytic granules is located next to the cSMAC, sketched in 2.16. It should be emphasized that the clusters do not carry out different functions, but collaborate on many tasks including the TCR signaling [83]. The description of the SMACs and their role can be found in [531].

Moving CTLs have a leading-edge enriched by the actin. Consequently, when the CTL binds to the APC actin is accumulated at the contact zone. Actin depletion at the contact zone initiates the formation of the cSMAC and is necessary for effective TCR signaling [74, 534]. Ritter et al. reported that the actin network dramatically reorganizes within the two minutes after the formation of the IS [74]. The authors observed a substantial loss of the actin density at the center of the IS and the actin relocation to the dSMAC. The depletion of the actin in the IS is correlated with the beginning of the MTOC repositioning. The MTOC arrives to the IS when the center is almost empty of the actin forming a ring-like structure located at the IS periphery, see Fig. 2.17. The contact between the two cells flattens the plasma membrane at the IS. In some cases, the membrane can invaginate to the CTL [5, 74]. To summarize, the IS is a flattened area surrounded by the actin ring.

Here, I will focus on the pulling forces and their location. The dynein motor protein is necessary for the repositioning since the depletion or the inhibition of dynein strongly impairs the MTOC movement [106, 538, 539]. There are still some open questions about how the dynein is recruited to the IS. Apparently, the dynein accumulation depends on the accumulation of the lipid second messenger diacylglycerol [538]. Sanchez et al. demonstrated the spatio-temporal correlation of the decrease of the actin density and dynein recruitment [182]. Although the actin filaments are never completely cleared from the IS, their density must drop under a certain value to enable the recruitment of the motor protein. The ADAP appears to be indispensable for the recruitment of dyneins to the IS, since its loss prevents MTOC translocation and dynein accumulation at the IS [118]. Both proteins move to the synapse, where they colocalize in the form of a ring in the pSMAC. It was suggested that the dynein in the pSMAC drives the repositioning via cortical sliding mechanism [9, 121]. Yi et al. [5] provided evidence that MTs are also pulled by the capture-shrinkage mechanism in the center of IS. To summarize, the dynein pulling via the cortical sliding and capture-shrinkage mechanism are accumulated at the periphery and in the narrow center of the IS, respectively.

At the end of this section, I will briefly summarize the properties of the IS that are crucial to my work. The IS is a complex structure divided into several clusters having a bull's eye arrangement surrounded by

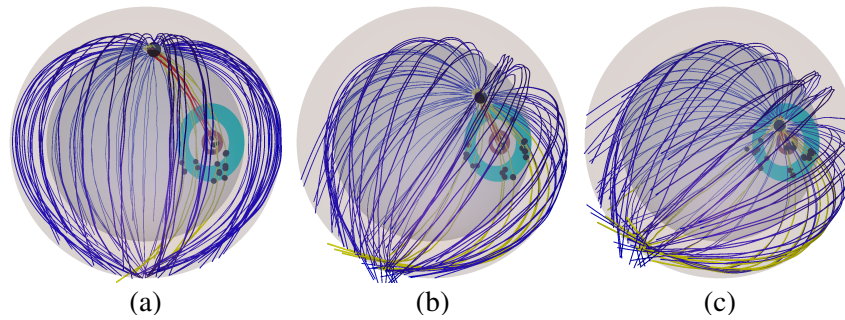


Figure 2.18.: Sketch of the combination of capture-shrinkage and cortical sliding mechanisms. The outer transparent sphere stands for plasma membrane and the inner sphere depicts the nucleus. The cyan and brown circle represent the periphery and the center of the IS, where cortical sliding and capture-shrinkage dyneins are located, respectively. The big black sphere represents the MTOC and small black spheres stand for dyneins. Blue, yellow and red lines represent unattached, cortical sliding and capture-shrinkage MTs, respectively. (a) At the beginning of the process, MTs intersecting the IS attach to dyneins. MTs passing through the center attach in end-on fashion to capture-shrinkage dyneins. Contrarily, MTs attached to cortical sliding dyneins at the periphery pass through the IS. (b) Capture-shrinkage MTs depolymerize as the MTOC approaches the IS. Cortical sliding MTs slide on the plasma membrane. Cortical sliding MTs create a wide stalk connecting the MTOC and the IS that encloses more narrow stalk between the MTOC and the center of the IS. (c) Capture-shrinkage MTs are depolymerized. The figure was made using the simulation software [Hornak2022B].

the ring of actin filaments. The dynein is accumulated at the periphery of the IS and in its center and pulls via two different mechanisms driving the MTOC repositioning.

2.9. MTOC repositioning during targeted killing

2.9.1. Experiments

The MTOC repositioning during the CTL targeted killing was first observed in 1982. Geiger et al. used electron microscopy to investigate the position of the MTOC in the CTL bound to the APC [540]. Already in this first experiment, the authors observed many important characteristics of the targeted killing. They reported that the CTL is polar and that the hit is strictly unidirectional, affecting the APC without harming the CTL. They also noted that the CTL interacts with and binds to APC predominantly by establishing a membrane region. Moreover, they reported that the MTOC in almost all CTL was moved towards the intercellular contact site. A year later, similar results were reported by Kupfer et al. who analyzed the targeted killing of the NK cell by light and immunofluorescence microscopy [541]. The NK-APC conjugates were observed. The binding of the NK cell triggers a sequence of events leading to a rapid repositioning of the Golgi apparatus and the MTOC inside the NK cell to the contact area. The authors proposed that the repositioning of the two organelles directs the secretory vesicles containing components inducing target cell lysis.

Kuhn et al. [9] investigated CTL directional killing by the means of polarization microscopy and computerized 3D reconstruction of tubulin. After the contact with the target cell, the MTOC transitioned to the IS during approximately three minutes, see Fig. 2.19. Subsequently, it wiggled around the contact zone. During this motion, the changes in the distance between the MTOC and the contact zone were relatively small compared to the ones between the MTOC and the IS center. When the CTL attached to two targets simultaneously, the MTOC exhibited large, often incomplete transitions in a direct line between the two contact sites.

The authors also observed the cortical sliding mechanism. During the process, the MTs were spanning from the MTOC to the contact zone on the cell cortex. The images also showed that the MTs straightened in the direction of the MTOC movement and that their interaction is not limited to their tips. In the case when the MTOC repolarized, the central zone was left devoid of MTs, since the majority

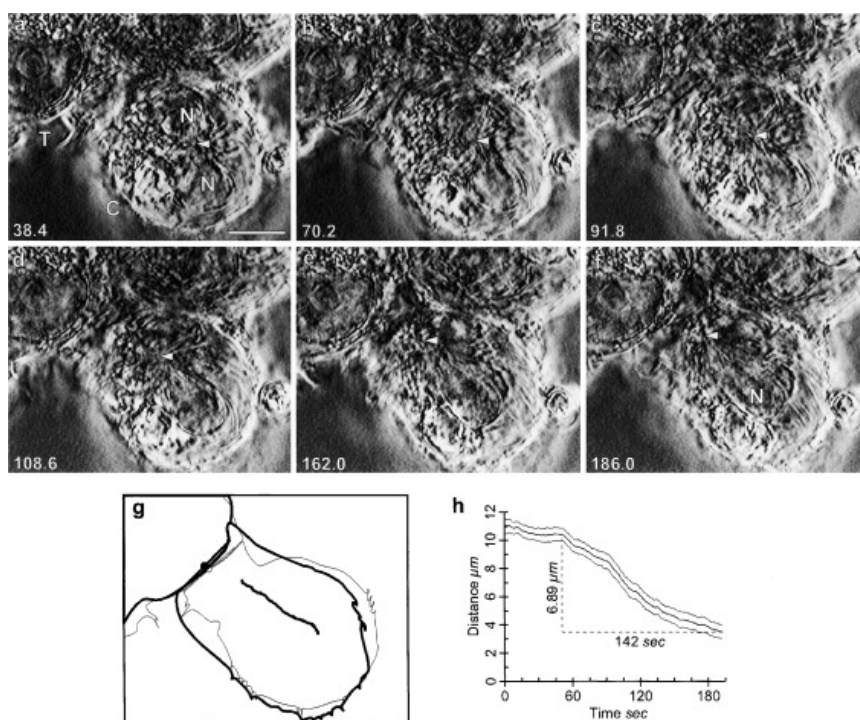


Figure 2.19.: Modulated polarization microscopy of the MTOC repositioning during the targeted killing. MTOC denoted by the white arrow was originally on the opposite side of the CTL nucleus (N) from the contact zone. (a-f) During approximately three minutes, the MTOC translocates to the IS. Scale bar, $5\mu\text{m}$. (g) The MTOC path. The beginning and ending outlines of the CTL are represented by light and bold lines, respectively. (h) The dependence of the mean distance between the MTOC and the center contact zone on time. The figure was taken from [9] with the permissions stated in the Appendix C.

of them extend out laterally from the MTOC toward the peripheries of the contact site. MTs bend sharply at the sites of contact with the cellular cortex and these bending points formed a roughly circular ring at the contact site. This supports the hypothesis that the MTs are attached to motor proteins at the pSMAC. The authors further hypothesized that the MTs can be one of the reasons why pSMAC takes the shape of the ring. Four years later, the same group reported that the dynein colocalizes with the ADAP ring in the pSMAC, where it can generate the forces necessary for the MT sliding [118].

Yi et al. [5] used optical trap to place a target cell so that the MTOC and the IS are initially diametrically opposed, which allowed for the dynamical imaging in a quantitative fashion. Following the formation of the IS, several MTs reach the center of the IS where they terminate in the end-on fashion. Over the next few seconds, they straighten and form a narrow stalk connecting the center of the IS with the MTOC. Subsequently, the MTs in the stalk shorten as the MTOC approaches the IS and the rates of depolymerization correspond to the rates of the MTOC repositioning. The effort to localize dynein was unsuccessful possibly due to their low amount. However, the authors reported that the plasma membrane penetrates into the CTL during the MTOC repositioning at the place where the MT stalk ends. Such indentations bear similarities with the ones appearing at the presumptive sites where the MT plus end is pulled at the membrane by the cortical dynein [542]. These results suggest that the MTOC is pulled by the capture-shrinkage mechanism, involving the end-on capture of MTs at the center of the IS, visualized in Fig. 2.18b. Since the center of the IS is relatively small, the stalk connecting the MTOC and the IS is narrow compared to the stalk of cortical sliding MTs, visualized in Fig. 2.18b.

To summarize, the works of Kuhn et al. and Yi et al. provided the evidence of the two mechanisms driving the repositioning. Cortical sliding and capture-shrinkage dyneins are anchored at the periphery and in the narrow center of the IS, respectively, see Fig. 2.18a. During the cortical sliding mechanism, the end

of the MT remains free, while the capture-shrinkage acts in an end-on fashion and the MTs depolymerize, see Fig. 2.18c. During both mechanisms, the MTs attached to dynein form a stalk connecting the MTOC and the IS. Since the center of the IS is substantially smaller compared to the entire IS, the cortical sliding stalk is substantially wider, see Fig. 2.18b.

Yi et al. also compared the MTOC speeds during the repositioning in the cells with and without the capture-shrinkage mechanism. To "turn off" the capture-shrinkage mechanism they used taxol, which is the inhibitor of MT depolymerization. They reported that the MTOC speeds in taxol-treated cells decreased by 71%. Moreover, they observed a substantially smaller percentage of complete repositionings. Based on these results the authors concluded that the capture-shrinkage is the main driving force of the repositioning. However, experiments were performed in only one configuration of the cell. The analysis of the role of the two mechanisms in various configurations of the cell was one of the main goals of my work.

Quann et al. [538] reported that the MTOC repositioning is preceded by the production of the diacylglycerol and the accumulation of dyneins at the IS. Moreover, they recorded the positions of the MTOC providing the timescale of the repositioning. Helper T cells were in contact with the glass coverslip and then used ultraviolet light to create a region of activated pMHC. The angle between the MTOC and the activated region was around ninety degrees. They observed that in such configuration the MTOC needs approximately three minutes to travel to the IS, which is consistent with the results from [9]. Moreover, they observed that the movement slows down when the MTOC approaches the IS, as was observed by [5].

The experimental results stated above are crucial for my work, since they provide the experimental evidence for the two mechanisms. Moreover, they measured the dependence of the MTOC-IS distance on the time during the repositioning. However, MTOC repositioning and the organization of the cytoskeletal filaments in immune reactions is a fascinating and a vivid topic. The recent works and the reviews can be found in [326, 543–545].

2.9.2. Models

Deterministic model

Kim and Maly [546] tested whether an MT pulling mechanism located in the IS can reposition the MTOC and therefore bring a killing apparatus. The cell has a shape of a sphere with flattened IS, see Fig. 2.20. MTs are connected in the MTOC and their movement opposed by the viscous drag is confined between the cell membrane and the rigid nucleus. The model simulates the pulling of the cortical sliding dyneins by the deterministic force proportional to the length of the filament closer to the IS than a threshold value

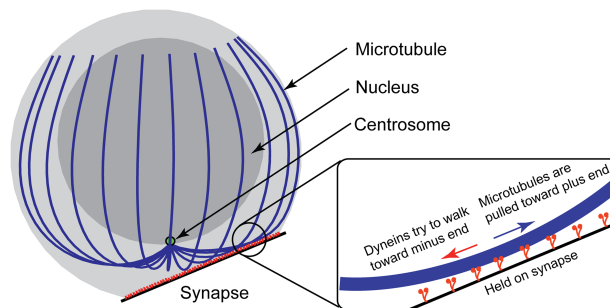


Figure 2.20.: Sketch of the deterministic mechanical model of the T Cell polarization. The flattened part represent the IS, where the MTs are pulled by the deterministic force. The figure was taken from [546] with permissions stated in the Appendix C.

The model reproduces the observations that the MTOC repositions to the IS and then oscillates close to it. However, some of the observations are in contradiction to experimental results. During the repositioning, long-range reorientation results in an asymmetrical arrangement of MTs, since a relatively tight "bundle" of filaments is formed at the leading side of the cytoskeleton. The creation of the bundle

results in the MTOC movement to the second IS if it is formed in the direction of the original MTOC motion. However, when the second IS is created in the opposite direction, the MTOC stays close to the first IS. The changes in the shape of the cytoskeleton observed in [5] were completely different since the side of the cytoskeleton leading the movement has a smaller amount of MTs. This contradiction may limit the predictions of the model.

Model with mobile dyneins

The model developed by Gros et al. takes into consideration the massive restructuring of the CTL to form the IS [547]. When the interface between the two cells is created, the actin filaments form a ring structure around the IS, whose center becomes actin-depleted, which allows dynein to be recruited to the IS [182]. The study proposes a model in which dynein is mobile and drags itself on the membrane while exerting force on the MTs. Dynein reorganizes in the synapse under the MTOC while stepping on the MT until they find a position on the filament and the force is sufficient to stall or unbind.

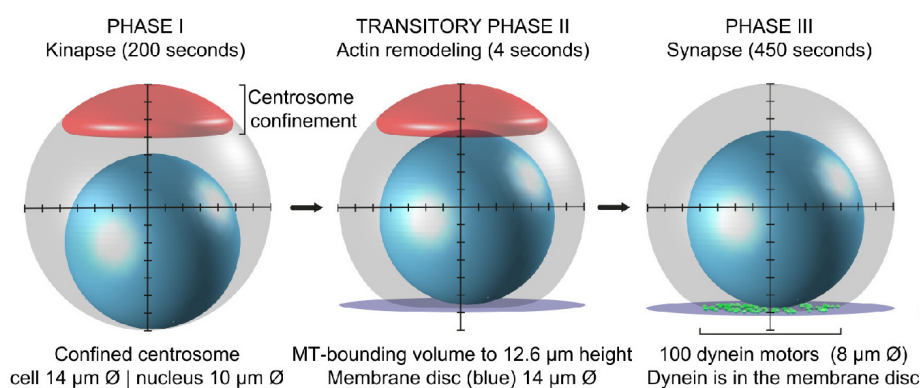


Figure 2.21.: The three phases of the model with the mobile dynein. The MTs move in the gray volume, the nucleus is blue, and the red part denotes the confinement of the MTOC. In the first phase, the MTOC is bound to the confinement and the MTs grow and shrink and achieve a steady state of the network. In the short second phase, the flattened IS is introduced. In the third phase, the MTOC is released from the confining cap and the dyneins are placed to the IS. The figure was reprinted from [547] with permissions stated in Appendix C.

The model is sketched in Fig. 2.21. The cytoskeleton in the model consisted of 150 growing and shrinking MTs. To assure the steady-state length distribution before the beginning of the repositioning, the simulation used a long initialization period during which the MTOC was confined in a spherical cap. During the transitory phase, actin is depleted from the center and form a dense structure at the periphery of the IS hindering the MTs from entering. Consequently, the MTs can make contact only with the central part of the IS. The side of the CTL with the IS is flattened to represent the contact between the two cells. Polarization starts after the addition of mobile dyneins on the flattened surface.

The model reproduced multiple aspects of the MTOC repositioning. Most importantly, dyneins accumulate into clusters in the IS and their pulling can create a MT stalk that was observed experimentally [5]. However, the MT bundles are created only if sufficient amount of motors has converged before the MTOC translocation. The authors further investigated the model with MT-capture-shrinkage dynein binding to the end of shrinking MTs. However, such model was less robust and required low unbinding rates to reposition the MTOC, possibly due to the simplified implementation (as authors admit). The capture-shrinkage dyneins still formed clusters, suggesting that the clustering may be independent of the mechanism.

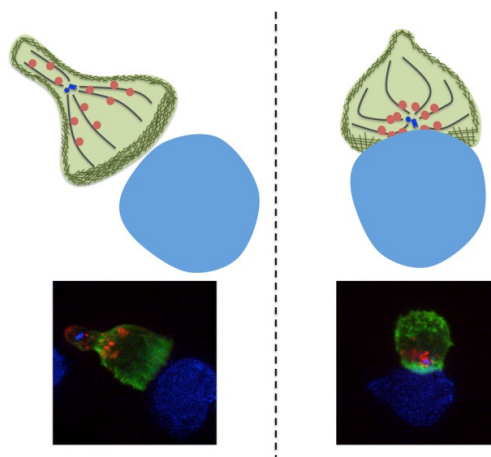


Figure 2.22.: Centrosome polarization brings lytic granules to the synapse. The continuous and intact actin cortex (green) in migrating cells provides a barrier restricting the secretion of lytic granules (red). Upon recognition of the APC (blue), the MTOC moves to the IS dragging the granules. The MTOC docks close to the cSMAC and brings the MTs and the lytic granules to the close proximity of the plasma membrane. Due to the low density of the actin cortex, lytic granules can secrete to the APC. The figure was taken from [534] with the permissions stated in the Appendix C.

Recent models

Several groups modeled the cytoskeletal dynamics during various biological processes. The reviews can be found in [548–550]. In the end, I would like to mention Cytosim, a cytoskeleton simulation suite developed in 2007 [551], that models basic elements of the filaments and motors, which can be combined to simulate different biological functions. The code is extensible and was used to model actin and MT assemblies in various functions in 1D, 2D and 3D. During the last few years, Cytosim was successfully used to model the cytoskeleton dynamics by various groups [547, 552, 553].

2.10. Secretion of lytic granules

The docking of the MTOC at the IS assures directional transport of specialized secretory lysosomes alongside the MTs, see Fig. 2.22. Subsequently, the granules are ejected towards the APC leading to its death. The secretion of lytic granules is therefore indispensable for the proper immune reaction and its defects lead to serious illnesses like hemophagocytic lymphohistiocytosis type 2–5 or Griscelli syndrome type 2 [87, 554]. The secretion is dictated by the TCR and signaling cascades initiated in the cSMAC [533, 554].

Stinchcombe et al. [555] found that the place of the secretion lies within the adhesion ring (colocalizing with pSMAC) close to the signaling region (cSMAC), sketched in Fig. 2.16. The authors also reported that the signaling protein organization is maintained during the secretion, which implies that the secretory and signaling function may take place simultaneously. The secretion of the granules is preceded by the accumulation of talin, a protein linking membrane proteins to the actin cytoskeleton, into a ring-like structure [556], see Fig. 2.23. The talin is localized into pSMAC and it surrounds the cSMAC containing signaling molecules including Lck and PKC- θ . The authors further investigated the mechanism of the secretion. The lytic granules accumulate around the Golgi apparatus and they tightly align with the plasma membrane. Subsequently, one can observe the formation of the large cleft between otherwise tightly associated plasma membranes of the two cells, sketched in Fig. 2.23d. They observed that the content of lytic granules like granzyme A and cathepsin D enters the cleft, see Fig. 2.23c, appears to be an indentation to the APC membrane. The authors suggested that the cleft is the site of exocytosis. If the CTL is connected to several different target cells, the CTL kills them separately, suggesting that the release is allowed at only one point at a time. The fact that the cytotoxic release is so carefully focused explains why the CTL can kill without any widespread damage [557].

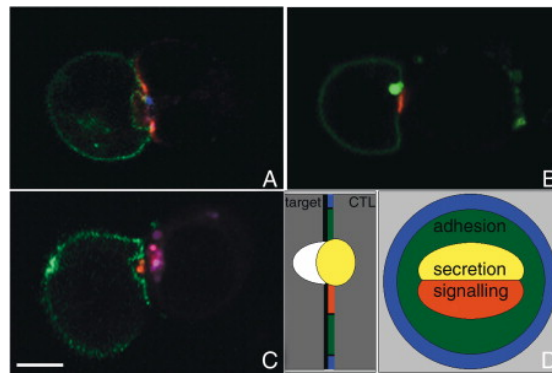


Figure 2.23.: Secretion of lytic granules to the APC. The cleft forms as an indentation in the APC membrane. (A–C) CTL (right) is conjugated to target cells (left, the membrane is green). (A) Talin is depicted as red, granzyme A is blue. (B) Signaling molecules Lck is red. The signaling domain appears intact. (C) Granzyme A (red) and cathepsin D (blue) enter the cleft between the two cells. (D) The model depicting the arrangement of the IS as seen in the section through the cell-cell contact site (left) and looking flat down to the IS from the side of CTL (right). Two distinctive domains, secretory and signaling are surrounded by the adhesion molecules assuring the contact between the two IS. The figure was taken from [555] with the permissions stated in the Appendix C.

Electron microscopy showed that the lytic granules are membrane delimited and have a diameter ranging from 0.5 to $2\mu\text{m}$. More recent flow cytometry analysis suggested that the granule population of differentiated human CTLs consists of individual granules having a continuous spectrum of sizes and containing various lytic molecule load [558, 559]. The lytic granules contain an arsenal of cytolytic proteins [554, 560]. The lytic ability of the CTL is dramatically increased by the combination of perforin and granzyme. It was shown that the perforin forms a pore at the cell membrane enabling the access of death-triggering granzymes to the cytosol [561, 562]. The perforin in the APC further creates the pores in the membrane allowing water and salts to pass into the cell leading to its death. The target may repair pores in the membrane caused by perforin, but its DNA is fragmented by the granzyme at the same time. Several types of granzymes could lead to apoptosis. However, granzyme B seems to be the most efficient [563, 564]. Whether the APC is killed by necrosis or apoptosis appears to depend on the target itself and the stage of the cell cycle [88]. The killing is very efficient and involves only a temporary contact between CTL and the target cell. CTLs are very effective serial killers since they can eliminate some of their targets within 2–10min [565, 566]. After the killing, they can detach from the APC and attack the following target around six minutes later [567].

2.11. Memory cells

The memory of the immune system is a crucial factor in the protection of health. Our ability to shape the immunological memory through vaccines is one of the greatest triumphs of modern science [568, 569].

The response of the T Cells increases with time and reaches the highest intensity 7 – 15 days after the stimulation. When the threat is eliminated, the population of the T Cell rapidly decreases and approximately 90% of lymphocytes die. A small fraction of the cells survive and keep the memory of the pathogen. The properties of those cells are changed: They can be easily activated (compared to naïve cells), they have an increased proliferative potential, and they can respond to a threat more rapidly [519]. Moreover, they can travel through secondary lymphoid organs and peripheral tissues that are poorly accessed by naïve or effector cells. Due to the memory cells, the reaction of the immune system in case of reinfection can be substantially faster. The memory cells are diverse and have multiple functions. This can be exemplified by helper cells, see Section 2.7, and CTLs that transform into central-memory (T_{CM}) and effector-memory (T_{EM}) T Cells, respectively. Upon antigen encounter, T_{EM} display immediate effector function against pathogen, while T_{CM} uses the time to proliferate and prepare the second round of effectors [570, 571]. The efficiency of the cytotoxicity of various types of memory cells were analyzed in 2022 by Knörck et al. [572]. The memory cells can last for decades and protect our body against certain pathogens for the rest of our lives [31].

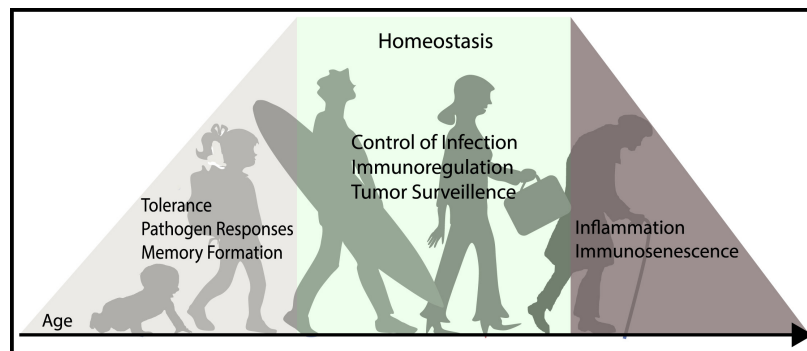


Figure 2.24.: Different roles of T Cells during aging. In early childhood, T Cells mediate pathogen clearance for several acute infections and develop memory responses, and establish tolerance to foreign antigens. During adulthood, the T Cell pool is more stable since it encounters a lesser amount of new threats and consequently generates fewer memory cells. T Cells maintain homeostasis by controlling chronic infections and surveil cancer cells, and maintain immunoregulation. The functions of the T Cells decline with the increasing age resulting in increased susceptibility to infection and cancer. The figure was taken from [50] with the permissions stated in the Appendix C.

2.12. Roles of T Cells in different stages of life

The critical role of T Cells in immunity changes and evolves during the different stages of the relatively long human life, sketched in Fig. 2.24 [50,573]. The first and the second decades of the life are critical, since immune memory is not yet established and various pathogens challenge the organism lacking the experience to handle them. Consequently, the infections are frequent and, as the childhood mortality before the invention of vaccination demonstrates, potentially lethal. In infancy and childhood naïve cells are the most represented to protect us against the overwhelming number of new antigens to which the body slowly builds tolerance. The naïve cells are activated into effector cells whose majority dies when the pathogens are defeated. The small fraction of the effector surviving after every infection contributes to the rising and diversifying amount of memory cells.

The increase in the number of memory cells stops at the beginning of adulthood. For the next few decades, the population of the memory cell is maintained and slowly gains the dominance over naïve cells [573,574]. The shift in dominance from naïve to memory cells suggests the change in the tasks of the immune system. In adulthood, fewer new antigens are encountered and the population of memory cells helps to deal with repeatedly encountered antigens. Moreover, the surveillance of tumors grows in importance with increasing age.

Despite its strengths, the weaknesses of the immune system begin to show already in adulthood. Mainly, adaptive immunity deteriorates since the body has difficulties maintaining a diverse repertoire of T Cells. Naïve and memory cells have a half-life from six to twelve months and fifteen to forty five days, respectively [575–577]. Thymic production of the new naïve cells diminishes with time due to the decrease of the volume of the functional thymic tissues [573,578,579]. At the beginning of adulthood, the thymus is responsible for 16% of the generated cells. At later stages of life, thymic contribution declines to < 1%. After the age of 50, almost the entire T Cell supply is generated from existing T Cells [580]. The insufficiency of this mechanism results in a decrease in the T Cell population and contraction of TCR diversity [575,581]. Aging affects various T Cell subsets differently, some types maintain their population even in the elderly while the number of others decreases rapidly [573,575]. The weakening of the adaptive immunity is increasingly clinically relevant as the person gets older and its failure is a major cause of mortality in the elderly [582].

2.13. MTOC repositioning during various cellular processes

The MTOC positioning is carefully regulated during the life of the cell and various cellular functions. The importance of the MTOC is given by multiple factors. First of all, as the MT organizing center, the MTOC is responsible for the maintenance of the cell's shape, it participates in cellular motility and

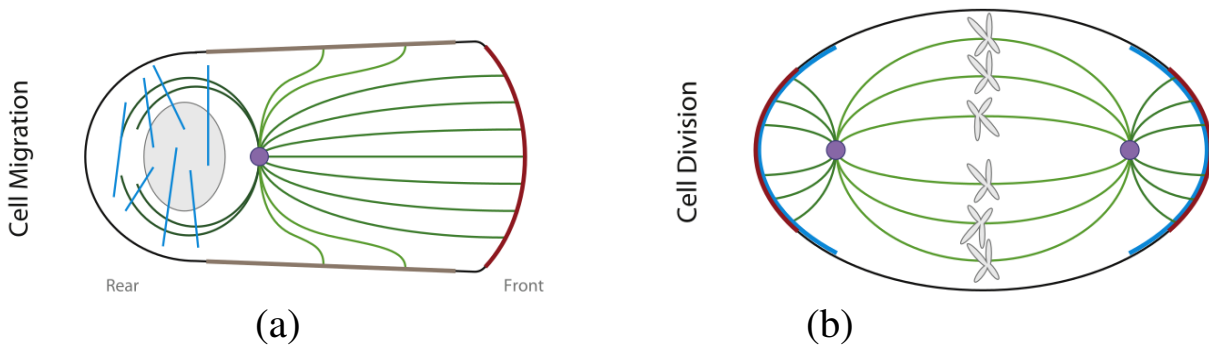


Figure 2.25.: Sketch of the MTOC repositioning in polarized cells. Green curved and blue straight lines represent MTs and straight lines actin, respectively. The MTOC is shown as a purple dot. (a) The MTOC positioning in migrating cells. The dyneins pull in the leading edge denoted by red and on sides denoted by grey. (b) The MTOC positioning during cell division. The red color denotes the area where MTs touch the plasma membrane, are captured and pulled by dyneins. The blue area denotes the area of signaling. The two MTOCs are connected by MTs that will be interrupted in the middle. The figure was taken from [584] with the permissions stated in the Appendix C.

plays a key role in crucial cellular processes like the cellular division [583, 584]. Moreover, the MTOC is also very important signaling platform [106]. The importance of the regulation of the MTOC position was discovered already in the nineteenth century. Theodor Boveri, who coined the name centrosome, provided evidence that following the duplication of the centrosome, the positioning of the two centrosomes determines the location of the MT spindle and therefore the orientation and the position of the division plane [585]. Spindle positioning can be determined both by intracellular and extracellular clues. The former can be exemplified by the large array of signals in single-cell organisms. The latter are for example the signals resulting from the cell adhesion to the extracellular matrix in multicellular organisms. The spindle orientation can have profound consequences on the basic structure of our organism. For example, the extracellular signals determine spindle orientation during epithelial morphogenesis and therefore have a deep impact on the tissue architecture, spreading or thickening [586–589].

During interphase, the MTOC is tightly associated with the nucleus and the interaction is facilitated by the cytoskeleton and various proteins of the nuclear envelope [590]. In non-polarized cells, the MTOC and the nucleus localize close to the center of the cell and the nucleus-centrosome axis has no preferential orientation. Due to its indispensable role in intracellular organization, the MTOC's position in the cell is tightly regulated to facilitate specific cellular functions. In polarized cells, the relative MTOC-nucleus position corresponds to the polarity axis. The position of the cytoskeleton reflects the geometry of the cell and is the result of the polarized forces acting on the MT cytoskeleton, especially by the MT-associated molecular motor proteins [122, 591]. This can be exemplified by the targeted killing in which the MTOC travels around the nucleus and positions itself between the nucleus and the IS. The purpose of this section is to show the analogies between the MTOC repositioning in the CTL with the MTOC dynamics during other biological functions.

In **migrating cells** the MTOC is usually positioned between the nucleus and the leading edge, which is thought to promote the directional movement [584, 592], sketched in Fig. 2.25a. Due to their pivotal role in cell mechanics, intracellular transport, and signaling, MTs play a key role in all essential events resulting from the cell migration. The MTOC placement in front of the nucleus may assure the contact of MTs with the leading edge of the cell. However, this concept is challenged by the case of migrating fibroblasts that position the MTOC behind the nucleus [593]. Regardless of the fact that the MTOC can be positioned behind or in front of the nucleus, the MTOC-nucleus axis appears to be in line with the direction of movement [584]. Although the MTOC positioning in various cells may appear similar, it can be achieved by distinct mechanisms: in astrocytes and neurons the MTOC transitions in front of the nucleus. In the case of fibroblasts, the nucleus moves while the MTOC stays close to the center of the cell [594]. The MTOC repositioning in migrating cells is actively controlled by the MTs as was demonstrated by the case of cells treated by a depolymerizing drug [592, 595]. Dyneins, which were thought to play a role in centrosome

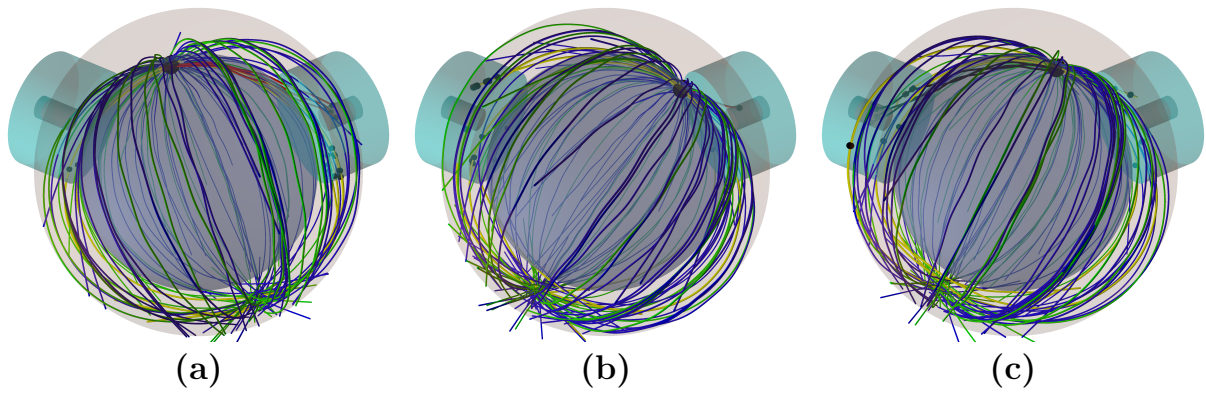


Figure 2.26.: MTOC repositioning in the cell with two IS. Snapshots from the time evolution of the MT cytoskeleton under the effect of both mechanisms with the same dynein density $400\mu\text{m}^{-2}$ in both IS. The outer transparent sphere stands for the cell membrane and the inner sphere depicts the nucleus. The blue and green lines represent unattached growing and shrinking MTs, respectively. The red, black and yellow lines depict MTs attached to capture-shrinkage dyneins in the right IS, left IS and to cortical sliding dyneins, respectively. The large cyan cylinders stand for the IS and the narrow brown cylinders represent their centers. Dyneins are depicted by small black dots. (a) MTs attach to capture-shrinkage and cortical sliding dyneins in the right IS and to cortical sliding dyneins in the left IS. They form a stalk and pull the MTOC towards the right IS. (b) Cortical sliding dyneins are attached to MTs in both IS. As the MTOC approaches, MTs detach from capture-shrinkage dyneins in the right IS. (c) Capture-shrinkage MTs form a stalk and pull the MTOC towards the left IS. The figure was made using the simulation software [Hornak2022B].

positioning in migrating cells, appear to be concentrated in the leading edge [594, 596]. To summarize, we can see several analogies with the MTOC repositioning in CTL: the MTOC moves, changes its relative position to the nucleus, and the movement results from the interplay of dynein motors and MT cytoskeleton.

During the **cell division**, the precise location of both mother and daughter centrioles is necessary to control the positioning of the mitotic spindle. In a large array of organisms, the positioning of the mitotic spindle is achieved by the forces of dynein located on the plasma membrane [597–599], sketched in Fig. 2.25b. This can be exemplified by mitotic spindle oscillations in *C. elegans* [107, 600–605]. They result from the cooperative attachment and detachment of dyneins to astral MTs [606–609]. In *C. elegans*, we have two distant locations of dynein accumulations on the opposite sides of the cell, sketched in Fig. 2.25b. As the MTs grow, they encounter the plasma membrane, are captured by dyneins, and then pulled towards the membrane. The oscillations occur since restoring forces pull the spindle back to the central location. The sources of the restoring forces were frequently discussed [225, 439, 600–602, 610–612]. MTs grow in all directions and therefore contact the plasma membrane on the other side. Consequently, restoring forces may simply result from the dynein pulling on the other side of the cell. Another possibility is that the restoring force is caused by the stiffness of MTs. As MTs grow, they encounter the plasma membrane and bend against it, which may result in forces opposing the movement.

One can observe similar MTOC transitions in the **CTL with two IS**, sketched in Fig. 2.26. The second IS is created when the CTL attacks the second APC before severing the contact with the first one. Consequently, MTs attach and dyneins from the opposite IS are in a constant tug-of-war. When one side wins the competition, the MTOC relocates towards the IS. Subsequently, the MTOC dwells for some time close to the IS, and then it travels to the second IS. Depending on the cell configuration and acting mechanisms, transitions may be continuous and fast, or slow and interrupted. Nevertheless, restoring forces are necessary to start a new transition. Kim and Maly [546] proposed that the MTOC transitions in the CTL with two IS are the consequence of the cooperative attachments and detachments of the dyneins in different IS. They hypothesized that the detachment of MTs on the trailing side of the MTOC takes place because the MTs are lifted off the pulling surface on the plasma membrane by viscous drag in the

cytoplasm. In [Hornak2022] we proposed a different scenario in which MTs detach at the close IS due to the MT stiffness forcing the MTs to lose the contact with the plasma membrane as the MTOC approaches the IS. Simultaneously, MTs attached in the distant IS are pulled by dyneins.

One can observe many similarities between the MTOC repositioning in the cell with two IS and mitotic spindle oscillations in *C. elegans*. In both cases, the cell exhibits two distinct areas of dynein accumulation. Moreover, the processes are influenced by the DI, since MTs growing and shrinking influence the number of MTs reaching the plasma membrane and the interaction. In both cases, the MTOC oscillates since it is pulled to one side and then pushed back to the central location by restoring forces that are at least partially provided by dyneins at the distant location.

To conclude, the MTOC dynamics in various biological functions often result from the interplay of MTs and dyneins. However, it would be a mistake to consider the MTOC dynamics completely different from other dynamic processes in the cell, since they employ similar mechanisms, which can be exemplified by the nuclear oscillations in *S.pombe* [613–615]. The analysis of the intracellular dynamics and interplay between motors and cytoskeleton filaments will certainly provide exciting topics for future research.

Chapter 3.

Computational model

Contents

3.1. Model of the cell with one immunological synapse	47
3.2. Model of the cell with two immunological synapses	48
3.3. Model of the microtubule	50
3.4. Model of the MTOC	51
3.5. Model of the dynein	52
3.6. Constrained Langevin dynamics	54
3.7. Projection with the constraints	55
3.8. Code and calculations	56

3.1. Model of the cell with one immunological synapse

We want to model a cell comprising the following elements: the plasma membrane, nucleus, microtubules (MTs), MTOC, IS, and dyneins. We model the membrane and the nucleus as two concentric spheres with the radii $R_{\text{Cell}} = 5\mu\text{m}$ and $R_{\text{nuc}} = 3.8\mu\text{m}$, respectively. The movement of MTs is confined between the plasma membrane and the nucleus and they are pulled by dyneins located in the IS via two mechanisms. The IS is divided into two areas: the center, where the dyneins pulling via the capture-shrinkage mechanism are located, and the whole IS, where dyneins pull via the cortical sliding mechanism, sketched in Fig. 3.1. The regions are modeled as intersections of the cell membrane with two cylinders with the same axis with radii $R_{\text{IS}} = 2\mu\text{m}$ for the complete IS and $R_{\text{CIS}} = 0.4\mu\text{m}$ for the central region.

The computational model of the cytoskeleton consists of a variable number of MTs sprouting from the rigid MTOC, sketched in Figs. 3.1a and d. In our model, MTs are represented by a bead-rod model with the flexural rigidity $2.2 \times 10^{-23}\text{Nm}^2$ [91]. MTs move under the influence of several forces: drag, forces of dyneins, noise, and bending. The model of the MT is described in detail in Section 3.3. We use constrained Langevin dynamic to model the motion of the filaments, see Section 3.6.

MTs sprout from the MTOC in every direction. Filaments sprouting in a direction parallel to the cell membrane continue to grow. However, MTs growing in the direction against the membrane or the nucleus soon hit the wall. Such MTs either bend in a direction parallel to the membrane or undergo the MT catastrophe. Long MTs, therefore, appear to sprout from the MTOC in one plane [5]. Consequently, we model the MTOC as a planar structure from which the MTs sprout to the cell's periphery in a direction given by the first segment, see Fig. 3.1d. The model of the MTOC is described in detail in Section 3.4.

Unattached dyneins are represented just by one point on the cell membrane and they scholastically attach to MTs with a rate decreasing with the rising distance from the MT. Attached dynein consists of an anchor point with the fixed position and an attachment point stepping on the MT. They are connected by an elastic stalk whose prolongation determines the force of the dynein. The stepping of the attachment point is stochastic and depends on the magnitude of the force and its orientation. If the force is parallel to the preferred direction of the stepping to the minus end, the dynein steps relatively quickly towards the MTOC. If the force has the opposite direction, the rate of stepping decreases with the increasing dynein force, and the movement stops at a stall force. If the force exceeds the stall force, the attachment point slowly steps to the plus end of the MT. The detachment rate increases exponentially with the force. The dynein model can be found in Section 3.5.

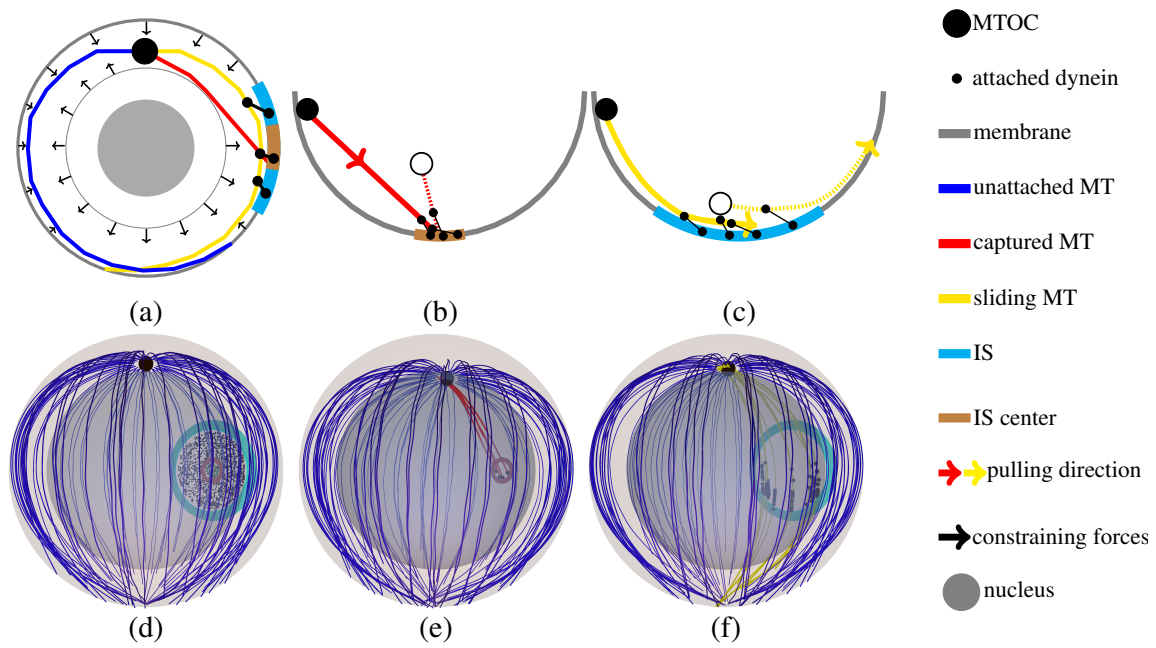


Figure 3.1.: Sketch of the model with one IS. (a) A two-dimensional sketch of the model is shown. MTs sprout from the MTOC to the periphery of the cell. MTs can remain unattached or attach to dyneins and be pulled by cortical sliding or capture-shrinkage mechanisms acting in the center or the whole IS, respectively. (b and c) Two-dimensional sketches of the capture-shrinkage and cortical sliding mechanisms. Small black points on the membrane and on the filaments represent the dynein anchor and attachment points, respectively, connected by the stalk. The filled black circle and the solid line, and the empty circle and the dashed line stand for the MTOC and the MT in earlier and later stage of the process, respectively. (b) Sketch of the capture-shrinkage mechanism. The plus end of the MT is fixated on the membrane and it depolymerizes as the MTOC approaches the IS. (c) Sketch of the cortical sliding mechanism. The plus end of the MT remains free and slides on the cell membrane. (d) A three-dimensional sketch of the cell cytoskeleton is shown. The cyan and brown disks represent the whole IS and its center, respectively. Black dots represent randomly distributed unattached dyneins in the center and the whole IS. (e and f) Three-dimensional sketches of the capture-shrinkage and cortical sliding mechanisms. (e) MTs attached to capture-shrinkage dyneins form a stalk connecting the center and the MTOC. (f) MTs intersecting the IS attach to cortical sliding dyneins located close to the filaments and slide on the cell membrane. Figures (d-f) were made using the simulation software [Hornak2022B].

Dyneins pull the MTs via two distinctive mechanisms. During the capture-shrinkage mechanism, the end of the MT is fixated on the cell membrane where it depolymerizes, sketched in Figs. 3.1b and e. During the cortical sliding mechanism, the plus end of the MT remains free and the MT moves tangentially alongside the cell membrane, sketched in Figs. 3.1c and f.

3.2. Model of the cell with two immunological synapses

This section will familiarize the reader with the augmentations of the model introduced to analyze the MTOC repositioning in the cell with two IS. The configuration of the cell is determined by the angle γ between the axes of the two IS, sketched in Fig. 3.2a. Both IS centers and the center of the cell are located on the xz plane of the coordinate system, sketched in Fig. 3.2c.

The main difference from the model with one IS is that now we have two distant locations where the dynein is accumulated. Dyneins in the same IS cooperate to pull the MTs in the same directions. However, dyneins from the opposite IS are in a constant tug-of-war, visualized in Fig. 3.2b. The consequence of opposing forces is the increase of the dynein force-dependent detachment rate expressed by Eq. 3.20. This may lead to the detachment of all capture-shrinkage dyneins acting on MTs and to the loss of the contact

between MTs plus ends and the plasma membrane. Consequently, contrarily to the previous case, the plus ends of capture-shrinkage MTs are no longer fixated on the plasma membrane when all dyneins detach.

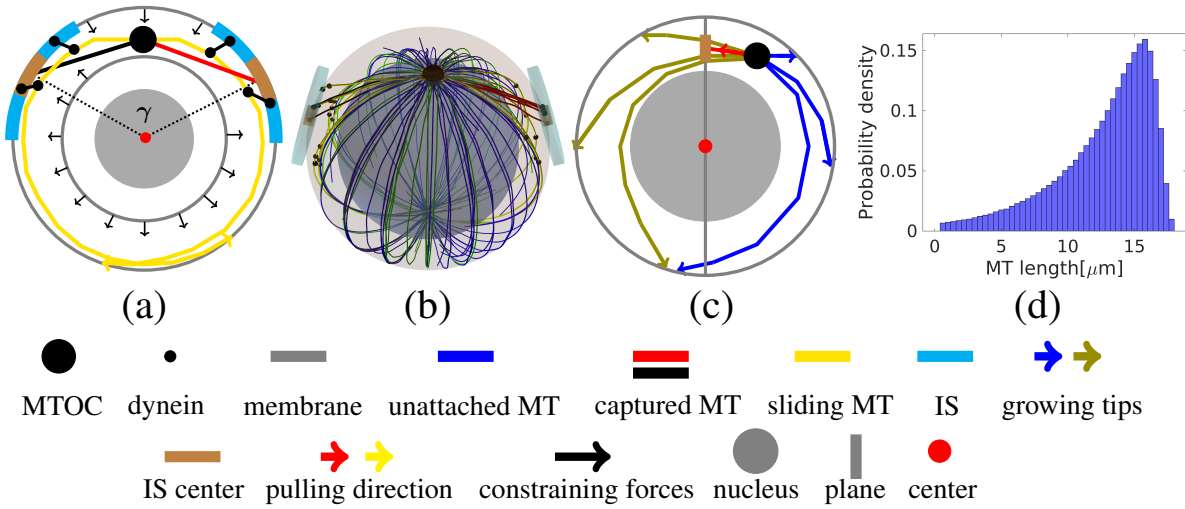


Figure 3.2.: Model of the cell with two IS. (a) A two-dimensional cross-section of the model is given. MTs can attach to dynein in both IS and are pulled by the capture-shrinkage and cortical sliding mechanisms. Small black dots on the filaments and the cell membrane represent attachment and anchor points, respectively, connected by the stalk. The configuration of the cell is defined by the angle γ between the axis of both IS represented by dashed lines. (b) A three-dimensional sketch of the model is given, $\gamma = \frac{2}{3}\pi$. The blue and the green lines denote unattached growing and shrinking MTs, respectively. Attached MTs are pulled by the two mechanisms in both IS. The figure was made using the simulation software [Hornak2022B]. (c) Two dimensional sketch of the growing MTs. The grey line represents the plane where the geometrical centers of both IS and the cell are located. Attached MTs pull the MTOC to the IS. Olive and blue arrows represent the growing tips of MTs pushing the MTOC from and to the IS, respectively. (d) Probability density of the MT length.

The model was augmented by the DI, since we hypothesized that it is indispensable for the MTOC transitions between the two IS. Contrarily to the cortical sliding, the capture-shrinkage mechanism acts in end-on fashion in the narrow center of the IS, sketched in Figs. 3.2a and b. The MT can attach to capture-shrinkage dyneins only when the plus end intersects the center of the IS. It is the permanent reconstruction of the cytoskeleton that allows the plus end of the MT to find the narrow center of the IS. Moreover, DI enables MTs depolymerized during the capture-shrinkage mechanism to regrow. Without the DI, the transitions between the two IS would result in a permanently damaged MT cytoskeleton composed mainly of depolymerized MTs. In our model, the growing and the shrinking speeds and the rescue rate are constant and the catastrophe rate increases with the MT length reflecting a higher catastrophe rate at the cell periphery. The implementation of the DI and its parameters are described in detail in Section 3.3. Fig. 3.2d shows the MT length distribution resulting from the used parameters of the DI. The distribution rises with the MT length until it reaches the maximum at the distance corresponding to the half of the circumference of the cell. Since the tips of MTs attached to cortical sliding dyneins remain free, they can shrink or grow even when attached.

The implementation of DI adds an additional force acting on MTs since the growing tips push against the cell membrane. Contrarily to other forces acting on MTs, this force can push the MTOC from the IS, sketched in Fig. 3.2c.

3.3. Model of the microtubule

We considered the MTs as inextensible since the prolongation of MTs are unlikely to influence the polarization. MTs are pulled by considerable longitudinal forces during the capture-shrinkage mechanism. However, it is hard to imagine that those forces would result in the prolongation of MTs, since their plus end is firmly anchored on the plasma membrane [5] and the rate of depolymerization corresponds to the MTOC speed. Consequently, the elasticity of MTs can hardly influence the MTOC dynamics. The situation is different when it comes to the cortical sliding, when the end of the MT is free and the MT can therefore prolong. However, the cortical sliding dyneins lack the concentration in a narrow place and therefore may exert considerably smaller forces [5]. Moreover, stochastically attached dyneins may pull by the force in the range of pN, which may hardly cause the prolongation of curved MT bound by the plasma membrane. Finally, the pulling force does not have to lead to the prolongation, but they can trigger depolymerization [212]. Consequently, it is unlikely that the MT prolongation influences the MTOC repositioning. Considering the flexural rigidity, I used the value $2.2 \times 10^{-23} \text{Nm}^2$ measured by Gittes et al. [91] giving the persistence length of approximately 5mm, which corresponds to the middle of the range of usually measured values.

We therefore model the MT as an inextensible polymer with a finite resistance to bending. The bending energy can be expressed as:

$$H = \frac{\kappa}{2} \int_0^L \left| \frac{\partial \vec{q}}{\partial s} \right|^2 ds, \quad (3.1)$$

where $\kappa = 2.2 \times 10^{-23} \text{Nm}^2$ is the bending rigidity, L is the length of the MT, $\vec{q} = \frac{\partial \vec{r}}{\partial s}$ is a unit tangent vector along the filament and $\vec{r}(s)$ is a position determined by an arc-length coordinate s [616]. The persistence length of the MT can be expressed:

$$l_p = \frac{\kappa}{k_B T} > 5 \cdot 10^{-3} \text{m}, \quad (3.2)$$

where $k_B = 1.38064852 \times 10^{-23} \text{J} \cdot \text{K}^{-1}$ is the Boltzmann constant and the temperature $T = 300 \text{K}$. The persistence length of the MT is longer than five millimeters and exceeds the diameter of the cell ($\sim 10 \mu\text{m}$) by two orders of magnitude.

The MT is represented by the bead-rod model. The filament is divided into N beads with coordinates $\vec{r}_0, \dots, \vec{r}_{N-1}$ connected by the $N - 1$ segments $\vec{l}_i = \vec{r}_{i+1} - \vec{r}_i$ of the same lengths, sketched in Fig. 3.3. If the MT is not growing or shrinking, the length of the MT and of all the segments is conserved in every step of the simulation:

$$|\vec{r}_i - \vec{r}_{i+1}| = k \quad i = 1, \dots, N - 1, \quad (3.3)$$

where $k = \frac{k}{N-1}$ is the length of the segment. The unit tangent vector between the two beads is expressed as:

$$\vec{q}_i = \frac{\vec{r}_{i+1} - \vec{r}_i}{|\vec{r}_{i+1} - \vec{r}_i|}. \quad (3.4)$$

The Hamiltonian can be discretized expressing the derivative of the unit vector as $\frac{\partial \vec{q}_i}{\partial s} = \frac{\vec{q}_{i+1} - \vec{q}_i}{k}$ we express:

$$\left| \frac{\partial \vec{q}_i}{\partial s} \right|^2 = \left(\frac{\vec{q}_{i+1} - \vec{q}_i}{k} \right)^2 = \frac{1}{k^2} (|\vec{q}_{i+1}|^2 + |\vec{q}_i|^2 - 2\vec{q}_{i+1} \cdot \vec{q}_i) = \frac{2}{k^2} (1 - \vec{q}_{i+1} \cdot \vec{q}_i). \quad (3.5)$$

Consequently, the Hamiltonian of the discretized MT is expressed:

$$H_d = \frac{\kappa}{k} \sum_0^{N-2} (1 - \vec{q}_{i+1} \cdot \vec{q}_i). \quad (3.6)$$

The bending force acting on the i th bead can be expressed as:

$$\vec{F}_i^{bend} = - \frac{\partial H_d}{\partial \vec{r}_i}. \quad (3.7)$$

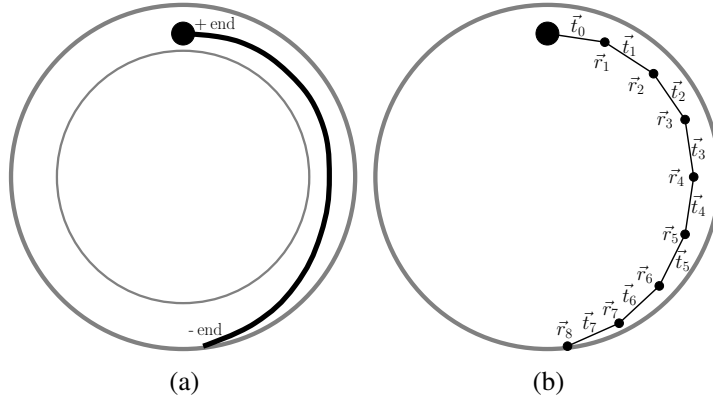


Figure 3.3.: A two-dimensional sketch of the MT discretization is given. The big grey circle, smaller circle and the black sphere represent the plasma membrane, nucleus and the MTOC, respectively. (a) The sketch of the MT in the cell. The MT movement is confined between the nucleus and the plasma membrane. The minus end of the MT is fixated in the MTOC. The plus end pushes against the cell membrane. (b) The sketch of the bead-rod model. The MT is represented by nine beads connected by the segments with the same length. The first bead of the MT is in the proximity of the MTOC.

In the model of the cell with two IS, DI was implemented. In such a case the MT randomly alternates between periods of growing and shrinking. Since the minus end of the MT is anchored in the MTOC, we consider the DI just at the plus end. The MT switches from growing to shrinking and vice versa by the events called catastrophe and rescue, respectively. To model the DI, one needs to define four parameters: polymerization and depolymerization speeds, catastrophe and rescue rates. The speed of the depolymerization (shrinking) is substantially faster than the polymerization (growing) speed and they were estimated as $v_s = 0.2\mu\text{ms}^{-1}$ and $v_g = 0.1\mu\text{ms}^{-1}$, respectively [93, 96, 101, 246, 246, 246, 251, 254, 254–256, 256, 256–262, 262–264, 264–266]. The catastrophe rate increases with the length of the MT and is expressed as:

$$c_r(L) = \exp((L - L_c)/b_c)s^{-1}, \quad (3.8)$$

where $L_c = \pi R_{\text{Cell}} + \frac{R_{\text{Cell}}}{2}$, $b_c = (L_0 - L_c)/\ln(r_c)$, $L_0 = \pi R_{\text{Cell}}$ and $r_c = 0.022$. The rescue rate was estimated as $r_r = 0.044s^{-1}$ [254, 256, 264, 266].

3.4. Model of the MTOC

The MTOC is modeled as a planar structure composed of twenty so-called sprouting points evenly distributed on a circle around the central point with the radius $R_{\text{MTOC}} = 0.5\mu\text{m}$, sketched in Fig. 3.4a. The structure is rigid since the distances between sprouting points and the center and the distances between two neighboring points are kept constant:

$$C_i^{\text{MTOC}} = |\vec{r}_i^{\text{mtoc}} - \vec{r}_c| = R_{\text{MTOC}} \quad i = 1, \dots, Q^{\text{MTOC}}, \quad (3.9)$$

where \vec{r}_i^{mtoc} is the position of the sprouting point, \vec{r}_c is the position of the central point. The distance d^{MTOC} between neighboring points is kept constant by additional Q^{MTOC} constraints:

$$C_i^{\text{MTOC}} = |\vec{r}_i^{\text{mtoc}} - \vec{r}_{i+1}^{\text{mtoc}}| = d^{\text{MTOC}} \quad i = Q^{\text{MTOC}} + 1, \dots, 2 \cdot Q^{\text{MTOC}}. \quad (3.10)$$

MTs sprout tangentially from the MTOC to the cell periphery in all directions. The direction of the sprouting is given by the orientation of the first segment. The second bead of the MT is connected to the sprouting point and the first bead is connected to a so-called "rear" point chosen randomly from the five most distant points of the MTOC, sketched in Fig. 3.4b. Therefore, the direction of the MT sprouting is given by the two points of the MTOC. From every sprouting point the same number of MT arises.

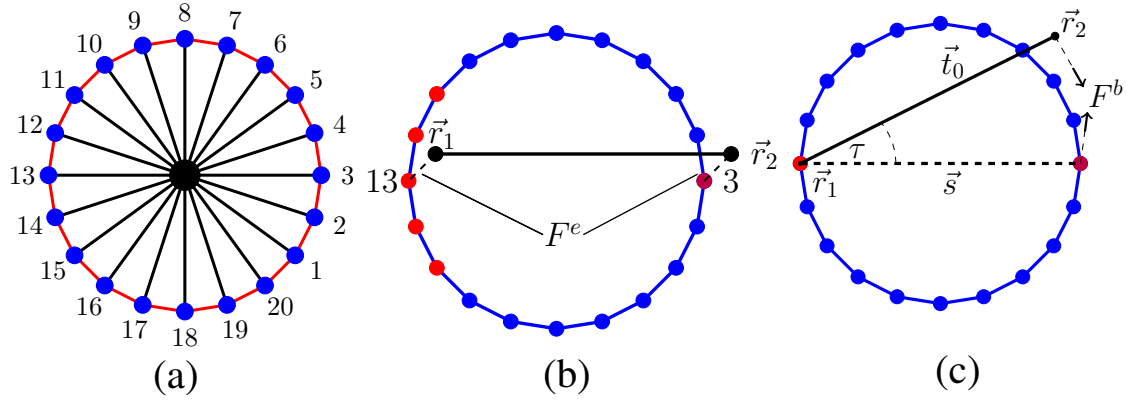


Figure 3.4.: Model of the MTOC. (a) The big black sphere represents the central point of the MTOC and the blue points represent twenty sprouting points. The black and red lines represent the constraints fixing the distance between the sprouting and the central point and between the two neighboring points, respectively. (b-c) Sketch of the forces connecting the MTOC and the MT. The small black dots and the black line represent the first two beads of the MT and the segment connecting them, respectively. The MT sprouts from the MTOC in the direction given by the first segment. The second and the first bead of the MT are connected to so-called sprouting (purple point) and rear point, respectively. The rear point is chosen randomly from the five most distant points (red points). In this case, the first and the second points of the MT are connected to the point 13 and 3, respectively. (b) Sketch of the elastic forces F^e connecting the MTOC and the MT given by the distance between MTOC and MT points depicted by the black dashed line. (c) The sketch of the bending forces F^b between the MT and the MTOC acting on the second bead of the MT and sprouting MTOC point. The bending force is given by the angle τ between the first segment of the MT \vec{t}_0 and the dashed line \vec{s} connecting the sprouting and the rear point. The forces push the beads towards each other decreasing the angle τ .

The first two beads of the MT are connected to the MTOC by elastic and bending forces, sketched in Figs. 3.4b and c. The elastic forces are expressed as:

$$|\vec{F}_2^e| = k_{\text{MTOC}} l_{\text{dm}}, \quad (3.11)$$

where $k_{\text{MTOC}} = 30 \cdot \text{pN}\mu\text{m}^{-1}$ is the chosen elastic modulus and l_{dm} is the distance between the MT and the MTOC points. Bending forces are given by the angle τ between the first segment and the line connecting the sprouting and the rear point, sketched in Fig. 3.4c. Bending forces acting on MT beads can be expressed:

$$\vec{F}_{\text{micro}}^b = \frac{b_{\text{MTOC}}}{|\vec{s}|^2} \left(-\frac{\vec{t}_0}{|\vec{t}_0|} + \frac{\vec{s}}{|\vec{s}|} \left(\frac{\vec{t}_0 \cdot \vec{s}}{|\vec{s}| |\vec{t}_0|} \right) \right), \quad (3.12a)$$

$$\vec{F}_{\text{MTOC}}^b = \frac{b_{\text{MTOC}}}{|\vec{t}_0|^2} \left(\frac{\vec{s}}{|\vec{s}|} - \frac{\vec{t}_0}{|\vec{t}_0|} \left(\frac{\vec{t}_0 \cdot \vec{s}}{|\vec{s}| |\vec{t}_0|} \right) \right), \quad (3.12b)$$

$$\vec{F}_0 = -\vec{F}_{\text{micro}}^b - \vec{F}_{\text{MTOC}}^b, \quad (3.12c)$$

where b_{MTOC} is the bending rigidity, \vec{s} is the segment between the sprouting and the rear points of the MTOC and \vec{t}_0 is the first segment of the MT. The forces \vec{F}_{MTOC}^b and \vec{F}_{micro}^b act on the sprouting point and the second bead of the MT, respectively. The force \vec{F}_0 acts on the first bead of the MT and the rear point of the MTOC.

3.5. Model of the dynein

An unattached dynein is modeled as a point located in the IS on the cell membrane. The attachment probability of the dynein decreases with the distance d_{md} between the point and the MT.

$$p_a = k_a \quad d_{\text{md}} \leq L_0 \quad (3.13)$$

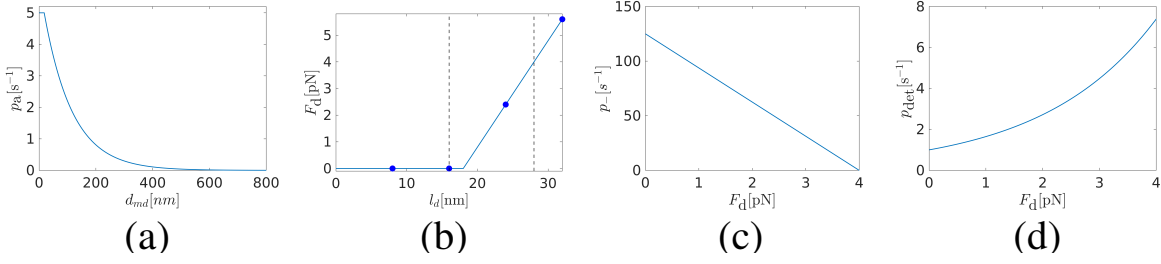


Figure 3.5.: Dynein’s force and rates. (a) The dependence of the attachment rate of dynein p_a on the distance d_{md} between the MT and the unattached dynein calculated using Eq. 3.13. (b) The dependence of the dynein force F_d on the length of the dynein stalk l_d , see Eq. 3.15. The blue points correspond to the lengths of the first fourth steps of the attachment points. The dashed lines represent the lengths of the stalk corresponding to the second step and to the stall force and delimit the probable length of the dynein stalk. (c) The dependence of the stepping rate p_- to the minus end of the MT on the dynein force F_d , see Eq. 3.18. (d) The dependence of the dynein detachment rate p_{det} on the dynein force F_d , see Eq. 3.20.

$$p_a = k_a \cdot \exp(-(d_{md} - L_0)/p_d) \quad d_{md} > L_0, \quad (3.14)$$

where $k_a = 5\text{s}^{-1}$ and $p_d = 0.1\mu\text{m}$ is a chosen parameter. Fig. 3.5a shows the dependence of the attachment probability on MT-dynein distance. The attached dynein consists of the attachment point stepping on the MT and the anchor point with the fixed position in the IS, sketched in Fig. 3.1. They are connected by a stalk whose relaxed length was estimated as $L_0 = 18\text{nm}$ [378, 617–619].

The force of the dynein motor is determined by the elastic properties of the stalk and by its prolongation:

$$F_d = 0 \quad l_d < L_0 \quad (3.15)$$

$$F_d = k_d \cdot (l_d - L_0) \quad l_d \geq L_0, \quad (3.16)$$

where $k_d = 400\text{pN}\mu\text{m}^{-1}$ is the estimated elastic modulus of the stalk [355, 620–623] and $l_d = |\vec{r}_{\text{anchor}} - \vec{r}_{\text{attach}}|$ is the length of the dynein stalk between the anchor and the attachment points. The dependence of the dynein force on the stalk length can be seen in Fig. 3.5b. The attachment point steps to the minus end of the MT with steps of various lengths [384–388, 624]. For the sake of simplicity, we considered the step length $d_{\text{step}} = 8\text{nm}$.

The force and its orientation determine the dynein stepping and the detachment probability. If the force is null or parallel to the preferred orientation of the dynein stepping (to the minus end), the dynein steps to the MTOC with the rate:

$$p_- = \frac{V_F}{d_{\text{step}}}, \quad (3.17)$$

where $V_F = 1000\text{nms}^{-1}$ is the estimated dynein forward speed [379, 382, 384, 385, 389–392, 625]. When the dynein force is opposite to the preferred direction, the rate of the dynein stepping decreases with the force:

$$p_- = \frac{V_F}{d_{\text{step}}} \left(1 - \frac{F_d}{F_S}\right) \quad F_d \leq F_S, \quad (3.18)$$

until it finally stops at the stall force estimated as $F_S = 4\text{pN}$ [384–387, 392, 626, 627], see Fig. 3.5c. If the dynein force $F_d > F_S$, the dynein steps to the plus end of the MT with the stepping rate:

$$p_+ = \frac{V_B}{d_{\text{step}}} \quad F_d \geq F_S, \quad (3.19)$$

where $V_B = 6\text{nms}^{-1}$ is the estimated backward speed [384, 384, 392, 393]. The detachment rate increases exponentially with the force:

$$p_{det} = \exp\left(\frac{F_d}{F_D}\right), \quad (3.20)$$

step	1	2	3	4
l_d [nm]	8	16	24	32
F_d [pN]	0	0	2.4	5.6
p_- [s^{-1}]	125	125	50	+
p_{det} [s^{-1}]	1	1	3.32	16.44

Table 3.1.: Dynein stepping. First row: the number of steps. Second row: distance l_d between the attachment and the anchor point. Third row: the force of dynein F_d . The force is null if $l_d < L_0$. Otherwise, it rises linearly with l_d . Fourth row: The stepping rate p_- to the minus end. The stepping rate decreases with the steps. At the fourth step the dynein stepping to the minus end is no longer possible and the attachment point walks to the plus end. Fifth row: The detachment rate rises exponentially with the distance.

where $F_D = 2\text{pN}$ is the estimated detachment force [392, 393, 628]. The dependence of the detachment rate on the force can be seen in Fig. 3.5d.

Fig. 3.5b and Table 3.1 show that the dynein force is zero at the first two steps, since the corresponding distances are smaller than the length of the relaxed stalk, see Eq. 3.15. Due to the high stepping rates at zero load given by Eq. 3.17, the dynein makes the first two steps very quickly. As the dynein force increases, the stepping rate to the minus end decreases and the detachment rate increases, see Figs. 3.5c and d and Table 3.1. Consequently, the distance between the anchor and the attachment point in the large majority of cases can be expected as $16\text{nm} < l_d < 28\text{nm}$, where the distance of 28nm corresponds to the stall force, see Fig. 3.5b.

3.6. Constrained Langevin dynamics

The motion of an unconstrained particle described with inertiales Langevin dynamics is expressed as:

$$\gamma \dot{x}_i = f_i + \eta_i, \quad (3.21)$$

where x_i is the position of the particle and η_i is a stochastic Langevin force, which is a non-differentiable function of time integrating random interactions with the molecules of the solvent, f_i is the sum of all other forces and γ is the drag coefficient of the particle.

In a constrained case, the molecule of N beads is bound by Q constraints [629]:

$$C_a(x_1, \dots, x_{3*N}) = c_a \quad a = 1, \dots, Q, \quad (3.22)$$

where c_a is a constant. Consequently, the movement of the beads must satisfy:

$$0 = \dot{C}_a = n_{ia} \cdot \dot{x}_i \quad a = 1, \dots, Q \quad (3.23)$$

where the matrix

$$n_{ia} = \frac{\partial C_a}{\partial x_i}. \quad (3.24)$$

Eq. 3.23 describes the simple requirement that the constraints must be kept constant. Consequently, the movement must be perpendicular to all constraints whose derivatives are expressed in the matrix in Eq. 3.24.

We can express the motion of the constrained particle as:

$$\gamma \dot{x}_i = f_i + \eta_i - n_{ia} \lambda_a, \quad (3.25)$$

where λ_a is the constraint force conjugate to the constraint a . Using the mobility tensor

$$H_{ik} = \frac{\mathbf{I}_{ik}}{\gamma}, \quad (3.26)$$

where \mathbf{I}_{ik} is the identity matrix, the equation 3.25 can be expressed as:

$$\dot{x}_i = H_{ij}[F_j^u - n_{ja}\lambda_a], \quad (3.27)$$

where $F_j^u = f_j + \eta_j$ is the unconstrained force acting on a particle. The instantaneous values of the forces λ_a are determined so that the constraints 3.23 are satisfied. This leads to the set of algebraic equations:

$$G_{a\nu}\lambda_\nu = n_{ia}H_{ij}F_j^u, \quad (3.28)$$

where

$$G_{a\nu} = n_{ia}H_{ij}n_{j\nu}. \quad (3.29)$$

Using the resulting values of the constrain forces, the equation of motion 3.27 can be expressed as:

$$\dot{x}_i = P_{ij}H_{jk}F_k^u, \quad (3.30)$$

where

$$P_{ij} = \mathbf{I}_{ij} - H_{ik}n_{ka}G_{a\nu}^{-1}n_{j\nu} \quad (3.31)$$

is a projection operator. If all the beads have an isotropic friction and the mobility tensor is expressed by (3.26), the projection operator 3.31 can be rewritten as:

$$P_{ij} = \mathbf{I}_{ij} - n_{ia}T_{a\nu}^{-1}n_{j\nu}, \quad (3.32)$$

where

$$T_{a\nu} = n_{ka}n_{k\nu}. \quad (3.33)$$

When expressing the motion of the beads using the projection operator, the forces are locally tangent to the $3N - Q$ dimensional hypersurface confining the system and the motion is perpendicular to the constraints.

3.7. Projection with the constraints

The coordinates of the fiber with N beads are stored in the vector $x = \{x_0, x_1, x_2, x_3, x_4, x_5, \dots\}$ of $3 \cdot N$ dimensions, the coordinates $\{x_0, x_1, x_2\}$ correspond to the first bead $\vec{r}_0 = \{x_0, x_1, x_2\}$, and $\{x_3, x_4, x_5\}$ to the second bead $\vec{r}_1 = \{x_3, x_4, x_5\}$. The constraint keeping the distance between the two particles can be expressed $C_0 = |\vec{r}_1 - \vec{r}_0| - k = \sqrt{(x_3 - x_0)^2 + (x_4 - x_1)^2 + (x_5 - x_2)^2} - k = 0$, where k is the fixed length of the segment. Its derivative with respect to x_0 is $\frac{\partial C_0}{\partial x_0} = \frac{x_0 - x_3}{|\vec{r}_1 - \vec{r}_0|} = \frac{x_0 - x_3}{k}$.

The movement of N beads of the MT is limited by $Q = N - 1$ constraints. Jacobian matrix $J_{ai} = \frac{\partial C_a}{\partial x_i}$ has dimensions $Q \times 3N$ and can be expressed as:

$$J = \frac{1}{k} \begin{pmatrix} x_0 - x_3 & x_1 - x_4 & x_2 - x_5 & x_3 - x_0 & x_4 - x_1 & x_5 - x_2 & 0 & 0 & 0 & \dots \\ 0 & 0 & 0 & x_3 - x_6 & x_4 - x_7 & x_5 - x_8 & x_6 - x_3 & x_7 - x_4 & x_8 - x_5 & \dots \\ \vdots & & & & & & & & & \ddots \end{pmatrix}. \quad (3.34)$$

The transposition of the Jacobi matrix results in the matrix n_{ia} , see Eq. 3.24. The matrix $T_{a\nu} = n_{ia}n_{i\nu}$ has dimensions $Q \times Q$ and it is a three-diagonal, symmetrical matrix:

$$T = \begin{pmatrix} 2 & -\vec{q}_0 \cdot \vec{q}_1 & 0 & 0 & \dots \\ -\vec{q}_0 \cdot \vec{q}_1 & 2 & -\vec{q}_1 \cdot \vec{q}_2 & 0 & \dots \\ 0 & -\vec{q}_1 \cdot \vec{q}_2 & 2 & -\vec{q}_2 \cdot \vec{q}_3 & \dots \\ 0 & 0 & -\vec{q}_2 \cdot \vec{q}_3 & 2 & \dots \\ \vdots & & & & \ddots \end{pmatrix}, \quad (3.35)$$

where

$$\vec{q}_i = \frac{\vec{r}_{i+1} - \vec{r}_i}{|\vec{r}_{i+1} - \vec{r}_i|}. \quad (3.36)$$

is the unit tangent vector. Consequently, $\vec{q}_i \cdot \vec{q}_{i+1}$ are the scalar products of the unit vectors expressing the orientations of neighboring segments. The projection operator is then calculated using matrices n_{ia} and T , see Eq. 3.32.

3.8. Code and calculations

The program listing is publicly available on GitHub [[Hornak2022B](#)]. I implemented the model in C++ on a computer cluster with Intel(R) Xeon(R) CPU E5-2660 0 @ 2.20GH processors, Linux operating system (Arch-Linux 4.1.7-hardened-r1) and compiler g++ 4.9.2 and performed simulation runs to generate the data shown in this publication. I prepared various movies and snapshots to visualize different simulations. The movies were made using the following steps: At specific times during the simulations the entire configuration of the system was saved. Consequently, Python was used to create POV-Ray files to generate snapshots that were later connected to create the movies.

Chapter 4.

Summary

Contents

4.1. Stochastic Model of T Cell Repolarization during Target Elimination (I)	57
4.2. Stochastic Model of T Cell Repolarization during Target Elimination (II)	59
4.3. Cytoskeleton rotation relocates mitochondria to the immunological synapse and increases calcium signals	62

4.1. Stochastic Model of T Cell Repolarization during Target Elimination (I)

The original research article was published on 7th April 2020 by the Biophysical Journal [Hornak2020]. I reprinted the article with permission from Elsevier, see Appendix B.

Summary

CTLs play a key role in our immune system since they are responsible for the elimination of the APC. The destruction takes place in three subsequent steps. First, the CTL establishes the IS composed of multiple activation clusters [81, 82, 114, 630]. Second, the CTL polarizes by rotating the MT cytoskeleton and repositioning the MTOC towards the IS under the influence of forces acting on microtubules [5–8]. Third, the CTL releases the lytic granules towards the APC leading to its death [11, 12, 555]. The dynein motor protein is indispensable for repositioning. Dynein steps on the MT while being anchored in the IS thus pulling the MTOC towards the IS. It was proposed that dynein acts via cortical sliding mechanism [118, 121], during which the free plus-end of the MT slides on the cell membrane. The IS periphery was indicated as the region where dyneins attach to MTs [9, 118]. It was suggested that dyneins are located at the periphery to facilitate interactions with MTs. Yi et al. [5] performed experiments in a specific configuration, in which the MTOC and the IS were initially diametrically opposed. They identified the capture-shrinkage mechanism as the main driving force. During this mechanism dynein acts in an end-on with the plus end of the MT fixated on the plasma membrane where it depolymerizes. Contrarily to cortical sliding, capture-shrinkage dyneins are located in the narrow center of the IS. Yi et al. also reported that the repositioning is biphasic since the MTOC movement changes orientation and substantially slows down when the MTOC is approximately $2\mu\text{m}$ from the IS.

Although it was observed in multiple experiments, many aspects of the internal mechanisms of the MTOC repositioning remained poorly understood. We investigated the MTOC repositioning during the targeted killing in the framework of a quantitative theoretical model for the molecular-motor-driven motion of the MT cytoskeleton. The MTOC repositioning is a complex interplay between molecular motors and the MT cytoskeleton composed of hundred of MTs. One MT can achieve the lengths approximately corresponding to half of the circumference of the CTL. Atomistic models offer the most accurate description of biopolymers, see Section 2.3.2. However, due to several reasons such as the computational costs, they are not suitable to model the complex network of long filaments. Additionally, the MTOC repositioning is a process that takes several minutes. Due to the complexity of our problem and timescale, we chose coarse-grained models. In our model, MTs are represented by a bead-rod model and their movement is modeled using constrained Langevin dynamics. The MT moves under the influence of bending, dynein forces, drag, stochastic forces, and restricting forces keeping them between the nucleus and the plasma membrane. Since the MTOC repositioning is relatively fast, the growth

and the shrinkage of MTs were neglected. MTs are connected to the MTOC modeled as a planar rigid structure. The attached dynein is represented by the fixed anchor point and the attachment point stepping on the MT and its force increases with the length of the stalk. The capture-shrinkage and cortical sliding dyneins are located in the center and the whole IS, respectively. The center and the whole IS are modeled as intersections of the cell sphere with two cylinders with the same axis, the radius of the center is five times smaller than the one of the IS. We analyzed the repositioning in the configuration, where the MTOC and the IS are initially diametrically opposed, which corresponds to the setup used in [5].

We started with the investigation of a situation when only the capture-shrinkage mechanism is present. In the first seconds of the simulations, the tips of MTs attach in the center of the IS. After the attachment to dynein, the attached MTs sprout from the MTOC in all directions. They are pulled by dynein, depolymerize and press the MTOC against the nucleus. Subsequently, the MTOC slides on the nucleus as it is pulled towards the IS. Attached MTs form a narrow stalk connecting the MTOC and the IS. Unattached MTs are pushed back by friction forces and, consequently, the MT cytoskeleton "opens". Such a change in MT cytoskeleton morphology, the cytoskeleton "opening", was experimentally observed in [5]. As the MTOC repositions to the IS, it gets to the point where the nucleus does not stand between the MTOC and the IS, corresponding approximately to the half of original MTOC-IS distance. Subsequently, the MTOC slows down and recedes from the nucleus, and is pulled by dynein to the plasma membrane. Therefore, one observes the decrease of the MTOC speed and the change of the direction of the movement as was previously reported in [5]. The slowing down of the MTOC at the end of the repositioning is caused by the detachment of dyneins. As the MTOC recedes from the nucleus, the whole cytoskeleton is dragged towards the plasma membrane and providing a new opposing force leading to dynein detachment. Therefore, we managed to recreate experimental observations and suggest an explanation. Intuitively, the speed of the MTOC rises with dynein density increasing the pulling force.

When the cortical sliding mechanism acts independently, one observes different behavior for low, medium, and high densities. When the densities are low, the MTOC speed increases with the density. In the area of medium densities, the repositioning is very fast and the dynamics is more complex. The MTOC moves to the IS, passes its center and returns back. In the area of high densities, the MTOC speed decreases with the dynein density. The three different behaviors are caused by the changes in cytoskeleton structure dependent on dynein density. In the area of low densities, only a fraction of MTs remains attached to dyneins, form a stalk and pull the MTOC to the IS. In the area of medium densities, dyneins are strong enough to hold a majority of MTs. Consequently, MTs bend to assume direction partially aligned with the MTOC movement. The large stalk results in strong forces leading to the fast movement, visualized in Fig. 4.1. Due to this large stalk, many MTs are attached at the end of the repositioning, pulling the MTOC pass the IS center to the periphery. When they detach, the MTOC is pulled back, see Fig. 4.1c. In the region of high densities, dyneins forces are strong to hold almost every microtubule pulling the MTOC in all directions. In such a case, the direction of the MTOC motion is not established and forces act in contradiction slowing down the MTOC movement. In our simulations, unattached dyneins were distributed uniformly in the IS. However, the attached cortical sliding dyneins are located predominantly at the IS periphery.

We compared the two mechanisms in terms of times and the final MTOC-IS distance indicating the efficiency of dynein force transmission and the completion of the repositioning, respectively. The times of capture-shrinkage repositioning are shorter, except with the relatively narrow region of medium densities. Capture-shrinkage always achieves shorter final distances and the difference is substantial in the area of low and high densities. Consequently, the capture-shrinkage mechanism substantially outperforms cortical sliding mechanism, even though the latter employs 25 times more dyneins due to the different dimensions of the IS and its center. Consequently, we report that the capture-shrinkage is largely superior in the considered setup.

Most importantly, we found that the two mechanisms act in a fascinating synergy. Surprisingly, the number of attached dyneins of one mechanism rises with the dynein density of the second mechanism. Cortical sliding mechanism supports the dominant capture-shrinkage by passing the microtubules to the center of the IS, where they can attach to capture-shrinkage dyneins. Capture-shrinkage supports cortical sliding by providing a firm anchor point and by pulling the MTOC to the cell membrane, which leads to the decrease of the distance between the filament and dynein motors resulting in the increase of the

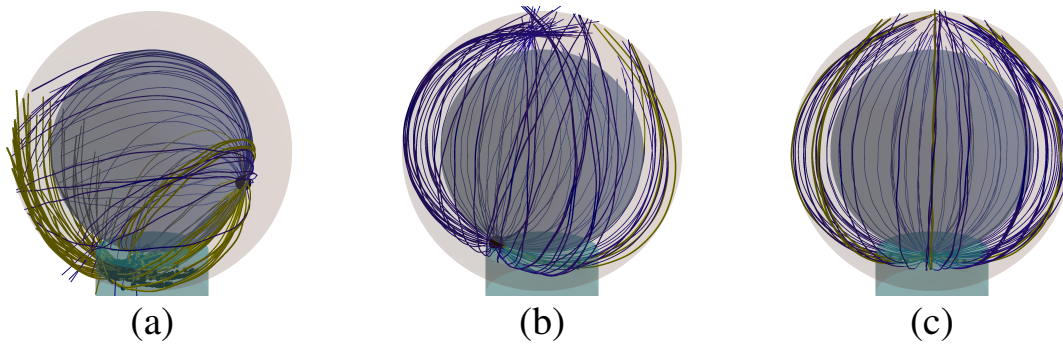


Figure 4.1.: Repositioning of the MTOC in the cell with one IS under the effects of cortical sliding mechanism. Snapshots from the time evolution of the MT cytoskeleton configuration in the cell with the medium cortical sliding dynein density, $\bar{\rho}_{IS} = 200\mu m^{-2}$. The MTOC is indicated by the large black sphere. Cyan cylinder indicates the IS where cortical sliding dyneins are located. Blue and yellow lines are unattached and attached MTs, respectively. The black spheres in the IS are the positions of dyneins attached to MTs. (a) MTOC approaches the IS. (b) MTOC pass the IS. (c) MTOC returns to the center of the IS. The figure was made using the simulation software [Hornak2022B].

attachment probability. This finding answers the role of the cortical sliding in the setup, where the capture-shrinkage mechanism is dominant. The combination of the two mechanisms results in a faster repositioning than a dominant mechanism with a higher dynein density. Consequently, the combination of the two mechanisms can reduce the area densities necessary for the effective repositioning and greatly saves resources.

To summarize, we analyzed the MTOC repositioning in the cell, where the MTOC and the IS are initially diametrically opposed. We confirmed that the capture-shrinkage mechanism is dominant and suggested the explanation for the biphasic nature of the repositioning. The attached cortical sliding dyneins are located predominantly at the periphery of the IS despite the uniform distribution of unattached dyneins. It was hypothesized in [9] that the dyneins are located at the periphery to facilitate the interactions with MTs. Our finding supports the hypothesis. Most importantly, we found that the two mechanisms act in synergy reducing the area densities necessary for the repositioning. Therefore, we found that the CTL performs the basic immune response with a stunning efficiency by employing two synergetically acting mechanisms and by placing the dyneins on the IS periphery.

4.2. Stochastic Model of T Cell Repolarization during Target Elimination (II)

The original research article [Hornak2022] was published on 5th April 2022 by the Biophysical Journal. I reprinted the article with permission from Elsevier, see Appendix B.

Summary

In the previous publication [Hornak2020], we analyzed the MTOC repositioning during the target elimination in the cell, where the MTOC and the IS are initially diametrically opposed, which is the experimental setup used in [5]. Here, we analyze situations that have not yet been analyzed experimentally, in which the angle β between the MTOC and the IS is arbitrary. Moreover, we focus on the MTOC repositioning in the cell with two IS.

The MTOC repositions due to forces of dyneins stepping to the minus-end of MTs while being anchored on the membrane. During the cortical sliding mechanism, the dynein attaches on the whole MT whose plus-end remains free. It was suggested that the dyneins acting via cortical sliding mechanism are anchored at the periphery of the IS [9, 118]. During the capture-shrinkage mechanism, dyneins

located in the narrow center of the IS capture the plus-end of the MT and depolymerize it by pulling it against the cell membrane [5, 122]. CTLs can attack two target cells simultaneously [9]. In such a case, one observes repeated, interrupted MTOC transitions between the two IS. The oscillatory behavior is caused by the accumulation of dyneins at two locations on the plasma membrane. The attachment and detachment of dynein is stochastic and the forces from two IS are in a constant tug-of-war. When one side wins the competition, the MTOC starts the repositioning. The oscillatory behavior of the MTOC is influenced by the MT dynamics. During its lifetime, MT switches randomly between the growing and shrinking in the process termed dynamic instability (DI) [92–102]. The process is indispensable for the transitions between the two IS, since it allows depolymerized MTs to regrow. Here, we analyze the interplay between the constantly evolving MT cytoskeleton and dyneins acting via two mechanisms in two IS to elucidate possible mechanisms leading to the oscillatory, stable, or bi-stable MTOC repositioning.

In the previous work [Hornak2020] we suggested a theoretical simulation model for the relocation of the MTOC after the IS formation. Here, the same model is used to study the repositioning in the cell with varying angle β between the MTOC and the IS. The ensuing enumeration familiarizes the reader with alterations and extensions made in the model to analyze the cytoskeleton dynamics in the cell with two IS. The configuration of such a cell is determined by the angle γ between the axes of both IS which are the lines connecting the center of the cell with the centers of IS. The motors from the different IS are in a tug-of-war increasing the force-detachment rate. The end of the capture-shrinkage MT is released when all dyneins detach. Mainly, we implemented the DI. In our model, the growing and shrinking speeds of the MT and the rescue rate are constant and the catastrophe rate is length-dependent to reflect the higher rate at the cell periphery [103, 250, 267]. Resulting MT length distribution rises monotonously until it reaches a peak at the length corresponding to the half of the cell circumference.

In the cell with one IS, the MTOC speed increases with the dynein density. The only exception is the cortical sliding mechanism when $\beta > 0.85\pi$, which can be explained by the three regimes of cortical sliding repositioning [Hornak2020]. The times of repositioning rise with β until they reach a maximum at $\beta = 0.7\pi$ and then they decrease. The times of repositioning increase with the angle when $\beta < 0.7\pi$ since both the initial MTOC-IS distance and the opposing force of the nucleus increase with β . Moreover, the number of MTs intersecting the IS decrease with the angle when $\beta < 0.5\pi$, resulting in the smaller amount of attached dyneins. The amount of MTs intersecting the IS substantially rises with the angle when $\beta > 0.7\pi$, leading to increased pulling forces compensating longer distances and the times of the MTOC repositioning decrease. The cortical sliding mechanism is faster when $\beta < 0.5\pi$ and substantially slower otherwise. Moreover, we report that the mechanisms act synergetically, since the combination of the two mechanisms with lower densities can outperform the dominant one with a high density. Similarly to the configuration when $\beta = \pi$, attached cortical sliding dyneins are located mainly at the periphery.

In the cell with two IS, when only the capture-shrinkage mechanism is present, the MTOC transitions between the two IS stochastically, but with well defined transition times. The MTOC transitions under the influence of capture-shrinkage mechanism are visualized in Fig 4.2. The underlying mechanism is the decrease of the number of attached dyneins with the decreasing MT length caused by the bending forces. The transition frequency and the MTOC dwell times close to the IS increase and decrease with the dynein density, respectively, since the rising density leads to a faster attachment initiating the new transition and to the increased pulling force resulting in higher MTOC speeds. The frequencies do not decrease monotonously with the distance between the two IS and are the highest when the angle between the two IS $\gamma = \pi$. Such behavior can be explained by the length distribution. As the angle γ rises, more MTs have a length corresponding to the circumferential distance between the two IS resulting in increased numbers of attached dyneins.

The dynamic is completely different when only the cortical sliding is acting. Contrarily to the capture-shrinkage dyneins, cortical sliding dyneins are always attached to MTs and in a constant tug-of-war. At $\gamma < \frac{2\pi}{3}$ the MTOC wiggles around the central position. When $\gamma \geq \frac{2\pi}{3}$ the transition frequency decreases with the angle γ and with the dynein density. If densities are small, the transition frequency is relatively high since the MTOC makes small transitions and does not approach the IS. As the density increases, the MTOC moves closer to the IS making the next transition less likely since the dyneins from the distant IS has to overcome dyneins from the close IS and the opposing force of the nucleus. This opposing force increases with the distance between the two IS causing that the transition frequency decreases

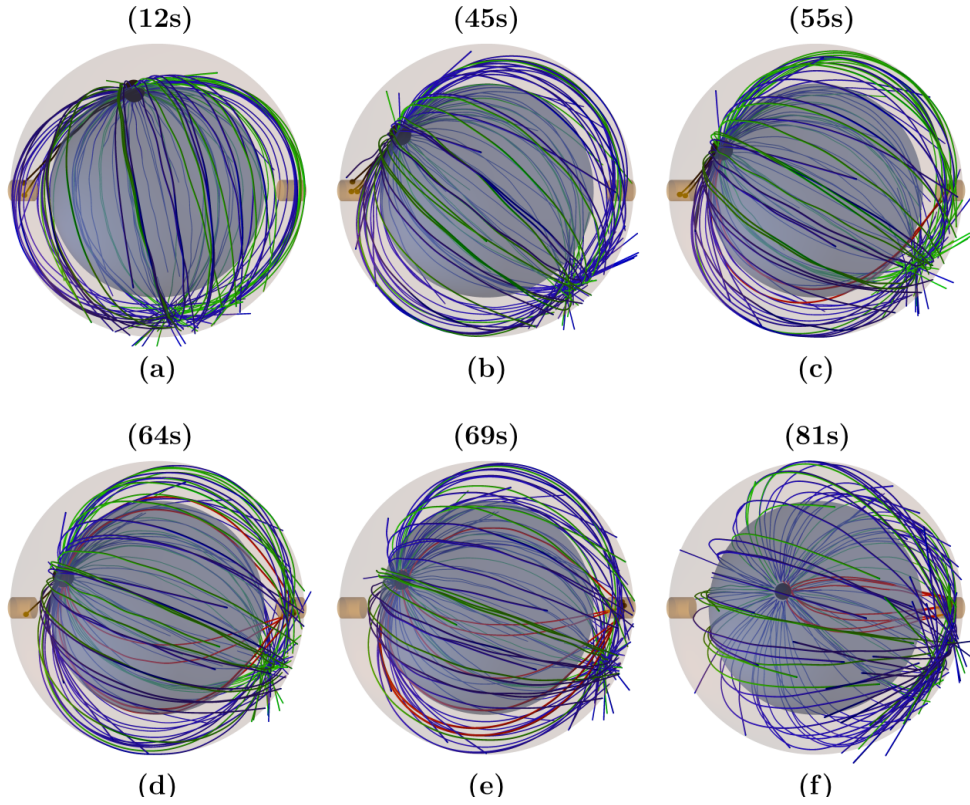


Figure 4.2.: Repositioning of the MTOC in the cell with two IS under the effects of capture-shrinkage mechanism. Snapshots from the time evolution of the MT cytoskeleton configuration in the cell with the same concentration of capture-shrinkage dyneins in both IS, $\rho_{IS}^1 = \rho_{IS}^2 = 400\mu\text{m}^{-2}$. The MTOC is indicated by the large black sphere. Brown cylinders indicate the centers of both IS where capture-shrinkage dyneins are located. Black and red lines represent MTs attached to capture-shrinkage dyneins and blue and green lines indicate growing and shrinking unattached MTs, respectively. Small black spheres in both IS represent attached dyneins. (a) MTs attach to dyneins in the left IS, form a stalk and the MTOC moves towards the left IS. (b) MTOC approaches the IS and MTs depolymerize. (c) Short MTs detach from the left IS. Simultaneously, the plus end of the MT intersect with the center of the distant IS and are captured by dynein. (d) Only one MT remains attached to the dynein in the left IS and additional MTs attach in the right IS. (e) All MTs are detached from the left IS and multiple MTs are attached in the distant IS. (f) MTs stalk is formed and the MTOC moves towards the right IS. The figure was made using the simulation software [Hornak2022B].

with the increasing angle γ . The frequency decreases to zero when $\gamma = \pi$. In such a configuration, the MTOC is pulled to the center of the IS as the density increases. Consequently, almost every MT is attached in the distant IS and dynein forces acting in contradiction prevent the MTOC from transitioning.

We further analyzed the configuration when the capture-shrinkage and the cortical sliding mechanisms are located in different IS. Multiple MTs always intersect relatively large IS and attach to cortical sliding dyneins. Contrarily, the MTs must intersect the narrow center of the IS by their plus-ends to attach to capture-shrinkage dyneins. The transition to the capture-shrinkage IS begins when the capture-shrinkage dyneins acting on multiple MTs overpower cortical sliding dyneins. As the MTOC approaches the IS, captured MTs detach and the MTOC initiates the transition back to the cortical sliding IS. The number of transitions increases with the dynein density if $\gamma < \pi$ due to increased pulling forces. When the two IS are diametrically opposed, the frequency increases until it reaches a maximum and then it decreases. The reason is that as the density increases, the MTOC travels closer to the capture-shrinkage IS and remains there since cortical sliding dyneins from the distant IS oppose each other. The configuration of the cell with different IS offers a way to compare the two mechanisms. In the case of low densities ($< 500\mu\text{m}^{-2}$), the MTOC is located predominantly at the cortical sliding IS. As the density increases, the MTOC

is increasingly located at the capture-shrinkage IS, indicating that the capture-shrinkage mechanism gains the upper hand. Consequently, the cortical sliding mechanism is stronger only when densities are low.

The transition frequency is the highest and the dwell times are the lowest when the two mechanisms act together. The reason is that at the end of the transition, the two mechanisms act together in the distant IS and against each other in the close IS. When the MTOC finishes transition, captured MTs are depolymerized and detach. Consequently, the capture-shrinkage dyneins remain unattached and cortical sliding dyneins act on a reduced number of MTs. Contrarily, both mechanisms share the load of opposing forces in the distant IS lowering their detachment rate. The transition frequency rises with the dynein density and, similarly to the case of capture-shrinkage, does not decrease with the angle γ and is the highest when $\gamma = \pi$.

To conclude, we found that the CTL performs repositioning with a stunning efficiency by employing the two mechanisms performing differently in various configurations of the cell. The combination of two synergistically acting mechanisms and the placement of dyneins at the IS periphery form an efficient machinery performing the basic immune response efficiency while saving resources. In the cell with the two IS, our model predicts that the MTOC transitions only when the capture-shrinkage mechanism is present at least in one IS. The behavior is the simplest when only the capture-shrinkage mechanism is present in both IS, since the MTOC transitions between the two IS in almost deterministic manner. Interrupted, incomplete transitions at small angle γ and long dwelling times close to one IS at high angle γ are typical for the cortical sliding mechanism. The synergy of the two mechanisms assure fast transitions between the two IS allowing the CTL to quickly kill two target cells simultaneously.

4.3. Cytoskeleton rotation relocates mitochondria to the immunological synapse and increases calcium signals

The original article [Hornak2016] was available online on 7th July 2016 by Cell Calcium. I reprinted the article with permission from Elsevier, see Appendix B.

Summary

Spatially resolved Ca^{2+} signals and Ca^{2+} microdomains are highly relevant for cellular functions. In T Cells, Ca^{2+} signaling after the IS formation is indispensable for downstream effector functions. During the polarization, the MT cytoskeleton rotates to reposition the MTOC towards the IS due to the forces of dynein motors [5, 121, 124]. Since Golgi apparatus, ER, and mitochondria are connected to MTs, they are dragged along with the cytoskeleton [631–636]. Therefore, the polarization is a complex process involving a massive rearrangement of the internal structure of the cell. Various signaling steps determining the CTL targeted killing depends on Ca^{2+} including the MTOC repositioning and the release of lytic granules [5, 124]. CRAC/Orai channels are the main source of the Ca^{2+} in the cell [157, 158]. The influx of Ca^{2+} through the Orai1 channels located at the IS is also controlled by the positions of mitochondria. Due to their functionality of absorption and redistribution, mitochondria acts as Ca^{2+} sinks at the IS [160, 169]. Consequently, they control local Ca^{2+} concentration and also Ca^{2+} dependent activity of CRAC channels. Absorbed Ca^{2+} is redistributed to the cytosol increasing the global concentration in the cell [160]. Here, we present the evidence that the rotation of the cytoskeleton during the MTOC repositioning is correlated with the relocation of mitochondria to the IS. Subsequently, we include the rotation into the model proposed in [156] and we analyze the dependence of the local and global Ca^{2+} concentrations on the angle of rotation of the mitochondria spindle.

First, we hypothesized that the rotation of the MT cytoskeleton and the relocation of mitochondria are correlated. In our experiments, T Cells were conjugated with APCs and the relocation of the fluorescently labeled MTs and mitochondria were visualized by the time-lapse microscopy. We found that after the IS formations, mitochondria location is closely connected with MTs and they were relocated towards the IS with the MT cytoskeleton rotation. These results support the aforementioned hypothesis.

We further hypothesized that the changes in the local Ca^{2+} concentration in the microdomain around the IS and the global concentration are connected to the mitochondria translation and their functionality

of absorption and redistribution. We developed a mathematical three-dimensional model for the spatio-temporal Ca^{2+} distribution in the cytosol, ER, and mitochondria. In our model, the cell membrane and the nucleus are represented by two concentric spheres. The mitochondria are represented by prolonged, thin compartments between the cell membrane and the nucleus and they form spindle-like arrangements motivated by their attachment to MTs sprouting from the MTOC. The IS is represented by a small circular region. Mitochondria spindle can be rotated by an angle around a chosen axis, the zero angle corresponds to the configuration where the spindle and the IS have the same axis. The compartments can exchange Ca^{2+} via channels and pumps. CRAC channels are located in the narrow center of the IS. PMCA pumps are in-homogeneously distributed on the cell membrane and we vary the percentage located at the IS. The outflux from the cell through PMCA pumps increases with the Ca^{2+} concentration. The effect of SERCA pumps and IP_3 receptors are modeled by in- and out-flux densities on the ER.

Using the model, we computed stationary distributions of Ca^{2+} in the experimental situation with blocked SERCA pumps, empty ER, and fully activated CRAC channels. When the spindle is fully polarized (zero spindle-IS angle), the global concentration increases and local concentration decreases with decreasing distance between the tips of mitochondria and the CRAC channels. Similarly, the local and global concentrations decrease and increase, respectively, with the decreasing spindle-IS angle. In both cases, the increase of the global concentration becomes more pronounced with the increasing PMCA pumps accumulation level at the IS. The reason is that the concentration of mitochondria is the biggest at the center of the spindle, which approaches the CRAC channels as the angle decreases. Mitochondria enter the microdomain under the IS and absorb Ca^{2+} lowering its local concentration. Mitochondria then redistribute Ca^{2+} to the rest of the cell, where fewer PMCA pumps are placed increasing the global concentration.

Subsequently, we extended our model with an immobile ER located underneath the IS. The ER was modeled using two distinctive geometries: one as a truncated cone, the other spindle-like. Under certain physiological conditions, an external stimulus can increase the cytosolic IP_3 concentration. Subsequently, IP_3 bind to the receptors on the surface of the ER permitting the Ca^{2+} outflux through the channel domain. To consider the negative feedback that the increased cytosolic Ca^{2+} concentration has on the IP_3 receptor channel capacity, the IP_3 flux depends on Ca^{2+} concentration. The influx of the CRAC channel decreases with increasing Ca^{2+} concentrations in the microdomain around the IS and in the ER [637]. When the concentration of the Ca^{2+} in the ER decreases, it is replenished by SERCAs.

We used the extended model to analyze Ca^{2+} dynamics under more physiologically relevant conditions in which SERCAs are not blocked. Moreover, an external stimulus is present for a certain time. We compute the time development of the Ca^{2+} concentration in various cellular compartments for different spindle-IS angles. The cytosolic Ca^{2+} concentration increases sharply after the beginning of the stimulus and then it decreases slightly until it reaches a plateau. The decrease deepens with the increasing spindle-IS angle. Local Ca^{2+} concentration rises at the beginning of the stimulus until it reaches a plateau value increasing with the spindle-IS angle. The decrease of the global and the increase of the local concentration with the angle is consistent with the previous results with blocked SERCAs and also with experimental results with unblocked SERCAs [160]. Both increase and decrease become more pronounced with the rising PMCA pumps accumulation at the IS. The ER concentration decreases after the beginning of the stimulus and the release of the Ca^{2+} from the ER contributes to the initial increase of global concentration. The increase of the cytosolic Ca^{2+} concentration permits SERCAs to replenish the ER. Consequently, the Ca^{2+} concentration in the ER decreases with the increasing spindle-IS angle, since PMCA pumps exports Ca^{2+} from the cell in the absence of mitochondria. After the end of the stimulus, Ca^{2+} concentrations in all compartments return to the baseline. The results were similar for both ER geometries indicating that the described effects are independent of the detailed changes of the ER shape.

To summarize, we found that mitochondria relocates towards the IS and their movement is correlated with the rotation of the MT cytoskeleton. We analyzed the Ca^{2+} dynamics with the compartment model of the cell including specific geometries of the mitochondria, IS and ER, model is sketched in Fig 4.3. The simulations predict the increase of the global and the decrease of the local Ca^{2+} concentrations when the center of mitochondria spindle approaches the IS, which is in agreement with experimental results [160]. Since the effect persists when the SERCAs are activated, we conclude that the ER does not control local and global Ca^{2+} concentrations after the T Cell activation, which is in agreement with the experimental

results [160]. Hoth et al. [638] demonstrated that in the cell with no IS formation or PMCA pumps accumulation CRAC channels partially inactivate if mitochondria do not accumulate Ca^{2+} . Our model predicts that in the case of the IS formation the changes in the activity of CRAC do not explain the control of the global and the local Ca^{2+} concentrations by mitochondria. However, PMCA pumps enrichment at the IS is indispensable. Consequently, the model demonstrates a hierarchy for the incoming Ca^{2+} after the IS formation. If the mitochondria are located at the IS, they absorb the majority of Ca^{2+} entering the cell. If they are absent, PMCA pumps export Ca^{2+} out of the cell. In the case when both PMCA pumps and mitochondria are absent, ER absorbs the Ca^{2+} via SERCAs finally inactivating the CRAC channels. To conclude, in the experimentally described setup where CRAC, mitochondria, PMCA pumps, and ER are localized close to the IS, Ca^{2+} gets deeper into the cytosol and its concentration at the IS is controlled.

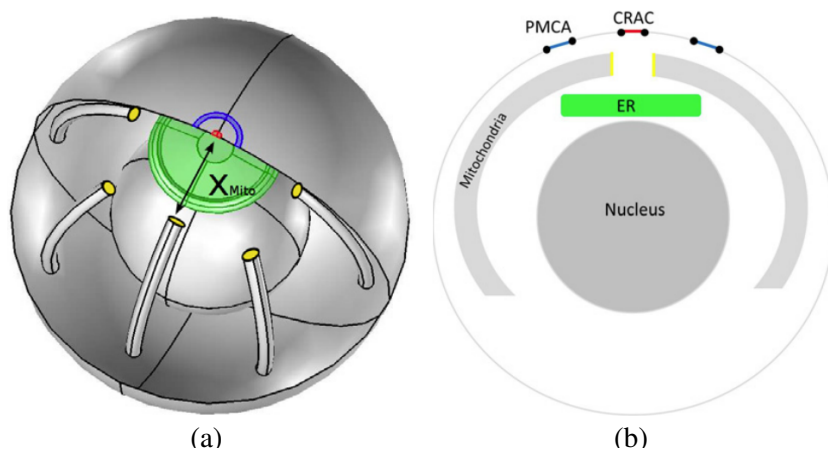


Figure 4.3.: Model for the analysis of Ca^{2+} diffusion in the T Cell. (a) The geometry of 3D model analyzing the influence of the mitochondria relocation on Ca^{2+} influx to the cell. The outer sphere, inner sphere and the circular region at the top of the cell represent the plasma membrane, nucleus and the IS, respectively. CRAC channels (red) and the PMCA pumps (blue) accumulate around the IS. The green compartment stands for the ER and the long rod-like objects with yellow tips represent mitochondria. The distance between the tips of the mitochondria and the center of the IS is denoted by the black double arrow. (b) Two dimensional profile of the geometry of the model. The figure was taken from [156] with the permissions stated in the Appendix C.

Chapter 5.

Summarizing discussions

5.1. What did we achieve?

Here, I provide a concluding discussion about the publications contained in this thesis and outline our achievements and contributions to the scientific community. I intend to put our most important results in a scientific context and suggest future possibilities.

Our model recapitulates several biological observations like the "opening" of the MT cytoskeleton [Hornak2020]. In the experiments, the plus ends of MTs intersecting the center of the IS attach to dynein and are pulled by the capture-shrinkage mechanism. Subsequently, they straighten and form a stalk connecting the MTOC and the IS. As the MTOC approaches the IS, the MTs in the stalk depolymerize. During the MT cytoskeleton rotation, unattached MTs are pushed back and the cytoskeleton "opens", see Fig. 1.4. We suggest that the "opening" of the cytoskeleton is caused by friction forces pushing unattached MTs back. This seemingly trivial process can have far-reaching consequences for the Ca^{2+} signaling in the cell. The CRAC channel is the main entry point for Ca^{2+} to the T Cell, see Section 1. Ca^{2+} is then absorbed and redistributed by the mitochondria relocated to the IS with the MTOC. Previous works including Peglow et al. [156] assumed the symmetric arrangement of mitochondria around the IS, which would imply that the Ca^{2+} is symmetrically distributed to the cell. MT cytoskeleton "opening" results in an asymmetric distribution of mitochondria around the IS, as was observed in [Hornak2016]. It is likely that the asymmetric positioning of mitochondria around the IS will result in an asymmetric absorption and redistribution of Ca^{2+} to the cell. This asymmetry might have profound consequences and may deserve further investigation.

The Ca^{2+} signaling in the T Cell is a complex process that plays a key role in a large array of cellular functions. However, I believe that our work contributed to this vivid field. Mainly, we demonstrated that the mitochondria are repositioned with the MTOC to the IS [Hornak2016]. Our model predicts that due to their ability of absorption and redistribution, the mitochondria reduce the local Ca^{2+} concentration in the microdomain around the CRAC channel and increase the global cytosolic concentration. In the cell configuration, where the CRAC channels, PMCA pumps, mitochondria, and ER are localized close to the IS, cytosolic Ca^{2+} concentration increases.

Yi et al. [5] reported that the MTOC repositioning can be divided into two phases. During the polarization phase, the MTOC travels quickly in a circular motion around the nucleus. In the docking phase, in which the MTOC travels approximately the last $2\mu\text{m}$, the MTOC moves slowly in a direct movement from the nucleus to the IS. Yi et al. hypothesized that the repulsive force emerges at the transition point between the two phases. The source of that force was elusive. One possible candidate is the actin network under the plasma membrane. Sanchez et al. observed that the actin is depleted from the center of the IS [182]. However, the interaction of the MTOC and MTs with actin ring on the periphery of the IS may slow down the movement. This biphasic movement was predicted by our model. We observed the gradual decrease of the MTOC speed and the change of the movement orientation, see Figs. 3 and 9 [Hornak2020], sketched in Fig. 5.1. However, our model shows that the emergence of the resistive force is not necessary. The MTOC simply slows down as a result of the gradual dynein detachment caused by the geometry of the cell and the interplay between the MT cytoskeleton and motors.

Combs et al. [118] demonstrated that dyneins are mainly localized on the periphery of the IS. Kuhn et al. [9] hypothesized that one of the reasons for the dynein accumulation at the periphery is to facilitate the interaction with MTs. We can support this hypothesis. In our model, unattached cortical sliding dyneins were uniformly distributed in the IS. However, regardless of the initial MTOC-IS distance MTs attach to

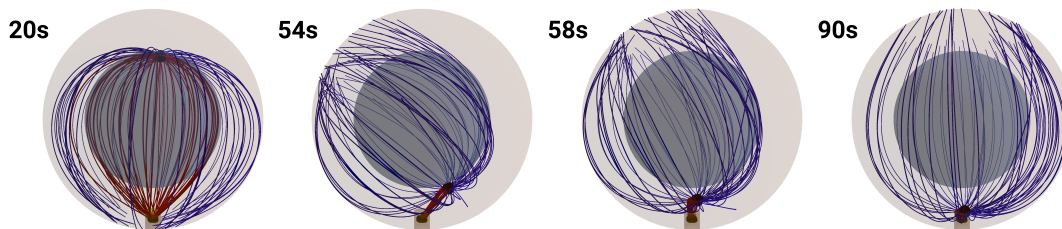


Figure 5.1.: Two phases of the MTOC repositioning. The plasma membrane and the nucleus are denoted by the outer and inner sphere, respectively. The big black sphere represents the MTOC and little black circles in the IS center (brown) stand for dynein. The MTs sprout from the MTOC to the IS periphery. They can remain unattached (blue) or attach (red) to capture-shrinkage dyneins. After 20s of the simulation, the MTOC is pushed to the nucleus by the forces acting on attached MTs. In this case, the polarization phase lasts 34s during which the MTOC transitions to approximately opposite side of the nucleus. The transition into the docking phase takes place between 54s and 58s of the simulation. To overcome the last $1.5\mu\text{m}$ the MTOC needs approximately the same time as to navigate around the entire nucleus. The figure was made using the simulation software [Hornak2022B].

dynein predominantly on the IS periphery, see Figs. 8 in [Hornak2020] and SFig. 8 in the supplementary material of [Hornak2022].

Yi et al. [5] identified the capture-shrinkage mechanism as the main driving force of the repositioning. The authors further asked the question about the role of the cortical sliding mechanism. We compared the two mechanisms in various configurations of the cell defined by the angle β between the initial positions of the MTOC and the IS. We found out that the cortical sliding is dominant when $\beta < \pi$ since it results in a faster repositioning, see Fig. 3 in [Hornak2022]. As the initial MTOC-IS distance increases, the capture-shrinkage mechanism becomes superior. These results confirm the findings from [5] identifying the capture-shrinkage mechanism as the main driving force in the configuration when $\beta = \pi$.

To summarize, we provided possible explanations for the dynein accumulation on the periphery of the IS, the opening of the cytoskeleton, and the biphasic movement. We also provided the analysis of the two mechanisms in various configurations.

Moreover, we also made several predictions. Observation of the MTOC repositioning under the sole influence of the cortical sliding mechanism revealed three different deformation characteristics depending on the dynein density, see Figs. 5, 7, and 8 in [Hornak2020]. This may open a possibility to experimentally investigate the dynein density from the cytoskeleton rotation and morphological changes.

Furthermore, we reported that the two mechanisms act in a synergy enhancing each other's effects. When the capture-shrinkage mechanism acts alone, attached MTs depolymerize, and unattached MTs are pushed back by friction forces resulting in the opening of the MT cytoskeleton. The opening prevents other MTs from intersecting the center of the IS and their attachment to capture-shrinkage dyneins. When the two mechanisms act together, MTs attached to cortical sliding dyneins prevent the friction forces from pushing the MTs and increase the probability that they will intersect the narrow center. Similarly, the capture-shrinkage mechanism helps cortical sliding by providing a firm anchor point and pulling the MTOC and the cytoskeleton to the cell membrane increasing the probability of attachment to cortical sliding dyneins. As was mentioned in Section 4, the synergy greatly saves the resources of the cell and results in a faster repositioning.

In this paragraph, I will outline morphological changes of the MT cytoskeleton induced by the two mechanisms. There is one morphological feature typical for the capture-shrinkage mechanism: the MT stalk connecting the center of the IS with the MTOC, see Fig. 5.2a. Cortical sliding cannot create the narrow stalk of MTs ending in the center of the IS. The cortical sliding mechanism has the advantage over the capture-shrinkage because it can act in the entire IS or large IS periphery. Consequently, a large stalk of MTs passing through the IS is a mark of the cortical sliding mechanism. The combination of the two mechanisms also results in distinctive morphological changes. In the cell where the MTOC and

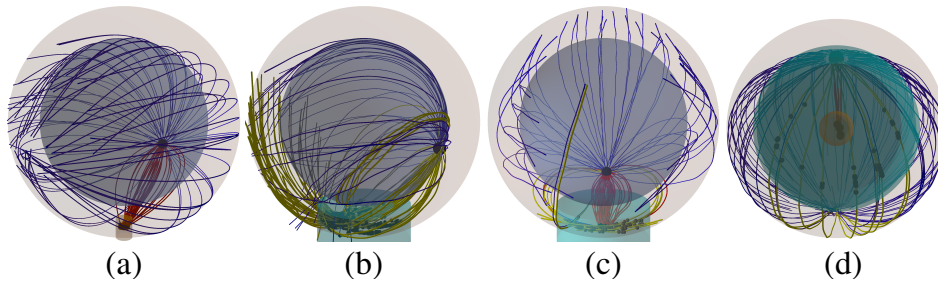


Figure 5.2.: Morphological changes of the MT cytoskeleton. Symbols and colors as in Fig. 5.1. The cyan cylinder represents the IS. MTOC repositioning in the cell where the IS and the MTOC were initially diametrically opposed. MTs are pulled by capture-shrinkage (a), cortical sliding (b), and both mechanisms (c). (a) Narrow stalk of MTs anchored on the plasma membrane connects the center of the IS and the MTOC. (b) MTOC repositioning pulled by cortical sliding mechanism. The large stalk of MTs passes through the entire IS. (c) Narrow stalk of capture-shrinkage MTs connects the center of the IS with the MTOC. Cortical sliding MTs form circular patterns on the periphery of the IS. (d) The MTOC repositioning driven by both mechanisms in the configuration of the cell where the initial MTOC-IS angle $\beta = 0.5\pi$ from the point of view located behind the IS. The stalk of capture-shrinkage MTs is substantially more narrow compared with the stalk of cortical sliding MTs. The figure was made using the simulation software [Hornak2022B].

the IS are initially diametrically opposed, the attachment of MTs to capture-shrinkage dyneins, their subsequent release, and attachment to cortical sliding dyneins results in a ring-like arrangement of cortical sliding MTs, see Fig. 5.2c, that was thoroughly described in [Hornak2020]. In the cell where $\beta < \pi$, the morphological changes are simpler, since the narrow stalk of capture-shrinkage MTs is located in the middle of the cortical sliding MT stalk, see SFig. 10 in the supplementary material [Hornak2022], visualized in Fig. 5.2d. To summarize, based on the changes in the MT structure, one can guess whether MTs are pulled by the capture-shrinkage mechanism, cortical sliding, or by both. Possibly, similar morphological changes could be observed in experiments, which could give a hint about the driving mechanism.

In the cell with two IS, our results suggest that one can estimate the presence of the two mechanisms based on the basic observations of the MTOC dynamics and MT cytoskeleton morphology. Similarly to the case of the cell with one IS, the MT stalk ending in the center of the IS is indicative of the capture-shrinkage mechanism. When the angle between the two IS is $< \frac{2}{3}\pi$, small fluctuations around the central position without ever reaching the center of one IS suggest the individually acting cortical sliding mechanism. When the IS are diametrically opposed, the cortical sliding mechanism causes long dwelling of the MTOC close to one IS. These results can provide a way how to interpret the observations in the future experiments observing the CTL target elimination.

Surprisingly, the cortical sliding mechanism acting independently does not lead to the MTOC repositioning in every configuration of the cell. This may impede the immune reactions, since the MTOC (and lytic granules) would dwell close to one IS and the CTL could not react to the second threat. It was demonstrated that the presence of the capture-shrinkage mechanism at least in one IS is necessary for the repeated transitions between the two IS.

The ability of the CTL to react to two targets simultaneously can be judged by the frequency of the MTOC transitions since a quickly rotating cytoskeleton could transition the lytic granules to both APCs. Moreover, it is crucial that the transition of the MTOC to the IS are complete, since an interrupted MTOC transition may result in the location of lytic arsenal of the CTL far away from the target. The combination of the two mechanisms leads to the highest frequency of the MTOC repositionings and smooth transitions. When the two mechanisms are combined, lower densities of both cortical sliding and capture-shrinkage dyneins lead to a faster MTOC movement than the individually acting capture-shrinkage mechanism with higher density. Consequently, the combination of the two mechanisms assures that the immune reaction is carried out efficiently while saving resources even in the cell with two IS.

5.2. "...things that have the appearance of having been designed with a purpose."

In this thesis, I demonstrated that the immune system often combines multiple players directing each other and enhancing each other's effects. The most obvious demonstration of this principle is the existence of the two branches of the immune system: innate and adaptive immunity. Innate immunity provides a fast response. Adaptive immunity protects against concrete threats. Both are important: while innate immunity provides the first line of defense, adaptive immunity harnesses resources. However, it would be a great mistake to think that they work separately. The innate immunity shapes the response of the adaptive branch and some cells of the adaptive immune system mark the threats for the destruction by the agents of the innate immunity. Similarly, the adaptive immune system employs various subsets of B and T cells helping each other to perform their functions. This can be exemplified by NKT cells helping to activate other subsets of T and B cells.

The same principle can be seen inside the CTL since the MTOC repositioning is driven by a wonderful machinery combining the actions of two players. Both cortical sliding and capture-shrinkage mechanisms are able to reposition the MTOC towards the IS independently. In a way, they cover each other's weaknesses, since they assure a fast MTOC repositioning in different cell configurations. But the synergy of the two mechanisms is definitely the most intriguing aspect of the machinery. The synergy allows the CTL to perform the repositioning quickly, efficiently, and reliably. The speed can be demonstrated by the fact that the MTOC repositions to the IS within a few minutes in every configuration of the cell. The efficiency of the mechanism can be demonstrated by the fact that the combination reduces the dynein area densities necessary for the repositioning and therefore saves the resources of the cell. In the real cell, where the MTOC has to push its way through an inhomogeneous environment, the synergy can increase the probability of complete repositioning. In the cell with two IS, the synergy enables the CTL to attack two targets at once. The efficiency of the repositioning is further enhanced by the placement of dyneins to the IS periphery facilitating the interaction with MTs.

At the end of this section, I have to go back to the first sentence in my thesis. It is the quote from Richard Dawkins: "Biology is the study of complicated things that have the appearance of having been designed with a purpose." This sentence can serve as a motto of my thesis since it underlines all of my findings. During my work on the topic, I was often mesmerized by the harmony of the process driven by a machinery that appears to be so well designed. However, the name and the work of Richard Dawkins suggest that I want to avoid expressions like "intelligent design". Nevertheless, nature provided the CTL with the machinery that can perform one of the key immune reactions with an elegant efficiency.

The purpose of this machinery, of target cell elimination, is clear. Some of the aspects, like the role of membrane fluctuations or the contribution of other motor proteins, are still elusive. The uncertainty in science always presents both a challenge and an opportunity. I believe that our work contributed to the lively scientific discussion about the topic of the CTL polarization. However, there are still many open questions left for tomorrow.

Chapter 6.

Original publications

Contents

6.1. Stochastic Model of T Cell Repolarization during Target Elimination (I)	69
6.1.1. Main Manuscript	69
6.1.2. Supplemental Material	86
6.2. Stochastic Model of T Cell Repolarization during Target Elimination (II)	100
6.2.1. Main Manuscript	100
6.2.2. Supplemental Material	121
6.3. Cytoskeleton rotation relocates mitochondria to the immunological synapse and increases calcium signals	129
6.3.1. Main Manuscript	129

6.1. Stochastic Model of T Cell Repolarization during Target Elimination (I)

The article is included in the thesis with the permission of Elsevier, see Appendix B.

6.1.1. Main Manuscript

Stochastic Model of T Cell Repolarization during Target Elimination I

Ivan Hornak¹ and Heiko Rieger^{1,*}¹Center for Biophysics (ZBP) and Department of Theoretical Physics, Saarland University, Saarbrücken, Germany

ABSTRACT Cytotoxic T lymphocytes (T) and natural killer cells are the main cytotoxic killer cells of the human body to eliminate pathogen-infected or tumorigenic cells (i.e., target cells). Once a natural killer or T cell has identified a target cell, they form a tight contact zone, the immunological synapse (IS). One then observes a repolarization of the cell involving the rotation of the microtubule (MT) cytoskeleton and a movement of the MT organizing center (MTOC) to a position that is just underneath the plasma membrane at the center of the IS. Concomitantly, a massive relocation of organelles attached to MTs is observed, including the Golgi apparatus, lytic granules, and mitochondria. Because the mechanism of this relocation is still elusive, we devise a theoretical model for the molecular-motor-driven motion of the MT cytoskeleton confined between plasma membrane and nucleus during T cell polarization. We analyze different scenarios currently discussed in the literature, the cortical sliding and capture-shrinkage mechanisms, and compare quantitative predictions about the spatiotemporal evolution of MTOC position and MT cytoskeleton morphology with experimental observations. The model predicts the experimentally observed biphasic nature of the repositioning due to an interplay between MT cytoskeleton geometry and motor forces and confirms the dominance of the capture-shrinkage over the cortical sliding mechanism when the MTOC and IS are initially diametrically opposed. We also find that the two mechanisms act synergistically, thereby reducing the resources necessary for repositioning. Moreover, it turns out that the localization of dyneins in the peripheral supramolecular activation cluster facilitates their interaction with the MTs. Our model also opens a way to infer details of the dynein distribution from the experimentally observed features of the MT cytoskeleton dynamics. In a subsequent publication, we will address the issue of general initial configurations and situations in which the T cell established two ISs.

SIGNIFICANCE Cytotoxic T lymphocytes are the main cytotoxic killer cells of the human body to eliminate target cells. The microtubule (MT) organizing center repositioning plays a key role in the killing process, and two underlying mechanisms are discussed: cortical sliding and capture-shrinkage. We devise a theoretical model for the molecular-motor-driven motion of the MT cytoskeleton confined between the membrane and the nucleus during T cell polarization and make quantitative predictions about the spatiotemporal evolution of the MT organizing center position and the MT cytoskeleton morphology comparable with experiments. It reveals the mechanism underlying the experimentally observed biphasic behavior and a remarkable synergy between capture-shrinkage and cortical sliding mechanisms. It also opens a way to infer dynein distribution from details of MT cytoskeleton dynamics.

INTRODUCTION

Cytotoxic T lymphocytes and natural killer (NK) cells have a key role in our immune system by finding and destruction of virus-infected and tumor cells, parasites, and foreign invaders. Once a T cell leaves the thymus, it circulates through the organism in search of a target cell. The directional

killing of a target cell is completed in three subsequent steps. First, T cell receptors bind to antigens on the surface of the target cell presented by the major histocompatibility complex (1–6), leading to the creation of a tight contact zone called the immunological synapse (IS) (7–9) composed of multiple supramolecular activation clusters (9–11). In the second step, the cell repolarizes by relocating the microtubule organizing center (MTOC) toward the IS (12–18) under the influence of forces exerted on MTs. Moreover, because mitochondria, the Golgi apparatus, and the endoplasmic reticulum are attached to MTs, these organelles are dragged along with the MT cytoskeleton

Submitted October 28, 2019, and accepted for publication January 30, 2020.

*Correspondence: h.rieger@physik.uni-saarland.de

Editor: Kevin Janes.

<https://doi.org/10.1016/j.bpj.2020.01.045>

© 2020 Biophysical Society.



Hornak and Rieger

(16,19–24). Consequently, the repolarization process involves massive rearrangements of the internal, MT-associated structure of the cell. In the third step, the T cell releases at the IS the cytotoxic material (e.g., the pore-forming protein perforin and the apoptosis-inducing granzyme) from vesicles, the lytic granules (25–29), toward the target cell, leading to its destruction (29–39). Although the lytic granule secretion can take place without MTOC repolarization (40) or before it (41), the MTOC-accompanied granule secretion may be required for the killing of resistant cells such as tumor cells.

The IS is partitioned into several supramolecular activation clusters (SMACs) including the distal SMAC, peripheral SMAC (pSMAC), and the central SMAC (cSMAC) (7,9,11,42,43), in which T cell receptors (cSMAC) and adhesion molecules are organized. Moreover, the engagement with the target cell results in the formation of actin and actomyosin networks at the IS (44). Dynein, a minus-end-directed (toward the MTOC) molecular motor protein anchored at the cell cortex, is absolutely necessary for the repolarization to take place, as was experimentally demonstrated with knock-out experiments (45) analogous to dynein exerting forces against anchor proteins fixed at the cell cortex during mitosis (46–49).

Once the T cell is activated, the adaptor protein ADAP forms a ring at the periphery of the IS with which dynein colocalizes (50,51). Concerning the underlying mechanism, it was proposed that the repolarization is driven by the cortical sliding mechanism (50,52), in which dyneins anchored at the cell cortex step on the MT toward the minus end and thus pull the MTOC toward the IS. The first experimental indications for cortical sliding came from observation of cytoskeleton movement using polarization light microscopy (17). Subsequent experiments indicate that the IS periphery, in particular the ring-shaped pSMAC, is the region where dyneins attach to and pull on MTs (17,50).

The repositioning was observed in various experiments. Focused activation of the photoactivable peptide-MHC on the glass surface was used in (53). In (16), the repositioning was observed alongside with the rotation of the mitochondria, which provided evidence that the mitochondria are dragged with the MT cytoskeleton. Detailed observations were made by Yi et al. (14), providing new insight into the mechanism of the repolarization. In (14), an optical trap was used to place a target cell so that the initial point of contact is in diametrical opposition to the current position of the MTOC, which allowed for dynamical imaging in a quantitative fashion. During the experiment, the deformations and changes in MT structures were observed and the position of the MTOC was tracked. First of all, Yi et al. (14) provided strong experimental evidence against the cortical sliding mechanism. Instead, the observations indicate that the MTOC is driven by a capture-shrinkage mechanism (54) localized in a narrow central region of the IS. The capture-shrinkage mechanism involves dynein interact-

ing in an end-on fashion with the plus end of a MT, which is fixed in a position on the membrane of the cell where the MT depolymerizes. The MT shrinkage part happens plausibly because dynein pulls the MT plus end against the cell membrane, which increases the force-dependent MT depolymerization rate (54).

In sequences of microscope pictures, (14) showed that MTs reach from the MTOC to the IS and bend alongside the cell membrane. Subsequently, MTs form a narrow stalk connecting the MTOC with the center of the IS. The plus end of MTs in the stalk, while captured in the center of the IS, straighten (probably under tension due to the dynein pulling at the plus end) and shrink by depolymerization at the capture point. Consequently, the MTOC is dragged toward the center of IS, which invaginates into the cell, further proving the location of the main pulling force. When the MT depolymerization was inhibited by taxol, the MTOC repositioning slowed down substantially. These observations supported the hypothesis that the capture-shrinkage mechanism plays a major role. However, the velocity of the MTOC repositioning is not always an advantage because time is necessarily for the killing of target cells in hostile environments (55) and might be beneficial for slower killing processes (56). Additionally, Yi et al. (14) reported that the repositioning is biphasic and that the two phases differ in the velocity of the MTOC and the orientation of its movement. In the first, so-called polarization phase, the MTOC travels quickly around the nucleus of the cell in a circular manner. The polarization phase ends when the MTOC is approximately $2 \mu\text{m}$ from the center of the IS. Subsequently, during the second, “docking” phase, the MTOC travels directly toward the IS with a substantially decreased velocity.

The cortical sliding mechanism alone was previously analyzed with a deterministic mechanical model (57), in which it was demonstrated that mechanism is capable of reorienting the MTOC into a position under the IS underneath certain conditions. Furthermore, oscillations between two ISs were studied in different situations. Nevertheless, the forces in the model were deterministic, neglecting the stochastic nature of dynein attachment, detachment, and stepping, leaving various experimental observations unexplained such as, for instance, the preferential attachment of MTs to a dynein anchored in the periphery of the IS.

Sarkar et al. (58) hypothesized that dynamic MTs find the central region of the IS, where they can be captured by a dynein by growing from the MTOC in random directions, analogous to the search and capture mechanism during the formation of the mitotic MT cytoskeleton. Once MTs attach to the dynein in the central region of the IS, the relocation of the MTOC starts, which is the process that is analyzed in this work.

Despite these detailed experimental observations, many aspects of the internal mechanisms driving the relocation of the MTOC during the T cell repolarization remain poorly

understood, like the cause of the transition from the polarization to the docking phase. Yi et al. argue that a resistive force emerges when the MTOC-IS distance is around 2 μm , leading to a reduction in the MTOC's velocity. The potential causes are physical impediments to the MTOC's translation or a reduced attachment or a force development of molecular motors. Moreover, the experiments of Yi et al. were performed with specific initial positions of the IS and the MTOC being diametrically opposed. The question arises whether the observed dominance of the capture-shrinkage mechanism would be robust in other naturally occurring situations in which the initial position of the MTOC is not in diametrical opposition to the IS. If capture-shrinkage is the truly dominant mechanism, what is the role of cortical sliding? Finally, why are cortically sliding MTs caught just on the periphery of the IS (17), and is it caused purely by the colocalization of dyneins with the ADAP ring (50)? The answers to these questions are still elusive, and in this work, we analyze them in the framework of a quantitative theoretical model for the relocation of the MTOC after the IS formation. Although this study focuses on the T cell, NK cells display the same kind of phenomenology: IS formation, MTOC relocation, and the release of lytic granules.

We distribute our analysis into two consecutive publications. In this first publication, we describe the theoretical model we use and present our results focusing on the experiments described in (14,17,50) and on an analysis of the two mechanisms: cortical sliding and capture-shrinkage. This comprises the setup in which the T cell has one IS and the initial positions of the IS and the MTOC are diametrically opposed to each other.

A subsequent, second, publication will focus on quantitative predictions of our model for situations that have not yet been analyzed experimentally. There, we will focus on the repolarization after initial configurations not realized in (43), which will also provide additional insight into the different effects of the two mechanisms, cortical sliding

and capture-shrinkage. Moreover, we will analyze the eventually oscillating MT/MTOC movement with two ISs.

METHODS

Computational model

The cell and its nucleus are modeled as two concentric spheres of the radius 5 and 3.8 μm , respectively. The model of the cytoskeleton consists of MTs and the MTOC; see Fig. 1. MTs are thin filaments with a diameter of ~ 25 nm (59–61). The measured values of the flexural rigidity vary between experiments (62,63); in our model, we take 2.2×10^{-23} nm² (64), yielding a persistence length larger than 5 μm that exceeds the size of the cell by three orders of magnitude. A single MT is represented by a bead-rod model (65). Because repolarization occurs on a timescale of seconds, the growth of MTs is neglected. The beads move under the influence of forces to be described below (and defined in detail in the [Supporting Materials and Methods](#): bending, drag, molecular motor, and stochastic forces). Assuming zero longitudinal elasticity of the MTs, we use constrained Langevin dynamics to model the motion of the MTs; see the [Supporting Materials and Methods](#). Repulsive forces acting on the MT segments confine the cytoskeleton between the nucleus and the cell membrane.

The MTOC is a large protein complex that has a complex structure composed of mother and daughter centrioles (66–69) embedded in the pericentriolar material (70–72). MTs nucleate from γ -tubulin-containing ring structures within the pericentriolar material mainly at the appendages of the mother centriole (66,73). MTs can sprout from the MTOC in all directions. MTs whose original direction is approximately parallel to the membrane of the cell will continue to grow to the cell periphery. Other MTs will soon hit the wall of the cell or its nucleus. Such MTs can either bend and assume a new direction parallel to the cell membrane or undergo the MT catastrophe. Therefore, long MTs are seemingly always sprouting from the MTOC in one plane, as can be seen in (14). Consequently, we model the MTOC as a planar, rigid polygon structure (Fig. S3) from which MTs emanate in random directions by fixing the positions and directions of their first segment (Fig. S4). MTs sprout from the MTOC to the cell periphery; see Fig. 1 a.

Unattached dynein is represented just with one point on the surface of the cell. If the dynein is closer to the MT than L_0 , protein attaches with a probability p_a . Dynein motors are distributed randomly in specific, spatially varying concentrations on the cell boundary. Attached dynein is represented by a fixed anchor point located on the cell boundary and an attachment point located on an MT, both being connected by an elastic stalk of a length L_0 (74,75). The force exerted on an MT F_i^{Dynein} depends on the stalk's

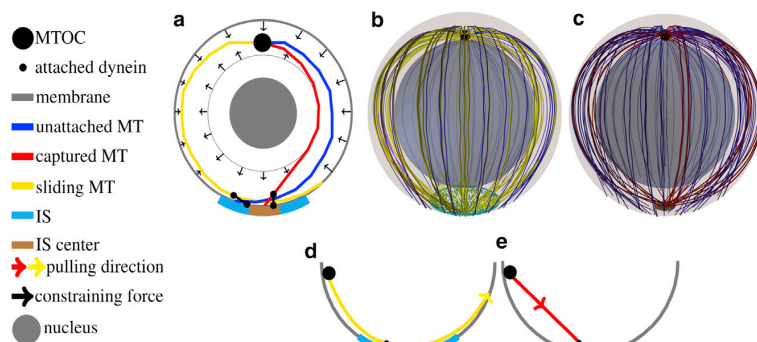


FIGURE 1 (a–c) Sketch of the model. (a) A two-dimensional cross-section of the model is shown. MTs sprout from the MTOC, and their movement is confined by constraining forces from the cell membrane and the nucleus. MTs are attached to dynein motors in the IS, and they are pulled by the capture-shrinkage or the cortical sliding mechanism. (b and c) A three-dimensional sketch of the cell model is given. The outer transparent and inner spheres represent the cell membrane and the nucleus of the cell, respectively. (b) The blue disk represents the IS, where cortical sliding dynein is anchored. Small green dots in the IS represent randomly distributed dynein. (c) The brown disk represents the central region of the IS where the capture-shrinkage dynein is anchored. (d and e) A sketch of the cortical sliding mechanism (d) and the capture-shrinkage mechanism (e) is shown. Small black dots on the MTs: attachment points. Note that MTs depolymerize when pulled by capture-shrinkage dynein toward the membrane. To see this figure in color, go online.

of the cortical sliding mechanism (d) and the capture-shrinkage mechanism (e) is shown. Small black dots on the MTs: attachment points. Note that MTs depolymerize when pulled by capture-shrinkage dynein toward the membrane. To see this figure in color, go online.

Hornak and Rieger

elastic modulus k_{Dynein} and its prolongation. The dynein stepping depends on the magnitude of the force and its orientation. If the force is parallel to the preferred direction of the stepping, the attachment point moves one step to the MT minus end (toward the MTOC) with a constant probability p_- . If the orientation of the force is opposite and its magnitude smaller than a stall force F_S , dynein makes one step toward the minus end with a force-dependent probability. If $|F_i^{\text{Dynein}}| > F_S$ and the force has an unfavorable direction, the dynein makes one step to the plus end with a constant probability p_+ . The steps of the dynein have varying lengths (75), but for simplicity, we set it to the most frequently measured value of $d_{\text{step}} = 8$ nm. The probability of detachment, p_{detach} , increases with the force.

Experimentally, two mechanisms by which the dynein act on MTs have been identified: cortical sliding (17), in which MTs under the effect of dynein move tangentially along the membrane, and capture-shrinkage (14), by which MTs under the effect of dynein are reeled in toward the membrane and concomitantly depolymerized (sketched in Fig. 1, *d* and *e*).

The IS is divided into two regions: the center, where dyneins act on MTs via the capture-shrinkage mechanism (14), and the complete IS, where dyneins act via the cortical sliding mechanism. Each region is modeled as an intersection of the cell sphere with a cylinder, 1, with radius $R_{\text{IS}} = 2$ μm for the complete IS and $R_{\text{CIS}} = 0.4$ μm for the central region. Dyneins are distributed randomly with uniform area density ρ_{IS} in the small central region, denoted as capture-shrinkage dynein, and density $\tilde{\rho}_{\text{IS}}$ in the larger region of the whole IS, denoted as cortical sliding dynein.

RESULTS

We analyzed the role of the cortical sliding and capture-shrinkage mechanisms and their combined effect during the repolarization by computer simulations of the model defined in the previous section. The density of dyneins anchored at the IS, $\tilde{\rho}_{\text{IS}}$, and the central region of the IS, ρ_{IS} , are unknown model parameters, which we therefore vary over a broad range between 0 (no anchored dynein) and 1000 μm^{-2} (the maximal number of anchored dynein because of the lateral size of dyneins; see Supporting Materials and Methods, Section S1.1.5). During the integration of the equation of motion, various quantities are calculated: the distance between the

center of the MTOC and the IS, d_{MIS} ; the number of dyneins attached to the MTs, N_{dm} ; the velocity of the MTOC, v_{MTOC} ; and the distance between the MTOC and the center of the cell, d_{MC} . For each point in the parameter space, these quantities were averaged over 500 simulation runs. Each simulation run is initialized with the mechanical equilibrium (minimal elastic energy) configuration of the MT/MTOC-system and all dyneins being detached. Results are shown with the standard deviation as error bars only when they are larger than the symbol size.

Capture-shrinkage mechanism

The repositioning process under the effect of the capture-shrinkage mechanism is visualized in Fig. 2. In Fig. 2, *a* and *d*, it can be seen that initially, the attached MTs aim from the MTOC in all directions. Subsequently, the stalk of MTs is almost formed in the middle phase of the repositioning (Fig. 2, *b* and *e*), and it is fully formed as the MTOC approaches the IS; see Fig. 2, *c* and *f* and Video S1 showing the time evolution of the MT cytoskeleton configuration under the effect of the capture-shrinkage mechanism with 100 MTs and the dynein density $\rho_{\text{IS}} = 100$ μm^{-2} .

The process can be divided into three phases based on the time evolution of the MTOC velocity; see Fig. 3 *b*. In the first phase, when the distance between the MTOC and the center of the IS is $\bar{d}_{\text{MIS}} > 8.8$ μm , the velocity changes rapidly in the first seconds of the process and then falls to a local minimum. In the second phase, the velocity continually increases to a maximum, and then in the third phase, it decreases again. By comparison of Fig. 3, *b* and *c*, it can be seen that the time evolution of the velocity corresponds to the time evolution of the number of dyneins acting on MTs. The evolution of the number of attached dyneins

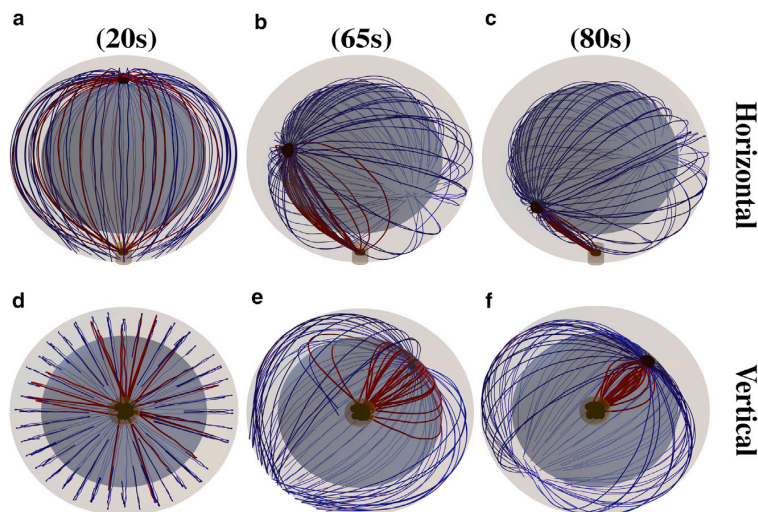


FIGURE 2 Snapshots from the time evolution of the MT cytoskeleton configuration under the effect of the capture-shrinkage mechanism alone (dynein density $\rho_{\text{IS}} = 100$ μm^{-2}). MTs are connected to the MTOC indicated by the large black sphere. Blue and red curves are unattached and attached MTs. Small black spheres in the IS represent dyneins. The brown cylinder indicates the center of the IS, where the capture-shrinkage dyneins are located. (*a* and *d*) $d_{\text{MIS}} = 9$ μm . Initially, the attached MTs sprout from the MTOC in all directions. (*b* and *e*) $d_{\text{MIS}} = 6$ μm . As time progresses, MTs form a stalk connecting the MTOC and the IS. (*c* and *f*) $d_{\text{MIS}} = 2.5$ μm . The stalk is fully formed, and it shortens as the MTOC approaches the IS. To see this figure in color, go online.

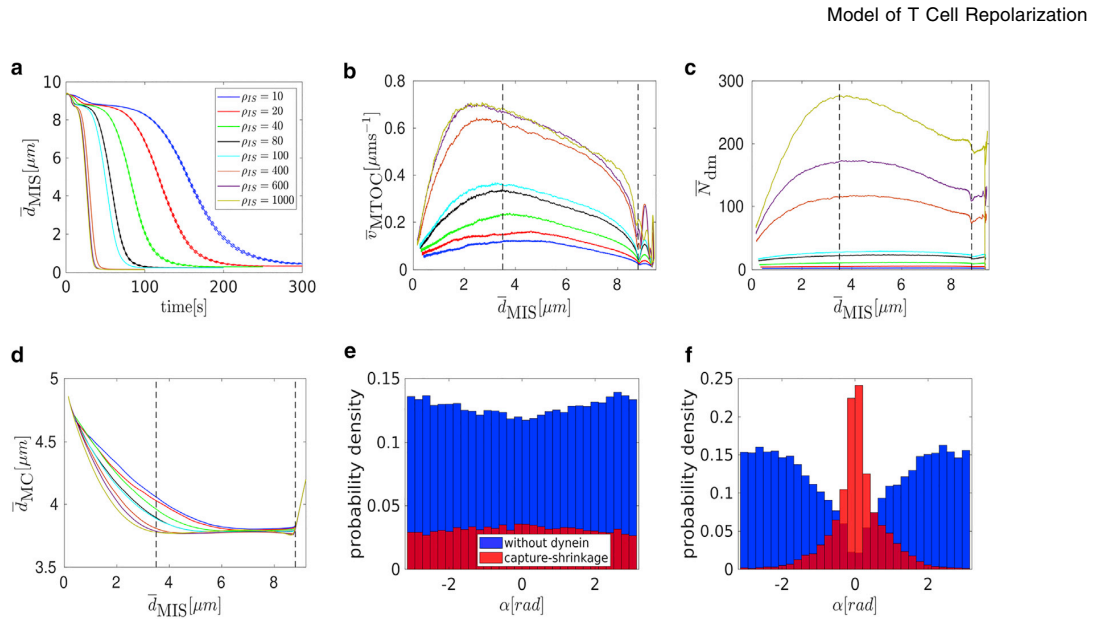


FIGURE 3 Capture-shrinkage mechanism: (a) the dependence of the average MTOC-IS distance \bar{d}_{MIS} on time. The error bars are represented by dashed lines and are plotted only if bigger than a symbol size. (b–d) Dependencies of the average MTOC velocity \bar{v}_{MTOC} (b), the number of dyneins acting on microtubules \bar{N}_{dm} (c), and the MTOC-center distance \bar{d}_{MC} (d) on the average MTOC-IS distance are shown. Black dashed lines denote transitions between different phases of the repositioning process. (e and f) Probability distributions of the angles between the first MT segments and the direction of the MTOC movement for a dynein density $\rho_{\text{IS}} = 100 \mu\text{m}^{-2}$ (e), $t = 1$ s, $\bar{d}_{\text{MIS}} \sim 9 \mu\text{m}$ are given. (f) $t = 60$ s, $\bar{d}_{\text{MIS}} \sim 5 \mu\text{m}$. To see this figure in color, go online.

during the first phase can be understood from an analysis of Figs. 2, a and b and 3 d. At the beginning of the simulations, a substantial number of MTs intersects the IS (visually demonstrated in Fig. 2, a and d), resulting in a fast increase of the number of attached dyneins. Because the MTs attached to dynein sprout from the MTOC in every direction (cf. Fig. 3 e), the MTOC moves toward the IS and, simultaneously, to the nucleus of the cell (see Fig. 3 d). As the MTOC approaches the nucleus of the cell, the nucleus starts to oppose the movement by repelling the MTs and, at the end of the first phase, the MTOC. Therefore, as the pulling force of the dyneins is opposed by the nucleus, the dyneins detach because the detachment rate is force dependent.

The increase of the number of attached dyneins \bar{N}_{dm} in the second phase can be explained by considering the fact that the MTOC slides over the surface of the nucleus and the MT stalk forms. At the beginning, the nucleus presents an obstacle between the MTOC and the IS; see Fig. 2 a. The opposing force from the nucleus decreases with the approach of the MTOC toward the IS. At the end of the repositioning, the nucleus no longer stands between the two objects; see Fig. 2, c and f. Therefore, the opposing force from the nucleus contributing to dynein detachment decreases. More importantly, attached MTs form the MT stalk. The angle α between the first segment of the MT and the direction of the MTOC movement is used to describe the deformation of the cytoskeleton structure and the stalk formation. At the beginning of the simulation (the first phase and the beginning of the second), attached MTs aim in every direction (see Fig. 3 e, visu-

alized in Fig. 2, a and d). Therefore, the dyneins pull in multiple directions, which makes them oppose each other, leading to dynein detachment. After a few seconds, the MTOC travels in the direction of the biggest pulling force. Consequently, the attached MTs form a stalk as the simulation progresses, and dyneins act in alignment; see Figs. 2, b and e and 3 f. They no longer oppose each other but share the load from opposing forces. Consequently, the detachment probability of dynein decreases with the opposing force, and the number of attached dyneins increases.

The number of dyneins decreases in the final phase when $\bar{d}_{\text{MIS}} < 3.5 \mu\text{m}$; see Fig. 3 c. Unattached MTs in the IS are pushed backward by viscous drag as the MTOC moves to the IS. As a result, one observes an “opening” of the MT cytoskeleton; cf. Figs. 2, c and f and 3 e. Unattached MTs do not intersect the IS (see Fig. 3 f) and cannot attach to dyneins. The attached MTs shorten because of the depolymerization, further lowering the probability of dynein attachment. Moreover, an opposing force arises from the cytoskeleton being dragged from the nucleus to the membrane (see Fig. 3 d), causing the detachment of dyneins because the detachment rate is force dependent.

To summarize, the trajectory of the MTOC toward the IS displays three phases, in which the two longer phases have also been reported in experiment (14), but not the short initial phase. First, the MTOC descends to the nucleus (see Fig. 3, a and d); then it moves to the IS quickly and slows down during the last $2 \mu\text{m}$ (see Fig. 3 b). Once the MTOC bypasses the nucleus, it moves away, switching

Hornak and Rieger

from a purely circular to partially radial movement (see Fig. 3 *d*). The variation of the MTOC velocity, its modulus, and its direction are clearly visible in Video S2, showing a simulation with a smaller nucleus radius $r_N = 3.3 \mu\text{m}$. Note that the duration of the complete repositioning process in the experiments is $\sim 60\text{--}90$ s, which our model predicts to be achieved by a dynein density of $80\text{--}200 \mu\text{m}^{-2}$.

Cortical sliding mechanism

For low, medium, and high densities, one observes for each a different characteristic behavior. In the regime of low dynein densities ($\tilde{\rho}_{\text{IS}} < 100 \mu\text{m}^{-2}$), the repolarization velocity increases with the dynein density, and the MTOC moves directly to the IS; see Fig. 5 *a*. For medium dynein densities ($100 \mu\text{m}^{-2} \leq \tilde{\rho}_{\text{IS}} < 500 \mu\text{m}^{-2}$), the MTOC movement is more complex; see Fig. 7 *a*. For high dynein densities ($\tilde{\rho}_{\text{IS}} > 500 \mu\text{m}^{-2}$), the repolarization velocity surprisingly decreases with $\tilde{\rho}_{\text{IS}}$; see Fig. 8 *a*.

Cortical sliding with low dynein densities

Video S3 shows MTOC repositioning under the effect of the cortical sliding mechanism with $\tilde{\rho}_{\text{IS}} = 60 \mu\text{m}^{-2}$. It shows MTs sprouting in all directions in the initial stage, the subsequent stalk formation, and the final slowing down of the MTOC. In Fig. 5 *b*, the dependence of the MTOC velocity on the MTOC-IS distance is shown. As in the case of the capture-shrinkage mechanism, the time evolution of the MTOC velocity can be divided into three phases. However, the transition points between the second and the third phase depend on the density $\tilde{\rho}_{\text{IS}}$. Similarly to the case of the capture-shrinkage mechanism, the behavior in the first phase can be explained by the interplay of fast-attaching dyneins and forces from the nucleus. In the second phase, the velocity of the MTOC increases despite a continuously decreasing number of attached dyneins (see Fig. 5, *b* and

c), which is due to the alignment of the MTs. Initially, attached MTs aim in all directions (see Fig. 5 *e*), as for the capture-shrinkage mechanism (cf. Fig. 4, *a* and *d*). Consequently, MTs whose original orientation does not correspond to the movement of the MTOC detach from dynein (see Figs. 4, *b* and *e* and 5 *f*). The probability density in the intermediate state of the repositioning ($\bar{d}_{\text{MIS}} \sim 5 \mu\text{m}$) shows that attached MTs are aligned and less in numbers. The MTOC does not significantly recede from the nucleus at the end of the repositioning (see Fig. 5 *d*), which implies that the MTs do not follow the cell membrane (with the capture-shrinkage mechanism, MTs always touch the membrane); see Fig. 4, *c* and *f*. Consequently, the attachment probability is lower and leads to the decrease in velocity in the third phase.

Cortical sliding with medium dynein densities

The differences between the behavior with low and medium dynein densities for the cortical sliding mechanism are analyzed in this section. Video S4 shows the repositioning with $\tilde{\rho}_{\text{IS}} = 200 \mu\text{m}^{-2}$. The repositioning is very fast, and the MT cytoskeleton is considerably deformed. Moreover, the MTOC passes the IS and subsequently returns to the center of IS. 5 s after the initialization, MTs in all directions are attached (see Fig. 6, *a* and *d*), but the direction of the MTOC motion is already established (see Fig. 7 *b*). Contrary to the case of low densities, the dynein forces are sufficiently strong to hold attached MTs. Subsequently, some MTs do not detach but take a direction partially aligned to the MTOC movement (see Fig. 7, *c* and *d*). Moreover, almost all MTs aligned with the MTOC motion are attached to dyneins (compare Figs. 5 *f* and 7 *d*). Consequently, the large majority of MTs are aligned with the direction of movement of the MTOC movement, causing a substantial increase of the MTOC velocity. By comparing the temporal evolution of the MTOC-IS distance $\bar{d}_{\text{IS}(t)}$ for small, medium, and large

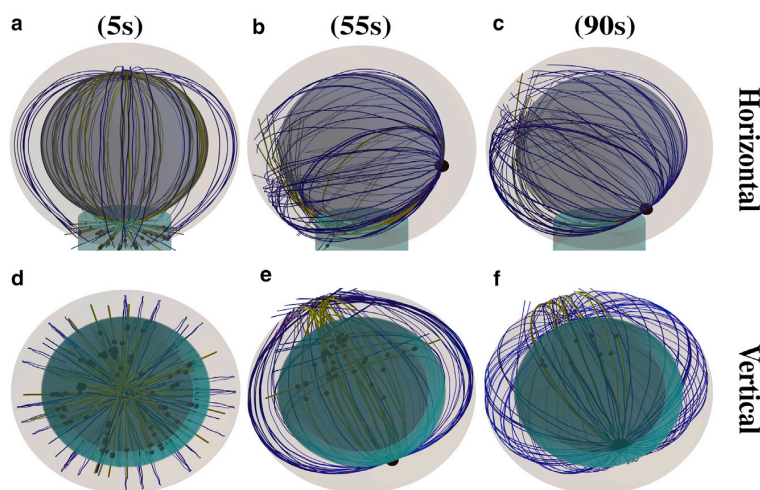


FIGURE 4 Snapshots from the time evolution of the MT cytoskeleton configuration under the effect of cortical sliding mechanism with a low dynein density, $\tilde{\rho}_{\text{IS}} = 60 \mu\text{m}^{-2}$. The cyan cylinder indicates the IS area. Blue and yellow lines are unattached and attached MTs, respectively. The black spheres in the IS are the positions of dyneins attached to MTs. (*a* and *d*) $\bar{d}_{\text{MIS}} = 9 \mu\text{m}$. Originally, the attached MTs aim from the MTOC in every direction. (*b* and *e*) $\bar{d}_{\text{MIS}} = 4.5 \mu\text{m}$. MTs attached to dynein aim predominantly in one direction. (*c* and *f*) $\bar{d}_{\text{MIS}} = 1.5 \mu\text{m}$. Just a few MTs remain under the actions of cortical sliding, and they rarely touch the surface of the cell in the IS. To see this figure in color, go online.

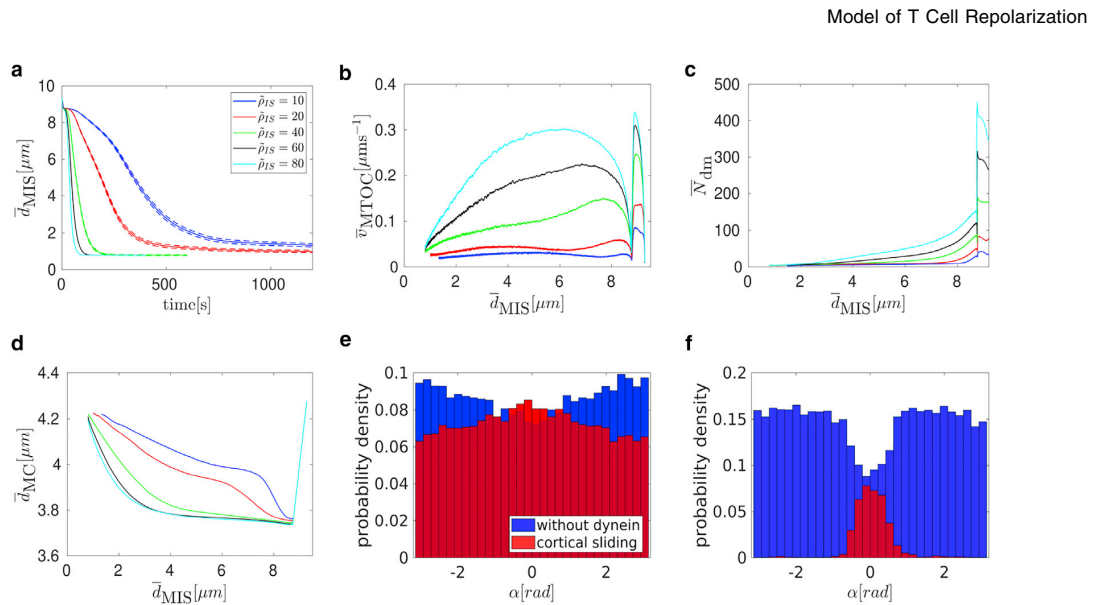


FIGURE 5 Cortical sliding with low dynein densities $\tilde{\rho}_{IS}$. (a) The dependence of the average MTOC-IS distance \bar{d}_{MIS} on time is shown. The error bars are represented by dashed lines and are plotted only if bigger than a symbol size. (b–d) Dependencies of the average MTOC velocity \bar{v}_{MTOC} (b), number of dyneins acting on MTs \bar{N}_{dm} (c), and the MTOC-center distance \bar{d}_{MC} (d) on the average MTOC-IS distance are shown. (e and f) Probability distributions of the angles α between the first MT segment and the MTOC motion, $\tilde{\rho}_{IS} = 60 \mu\text{m}^{-2}$, are shown. (e) $t = 5$ s, $\bar{d}_{MIS} \sim 9 \mu\text{m}$. (f) $t = 65$ s, $\bar{d}_{MIS} \sim 5 \mu\text{m}$. To see this figure in color, go online.

dynein densities (Figs. 5 a, 7 a, and 8 a), one observes that the velocity of the MTOC is maximal for medium densities of cortical sliding dyneins (see also Fig. 9, a and b below). Moreover, by comparing the configuration snapshots for low and high densities (Fig. 4, b and e and 6, b and e), one observes that the strong forces exerted at high dynein densities cause large deformations of the MT cytoskeleton.

Because of the deformation of the cytoskeleton, a large number of MTs are attached to dynein at the end of the repositioning (see Fig. 7 d), and dyneins are predominantly found at the opposite side of the IS (compared to the MTOC). Because of the attachment, the MTOC passes the center of the IS (see Fig. 7 a) and the anchor points of certain dynein motors (see Fig. 6, c and f). The MTs are attached to anchor points, so the probability density of α changes, and the majority of MTs are behind the MTOC (see Fig. 7 e). When the MTOC returns to the IS, the probability density levels (see Fig. 7 f), and dynein detaches.

Cortical sliding with high dynein densities

An example for repositioning under the effect of cortical sliding with a high dynein density $\tilde{\rho}_{IS} = 1000 \mu\text{m}^{-2}$ is shown in Video S5. As the area density $\tilde{\rho}_{IS}$ rises, the MTs are more and more attached at the periphery (see Fig. 8 d). This is further demonstrated by Fig. 8, e and f (the center of the IS is almost depopulated when $\tilde{\rho}_{IS} = 1000 \mu\text{m}^{-2}$). The reason is that there are a sufficient number of dyneins to firmly catch the MTs passing just the periphery of the IS. The higher number of MTs also logically means bigger pulling forces on

MTs. In a spherical cell, dyneins act in competition, which leads to dynein detachment. The bigger the competition is, the more frequent the detachment, as can be seen in Fig. 8 b, in which the highest number of attached dyneins corresponds to the lowest area density.

Constantly attaching and detaching dyneins does not allow MTs to align with the direction of the MTOC movement. Subsequently, the MTOC “lingers” behind the nucleus before it moves to the IS as the dominant orientation of attached MTs forms slowly. The duration of this inactivity rises with $\tilde{\rho}_{IS}$ (see Fig. 8 a). Even when the dominant direction is established, MTs are still attached in every direction, slowing down the movement (see Fig. 8 c). Therefore, the slowing in the third section (cf. Fig. 8 a) is caused by two effects: first, the misalignment of MTs, resulting in contradictory pulling forces and a lower number of attached dyneins; second, the increasing probability of attachment at the periphery, resulting in MTs being pulled to different places and increasingly contradicting each other as the MTOC approaches the IS.

Comparison of cortical sliding and capture-shrinkage

In this section, two mechanisms are compared in terms of MTOC velocity: times and final MTOC-IS distances. The biological motivation is that the velocity (times) indicates the efficiency of transmission of the force of dynein on the cytoskeleton, and the final distance determines the

Hornak and Rieger

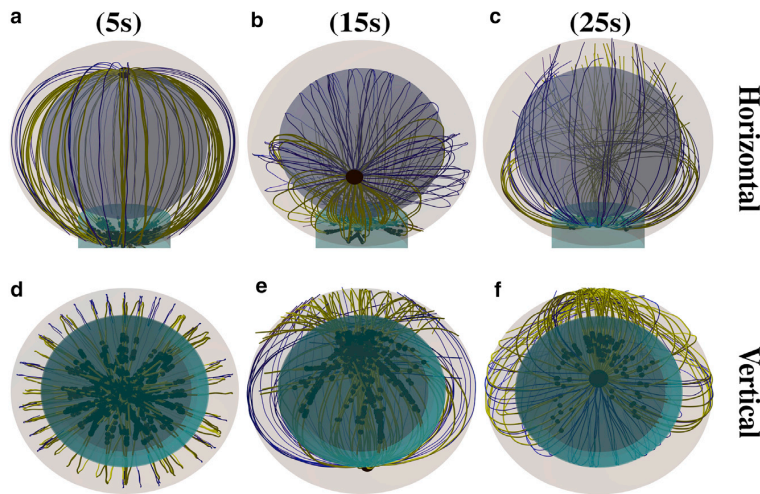


FIGURE 6 Snapshots from the time evolution of the MT cytoskeleton configuration under the effect of cortical sliding alone, with a medium area density of the dynein $\bar{\rho}_{IS} = 200 \mu\text{m}^{-2}$ from two perspectives. (a and c) $\bar{d}_{MIS} = 9 \mu\text{m}$. MTs sprout from the MTOC in all directions. (b and d) $\bar{d}_{MIS} = 5 \mu\text{m}$. The majority of MTs are attached, and the MT cytoskeleton is deformed. (c and e) $\bar{d}_{MIS} = 1 \mu\text{m}$. At the end of the repositioning, the MTOC passed the center of the IS, and attached MTs aim in all directions. To see this figure in color, go online.

completion of the repositioning. In the previous sections, the repositioning was divided into three phases based on the MTOC velocity (see Figs. 3 and 5), which enabled the analysis of the dynamics based on the attached dyneins and deformations of the cytoskeleton structure.

To analyze average velocity, the repositioning is divided into three phases based on the MTOC-IS distance: the activation, the first, and the second phase. This approach will later enable a comparison with experimental results. The activation phase ends when $d_{MIS} \leq 8.2 \mu\text{m}$ (identical with the first phase based on the MTOC velocity). Although the activation phase is important for the observation of the influence of dynein motors (see Figs. 3 c, 5 c, and 8 b), the phase lacks experimental analogy because in reality, the IS, along with a high dynein area density, is not created instantly. Therefore, it will not be further analyzed. In the first phase, the MTOC-IS distance $8.2 \mu\text{m} > d_{MIS} > d_f + 1 \mu\text{m}$, where d_f is the final MTOC-IS distance, which depends on the area density and mechanism. The second phase comprises the last micrometer of the MTOC journey.

The MTOC velocity in the capture-shrinkage repositioning increases with the area density of dyneins for both phases (see Fig. 9 a). The development of the average MTOC velocity of the cortical sliding repolarization is more difficult because it rises to its maximum (middle densities) (see Fig. 9 a) and then falls sharply. The velocity of the cortical sliding repositionings is lower except when considering middle area densities of the cortical sliding dynein. Moreover, for the low and high densities, the velocity of capture-shrinkage is more than two times the velocity of cortical sliding (see Fig. 9 a). The times of repositioning evolve accordingly (see Fig. 9 c). Times are longer for the case of capture-shrinkage only when ρ corresponds to the middle densities of cortical sliding (see Fig. 9 a).

The final MTOC-IS distance decreases with the rising ρ in the case of sole capture-shrinkage (see Fig. 9 b). In the case

of cortical sliding, the situation is more complicated because of the lack of an anchor point. The large final distances at low area densities are caused by the insufficient pulling force. The shortest distance is at the end of low area densities $\rho = 80 \mu\text{m}^{-2}$, which is caused by the fact that the formation of the narrow MT stalk, in which MTs pull in alignment, is limited just to low densities (see Figs. 5 e, 7 c, and 8 c). Then, we can observe a steady rise in final distances caused by the growing attachment of MTs at the peripheries as $\bar{\rho}_{IS}$ causes the increasing competition of pulling forces in the final stages of the polarization.

Fig. 9 c explains the lower MTOC velocity for cortical sliding. First of all, let us notice that the three regimes of the cortical sliding behavior are visible in Fig. 9 c. We can see that the increasing $\bar{\rho}_{IS}$ causes MT attachment on the periphery of the IS, as was already suggested by Fig. 8, d-f. Moreover, the attached dynein is always predominantly at the periphery because the average distance for the uniform distribution of dynein is $\bar{r}_{IS} = (1/2)R_{IS} = 1 \mu\text{m}$. Therefore, as the MTOC approaches the IS, MTs are pulled to different locations, and the forces of dynein oppose each other and cause the dynein detachment.

The capture-shrinkage mechanism is faster, with the relatively narrow exception of the middle area densities. Cortical sliding never achieves shorter distances in comparison to capture-shrinkage; moreover, in the case of high or low densities, the final distances differ substantially. Fig. 9 shows the dependencies on area density. Nevertheless, in the case of capture-shrinkage, we consider just the density in the center of the IS. We should remind the reader that the radii of the center and the entire IS are $R_{CIS} = 0.4 \mu\text{m}$ and $R_{IS} = 2 \mu\text{m}$. Because the number of dyneins depends on the area, the number of dyneins in the IS $N_{IS} = 25 \times N_{CIS}$, where N_{CIS} is the number of dyneins in the center of the IS. Consequently, Fig. 9 confirms that the capture-shrinkage mechanism is the main driving force of the repositioning because

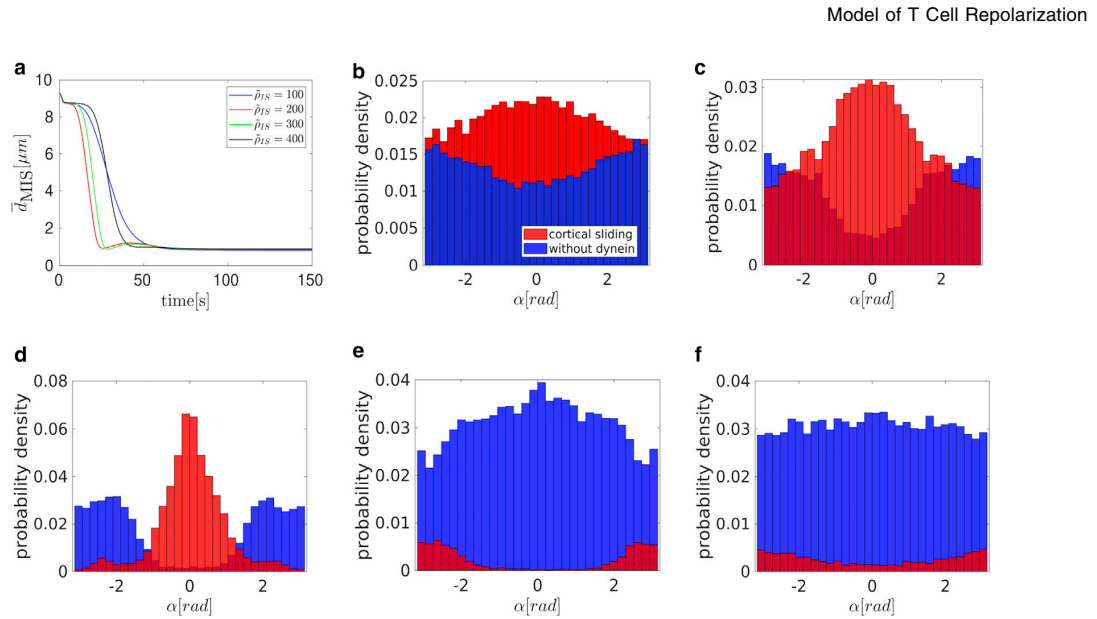


FIGURE 7 Cortical sliding mechanism with medium dynein densities $\tilde{\rho}_{IS}$. (a) The dependence of the MTOC-IS distance \bar{d}_{MIS} on time is shown. Probability distributions of the angles α between the first MT segment and the MTOC motion, $\tilde{\rho}_{IS} = 200 \mu\text{m}^{-2}$, are shown. (b) $t = 5 \text{ s}$, $\bar{d}_{MIS} \sim 9 \mu\text{m}$. (c) $t = 15 \text{ s}$, $\bar{d}_{MIS} \sim 6 \mu\text{m}$. (d) $t = 20 \text{ s}$, $\bar{d}_{MIS} \sim 2.5 \mu\text{m}$. (e) $t = 25 \text{ s}$, $\bar{d}_{MIS} \sim 1.5 \mu\text{m}$, other side of IS. (f) $t = 60 \text{ s}$, $\bar{d}_{MIS} \sim 0.8 \mu\text{m}$. To see this figure in color, go online.

this mechanism produces bigger or comparable velocities with just 4% of the dynein motors of cortical sliding. Moreover, the MTOC comes closer to the IS, meaning that the capture-shrinkage mechanism is more likely to finish repositioning. To summarize, considering the lower number of dyneins, the capture-shrinkage mechanism is largely superior in the considered setup. The most important difference between the two mechanisms is the firm, narrow anchor point in case of the capture-shrinkage mechanism. It assures a firm attachment of the MTs (see Fig. 3 f) and a geometrical alignment of the pulling forces in all stages of repositioning. The capture-shrinkage mechanism was identified as the main driving force of the repositioning (14), and our model fully supports this statement. In the next section, we will scrutinize the role of cortical sliding.

Combination of capture-shrinkage and cortical sliding

In this section, the interplay between the two mechanisms is analyzed. A comparison of Video S6 (capture-shrinkage, with $\rho_{IS} = 60 \mu\text{m}^{-2}$, $\tilde{\rho}_{IS} = 0 \mu\text{m}^{-2}$) and Video S7 (both mechanisms combined, $\tilde{\rho}_{IS} = \rho_{IS} = 60 \mu\text{m}^{-2}$) demonstrates the difference between the MT cytoskeleton dynamics under the effect of capture-shrinkage alone and under the effect of both mechanisms combined. The videos show the first few seconds of the process. In the case of sole capture-shrinkage, only long enough MTs attach to the center of the IS. One clearly sees in Video S7 that MTs intersecting the IS and attached to cortical sliding dynein are passed to the center of the IS, where they are captured by cortical

sliding dynein. Video S8 shows the complete repositioning of the MTOC under the effect of both mechanisms combined ($\tilde{\rho}_{IS} = \rho_{IS} = 60 \mu\text{m}^{-2}$).

A quantitative analysis in Fig. 10, a and b shows that the repolarization velocity increases with the cortical sliding density $\tilde{\rho}_{IS}$ as expected. Quite unexpectedly, it turns out that the average number of attached capture-shrinkage dyneins depends on the density of cortical sliding dyneins $\tilde{\rho}_{IS}$ and increases with it, as demonstrated by Fig. 10 c.

This finding indicates a synergy of the two mechanisms, capture-shrinkage and cortical sliding, and can be explained by the alignment of the MTs during repositioning. The MTs attached to the cortical sliding dyneins tend to align with the MTOC movement, as demonstrated by Fig. 10 e, in which the dominant central peak in direction $\alpha = 0$ is caused by capture-shrinkage dyneins, and cortical sliding dyneins provide only two small peaks from angles toward the periphery of the IS. As MTs align with the MTOC movement, they are captured by the capture-shrinkage dyneins in the central region of the IS, and the number of cortical sliding dyneins drops dramatically, as shown in Fig. 10 d.

A comparison of the probability densities shown in Fig. 3 f for capture-shrinkage alone and Fig. 5 f for cortical sliding alone reveals the mechanism by which cortical sliding supports capture-shrinkage. Fig. 3 f shows that the unattached MTs are pushed back by friction forces, which leads to the opening of the MT cytoskeleton such that MTs cannot intersect the narrow center of the IS anymore (visualized in Fig. 2 f). Attached MTs align with the MTOC movement in the case of cortical sliding (cf. Fig. 5 f). Therefore, when both mechanisms are combined, MTs attached by the

Hornak and Rieger

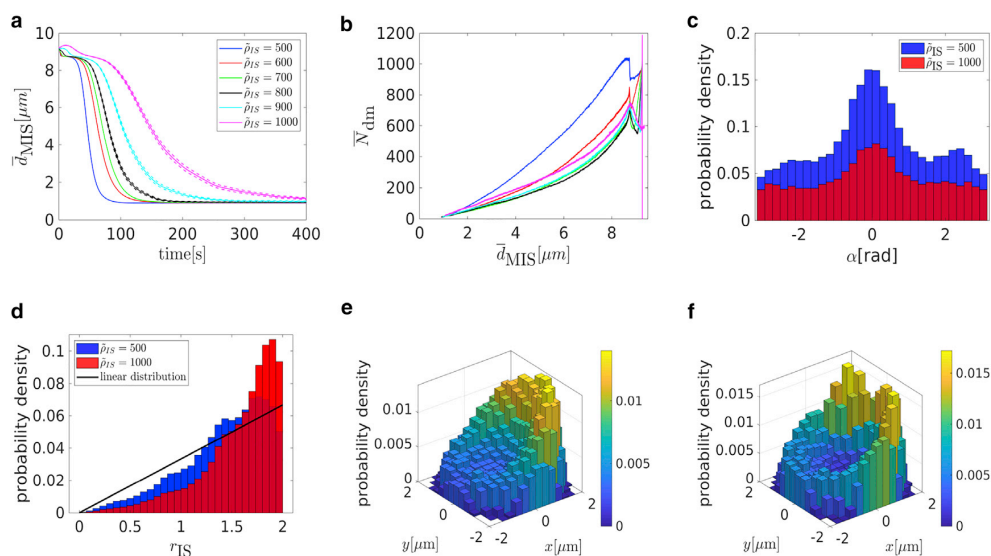


FIGURE 8 Cortical sliding with high dynein densities $\bar{\rho}_{\text{IS}}$. (a) The dependence of the average MTOC-IS distance \bar{d}_{MIS} on time is shown. The error bars are represented by dashed lines and are plotted only if bigger than a symbol size. (b) The dependence of the average number of dyneins \bar{N}_{dm} on the MTOC-IS distance is shown. (c) Probability distribution of the angle α between the first MT segment of attached MTs and the direction of the MTOC motion, $\bar{d}_{\text{MIS}} \sim 5 \mu\text{m}$, is shown. (d) The probability distribution of the distance of attached dynein anchor points from the axis of the IS r_{IS} when $\bar{d}_{\text{MIS}} \sim 5 \mu\text{m}$ is shown. (e and f) The two-dimensional probability density of attached dyneins in the IS, $\bar{d}_{\text{MIS}} = 5 \mu\text{m}$, is shown. (e) Area density of cortical sliding dyneins $\bar{\rho}_{\text{IS}} = 500 \mu\text{m}^{-2}$. (f) $\bar{\rho}_{\text{IS}} = 1000 \mu\text{m}^{-2}$. To see this figure in color, go online.

cortical sliding dyneins are not pushed back by friction, they align with the MTOC movement, and the attachment probability of the capture-shrinkage dynein increases. Comparing the probability density of the angle α for cortical sliding alone (Fig. 5 f) with the one for the combined mechanisms (Fig. 10 e) demonstrates impressively that most MTs attached to cortical sliding dyneins have detached and attached to capture-shrinkage dyneins.

These observations suggest an answer to the question about the role of the cortical sliding: it passes the MTs to the more efficient capture-shrinkage mechanism. Additionally, it provides a bigger pulling force than for cortical sliding alone because of the fact that the capture-shrinkage mechanism also supports cortical sliding. By comparison of Figs. 5 c and 8 b with Fig. 10 d, one realizes that the dependencies of the number of cortical sliding dyneins on the MTOC-IS distance are very different. As the MTOC approaches the IS, the number of dyneins acting on MTs decreases in the case of sole cortical sliding (cf. Figs. 5 c and 8 b) but rises for the case of the combined mechanisms (cf. Fig. 10 d). The reason lies in the firm anchoring of MTs in the center of the IS and the emergence of the remarkable “arc” formations of attached dynein (cf. Fig. 11, b and c).

The velocity of the capture-shrinkage processes explains this surprising finding. The capture-shrinkage mechanism is more efficient because the MTs shorten because of depolymerization, align with the MTOC movement, and are pulled to the same place. Slower stepping in the cortical sliding

mechanism will result in MT lengths between the MTOC and the IS far longer than the direct distance. Therefore, MTs have to bend (see Fig. 11, e–g), which explains the “arc” patterns of attached dyneins in the IS. In other words, firm anchoring of capture-shrinkage pushes the cortical sliding MTs against the IS, causing further attachment. By comparison of Fig. 5 d and Fig. 11 a, one observes that the MTOC approaches the IS more closely in the case of combined mechanisms than in the case of cortical sliding, which is another proof of the pulling of the MTOC toward the center of the IS. We conclude that the cortical sliding mechanism supports the dominant capture-shrinkage mechanism by “passing” the MTs, and the capture-shrinkage mechanism supports the cortical sliding mechanism by providing the anchoring and pushing the MTs against the IS.

This synergy is also indicated by Fig. 11 d, which shows the total repositioning times as a function of the density of capture-shrinkage dynein for various fixed values of the cortical sliding dynein. Although the repositioning time does not decrease further for large values of the capture-shrinkage dynein density ($\rho_{\text{IS}} > 600 \mu\text{m}^{-2}$), it can actually be decreased further by increasing cortical sliding dynein. Consequently, the combination of the two mechanisms with relatively low area densities is faster than the dominant mechanism alone with maximal area density (compare cases $\rho_{\text{IS}} = 200 \mu\text{m}^{-2}$ with various $\bar{\rho}_{\text{IS}}$ with the case of $\rho_{\text{IS}} = 1000 \mu\text{m}^{-2}$ in Fig. 11 d). Further parameter variations supporting this result can be found in the Supporting Materials and

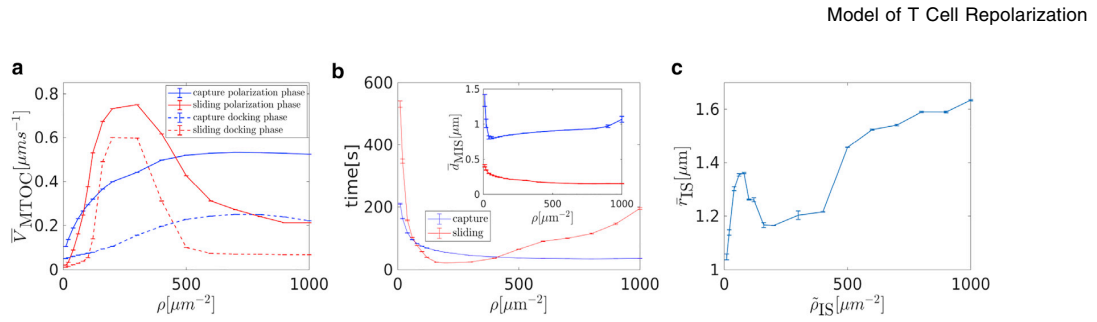


FIGURE 9 Comparison of the capture-shrinkage and the cortical sliding mechanisms in terms of the average MTOC velocity in both phases \bar{v}_{MTOC} , times of repositioning, and the final MTOC-IS distance \bar{d}_{MIS} . (a) The MTOC velocity in the first and the second phase is shown. (b) Repositioning times are shown. Final MTOC-IS distances are shown in the inset. (c) The dependence of the average distance \bar{r}_{IS} of attached dynein motors from the axis of the IS on dynein area density $\hat{\rho}_{\text{IS}}$ for the case of sole cortical sliding is shown. The error bars are represented by dashed lines and are plotted only if bigger than a symbol size. To see this figure in color, go online.

Methods, Section S3.3.3. The effect is certainly advantageous for the cell because the cortical sliding mechanism is not as efficient as the capture-shrinkage mechanism, considering the large amount of dynein required.

DISCUSSION

We have analyzed the experiments of (14) with a mechanistic model for the relocation of the MTOC in T cells. By using biologically realistic values for the model parameters such as the number and the stiffness of MTs, dynein pulling forces and detachment probabilities, and cytosol viscosity, we can recapitulate for a wide range of dynein densities the experimental observations of (14). In particular,

the timescale for the completion of the relocation process, as well as the MTOC velocities predicted by the model, agrees well with the experimental results.

Our model predicts that the cytoskeleton deforms substantially during the MTOC-repositioning process because of the combined effects of the capture-shrinkage mechanism and friction forces. The captured MTs form a narrow stalk between the MTOC and the IS, straightening under the tension caused by dynein motors acting on it and causing the rotation of the whole MT cytoskeleton toward it. Concomitantly, unattached MTs are pushed backward by the emerging viscous drag “opening” the MT cytoskeleton (cf. Fig. 2, *e* and *f*). Thus, our model provides a mechanistic explanation of the MT cytoskeleton opening that is also

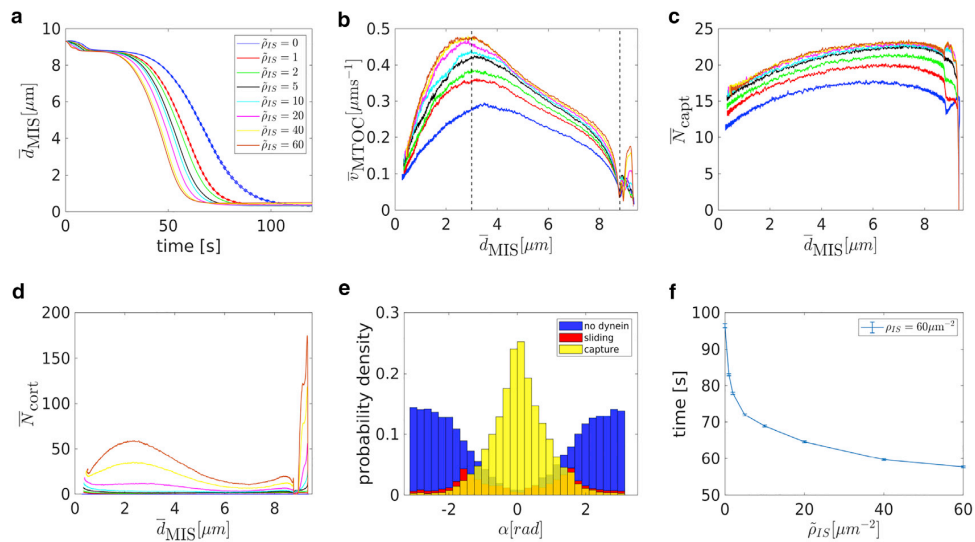


FIGURE 10 Combination of capture-shrinkage and cortical sliding: (a) dependence of the average MTOC-IS distance \bar{d}_{MIS} on time. Dependence of the average MTOC velocity \bar{v}_{MTOC} (b), the average number of attached capture-shrinkage dyneins \bar{N}_{capt} (c), and the average number of attached cortical sliding dyneins \bar{N}_{cort} (d) on the average MTOC-IS distance is shown (cortical sliding densities corresponding to different line colors in *b*–*d* are the same as in *a*). (e) The probability density of the angles α between the first MT segment and the direction of the MTOC motion is shown; $t = 50$ s, $\bar{d}_{\text{MIS}} \sim 5$ μm , $\hat{\rho}_{\text{IS}} = \rho_{\text{IS}}$ = 60 μm^{-2} . (f) Dependence of times of repositioning on cortical sliding area density $\hat{\rho}_{\text{IS}}$ is shown. The error bars are represented by dashed lines and are plotted only if bigger than a symbol size. To see this figure in color, go online.

Hornak and Rieger

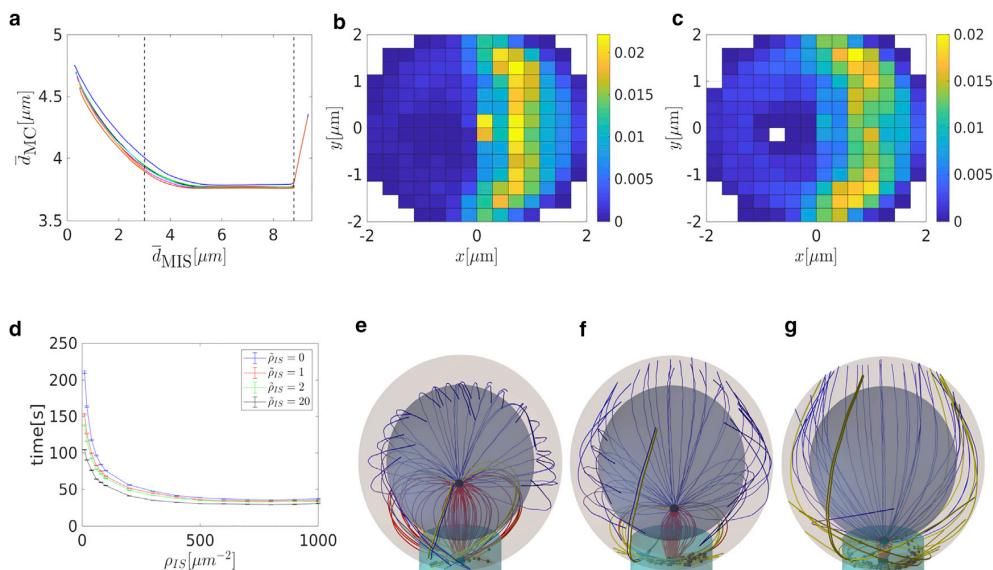


FIGURE 11 Combination of capture-shrinkage and cortical sliding. (a) Dependence of the average distance between the center of the cell and the MTOC \bar{d}_{MC} on the average MTOC-IS distance \bar{d}_{MIS} is shown. (b and c) A probability density plot for the spatial distribution of attached dynein is given. (b) $t = 50$ s, $\bar{d}_{MIS} \sim 4.5$ μm . (c) $t = 60$ s, $\bar{d}_{MIS} \sim 1.5$ μm . (d) Repositioning times as a function of the density of capture-shrinkage dynein ρ_{IS} for four different values of the cortical sliding area density $\bar{\rho}_{IS}$ are shown. The error bars are represented by dashed lines and are plotted only if bigger than a symbol size. (e–g) Snapshots from simulation are given. The blue, red, and bold yellow curves correspond to MTs without dynein and with capture-shrinkage and cortical sliding, respectively. Black dots depict positions of attached dynein motors. (e) $d_{MIS} = 4.5$ μm , (f) $d_{MIS} = 2.5$ μm , and (g) $d_{MIS} = 1$ μm . To see this figure in color, go online.

clearly visible in the experiments, as, for instance, in Fig. 5 A of (14). The opening can also be seen in the case of combined mechanisms, although for partially different reasons (Fig. 11, e–g).

The MT cytoskeleton opening might have interesting consequences for the distribution of Ca^{2+} in the cell, which is highly relevant for cell function. As the cytoskeleton rotates, the mitochondria are dragged with it (16) until they approach the IS. Because of the MT cytoskeleton opening, the mitochondria are positioned asymmetrically around the IS, resulting in an asymmetric absorption and redistribution of Ca^{2+} by the mitochondria. Consequently, an asymmetric distribution of Ca^{2+} arises around the IS, the function of which might deserve further investigation.

The detailed analysis of the MT cytoskeleton arrangement for the cortical sliding mechanism revealed three different deformation characteristics depending on three regimes for the dynein density (Cortical-Sliding Mechanism). This observation opens an interesting experimental perspective to estimate the dynein distribution from the MT cytoskeleton deformation during the MTOC repositioning.

Moreover, our model also predicts a biphasic behavior of the relocation process, as reported for the experiments in (14). Figs. 3 a and 10 a bear a clear resemblance to Fig. 3 D of (14). We showed that after a short initial period in which MTs start to attach to the dynein, the first phase observed experimentally corresponds in our model to the circular motion of the MTOC around the nucleus and the second phase to

the last 1 μm of the MTOC movement, when it detaches from the nucleus and moves more or less straight to the IS with a substantially reduced velocity for both mechanisms (capture-shrinkage and cortical sliding) and a large range of dynein densities. During the latter phase, the MTOC increases its distance from the cell center by approximately 1 $\mu\text{m} \sim 0.2 \times R_{\text{Cell}}$, which is close to the value reported in (14).

It was hypothesized in (14) that a resistive force emerges at the transition point between the phases, causing slowing down of the MTOC. Our model shows that the assumption of a resistive force is not necessary to explain the biphasic behavior: the velocity of the MTOC is only determined by the number of motors pulling on the MTs and on MT alignment (Figs. 3, 5 a, and 8). The reason for the slowing down is therefore simply the decrease of the number of dyneins attached to the MTs, which again is a consequence of the changing geometry and forces during the movement of the MTOC, i.e., a consequence of the interplay between the MT cytoskeleton and motors.

Experimentally, it was also observed that a treatment with taxol substantially reduced the velocity of the repositioning. Taxol impedes depolymerization of the MTs, which we could mimic in our model by reducing the capture-shrinkage efficiency. With this modification, our model reproduces the experimental observation (Fig. S10, a and b).

An interesting prediction of our model is that the two mechanisms, capture-shrinkage and cortical sliding, appear to act in remarkable synergy (Combination of Capture

Shrinkage and Cortical Sliding), which provides an answer to the question about the role of cortical sliding (14). Cortical sliding passes the MTs to the more efficient capture-shrinkage mechanism, which in return provides a firm anchor point. Therefore, cortical sliding is useful even in the configuration when capture-shrinkage is dominant. The synergy has a very practical effect because the combination of mechanisms with relatively low area densities can be faster than only the dominant mechanism with much higher area density Fig. 11 *d*. Therefore, the synergy of the two mechanisms can substantially reduce the area densities necessary for an effective repositioning and reduces the necessary resources (dynein). In our model, the cytoskeleton does not have to force its way through multiple organelles with complex structure, and the synergy manifests itself mainly in the velocity of the repositioning process. But one could speculate that in the real cell, the synergy can actually make the difference between completed and no repositioning.

It was proven in (50) that dyneins colocalize with the ADAP ring in the pSMAC. Moreover, in (17) it was hypothesized that the MTs are part of the reason why the pSMAC takes the form of a ring. Additionally, (17) reported the sharp turns in MTs upon interaction with the pSMAC and that the MTs do not project directly to the cSMAC. In our model, the cortical sliding dynein is homogeneously distributed over the entire IS; nevertheless, we observe that dyneins attach to MTs predominantly at the periphery of the IS (cf. Fig. 8, *d–f*). If both mechanisms are present, attached cortical sliding dyneins are even completely absent in the central region (cf. Fig. 11). We therefore conclude, like (17), that cortical sliding MTs do not project directly into the cSMAC and identify the periphery of the IS as the region where cortical sliding MTs are anchored. In agreement with the experiments (17), we observe that cortical sliding MTs turn upon contact with the periphery (Fig. 11, *e–g*), twist, and contribute to the formations of dynein “arcs.” Because the dynein in the central region of the IS does not contribute to the MTOC repositioning via cortical sliding, one could hypothesize that the pSMAC takes the shape of a ring to facilitate interaction with MTs (17).

We presented a numerical analysis of the repositioning in the case in which the MTOC and the IS are initially at the opposite sides of the cell. Even a case so restricted brought interesting results, enabling comparison with experiments and a proposed explanation for the experimental observable. We found that the cell performs the repositioning with great efficiency. The dyneins are placed only at the peripheries of the IS (pSMAC), which is the place where they are used the most, evacuating less-used regions. Moreover, we introduced a synergy of two mechanisms that minimizes the necessary area density of dynein.

In this work, we presented the results of our theoretical analysis of the MTOC repositioning that are relevant for the experimental setup in (14), in which the IS and the initial

position of the MTOC are diametrically opposed. Here, it turned out that even if both mechanisms (capture-shrinkage and cortical sliding) are at work, capture-shrinkage is always dominant, as reported in (14). In a second part of this work (unpublished data), we will examine other initial positions of the MTOC and the IS that will naturally occur in biologically relevant situations, and we will investigate under which circumstances cortical sliding will become the dominant mechanism over capture-shrinkage. Moreover, we will further demonstrate the synergy of two mechanisms introduced in this work and prove that it has more far-reaching effects in other initial configurations than the one studied here. Also, in the situation in which the T cell establishes two ISs, interesting dynamical behavior of the MTOC can be expected and will be analyzed in detail. In the end, we will see that in T cells the two mechanisms (capture-shrinkage and cortical sliding) and the spatial distribution of dynein are combined so as to minimize the number of dyneins necessary for polarization and to minimize the damage of the MT cytoskeleton.

SUPPORTING MATERIAL

Supporting Material can be found online at <https://doi.org/10.1016/j.bpj.2020.01.045>.

AUTHOR CONTRIBUTIONS

H.R. designed the research. I.H. performed calculations, prepared figures, and analyzed the data. I.H. and H.R. wrote the manuscript.

ACKNOWLEDGMENTS

The authors thank Bin Qu and Renping Zhao for helpful discussions.

This work was financially supported by the German Research Foundation within the Collaborative Research Center SFB 1027.

SUPPORTING CITATIONS

References (76–130) appear in the [Supporting Material](#).

REFERENCES

1. Rudolph, M. G., R. L. Stanfield, and I. A. Wilson. 2006. How TCRs bind MHCs, peptides, and coreceptors. *Annu. Rev. Immunol.* 24:419–466.
2. Garcia, K. C. 2012. Reconciling views on T cell receptor germline bias for MHC. *Trends Immunol.* 33:429–436.
3. Zinkernagel, R. M., and P. C. Doherty. 1974. Restriction of in vitro T cell-mediated cytotoxicity in lymphocytic choriomeningitis within a syngeneic or semiallogeneic system. *Nature.* 248:701–702.
4. Attaf, M., M. Legut, ..., A. K. Sewell. 2015. The T cell antigen receptor: the Swiss army knife of the immune system. *Clin. Exp. Immunol.* 181:1–18.
5. Wucherpfennig, K. W. 2004. T cell receptor crossreactivity as a general property of T cell recognition. *Mol. Immunol.* 40:1009–1017.
6. Babbitt, B. P., P. M. Allen, ..., E. R. Unanue. 1985. Binding of immunogenic peptides to Ia histocompatibility molecules. *Nature.* 317:359–361.

Hornak and Rieger

7. Monks, C. R., B. A. Freiberg, ..., A. Kupfer. 1998. Three-dimensional segregation of supramolecular activation clusters in T cells. *Nature*. 395:82–86.
8. Dustin, M. L., M. W. Olszowy, ..., A. S. Shaw. 1998. A novel adaptor protein orchestrates receptor patterning and cytoskeletal polarity in T-cell contacts. *Cell*. 94:667–677.
9. Dustin, M. L., A. K. Chakraborty, and A. S. Shaw. 2010. Understanding the structure and function of the immunological synapse. *Cold Spring Harb. Perspect. Biol.* 2:a002311.
10. Huang, Y., D. D. Norton, ..., R. L. Wange. 2005. Deficiency of ADAP/Fyb/SLAP-130 destabilizes SKAP55 in Jurkat T cells. *J. Biol. Chem.* 280:23576–23583.
11. André, P., A. M. Benoliel, ..., P. Bongrand. 1990. Use of conjugates made between a cytolytic T cell clone and target cells to study the redistribution of membrane molecules in cell contact areas. *J. Cell Sci.* 97:335–347.
12. Geiger, B., D. Rosen, and G. Berke. 1982. Spatial relationships of microtubule-organizing centers and the contact area of cytotoxic T lymphocytes and target cells. *J. Cell Biol.* 95:137–143.
13. Kupfer, A., D. Louvard, and S. J. Singer. 1982. Polarization of the Golgi apparatus and the microtubule-organizing center in cultured fibroblasts at the edge of an experimental wound. *Proc. Natl. Acad. Sci. USA*. 79:2603–2607.
14. Yi, J., X. Wu, ..., J. A. Hammer. 2013. Centrosome repositioning in T cells is biphasic and driven by microtubule end-on capture-shrinkage. *J. Cell Biol.* 202:779–792.
15. Stinchcombe, J. C., E. Majorovits, ..., G. M. Griffiths. 2006. Centrosome polarization delivers secretory granules to the immunological synapse. *Nature*. 443:462–465.
16. Maccari, I., R. Zhao, ..., H. Rieger. 2016. Cytoskeleton rotation relocates mitochondria to the immunological synapse and increases calcium signals. *Cell Calcium*. 60:309–321.
17. Kuhn, J. R., and M. Poenie. 2002. Dynamic polarization of the microtubule cytoskeleton during CTL-mediated killing. *Immunity*. 16:111–121.
18. Hui, K. L., and A. Upadhyaya. 2017. Dynamic microtubules regulate cellular contractility during T-cell activation. *Proc. Natl. Acad. Sci. USA*. 114:E4175–E4183.
19. Kupfer, A., and G. Dennert. 1984. Reorientation of the microtubule-organizing center and the Golgi apparatus in cloned cytotoxic lymphocytes triggered by binding to lysable target cells. *J. Immunol.* 133:2762–2766.
20. Kupfer, A., S. L. Swain, ..., S. J. Singer. 1986. The specific direct interaction of helper T cells and antigen-presenting B cells. *Proc. Natl. Acad. Sci. USA*. 83:6080–6083.
21. Gurel, P. S., A. L. Hatch, and H. N. Higgs. 2014. Connecting the cytoskeleton to the endoplasmic reticulum and Golgi. *Curr. Biol.* 24:R660–R672.
22. Lee, C., and L. B. Chen. 1988. Dynamic behavior of endoplasmic reticulum in living cells. *Cell*. 54:37–46.
23. Waterman-Storer, C. M., and E. D. Salmon. 1998. Endoplasmic reticulum membrane tubules are distributed by microtubules in living cells using three distinct mechanisms. *Curr. Biol.* 8:798–806.
24. Palmer, K. J., P. Watson, and D. J. Stephens. 2005. The role of microtubules in transport between the endoplasmic reticulum and Golgi apparatus in mammalian cells. *Biochem. Soc. Symp.* 72:1–13.
25. Müllbacher, A., P. Waring, ..., M. M. Simon. 1999. Granzymes are the essential downstream effector molecules for the control of primary virus infections by cytolytic leukocytes. *Proc. Natl. Acad. Sci. USA*. 96:13950–13955.
26. Lowin, B., M. C. Peitsch, and J. Tschopp. 1995. Perforin and granzymes: crucial effector molecules in cytolytic T lymphocyte and natural killer cell-mediated cytotoxicity. *Curr. Top. Microbiol. Immunol.* 198:1–24.
27. Voskoboinik, I., M. J. Smyth, and J. A. Trapani. 2006. Perforin-mediated target-cell death and immune homeostasis. *Nat. Rev. Immunol.* 6:940–952.
28. Grossman, W. J., P. A. Revell, ..., T. J. Ley. 2003. The orphan granzymes of humans and mice. *Curr. Opin. Immunol.* 15:544–552.
29. Krzewski, K., and J. E. Coligan. 2012. Human NK cell lytic granules and regulation of their exocytosis. *Front. Immunol.* 3:335.
30. Yannelli, J. R., J. A. Sullivan, ..., V. H. Engelhard. 1986. Reorientation and fusion of cytotoxic T lymphocyte granules after interaction with target cells as determined by high resolution cinemicrography. *J. Immunol.* 136:377–382.
31. Pasternack, M. S., C. R. Verret, ..., H. N. Eisen. 1986. Serine esterase in cytolytic T lymphocytes. *Nature*. 322:740–743.
32. Poo, W. J., L. Conrad, and C. A. Janeway, Jr. 1988. Receptor-directed focusing of lymphokine release by helper T cells. *Nature*. 332:378–380.
33. Kupfer, H., C. R. Monks, and A. Kupfer. 1994. Small splenic B cells that bind to antigen-specific T helper (Th) cells and face the site of cytokine production in the Th cells selectively proliferate: immunofluorescence microscopic studies of Th-B antigen-presenting cell interactions. *J. Exp. Med.* 179:1507–1515.
34. Stinchcombe, J. C., G. Bossi, ..., G. M. Griffiths. 2001. The immunological synapse of CTL contains a secretory domain and membrane bridges. *Immunity*. 15:751–761.
35. Haddad, E. K., X. Wu, ..., P. A. Henkart. 2001. Defective granule exocytosis in Rab27a-deficient lymphocytes from Ashen mice. *J. Cell Biol.* 152:835–842.
36. Griffiths, G. M. 1997. Protein sorting and secretion during CTL killing. *Semin. Immunol.* 9:109–115.
37. Stinchcombe, J. C., D. C. Barral, ..., G. M. Griffiths. 2001. Rab27a is required for regulated secretion in cytotoxic T lymphocytes. *J. Cell Biol.* 152:825–834.
38. Calvo, V., and M. Izquierdo. 2018. Imaging polarized secretory traffic at the immune synapse in living T lymphocytes. *Front. Immunol.* 9:684.
39. Kupfer, A., G. Dennert, and S. J. Singer. 1985. The reorientation of the Golgi apparatus and the microtubule-organizing center in the cytotoxic effector cell is a prerequisite in the lysis of bound target cells. *J. Mol. Cell. Immunol.* 2:37–49.
40. Golstein, P., and G. M. Griffiths. 2018. An early history of T cell-mediated cytotoxicity. *Nat. Rev. Immunol.* 18:527–535.
41. Bertrand, F., S. Müller, ..., S. Valitutti. 2013. An initial and rapid step of lytic granule secretion precedes microtubule organizing center polarization at the cytotoxic T lymphocyte/target cell synapse. *Proc. Natl. Acad. Sci. USA*. 110:6073–6078.
42. Lin, J., M. J. Miller, and A. S. Shaw. 2005. The c-SMAC: sorting it all out (or in). *J. Cell Biol.* 170:177–182.
43. Choudhuri, K., and M. L. Dustin. 2010. Signaling microdomains in T cells. *FEBS Lett.* 584:4823–4831.
44. Hammer, J. A., J. C. Wang, ..., A. T. Pedrosa. 2019. Origin, organization, dynamics, and function of actin and actomyosin networks at the T cell immunological synapse. *Annu. Rev. Immunol.* 37:201–224.
45. Martín-Cófreces, N. B., J. Robles-Valero, ..., F. Sánchez-Madrid. 2008. MTOC translocation modulates IS formation and controls sustained T cell signaling. *J. Cell Biol.* 182:951–962.
46. Nguyen-Ngoc, T., K. Afshar, and P. Gönczy. 2007. Coupling of cortical dynein and G α proteins mediates spindle positioning in *Caenorhabditis elegans*. *Nat. Cell Biol.* 9:1294–1302.
47. Saito, T. T., D. Okuzaki, and H. Nojima. 2006. Mcp5, a meiotic cell cortex protein, is required for nuclear movement mediated by dynein and microtubules in fission yeast. *J. Cell Biol.* 173:27–33.
48. Yamashita, A., and M. Yamamoto. 2006. Fission yeast Num1p is a cortical factor anchoring dynein and is essential for the horse-tail nuclear movement during meiotic prophase. *Genetics*. 173:1187–1196.

49. Ananthanarayanan, V., M. Schattat, ..., I. M. Tolić-Nørrelykke. 2013. Dynein motion switches from diffusive to directed upon cortical anchoring. *Cell*. 153:1526–1536.
50. Combs, J., S. J. Kim, ..., M. Poenie. 2006. Recruitment of dynein to the Jurkat immunological synapse. *Proc. Natl. Acad. Sci. USA*. 103:14883–14888.
51. Hashimoto-Tane, A., T. Yokosuka, ..., T. Saito. 2011. Dynein-driven transport of T cell receptor microclusters regulates immune synapse formation and T cell activation. *Immunity*. 34:919–931.
52. Stinchcombe, J. C., and G. M. Griffiths. 2014. Communication, the centrosome and the immunological synapse. *Philos. Trans. R. Soc. Lond. B Biol. Sci.* 369:20130463.
53. Quann, E. J., E. Merino, ..., M. Huse. 2009. Localized diacylglycerol drives the polarization of the microtubule-organizing center in T cells. *Nat. Immunol.* 10:627–635.
54. Laan, L., N. Pavin, ..., M. Dogterom. 2012. Cortical dynein controls microtubule dynamics to generate pulling forces that position microtubule asters. *Cell*. 148:502–514.
55. Breart, B., F. Lemaître, ..., P. Bousso. 2008. Two-photon imaging of intratumoral CD8+ T cell cytotoxic activity during adoptive T cell therapy in mice. *J. Clin. Invest.* 118:1390–1397.
56. He, J.-S., and H. L. Ostergaard. 2007. CTLs contain and use intracellular stores of FasL distinct from cytolytic granules. *J. Immunol.* 179:2339–2348.
57. Kim, M. J., and I. V. Maly. 2009. Deterministic mechanical model of T-killer cell polarization reproduces the wandering of aim between simultaneously engaged targets. *PLoS Comput. Biol.* 5:e1000260.
58. Sarkar, A., H. Rieger, and R. Paul. 2019. Search and capture efficiency of dynamic microtubules for centrosome relocation during IS formation. *Biophys. J.* 116:2079–2091.
59. Cooper, G. M. 2000. *The Cell: A Molecular Approach*, Second Edition. Sinauer Associates, Sunderland, MA.
60. Li, H., D. J. DeRosier, ..., K. H. Downing. 2002. Microtubule structure at 8 Å resolution. *Structure*. 10:1317–1328.
61. Meurer-Grob, P., J. Kasparian, and R. H. Wade. 2001. Microtubule structure at improved resolution. *Biochemistry*. 40:8000–8008.
62. Jia, K., and X. Liu. 2017. Measuring the flexural rigidity of actin filaments and microtubules from their thermal fluctuating shapes: a new perspective. *J. Mech. Phys. Solids*. 101:64–92.
63. Takasone, T., S. Juodkazis, ..., H. Misawa. 2002. Flexural rigidity of a single microtubule. *Jpn. J. Appl. Phys.* 41:3015–3019.
64. Gittes, F., B. Mickey, ..., J. Howard. 1993. Flexural rigidity of microtubules and actin filaments measured from thermal fluctuations in shape. *J. Cell Biol.* 120:923–934.
65. Broedersz, C., and F. MacKintosh. 2014. Modeling semiflexible polymer networks. *Rev. Mod. Phys.* 86:995–1036.
66. Chrétien, D., B. Buendia, ..., E. Karsenti. 1997. Reconstruction of the centrosome cycle from cryoelectron micrographs. *J. Struct. Biol.* 120:117–133.
67. Winey, M., and E. O’Toole. 2014. Centriole structure. *Philos. Trans. R. Soc. Lond. B Biol. Sci.* 369:20130457.
68. Guichard, P., V. Hachet, ..., P. Gönczy. 2013. Native architecture of the centriole proximal region reveals features underlying its 9-fold radial symmetry. *Curr. Biol.* 23:1620–1628.
69. Bernhard, W., and E. De Harven. 1956. Electron microscopic study of the ultrastructure of centrioles in vertebra. *Z. Zellforsch. Mikrosk. Anat.* 45:378–398.
70. Woodruff, J. B., O. Wueseke, and A. A. Hyman. 2014. Pericentriolar material structure and dynamics. *Philos. Trans. R. Soc. Lond. B Biol. Sci.* 369:20130459.
71. Moritz, M., M. B. Braunfeld, ..., D. A. Agard. 2000. Structure of the gamma-tubulin ring complex: a template for microtubule nucleation. *Nat. Cell Biol.* 2:365–370.
72. Robbins, E., G. Jentzsch, and A. Micali. 1968. The centriole cycle in synchronized HeLa cells. *J. Cell Biol.* 36:329–339.
73. Moritz, M., M. B. Braunfeld, ..., D. A. Agard. 1995. Microtubule nucleation by gamma-tubulin-containing rings in the centrosome. *Nature*. 378:638–640.
74. Burgess, S. A., M. L. Walker, ..., K. Oiwa. 2003. Dynein structure and power stroke. *Nature*. 421:715–718.
75. Belyy, V., M. A. Schlager, ..., A. Yildiz. 2016. The mammalian dynein-dynactin complex is a strong opponent to kinesin in a tug-of-war competition. *Nat. Cell Biol.* 18:1018–1024.
76. Puchkov, E. O. 2013. Intracellular viscosity: methods of measurement and role in metabolism. *Biochem. Moscow Suppl. Ser. A*. 7:270–279.
77. Bausch, A. R., W. Möller, and E. Sackmann. 1999. Measurement of local viscoelasticity and forces in living cells by magnetic tweezers. *Biophys. J.* 76:573–579.
78. Howard, J. 2001. *Mechanics of Motor Proteins and the Cytoskeleton*. Sinauer Associates, Sunderland, MA.
79. Leith, D. 1987. Drag on nonspherical objects. *Aerosol Sci. Technol.* 6:153–161.
80. Bereiter-Hahn, J., and M. Vöth. 1994. Dynamics of mitochondria in living cells: shape changes, dislocations, fusion, and fission of mitochondria. *Microsc. Res. Tech.* 27:198–219.
81. Jakobs, S. 2006. High resolution imaging of live mitochondria. *Biochim. Biophys. Acta*. 1763:561–575.
82. Chaudhuri, A. 2016. Cell biology by the numbers. *Yale J. Biol. Med.* 89:425–426.
83. Fawcett, D. W. 1966. An atlas of fine structure. The cell. Its organelles and inclusions. *Ann. Intern. Med.* 64:968.
84. Jakobs, S., and C. A. Wurm. 2014. Super-resolution microscopy of mitochondria. *Curr. Opin. Chem. Biol.* 20:9–15.
85. Xu, H., W. Su, ..., H. Wang. 2013. The asymmetrical structure of Golgi apparatus membranes revealed by in situ atomic force microscope. *PLoS One*. 8:e61596.
86. Ladinsky, M. S., D. N. Mastronarde, ..., L. A. Staehelin. 1999. Golgi structure in three dimensions: functional insights from the normal rat kidney cell. *J. Cell Biol.* 144:1135–1149.
87. Day, K. J., L. A. Staehelin, and B. S. Glick. 2013. A three-stage model of Golgi structure and function. *Histochem. Cell Biol.* 140:239–249.
88. Huang, S., and Y. Wang. 2017. Golgi structure formation, function, and post-translational modifications in mammalian cells. *F1000 Res.* 6:2050.
89. Westrate, L. M., J. E. Lee, ..., G. K. Voeltz. 2015. Form follows function: the importance of endoplasmic reticulum shape. *Annu. Rev. Biochem.* 84:791–811.
90. English, A. R., and G. K. Voeltz. 2013. Endoplasmic reticulum structure and interconnections with other organelles. *Cold Spring Harb. Perspect. Biol.* 5:a013227.
91. English, A. R., N. Zurek, and G. K. Voeltz. 2009. Peripheral ER structure and function. *Curr. Opin. Cell Biol.* 21:596–602.
92. Shibata, Y., G. K. Voeltz, and T. A. Rapoport. 2006. Rough sheets and smooth tubules. *Cell*. 126:435–439.
93. Hu, J., W. A. Prinz, and T. A. Rapoport. 2011. Weaving the web of ER tubules. *Cell*. 147:1226–1231.
94. Alberts, B., A. Johnson, ..., P. Walter. 2007. *Molecular Biology of the Cell*, Fifth Edition. Garland Science, New York.
95. Goodenough, U. W., B. Gebhart, ..., J. E. Heuser. 1987. High-pressure liquid chromatography fractionation of Chlamydomonas dynein extracts and characterization of inner-arm dynein subunits. *J. Mol. Biol.* 194:481–494.
96. Gee, M. A., J. E. Heuser, and R. B. Vallee. 1997. An extended microtubule-binding structure within the dynein motor domain. *Nature*. 390:636–639.
97. Goodenough, U., and J. Heuser. 1984. Structural comparison of purified dynein proteins with in situ dynein arms. *J. Mol. Biol.* 180:1083–1118.

Hornak and Rieger

98. Schmidt, H., E. S. Gleave, and A. P. Carter. 2012. Insights into dynein motor domain function from a 3.3-Å crystal structure. *Nat. Struct. Mol. Biol.* 19:492–497, S1.
99. Leduc, C., O. Campàs, ..., J. Prost. 2004. Cooperative extraction of membrane nanotubes by molecular motors. *Proc. Natl. Acad. Sci. USA.* 101:17096–17101.
100. Kamiya, N., T. Mashimo, ..., H. Nakamura. 2016. Elastic properties of dynein motor domain obtained from all-atom molecular dynamics simulations. *Protein Eng. Des. Sel.* 29:317–325.
101. Lindemann, C. B., and A. J. Hunt. 2003. Does axonemal dynein push, pull, or oscillate? *Cell Motil. Cytoskeleton.* 56:237–244.
102. Sakakibara, H., H. Kojima, ..., K. Oiwa. 1999. Inner-arm dynein c of *Chlamydomonas* flagella is a single-headed processive motor. *Nature.* 400:586–590.
103. Sakakibara, H., and K. Oiwa. 2011. Molecular organization and force-generating mechanism of dynein. *FEBS J.* 278:2964–2979.
104. Gennerich, A., A. P. Carter, ..., R. D. Vale. 2007. Force-induced bidirectional stepping of cytoplasmic dynein. *Cell.* 131:952–965.
105. Toba, S., T. M. Watanabe, ..., H. Higuchi. 2006. Overlapping hand-over-hand mechanism of single molecular motility of cytoplasmic dynein. *Proc. Natl. Acad. Sci. USA.* 103:5741–5745.
106. Mallik, R., D. Petrov, ..., S. P. Gross. 2005. Building complexity: an in vitro study of cytoplasmic dynein with in vivo implications. *Curr. Biol.* 15:2075–2085.
107. Mallik, R., B. C. Carter, ..., S. P. Gross. 2004. Cytoplasmic dynein functions as a gear in response to load. *Nature.* 427:649–652.
108. Reck-Peterson, S. L., A. Yildiz, ..., R. D. Vale. 2006. Single-molecule analysis of dynein processivity and stepping behavior. *Cell.* 126:335–348.
109. Kural, C., H. Kim, ..., P. R. Selvin. 2005. Kinesin and dynein move a peroxisome in vivo: a tug-of-war or coordinated movement? *Science.* 308:1469–1472.
110. Torisawa, T., M. Ichikawa, ..., K. Furuta. 2014. Autoinhibition and cooperative activation mechanisms of cytoplasmic dynein. *Nat. Cell Biol.* 16:1118–1124.
111. Müller, M. J. I., S. Klumpp, and R. Lipowsky. 2008. Tug-of-war as a cooperative mechanism for bidirectional cargo transport by molecular motors. *Proc. Natl. Acad. Sci. USA.* 105:4609–4614.
112. King, S. J., and T. A. Schroer. 2000. Dynactin increases the processivity of the cytoplasmic dynein motor. *Nat. Cell Biol.* 2:20–24.
113. Nishiura, M., T. Kon, ..., K. Sutoh. 2004. A single-headed recombinant fragment of *Dictyostelium* cytoplasmic dynein can drive the robust sliding of microtubules. *J. Biol. Chem.* 279:22799–22802.
114. Kon, T., M. Nishiura, ..., K. Sutoh. 2004. Distinct functions of nucleotide-binding/hydrolysis sites in the four AAA modules of cytoplasmic dynein. *Biochemistry.* 43:11266–11274.
115. Cho, C., S. L. Reck-Peterson, and R. D. Vale. 2008. Regulatory ATPase sites of cytoplasmic dynein affect processivity and force generation. *J. Biol. Chem.* 283:25839–25845.
116. Kikushima, K., T. Yagi, and R. Kamiya. 2004. Slow ADP-dependent acceleration of microtubule translocation produced by an axonemal dynein. *FEBS Lett.* 563:119–122.
117. Walter, W. J., B. Brenner, and W. Steffen. 2010. Cytoplasmic dynein is not a conventional processive motor. *J. Struct. Biol.* 170:266–269.
118. Ikuta, J., N. K. Kamisetty, ..., R. Yokokawa. 2014. Tug-of-war of microtubule filaments at the boundary of a kinesin- and dynein-patterned surface. *Sci. Rep.* 4:5281.
119. Kunwar, A., S. K. Tripathy, ..., S. P. Gross. 2011. Mechanical stochastic tug-of-war models cannot explain bidirectional lipid-droplet transport. *Proc. Natl. Acad. Sci. USA.* 108:18960–18965.
120. Klein, S., C. Appert-Rolland, and L. Santen. 2015. Motility states in bidirectional cargo transport. *EPL.* 111:68005.
121. Roberts, A. J., N. Numata, ..., S. A. Burgess. 2009. AAA+ Ring and linker swing mechanism in the dynein motor. *Cell.* 136:485–495.
122. Imai, H., T. Shima, ..., S. A. Burgess. 2015. Direct observation shows superposition and large scale flexibility within cytoplasmic dynein motors moving along microtubules. *Nat. Commun.* 6:8179.
123. Mizuno, N., A. Narita, ..., M. Kikkawa. 2007. Three-dimensional structure of cytoplasmic dynein bound to microtubules. *Proc. Natl. Acad. Sci. USA.* 104:20832–20837.
124. Montesi, A., D. C. Morse, and M. Pasquali. 2005. Brownian dynamics algorithm for bead-rod semiflexible chain with anisotropic friction. *J. Chem. Phys.* 122:84903.
125. Fixman, M. 1978. Simulation of polymer dynamics. I. General theory. *J. Chem. Phys.* 69:1527–1537.
126. Hinch, E. J. 1994. Brownian motion with stiff bonds and rigid constraints. *J. Fluid Mech.* 271:219–234.
127. Grassia, P. S., E. J. Hinch, and L. C. Nitsche. 1995. Computer simulations of Brownian motion of complex systems. *J. Fluid Mech.* 282:373–403.
128. Grassia, P., and E. J. Hinch. 1996. Computer simulations of polymer chain relaxation via Brownian motion. *J. Fluid Mech.* 308:255–288.
129. Pasquali, M., and D. C. Morse. 2002. An efficient algorithm for metric correction forces in simulations of linear polymers with constrained bond lengths. *J. Chem. Phys.* 116:1834–1838.
130. Nedelec, F., and D. Foethke. 2007. Collective Langevin dynamics of flexible cytoskeletal fibers. *New J. Phys.* 9:427.

6.1.2. Supplemental Material

Biophysical Journal, Volume 118

Supplemental Information

Stochastic Model of T Cell Repolarization during Target Elimination I

Ivan Hornak and Heiko Rieger

Stochastic model of T Cell repolarization during target elimination (I)

SUPPLEMENTARY MATERIAL

Ivan Hornak, Heiko Rieger

1 Model of the cell

1.1 Microtubules

The microtubules(MTs) are represented as semiflexible filaments, therefore the Hamiltonian of a single MT is given by:

$$H = \frac{\kappa}{2} \int_0^L \left| \frac{\partial \vec{t}}{\partial s} \right|^2, \quad (1)$$

where κ is bending rigidity($2.2 * 10^{-23} \text{Nm}^2$), L is the length of MT, s is arc length, $\vec{t} = \frac{\partial \vec{r}}{\partial s}$ is unit tangent vector and $\vec{r}(s)$ is a position (1). A single MT is represented as a chain of N beads with coordinates $\vec{r}_1, \dots, \vec{r}_N$ connected by $N - 1$ tangents $\vec{t}_i = \vec{r}_{i+1} - \vec{r}_i$ of the length $k = L/(N - 1)$. In the present model, the length $k = 0.8 \mu\text{m}$ was used. Since the MT is an inextensible polymer discretized into N beads, $N - 1$ constraints must be fulfilled:

$$C_i^{\text{micro}} = |\vec{r}_i - \vec{r}_{i+1}| = k \quad i = 1, \dots, N - 1 \quad (2)$$

The length of the MTs varies considerably, but since short MTs are not relevant for repositioning, we include only just MTs that reach from the MTOC to the IS in the first seconds of repositioning. The maximum length of a MT should be $L > \pi * R_{\text{Cell}}$ to always reach the IS in the first stages of repolarization, the length must be $L > \frac{3}{4} * \pi * R_{\text{Cell}}$. Thus, the number of beads N is uniformly distributed between 15 and 20.

1.1.1 Bending forces of the microtubule

The Hamiltonian for the discretized MT can be expressed as:

$$H_{\text{bend}} = \kappa_d \sum_{i=0}^{N-2} \left(1 - \frac{\vec{t}_i \vec{t}_{i+1}}{|\vec{t}_i| |\vec{t}_{i+1}|} \right), \quad (3)$$

where $\kappa_d = \kappa/k$ is the bending rigidity of the discretized model. The bending force acting on bead i is the derivative of the discretized Hamiltonian with the respect to \vec{r}_i :

$$\vec{F}_i^{\text{bend}} = - \frac{\partial H_{\text{bend}}}{\partial \vec{r}_i}. \quad (4)$$

If we consider the simplest case (sketched in Fig. 2) of three points with coordinates \vec{r}_1 , \vec{r}_2 and \vec{r}_3 connected with the tangents \vec{t}_1 and \vec{t}_2 , the bending forces acting on the beads are:

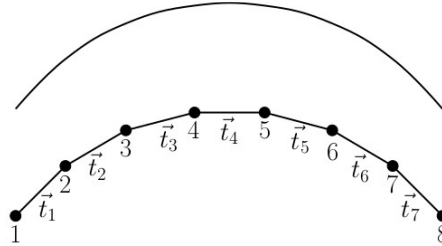


Figure 1: Bead-rod model of the microtubule. The MT is divided into 8 point connected by 7 rods. The circles correspond to the positions of the beads. The lengths of rods connecting beads remain constant.

$$\vec{F}_1^{\text{bend}} = \frac{\kappa_d}{|\vec{t}_1|} \left(- \frac{\vec{t}_2}{|\vec{t}_2|} + \frac{\vec{t}_1}{|\vec{t}_1|} \left(\frac{\vec{t}_1 \cdot \vec{t}_2}{|\vec{t}_2| |\vec{t}_1|} \right) \right), \quad (5a)$$

$$\vec{F}_3^{\text{bend}} = \frac{\kappa_d}{|\vec{t}_2|} \left(\frac{\vec{t}_1}{|\vec{t}_1|} - \frac{\vec{t}_2}{|\vec{t}_2|} \left(\frac{\vec{t}_1 \cdot \vec{t}_2}{|\vec{t}_2| |\vec{t}_1|} \right) \right) \quad (5b)$$

$$\vec{F}_2^{\text{bend}} = -\vec{F}_3^{\text{bend}} - \vec{F}_1^{\text{bend}}. \quad (5c)$$

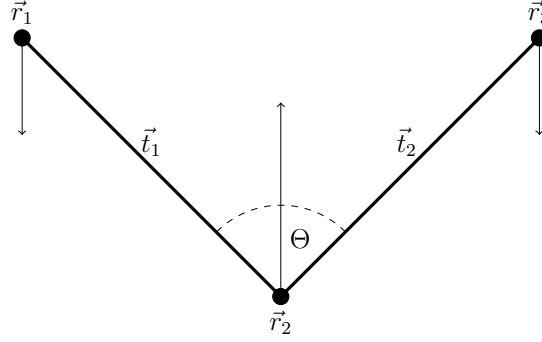


Figure 2: The sketch of bending forces acting on the MT composed of three beads. The filled circles represent the beads of the MT. The bending force is determined by the angle Θ between the tangents \vec{t}_1 and \vec{t}_2 . The narrow arrows depict bending forces acting on beads.

1.1.2 Drag coefficient

The drag force on an object depends on the speed of the object, the viscosity μ of the fluid, the size, and the shape of the object. The intracellular viscosity is very hard to measure or estimate, since the space between the nucleus and cell membrane is far from homogenous. The viscosity of aqueous domains of cell cytoplasm corresponds to the viscosity of water (2). On the other hand, in other microdomains, the local viscosity differs from the viscosity of water by more than three orders of magnitude (3). The effective viscosity in our model was chosen as:

$$\mu \sim 30\mu_w = 0.03\text{Pa} \cdot \text{s}, \quad (6)$$

where $\mu_w = 0.9775\text{mPa} \cdot \text{s}$ is the viscosity of water at temperature of $T = 21^\circ\text{C}$.

The MT is divided into segments of a cylindrical shape whose length is substantially bigger than the diameter. The drag depends on the object's area projected normal to the direction of the motion. Therefore, drag forces for the motions parallel and perpendicular to the object are defined as $F = \gamma_{\parallel}\dot{x}$ and $F = \gamma_{\perp}\dot{x}$, respectively, where \dot{x} is speed of the object. Parallel γ_{\parallel} and perpendicular γ_{\perp} drag coefficients (4) are defined for the case of a cylinder in the fluid with viscosity μ as:

$$\gamma_{\parallel} = \frac{2\pi\mu k}{\ln(k/d) - 0.2} \quad (7a)$$

$$\gamma_{\perp} = \frac{4\pi\mu k}{\ln(k/d) + 0.84}, \quad (7b)$$

where k and d are the length and the diameter of the cylinder, respectively. Therefore, the friction of the cylinder is anisotropic $\gamma_{\perp} \sim 2\gamma_{\parallel}$. However, the anisotropy is hard to implement, as the orientation of segments varies. Therefore, the anisotropy is not implemented. For the case of simplicity, the perpendicular drag coefficient is considered in the simulation to the beads of MT and the same drag coefficient is attributed to all MTOC points.

1.2 Drag force of organelles

EM, Golgi and mitochondria are the organelles with different structures and sizes. However, their drag force can be estimated from their volume and surfaces. A dynamic shape factor(5), K_{sf} , can be defined to calculate the drag coefficient of the nonspherical particle:

$$\gamma = 3\pi d_v \mu K_{sf}, \quad (8)$$

where d_v is the diameter of the sphere with the same volume as the object. The drag force can be divided between the form drag, coming from the pressure on the surface, and tangential shear stress. Form drag is determined by the objects area projected normal to the direction of the motion. It can be expressed through the Stokes law form drag on a sphere, whose projected area equals to the projected area of a nonspherical object. The diameter of such a sphere is d_n . The friction force on the surface can be expressed by the friction on the sphere with the same effective surface, which has the diameter d_s . The dynamic shape factor can be defined as:

$$K_{sf} = \frac{d_n + 2d_s}{3d_v}. \quad (9)$$

The number of mitochondria were measured(just the case of one cell) in (6) (44 mitochondria in a T-Cell). The size and shape of MTs varies greatly, since they can shrink, grow, go through fission and fusion (7–11). We consider the

most common spherocylindrical shape approximated by the cylinder, whose diameter and the length were estimated as $0.75\mu\text{m}$ and $1.5\mu\text{m}$, respectively. Golgi apparatus is a very complex structure composed from multiple classes of cisternae differing in form, function and composition that are stacked in various ways (12–15). The endoplasmic reticulum (ER) is also a complex organelle composed from a bilayer forming nuclear envelope and a network of sheets and dynamic tubules (16–20). Golgi, ER and mitochondria are connected to cytoskeleton (21) and (6).

For the rough approximate evaluation of drag force we consider the estimates from (22), table 12. The major organelles including EM and Golgi are close to the center and they are in contact. Consequently, effective viscosity in the regions close to the nucleus of the cell is different from more aqueous domain close to the cell membrane where the rotation of the cytoskeleton takes place. Therefore, we assume that the effective viscosity of the medium in which EM and Golgi travel is $\mu_2 = 10 * \mu$. We will express the drag coefficient of organelles as a function of viscosity and compare it with the drag coefficient of the cytoskeleton. For the estimate of the cytoskeleton drag coefficient, the cytoskeleton of 100 MTs was considered and the drag coefficient were calculated using (9).

$$\gamma_{\text{GSER}} \sim 0.00131\mu \quad (10)$$

$$\gamma_{\text{RER}} \sim 0.00160\mu \quad (11)$$

$$\gamma_{\text{Mito}} \sim 0.00257\mu \quad (12)$$

$$\gamma_{\text{Cyto}} \sim 0.00270\mu \quad (13)$$

From the equations (10) it can be seen that the $\gamma_{\text{total}} = (\gamma_{\text{Cyto}} + \gamma_{\text{Mito}} + \gamma_{\text{RER}} + \gamma_{\text{GSER}}) \sim 3 * \gamma_{\text{Cyto}}$. Consequently, to consider the drag force from the organelles in the cell, the drag coefficient of MT is tripled. Thus, the equation (7) can be rewritten as:

$$\gamma_{\parallel} = 3 * \frac{2\pi\mu k}{\ln(k/d) - 0.2} \quad (14a)$$

$$\gamma_{\perp} = 3 * \frac{4\pi\mu k}{\ln(k/d) + 0.84}. \quad (14b)$$

1.3 Confinement of the cytoskeleton

The cytoskeleton moves between the wall of the cell and the nucleus. They have a spherical shape and they are modeled as force fields. The force of the wall is null if $|\vec{r}_i| \leq R$. Otherwise, the force acting on the bead of the MT or the MTOC is expressed as:

$$\vec{F}_i^{\text{wall}} = -1 \frac{\vec{r}_i}{|\vec{r}_i|} k_1 \exp(k_2(|\vec{r}_i| - R)), \quad (15)$$

where R is the radius of the cell and $k_1 = 20\text{pN}\mu\text{m}^{-1}$ and $k_2 = 1\text{m}^{-1}$ are chosen constants. The force of nucleus is null if $|\vec{r}_i| > R_{\text{nucleus}}$ (radius of the nucleus). Otherwise, it can be expressed by:

$$\vec{F}_i^{\text{nucleus}} = \frac{\vec{r}_i}{|\vec{r}_i|} k_1 \exp(k_2(R_{\text{nuc}} - |\vec{r}_i|)), \quad (16)$$

where R_{nuc} is the radius of the nucleus.

1.4 Dynein motors

Unfortunately, since the results from the measurements differ greatly, the mechanical properties of dynein remain uncertain. Therefore, the parameters in this section are estimations. The dynein has an anchor and attachment points connected by a stalk. The anchor point has a stable position and the attachment point walks on the MT. The force acting on the MT is determined by the length of the stalk, whose relaxed length was estimates as $L_0 = 18\text{nm}$ (23–26).

Unattached dynein is represented just with one point on the surface of the cell. If the dynein is closer to the MT than L_0 , the motor protein can attach to the filament. Fluctuations of the membrane can move the dynein motor to the MT. Therefore, the attachment probability is defined as:

$$p_a = 5s^{-1} \quad d_{md} \leq L_0 \quad (17)$$

$$p_a = 5 \cdot \exp(-(d_{md} - L_0)/p_d)s^{-1} \quad d_{md} > L_0, \quad (18)$$

where d_{md} is the distance of the dynein point to the closest point of the MT and $p_d = 10^{-7}$ is a chosen parameter. If the MT is attached, the anchor and attachment points of the dynein motor are placed to the same point on the MT. Attachment probability of dynein is unknown; therefore, the attachment probability p_a corresponding to the attachment ratio of kinesin is considered (27). The force of dynein motor comes from the elastic properties of the stalk:

$$|F_i^{\text{Dynein}}| = 0, \quad |\vec{r}_{\text{Dynein}}| < L_0 \quad (19)$$

$$\vec{F}_i^{\text{Dynein}} = k_{\text{Dynein}} (|\vec{r}_{\text{Dynein}}| - L_0) \frac{\vec{r}_{\text{Dynein}}}{|\vec{r}_{\text{Dynein}}|} \quad |\vec{r}_{\text{Dynein}}| > L_0, \quad (20)$$

where $\vec{r}_{\text{Dynein}} = \vec{r}_{\text{anchor}} - \vec{r}_{\text{attach}}$ is the distance between the anchor and the attachment points. The measurements of elastic modulus of the stalk differ (28–31), therefore, the elastic modulus was estimated to $k_{\text{Dynein}} = 400\text{pN}\mu\text{m}^{-1}$ (32). If the force is null or parallel to the preferred direction of stepping, the probability of stepping to the minus end is:

$$p_- = \frac{V_F}{d_{\text{step}}}, \quad (21)$$

where V_F is the forward speed of dynein and d_{step} is the length of the step. The steps of dynein have multiple lengths (33–38). Nevertheless, just the most frequently measured length $d_{\text{step}} = 8\text{nm}$ is considered. The forward speed was estimated or measured in various sources (33, 34, 39–45). For our purposes it is estimated to be $V_F = 1000\text{nms}^{-1}$. In the case of the force of the dynein being in the opposite direction to the preferred movement and smaller than a stall force F_S , the attachment point steps to the minus end with probability:

$$p_- = \frac{V_F}{d_{\text{step}}} \left(1 - \frac{|F^{\text{Dynein}}|}{F_S}\right). \quad (22)$$

The value of the stall force varies greatly (33, 33–36, 40, 46) and (47), we estimate it as $F_S = 4\text{pN}$. If the force aims to the plus end and it is bigger than the stall force, dynein steps to the plus end with probability:

$$p_+ = \frac{V_B}{d_{\text{step}}}. \quad (23)$$

Backward stepping speed is force dependent (33) and the measured values also differ (40), (48). Our estimate is $V_B = 6.0\text{nm}\cdot\text{s}^{-1}$ (33).

The probability of detachment is expressed as:

$$p_{\text{detach}} = \exp\left(\frac{|F_d|}{F_D}\right), \quad (24)$$

where the detachment force (40, 48, 49) was estimated as $F_D = F_S/2$. When the attachment point of dynein motor is not on a bead of MT, the force is acting on a point of a segment between two beads. In such a case, the force has to be transmitted to the two closest beads. Since the mechanism of stepping and detachment of dynein is uncertain, we use the model for kinesin stepping (50).

Dynein plays a role in two mechanisms. During the cortical sliding mechanism acting in the whole IS, the MT slides on the membrane and its plus-end remains free. MT depolymerizes in the fixed position on the membrane of the cell during capture-shrinkage mechanism acting in the center of the IS. Without the effects of dynein, MT detaches from fixed position.

The densities of capture-shrinkage dyneins, ρ_{IS} , and cortical sliding dynein $\tilde{\rho}_{IS}$ vary through the range that could be expected during the T-Cell activation, $0 < \rho_{IS}, \tilde{\rho}_{IS} < \rho_{\text{MAX}}$. The maximum density of dyneins were estimated considering its structure and size. The dynein comprises a long stalk and a ring-like head containing six AAA+ modules whose diameter is comparable with the length of the stalk (51, 52), and N- and C-terminal regions. The size of the dynein motor can be also estimated from the distance d_{hm} between the head domain of the dynein and the center of the attached MT (53), $d_{\text{hm}} = 28\text{nm}$, which substantially exceeds the length of the dynein stalk. For the case of simplicity, we compute the area of plasma membrane covered by one dynein as $a_d = \pi * L_0^2$, where L_0 is the length of the stalk. The number of dynein N_{dynein} in $1\mu\text{m}^2$ is calculated as

$$N_{\text{dynein}} = \frac{1^{-12}}{a_d} \sim 1000. \quad (25)$$

Consequently, $\rho_{\text{MAX}} = 1000\mu\text{m}^{-2}$.

1.5 Microtubule organizing center (MTOC)

The MTOC is modeled as a planar, polygonal structure, composed from so-called sprouting points (points of MT sprouting). If MTOC has Q^{MTOC} sprouting points, then the equal number of constraints holds them in a specified distance from MTOC center (black lines in Fig. 3). Therefore, the i th constraint is defined as:

$$C_i^{\text{MTOC}} = |\vec{r}_i^{\text{mtoc}} - \vec{r}_c| = R_{\text{MTOC}} \quad i = 1, \dots, Q^{\text{MTOC}}, \quad (26)$$

where \vec{r}_i^{mtoc} is the position of i th sprouting point and \vec{r}_c is the position of the center of the MTOC. Moreover, additional Q^{MTOC} bonds keep the neighboring points in a constant distance d^{MTOC} (blue lines in Fig. 3).

$$C_i^{\text{MTOC}} = |\vec{r}_i^{\text{mtoc}} - \vec{r}_{i+1}^{\text{mtoc}}| = d^{\text{MTOC}} \quad i = Q^{\text{MTOC}} + 1, \dots, 2 \cdot Q^{\text{MTOC}}, \quad (27)$$

When MT is created, the so-called "sprouting point" and "rear point" on the MTOC are chosen 4. The second bead of the MT is attached to the sprouting point and the first bead to the rear point. Consequently, the original MT orientation is given by the direction from the rear point to the sprouting point. Every MTOC point is the sprouting point to the same number of MTs. The rear point is chosen from the points at the approximately opposite side (relatively to sprouting point) of the MTOC 4a, which gives a variety of the initial MT orientations. Elastic force 4a anchors the MT in the MTOC, while bending force 4b forces the MT to be aligned with the line connecting sprouting and rear points. The combination of two forces assures anchoring of the MT and limitation of changes in orientation, simulating the effect of PCM.

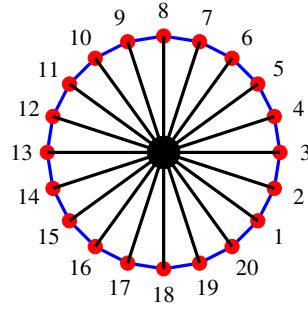


Figure 3: Sketch of the MTOC with $N_{\text{MTOC}} = 20$ MT sprouting points represented by red spheres. The black sphere in the middle depicts the center of the MTOC. Black lines connecting the points with the center and blue lines connecting the neighboring points are nondeformable.

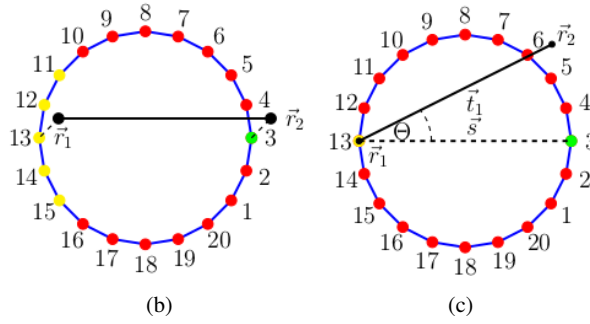


Figure 4: The sketch of the MTOC and forces connecting the MTOC with MTs. The black line denotes the first segment of microtubule. (a) Dashed lines depict the elastic forces connecting two points of microtubule to two MTOC points. The green point represents the sprouting point and yellow points depict possible rear points. (b) Bending force minimizes the angle Θ between the first segment of microtubule \vec{t}_1 and the line \vec{s} connecting sprouting (green) and rear (yellow) point.

1.5.1 Connecting microtubule and MTOC

The first segment of the MT is inside the MTOC 4a. The second and the first the MT beads are attached by elastic forces to the sprouting point and the rear point, respectively 4a. Elastic forces acting on a MT bead can be written as:

$$\vec{F}_2^{\text{elas}} = k_3 |\vec{d}_2| \cdot \frac{\vec{d}_2}{|\vec{d}_2|}, \quad (28)$$

where $k_3 = 30 \cdot \text{pN}\mu\text{m}^{-1}$ is a spring constant and $\vec{d}_2 = \vec{r}_s^{\text{MTOC}} - \vec{r}_2^{\text{micro}}$, where \vec{r}_s^{MTOC} and \vec{r}_2^{micro} are MTOC sprouting point and the second bead of MT, respectively. Analogically, we can define the forces between the first bead of the MT and the MTOC rear point. Bending forces 4b are calculated via:

$$\vec{F}_{\text{MTOC}}^{\text{bend}} = \frac{\kappa}{|\vec{s}|^2} \left(-\frac{\vec{t}_1}{|\vec{t}_1|} + \frac{\vec{s}}{|\vec{s}|} \left(\frac{\vec{t}_1 \cdot \vec{s}}{|\vec{s}||\vec{t}_1|} \right) \right) \quad (29a)$$

$$\vec{F}_{\text{micro}}^{\text{bend}} = \frac{\kappa}{|\vec{t}_1|^2} \left(\frac{\vec{s}}{|\vec{s}|} - \frac{\vec{t}_1}{|\vec{t}_1|} \left(\frac{\vec{t}_1 \cdot \vec{s}}{|\vec{s}||\vec{t}_1|} \right) \right), \quad (29b)$$

$$\vec{F}_0 = -\vec{F}_{\text{micro}}^{\text{bend}} - \vec{F}_{\text{MTOC}}^{\text{bend}} \quad (29c)$$

where \vec{s} is the segment between the two beads of the MTOC, \vec{t}_1 is the first segment of MT. The forces $\vec{F}_{\text{MTOC}}^{\text{bend}}$ and $\vec{F}_{\text{micro}}^{\text{bend}}$ act on the sprouting point and the second bead of MT, respectively. The force \vec{F}_0 acts on the first bead of the MT and the rear point.

2 Constrained Langevin dynamics

Using Langevin dynamics, the motion of an unconstrained particle with the position x_i can be expressed:

$$\gamma_i \dot{x}_i = f_i + \eta_i, \quad (30)$$

where η_i is a random Langevin force, which is a stochastic, non-differentiable function of time that integrates random interactions with the molecules of the solvent. The force f_i is the sum of all other forces and it depends on the object and γ is the drag coefficient. In a constrained case, N beads in 3D have to satisfy Q constraints (54):

$$C_a(x_1, \dots, x_{3*N}) = c_a \quad a = 1, \dots, Q \quad (31)$$

The constraints have to remain constant in every instance. Therefore, the movement of the beads must satisfy:

$$0 = \dot{C}_a = n_{ia} \cdot \dot{x}_i \quad a = 1, \dots, Q \quad (32)$$

where

$$n_{ia} = \frac{\partial C_a}{\partial x_i}. \quad (33)$$

The motion of a constrained bead can be expressed:

$$\gamma \dot{x}_i = f_i + \eta_i - n_{ia} \lambda_a, \quad (34)$$

where λ_a is the constraint force conjugate to the constraint μ .

2.1 Mid-Step algorithm

Mid-Step algorithm was proposed by Fixman and further generalized by Hinch and Grassia (55–58) The algorithms was elaborated for specific cases by Morse and Pasquali (54) and (59). Using the mobility tensor

$$H_{ik} \gamma = \mathbf{I}_{ik}, \quad (35)$$

the equation (34) can be rewritten as:

$$\dot{x}_i = H_{ij} [F_j^u - n_{ja} \lambda_a], \quad (36)$$

where $F_j^u = f_j + \eta_j$ is unconstrained force. The values of λ_a for $a = 1, \dots, Q$ can be calculated from the conditions (32) at every instant. It will result in the set of algebraic equations:

$$G_{av} \lambda_v = n_{ia} H_{ij} F_j^u, \quad (37)$$

where

$$G_{av} = n_{ia} H_{ij} n_{jv}. \quad (38)$$

If the constraint forces are expressed by (37), we get the equation of motion from (34):

$$\dot{x}_i = P_{ij} H_{jk} F_k^u, \quad (39)$$

where

$$P_{ij} = \mathbf{I}_{ij} - H_{ik} n_{ka} G_{av}^{-1} n_{jv} \quad (40)$$

is a projection operator. In the case when the mobility tensor is expressed by (35), equation 40 can be rewritten as:

$$P_{ij} = \mathbf{I}_{ij} - n_{ia} T_{av}^{-1} n_{jv}, \quad (41)$$

where

$$T_{av} = n_{ia} n_{iv}. \quad (42)$$

The dynamical projection operator is used to project forces to $3N - Q$ dimensional hypersurface. Therefore, they are locally perpendicular to the constraints.

The mid-step algorithm proposed by Hinch is for the case of mobility tensor (35) composed by four following substeps:

1. Generate unprojected random forces η_i and unprojected forces f_i at initial position x_i^0 ;
2. Construct projected random force $\eta_i^P = P_{ij} \eta_j$ and $f_i^P = P_{ij} f_j$;
3. Calculate midstep position $x_i^{1/2} = x_i^0 + \dot{x}_i^0 \Delta t / 2$, where the mobility in the original configuration \dot{x}_i^0 is calculated via (39) and Δt is the time step;
4. Calculate updated bead positions $x_i^1 = x_i^0 + \dot{x}_i^{1/2} \Delta t$, where $\dot{x}_i^{1/2}$ is evaluated with the deterministic and normal vectors from mid position, but with the same projected random force from initial configuration.

Mid-step algorithm uses the projection operator (40) that alongside with the mid position calculation minimizes the perturbations of constraints. Nevertheless, perturbations cannot be eliminated. Therefore, the MT has to be resized to fulfill the constraints. In such operation, the angles between \vec{t}_i and \vec{t}_{i+1} , where $i = 1, \dots, N - 1$ are conserved, the first bead of MT remains constant and MT regrows from the MTOC. Consequently, the bending energy of the MT remains unchanged.

3 Additional results

3.1 Influence of random forces

Random forces acting on the MTs have small effects since the motion of the MTs is constrained. Fig. 5a suggests that random forces perpendicular to the cell membrane (red) have no effect since microtubule curvature is given by the interplay of bending forces and the force of the membrane. The green forces, acting parallel to the segments of the MTs have also no impact, because the MT is attached to the MTOC, making it a part of a very massive structure. Consequently, just random forces depicted in purple in 5b can result in movement, making the random noise effectively one-dimensional. However, the MT is still rigid structure, random forces act in contradiction and filament is bound to MTOC, which seriously limits the movement of upper beads. Therefore, the influence of random noise can be expected to be negligible. Moreover, the capture-shrinkage mechanism fixates the MT on both sides, further minimizing the effect of the random force. In Figs. 6a and 6b we can see that the repositioning curves are almost identical for the case of the capture-shrinkage mechanism. The Figs. 6c and 6d demonstrate that the developments of the number of attached dyneins also do not differ. During cortical sliding repositionings the effect of the random forces is also negligible 7.

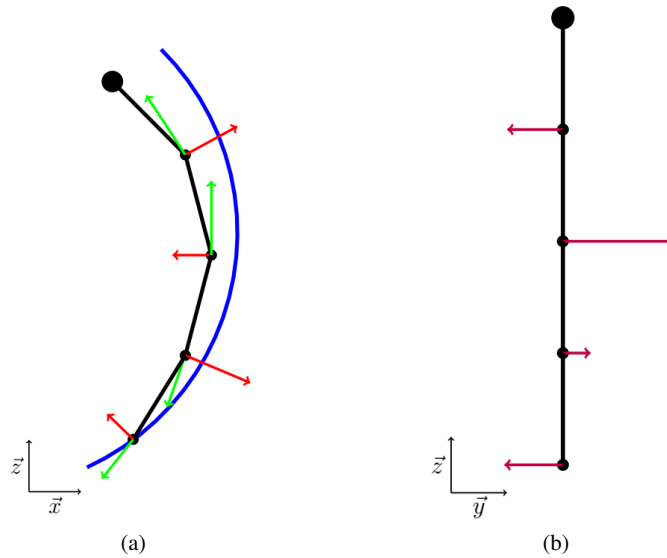


Figure 5: Sketch of random forces acting on the MT from two perspectives. The big circle represents MTOC and smaller circles represent beads of microtubule. Blue arc depicts membrane of the cell. Red, green and purple lines representing random forces acting on every bead are perpendicular.

3.2 Comparison of two cases with different number of microtubules

The cytoskeleton of $M_{\text{micro}} = 100$ MTs (examined in previous section) is compared with the cytoskeleton of $M_{\text{micro}} = 40$. We define $n_{\text{dm}}(t) = \frac{N_{\text{dm}}(t)}{M_{\text{micro}}}$ to examine the ratio of the attached dyneins and the number of the MTs in a cytoskeleton. Fig. 8a depicts repolarization curves of two cytoskeletons for the case of the capture-shrinkage mechanism. The polarization exhibits a triphasic behavior for both cases 8b.

We define $n_{\text{max}} = \max(n_{\text{dm}}(t))$. In Figs 8c it can be seen that n_{max} is always bigger for the case of smaller cytoskeleton (caused by the small area of the center of IS and limited number of dynein). The Figs. 8c and 8d explain the differences of speed in terms of the number of motors. When the area density is small, the smaller cytoskeleton is pulled with relatively higher force. As the concentration increases, the maximum speed is achieved ($\rho_{\text{IS}} \sim 600 \mu\text{m}^{-2}$). Subsequent increase of pulling force has no effect.

Figs. 9a and 9b depicting the repositioning under the influence of the cortical sliding mechanism shows the three regimes for both cytoskeletons. In both cases, n_{max} rises at the beginning, it reaches its maximum when $\tilde{\rho}_{\text{IS}} \sim 200 \mu\text{m}^{-2}$ and then it decreases swiftly and then steadily 9c. For smaller densities, the number of dyneins per MT are smaller for the bigger cytoskeleton. The situation is opposite when considering high area densities. Since the attached MTs aim in different directions, dyneins compete in the area of higher densities. As the number of the MT decreases, the pulling forces acting on individual filaments increase, leading to faster detachment. The MTOC speed increases when $\tilde{\rho}_{\text{IS}} < 200 \mu\text{m}^{-2}$ and then it decreases. We can see in 9d that the speed decreases for both cases even when n_{max} stays approximately the same, which is the consequence of dynein acting predominantly at the periphery.

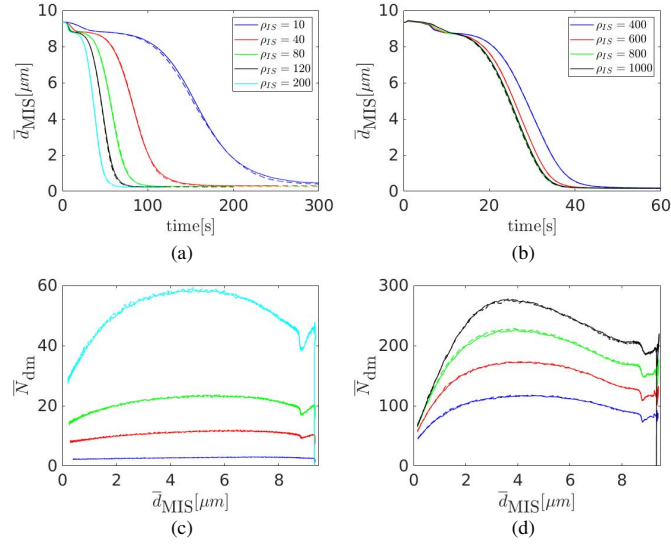


Figure 6: Combination of the capture-shrinkage mechanism and random forces. Solid lines stand for the sole capture shrinkage and dashed lines for the combination with random forces. Legends in (a), (b) apply for (c), (d), respectively. (a)(b) Dependence of the average MTOC-IS distance \bar{d}_{MIS} on time, (c)(d) Dependence of the average number of dynein \bar{N}_{dm} motors on MTOC-IS distance \bar{d}_{MIS} .

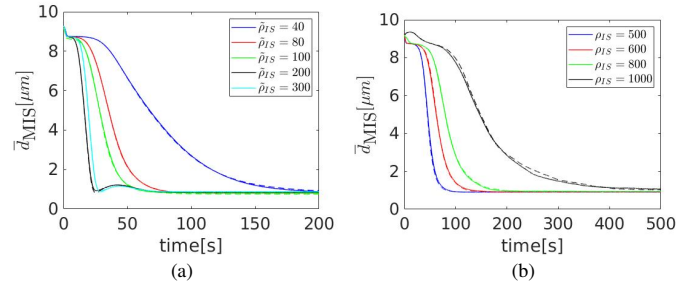


Figure 7: Combination of the cortical sliding mechanism and random forces. Solid lines stand for the sole cortical sliding and dashed lines for the combination with random forces. (a)(b) Dependence of the average MTOC-IS distance \bar{d}_{MIS} on time.

3.3 Capture-shrinkage and cortical sliding combined

As can be seen in Fig. 10b, addition of the small area density of capture-shrinkage dyneins in the center of IS causes substantial decrease of differences between times of polarization. Moreover, the three regimes of behavior based on the area density of cortical sliding dyneins is not observed in the presence of the capture-shrinkage mechanism. Surely, the third regime presents a disadvantage, since the pulling force of dynein is wasted in unproductive competitions. Therefore, the synergy of two mechanisms proves once more to be highly effective, since it does not only removes the third regime, but also greatly reduces the times of repositioning when the area density of cortical sliding $\bar{\rho}_{IS} < 100\mu\text{m}^{-2}$. Fig. 10a depicts times of repositioning for different sets of combined mechanisms since the capture-shrinkage area density varies and cortical sliding density remains constant. We can see that the times of repositioning are in general shorter for the case of combined mechanisms. Moreover, even when the area densities correspond to the second regime, the times of repositioning are comparable. Combined cases, however, have just 15% of the number of dyneins. Additionally, we can notice that the increase of area densities when $\bar{\rho}_{IS} > 500\mu\text{m}^{-2}$ presents no advantage since it causes slowing down of repositioning in the absence of capture-shrinkage and has no effect when the mechanisms are combined. Fig. 10c shows that the attached dyneins are predominantly located on the periphery of IS even in the case when $\bar{\rho}_{IS} > \rho_{IS}$.

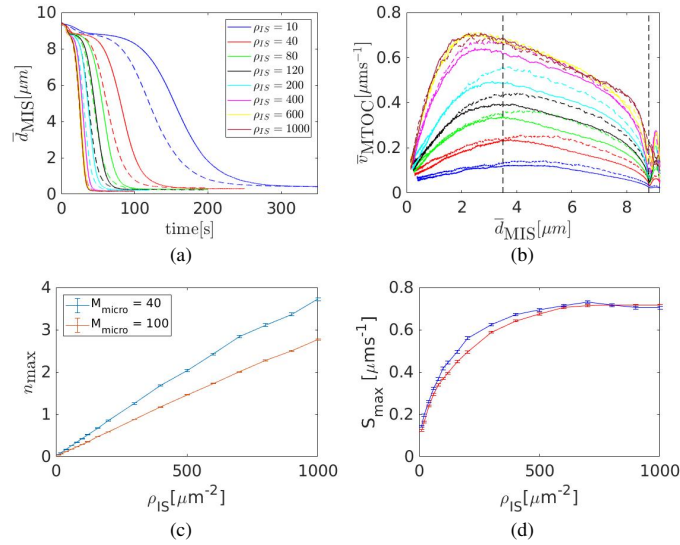


Figure 8: Capture-shrinkage mechanism for two cytoskeletons with different numbers of microtubules: $M_{\text{micro}} = 100$ (solid lines) and $M_{\text{micro}} = 40$ (dashed lines). (a) Dependence of average MTOC-IS distance \bar{d}_{MIS} on time. (b) Dependence of average MTOC speed \bar{v}_{MTOC} on \bar{d}_{MIS} . (c) Dependence of the maximum number of attached dyneins per microtubule n_{max} on area density ρ_{IS} . (d) Dependence of the maximum speed S_{max} on ρ_{IS} .

4 Commentary on modeling approaches

4.1 Cytosim

Cytosim is widely accepted as an efficient tool for the simulations of fibers (60). Although there are many similarities between the models, we decided not to use Cytosim. The first reason is our goal to examine the role of Brownian motion. The implicit integration used by Cytosim has a numerical error that could influence the precision of calculation in the absence of thermal noise. The second reason is the simplified calculation of the bending forces used by Cytosim. The advantage of such an approach, which enables to express the bending forces as a result of a matrix-vector multiplication, is a great efficiency of calculation. Nevertheless, the procedure is valid only if the angles between subsequent segments remain small. This presents a drawback, since the angles between the segment increase as the radius of the cell decrease. More importantly, substantial curvature of the MTs can be expected during repositioning (61)(See 4.4). Moreover, the "reshaping" of the objects due to the numerical impressions is done to keep the center of mass constant. Since the rigidity of MTOC is an important part of our model, reshaping is done to keep the first the bead of the MT (therefore MTOC-MT forces) constant.

4.2 Model using deterministic force

Kim and Maly (62) modeled the cortical sliding mechanism using the deterministic force. Although this model has various merits, it leads to the contradiction with some experimental observable: for example MTs stalk going through the center (62). This presents a drawback since various biological functions depend on the distribution of MTs.

References

1. Broedersz, C., and F. MacKintosh, 2014. Modeling semiflexible polymer networks. *Rev. Mod. Phys.* 86:995–1036.
2. Puchkov, E. O., 2013. Intracellular viscosity: Methods of measurement and role in metabolism. *Biochem. Moscow Suppl. Ser. A* 7:270–279.
3. Bausch, A. R., W. Möller, and E. Sackmann, 1999. Measurement of local viscoelasticity and forces in living cells by magnetic tweezers. *Biophys J* 76:573–579.
4. Howard, J., 2001. *Mechanics of Motor Proteins and the Cytoskeleton*. Sinauer Associates is an imprint of Oxford University Press, Sunderland, Mass, new edition.
5. Leith, D., 1987. Drag on Nonspherical Objects. *Aerosol Science and Technology* 6:153–161.

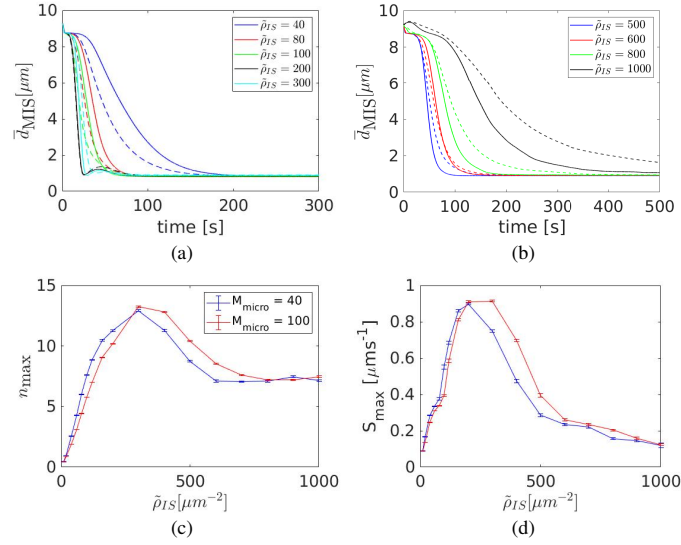


Figure 9: Cortical sliding mechanism for two cytoskeletons with different numbers of microtubules $M_{\text{micro}} = 100$ (solid lines) and $M_{\text{micro}} = 40$ (dashed lines). (a)(b) Dependence of average MTOC-IS distance \bar{d}_{MIS} on time. (c) Dependence of the number of attached dyneins per microtubule n_{max} on the area density $\tilde{\rho}_{\text{IS}}$. (d) Dependence of the maximum speed S_{max} on $\tilde{\rho}_{\text{IS}}$.

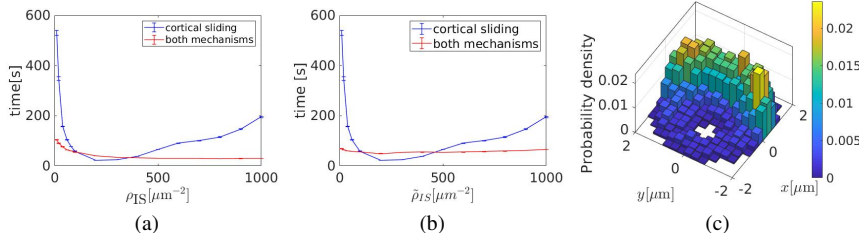


Figure 10: Combination of the capture-shrinkage and the cortical sliding mechanisms. (a)(b) Times of repositioning for the sole cortical sliding and combinations of two mechanisms. (a) In the combined case the capture-shrinkage area density varies, cortical sliding area density is constant $\tilde{\rho}_{\text{IS}} = 20 \mu\text{m}^{-2}$. (b) In the combined case the cortical sliding area density $\tilde{\rho}_{\text{IS}}$ varies and capture-shrinkage area density is constant $\rho_{\text{IS}} = 60 \mu\text{m}^{-2}$. (c) Two dimensional probability density of attached dynein $\tilde{\rho}_{\text{IS}} = 60 \mu\text{m}^{-2}$, $\rho_{\text{IS}} = 20 \mu\text{m}^{-2}$, $\bar{d}_{\text{MIS}} = 4.5 \mu\text{m}$.

6. Maccari, I., R. Zhao, M. Peglow, K. Schwarz, I. Hornak, M. Pasche, A. Quintana, M. Hoth, B. Qu, and H. Rieger, 2016. Cytoskeleton rotation relocates mitochondria to the immunological synapse and increases calcium signals. *Cell Calcium* 60:309–321.
7. Bereiter-Hahn, J., and M. Vöth, 1994. Dynamics of mitochondria in living cells: shape changes, dislocations, fusion, and fission of mitochondria. *Microsc. Res. Tech.* 27:198–219.
8. Jakobs, S., 2006. High resolution imaging of live mitochondria. *Biochimica et Biophysica Acta (BBA) - Molecular Cell Research* 1763:561–575.
9. Chaudhuri, A., 2016. Cell Biology by the Numbers. *Yale J Biol Med* 89:425–426.
10. 1966. An Atlas of Fine Structure. The Cell. Its Organelles and Inclusions. *Ann Intern Med* 64:968.
11. Jakobs, S., and C. A. Wurm, 2014. Super-resolution microscopy of mitochondria. *Current Opinion in Chemical Biology* 20:9–15.
12. Xu, H., W. Su, M. Cai, J. Jiang, X. Zeng, and H. Wang, 2013. The Asymmetrical Structure of Golgi Apparatus Membranes Revealed by In situ Atomic Force Microscope. *PLoS One* 8.
13. Ladinsky, M. S., D. N. Mastrorarde, J. R. McIntosh, K. E. Howell, and L. A. Staehelin, 1999. Golgi Structure in Three Dimensions: Functional Insights from the Normal Rat Kidney Cell. *J Cell Biol* 144:1135–1149.

14. Day, K. J., L. A. Staehelin, and B. S. Glick, 2013. A Three-Stage Model of Golgi Structure and Function. *Histochem Cell Biol* 140:239–249.
15. Huang, S., and Y. Wang, 2017. Golgi structure formation, function, and post-translational modifications in mammalian cells. *F1000Res* 6.
16. Westrate, L. M., J. E. Lee, W. A. Prinz, and G. K. Voeltz, 2015. Form follows function: the importance of endoplasmic reticulum shape. *Annu. Rev. Biochem.* 84:791–811.
17. English, A. R., and G. K. Voeltz, 2013. Endoplasmic reticulum structure and interconnections with other organelles. *Cold Spring Harb Perspect Biol* 5:a013227.
18. English, A. R., N. Zurek, and G. K. Voeltz, 2009. Peripheral ER structure and function. *Curr. Opin. Cell Biol.* 21:596–602.
19. Shibata, Y., G. K. Voeltz, and T. A. Rapoport, 2006. Rough sheets and smooth tubules. *Cell* 126:435–439.
20. Hu, J., W. A. Prinz, and T. A. Rapoport, 2011. Weaving the Web of ER Tubules. *Cell* 147:1226–1231.
21. Gurel, P., A. Hatch, and H. Higgs, 2014. Connecting the Cytoskeleton to the Endoplasmic Reticulum and Golgi. *Current Biology* 24:R660–R672.
22. Alberts, B., A. Johnson, J. Lewis, M. Raff, K. Roberts, and P. Walter, 2007. *Molecular Biology of the Cell*, 5th Edition. Garland Science, New York, 5th edition edition.
23. Goodenough, U. W., B. Gebhart, V. Mermall, D. R. Mitchell, and J. E. Heuser, 1987. High-pressure liquid chromatography fractionation of *Chlamydomonas* dynein extracts and characterization of inner-arm dynein subunits. *Journal of Molecular Biology* 194:481–494.
24. Gee, M. A., J. E. Heuser, and R. B. Vallee, 1997. An extended microtubule-binding structure within the dynein motor domain. *Nature* 390:636–639.
25. Goodenough, U., and J. Heuser, 1984. Structural comparison of purified dynein proteins with in situ dynein arms. *Journal of Molecular Biology* 180:1083–1118.
26. Schmidt, H., E. S. Gleave, and A. P. Carter, 2012. Insights into dynein motor domain function from a 3.3 Å crystal structure. *Nat Struct Mol Biol* 19:492–S1.
27. Leduc, C., O. Campàs, K. B. Zeldovich, A. Roux, P. Jolimaître, L. Bourel-Bonnet, B. Goud, J.-F. Joanny, P. Bassereau, and J. Prost, 2004. Cooperative extraction of membrane nanotubes by molecular motors. *Proc. Natl. Acad. Sci. U.S.A.* 101:17096–17101.
28. Kamiya, N., T. Mashimo, Y. Takano, T. Kon, G. Kurisu, and H. Nakamura, 2016. Elastic properties of dynein motor domain obtained from all-atom molecular dynamics simulations. *Protein Eng Des Sel* 29:317–325.
29. Burgess, S. A., M. L. Walker, H. Sakakibara, P. J. Knight, and K. Oiwa, 2003. Dynein structure and power stroke. *Nature* 421:715–718.
30. Lindemann, C. B., and A. J. Hunt, 2003. Does axonemal dynein push, pull, or oscillate? *Cell Motil. Cytoskeleton* 56:237–244.
31. Sakakibara, H., H. Kojima, Y. Sakai, E. Katayama, and K. Oiwa, 1999. Inner-arm dynein c of *Chlamydomonas* flagella is a single-headed processive motor. *Nature* 400:586–590.
32. Sakakibara, H., and K. Oiwa, 2011. Molecular organization and force-generating mechanism of dynein. *The FEBS Journal* 278:2964–2979.
33. Gennerich, A., A. P. Carter, S. L. Reck-Peterson, and R. D. Vale, 2007. Force-Induced Bidirectional Stepping of Cytoplasmic Dynein. *Cell* 131:952–965.
34. Toba, S., T. M. Watanabe, L. Yamaguchi-Okimoto, Y. Y. Toyoshima, and H. Higuchi, 2006. Overlapping hand-over-hand mechanism of single molecular motility of cytoplasmic dynein. *PNAS* 103:5741–5745.
35. Mallik, R., D. Petrov, S. A. Lex, S. J. King, and S. P. Gross, 2005. Building complexity: an in vitro study of cytoplasmic dynein with in vivo implications. *Curr. Biol.* 15:2075–2085.
36. Mallik, R., B. C. Carter, S. A. Lex, S. J. King, and S. P. Gross, 2004. Cytoplasmic dynein functions as a gear in response to load. *Nature* 427:649–652.
37. Reck-Peterson, S. L., A. Yildiz, A. P. Carter, A. Gennerich, N. Zhang, and R. D. Vale, 2006. Single-Molecule Analysis of Dynein Processivity and Stepping Behavior. *Cell* 126:335–348.

38. Kural, C., H. Kim, S. Syed, G. Goshima, V. I. Gelfand, and P. R. Selvin, 2005. Kinesin and dynein move a peroxisome in vivo: a tug-of-war or coordinated movement? *Science* 308:1469–1472.
39. Torisawa, T., M. Ichikawa, A. Furuta, K. Saito, K. Oiwa, H. Kojima, Y. Y. Toyoshima, and K. Furuta, 2014. Autoinhibition and cooperative activation mechanisms of cytoplasmic dynein. *Nature Cell Biology* 16:1118–1124.
40. Müller, M. J. I., S. Klumpp, and R. Lipowsky, 2008. Tug-of-war as a cooperative mechanism for bidirectional cargo transport by molecular motors. *Proc. Natl. Acad. Sci. U.S.A.* 105:4609–4614.
41. King, S. J., and T. A. Schroer, 2000. Dynactin increases the processivity of the cytoplasmic dynein motor. *Nat Cell Biol* 2:20–24.
42. Nishiura, M., T. Kon, K. Shiroguchi, R. Ohkura, T. Shima, Y. Y. Toyoshima, and K. Sutoh, 2004. A single-headed recombinant fragment of Dictyostelium cytoplasmic dynein can drive the robust sliding of microtubules. *J. Biol. Chem.* 279:22799–22802.
43. Kon, T., M. Nishiura, R. Ohkura, Y. Y. Toyoshima, and K. Sutoh, 2004. Distinct Functions of Nucleotide-Binding/Hydrolysis Sites in the Four AAA Modules of Cytoplasmic Dynein. *Biochemistry* 43:11266–11274.
44. Cho, C., S. L. Reck-Peterson, and R. D. Vale, 2008. Regulatory ATPase sites of cytoplasmic dynein affect processivity and force generation. *J. Biol. Chem.* 283:25839–25845.
45. Kikushima, K., T. Yagi, and R. Kamiya, 2004. Slow ADP-dependent acceleration of microtubule translocation produced by an axonemal dynein. *FEBS Letters* 563:119–122.
46. Walter, W. J., B. Brenner, and W. Steffen, 2010. Cytoplasmic dynein is not a conventional processive motor. *J. Struct. Biol.* 170:266–269.
47. Belyy, V., M. A. Schlager, H. Foster, A. E. Reimer, A. P. Carter, and A. Yildiz, 2016. The mammalian dynein-dynactin complex is a strong opponent to kinesin in a tug-of-war competition. *Nat. Cell Biol.* 18:1018–1024.
48. Ikuta, J., N. K. Kamisetty, H. Shintaku, H. Kotera, T. Kon, and R. Yokokawa, 2014. Tug-of-war of microtubule filaments at the boundary of a kinesin- and dynein-patterned surface. *Scientific Reports* 4:5281.
49. Kunwar, A., S. K. Tripathy, J. Xu, M. K. Mattson, P. Anand, R. Sigua, M. Vershinin, R. J. McKenney, C. C. Yu, A. Mogilner, and S. P. Gross, 2011. Mechanical stochastic tug-of-war models cannot explain bidirectional lipid-droplet transport. *Proc. Natl. Acad. Sci. U.S.A.* 108:18960–18965.
50. Klein, S., C. Appert-Rolland, and L. Santen, 2015. Motility states in bidirectional cargo transport. *EPL* 111:68005.
51. Roberts, A. J., N. Numata, M. L. Walker, Y. S. Kato, B. Malkova, T. Kon, R. Ohkura, F. Arisaka, P. J. Knight, K. Sutoh, and S. A. Burgess, 2009. AAA+ Ring and Linker Swing Mechanism in the Dynein Motor. *Cell* 136:485–495.
52. Imai, H., T. Shima, K. Sutoh, M. L. Walker, P. J. Knight, T. Kon, and S. A. Burgess, 2015. Direct observation shows superposition and large scale flexibility within cytoplasmic dynein motors moving along microtubules. *Nature Communications* 6:1–11.
53. Mizuno, N., A. Narita, T. Kon, K. Sutoh, and M. Kikkawa, 2007. Three-dimensional structure of cytoplasmic dynein bound to microtubules. *PNAS* 104:20832–20837.
54. Montesi, A., D. C. Morse, and M. Pasquali, 2005. Brownian dynamics algorithm for bead-rod semiflexible chain with anisotropic friction. *J. Chem. Phys.* 122:084903.
55. Fixman, M., 1978. Simulation of polymer dynamics. I. General theory. *J. Chem. Phys.* 69:1527–1537.
56. Hinch, E. J., 1994. Brownian motion with stiff bonds and rigid constraints. *Journal of Fluid Mechanics* 271:219–234.
57. Grassia, P. S., E. J. Hinch, and L. C. Nitsche, 1995. Computer simulations of Brownian motion of complex systems. *Journal of Fluid Mechanics* 282:373–403.
58. Grassia, P., and E. J. Hinch, 1996. Computer simulations of polymer chain relaxation via Brownian motion. *Journal of Fluid Mechanics* 308:255–288.
59. Pasquali, M., and D. C. Morse, 2002. An efficient algorithm for metric correction forces in simulations of linear polymers with constrained bond lengths. *The Journal of Chemical Physics* 116:1834–1838.
60. Nedelec, F., and D. Foethke, 2007. Collective Langevin dynamics of flexible cytoskeletal fibers. *New J. Phys.* 9:427–427.
61. Kuhn, J. R., and M. Poenie, 2002. Dynamic Polarization of the Microtubule Cytoskeleton during CTL-Mediated Killing. *Immunity* 16:111–121.
62. Kim, M. J., and I. V. Maly, 2009. Deterministic Mechanical Model of T-Killer Cell Polarization Reproduces the Wandering of Aim between Simultaneously Engaged Targets. *PLOS Computational Biology* 5:e1000260.

6.2. Stochastic Model of T Cell Repolarization during Target Elimination (II)

The article is included in the thesis with the permission of Elsevier, see Appendix [B](#).

6.2.1. Main Manuscript

Stochastic model of T cell repolarization during target elimination (II)

Ivan Hornak^{1,*} and Heiko Rieger¹¹Department of Theoretical Physics, Center for Biophysics, Saarland University, Saarbrücken, Germany

ABSTRACT Cytotoxic T lymphocytes (T cells) and natural killer cells form a tight contact, the immunological synapse (IS), with target cells, where they release their lytic granules containing perforin/granzyme and cytokine-containing vesicles. During this process the cell repolarizes and moves the microtubule organizing center (MTOC) toward the IS. In the first part of our work we developed a computational model for the molecular-motor-driven motion of the microtubule cytoskeleton during T cell polarization and analyzed the effects of cortical-sliding and capture-shrinkage mechanisms. Here we use this model to analyze the dynamics of the MTOC repositioning in situations in which 1) the IS is in an arbitrary position with respect to the initial position of the MTOC and 2) the T cell has two IS at two arbitrary positions. In the case of one IS, we found that the initial position determines which mechanism is dominant and that the time of repositioning does not rise monotonously with the MTOC-IS distance. In the case of two IS, we observe several scenarios that have also been reported experimentally: the MTOC alternates stochastically (but with a well-defined average transition time) between the two IS; it wiggles in between the two IS without transiting to one of the two; or it is at some point pulled to one of the two IS and stays there. Our model allows one to predict which scenario emerges in dependency of the mechanisms in action and the number of dyneins present. We report that the presence of capture-shrinkage mechanism in at least one IS is necessary to assure the transitions in every cell configuration. Moreover, the frequency of transitions does not decrease with the distance between the two IS and is the highest when both mechanisms are present in both IS.

SIGNIFICANCE Repositioning of the microtubule organizing center (MTOC) plays a key role in the process of target cell elimination of cytotoxic killer cells (T cells and natural killer cells). We use a recently established model for the molecular-motor-driven motion of the MT cytoskeleton confined between the membrane and the nucleus during T cell polarization to make quantitative predictions about the MTOC dynamics and the MT cytoskeleton morphology comparable with experiments. In the presence of two IS it predicts oscillatory, fluctuating, or bistable MTOC dynamics in dependency of the dynein distribution and the action of a cortical-sliding or a capture-shrinkage mechanism, which allows experimental conclusions on the basis of the measurement of MTOC trajectories.

INTRODUCTION

T cells have a key role in the adaptive branch of our immune system by finding and destroying virus-infected and tumor cells, parasites, and foreign invaders. Cytotoxic killing of a target cell is achieved in three subsequent steps. First, the T cell binds to the surface of the target cell and creates a tight contact zone called immunological synapse (IS) (1–9). Second, the T cell relocates the microtubule organizing center (MTOC) toward the IS by a massive movement of the entire microtubule (MT) cytoskeleton due to

forces acting on MTs (10–16). This process involves the repositioning of mitochondria, the Golgi apparatus, and the endoplasmic reticulum, since the organelles are bound to the cytoskeleton and relocate with it (14,17–22). In the third step, the T cell releases the cytotoxic material from the lytic granules toward the target cell, leading to its death by necrosis or apoptosis (23–28). The secretion of lytic granules can take place without the MTOC repolarization (29), or before it (30). However, it does not make the repositioning redundant, since the MTOC-accompanied granule secretion may be crucial for the killing of resistant cells.

The IS is divided into several supramolecular activation clusters (SMACs) including ring-shaped peripheral SMAC (pSMAC) (7,9,31–33). Dynein, a minus-end-directed (toward the MTOC) molecular motor protein, is indispensable

Submitted June 28, 2021, and accepted for publication February 16, 2022.

*Correspondence: hornak@lusi.uni-sb.de

Editor: Kevin A. Janes.

<https://doi.org/10.1016/j.bpj.2022.02.029>

© 2022 Biophysical Society.



for the repositioning as was shown by knockout experiments (34–38). The dynein colocalizes with the adapter protein ADAP that forms a ring at the IS periphery after activation of the T cell (39,40). Dynein plays a key role in the two mechanisms proposed to drive the repositioning: cortical sliding and capture shrinkage. In the cortical-sliding mechanism the dyneins step to the minus-end of MTs (toward the MTOC) while being anchored on the cell membrane and therefore pull the MTOC toward the IS (15,39,41). It was indicated that the ring-shaped pSMAC is the place where attached dyneins are anchored (15,39). It was shown in (42) that the recruitment of the dynein to the IS is correlated and promoted by the depletion of cortical actin filaments from the same place.

A detailed analysis of the capture-shrinkage process was performed by Yi et al. (12). An optical trap was used to place the target cell so that the IS (contact zone) is initially diametrically opposed to the MTOC. This well-defined initial configuration allowed quantitative dynamical imaging including observation of the MT cytoskeleton morphology. They provided strong evidence that the repositioning is driven by a capture-shrinkage mechanism (43) involving the depolymerization of the caught MT in a confined area in the center of the IS. It was shown (12) that MTs bend alongside the cell membrane to reach the IS. Consequently, the MTs caught by their plus-end in the center of the IS straighten, form a narrow stalk, and depolymerize at the capture-point. The MTOC is pulled to the center of the IS, which invaginates the cell, indicating the location of the main pulling force. The capture-shrinkage mechanism was identified as the main driving force of the repositioning, since inhibiting the MT depolymerization substantially slowed down the repositioning. Yi et al. (12) reported that the repositioning can be divided into two phases that differ in the MTOC speed and the direction of its motion. In the first so-called polarization phase, the MTOC travels quickly in a circular motion around the nucleus. In the second, docking phase, the MTOC moves slowly and directly toward the IS.

T cells can attack two target cells simultaneously, in which case two IS are established (15). In this case, the MTOC transits repeatedly between the two IS (15), reminiscent of mitotic spindle oscillations in *Caenorhabditis elegans* (35,44–49). These spontaneous spindle oscillations have been explained by the cooperative attachment and detachment of cortical force generators to astral microtubules (50–53). For MTOC oscillations in T cells with two synapses a similar scenario has been proposed in connection with cortical-sliding mechanism (54). There it has been hypothesized that MTs on the trailing side of the MTOC are lifted off the pulling surface by viscous drag in the cytoplasm, leading to their detachment from cortical motors. Here we propose a different mechanism, which also works for capture shrinkage as reported in (12) and which relies on dynamic MTs, similar to, for instance, meiotic nuclear oscillations in *Schizosaccharomyces pombe* (55–57).

The interplay between dyneins and filaments is influenced by dynamic MTs, which constantly grow and shrink: periods of grow alternate with periods of rapid depolymerization in a process called dynamic instability (DI) (58–68). This process allows the cytoskeleton to adopt itself to the needs and functions of the cell to perform substantial shape changes through the cell cycle (61,69–71). Transitions between two IS would not be possible without the DI of MTs: at the end of the repositioning process toward one IS, the MT cytoskeleton is deformed and capture-shrinkage MTs are depolymerized (12,72). Due to DI, the depolymerized MTs regrow and the deformed cytoskeleton can restructure.

The main reason for MTOC oscillations in T cells with two IS as well as mitotic spindle oscillations to occur is that one has two distinct locations of dynein accumulation on the cell boundary, where motors can catch the MTs. The attachment of dynein is stochastic and one location wins the tug-of-war between the attached dyneins, resulting in MTOC relocation toward that location. In both cases, dyneins detach as the MTOC approaches. In the case of spindle oscillation, two restoring forces pushing the spindle back to the center were considered: the cortical pushing of the MT polymerization-driven growth against a barrier followed by the bending of the filaments, and the pulling force of the dyneins opposite to the movement of the MTOC (44–46,73–77). The purpose of our theoretical study is to elucidate the potential mechanisms for cooperative dynein attachment and detachment leading to stable, bistable, or oscillatory MTOC relocation in T cells with two IS.

COMPUTATIONAL MODEL

We use the computational model introduced in (72). The cell membrane and the nucleus are represented by two spheres with radius $5 \mu\text{m}$ and $3.8 \mu\text{m}$, respectively. MTs sprout from the MTOC to the cell periphery, as sketched in Fig. 1, *a* and *b*. They are modeled by a bead-rod model with constrained Langevin dynamics. The MTs move under the influence of several forces—bending, drag, molecular motors, noise, and repulsive forces—keeping them between the nucleus and the cell membrane. The MTOC moves to the IS due to the pulling force of dyneins acting via two mechanisms: cortical sliding during which the plus-end of the MT remains free and the filament slides tangentially along the plasma membrane; and capture shrinkage, by which dyneins capture the tip of the MT and depolymerize it by pulling it against the membrane, as sketched in Fig. 1 *c*. Dyneins acting via cortical sliding and capture shrinkage are located in the complete IS and the narrow center, respectively. The two regions are represented by intersections of the cell sphere with cylinders with radius $R_{\text{IS}} = 2 \mu\text{m}$ for the complete IS and $R_{\text{CIS}} = 0.4 \mu\text{m}$ for the center, as sketched in Fig. 1. Note that we assume the dyneins to be immobile and firmly fixed at the cell boundary. This is in contrast to a recently proposed model in which

Hornak and Rieger

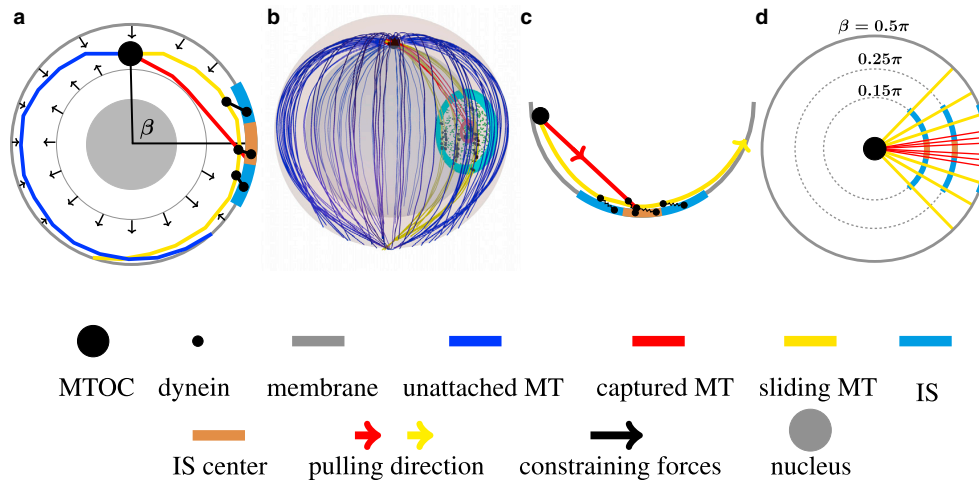


FIGURE 1 Sketch of the model of the cell with one IS. (a) A two-dimensional cross-section of the model is shown. The movement of the MTs sprouting from the MTOC is confined between the nucleus and the cell membrane. MTs are pulled by the cortical-sliding and capture-shrinkage mechanisms employing dynein motors in the IS and its center, respectively. Small black dots on the membrane and on the MTs represent dynein's anchor and attachment points, respectively. Angle β denotes the angle between the IS and the initial position of the MTOC. (b) Three-dimensional sketch. The plasma membrane and the nucleus are represented by the transparent outer and inner spheres, respectively. Small green spheres represent unattached dyneins in the IS and its center encircled by the cyan and brown rings, respectively. (c) Sketch of the cortical-sliding mechanism and the capture-shrinkage mechanism. Small black dots represent dynein's anchor and attachment points. When an MT is pulled by the capture-shrinkage mechanism, the plus-end of the MT is anchored at the center of the IS and depolymerizes. Cortical-sliding MTs slide on the surface and the MT plus-end remains free. (d) Sketch of MTs intersecting the IS and its center in the cells with different angles β . The percentage of MTs intersecting the IS is given by the ratio of the diameter of the IS to the cell circumference corresponding to angle β depicted by dashed circles. It is minimal at $\beta = 0.5\pi$. To see this figure in color, go online.

dyneins can more or less freely (dependent upon assumed friction coefficients) move in an actin-depleted zone of the IS (78) and thus self-organize into clusters at the boundary of the actin-depleted zone. This is an interesting hypothesis that has still to be confirmed or refuted by experiments, but we do not expect dyneins that can move within a restricted region of the IS to alter our main conclusions substantially, for which reason we stick to our original model of a predefined dynein location (72). In (72) we focused on the analysis of the MTOC repositioning process in the experimental setup used in (12), in which the MTOC and the IS are initially diametrically opposed. Here we consider naturally occurring situations, in which the angle β between the MTOC and the IS (see Fig. 1 a) is arbitrary, and situations in which the T cell attaches simultaneously to two target cells and thus forms two IS (15).

To analyze the situation with two IS, we augmented our model presented in (72) in several ways. The configuration of a cell with two IS is defined by the angle γ between the lines connecting the centers of IS with the center of the cell, sketched in Fig. 2 a. Both IS and the center of the cell are located on the xz plane of the coordinate system, sketched in Fig. 2 b and visually demonstrated in Fig. 2 c. The dyneins from both IS are in a tug-of-war leading to an increase of the detachment rate (72). When all capture-shrinkage dyneins detach from the MT, the plus-end is no longer fixed on the cell membrane. Most importantly, we included the dynam-

ical instability of MTs (59,61,62,65,79), since we hypothesized that transitions between two IS rely on DI. The measured values of parameters of DI differ (59,80–89); they depend on the cell phase (90,91) and on the distance from the cell membrane (92–95). We take the following estimates from the literature: growth velocity $v_g = 0.1 \mu\text{m s}^{-1}$ (62,83,89,96), although it might depend mildly on load and MT plus-end location (67,93); shrinking velocity $v_s = 0.2 \mu\text{m s}^{-1}$; rescue rate (the transition rate from shrinkage to growth) $r_r = 0.044 \text{ s}^{-1}$ (80,82,97,98); and a length-dependent catastrophe rate (transition rate from growth to shrinkage) $c_r(L) = \exp((L - L_c)/b_c) \text{ s}^{-1}$, where $L_c = \pi R_{\text{Cell}} + \frac{R_{\text{Cell}}}{2}$, $b_c = (L_0 - L_c)/\ln(r_c)$, $L_0 = \pi R_{\text{Cell}}$, and $r_c = 0.022$, reflecting a lower catastrophe rate close to the MTOC and a higher one at the cell periphery (69,92,99). The MT length distribution resulting from the DI with aforementioned parameters is shown in Fig. 2 f. Due to the DI, growing and shrinking MTs coexist in a dynamically changing cytoskeleton affected by the two mechanisms in both IS, as visualized in Fig. 2 c. The DI adds another force acting on MTs, since the growing tips of filaments are pushed against the cell membrane, sketched in Fig. 2 e. In contrast to the dynein forces, growing tips can push the MTOC from both IS and the xz plane. Since the plus-end of the MTs remains free during the cortical-sliding mechanism, the MTs can grow or shrink even when attached. The MT length influences the contact between MTs and the dyneins on the cell membrane. The MTOC is

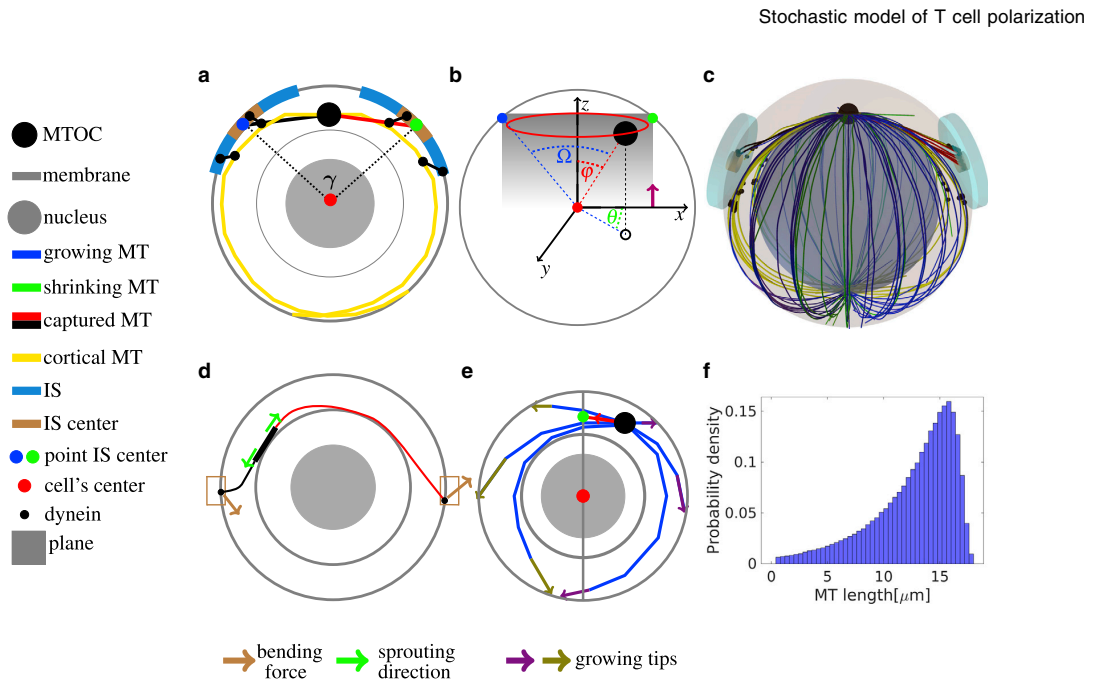


FIGURE 2 Sketch of the model of the cell with two IS. (a) γ denotes the angle between the two IS. Small black dots on the membrane and MTs represent dynein anchor and attachment points, respectively. MTs can attach to capture-shrinkage or cortical-sliding dyneins in both IS. (b) Sketch of the azimuthal (θ), polar (ϕ) and MTOC-IS (Ω) angle. The positions of the centers of both IS and the cell are located in the gray-shaded xz plane. When $\gamma < \pi$ both IS are located in the upper hemisphere ($z > 0$) denoted by the magenta arrow. The polar angle ϕ denotes the cone with the vertex located in the center of the cell indicated by the red circle and the red dashed line. The azimuthal angle θ denotes the angle between the x axis and the dashed black line connecting the center of the cell with the projection of the MTOC position on the xy plane depicted by the small black circle. The angle Ω denotes the angle between the line connecting the MTOC with the cell center (red dashed line) and the axis of the IS depicted by the blue dashed line. (c) Three-dimensional snapshot of an initial configuration of the model with $\gamma = \frac{3}{4}\pi$. The point of view is located on the yz plane in the upper hemisphere ($z > 0$) at the angle $\frac{\pi}{4}$ of the y axis. Growing and shrinking MTs radiate from the MTOC toward the cell periphery and can be pulled by the two mechanisms in both IS. Dyneins in one IS cooperate and dyneins from different IS are in a tug-of-war. (d) Sketch of bending forces acting on MTs attached to a capture-shrinkage. The thick black segment and the brown rectangles represent the plane of the MTOC and the centers of IS, respectively. The small black circles represent dyneins at points where they capture the plus-end of MTs. Since attached MTs sprout from the MTOC, bending forces push the long MT against the cell membrane and pull the short MT from it. (e) Two-dimensional sketch of the forces pulling the MTOC toward and away from the IS. The gray line represents the xz plane on which the centers of the cell and both IS are located. The red line stands for the MT attached in the IS. Dynein forces acting on the red MT pull the MTOC to the xz plane where the IS is located. The growing olive and violet plus-end of MTs push the MTOC from the xz plane and toward it, respectively. (f) Probability density of MT length. To see this figure in color, go online.

modeled as a planar structure (72), and the MT sprouts from the MTOC radially. The short MTs have to bend to stay in contact with the dyneins on the membrane, as sketched in Fig. 2 d. Once the dyneins detach, the tip recedes from the membrane, making the reattachment unlikely. On the other hand, bending forces press the tip of a long MT against the cell membrane where it can attach to dyneins.

We analyzed the role of the cortical-sliding and capture-shrinkage mechanisms during the MTOC repositioning in the cell with one and two IS by computer simulations of the model as defined in (72) and above. We mainly focused on the dependence of the repositioning process from initial conditions (angle β in Fig. 1 a for one IS) or double-IS arrangement (angle γ in Fig. 2 a for two IS), and from the cortical-sliding dynein density $\hat{\rho}_{IS}$ and capture-shrinkage dynein density ρ_{IS} . Since both densities are unknown, we varied them over the whole range from 10 to 1000 μm^{-2} : lower densities fail to relocate the MTOC at all, and larger densities are not realistic due to steric repulsion between

the dyneins. The angles β and γ were varied between 0.2π and π ; smaller values appear unrealistic for geometric reasons (IS and MTOC size) while larger values can be mapped on the considered interval.

We implemented the model in C++ on a computer cluster with Intel(R) Xeon(R) CPU E5-2660 0 @ 2.20GH processors, Linux operating system (Arch-Linux 4.1.7-hardened-r1), and compiler g++ 4.9.2 and performed simulation runs to generate the data shown in this publication. The program listing is publicly available on GitHub (100). The snapshots from the simulations and videos in supporting material were made in POV-Ray.

RESULTS

Repositioning time scales

Before we present the results of computer simulations of the model defined in the previous section, we give an estimate

Hornak and Rieger

for the time scale of the MTOC repositioning process based on the antagonistic interplay of friction and pulling forces acting on the MT cytoskeleton and compare it with the repositioning times from experiments.

The MTOC position during the repositioning was traced in several experiments (14,15,101). The MTOC was originally located approximately at the opposite side of the target cell, and its repositioning to the IS took more than 3 min. The repositioning was faster in the experiments performed by Yi et al. (12) where the MTOC gets to the IS (distance $< 2 \mu\text{m}$) on average in ca. 2 min. The increased speed is likely caused by the experimental setup in which the MTOC and the target cell are initially diametrically opposed. In such a configuration all MTs that are long enough intersect the center of the IS, visually demonstrated in Fig. S2, *b* and *g*, and their plus-ends attach and are pulled by capture-shrinkage dyneins. Moreover, all MTs long enough to reach the IS can attach to cortical-sliding dyneins. When $\beta < \pi$, fewer dyneins are attached to MTs, since just a fraction of MTs intersect the IS and its center, see Fig. S1 *c* and visually in Fig. S2. Consequently, the initial diametrical opposition of the MTOC and the IS may result in higher pulling forces.

In what follows, we estimate the time scales as one would predict them on the basis of our model assumptions. The drag force acting on an MT moving with velocity v is $F_{\text{drag}} = \gamma_{\text{MT}} \times v$, where γ_{MT} is the drag coefficient. For a cylindrical object of length L and diameter d it is given by (102)

$$\gamma_{\text{MT}} = \frac{4\pi\mu L}{\ln(L/d) + 0.84}, \quad (1)$$

where μ is the viscosity of the surrounding liquid, the cytoplasm, which is e times the viscosity of water, $\mu = e \times \mu_w \approx 10^{-3} \text{N s m}^{-2} = e \times 10^{-3} \text{N s m}^{-2}$, and we estimate it to be $e \approx 30$ (72). Note that for simplicity we do not discriminate between movement of the cylindrical object in the longitudinal or in the transverse direction. Taking the average length of the MT to be $L = 10 \mu\text{m}$ and its diameter to be $d = 25 \text{nm}$, we have $\gamma_{\text{MT}} \approx \mu \times 18.4 \mu\text{m}$. The drag coefficient of the whole cytoskeleton with N_{MT} MTs is $\gamma_{\text{cyto}} = N_{\text{MT}} \times \gamma_{\text{MT}}$. Mitochondria, Golgi apparatus (103–106), and endoplasmic reticulum (107–111) are massive organelles entangled with the cytoskeleton (14,19) and dragged with it, thereby increasing the drag coefficient by a factor g , i.e., $\gamma_{\text{eff}} = g \times \gamma_{\text{cyto}}$, which was estimated to be $g \approx 3$ (72).

The force pulling on the cytoskeleton is given by the number of dyneins attached to MTs times the average forces exerted by a dynein motor: $F = N_{\text{dyn}} \times F_{\text{dyn}}$, the latter is in the pico-Newton range, $F_{\text{dyn}} = f \times 10^{-12} \text{N}$, with $f \approx 1$. Consequently, the velocity of the whole cytoskeleton movement when N_{dyn} are pulling is

$$v = \frac{F_{\text{dyn}}}{\gamma_{\text{eff}}} \approx 54 \times \frac{N_{\text{dyn}}}{N_{\text{MT}}} \times \frac{f}{e g} \frac{\mu\text{m}}{\text{s}}. \quad (2)$$

Inserting the estimates $f = 1$, $e = 30$, $g = 3$, and evaluating the r.h.s. for $N_{\text{MT}} = 100$ MTs and $N_{\text{dyn}} = 10 - 50$ attached dyneins, one obtains a velocity $v = 3.6 - 18 \mu\text{m min}^{-2}$, a range that agrees well with the experimentally determined MTOC velocities (12). For an initial MTOC position diametrically opposed to the IS the MTOC would have to travel a distance $D = \pi R_{\text{Cell}}$, where R_{Cell} is the radius of the cell, and with $R_{\text{Cell}} \approx 5 \mu\text{m}$ and the above velocity estimate the whole relocation process would need 1–4 min, which also agrees with the experimentally reported relocation times (12).

Since the number of attached dyneins is the central quantity determining the speed of the relocation process, let us relate to the dynein density and the attachment rates that we use in our model. For the capture-shrinkage mechanism we assume dynein to be concentrated in a central region of the IS with radius $R_{\text{CIS}} = 0.4 \mu\text{m}$ (i.e., an area of $0.5 \mu\text{m}^2$) and with a dynein density ρ_{IS} . At medium density of $\rho_{\text{IS}} = 100 \mu\text{m}^{-2}$ we have 50 dyneins located in this area and, since most MTs in our model reach this area, they could in principle all be attached: the average distance between dyneins is $D_{\text{d2}} = \rho_{\text{IS}}^{-1/2} = 100 \text{nm}$ for the assumed dynein density and with the attachment rate decreasing exponentially with the distance (see Eq. 4 in supporting material) one has $p_a \approx 2 \text{s}^{-1}$, implying that attachment is fast in comparison with the duration of the relocation process. Actually, in our simulations we observe that initially ca. one-quarter of all MTs get attached to dynein, some of them even attached simultaneously to two dyneins. Consequently for $\rho_{\text{IS}} = 100 \mu\text{m}^{-2}$ we have indeed initially 25–50 dyneins attached to MTs, resulting in an initial MTOC velocity of $v_{\text{MTOC}} = 9 - 18 \mu\text{m min}^{-2}$. In the later stage of the relocation process competing forces will slow down the MTOC velocity, which will be revealed by the actual simulations reported below.

These rough estimates hold for our model framework as well and can be elaborated more on the basis of more detailed model assumptions. Force exerted by attached dynein is assumed to depend on the length of the stalk between the attachment and the anchor point l_d and is expressed as $F_d = 0$ if $l_d < L_0$ and $F_d = k_d(l_d - L_0)$ otherwise, where $L_0 = 18 \text{nm}$ is the length of the relaxed stalk and $k_d = 400 \text{pN } \mu\text{m}^{-1}$ is the elastic modulus of the stalk, see Fig. S1 *a*. In our model, the dynein makes steps with the length $d_{\text{step}} = 8 \text{nm}$ toward the minus-end of the MT. The stepping is very fast at zero load (the first two steps) and slows down as the force increases (72), and the movement stops at the stall force $F_S = 4 \text{pN}$. Since the MT depolymerizes and moves, the distance between the attachment and the anchor point can differ from the multiples of the dynein step. Consequently, the length of the stalk is $l_1 < l_d < l_2$ where l_1 and l_2 are the lengths corresponding to the second step and to the stall force, respectively, see Fig. S1 *a*. The average dynein force $\bar{F}_d = 1.66 \text{pN}$ is calculated as the integral of the force between l_1 and l_2 divided by their distance.

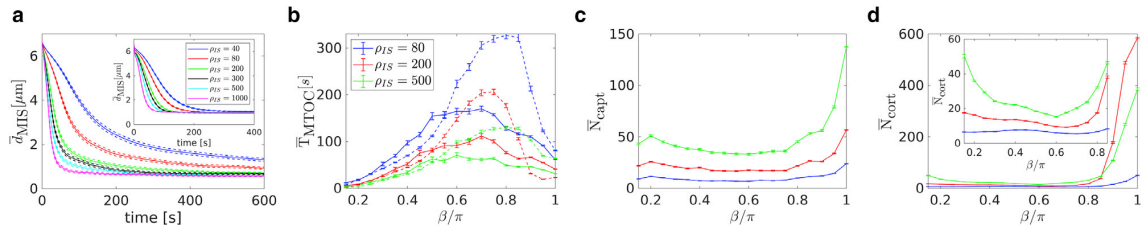


FIGURE 3 Repositioning under the influence of the capture-shrinkage and cortical-sliding mechanisms for different angles β between the IS and the initial position of the MTOC. (a) Dependence of the average MTOC-IS distance \bar{d}_{MIS} on time. $\beta = 0.5\pi$. The error bars are represented by dashed lines. (b) Dependence of the averaged times \bar{T}_{MTOC} (MTOC-IS distance $d_{\text{MIS}} < 1.5 \mu\text{m}$) on the angle β . Capture-shrinkage and cortical-sliding mechanisms are represented by solid and dashed lines, respectively. (c and d) Dependencies of the mean numbers of attached dyneins \bar{N} averaged over simulation runs on the angle β . (c) Capture-shrinkage mechanism. (d) Cortical-sliding mechanism. Dependencies are plotted with error bars. To see this figure in color, go online.

At the beginning of the repositioning the number of attached dyneins increases rapidly, see Fig. S3. The detachment rate of the dynein increases exponentially with the dynein force (Eq. S3). The detachment rate corresponding to the average dynein force is $p_{\text{det}}(\bar{F}_d) = 2.29 \text{ s}^{-1}$, see Fig. S1 b. Consequently, dyneins are expected to detach in less than half a second. The attachment rate of the dynein decreases exponentially with the distance from the filament (72). When the distance between the dynein and the filament $d_{\text{md}} = 95 \text{ nm}$, the attachment rate equals detachment rate of the average dynein force $p_a(d_{\text{md}}) = p_{\text{det}}(\bar{F}_d)$, see Fig. S1 b. Consequently, the dyneins located closer to the filament are expected to attach faster than dyneins detach on average. The fraction of MTs intersecting the IS, q_{IS} (or the central region of the IS, q_{CIS}), shown in Fig. S1 c, is given by the ratio of the diameter of the IS (or diameter of the center of the IS) and the circumference $c(\beta)$ of the circle of latitude at angle β (see Fig. 1 d): $q_{\text{IS}} = \min(1, 2R_{\text{IS}}/c(\beta))$, with $c(\beta) = 2\pi r(\beta)$, where $r(\beta) = R_{\text{cell}}\sin(\beta)$ is the radius of the circle.

The number of attached dyneins can then be estimated by the number of dyneins that are closer than $d_{\text{md}} = 95 \text{ nm}$ to an MT:

$$\bar{N}_{\text{dm}} = N_{\text{MT}} \times q_{\text{CIS}} \times n_{\text{dm}}, \quad (3)$$

where $N_{\text{MT}} = 100$ is the number of MTs and $n_{\text{dm}} = \pi \times d_{\text{md}}^2 \times \rho_{\text{IS}}$ is the number of dyneins in the proximity of the filament. It can be seen in Fig. S3 that the number of attached dyneins approaches the estimated number of dyneins regardless of the angle and the dynein density. With this β -dependent estimate of the β -dependent number of attached dyneins, we can perform again the calculation of the estimated MTOC velocity and the relocation time as above.

Fig. S1 d shows the dependence of the estimated time of the repositioning T_{est} on the angle β . The repositioning time increases with the angle until they reach a maximum at $\beta \sim 0.6\pi$ and then they decrease, see Fig. S1 d. The decrease when $\beta \leq 0.5\pi$ can be explained by the fact that the distance is increasing and the q_{CIS} decreases with β , see Fig. S1 d.

The ratio q_{CIS} increases sharply when $\beta > 0.65\pi$ and the increased pulling force results in faster repositioning. This may offer an explanation as to why the time of repositioning is the shortest in the experimental setup when the MTOC and the IS are initially diametrically opposed (12).

Repositioning with one IS

In the first part of our work (72), we analyzed the repositioning in the cell where the MTOC and the IS are initially diametrically opposed. In this section we present the results of the computer simulation of the model with one IS, located at an angle β with respect to the initial position of the MTOC, see Fig. 1. Fig. 3 a shows that as expected the repositioning becomes faster with increasing dynein density for both mechanisms. Moreover, we found that the time scale for the completion of the relocation process agrees for a wide range of dynein densities. In addition, the MTOC dynamic has the same characteristic as in the case of $\beta = \pi$, which was analyzed in detail in (72). The MTOC travels to the IS and its speed decreases with the MTOC-IS distance. Additional analysis of the repositioning for the cases of $\beta = 0.75, 0.5, 0.25\pi$ can be found in sections 3.1 and 3.2 of supporting material. Here we focus on the average repositioning time \bar{T}_{MTOC} and its dependence on the angle β : Fig. 3 b shows that \bar{T}_{MTOC} increases with the angle β to a maximum at $\beta \sim 0.75\pi$ and then decreases. \bar{T}_{MTOC} depends on the initial MTOC-IS distance, opposing forces and the pulling force of dynein motors. The opposing forces increase with the angle β since the nucleus increasingly presents an obstacle on the path of the MTOC. For $\beta = 0.25\pi$ the nucleus does not intersect the line between the initial positions of the MTOC and the IS, visually demonstrated in supporting material and Fig. S2, b–k. Contrarily, the MTOC has to navigate around the entire nucleus when $\beta = \pi$.

Fig. 3, c and d show that the number of attached dyneins decreases with β to a minimum at approximately $\beta = 0.6\pi$ and then increases sharply. This can easily be explained by the number of MTs intersecting the IS given by the ratio of the diameter of the IS (or its center) and the circumference

Hornak and Rieger

of the circle of latitude at angle β (see Figs. 1 *d* and S1 *c*): $q_{\text{IS}} = \min(1, 2R_{\text{IS}}/c(\beta))$, with $c(\beta) = 2\pi r(\beta)$, where $r(\beta) = R_{\text{cell}}\sin(\beta)$ is the radius of the circle. In the special case of $\beta = \pi$ all MTs long enough intersect the IS, as visualized in Fig. S2, *c* and *h*. However, when $\beta = 0.5\pi$ the IS is intersected only by MTs sprouting from the MTOC toward it, visually in Figs. 1, *b* and *d* and 2, *a* and *e*. The ratio decreases with the angle β until it reaches the minimum at $\beta = 0.5\pi$ and then it increases sharply, see Fig. S1 *c*, visually demonstrated in Fig. 1 *d*. In the simulations the minimum is slightly shifted from $\beta = \pi/2$ to 0.6π , as visible in Fig. 3, *c* and *d*, because dyneins detach due to an increasing opposing force of the nucleus. Subsequently, the number of dynein increases due to the fact that the increasing percentage of MTs intersects the IS, compare Fig. 3, *c* and *d* with Fig. S1 *c*. By comparing Fig. 3, *c* and *d* one observes that the number of attached cortical-sliding dyneins increases more sharply with increasing β , due to the fact that a part of the relatively large IS is located in the diametrical opposition of the IS for $\beta > 0.9\pi$ and the MTs sprouting from the MTOC in all directions can attach to dynein. The number of attached capture-shrinkage dyneins at $\beta = 0.15\pi$ is smaller than for $\beta = 0.2\pi$ due to the fact that owing to the short MTOC-IS distances the MTOC is dragged toward the IS and the number of dyneins quickly decreases, see Fig. S5.

The repositioning time, \bar{T}_{MTOC} , increases with β between 0 and $\beta < 0.7\pi$, since the distance and opposing force increase and the number of attached dyneins decrease, see Fig. 3, *b-d*. It can be seen in Fig. 3 *b* that the increase of \bar{T}_{MTOC} is sharper for cortical sliding when $\beta > 0.5\pi$ due to the different behavior of the number of attached dyneins, cf. Figs. S5 and S7. When $\beta > 0.8$, \bar{T}_{MTOC} decreases rapidly due to the sharp increase of pulling force.

The repositioning time offers a way to compare the performance of the two mechanisms for different configurations of the cell. It can be seen that the cortical-sliding mechanism outperforms the capture-shrinkage mechanism when $\beta < 0.5\pi$ and is substantially slower otherwise. The only exception is the case of cortical-sliding mechanism when the density $\tilde{\rho}_{\text{IS}} = 200 \mu\text{m}^{-2}$ since it results in the fastest repositioning when $\beta \geq 0.85\pi$. The speed of the process can be explained by the three regimes of cortical-sliding repositioning analyzed in (72). The difference between the repositioning times for the two mechanisms decreases as the dynein density increases, see Fig. 3 *b*.

In our model the cortical-sliding dynein was distributed equally over the entire IS. However, we observe that the large majority of attached cortical-sliding dyneins is located at the periphery of the IS, see Fig. S8. In the case of combined mechanisms, the attached cortical-sliding dyneins are completely absent in the center of the IS, see Fig. S10 *c*. It was hypothesized (15) that the dynein colocalizes with the ADAP ring at the periphery of the IS to facilitate the interaction with MTs. This finding supports the aforementioned hypothesis.

It was also shown in (72) that the mechanisms act in synergy regardless the initial configuration of the cell, see Fig. S10, *a* and *b*, since the dominant mechanism is always supported by the secondary one. The cortical-sliding mechanism supports the capture-shrinkage mechanism by passing MTs to it, see Fig. S10, *f* and *i*. The capture-shrinkage mechanism supports cortical sliding by providing a firm anchor point and pulling the MTOC from the nucleus, see Fig. S10, *g* and *h*. When the MTOC recedes from the nucleus, MTs copy the cell membrane more closely and the attachment to cortical sliding is more likely, see Fig. S10 *e*. The dyneins of the two mechanisms pull in alignment sharing the load from opposing forces, resulting in decreased detachment probability. The combination of two mechanisms with low area densities can be faster than the dominant mechanism with high densities (72), Fig. S10, *a* and *b*.

Repositioning in the T cell with two IS

In this section we present the results of the computer simulation of the model with two IS, as sketched in Fig. 2. The configuration of the cell is defined by the angle γ between the two IS, sketched in Fig. 2 *a*. The densities of dyneins anchored at both IS, $\tilde{\rho}_{\text{IS}}^1$ and $\tilde{\rho}_{\text{IS}}^2$, and the central region of the IS, ρ_{IS}^1 and ρ_{IS}^2 , are unknown model parameters, which we therefore vary over a broad range between 0 (no anchored dynein) and $1000 \mu\text{m}^{-2}$. We calculate and analyze the following quantities: the transition frequency between the two IS, $N_{\text{tr}} \text{min}^{-1}$; the dwell times at one IS, which is defined as the time interval during which the MTOC-IS distance is smaller than $3 \mu\text{m}$, T_{d} ; and the longitudinal and transverse fluctuations of the MTOC by determining the time-averaged probability distribution of the polar, azimuthal, and MTOC-IS angles, φ , θ , and Ω , respectively, which are defined as sketched in Fig. 2 *b*. For each point in the parameter space, these quantities were averaged over 500 simulation runs. Each simulation run is initialized with all dyneins being detached. Results are shown with the standard deviation as error bars.

Capture-shrinkage mechanism

Video S1 shows the repositioning with two IS with the same density of capture-shrinkage dyneins $\rho_{\text{IS}}^1 = \rho_{\text{IS}}^2 = 400 \mu\text{m}^{-2}$. In the first seconds of the simulation, MTs attach to dyneins at the left IS, visualized in Fig. 4 *a*, and the MTOC is dragged toward it. Captured MTs shorten and depolymerize, see Fig. 4 *b*. As the MTOC approaches the left IS, we observe that the number of attached MTs decreases as MTs detach and reattach in the center of the IS. Simultaneously, the plus-end of MTs intersect with the distant IS and are captured by dyneins, visually demonstrated in Fig. 4 *c*. Finally, all MTs are detached from the left IS at the end of the transition and the MTOC moves to the right IS. Due to the DI, MTs grow (blue lines) and

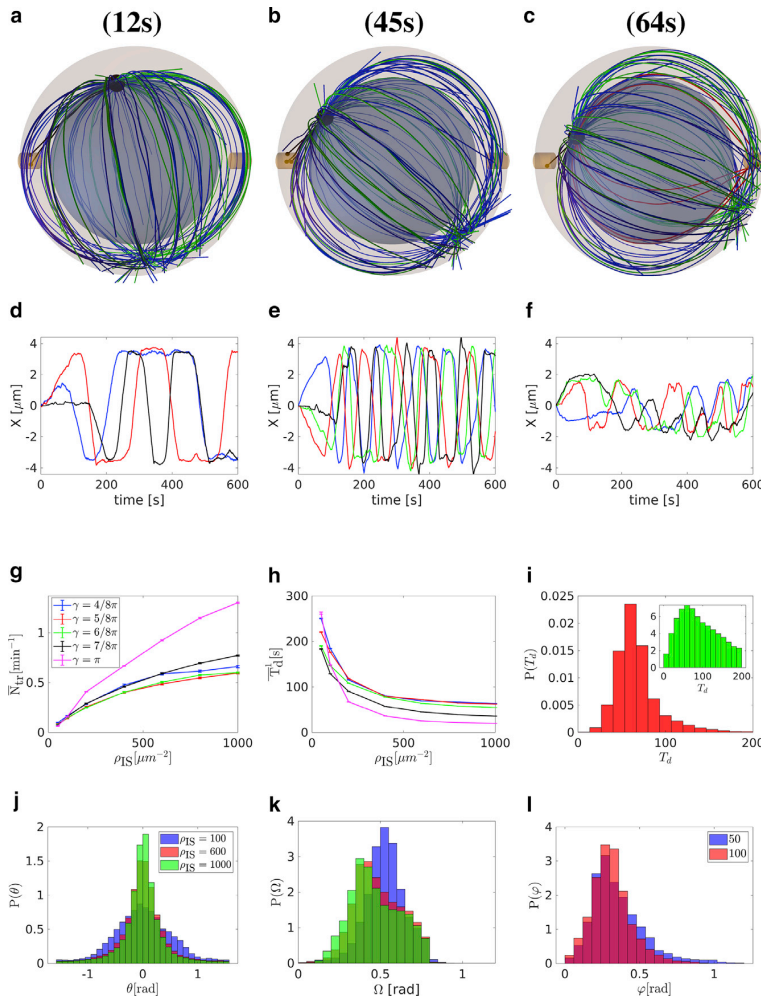


FIGURE 4 Capture-shrinkage mechanism with two IS with the same dynein density $\rho_{IS}^1 = \rho_{IS}^2 = \rho_{IS}$. (a–c) Snapshots from the time evolution of the MT cytoskeleton configuration with capture-shrinkage mechanism, $\rho_{IS} = 400 \mu\text{m}^{-2}$. Symbols and colors as in Fig. 2. (a) MTs attach to dyneins in the left IS and form a stalk, and the MTOC moves toward the left IS. (b) MTOC approaches the IS and MTs depolymerize. (c) Short MTs detach from the left IS. Simultaneously, the plus-end of the MT intersects with the center of the distant IS and is captured by dynein. (d–f) Examples of the time evolution of the MTOC position in 600 s of the simulation. The time evolutions of x coordinate of the MTOC are shown. Both IS are located in the xz plane and the MTOC is originally located at the same distance from both IS, $x = 0$. (d and e) $\gamma = \pi$. (d) $\rho_{IS} = 200 \mu\text{m}^{-2}$. (e) $\rho_{IS} = 800 \mu\text{m}^{-2}$. (f) $\gamma = \frac{1}{2}\pi$, $\rho_{IS} = 800 \mu\text{m}^{-2}$. (g) Dependencies of the average transition frequency between two IS per minute \bar{N}_{tr} . (h) Average dwell time that the MTOC spends next to the IS \bar{T}_d (h on dynein density ρ_{IS} . Dependencies are plotted with error bars only if bigger than a symbol size. (i) Probability densities of dwell times for angle between the axis of two IS. $\gamma = \pi$, $\rho_{IS} = 200 \mu\text{m}^{-2}$. Inset: dwell time distribution in a log-lin plot demonstrating the exponential tail. Dwell times were collected from 1280 simulation runs. (j–l) $\gamma = \frac{1}{2}\pi$. Probability densities of the azimuthal angle θ (j), MTOC-IS angle Ω (k), and polar angle φ (l). To see this figure in color, go online.

shrink (green lines). The MT cytoskeleton is not damaged permanently by the capture-shrinkage mechanism, since short filaments regrow due to the polymerization. Therefore, the MTOC relocates back and forth between the two IS until one IS is removed. In Fig. 4, d–f we see that the time evolution of the MTOC position follows a recurring pattern already seen in the video: the MTOC travels to one IS, remains in its close proximity for a time, and then repositions to the second IS. This pattern is caused by two effects: the MTs lose contact with the close IS (to which it moves) and establish a contact with the distant IS. The similar process for the case $\gamma = \frac{3\pi}{4}$ is shown in Video S2.

The physical mechanism underlying the MTOC transition from one IS to the other and back is the decrease of the dynein attachment probability with decreasing MTOC-IS distance due to strong bending of attached filaments at short distances, as sketched in Fig. 2 d. The MTOC is a planar structure and

MTs sprout from the MTOC tangentially. At large MTOC-IS distances the MT bends around the nucleus and bending forces press the plus-end against the cell membrane, where it can be captured by dyneins. At small MTOC-IS distances an attached MT has to bend to stay in contact with the IS. When a short MT detaches from dyneins the plus-end recedes from the IS, making reattachment unlikely. The attachment probability of the MT in the IS depends on the circumferential MTOC-IS distance, since only MTs having a length roughly corresponding to it can attach in the IS. Fig. 2 f shows that the probability density of the MT length steadily increases before reaching a peak at $L_{MT} \sim 15.8 \mu\text{m}$, corresponding to the circumferential distance between two IS when $\gamma = \pi$. Consequently, the probability of the MT attachment in the distant IS increases as the MTOC recedes, since an increasing number of MTs have a length corresponding to the circumferential MTOC-IS distance.

Hornak and Rieger

By comparing Fig. 4, *d* and *e*, one realizes that when the density increases, transitions are faster and the MTOC remains close to the IS for a shorter time. Fig. 4 *g* shows that the transition frequency increases with the dynein density. Dwell times decrease with the increasing dynein density and increasing angle γ , cf. Fig. 4 *h*. One would expect that the transition frequency decreases with the rising distance between two IS (increasing with γ). Surprisingly, it decreases with γ only when $\gamma \leq \frac{3\pi}{4}$ and is the maximal when $\gamma = \pi$.

The dynein detachment probability is force dependent and its pulling force is constantly opposed by forces of the friction and from the nucleus. As the density increases, more dyneins share the load from opposing forces and the detachment probability decreases, leading to shorter dwell times, cf. Fig. 4 *h*. Fig. 4 *i* shows the probability distribution of dwell times, and from the log-lin scale of the same plot in the inset one concludes that the dwell time distribution has an exponential tail. An increased dynein number leads to faster MTOC movement and shorter dwell times, which again result in an increased transition frequency.

The transition frequency does not decrease monotonously with increasing angle γ , since the probability of dynein attachment increases with the circumferential distance between two IS. At the end of the MTOC transition, only MTs having a length roughly corresponding to the circumferential distance between two IS can attach at the distant IS, as visualized in Fig. 4 *c*. The MT length distribution increases until it reaches maximum, corresponding approximately to the half of the cell circumference, cf. Fig. 2 *f*. Consequently, the probability that a plus-end intersects with the center of the IS at the end of MTOC transitions increases with the angle γ . The transition frequency decreases with the angle when $\gamma \leq \frac{3\pi}{4}$ because the MTOC travels longer distances and the increase of probability density is not significant. When $\gamma > \frac{3\pi}{4}$ the increasing distance is compensated by a higher number of MTs intersecting with the center of the distant IS, leading to shorter dwell times and faster MTOC movement, see Fig. 4, *e-h*. The case of $\gamma = \pi$ has the additional geometrical advantage that all MTs with sufficient length intersect the distant IS at the end of transitions, visually demonstrated in Fig. 4 *c*.

The increasing number of attached MTs influences the continuity of the MTOC transitions. When $\gamma = \pi$, the movement of the MTOC is regular and uninterrupted, see Fig. 4 *e*. On the other hand, for the smallest value of γ , i.e., the shortest distance between the two IS, the movement of the MTOC is highly irregular, see Fig. 4 *f*: the MTOC stops and stalls before resuming the movement to the IS (blue, green). In some cases the MTOC does not finish the journey and returns to the original location (black). When $\gamma = \pi$ a relatively high number of MTs intersects with the center of the distant IS with their plus-end, see Fig. 2 *f*. Since the MTOC is pulled by dyneins acting on multiple MTs, transitions are smooth and uninterrupted. When $\gamma = \pi/2$

only a limited number of MTs is pulled, resulting in easily interrupted transitions.

The longitudinal and transverse fluctuations of the MTOC along its path from one IS to the other can be described by the distribution of the polar and azimuthal angle, φ and θ , sketched in Fig. 2 *b*. The standard deviation of the azimuthal angle decreases with the increasing dynein density when $\gamma \leq \frac{3\pi}{4}$ and increases when $\gamma = \pi$, see Fig. S11 *a*. Two forces act on cytoskeleton: forces of dynein pulling the MTOC toward the IS and the forces of the tips of growing MTs on the cell membrane pushing the MTOC to all directions, sketched in Fig. 2 *e*. When $\gamma < \frac{3\pi}{4}$, only a small fraction of MTs sprouting from the MTOC intersect the distant IS at the end of the transition, see Fig. 2 *f*. Since the stalk pulls the MTOC either within the xz plane or toward it, sketched in Fig. 2 *e*, the azimuthal angle can only decrease during transitions. At the end of the transition, the dynein detach and forces from growing MT tips can push the MTOC from the xz plane, sketched in Fig. 2 *e*, increasing the azimuthal angle. Consequently, the standard deviation of the azimuthal angle decreases with dwell times and therefore decreases with dynein density, see Figs. 4 *h* and S11 *a*. Fig. 4 *j* shows that when $\gamma = \frac{\pi}{2}$ the peak of the probability distribution of the azimuthal angle is located at $\theta = 0$ and narrows for higher dynein densities, resulting in a reduced standard deviation. When $\gamma \geq \frac{7}{8}\pi$ the transitions can increase the azimuthal angle of the MTOC, since the MTs sprouting in multiple directions can attach to the IS, as visualized in Fig. 4. In contrast to the case $\gamma < \frac{7}{8}\pi$, the azimuthal angle increases as the dwell time decreases when $\gamma = \pi$, since the azimuthal angles are low when the MTOC is in the proximity of the IS and the transitions pull it from the plane, increasing azimuthal angles of the MTOC, see Fig. S11, *a* and *c*.

When $\gamma < \pi$ the standard deviation of the polar angle slightly decreases with the dynein density when $\rho_{IS} < 100 \mu\text{m}^2$ and then increases, see Fig. S11 *b*. The standard deviation of the polar angle depends on its range. When $\rho_{IS} \geq 100 \mu\text{m}^2$ the MTOC transitions between two IS, see Figs. 4, *g* and *h*, and the rising dynein force pulls the MTOC closer to the IS, see Fig. 4 *k*, increasing the range of the polar angle. The density of $\rho_{IS} = 50 \mu\text{m}^2$ is an exceptional case since the MTOC does not transition, see Fig. 4 *g*, since the dynein density is too small to establish the MT stalk. Consequently, forces from the growing MTs can push the MTOC from both IS increasing the polar angle, see Fig. S4 *l*. Obviously, the standard deviation of the polar angle increases with γ , see Fig. S11. When $\gamma = \pi$, the standard deviation is the largest and increases monotonously with dynein density. When $\gamma < \pi$ dyneins always pull the MTOC to the IS located in upper hemisphere, sketched in Fig. 2 *b*. When $\gamma = \pi$ the MTOC can travel through the lower hemisphere, thus increasing the range of the polar angle. Consequently, the standard deviation of the polar angle increases with the transition frequency, compare

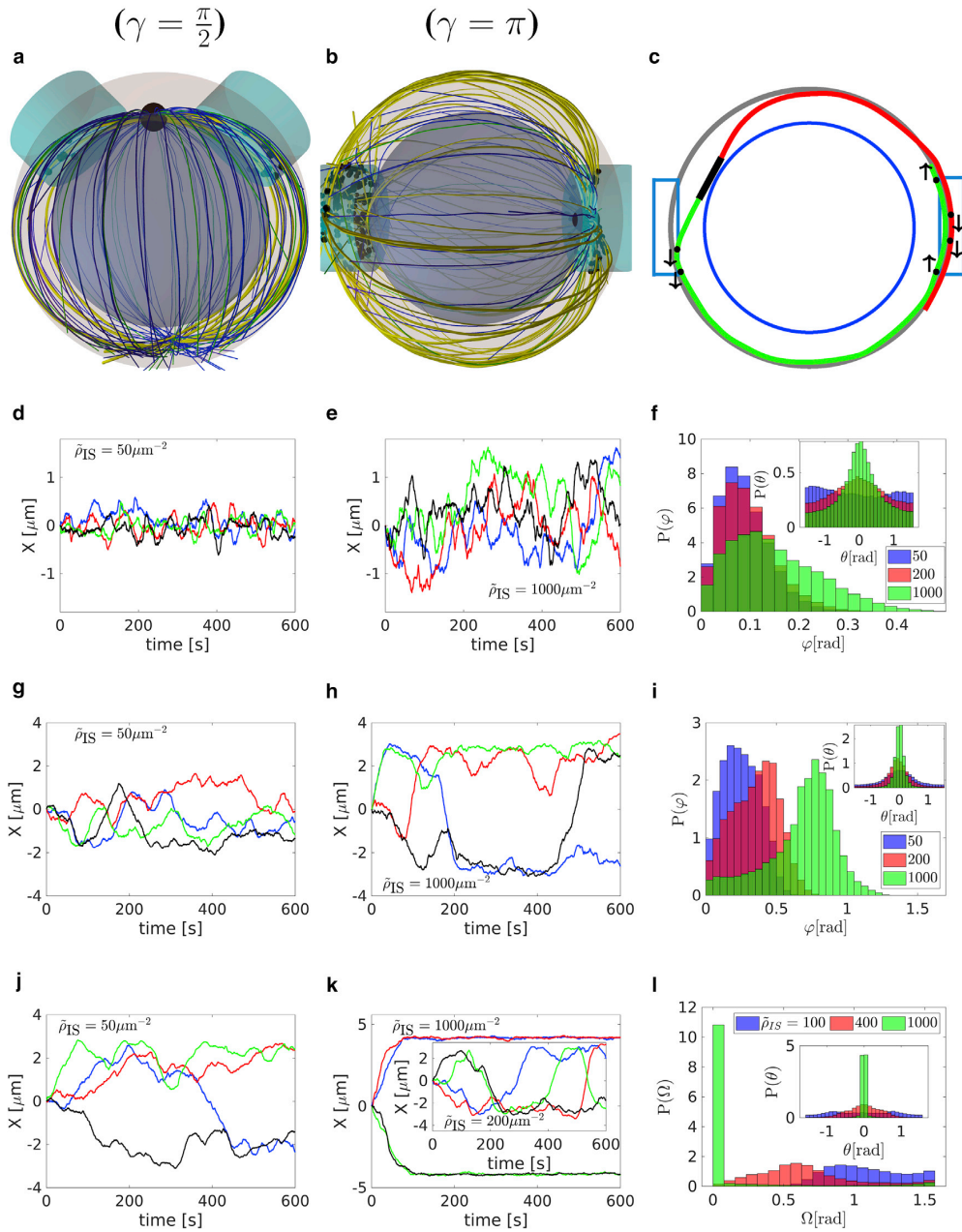


FIGURE 5 Cortical-sliding mechanism with two IS with the same dynein density $\hat{\rho}_{IS}^1 = \hat{\rho}_{IS}^2 = \bar{\rho}_{IS}$. (a and b) Snapshots from the time evolution of the MT cytoskeleton configuration with the cortical-sliding mechanism acting at both IS. Symbols and colors as in Fig. 2. (a) $\gamma = 0.5\pi$, $\bar{\rho}_{IS} = 200 \mu\text{m}^{-2}$. MTs attach in both IS and dyneins remain in a tug-of-war for the rest of the simulation. (b) $\gamma = \pi$, $\bar{\rho}_{IS} = 1000 \mu\text{m}^{-2}$. The MTOC is located close to the center of the IS. Almost all MTs are attached to dyneins and they sprout from the MTOC in all directions. (c) Sketch of dynein forces when $\gamma = \pi$ and with the MTOC in the close proximity of the IS. The cell membrane and the nucleus are represented by the gray and blue circle, respectively. The black line and the cyan rectangles denote the MTOC and two IS, respectively. Black dots and arrows denote dynein motors and directions of pulling forces, respectively. The green MT is attached to dyneins in both IS and the red MT is attached only by dyneins in the distant IS. (d and e) Examples of the time evolution of the MTOC position for $\gamma = \pi/2$. The time evolutions of x coordinate of the MTOC are shown, (d) for $\bar{\rho}_{IS} = 50 \mu\text{m}^{-2}$, (e) for $\bar{\rho}_{IS} = 1000 \mu\text{m}^{-2}$. (f) Probability

(legend continued on next page)

Hornak and Rieger

Figs. S11 b and 4 g. Similarly to the case $\gamma < \beta$, the MTOC is pulled closer to the IS as the dynein density increases, see **Fig. S11 d**.

We further analyzed the capture-shrinkage scenario with different dynein densities at the two IS. As in the case of equal densities, dynein detaches when the MTOC approaches the IS and MTs attach at the second IS, visually in **Fig. 4 c**. We fixed the density in IS₁ $\rho_{IS}^1 = 600 \mu\text{m}^{-2}$ and we vary the density in IS₂ $50 \mu\text{m}^{-2} \leq \rho_{IS}^2 \leq 1000 \mu\text{m}^{-2}$. From **Fig. S12 a** one can see that the MTOC transitions between two IS even when dynein densities are different. The MTOC is predominantly located closer to the IS with higher dynein density. Average MTOC-IS₁ angle $\bar{\Omega}$ steadily increases with ρ_{IS}^2 and $\bar{\Omega} = \frac{\gamma}{2}$ when $\rho_{IS}^2 = \rho_{IS}^1$, see **Fig. S12 b**. Moreover, the dwell times are substantially larger for the IS with higher density, see **Fig. S12 c**.

Cortical-sliding mechanism

In contrast to the capture-shrinkage mechanism, cortical-sliding dyneins are distributed in a relatively large IS and can attach at any position on an MT. Since multiple filaments intersect with the IS in every instant, MTs are always simultaneously attached at both IS, as visualized in **Fig. 5, a** and **b**.

By comparison of **Fig. 5, d–l** one realizes that as the angle γ increases, the MTOC transitions become more continuous and less frequent. When $\gamma < \frac{3\pi}{4}$, the transition frequency increases before reaching the peak at $\tilde{\rho}_{IS} = 200 \mu\text{m}^{-2}$ and then declines, see **Fig. S13 a**. It steadily decreases with the rising dynein density when $\gamma > \frac{3\pi}{4}$. The case of $\gamma = \pi$ is unique since the transition frequency decreases to zero. Moreover, it is the only case when standard deviation of the polar angle decreases with rising dynein density, see **Fig. S13 b**. The standard deviations of the azimuthal angle steadily decrease with the dynein density, see **Fig. S13 c**.

When $\gamma < \frac{3\pi}{4}$ relatively large IS are located close to each other, visually demonstrated in **Fig. 5 a**. The dynein detach when the MTOC approaches the IS (see section 3.2 of [supporting material](#)) and the pulling force decreases. MTs are being pulled by dyneins in the second IS at the same time. These two effects result in minimal MTOC fluctuations around the central position, see **Fig. 5 d**, and in a relatively high transition frequency between two hemispheres, see **Fig. S13 a**. By comparison of azimuthal angles in **Fig. 5, f** and **i** one realizes that the MTOC fluctuations have a strong lateral component when $\gamma \leq \frac{3\pi}{4}$, which is stronger than the parallel one when $\tilde{\rho} = 50 \mu\text{m}^{-2}$. This is due to the fact that dyneins located at the peripheries of both IS can cooperate while pulling the MTOC from the xz plane but are always in competi-

tion when pulling the MTOC parallel to the plane. The MTOC movement becomes more aligned with the xz plane, see **Fig. 5 f**, as the dynein density increases, leading to a slight increase in the transition frequency, see **Fig. S13 a**. As the density further increases, $\tilde{\rho} > 200 \mu\text{m}^{-2}$, the MTOC is increasingly pulled from the central position to the IS, see **Fig. 5, e** and **f**. The number of transitions decreases since the MTOC travels a longer distance. Moreover, as the MTOC approaches one IS the forces of nucleus oppose the movement to the distant IS, giving the advantage to the dynein at the close IS in the constant tug-of-war.

When $\frac{3\pi}{4} \leq \gamma < \pi$ and dynein densities are low, the constant competition between dyneins from both IS leads to short, interrupted transitions between two IS, see **Fig. 5 g**. The MTOC moves around the central position (green), and transitions between two IS are very slow (blue) or interrupted (red), or the MTOC dwells in one hemisphere for a long time (black). As in the previous case, the MTOC is increasingly pulled from the central position to the IS with rising density, see **Fig. 5 h** and **i**. Transitions to the distant IS become more unlikely due to the fact that the dyneins from the distant IS are opposed by the forces of dyneins from the close IS and from the nucleus. When $\tilde{\rho} = 1000 \mu\text{m}^{-2}$ the MTOC dwells in one hemisphere and rarely transitions, see **Fig. 5, h** and **i**. Since the MTOC stays longer in the proximity of the IS located at the xz plane as the density increases, the peak of azimuthal angle probability distributions narrows, see **Fig. 5 i**. **Video S3** shows the process for the case $\gamma = \frac{3}{4}\pi$ and $\tilde{\rho} = 600 \mu\text{m}^{-2}$.

In **Fig. 5, j** and **k** it can be seen that the MTOC trajectories are fundamentally different for lower and higher densities when $\gamma = \pi$. Moreover, the transition frequency is higher than in the case of $\gamma = \frac{7\pi}{8}$, since the higher number of MTs intersect the distant IS when IS are in diametrical opposition, visually demonstrated in **Fig. 5 b**. When the density is low, the MTOC transitions between two IS, never reaching their center, see **Fig. 5, j** and **l**. As the density increases, the MTOC approaches closer to the IS, see **Fig. 5, k** and **l**. When $\tilde{\rho}_{IS} > 600 \mu\text{m}^{-2}$, dynein forces are strong enough to pull the MTOC to the center of the IS, where it remains for the rest of the simulation, see **Fig. 5, k** and **l**. In such a case the majority of MTs are attached in the distant IS, visually demonstrated in **Fig. 5 b**. Since MTs attached at the distant IS are sprouting from the MTOC in every direction, the dyneins act in a competition, sketched in **Fig. 5 c**. If the MTOC recedes from the center of the IS, the dyneins at the close IS pull the MTOC back alongside the part of the dyneins in the distant IS. Contrarily to the cases when $\beta < \pi$ the MTOC can travel to the distant IS in all directions, resulting in substantial deviations from the xz plane, see the inset of **Fig. 5 l**. The peak of the probability density of the

distribution of the polar angle φ (main plot) and the azimuthal angle θ (inset). (*g–i*) The same as (*d–f*) for $\gamma = \frac{2\pi}{3}$. (*j* and *k*) Examples of the time evolution of the MTOC position for $\gamma = \pi$, (*j*) for $\tilde{\rho}_{IS} = 50 \mu\text{m}^{-2}$, (*k*) for $\tilde{\rho}_{IS} = 1000 \mu\text{m}^{-2}$ (main plot) and $\tilde{\rho}_{IS} = 200 \mu\text{m}^{-2}$ (inset). (*l*) Probability distribution of the MTOC-IS angle Ω and the azimuthal angle (inset). To see this figure in color, go online.

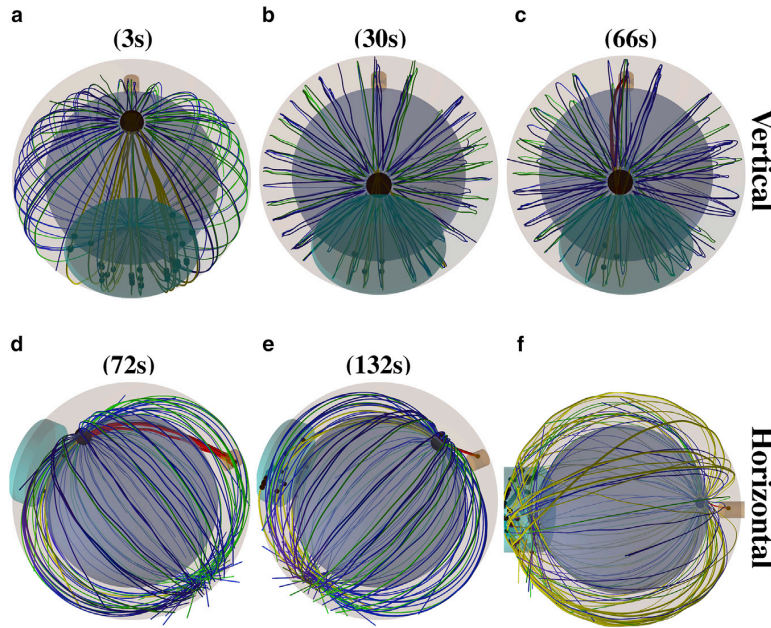


FIGURE 6 Snapshots from the time evolution of the MT cytoskeleton configuration under the effects of both capture-shrinkage and cortical-sliding mechanisms from two perspectives in different IS with the same dynein densities. $\gamma = \frac{3\pi}{4}$, $\rho_{IS}^1 = \rho_{IS}^2 = \rho = 400 \mu\text{m}^{-2}$, $\tilde{\rho}_{IS}^2 = \tilde{\rho}_{IS}^1 = 0 \mu\text{m}^{-2}$. Symbols and colors as in Fig. 2. (a) Initially, MTs attach only to the cortical-sliding dynein at the left IS since no plus-end of MTs intersect with the center of the right IS. (b) Cortical-sliding dyneins detach as the MTOC approaches the left IS. (c) The plus-end of an MT intersects with the center of the right IS and is captured by dynein. (d) Several MTs form a stalk connecting the center of the right IS with the MTOC and overpower cortical sliding at the left IS. (e) As the MTOC approaches the right IS, capture-shrinkage MTs detach from the dyneins. Simultaneously, MTs attach to cortical-sliding dyneins at the left IS. (f) Snapshots from the time evolution of the MT cytoskeleton. $\rho = 1000 \mu\text{m}^{-2}$, $\gamma = \pi$. The MTOC is located close to the center of the right IS. Almost all MTs are attached to cortical-sliding dyneins at the left IS and they sprout from the MTOC in all directions, resulting in contradictory pulling forces. To see this figure in color, go online.

angle θ becomes more narrow with rising density, since the MTOC is increasingly located closer to the IS, see Fig. 5 l. Video S4 shows the process for the case $\gamma = \pi$ and $\tilde{\rho} = 1000 \mu\text{m}^{-2}$.

In general, the MTOC is located closer to the xz plane as the density increases, see Fig. 5, f, i, and l. Consequently, the standard deviation of the horizontal angle decreases with the dynein density, see Fig. S13 c. At the same time the standard deviation of the polar angle increases, see Fig. S13 b, due to its increased range, see Fig. 5, f and i. The only exception is the case of $\gamma = \pi$. Small and still decreasing transition frequency causes decreasing range MTOC-IS₁ angles, see Figs. S13 a and 5 l, leading to the decreased standard deviation of the polar angle, see Fig. S13 b.

Capture-shrinkage and cortical-sliding mechanisms in different IS

In this section, we analyze the scenario when two IS employ different mechanisms. Cortical sliding has multiple advantages over the capture-shrinkage mechanism. Given the radii of the whole IS and its center $R_{IS} = 2 \mu\text{m}^{-2}$ and $R_{CIS} = 0.4 \mu\text{m}^{-2}$, respectively, the surface of the whole IS is 25-times larger than the surface of the IS center. Moreover, the cortical-sliding dyneins attach on the whole MT, with capture shrinkage just at the end. Consequently, multiple filaments are attached to cortical-sliding dyneins during the entire simulation. The capture-shrinkage dynein attach only when the tip of the MT intersects with the narrow center of the IS, making the attachment of capture-shrinkage dyneins far less frequent. All capture-shrinkage dyneins

can be unattached for a long time. On the other hand, the capture-shrinkage mechanism has the advantage that the attached MTs form a narrow stalk assuring the alignment of dynein forces, as visualized in Fig. 6 d.

The resulting repositioning process is shown in Video S5, $\rho_{IS}^1 = \tilde{\rho}_{IS}^2 = 400 \mu\text{m}^{-2}$. The capture-shrinkage dyneins are located in the right IS₁. The MTOC moves to the left IS, since the MTs attach immediately to cortical-sliding dyneins and the center of the right IS is not intersected by plus-ends of MTs, visualized in Fig. 6 a. When the MTOC approaches the left IS, the cortical-sliding dyneins detach and, simultaneously, the tips of MTs passing through the center of the right IS attach to capture-shrinkage dyneins, visually demonstrated in Fig. 6, b and c. Since the capture-shrinkage mechanism is opposed by cortical sliding, MTs can detach from the capture-shrinkage dyneins. It takes several MTs to attach in the center of the IS at the same time to compete with the force of cortical-sliding dyneins. As the force of capture-shrinkage dyneins outweighs the force of the cortical-sliding dyneins, the MTOC moves to the right center in the direction given by the MT stalk, visualized in Fig. 6 d. The capture-shrinkage dyneins detach when the MTOC approaches the right IS. Simultaneously, cortical-sliding dyneins attach at the left IS, visually demonstrated in Fig. 6 e, and the MTOC moves again to the left IS.

Fig. 7 a shows that when $\gamma < \pi$ the transition frequency steadily increases with the dynein density. Fig. 7 b shows that when the densities are low, the average angle between the MTOC and the capture-shrinkage IS₁ is $\Omega \gg \frac{\pi}{2}$, indicating

Hornak and Rieger

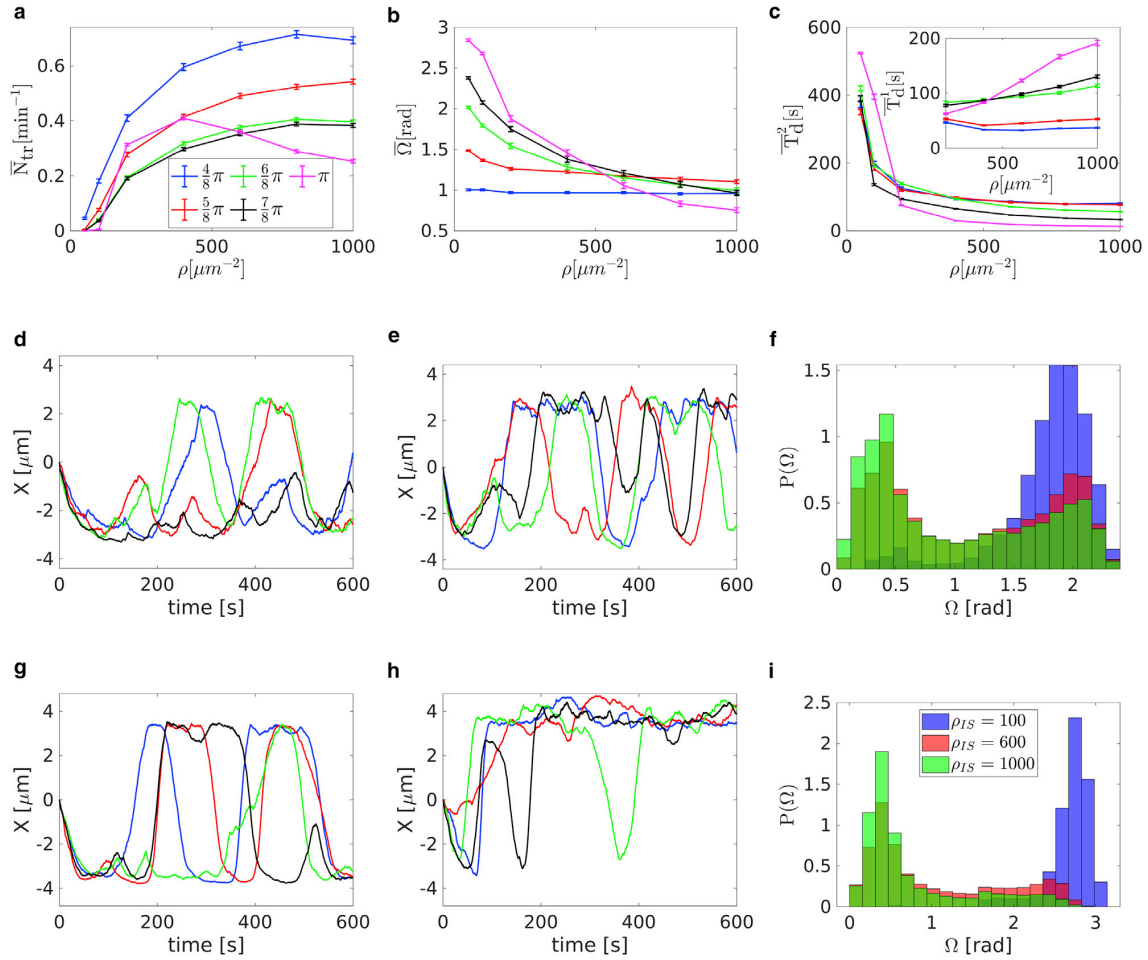


FIGURE 7 Capture-shrinkage and cortical-sliding mechanisms in different IS with the same dynein densities. $\rho_{IS}^1 = \bar{\rho}_{IS}^2 = \rho$, $\rho_{IS}^2 = \bar{\rho}_{IS}^1 = 0 \mu\text{m}^{-2}$. Cortical-sliding IS₂ is located in the hemisphere $x < 0$. (a–c) Dependencies of the average transition frequency \bar{N}_{tr} between two IS (a), the average angle between the MTOC and the capture-shrinkage IS₁ $\bar{\Omega}$ (b), and average dwell times \bar{T}_d^1 and \bar{T}_d^2 that the MTOC spends next to the capture-shrinkage IS₁ and the cortical-sliding IS₂, respectively (c), on the dynein density ρ . The dwell times \bar{T}_d^1 are given for $\rho \geq 200 \mu\text{m}^{-2}$ since the MTOC does not reach the IS₁ when $\rho < 200 \mu\text{m}^{-2}$. Dependencies are plotted with error bars only if bigger than a symbol size. (d and e) Examples of the time evolution of the MTOC position in 600 s of simulation. The time evolutions of x coordinate of the MTOC are shown, $\gamma = \frac{3\pi}{4}$. (d) $\rho = 200 \mu\text{m}^{-2}$, (e) $\rho = 1000 \mu\text{m}^{-2}$. (f) Probability distribution of the angle Ω between the MTOC and the capture-shrinkage IS₁, $\gamma = \frac{3\pi}{4}$. (g and h) Examples of the time evolution of the MTOC position in 600 s of simulation, $\gamma = \pi$. (g) $\rho = 200 \mu\text{m}^{-2}$, (h) $\rho = 1000 \mu\text{m}^{-2}$. (i) Probability distribution of the angle Ω between the MTOC and the capture-shrinkage IS₁, $\gamma = \pi$. To see this figure in color, go online.

that the MTOC is predominantly located closer to the cortical-sliding IS₂. Moreover, the angle decreases with the increasing dynein density. Average dwell times \bar{T}_d^2 close to cortical-sliding IS₂ and \bar{T}_d^1 close to capture-shrinkage IS₁ decrease and increase with increasing density, respectively, see Fig. 7 c.

It can be seen in Fig. 7, d, e, g, and h that initially the MTOC travels to the cortical-sliding IS₂ in all cases except one. The MTOC travels to the capture-shrinkage IS₁ only in a highly improbable scenario when plus-ends of multiple

MTs intersect the narrow IS center. When $\gamma = \frac{3\pi}{4}$ and $\rho = 200 \mu\text{m}^{-2}$ the MTOC dwells in the proximity of the cortical-sliding IS₂, see Fig. 7, d and f. The transitions to the capture-shrinkage IS₁ are interrupted and the MTOC travels back to the cortical-sliding IS₂ (black). When the MTOC finishes the transitions to the IS₁, it dwells in its proximity for a short time and then returns to the IS₂ (blue, red). Multiple transitions to IS₁ rarely occur (green). Interrupted transitions to IS₁ can be explained by constantly attached cortical-sliding dyneins overpowering the force of the

capture-shrinkage mechanism. If the MTOC finishes transition to the IS₁, capture-shrinkage dyneins detach and cortical sliding pulls the MTOC back to the IS₂. To conclude, cortical sliding has dominance over the capture-shrinkage mechanism when $\rho_{IS} < 600 \mu\text{m}^{-2}$, since the MTOC is located predominantly closer to the IS₂, see Fig. 7, b–d and f.

Fig. 7 e shows that when $\rho = 1000 \mu\text{m}^{-2}$ the transitions toward the capture-shrinkage IS₁ are mostly uninterrupted, indicating that the capture-shrinkage mechanism can compete with cortical-sliding dyneins by capturing several MTs and forming MT stalk, as visualized in Fig. 6 d. Moreover, the MTOC dwells longer close to the capture-shrinkage IS₁, see Fig. 7, c, e, and f, resulting in the decrease of the average MTOC-IS₁ angle, see Fig. 7 b. Therefore, the capture-shrinkage mechanism gains dominance over the cortical-sliding mechanism as the dynein density increases.

When $\gamma < \pi$, the transition frequency increases with the dynein density, see Fig. 7 a, and therefore increases as the capture-shrinkage mechanism becomes dominant. The increasing density of capture-shrinkage dyneins increases the probability of dynein attachment and the formation of MT stalks that can overcome the cortical-sliding mechanism. The formation of the MT stalks results in complete transitions toward the capture-shrinkage IS₁ and in the steep decrease of cortical-sliding dwell times, see Fig. 7, c and e. However, the capture-shrinkage dwell times increase only slightly with the increasing density, see Fig. 7 c. Regardless of dynein density, motors detach at the end of the transition and depolymerized MTs are unlikely to reattach, visually demonstrated in Fig. 2 d. Consequently, as the dynein density increases, the capture-shrinkage mechanism becomes more able to pull the MTOC but remains unable to hold it, leading to the increased transition frequency.

The case of $\gamma = \pi$ is unique, since the transition frequency increases with the dynein density before reaching the peak at $\rho = 400 \mu\text{m}^{-2}$ before slowly decreasing, see Fig. 7 a. The MTOC trajectories differ when considering multiple dynein densities. When $\rho = 200 \mu\text{m}^{-2}$, the MTOC moves similarly to the case when $\gamma < \pi$. The MTOC transitions to one IS, dwells there, then moves to the second IS, see Fig. 7 g. Fig. 7 i shows that the MTOC is predominantly located closer to the cortical-sliding IS when the dynein density is low. When $\rho = 1000 \mu\text{m}^{-2}$, the MTOC dwells in the proximity of the capture-shrinkage IS₁, see Fig. 7 l, and the transitions to the cortical-sliding IS₂ are infrequent and unfinished, see Fig. 7 h. When $\rho \geq 600 \mu\text{m}^{-2}$, the dynein force is strong enough to pull the MTOC to the close proximity of the center of the capture-shrinkage IS₁, Fig. 7 i. In such a case almost all MTs are attached to the cortical-sliding dynein at the distant IS₂, visually demonstrated in Fig. 6 f. The MTOC stays in the proximity of the capture-shrinkage IS₁, see Fig. 7 i, since the cortical-sliding dyneins pull the MTOC in different directions and oppose each other. Moreover, the MTOC is

pulled back to the close IS by MTs occasionally attached to capture-shrinkage dyneins in the center of the IS₁, visually depicted by the red short MT in Fig. 6 f. Video S6 shows the process for $\gamma = \pi$ and $\rho_{IS}^1 = \tilde{\rho}_{IS}^2 = 1000 \mu\text{m}^{-2}$.

The transition frequency decreases with the distance between the two IS when $\gamma \leq \frac{2\pi}{3}$, see Fig. 7 a, since the MTOC has to travel longer distance. When $\gamma > \frac{2\pi}{3}$ the distance is compensated by the increased attachment probability in the center of the IS caused by the increased probability density of MTs length corresponding to the circumferential distance between the two IS, see Fig. 2 f. An increased number of attached capture-shrinkage MTs leads to the decreased cortical-sliding dwelling times as the γ increases, see Fig. 7. The capture-shrinkage dwell times increase with γ , since the higher number of MTs pulls the MTOC closer to the IS, see Fig. 7, f and i.

Combined mechanisms in both IS

The time evolution of the cytoskeleton under the effect of both mechanisms with equal densities in both IS $\tilde{\rho}_{IS}^1 = \tilde{\rho}_{IS}^2 = \rho_{IS}^1 = \rho_{IS}^2 = 400 \mu\text{m}^{-2}$, $\gamma = \frac{3\pi}{4}$, is shown in the Video S7. During the simulation, the MTOC repeatedly transitions between the two IS. The snapshots of one transition can be seen in Fig. 8. At the end of the transition, the MTs intersecting with the center of the distant IS are captured by dyneins, as visualized in Fig. 8 a. The cortical-sliding dyneins in the right IS have to compete with both mechanisms from the left IS and detach. Consequently, the MTOC is pulled to the left IS by both mechanisms and the movement is not opposed by the forces from the right IS, visualized in Fig. 8 b. As the MTOC approaches the left IS, capture-shrinkage MTs detach. Simultaneously, MTs are captured on the other side of the cell. Consequently, the stalk connecting the MTOC and the IS is formed and both mechanisms pull the MTOC to the right IS, as visualized in Fig. 8 c. As the MTOC approaches the right IS, dyneins of both mechanisms detach. Simultaneously, dyneins attach in the distant IS and initialize the next transition.

Fig. 8 d shows that the transition frequency increases with the dynein density. Moreover, the transition frequency decreases with the increasing angle γ only when $\gamma \leq \frac{3\pi}{4}$ and reaches the maximum when $\gamma = \pi$. Surprisingly, dwell times in the proximity of the IS do not steadily decrease with the dynein density despite the continuous decrease of the time that the MTOC spends in one hemisphere, see Fig. 8 e. The dwell times decrease with the dynein density until they reach a minimum when $\rho \sim 400 \mu\text{m}^{-2}$ and then slightly increase. The standard deviation of the polar angle slightly increases and decreases when $\gamma < \pi$ and $\gamma = \pi$, respectively.

By comparison between Figs. 4, d–f and 8, g and h, one realizes that the MTOC trajectories under the effects of both mechanisms follow the same pattern as in the case of the sole capture-shrinkage mechanism: the MTOC travels

Hornak and Rieger

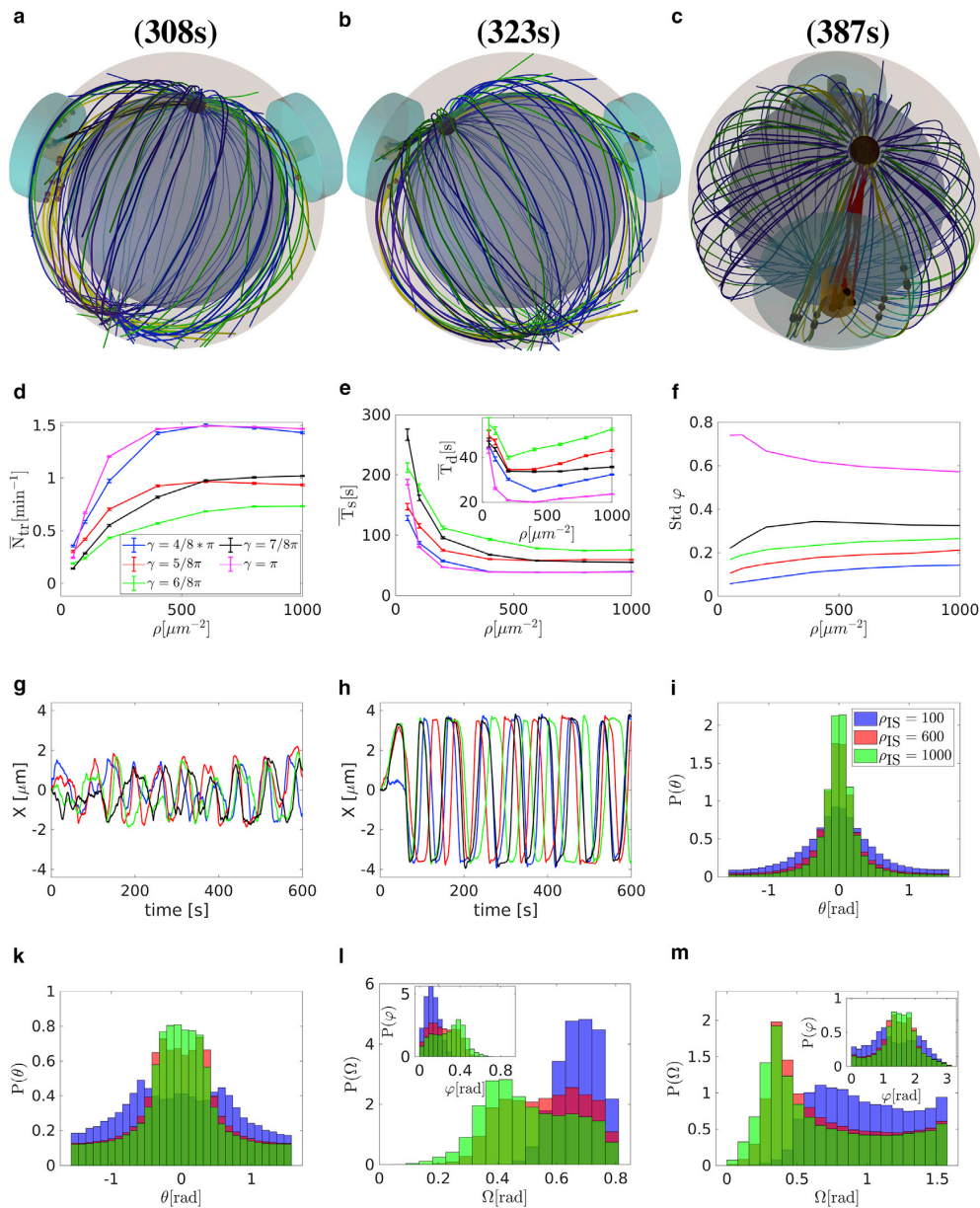


FIGURE 8 Combination of capture-shrinkage and cortical-sliding mechanisms with the same dynein density in both IS, $\rho_{IS}^1 = \rho_{IS}^2 = \rho_{IS}^1 = \rho_{IS}^2 = \rho$. (a–c) Snapshots from the time evolution of the MT cytoskeleton. $\rho = 400 \mu\text{m}^{-2}$, $\gamma = \frac{3\pi}{4}$. Symbols and colors as in Fig. 2. (a) MTs intersecting with the center of the left IS attach to capture-shrinkage dyneins. Cortical-sliding dyneins attach to MTs at the periphery of both IS. (b) MTs captured in the left IS depolymerize as the MTOC approaches. Both capture-shrinkage and cortical-sliding MTs detach from dyneins. (c) Snapshot from the perspective of the right IS. MTs detached from the capture-shrinkage dyneins in the left IS. Simultaneously, MTs intersect with the center of the right IS and are captured by dyneins. Cortical-sliding dyneins attach at the right IS and detach at the left IS. (d–f) Dependencies of the average transition frequency \bar{N}_{tr} (d), the time that the MTOC spends in one hemisphere \bar{T}_s (e), and the dwell time in the proximity of the IS \bar{T}_d (e), and the standard deviation of the polar angle φ (f) on the dynein density ρ . (d and e) Dependencies are plotted with error bars. (g and h) Examples of the time evolution of the MTOC position in 600 s of simulation. The time evolutions of x coordinate of the MTOC are shown, $\rho = 600 \mu\text{m}^{-2}$. (g) $\gamma = \frac{\pi}{2}$, (h) $\gamma = \pi$. (l and k) Probability distributions of the azimuthal angle θ . (i) $\gamma = \frac{\pi}{2}$, (k) $\gamma = \pi$. (l and m) Probability distributions of the angle Ω between the MTOC and the IS and the polar angle φ . (l) $\gamma = \frac{\pi}{2}$, (m) $\gamma = \pi$. To see this figure in color, go online.

TABLE 1 Synopsis of cortical sliding/capture shrinkage

	Capture shrinkage	Cortical sliding	Different mechanisms	Combined mechanisms
Transition frequencies N_{tr}	N_{tr} increases with ρ_{IS} and maximal for $\gamma = \pi$	N_{tr} decreases with γ , and $\bar{\rho}_{IS}$ for $\gamma \geq \frac{2\pi}{3}$	N_{tr} increases with ρ ; $\gamma < \pi$; N_{tr} depends non-monotonously on ρ for $\gamma \approx \pi$	N_{tr} increases with ρ , maximal for $\gamma = \pi$
Dwell times T_D	T_D decreases with ρ_{IS}	MTOC does not come close to one of the two IS for $\bar{\rho}_{IS} < 600 \mu\text{m}^2$ and $\gamma < \frac{2\pi}{3}$, only fluctuates between the two hemispheres	T_D decreases and increases with ρ at the sliding, shrinkage IS, respectively	T_D decreases and then increases with ρ
Angles: azimuthal θ /Polar φ ; MTOC-IS Ω	fluctuations of θ decrease with ρ_{IS} for $\gamma < \frac{2\pi}{3}$, but increase for $\gamma \approx \pi$	fluctuations of φ and Ω decrease for increasing $\bar{\rho}_{IS}$ when $\gamma \approx \pi$	Ω decreases and MTOC is closer to shrinkage IS as ρ increases	fluctuations of φ increase with ρ , except when $\gamma \approx \pi$, when they decrease
MT cytoskeleton morphology	MTs form a stalk connecting the MTOC and the IS. Dyneins in IS can remain unattached for a time	MTs always intersect the IS. MTOC stays at one of the two IS for $\bar{\rho}_{IS} > 600 \mu\text{m}^2$	MT stalk connects MTOC and shrinkage IS. Capture shrinkage becomes dominant as ρ increases	captured MTs shrink and detach. Sliding dynein acts on reduced number of MTs at close IS

to one IS, dwells in its close proximity, then transitions to the second IS. Moreover, the transitions between two IS are regular and continuous when $\gamma = \pi$ and incomplete and irregular when $\gamma = \frac{\pi}{2}$. As in the case of the capture-shrinkage mechanism, increasing circumferential distance between the two IS increases the probability that the plus-end of an MT is captured in the center of the distant IS due to the increasing probability density of MT length, see Fig. 2 f. Consequently, the dynein acts on an increased number of filaments as the γ increases, assuring continuous transition.

The combination of mechanisms leads to the unprecedented transition frequency and shortest dwell times, compare Figs. 4, 7, and 8. The reason is that the capture-shrinkage mechanism supports the cortical-sliding mechanism at the distant IS and hinders it at the close IS. At the end of the transitions, capture-shrinkage MTs are depolymerized and the cortical-sliding dyneins can attach to a lower number of MTs. Contrarily, MTs attach to the capture-shrinkage dyneins in the distant center and the two mechanisms pull in alignment sharing the load from opposing forces, as visualized in Fig. 8 c. Consequently, the MTOC is pulled to the distant IS by two mechanisms and to the close IS just by the cortical sliding acting on a reduced number of MTs.

The dwell times decrease with the rising dynein density, see Fig. 8 e, due to the higher pulling force. The slight increase of dwelling times when $\rho > 400 \mu\text{m}^{-2}$ is caused by the fact that the MTOC travels closer to the IS, see Fig. 8, l and m, and spends more time in the proximity of the IS. The monotonously decreasing times that the MTOC spends in one hemisphere indicate that the process gets faster with the dynein density despite the slightly increased dwelling times, see Fig. 8 e.

When $\gamma < \pi$, the standard deviation of the polar angle increases with the dynein density, see Fig. 8 f, because the MTOC is pulled closer to the IS and the angle has a wider range, see Fig. 8 l. The standard deviation of the polar angle is the largest when $\gamma = \pi$, since the MTOC can transition between IS through the lower hemisphere, sketched in Fig. 2 b. The standard deviation slightly decreases with the density. The reason lies in the fast speed of the MTOC transitions that leads to the fast transition from one IS to the second. Fig. 8 m shows that the MTOC is increasingly located closer to the IS when $\gamma = \pi$. The deviations from the xz plane decrease with the rising density, Fig. 8 i and k. The probability density does not have a peak at $\theta = 0$ when $\gamma = \pi$ at low densities, see Fig. 8 k, since the transitions pull the MTOC from the xz plane and the force is often insufficient to finish the transition in the close proximity of the IS center.

Synopsis of cortical sliding/capture shrinkage

Here, and in Table 1, we present a brief synopsis of the main differences that our model predicts when different mechanisms operate in both or in individual IS. When

Hornak and Rieger

only the cortical-sliding mechanism is acting, the transition frequency decreases with increasing angle γ , see Fig. S13 *a*. Contrarily to the capture-shrinkage mechanism, cortical-sliding dyneins are in a constant tug-of-war. When the dynein densities are small, the MTOC wiggles around the central position, see Fig. 5, *d, g, and j*. As the dynein density increases, one IS gains the upper hand and pulls the MTOC to the IS, see Fig. 5, *f, I, and l*. A subsequent transition to the distant IS is unlikely, since the dyneins from the distant IS have to overcome the forces from the close IS and the forces from the nucleus increasing with γ .

The mechanisms can be compared by locating them in different IS. One observes that for $\rho_{IS} < 600 \mu\text{m}^{-2}$, the average angle between the MTOC and the capture-shrinkage IS $\bar{\Omega} > \frac{\gamma}{2}$, indicating that the MTOC is located closer to the cortical-sliding IS₂, see Fig. 7 *b*. As the density increases, the capture-shrinkage mechanism gains the upper hand and the MTOC is located closer to the capture-shrinkage IS₁, see Fig. 7, *b, f, and i*. One can therefore conclude that the cortical-sliding mechanism is stronger only when $\rho_{IS} < 600 \mu\text{m}^{-2}$ and weaker otherwise. When $\gamma = \pi$, the transition frequency decreases with increasing dynein density when $\rho_{IS} > 400 \mu\text{m}^{-2}$. As the dynein density increases the MTOC moves closer to the IS and dwells there, since cortical-sliding dyneins act against each other, as visualized in Fig. 6 *f*.

When the two mechanisms act together in both IS, the transition frequency is the highest and the dwell times are the lowest. The high transition frequency is due to the fact that as the MTOC is located in the proximity of one IS; the two mechanisms work together in the distant IS and oppose each other at the closer IS. As the MTOC approaches the IS, the captured MTs depolymerize and at the end detach from dyneins. Consequently, the capture-shrinkage mechanism cannot keep the MTOC at the close IS and the cortical-sliding mechanism acts on a reduced number of MTs. On the other hand, the dyneins from both mechanisms cooperate at the distant IS and share the load from opposing forces, reducing their detachment rate.

Surprisingly, when only the capture-shrinkage mechanism is acting, the transition frequency slightly decreases with increasing angle γ for $\gamma \leq \frac{2\pi}{3}$ and increases otherwise, see Fig. 4. This behavior can be explained by the shape of the MT length distribution, see Fig. 2 *f*. As the angle γ increases, increasing numbers of MTs have a length corresponding to the circumferential distance between two IS. Increasing numbers of attached MTs result in stronger pulling forces as well as higher transition frequency and smaller dwelling times.

DISCUSSION

The cell can polarize with stunning efficiency by employing two mechanisms performing differently in various cell configurations. In our computational model, the synergy of the two mechanisms manifests itself in reduced relocation

times. In a real cell where the cytoskeleton is dragged through the inhomogeneous environment of organelles and filaments, the synergy can make a difference between complete and unfinished repositioning. Thus it appears that the location of dyneins on the IS periphery and the combination of two synergetically acting mechanisms together form a complex, efficient machinery, ensuring that the crucial immune response of human body is carried out efficiently while saving resources.

In situations in which the T cell has two IS, several scenarios have been observed experimentally (15) and are also predicted by our model: the MTOC alternates stochastically (but with a well-defined average transition time) between the two IS; it wiggles in between the two IS without transiting to one of the two; or it is at some point pulled to one of the two IS and stays there. We have analyzed with the help of our model which scenario emerges in dependency of the mechanisms in action and the number of dyneins present.

The emerging behavior of the MTOC is simplest when in both IS only the capture-shrinkage mechanism is acting: the frequency of transitions between the two IS increases monotonously with increasing ρ_{IS} and the dwell time at an IS decreases. The longitudinal fluctuations, described by the polar angle φ , also decrease with increasing ρ_{IS} , which means that the MTOC transits without much back and forth movement to the other IS when the dynein density is large. On the other hand, the transverse fluctuations do not depend significantly on ρ_{IS} . This nearly deterministic oscillatory behavior of the MTOC position is based on the presence of a mechanism detaching the pulling dyneins due to strong bending forces acting on the MT when the MTOC gets close to the center of an IS, cf. Fig. 2 *d*.

The situation becomes more complex as soon as cortical sliding plays a role, either in both IS or in one. If it is present in both, i.e., cortical sliding only, at both IS many MTs can attach to dynein and the resulting attached dynein populations are in a persistent tug-of-war, leading to stochastic alternations between the two hemispheres of the cell but without ever reaching the center of one IS. Except for very high dynein densities, when one IS can have a sufficiently strong, stochastic majority of attached dyneins it pulls the MTOC toward it and keeps it there, since no mechanism forcing the dyneins to detach is present in cortical sliding. Therefore, our model predicts that capture shrinkage is necessary to decide the tug-of-war that arises when two IS with low to medium dynein densities are present. In addition it predicts that when both mechanisms are present they can act even synergetically, since their cooperation results in the largest number of transitions. This observation suggests that the combination of the two mechanisms, capture shrinkage and cortical sliding, would actually allow the cell to kill two targets simultaneously.

Our results suggest that one may obtain insight into intracellular processes based on basic observations of the MTOC dynamics and cytoskeleton morphology. Regardless of the

number of the IS, the stalk of MTs sprouting from the MTOC and ending in the center of the IS is indicative of the capture-shrinkage mechanism. Its presence is also suggested by uninterrupted transitions and small dwelling times. Incomplete, interrupted transitions at small angle γ and long dwelling at one IS when $\gamma \geq \frac{2\pi}{3}$ are characteristic of the cortical-sliding mechanism. Moreover, the MTOC dynamics in the cell with two IS may offer a way to estimate the MT length distribution. Since the number of transitions does not decrease with increasing distance between the two IS and it is maximal when the distance corresponds to the peak of the length distribution, the experimental observations of the repositioning in the cell with two IS in different configurations may suggest the distribution of MT lengths.

In conclusion, we provided here a fairly complete picture of MTOC repositioning with one or two IS, under the model assumption of a fixed (spherical) cell shape. It would certainly be rewarding to include a deformable, semiflexible (due to the actin cortex) cell boundary interacting mechanically with the forces exerted by the semiflexible MTs. Another open question concerns the way in which dyneins are spatially organized in the membrane: do they self-organize (42,78,112) or are they more or less firmly anchored in the actin cortex, as we assumed in our model? Probably more experimental insight is necessary to decide this question.

From a broader perspective, MTOC/centrosome precise positioning is also crucial for other cell functions: in addition to the polarized immune response of lymphocytes considered here, it also determines either the axis of cell division or the direction of cell migration (113). In the latter contexts the centrosome is subjected to a force field of pulling and pushing forces that are mediated by cortical dynein and centrosome nucleated MTs, respectively. Our model included mainly pulling forces, as centrosome positioning in T cells is largely dependent on dynein, but a recent study (114) indicated that myosin-mediated pushing forces might also play a role in this process: dynein and myosin II accumulate at opposite cell poles following IS formation. While the dynein-dependent mechanism generates pulling forces at the IS, the asymmetric distribution of non-muscle myosin creates pushing forces from the opposite pole. Possibly the last phase of MTOC repositioning, the slow final approach toward the IS, is supported by these pushing forces—a hypothesis that could quantitatively be tested by our model, augmented also by an elastic and spatially inhomogeneous active cell boundary.

SUPPORTING MATERIAL

Supporting material (Vodeps S8–S10) can be found online at <https://doi.org/10.1016/j.bpj.2022.02.029>.

AUTHOR CONTRIBUTIONS

I.H. and H.R. designed the research. I.H. performed calculations, prepared figures, and analyzed the data. I.H. and H.R. wrote the manuscript.

ACKNOWLEDGMENTS

This work was financially supported by the German Research Foundation (DFG) within the Collaborative Research Center SFB 1027.

REFERENCES

- Rudolph, M. G., R. L. Stanfield, and I. A. Wilson. 2006. How TCRs bind MHCs, peptides, and coreceptors. *Annu. Rev. Immunol.* 24:419–466.
- Garcia, K. C. 2012. Reconciling views on T cell receptor germline bias for MHC. *Trends Immunol.* 33:429–436.
- Zinkernagel, R. M., and P. C. Doherty. 1974. Restriction of *in vitro* T cell-mediated cytotoxicity in lymphocytic choriomeningitis within a syngeneic or semiallogeneic system. *Nature.* 248:701.
- Attaf, M., M. Legut, ..., A. K. Sewell. 2015. The T cell antigen receptor: the Swiss army knife of the immune system. *Clin. Exp. Immunol.* 181:1–18.
- Wucherpfennig, K. W. 2004. T cell receptor crossreactivity as a general property of T cell recognition. *Mol. Immunol.* 40:1009–1017.
- Babbitt, B. P., P. M. Allen, ..., E. R. Unanue. 1985. Binding of immunogenic peptides to Ia histocompatibility molecules. *Nature.* 317:359.
- Monks, C. R., B. A. Freiberg, ..., A. Kupfer. 1998. Three-dimensional segregation of supramolecular activation clusters in T cells. *Nature.* 395:82–86.
- Dustin, M. L., M. W. Olszowy, ..., A. S. Shaw. 1998. A novel adaptor protein orchestrates receptor patterning and cytoskeletal polarity in T-cell contacts. *Cell.* 94:667–677.
- Dustin, M. L., A. K. Chakraborty, and A. S. Shaw. 2010. Understanding the structure and function of the immunological synapse. *Cold Spring Harb Perspect. Biol.* 2:a002311.
- Geiger, B., D. Rosen, and G. Berke. 1982. Spatial relationships of microtubule-organizing centers and the contact area of cytotoxic T lymphocytes and target cells. *J. Cell Biol.* 95:137–143.
- Kupfer, A., D. Louvard, and S. J. Singer. 1982. Polarization of the Golgi apparatus and the microtubule-organizing center in cultured fibroblasts at the edge of an experimental wound. *Proc. Natl. Acad. Sci. U S A.* 79:2603–2607.
- Yi, J., X. Wu, ..., J. A. Hammer. 2013. Centrosome repositioning in T cells is biphasic and driven by microtubule end-on capture-shrinkage. *J. Cell Biol.* 202:779–792.
- Stinchcombe, J. C., E. Majorovits, ..., G. M. Griffiths. 2006. Centrosome polarization delivers secretory granules to the immunological synapse. *Nature.* 443:462–465.
- Maccari, I., R. Zhao, ..., H. Rieger. 2016. Cytoskeleton rotation relocates mitochondria to the immunological synapse and increases calcium signals. *Cell Calcium.* 60:309–321.
- Kuhn, J. R., and M. Poenie. 2002. Dynamic polarization of the microtubule cytoskeleton during CTL-mediated killing. *Immunity.* 16:111–121.
- Hui, K. L., and A. Upadhyaya. 2017. Dynamic microtubules regulate cellular contractility during T-cell activation. *Proc. Natl. Acad. Sci. U S A.* 114:E4175–E4183.
- Kupfer, A., and G. Dennert. 1984. Reorientation of the microtubule-organizing center and the Golgi apparatus in cloned cytotoxic lymphocytes triggered by binding to lysable target cells. *J. Immunol.* 133:2762–2766.
- Kupfer, A., S. L. Swain, ..., S. J. Singer. 1986. The specific direct interaction of helper T cells and antigen-presenting B cells. *Proc. Natl. Acad. Sci. U S A.* 83:6080–6083.
- Gurel, P., A. Hatch, and H. Higgs. 2014. Connecting the cytoskeleton to the endoplasmic reticulum and Golgi. *Curr. Biol.* 24:R660–R672.
- Lee, C., and L. B. Chen. 1988. Dynamic behavior of endoplasmic reticulum in living cells. *Cell.* 54:37–46.

Hornak and Rieger

21. Waterman-Storer, C. M., and E. D. Salmon. 1998. Endoplasmic reticulum membrane tubules are distributed by microtubules in living cells using three distinct mechanisms. *Curr. Biol.* 8:798–806.
22. Palmer, K. J., P. Watson, and D. J. Stephens. 2005. The role of microtubules in transport between the endoplasmic reticulum and Golgi apparatus in mammalian cells. *Biochem. Soc. Symp.* 72:1–13.
23. Müllbacher, A., P. Waring, ..., M. M. Simon. 1999. Granzymes are the essential downstream effector molecules for the control of primary virus infections by cytolytic leukocytes. *PNAS.* 96:13950–13955.
24. Lowin, B., M. C. Peitsch, and J. Tschopp. 1995. Perforin and granzymes: crucial effector molecules in cytolytic T lymphocyte and natural killer cell-mediated cytotoxicity. *Curr. Top. Microbiol. Immunol.* 198:1–24.
25. Voskoboinik, I., M. J. Smyth, and J. A. Trapani. 2006. Perforin-mediated target-cell death and immune homeostasis. *Nat. Rev. Immunol.* 6:940–952.
26. Grossman, W. J., P. A. Revell, ..., T. J. Ley. 2003. The orphan granzymes of humans and mice. *Curr. Opin. Immunol.* 15:544–552.
27. Krzewski, K., and J. E. Coligan. 2012. Human NK cell lytic granules and regulation of their exocytosis. *Front. Immunol.* 3:335.
28. Groscurth, P., and L. Filgueira. 1998. Killing mechanisms of cytotoxic T lymphocytes. *Physiology.* 13:17–21.
29. Golstein, P., and G. M. Griffiths. 2018. An early history of T cell-mediated cytotoxicity. *Nat. Rev. Immunol.* 18:527–535.
30. Bertrand, F., S. Müller, ..., S. Valitutti. 2013. An initial and rapid step of lytic granule secretion precedes microtubule organizing center polarization at the cytotoxic T lymphocyte/target cell synapse. *Proc. Natl. Acad. Sci. U.S.A.* 110:6073–6078.
31. Andre, P., A. M. Benoliel, ..., P. Bongrand. 1990. Use of conjugates made between a cytolytic T cell clone and target cells to study the redistribution of membrane molecules in cell contact areas. *J. Cell Sci.* 97:335–347.
32. Lin, J., M. J. Miller, and A. S. Shaw. 2005. The c-SMAC. *J. Cell Biol.* 170:177–182.
33. Choudhuri, K., and M. L. Dustin. 2010. Signaling microdomains in T cells. *FEBS Lett.* 584:4823–4831.
34. Martín-Cófreces, N. B., J. Robles-Valero, ..., F. Sánchez-Madrid. 2008. MTOC translocation modulates IS formation and controls sustained T cell signaling. *J. Cell Biol.* 182:951–962.
35. Nguyen-Ngoc, T., K. Afshar, and P. Gönczy. 2007. Coupling of cortical dynein and G α proteins mediates spindle positioning in *Caenorhabditis elegans*. *Nat. Cell Biol.* 9:1294–1302.
36. Saito, T. T., D. Okuzaki, and H. Nojima. 2006. Mcp5, a meiotic cell cortex protein, is required for nuclear movement mediated by dynein and microtubules in fission yeast. *J. Cell Biol.* 173:27–33.
37. Yamashita, A., and M. Yamamoto. 2006. Fission yeast Num1p is a cortical factor Anchoring dynein and is essential for the horse-tail nuclear movement during meiotic prophase. *Genetics.* 173:1187–1196.
38. Ananthanarayanan, V., M. Schattat, ..., I. M. Tolić-Nørrelykke. 2013. Dynein motion switches from diffusive to directed upon cortical anchoring. *Cell.* 153:1526–1536.
39. Combs, J., S. J. Kim, ..., M. Poenie. 2006. Recruitment of dynein to the Jurkat immunological synapse. *Proc. Natl. Acad. Sci. U.S.A.* 103:14883–14888.
40. Hashimoto-Tane, A., T. Yokosuka, ..., T. Saito. 2011. Dynein-driven transport of T cell receptor microclusters regulates immune synapse formation and T cell activation. *Immunity.* 34:919–931.
41. Stinchcombe, J. C., and G. M. Griffiths. 2014. Communication, the centrosome and the immunological synapse. *Philos. Trans. R. Soc. Lond. B Biol. Sci.* 369:20130463.
42. Sanchez, E., X. Liu, and M. Huse. 2019. Actin clearance promotes polarized dynein accumulation at the immunological synapse. *PLoS One.* 14:e0210377.
43. Laan, L., N. Pavin, ..., M. Dogterom. 2012. Cortical dynein controls microtubule dynamics to generate pulling forces that position microtubule asters. *Cell.* 148:502–514.
44. Grill, S. W., K. Kruse, and F. Jülicher. 2005. Theory of mitotic spindle oscillations. *Phys. Rev. Lett.* 94:108104.
45. Kozłowski, C., M. Srayko, and F. Nedelec. 2007. Cortical microtubule contacts position the spindle in *C. elegans* embryos. *Cell.* 129:499–510.
46. Grill, S. W., and A. A. Hyman. 2005. Spindle positioning by cortical pulling forces. *Dev. Cell.* 8:461–465.
47. Kruse, K., and F. Jülicher. 2005. Oscillations in cell biology. *Curr. Opin. Cell Biol.* 17:20–26.
48. Colombo, K., S. W. Grill, ..., P. Gönczy. 2003. Translation of polarity cues into asymmetric spindle positioning in *Caenorhabditis elegans* embryos. *Science.* 300:1957–1961.
49. Grill, S. W., J. Howard, ..., A. A. Hyman. 2003. The distribution of active force generators controls mitotic spindle position. *Science.* 301:518–521.
50. Grill, S. W., P. Gönczy, ..., A. A. Hyman. 2001. Polarity controls forces governing asymmetric spindle positioning in the *Caenorhabditis elegans* embryo. *Nature.* 409:630–633.
51. Siller, K. H., and C. Q. Doe. 2009. Spindle orientation during asymmetric cell division. *Nat. Cell Biol.* 11:365–374.
52. Couwenbergs, C., J.-C. Labbé, ..., M. Gotta. 2007. Heterotrimeric G protein signaling functions with dynein to promote spindle positioning in *C. elegans*. *J. Cell Biol.* 179:15–22.
53. Pecreaux, J., J.-C. Röper, ..., J. Howard. 2006. Spindle oscillations during asymmetric cell division require a threshold number of active cortical force generators. *Curr. Biol.* 16:2111–2122.
54. Kim, M. J., and I. V. Maly. 2009. Deterministic mechanical model of T-killer cell polarization reproduces the wandering of aim between simultaneously engaged targets. *PLoS Comput. Biol.* 5:e1000260.
55. Vogel, S. K., N. Pavin, ..., I. M. Tolić-Nørrelykke. 2009. Self-Organization of dynein motors generates meiotic nuclear oscillations. *PLoS Biol.* 7:e1000087.
56. Ding, D. Q., Y. Chikashige, ..., Y. Hiraoka. 1998. Oscillatory nuclear movement in fission yeast meiotic prophase is driven by astral microtubules, as revealed by continuous observation of chromosomes and microtubules in living cells. *J. Cell Sci.* 111 (Pt 6):701–712.
57. Yamamoto, A., R. R. West, ..., Y. Hiraoka. 1999. A cytoplasmic dynein heavy chain is required for oscillatory nuclear movement of meiotic prophase and efficient meiotic recombination in fission yeast. *J. Cell Biol.* 145:1233–1249.
58. Walker, R. A., E. T. O'Brien, ..., E. D. Salmon. 1988. Dynamic instability of individual microtubules analyzed by video light microscopy: rate constants and transition frequencies. *J. Cell Biol.* 107:1437–1448.
59. Mitchison, T., and M. Kirschner. 1984. Dynamic instability of microtubule growth. *Nature.* 312:237–242.
60. Vorob'ev, I. A., and I. S. Grigor'ev. 2003. Dynamics and the life cycle of cell microtubules. *Tsitol Genet.* 37:22–38.
61. Horio, T., and T. Murata. 2014. The role of dynamic instability in microtubule organization. *Front. Plant Sci.* 5:511.
62. Brouhard, G. J. 2015. Dynamic instability 30 years later: complexities in microtubule growth and catastrophe. *Mol. Biol. Cell.* 26:1207–1210.
63. Mandelkow, E. M., E. Mandelkow, and R. A. Milligan. 1991. Microtubule dynamics and microtubule caps: a time-resolved cryo-electron microscopy study. *J. Cell Biol.* 114:977–991.
64. Bieling, P., L. Laan, ..., T. Surrey. 2007. Reconstitution of a microtubule plus-end tracking system *in vitro*. *Nature.* 450:1100–1105.
65. Desai, A., and T. J. Mitchison. 1997. Microtubule polymerization dynamics. *Annu. Rev. Cell Dev. Biol.* 13:83–117.
66. Kerssemakers, J. W. J., E. Laura Munteanu, ..., M. Dogterom. 2006. Assembly dynamics of microtubules at molecular resolution. *Nature.* 442:709–712.

67. Schek, H. T., M. K. Gardner, ..., A. J. Hunt. 2007. Microtubule assembly dynamics at the nanoscale. *Curr. Biol.* 17:1445–1455.
68. Gardner, M. K., A. J. Hunt, ..., D. J. Odde. 2008. Microtubule assembly dynamics: new insights at the nanoscale. *Curr. Opin. Cell Biol.* 20:64–70.
69. Myers, K. A., K. T. Applegate, ..., C. M. Waterman. 2011. Distinct ECM mechanosensing pathways regulate microtubule dynamics to control endothelial cell branching morphogenesis. *J. Cell Biol.* 192:321–334.
70. Lacroix, B., G. Letort, ..., J. Dumont. 2018. Microtubule dynamics scale with cell size to set spindle length and assembly timing. *Dev. Cell.* 45:496–511.e6.
71. Fuesler, J., and H.-J. Li. 2012. Dynamic instability – a common denominator in prokaryotic and eukaryotic DNA segregation and cell division. *Cell Mol. Biol. Lett.* 17:542–548.
72. Hornak, I., and H. Rieger. 2020. Stochastic model of T cell repolarization during target elimination I. *Biophys. J.* 118:1733–1748.
73. Wu, H.-Y., E. Nazockdast, ..., D. J. Needleman. 2017. Forces positioning the mitotic spindle: theories, and now experiments. *BioEssays.* 39:1600212.
74. Garzon-Coral, C., H. A. Fantana, and J. Howard. 2016. A force-generating machinery maintains the spindle at the cell center during mitosis. *Science.* 352:1124–1127.
75. Howard, J. 2006. Elastic and damping forces generated by confined arrays of dynamic microtubules. *Phys. Biol.* 3:54–66.
76. Pécéréaux, J., S. Redemann, ..., J. Howard. 2016. The mitotic spindle in the one-cell *C. elegans* embryo is positioned with high precision and stability. *Biophys. J.* 111:1773–1784.
77. Dogterom, M., and B. Yurke. 1997. Measurement of the force-velocity relation for growing microtubules. *Science.* 278:856–860.
78. Gros, O. J., H. G. J. Damstra, ..., F. Berger. 2021. Dynein self-organizes while translocating the centrosome in T-cells. *MBoC.* 32:855–868.
79. Zhang, R., G. Alushin, ..., E. Nogales. 2015. Mechanistic origin of microtubule dynamic instability and its modulation by EB proteins. *Cell.* 162:849–859.
80. Cassimeris, L., N. K. Pryer, and E. D. Salmon. 1988. Real-time observations of microtubule dynamic instability in living cells. *J. Cell Biol.* 107:2223–2231.
81. Sammak, P. J., and G. G. Borisy. 1988. Direct observation of microtubule dynamics in living cells. *Nature.* 332:724–726.
82. Belmont, L. D., A. A. Hyman, ..., T. J. Mitchison. 1990. Real-time visualization of cell cycle-dependent changes in microtubule dynamics in cytoplasmic extracts. *Cell.* 62:579–589.
83. Zwetsloot, A., G. Tut, and A. Straube. 2018. Measuring microtubule dynamics. *Essays Biochem.* 62:725–735.
84. Steinberg, G., R. Wedlich-Soldner, ..., I. Schulz. 2001. Microtubules in the fungal pathogen *Ustilago maydis* are highly dynamic and determine cell polarity. *J. Cell Sci.* 114:609–622.
85. Yvon, A. M., and P. Wadsworth. 1997. Non-centrosomal microtubule formation and measurement of minus end microtubule dynamics in A498 cells. *J. Cell Sci.* 110:2391–2401.
86. Carminati, J. L., and T. Stearns. 1997. Microtubules orient the mitotic spindle in yeast through dynein-dependent interactions with the cell cortex. *J. Cell Biol.* 138:629–641.
87. Adames, N. R., and J. A. Cooper. 2000. Microtubule interactions with the cell cortex causing nuclear movements in *Saccharomyces cerevisiae*. *J. Cell Biol.* 149:863–874.
88. Drummond, D. R., and R. A. Cross. 2000. Dynamics of interphase microtubules in *Schizosaccharomyces pombe*. *Curr. Biol.* 10:766–775.
89. Van Damme, D., K. Van Poucke, ..., D. Geelen. 2004. *In vivo* dynamics and differential microtubule-binding activities of MAP65 proteins. *Plant Physiol.* 136:3956–3967.
90. Yamashita, N., M. Morita, ..., Y. Mimori-Kiyosue. 2015. Three-dimensional tracking of plus-tips by lattice light-sheet microscopy permits the quantification of microtubule growth trajectories within the mitotic apparatus. *JBO.* 20:101206.
91. Tirnauer, J. S., E. O’Toole, ..., D. Pellman. 1999. Yeast Bim1p promotes the G1-specific dynamics of microtubules. *J. Cell Biol.* 145:993–1007.
92. Komarova, Y. A., I. A. Vorobjev, and G. G. Borisy. 2002. Life cycle of MTs: persistent growth in the cell interior, asymmetric transition frequencies and effects of the cell boundary. *J. Cell Sci.* 115:3527–3539.
93. Alieva, I. B., E. A. Zemskov, ..., A. D. Verin. 2010. Microtubules growth rate alteration in human endothelial cells. *J. Biomed. Biotechnol.* 2010:671536.
94. Brunner, D., and P. Nurse. 2000. CLIP170-like tip1p spatially organizes microtubular dynamics in fission yeast. *Cell.* 102:695–704.
95. Rusan, N. M., C. J. Fagerstrom, ..., P. Wadsworth. 2001. Cell cycle-dependent changes in microtubule dynamics in living cells expressing green fluorescent protein- α tubulin. *Mol. Biol. Cell.* 12:971–980.
96. Trushko, A., E. Schäffer, and J. Howard. 2013. The growth speed of microtubules with XMAP215-coated beads coupled to their ends is increased by tensile force. *PNAS.* 110:14670–14675.
97. Sheldon, E., and P. Wadsworth. 1993. Observation and quantification of individual microtubule behavior *in vivo*: microtubule dynamics are cell-type specific. *J. Cell Biol.* 120:935–945.
98. Fees, C. P., and J. K. Moore. 2019. A unified model for microtubule rescue. *MBoC.* 30:753–765.
99. Tischer, C., D. Brunner, and M. Dogterom. 2009. Force- and kinesin-8-dependent effects in the spatial regulation of fission yeast microtubule dynamics. *Mol. Syst. Biol.* 5:250.
100. Ihornak - Overview. <https://github.com/ihornak>.
101. Quann, E. J., E. Merino, ..., M. Huse. 2009. Localized diacylglycerol drives the polarization of the microtubule-organizing center in T cells. *Nat. Immunol.* 10:627–635.
102. Howard, J. 2001. Mechanics of Motor Proteins and the Cytoskeleton, new edition. Sinauer Associates.
103. Xu, H., W. Su, ..., H. Wang. 2013. The asymmetrical structure of Golgi apparatus membranes revealed by *in situ* atomic force microscope. *PLoS One.* 8:e61596.
104. Ladinsky, M. S., D. N. Mastronarde, ..., L. A. Staehelin. 1999. Golgi structure in three dimensions: functional insights from the normal rat kidney cell. *J. Cell Biol.* 144:1135–1149.
105. Day, K. J., L. A. Staehelin, and B. S. Glick. 2013. A three-stage model of Golgi structure and function. *Histochem. Cell Biol.* 140:239–249.
106. Huang, S., and Y. Wang. 2017. Golgi structure formation, function, and post-translational modifications in mammalian cells. *F1000Res.* 6:2050.
107. Westrate, L. M., J. E. Lee, ..., G. K. Voeltz. 2015. Form follows function: the importance of endoplasmic reticulum shape. *Annu. Rev. Biochem.* 84:791–811.
108. English, A. R., and G. K. Voeltz. 2013. Endoplasmic reticulum structure and interconnections with other organelles. *Cold Spring Harb Perspect. Biol.* 5:a013227.
109. English, A. R., N. Zurek, and G. K. Voeltz. 2009. Peripheral ER structure and function. *Curr. Opin. Cell Biol.* 21:596–602.
110. Shibata, Y., G. K. Voeltz, and T. A. Rapoport. 2006. Rough sheets and smooth tubules. *Cell.* 126:435–439.
111. Hu, J., W. A. Prinz, and T. A. Rapoport. 2011. Weaving the web of ER tubules. *Cell.* 147:1226–1231.
112. Hooikaas, P. J., H. G. Damstra, ..., A. Akhmanova. 2020. Kinesin-4 KIF21B limits microtubule growth to allow rapid centrosome polarization in T cells. *eLife.* 9:e62876.
113. Elric, J., and S. Etienne-Manneville. 2014. Centrosome positioning in polarized cells: common themes and variations. *Exp. Cell Res.* 328:240–248.
114. Liu, X., T. M. Kapoor, ..., M. Huse. 2013. Diacylglycerol promotes centrosome polarization in T cells via reciprocal localization of dynein and myosin II. *Proc. Natl. Acad. Sci. U.S.A.* 110:11976–11981.

6.2.2. Supplemental Material

Stochastic model of T Cell repolarization during target elimination (II)

SUPPLEMENTARY MATERIAL

Ivan Hornak, Heiko Rieger

1 Dynein attachment during the first few seconds

When $\beta < \pi$ only a fraction of MTs intersect the center of the IS, visually demonstrated in Fig. S1, and their number is given by the ratio q_{CIS} , see Fig. 3c in the main text. Considering the number of MT intersecting with the center of the IS, the number of attached dyneins can be estimated using Eq. 3 in the main text.

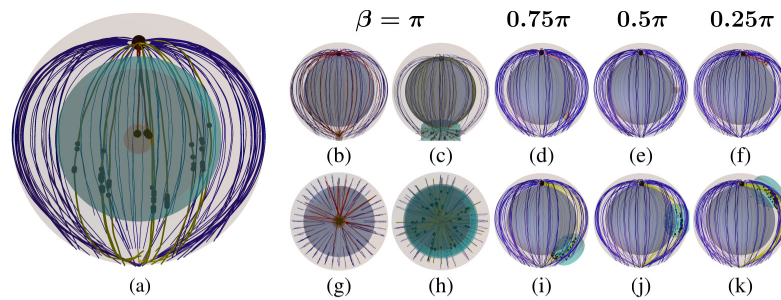


Fig. S1: Snapshots from the beginning of simulations with different angles β between the IS and the initial position of the MTOC, sketched in Fig. 1a in the main text. The plasma membrane and the nucleus are represented by the transparent outer and inner sphere, respectively. The cyan and small brown cylinder denote the complete IS and its center, respectively. Unattached (blue), capture-shrinkage (red) and cortical sliding (yellow) MTs sprout from the MTOC depicted by the big black sphere. Small black spheres represent attached dyneins. (a) Snapshot from the beginning of the simulation with $\beta = 0.5\pi$ from the perspective of the IS. Just a fraction of MTs pass through the IS and its center. (b)(g) Cell with the center of the IS from the horizontal and vertical perspective, respectively. (c)(h) Cell with the whole IS from the horizontal and vertical perspective, respectively. (d)(e)(f) Cells with the center of the IS. (i)(j)(k) Cells with the whole IS.

It can be seen in Figs. S2(a-f) that the number of attached dyneins initially sharply increases due to the fast attachment of the dyneins. As the time progresses, dyneins detach and the number of attached dyneins decreases and subsequently approaches the estimated values. The number of dyneins is lower than the estimated value when $\rho_{\text{IS}} = 500 \mu\text{m}^{-2}$, which can be explained by the fact that the stronger force results in a faster movement and bigger opposing forces increase the probability of the dynein detachment. Moreover, the dynein force presses the MTOC stronger against the nucleus, see Figs. S4(d-f).

The estimates of attached dyneins are lower when $\beta > 0.8\pi$, see Figs. S2(g-i), since only a fraction of MTs are long enough to reach the IS. As was stated in the first part of our work (1), the number of MT beads is uniformly distributed between 15 and 20. Consequently, only 66, 33, 17% of MTs are long enough to reach the IS when $\beta = 0.8, 0.9, 0.95\pi$, respectively. The number of attached dyneins are lower than estimates when $\beta > 0.5\pi$, see Figs. S2(g-i), due to the fact that the nucleus intersects the path of the MTOC to the IS, as visualized in Figs. S1b-d, and the repulsive force from the nucleus increases the dynein detachment probability.

The number of attached dyneins differ from the estimates for the cases $\beta = 0.15\pi$ and $\beta = \pi$, see Figs. S2j and k. When $\beta < 0.25\pi$ the cytoskeleton is immediately dragged to the IS due to the short initial MTOC-IS distance and dyneins detach, see Figs. S4c and f. In the case of $\beta = \pi$, every MT with the sufficient length intersects the center of the IS, visualized in Figs. S1b and g. Around 20% of MTs have a sufficient length to reach the IS in the first seconds of the simulation. The number of dyneins estimated by the Eq. 3 in the main text would be greater than the number of dyneins in the IS. To avoid this contradiction, we assume that all dyneins attach during the first seconds of the simulation. It can be seen in Fig. S2k that the measured number of attached dyneins is substantially lower. It can be explained by the fact that dyneins act on MTs sprouting in all orientation from the IS, visualized in Figs. S1b and g, and therefore act in competition and mutually increase force-dependent detachment rate (1).

2 Additional results for one IS: β -dependence for different mechanisms

2.1 Capture-Shrinkage mechanism

The supplementary Movie S8 shows the MTOC repositioning under the effect of the capture-shrinkage mechanism, $\rho_{\text{IS}} = 300 \mu\text{m}^{-2}$, $\beta = 0.75\pi$. The process is also visualized for the case of $\beta = 0.75\pi$ in Fig. S3. At the beginning of the simulation, only a small fraction of MTs intersects the IS and they sprout from the MTOC in one direction (visualized

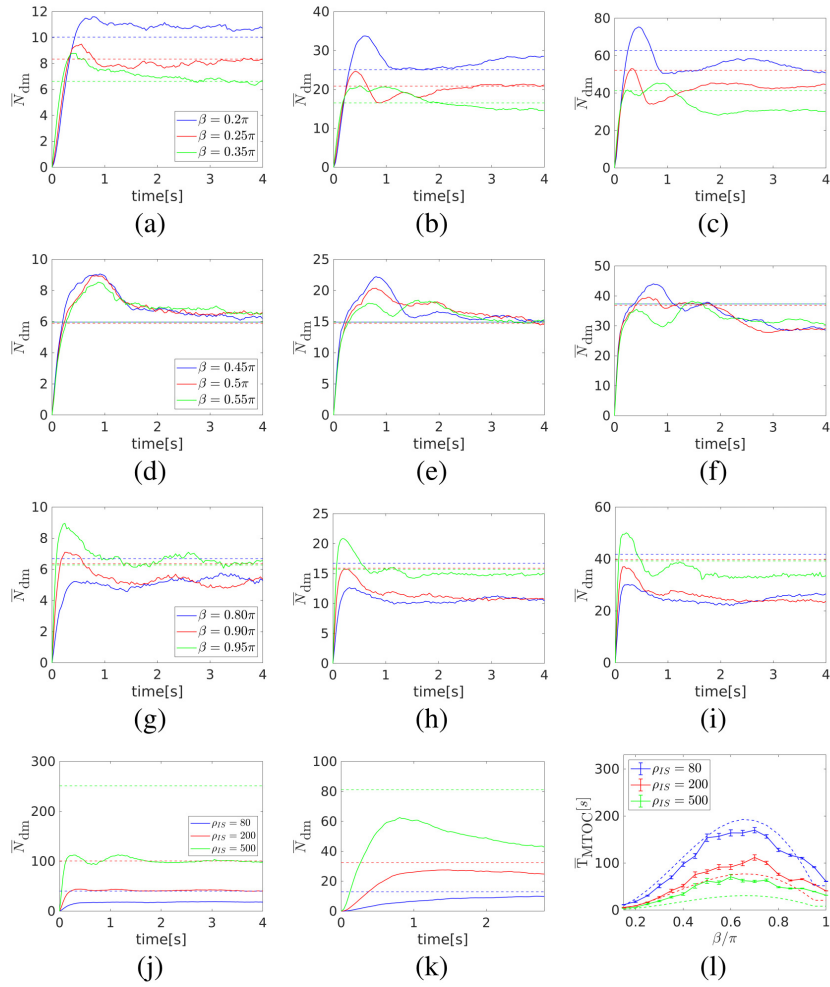


Fig. S2: The dependence of the average number of dyneins \bar{N}_{dm} on the time during the first seconds of repositioning. The dashed lines represent estimations. (a, d and g) $\rho_{IS} = 80\mu\text{m}^{-2}$. (b, e and h) $\rho_{IS} = 200\mu\text{m}^{-2}$. (c, f and i) $\rho_{IS} = 500\mu\text{m}^{-2}$. (j) $\beta = \pi$ (k) $\beta = 0.15\pi$ (l) Comparison of the measured (solid) and estimated (dashed) times of the repositioning.

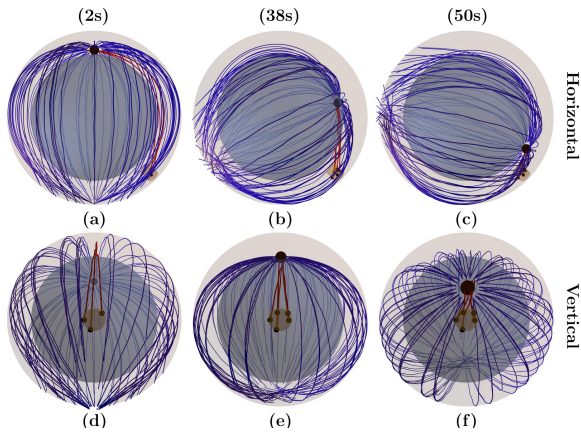
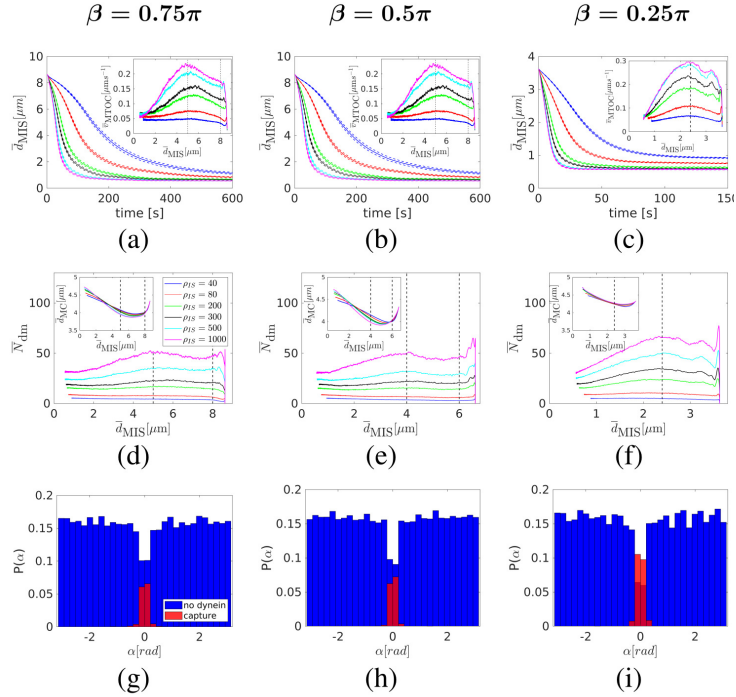


Fig. S3: Snapshots from the time evolution of the spindle configuration under the effect of the capture-shrinkage mechanism (dynein density $\rho_{IS} = 300\mu\text{m}^{-2}$, initial angle between MTOC and IS $\beta = 0.75\pi$). MTs connect to the MTOC represented by the large black sphere. Blue and red curves represent unattached and attached MTs, respectively. The brown cylinder depicts the center of the IS, where the capture-shrinkage dyneins represented by small black spheres are located. (a and d) $d_{MIS} \sim 8.0\mu\text{m}$. A stalk connecting the MTOC and IS is formed. (b and e) $d_{MIS} \sim 4\mu\text{m}$. The stalk shortens and the MTOC approaches the IS. (c and f) $d_{MIS} \sim 1\mu\text{m}$. The MTs in stalk depolymerized and MTOC is in the close proximity of the IS.

Fig. S4: Capture-shrinkage mechanism: (a-c) Dependence of the average MTOC-IS distance \bar{d}_{MIS} on time. Dependences of the average MTOC velocity \bar{v}_{MTOC} in insets (a-c), the average number of dyneins acting on microtubules \bar{N}_{dm} (d-f) and the MTOC-center distance \bar{d}_{MC} in the insets of (d-f) on the average MTOC-IS distance. Black dashed lines denote transitions between different phases of the repositioning process. (g)(h)(i) Probability densities of the angle α between the first MT segments and the direction of the MTOC movement for the dynein density $\rho_{\text{IS}} = 300 \mu\text{m}^{-2}$ at the beginning of the simulation. (g and h) Time $t = 10\text{s}$. (i) $t = 5\text{s}$.



in Figs. S3a and d. The MTs attach to dynein at the beginning of the simulation and form a narrow stalk connecting the MTOC and the IS. As the MTOC approaches the IS, unattached MTs are pushed back by the friction forces and the spindle "opens", visually demonstrated in Figs. 3e and f. As the time progresses, the stalk of MTs shortens and the MTOC approaches the IS, see Figs S3b, c, e and f.

When $\beta > 0.25\pi$, the process can be divided into three phases based on the time evolution of the MTOC velocity, see Figs. S4a and 4b. In the first phase comprising approximately the first $0.5 \mu\text{m}$ of the MTOCs trajectory, the velocity increases and then in some cases decreases to a local minimum. In the second phase, the velocity slightly increases until it reaches a maximum and then in the third phase, it declines again. By comparison of Figs. S4ab and S4de one realizes that the time evolution of the velocity is determined by the time evolution of the number of attached dyneins, which can be understood by considering the forces from the nucleus. At the beginning of the simulations, MTs intersects the IS (visually demonstrated in Figs. S3a and d) leading to the dynein attachment and the formation of a narrow MT stalk, see Figs. S4g-i, visually Fig. S3a and d. As the MTOC moves to the IS in the direction given by the MT stalk, it is pressed against the nucleus, see Figs. S4d and e, visually demonstrated by Figs. S1 and S3. The opposing forces of the nucleus repel the MTs resulting in the detachment of dyneins, see Figs. S4d and e, because the detachment rate is force dependent. The force from the nucleus decreases as the MTOC slides on its surface, causing the slight increase of the MTOC velocity despite the constant pulling force (compare Figs. S4ab and S4de). The number of attached dyneins remains approximately constant in the second phase, see Figs. S4d and e, since unattached MTs in opening cytoskeleton are pushed back by friction forces and unlikely to attach to dynein, visualized in Figs. S3d-f. The decrease of the number of attached dynein in the third phase can be explained by the shortening of the MTs in the stalk due to the depolymerization lowering the probability of dynein attachment. More importantly, the detachment probability increases due to the opposing force of the cytoskeleton being dragged from the nucleus to the membrane, see Figs. S4d and e. Consequently, the repositionings have similar characteristics as the one in the cell when $\beta = \pi$ (1).

When $\beta = 0.25\pi$ the repositioning has only two phases as can be seen in Fig. S4f, since the velocity of the MTOC rises quickly and then continuously decreases. Due to the short initial MTOC-IS distance the nucleus does not present an obstacle and MTOC is pulled directly to the cell membrane, see Fig. S4f. Therefore, the number of attached dyneins decreases due to the same causes as in the third phase when $\beta > 0.25\pi$, compare Figs. S4de and f.

2.2 Cortical Sliding mechanism

The repositioning process under the effect of the cortical sliding mechanism is visually demonstrated in Fig. S5 and in the supplementary Movie S9, $\rho_{\text{IS}} = 300 \mu\text{m}^{-2}$, $\beta = 0.75\pi$. In contrast to the capture-shrinkage, MTs attach to the cortical sliding dynein in the whole IS, which is substantially larger than its center. Figs. S5a and d shows that the MTOC is pulled to the IS by MTs aligned in a large stalk. As the MTOC approaches the IS, dyneins detach and remaining attached dyneins are increasingly located at the periphery of the IS, visually demonstrated in Figs. S5b and e. Almost all dyneins detach at the end of the repositioning, see Figs. S5c and f.

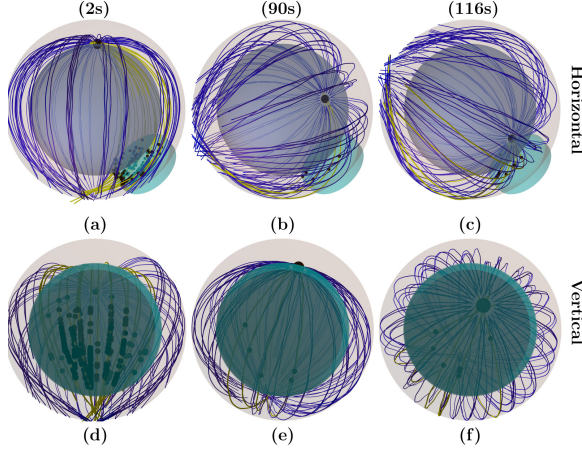


Fig. S5: Snapshots from the time evolution of the MT cytoskeleton under the effect of the cortical sliding mechanism (dynein density $\rho_{IS} = 300\text{m}^{-2}$, $\beta = 0.75\pi$). The cyan cylinder denotes the area of the IS. Blue and yellow lines represent unattached and attached MTs, respectively. The small black spheres in the IS stand for the positions of dyneins attached to MTs. (a and d) $d_{MIS} \sim 8.0\mu\text{m}$. A stalk connecting the MTOC and IS is formed. The attached MTs are sprouting from the MTOC in one direction since the beginning. (b and e) $d_{MIS} \sim 7.5\mu\text{m}$. The number of attached dyneins decreased and motors are attached in one half of the IS and mainly at its periphery. (c and f) $d_{MIS} \sim 1\mu\text{m}$. The MTOC is in the close proximity of the IS. Dyneins are attached to MTs solely on the periphery of the IS.

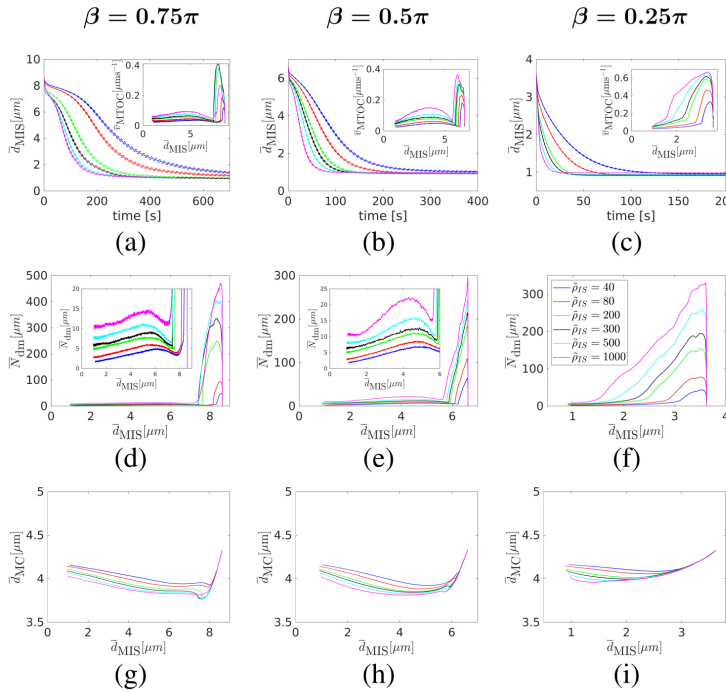


Fig. S6: Cortical sliding mechanism. (a-c) The dependence of the average MTOC-IS distance \bar{d}_{MIS} on the time is shown. Inset: the dependence of the average MTOC velocity \bar{v}_{MTOC} on the average MTOC-IS distance are shown. The dependencies of the average number of dyneins acting on MTs \bar{N}_{dm} (d-f), the average distance between the MTOC and the center of the cell \bar{d}_{MC} (g-i) on the average MTOC-IS distance are shown.

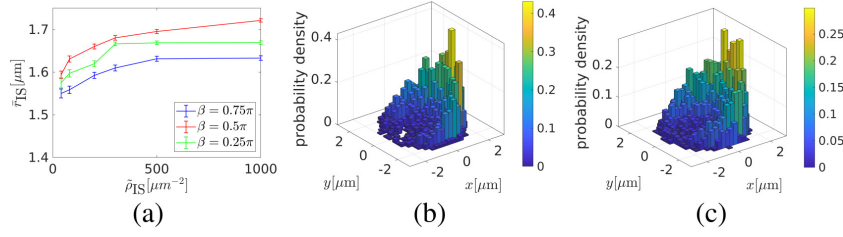
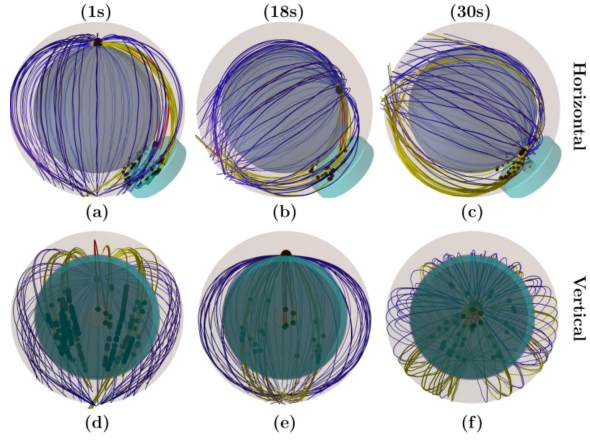


Fig. S7: Attached cortical sliding dyneins. (a) The dependence of the average distance \bar{r}_{IS} of attached cortical sliding dyneins from the axis of the IS on dynein area density $\hat{\rho}_{IS}$ is shown. (b-c) The two-dimensional probability density of attached dyneins in the IS in the middle of the repositioning, $\bar{d}_{MIS} = 3\mu\text{m}$, $\beta = 0.5\pi$, is shown. (b) $\hat{\rho}_{IS} = 80\mu\text{m}^{-2}$. (c) $\hat{\rho}_{IS} = 1000\mu\text{m}^{-2}$.

Fig. S8: Snapshots from the time evolution of the MT cytoskeleton under the combined effect of both mechanisms (dynein density $\rho_{IS} = \hat{\rho}_{IS} = 300\mu\text{m}^{-2}$, $\beta = 0.5\pi$). The cyan and brown cylinders denote the IS and its center, respectively. Blue, yellow and red lines represent unattached, cortical sliding and capture-shrinkage MTs, respectively. The small black spheres in the IS stand for the positions of the dyneins attached to MTs. (a and d) $d_{MIS} \sim 8\mu\text{m}$. A stalk of capture-shrinkage MTs connecting the MTOC and the center of the IS is formed at the beginning. Cortical sliding MTs attach at the periphery of the IS and do not intersect the center of the IS. (b and e) $d_{MIS} \sim 4\mu\text{m}$. The capture-shrinkage MTs in the stalk shorten and the MTOC approaches the IS. The MTOC slides on the surface of the nucleus. (c and f) $d_{MIS} \sim 1\mu\text{m}$. The MTs in the stalk are depolymerized and the MTOC is in the close proximity of the IS. The MTOC detached from the nucleus and moves to the membrane. Cortical sliding dyneins are attached at the IS periphery.



Similarly to the previous case of the capture-shrinkage mechanism, the repositioning can be divided into three phases when $\beta > 0.25\pi$. Contrarily, the transition points between the phases depend on the density $\hat{\rho}_{IS}$, see Figs. S6a and b. The time evolution of the velocity of the MTOC is determined by the number of dyneins, compare Figs. S6a and b with Figs. S6d and e. The stalk of MTs connecting the MTOC and the IS is formed at the beginning of the simulation, visually in Figs. S5a and d, and the dynein quickly attach to MTs. Due to the opposing force of the nucleus the number of dynein decreases during the first phase, see insets of Figs. S6d and e. The decrease is steeper than in the previous case, compare Figs. S4d and e with S6d and e, due to the fact that the cortical sliding lacks a firm anchor point characteristic for the capture-shrinkage. In the second phase, the number of dynein rises, see insets of Fig. S6d and e, since the opposing force of the nucleus decreases as the MTOC slides on the surface. The number of attached dyneins decreases in the third phase because the MTOC does not recede substantially from the nucleus of the cell, see Figs. S6g-i, indicating that the MTs do not follow the membrane resulting in the lower attachment probability of dynein, visually demonstrated in Figs. S5c and f.

The MTOC displays only one phase when $\beta = 0.25\pi$, see Figs. S6c and f because of short initial distance and the fact that the MTOC is not an obstacle on the MTOC's journey, visualized in Figs. S1f and k. The number of attached dynein decreases from the beginning of the simulation, see Fig. S6f, since the MTs do not copy the cell membrane as the MTOC approaches the IS.

Fig. S7 shows that similarly to the case of $\beta = \pi$ (1) the attached dyneins are located predominantly at the periphery of the IS and their average distance from the axis of the IS slightly increases with the density. Consequently, we report that attached dyneins are predominantly located on the periphery of the IS regardless of the initial configuration of the cell.

2.3 Combined mechanisms

The supplementary Movie S10 shows the MTOC repositioning under the combined effects of both mechanism, $\rho_{IS} = \tilde{\rho}_{IS} = 300\mu\text{m}^{-2}$, $\beta = 0.5\pi$. At the beginning of the simulation, MTs intersecting the center of the IS attach to capture-shrinkage dyneins and form a narrow stalk connecting the MTOC and the IS, visually demonstrated in Figs. S8a and d. Cortical sliding dynein attach and pull MTs in the periphery of the IS. Consequently, the MTs in the stalk shorten and the MTOC slides on the surface of the cell towards the IS, visually Figs. S8b and e. At the end of the repositioning, the MTOC recedes from the nucleus and is pulled to the center of the IS by capture-shrinkage MTs, visually Figs. S8c and f.

We examine the combined effect of the mechanisms in two initial configurations: $\beta = 0.5, 0.75\pi$. When $\beta = 0.25\pi$ the repositioning is already very fast, see Figs. S4 and S6 and Fig. 4b in the main text, and the combination is not needed for an efficient repositioning. The interplay of the two mechanisms when $\beta = \pi$ was previously analyzed in the first part of our work (1). Figs. S9a and b shows that the combination of the two mechanisms always leads to a faster repositioning. Moreover, two mechanisms with relatively small dynein densities can outperform the dominant mechanism with a substantially larger density. For example when $\beta = 0.75\pi$, the capture-shrinkage mechanism with the density $\rho_{IS} = 1000\mu\text{m}^{-2}$ is slower than any combination of mechanisms where $\tilde{\rho}_{IS}, \rho_{IS} \geq 200\mu\text{m}^{-2}$, see Fig. S9a. It generally holds for both angles β that the combination of two mechanisms when $\tilde{\rho}_{IS}, \rho_{IS} \geq 200\mu\text{m}^{-2}$ is faster than an individual mechanism.

The capture-shrinkage mechanism was identified as the dominant mechanism when $\beta = 0.75\pi$. Fig. S9a shows that the repositioning gets faster with the rising cortical sliding density. Moreover, the average number of attached capture-shrinkage dyneins increases with the cortical sliding density, see Fig. S9d. This can be explained by the alignment of cortical sliding MTs in the direction of the MTOC movement, see Fig. S9f. In the case when capture-shrinkage acts alone, the unattached MTs are unlikely to attach to capture-shrinkage, since they are pushed back by friction forces, visually demonstrated in Fig. S3. MTs attached to cortical sliding tend to align to the MTOC movement, see Figs. S9f and i and visually demonstrated by the Fig. S8. Due to the alignment they are not pushed back by friction forces and they are more likely to be captured in the narrow center of the IS. Figs. S9f and i shows that the dominant central peak of the cortical sliding MTs is interrupted in the middle by the narrow peak of capture-shrinkage MTs proving that cortical sliding MTs are passed to the capture-shrinkage mechanism. Therefore, the cortical sliding mechanism gives capture-shrinkage substantial advantage compared to the case when capture-shrinkage acts alone by increasing the probability that the MT will attach to dyneins in the center of the IS.

Furthermore, the cortical sliding helps capture-shrinkage dyneins because they share the load from opposing forces. The sharing of forces leads to the decrease of the force dependent detachment probability and to the increase of attached capture-shrinkage dyneins. To summarize, cortical sliding supports capture-shrinkage by increasing the attachment probability by aligning the MTs with the MTOC movement and by decreasing the detachment probability by sharing the load from opposing forces.

Fig. S9e demonstrates that when the density of cortical sliding dyneins is fixed, the repositioning gets faster with the increasing capture-shrinkage density. Moreover, the number of attached cortical sliding dyneins increases with the rising capture-shrinkage density mainly at the end of the repositioning. This may come as a surprise, since the presence of capture-shrinkage decreases the number of cortical sliding MTs due to their attachment in the center of the IS, see Fig. S9f and i. Moreover, dyneins in the part of the IS behind the center (from the MTOC's perspective) cannot attach to MTs, see Fig. S9c, since they are distant from any filament. Fig. 9c clearly demonstrates that the attached cortical sliding dyneins form interesting "slashed" patterns indicating that the dyneins behind IS remain unattached. Seemingly, the capture-shrinkage mechanism harms the cortical sliding by stealing the MTs and by preventing it to reach a part of the IS.

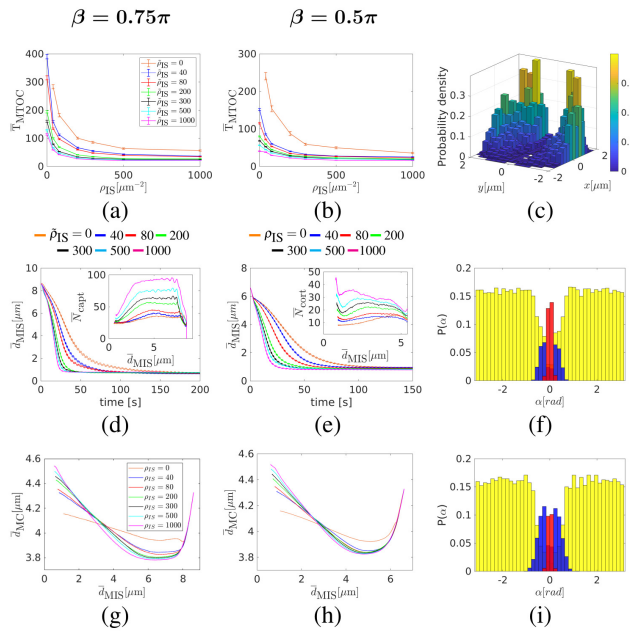
However, the capture-shrinkage dynein pull in alignment towards the center of the IS and provide a firm anchor point that the cortical sliding is otherwise missing. Figs. S6g-i clearly demonstrates that the MTOC does not substantially recede from the nucleus in the case of the sole cortical sliding. Consequently, MTs do not copy the cell membrane and the dynein attachment probability decreases. The pulling force of capture-shrinkage dyneins causes that the membrane is followed more closely in the case of combined mechanisms, see Figs. S9g-h, resulting in the increase of the number of attached cortical sliding dyneins, see Fig. S9e. Additionally, capture-shrinkage dyneins share the load from opposing forces leading to the decrease of the detachment probability of cortical sliding dyneins and therefore to the bigger number of attached dyneins.

To conclude, the cortical sliding mechanism supports capture shrinkage by passing the MTs. Capture-shrinkage promotes cortical sliding by providing it a firm anchor point. The two mechanisms support each other by sharing the load from opposing forces. To conclude, the mechanisms act in a fascinating synergy in every configuration of the cell.

References

1. Hornak, I., and H. Rieger, 2020. Stochastic Model of T Cell Repolarization during Target Elimination I. *Biophys. J.* .

Fig. S9: Combination of capture-shrinkage and cortical sliding mechanisms: (a and b) Dependence of the averaged times \bar{T}_{MTOC} (MTOC-IS distance $d_{\text{MIS}} < 1.5\mu\text{m}$) on the capture-shrinkage dyneins density ρ_{IS} . Cortical sliding densities are given by the color. (c) The two-dimensional probability density of attached dyneins in the IS is shown, $\beta = 0.75\pi$, $\tilde{\rho}_{\text{IS}} = \rho_{\text{IS}} = 500\mu\text{m}^{-2}$, the MTOC-IS distance $d_{\text{MIS}} \sim 3.5\mu\text{m}$. (d) Dependence of the average MTOC-IS distance \bar{d}_{MIS} on time. In the inset: Dependence of the average number of attached capture-shrinkage dyneins \bar{N}_{capt} on the average MTOC-IS distance \bar{d}_{MIS} . $\beta = 0.75\pi$, $\tilde{\rho}_{\text{IS}} = 500\mu\text{m}^{-2}$. The cortical sliding density $\tilde{\rho}_{\text{IS}}$ is given by the color. (e) Dependence of the average MTOC-IS distance on time. In the inset: Dependence of the average number of attached cortical-sliding dyneins \bar{N}_{cort} on the average MTOC-IS distance. $\beta = 0.5\pi$, $\tilde{\rho}_{\text{IS}} = 500\mu\text{m}^{-2}$. The capture-shrinkage density ρ_{IS} is given by the color. (f) The probability density of the angle α between the first MT segment and the direction of the MTOC motion is shown. $\tilde{\rho}_{\text{IS}} = \rho_{\text{IS}} = 200\mu\text{m}^{-2}$, $t = 10\text{s}$, $\bar{d}_{\text{MIS}} \sim 4\mu\text{m}$, $\beta = 0.5\pi$. (g and h) The dependence of the average MTOC-center distance \bar{d}_{MC} on the average MTOC-IS distance \bar{d}_{MIS} . $\tilde{\rho}_{\text{IS}} = 40\mu\text{m}^{-2}$. Capture-shrinkage density ρ_{IS} is given by the color. (i) The probability density of the angle α between the first MT segment and the direction of the MTOC motion is shown. $\tilde{\rho}_{\text{IS}} = \rho_{\text{IS}} = 200\mu\text{m}^{-2}$, $t = 10\text{s}$, $\bar{d}_{\text{MIS}} \sim 8\mu\text{m}$, $\beta = 0.75\pi$.



6.3. Cytoskeleton rotation relocates mitochondria to the immunological synapse and increases calcium signals

The article is included in the thesis with the permission of Elsevier, see [Appendix B](#).

6.3.1. Main Manuscript



Cytoskeleton rotation relocates mitochondria to the immunological synapse and increases calcium signals



Ilaria Maccari^{a,1}, Renping Zhao^b, Martin Peglow^a, Karsten Schwarz^a, Ivan Hornak^a, Mathias Pasche^{c,2}, Ariel Quintana^{b,3}, Markus Hoth^{b,*}, Bin Qu^b, Heiko Rieger^{a,*}

^a Theoretical Physics, Saarland University, 66041 Saarbrücken, Germany

^b Biophysics, Center for Integrative Physiology and Molecular Medicine (CIPMM), School of Medicine, Saarland University, 66421 Homburg, Germany

^c Physiology, Center for Integrative Physiology and Molecular Medicine (CIPMM), School of Medicine, Saarland University, 66421 Homburg, Germany

ARTICLE INFO

Article history:

Received 20 May 2016

Received in revised form 24 June 2016

Accepted 24 June 2016

Available online 7 July 2016

Keywords:

Mitochondria

CRAC channels

Orai channels

Plasma membrane calcium ATPase (PMCA)

Immunological synapse (IS)

Rotation model

ABSTRACT

Ca²⁺ microdomains and spatially resolved Ca²⁺ signals are highly relevant for cell function. In T cells, local Ca²⁺ signaling at the immunological synapse (IS) is required for downstream effector functions. We present experimental evidence that the relocation of the MTOC towards the IS during polarization drags mitochondria along with the microtubule network. From time-lapse fluorescence microscopy we conclude that mitochondria rotate together with the cytoskeleton towards the IS. We hypothesize that this movement of mitochondria towards the IS together with their functionality of absorption and spatial redistribution of Ca²⁺ is sufficient to significantly increase the cytosolic Ca²⁺ concentration. To test this hypothesis we developed a whole cell model for Ca²⁺ homeostasis involving specific geometries for mitochondria and use the model to calculate the spatial distribution of Ca²⁺ concentrations within the cell body as a function of the rotation angle and the distance from the IS. We find that an inhomogeneous distribution of PMCA pumps on the cell membrane, in particular an accumulation of PMCA at the IS, increases the global Ca²⁺ concentration and decreases the local Ca²⁺ concentration at the IS with decreasing distance of the MTOC from the IS. Unexpectedly, a change of CRAC/Orai activity is not required to explain the observed Ca²⁺ changes. We conclude that rotation-driven relocation of the MTOC towards the IS together with an accumulation of PMCA pumps at the IS are sufficient to control the observed Ca²⁺ dynamics in T-cells during polarization.

© 2016 Elsevier Ltd. All rights reserved.

1. Introduction

Organelle polarization is a fundamental biological process for many cellular functions [1–5]. Cytotoxic T lymphocytes (CTL) and natural killer (NK) cells are highly polarized during cell migration and immunological synapse (IS) formation with their cognate target cells like tumor cells or virus infected cells [6–8]. Polarity is often controlled by actin polymerization induced by Cdc42 [9] or Arp2/3-dependent actin nucleation [10]. The specificity of target cell killing

is, among other mechanisms, guaranteed through polarized secretion of lytic granules (LG) containing perforin and granzymes at the IS [11–13]. The microtubule organizing center (MTOC, centrosome) is a key organelle involved in repositioning of LG towards the IS following actin depletion [14], and secretion of LG at the IS is one of the central polarization steps in CTL and NK cells [4,15]. The MTOC moves to the IS within several minutes of IS formation [13,16]. This directed movement requires the motor protein dynein [17] which according to the favored mechanism, mediates MTOC repositioning to the IS by generating force through microtubule binding at the outer ring of actin at the IS. This process is also referred to as cortical sliding mechanism. This view has recently been challenged by Yi et al. [18] who present a series of experiments favoring a mechanism that dynein mediates MTOC repositioning through a “microtubule end-on capture-shrinkage mechanism”, by which dyneins act on microtubules docked at the center of the IS and not at the outer actin ring. Regardless of the model, the MTOC is considered a master regulator of T cell polarization [17] and it is most

* Corresponding authors.

E-mail addresses: markus.hoth@uks.eu (M. Hoth), h.rieger@mx.uni-saarland.de (H. Rieger).

¹ Present address: Physics Department, “La Sapienza” University of Rome, 00185 Rome, Italy.

² Present address: MRC Laboratory for Molecular Biology, Cambridge CB2 0QH, England, UK.

³ Present address: Division of Signalling and Gene Expression, La Jolla Institute for Allergy and Immunology, La Jolla, CA 92037, United States.

<http://dx.doi.org/10.1016/j.ceca.2016.06.007>

0143-4160/© 2016 Elsevier Ltd. All rights reserved.

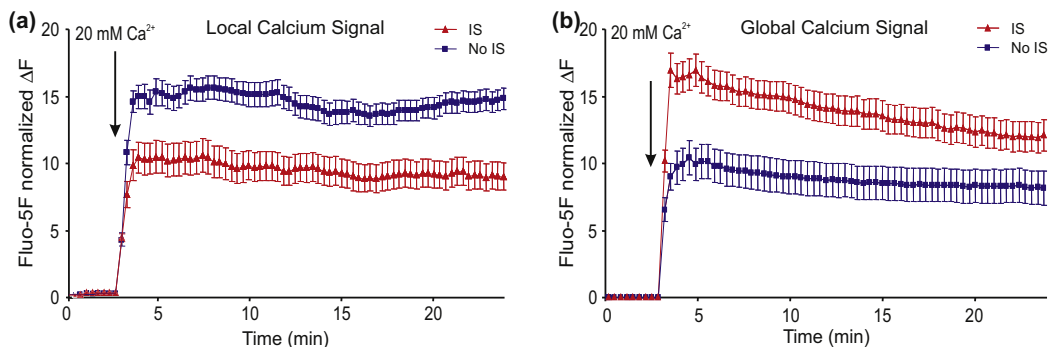


Fig. 1. Mitochondrial localization at the IS modulates local and global Ca^{2+} levels. Fluo-5F/AM loaded Jurkat E6.1 T-cells were settled either on anti-CD3 antibody-coated coverslips (inducing IS formation) or on poly-L-ornithine-coated coverslips (no IS formation). Ca^{2+} stores were depleted by 5–7 min thapsigargin ($1 \mu\text{M}$) pre-treatment in Ca^{2+} free solution and subsequently, cells were exposed to 20 mM Ca^{2+} . **(a)** Mean normalized fluorescence of Fluo-5F by TIRFM of 33 (with IS formation, red trace) and 37 (no IS formation, blue trace) cells over time (at 20 min, $p < 0.0001$) representing local Ca^{2+} signals at the plasma membrane. **(b)** Mean normalized fluorescence of Fluo-5F by epifluorescence microscopy of 17 (with IS formation, red trace) and 18 (no IS formation, blue trace) cells over time (at 20 min, $p = 0.036$) representing global Ca^{2+} signals. (For interpretation of the references to color in this figure legend, the reader is referred to the web version of this article.)

likely guiding other organelles like the Golgi apparatus [19,20], mitochondria [21–24] and LG [13] to the IS.

Several of the signaling steps governing CTL and/or NK cell dependent target cell death are Ca^{2+} dependent: (1) MTOC relocalization to the IS [18]; (2) mitochondria relocalization to the IS [24,25]; (3) secretion of LG at the IS [26–28]; (4) perforin-dependent lysis of target cells [29]. While the exact molecular mechanisms of how Ca^{2+} is involved in regulating these processes are not resolved yet, it is clear that Ca^{2+} influx through Orai (mostly Orai1) channels is the main Ca^{2+} source [28,30,31]. Ca^{2+} influx at the IS through Orai1 channels is among other factors controlled by mitochondrial positioning at the IS. There, mitochondria act as Ca^{2+} sinks, whereby they control Ca^{2+} dependent activity of Orai channels and local Ca^{2+} concentrations at the IS as well as global cytosol Ca^{2+} concentrations ($[\text{Ca}^{2+}]_{\text{cyt}}$) [23,32,33].

In this paper we show that cytoskeleton rotation relocates mitochondria to the immunological synapse. Unexpectedly, repositioning of mitochondria alone can modulate the global cytosolic Ca^{2+} concentration, independent of any influence of mitochondrial position on CRAC/Orai channel activity. We determine the geometric path that mitochondria take during relocation towards the IS and show that it is correlated with a rotation of the MTOC and microtubule network. We implement this rotation into a model for spatiotemporal Ca^{2+} dynamics in T-cells that we proposed recently [33] and present the predictions of this model about the dependence of the global and local Ca^{2+} concentration on the rotation angle of the cytoskeleton/mitochondria system.

2. Results

2.1. Mitochondria relocation correlates with Ca^{2+} increase

In 2011, we have shown that mitochondrial relocation to the IS decreases local cytosolic Ca^{2+} levels but increases global ones [23]. We confirm these findings by an independent set of experiments in human Jurkat T-cells (Fig. 1) similar to the experiments shown in Fig. 4C and D of our previous publication [23]. In case an IS is induced by anti-CD3 antibodies on the coverslip, mitochondria localize to the IS as shown by Quintana et al. [23] and the local Ca^{2+} signals at the plasma membrane are lower compared to conditions in which no IS was formed (Fig. 1a). In contrast the global Ca^{2+} signals are higher in case of IS formation (Fig. 1b). Localization of mitochondria at the IS thus decreases the local Ca^{2+} levels compared to experiments where no IS is formed but increases the global ones. In

conclusion mitochondrial localization relative to CRAC channels at the IS determines local and global Ca^{2+} concentrations.

2.2. Mitochondria relocation correlates with cytoskeleton movement

Whereas it is undisputed that mitochondria relocate to the IS, the exact mechanisms of the relocalization process have not been resolved. Mitochondrial fusion/fission [21] and cytoskeletal reorganization are very likely involved [3,5] but the exact mechanisms are not understood. Considering the MTOC relocalization to the IS [13,16,19,20] and its potential to guide other organelles there, it is reasonable to assume that the MTOC and mitochondrial movement could be correlated. We thus tested the hypothesis that mitochondria translocation and microtubule network reorientation towards the IS are correlated. We fluorescently labeled microtubules (with EMTB-3 \times GFP) and mitochondria (with MitoTracker or DsRed2-Mito-7) in CTL. CTL were conjugated with target cells at 37°C and translocation of microtubule network and mitochondria was visualized by time lapse microscopy. We found that mitochondrial localization was closely associated with microtubules (Fig. 2a). Following contact between CTL and a target cell, mitochondria were passively translocated to the IS along with microtubule network reorientation (Fig. 2a and Supplementary Movie 1). Moreover, we observed that occasionally mitochondria could actively move along microtubule tracks (Fig. 2b and Supplementary Movie 2). These results show that mitochondria relocation correlates with cytoskeleton rearrangement, especially microtubule network reorientation towards the IS.

2.3. Quantitative analysis of cytoskeleton and mitochondria rotation

For each time frame we extracted the three-dimensional positions of the MTOC, the IS, the cell center, and individual mitochondria using a higher time resolution for 3D pictures as described in the Materials and Methods section. The position data for all objects in a single frame were brought into a standard coordinate system by two rotations and one translation, such that MTOC, IS, and cell center lie in one plane, the x-z plane, and the rotation axis is parallel along the y-axis. We assume that the MTOC (in this case located at 90°) moves towards the IS. In Fig. 3a we sketch the movement of mitochondria that one expects in case mitochondria are attached to the microtubules: in the right half space they are rotated

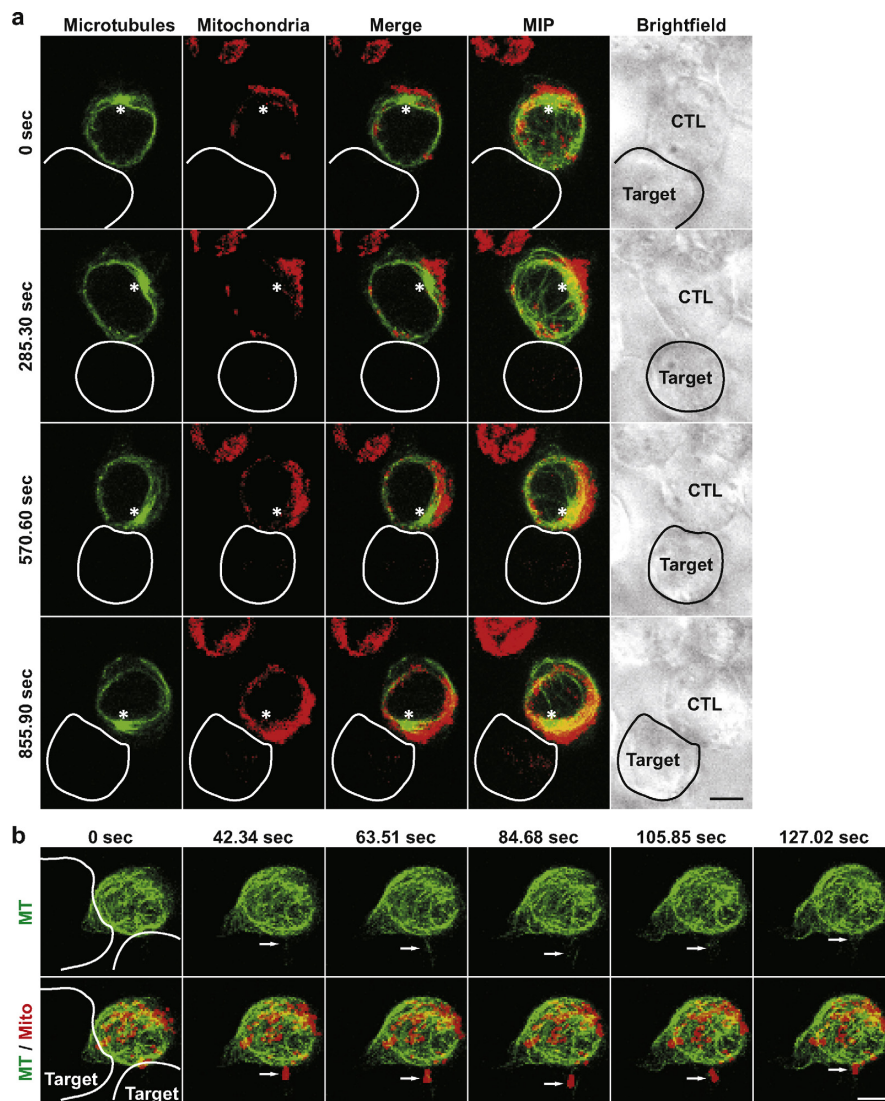


Fig. 2. Microtubules and mitochondria rotate together towards the IS during polarization. CTL were conjugated with SEA/SEB-pulsed Raji cells (target). **(a)** Mitochondria are translocated along with microtubule network. Microtubules and mitochondria were labeled by EMTB-3 × GFP and MitoTracker Deep Red, respectively. The time lapse was taken at 37 °C every 21.17 s by a confocal microscope with a 63× objective. MTOC is marked by the asterisk. MIP: maximum intensity projection. **(b)** Mitochondria can be actively transported along microtubules. Microtubules and mitochondria were labeled by EMTB-3 × GFP and DsRed2-Mito-7. The time lapse was taken at 37 °C every 19.02 s by a confocal microscope with a 63× objective. The maximum intensity projections are shown. Arrowheads highlight the transported mitochondrion and the corresponding microtubule. Scale bars are 5 μm.

towards the IS, in the left half space they are rotated away from it. Consequently vectors pointing from the center to mitochondria on the right half space decrease their angle with the vector from the center to the IS in the same way as the vector pointing from the center to the MTOC. In the left half space the mitochondria angles increase.

In Fig. 3b we show a histogram for the mitochondria angles extracted from tracking data acquired with a spinning disk confocal microscope (see Materials & Methods), in which CTL were settled on CD3/CD28 antibody-coated coverslips and IS was formed between CTL and coverslips. We analyzed two time points: before (at 0 s) and after polarization (at 186 s). Compared to the angles before polarization, the distribution after polarization is systematically

shifted to the lower angles as expected from a rotation. The histogram for the mitochondria angles in the left half space is shown in Fig. 3c: here the angles after polarization are systematically shifted to larger values as expected from a rotation. In conclusion, a correlated rotation model of MTOC and the microtubules with attached mitochondria explains the observed mitochondria movement during IS formation very well.

The number of mitochondria data points in the left half space (Fig. 3c) is much smaller than the number of data points in the right half space (Fig. 3b). The reason is a displacement of microtubules from the left into the right half space during the repositioning of the MTOC as is clearly visible in Fig. 5A of Ref. [18]. This displacement is mechanically plausible: When microtubules are caught by

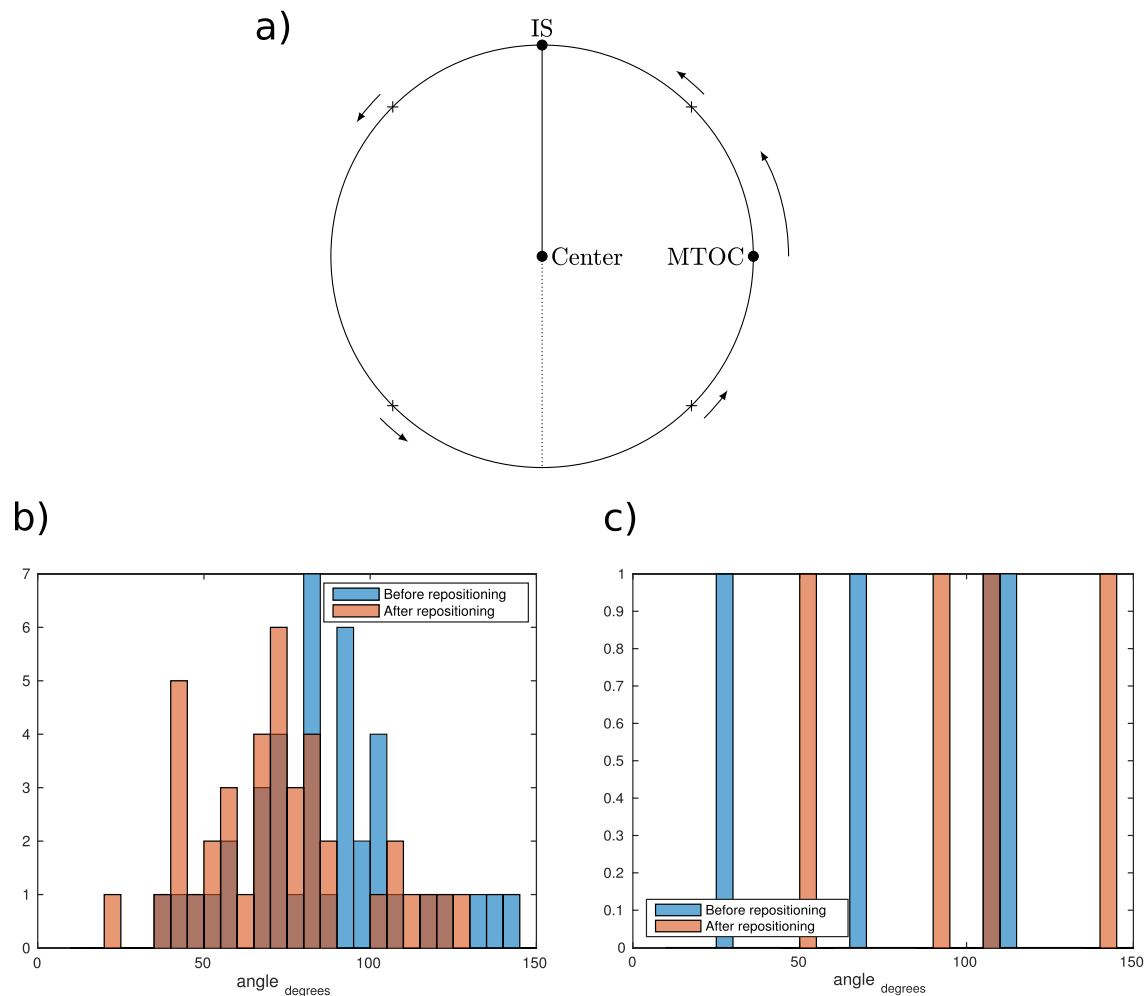


Fig. 3. Rotation angle of mitochondria increases during polarization. (a) Sketch of the rotational movement of MTOC and mitochondria in the plane perpendicular to the rotation axis. Mitochondria in the right half space rotate towards the IS, mitochondria in the left half space rotate away from the IS. (b) Histogram of the rotation angle of mitochondria in the right half plane at the beginning and the end of the polarization. Acquisitions from spinning disk confocal were analyzed. (c) Same as (b) for the left half space.

dynein, they are pulled towards the IS, and, consequently, the whole structure of microtubules and MTOC is repositioned. This movement is opposed by friction of the solvent in the cell that push microtubules in direction opposed to the movement. Microtubules caught by dynein have fixed position, but the position of the other microtubules relative to cytoskeleton change, and the microtubule structure “opens” in the direction towards IS as observable in Fig. 5A of Ref. [18].

2.4. Mathematical modeling reveals the mechanism for experimentally observed Ca^{2+} increase during polarization

We hypothesize that the observed changes in local and global Ca^{2+} concentration are intimately connected to the observed rotational relocation of the mitochondria towards the IS and that the underlying mechanism is the spatial rearrangement of Ca^{2+} sources, sinks and compartments during the observed mitochondrial movement. To test this, we formulated a mathematical three-dimensional (3D) model for the spatiotemporal distribution

of Ca^{2+} in the cell cytosol, the mitochondria and the ER as a function of the geometry and spatial arrangement of mitochondria within the cell, as we have observed them experimentally.

Our 3D full cell Ca^{2+} model assumes a spherical cell with a concentric nucleus and a spindle-like arrangement of thin, cylindrical mitochondria compartments between nucleus and plasma membrane (see Figs. 4a and 5a for a sketch). The spindle-like arrangement is motivated by the spindle formed by microtubules emanating from a MTOC, c.f. Fig. 2a and [18], and the observation that mitochondria are predominantly attached to microtubules and form filamentous structures [34,35]. The whole spindle can be rotated around an arbitrary axis by a specific angle, with zero angle corresponding to the configuration when the spindle center and the center of the IS match. The IS is defined as a small circular region at the north pole of the sphere.

The compartments can exchange Ca^{2+} through the compartment boundaries via channels and pumps which are distributed homogeneously or in-homogeneously over the compartment surfaces, defined quantitatively as Ca^{2+} flux per area. CRAC channels

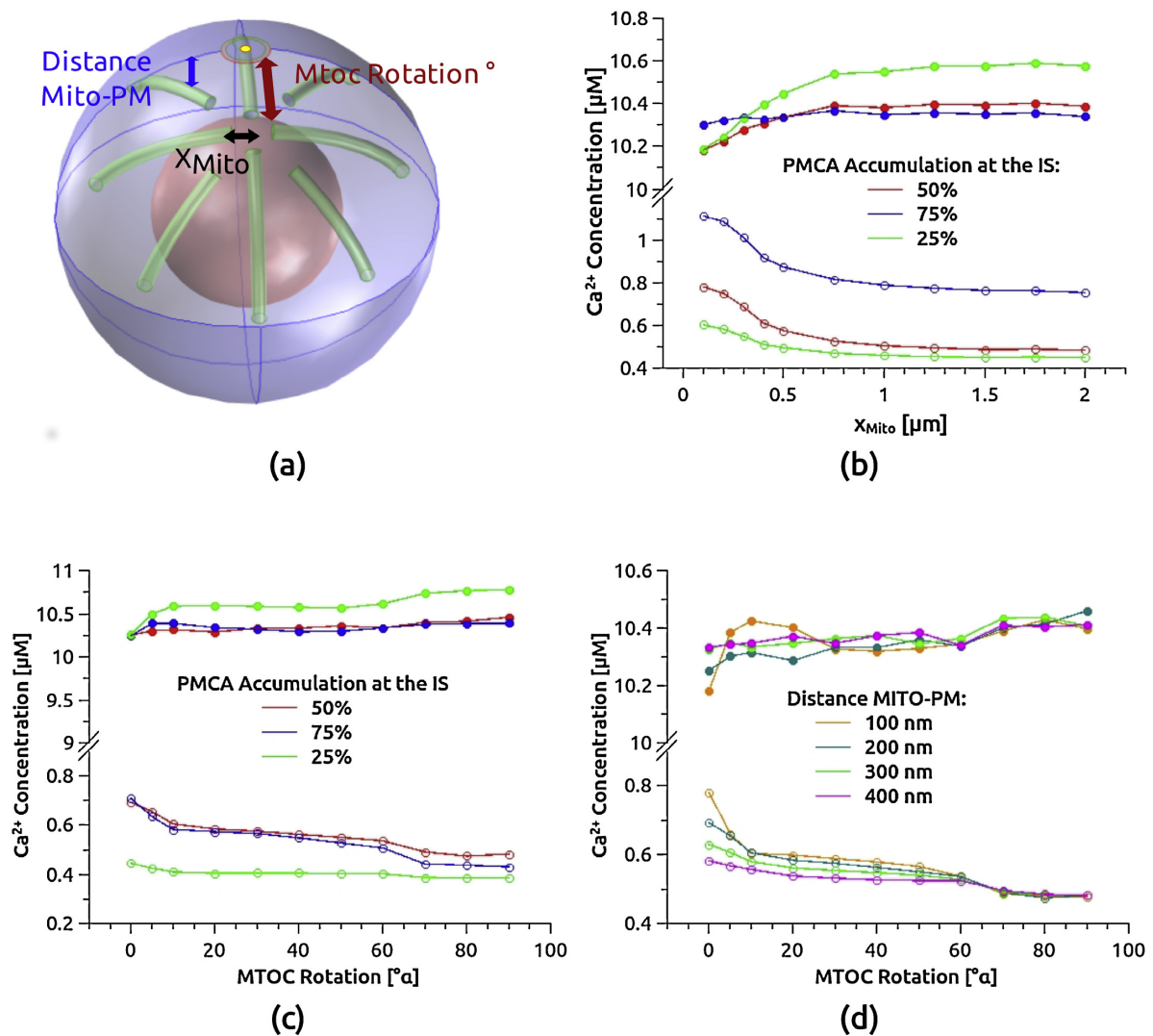


Fig. 4. Ca²⁺ concentrations depend on mitochondria rotation angle – model prediction for blocked SERCAs. **(a)** Sketch of the cell boundary (outer sphere), cell nucleus (inner sphere), IS (red circle), CRAC channels (yellow) and mitochondria geometry (green) for the model with depleted ER and blocked SERCAs. **(b)** Stationary value of the global (bottom curves) and local (top curves) Ca²⁺ concentrations predicted by the model as a function of the distance, x_{mito} , of the tip of the mitochondria from the CRAC channels in the fully polarized state (rotation angle $\alpha = 0$). **(c)** Stationary value of the global (bottom curves) and local (top curves) Ca²⁺ concentrations predicted by the model as a function of the rotation angle α for different levels of PMCA accumulation at the IS. **(d)** The same as in (c) but for different distances between mitochondria and plasma membrane. (For interpretation of the references to color in this figure legend, the reader is referred to the web version of this article.)

are located in the center of the IS in agreement with previous studies [23,36], PMCA pumps are in-homogeneously distributed over the plasma membrane with a higher concentration at the IS and a lower concentration on the rest of the PM in agreement with previous data [23]. The effect of mitochondrial Ca²⁺ uniporter and Na/Ca exchanger is described by in- and out-flux densities on the mitochondrial membranes. Similarly, the effect of IP₃ receptors and SERCA pumps on the Ca²⁺ content of the ER is described by in- and out-flux densities on the ER boundary. The precise definition and flux dependencies on Ca²⁺ concentrations in the different compartments can be found in the Materials and Methods section.

First we consider the experimental situation described above, in which SERCAs are blocked by thapsigargin, ER is empty and there-

fore CRAC channels fully activated. We computed the stationary Ca²⁺ distribution for different rotation angles as predicted by our model and show the results in Fig. 4. Fig. 4b shows the result for the fully polarized mitochondrial spindle (rotation angle $\alpha = 0$) as a function of the distance x_{mito} between the tips of the mitochondria and the CRAC channels for different PMCA accumulation levels. As already observed before [33], the global Ca²⁺ concentration increases with decreasing distance x_{mito} , whereas the local Ca²⁺ decreases. The variation becomes more pronounced the larger the PMCA accumulation level at the IS is. Next we fixed x_{mito} and varied the rotation angle α . As shown in Fig. 4c the global Ca²⁺ concentration increases with decreasing rotation angle of the mitochondrial spindle, most sharply for the smallest angle. The increase is again the more pronounced the higher the percentage of PMCA pumps

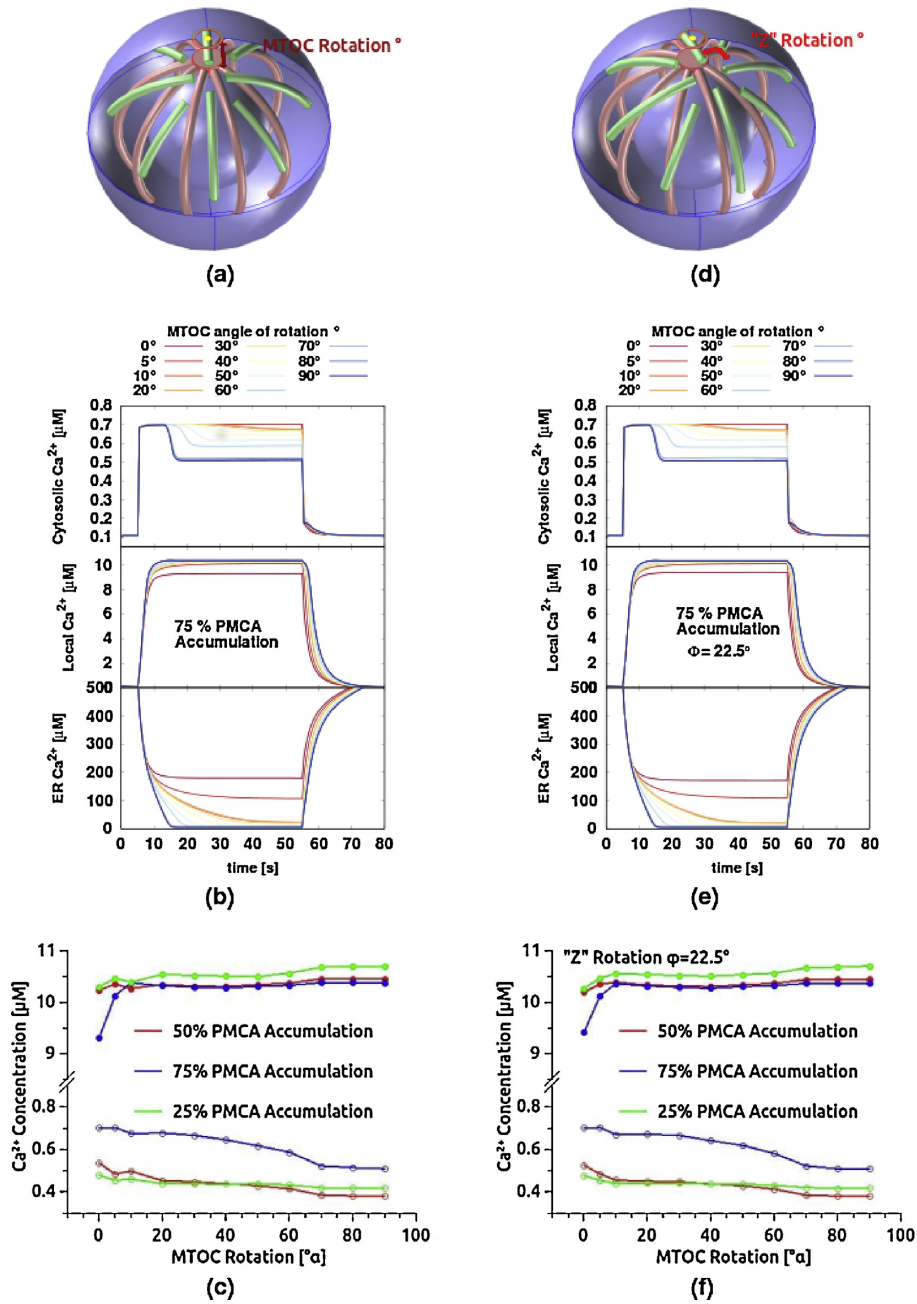


Fig. 5. Ca^{2+} concentrations depend on mitochondria rotation angle – model prediction with working SERCAs and spindle ER geometry. (a) Sketch of the mitochondria (green) and a spindle ER geometry (red). (b) Time course of Ca^{2+} concentrations in the cytosol (top), at the IS (middle), and in the ER (bottom) for the geometry in a. CRAC channels are activated at $t = 10$ s and deactivated at $t = 60$ s (c) Plateau value (at $t = 40$ s) of the cytosol (global) and IS (local) Ca^{2+} concentrations as a function of the rotation angle of the mitochondrial network for different ratio of PMCA accumulation at the IS. (d) Same as in (a) but with mitochondria spindle rotated by 22.5° . (e) Same as in (b) but for geometry d. (f) Same as in (c) but for geometry (d). (For interpretation of the references to color in this figure legend, the reader is referred to the web version of this article.)

accumulated at the IS. Simultaneously the local Ca^{2+} concentration at the IS decreases with decreasing rotation angle of the mitochondrial spindle, again more strongly with higher PMCA accumulation at the IS. The strength of the effect also depends on the distance between the mitochondria and the plasma membrane: the larger

the distance the weaker the concentration changes with rotation angle (see Fig. 4d).

The physical reason for Ca^{2+} concentration changes is the following: with decreasing rotation angle the center of the mitochondrial spindle comes closer to the IS. The density of mito-

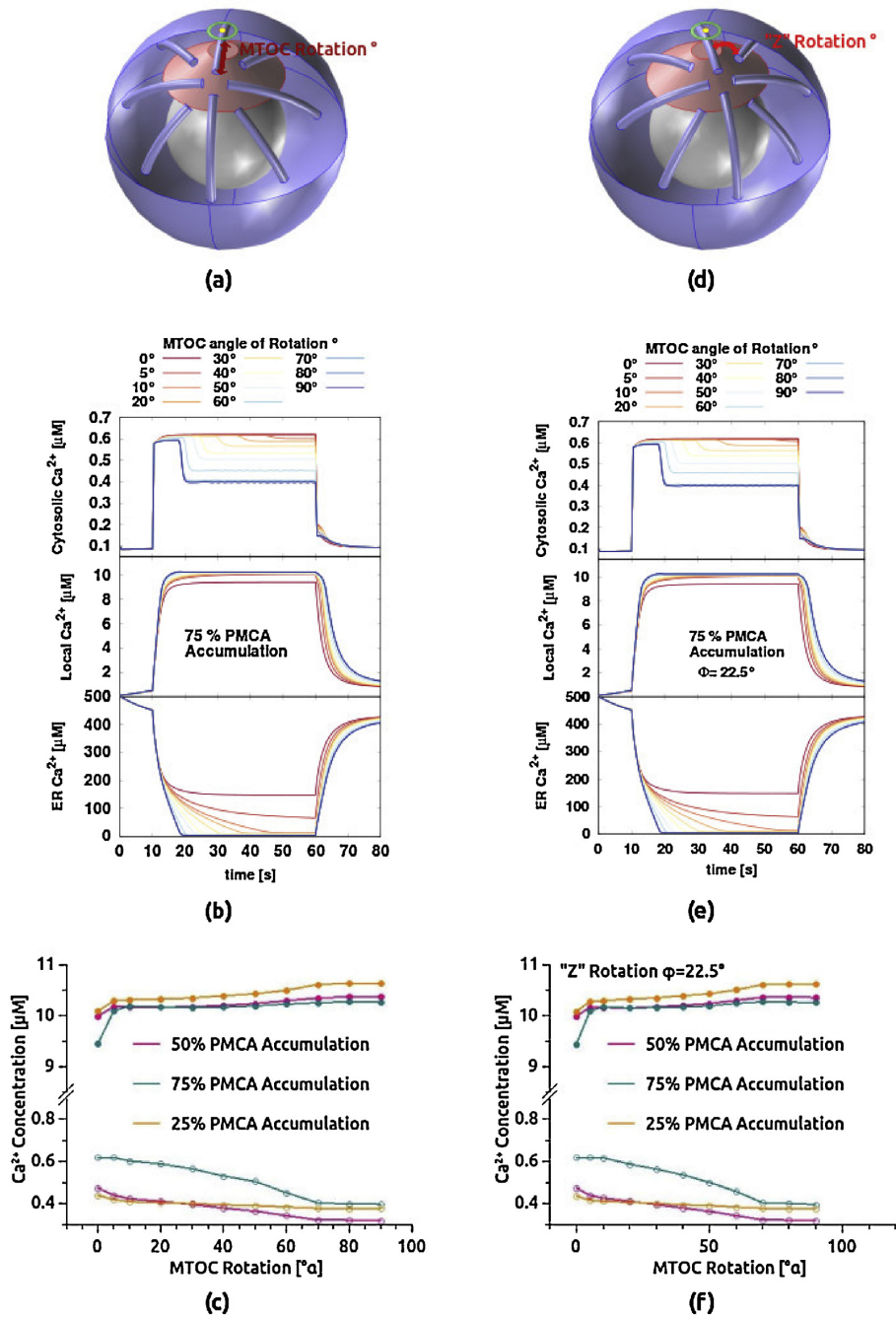


Fig. 6. Ca^{2+} concentrations depend on mitochondria rotation angle – model prediction with working SERCAs and truncated cone ER geometry. (a) Sketch of the mitochondria (green) and a truncated cone ER geometry (red). (b) Time course of Ca^{2+} concentrations in the cytosol (top), at the IS (middle), and in the ER (bottom) for the geometry in (a). CRAC channels are activated at $t = 10$ s and deactivated at $t = 60$ s (c) Plateau value (at $t = 40$ s) of the cytosol (global) and IS (local) Ca^{2+} concentrations as a function of the rotation angle of the mitochondrial network for different ratios of PMCA accumulation at the IS. (d) Same as in (a) but with mitochondria spindle rotated by 22.5° . (e) Same as in (b) but for geometry (d). (f) Same as in (c) but for geometry (d). (For interpretation of the references to color in this figure legend, the reader is referred to the web version of this article.)

chondria is highest at the center of the spindle, which means that more Ca^{2+} is transported into the mitochondrial compartment when the spindle center, supposed to be co-localized with the MTOC, comes close to the center of the IS, where the CRAC channels are located. Here the mitochondria take up the Ca^{2+} entering the microdomain underneath the IS, thereby decreasing the local Ca^{2+} concentration, and distribute it via internal diffusion along the mitochondrial lumen deeper into the cell, and release it into the cytosol, where less PMCAs are located, thereby increasing the global Ca^{2+} concentration.

2.5. Mathematical modeling predicts global Ca^{2+} increase during polarization under physiological conditions

Next we ask whether the Ca^{2+} concentration changes and the identified underlying mechanism observed with blocked SERCAs is relevant under more physiologically relevant conditions without administration of thapsigargin. We added a third compartment to our model, the ER, for which we assumed two different geometries: one also spindle-like, the other a truncated cone, both with fixed positions underneath the IS, see Figs. 5a and 6a, and in Figs. 5d and 6d for mitochondria rotated by 22.5° around the z-axis. The location of the ER is attributed to the fact that a part of the ER plasma membrane should be close to the IS to ensure CRAC channel formation through STIM-ORAI interaction. Ca^{2+} in- and out-flux is again modeled by a homogeneous density of SERCAs and IP_3 -receptors, respectively, over the ER surface. The CRAC channel capacity now depends on the ER calcium concentration as originally proposed by Putney [37], a concept that has been widely recognized in many cell types. The precise definition and flux dependencies on Ca^{2+} concentrations in the different compartments are found in the Materials and Methods section.

Under physiological conditions an external stimulus, for instance provided by ligand binding to a G protein coupled or tyrosine kinase receptor, will increase the cytosolic IP_3 concentration. IP_3 binds to IP_3 receptors on the ER membrane allowing Ca^{2+} outflux from the ER through the channel domain of the receptors. The negative feedback that increased cytosolic Ca^{2+} has on the IP_3 receptor channel capacity, potentially leading to Ca^{2+} oscillations [38], is also considered in our simulations via the Ca^{2+} concentration dependent flux J_{IP_3} . Once Ca^{2+} is released from the ER, CRAC channels open and SERCAs start to replenish the ER with Ca^{2+} . Consequently the dynamics of Ca^{2+} concentration is more complex than in the case of blocked SERCAs.

We assume the presence of an external stimulus between time $t = 10$ s and $t = 40$ s and computed the time course of the Ca^{2+} concentration in the different compartments for different rotation angles as predicted by our model. The results are shown in Fig. 5b for the spindle-like ER and in Fig. 5e with mitochondria rotated by 22.5° around the z-axis. The cytosolic Ca^{2+} concentration increases rapidly as soon as the stimulus starts and then decreases again slightly as usually reported in T cells, depending on how close the mitochondrial spindle center is to the IS, until a plateau value is reached. The plateau value is higher the smaller the rotation angle, i.e. the closer the mitochondrial spindle center is to the IS, and the local Ca^{2+} concentration at the IS is lower for smaller rotation angles, both in accordance with what is observed with blocked SERCAs (Fig. 1a and b, and [23]) but also consistent with the experiments with unblocked SERCAs [23]. The absolute value of the local Ca^{2+} concentration is around $10 \mu\text{mol}$, which is in good agreement with recent simulations at the ER-plasma membrane junction with clustered Orai1 channels [39]. It is an average over a pre-defined region around the CRAC channel and because of the steep Ca^{2+} gradient there depends on the size of this region. Therefore it cannot be compared directly with the experimental measurement depicted in Fig. 1.

The initial overshoot in the global Ca^{2+} concentration is due to the additional Ca^{2+} released by the ER and softens for smaller rotation angles. CRAC channels inactivation and PMCA modulation may also contribute to the overshoot. The ER Ca^{2+} concentration reaches a plateau, which is close to zero for large rotation angles but significantly larger than zero for small rotation angles. Once the stimulus is removed (at $t = 40$ s) all Ca^{2+} concentrations go back to baseline.

The mechanism of Ca^{2+} redistribution within the cell interior by the mitochondria and preventing Ca^{2+} entering the cell through the CRAC channels from being transported out again through the PMCA pumps is working in the physiological situation considered here, too. In addition the increased cytosolic Ca^{2+} concentration for small rotation angles lets the SERCAs replenish the ER at least partially, having an only minor effect on CRAC channel capacity.

In Fig. 5c and f we show the plateau values of global and local Ca^{2+} concentrations during stimulation for different PMCA pump accumulations at the IS as a function of the rotation angle. We observe qualitatively the same behavior as in the case of blocked SERCAs, i.e. a strong increase of the global Ca^{2+} concentration and decrease of the local one for a high accumulation of PMCAs at the IS.

Fig. 6 shows the results for the truncated cone ER geometry: Fig. 6a is a sketch of the compartment geometry, Fig. 6d with mitochondria rotated by 22.5° around the z-axis. The time course of the Ca^{2+} concentrations in the different compartments, shown in Fig. 6b and e, are similar to the spindle-like ER geometry (Fig. 5b and e), also the plateau values of the global and local Ca^{2+} concentrations show similar rotation angle dependencies. These results indicate that the reported effects are independent of the details of the ER geometry.

2.6. Calcium concentration is further increased by mitochondrial movement along microtubules towards the IS

In the work by Morlino et al. [22], it was observed that after MTOC relocation to the IS mitochondria move actively by Miro-1 modulated motors along microtubules towards the IS and increase. The effect of such an additional movement with fully polarized microtubules on the global and local Ca^{2+} concentration as predicted by our model can be seen from Fig. 4b: decreasing the distance, x_{mito} , between the tips of the mitochondria and the CRAC channels increases the global Ca^{2+} concentration and decreases the local one, depending on the degree of PMCA accumulation at the IS.

3. Discussion

Following T cell activation, mitochondria localize to the IS [21–24] and control local and global Ca^{2+} concentrations in T cells [23,32,33]. The MTOC as a key guiding organelle moves to the IS within several minutes of IS formation [13,16]. We present experimental evidence that during polarization of T-cells following target cell contact, the microtubule network rotates towards the IS and drags mitochondria with it. Based on the observed geometric paths of mitochondria during polarization we have developed a full three-dimensional (3D) compartment model for the Ca^{2+} dynamics in T-cells, which includes specific geometries and spatial arrangements of mitochondria, ER, and immunological synapse as well as localization aspects of Orai channels and PMCA at the IS. A potential regulation of PMCA by STIM1, as reported by Ritchie et al. [40], was not included in the model, however the pump rates are in accordance with values reported in the literature [41] and should thus reflect reasonable Ca^{2+} pump rates in T cells.

The model predicts an increase of global Ca^{2+} and a decrease in local Ca^{2+} concentration in case the mitochondrial structure is rotated towards the IS and a fraction of PMCA pumps accumu-

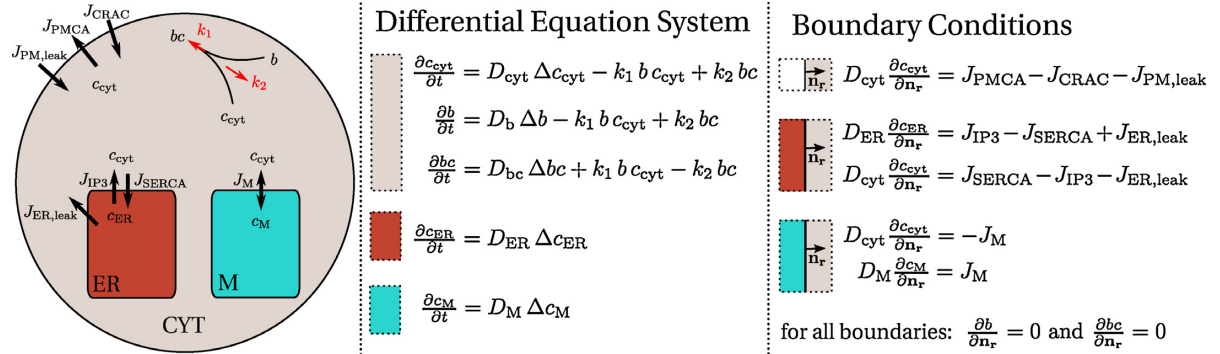


Fig. 7. Sketch of the mathematical model for the intracellular Ca^{2+} dynamics. For the figure description see Materials and Methods section.

lates at the IS, in agreement with experimental observations in thapsigargin-treated cells and in cells without thapsigargin present [23]. Once the cytoskeleton is fully polarized the mitochondria can still move further towards the IS along the microtubules, which the model predicts to increase global Ca^{2+} concentration even further and decrease local Ca^{2+} more.

The physical mechanism underlying the increase of the global Ca^{2+} concentration is, according to our model, the following: with decreasing rotation angles the center of the mitochondrial spindle comes closer to the IS. The density of mitochondria is highest at the center of the spindle, which means that more Ca^{2+} is transported into the mitochondrial compartment when the spindle center, supposed to be co-localized with the MTOC, comes close to the center of the IS, where the CRAC channels are located. Here the mitochondria take up the Ca^{2+} entering the microdomain underneath the IS, thereby decreasing the local Ca^{2+} concentration, and distribute it via internal diffusion along the mitochondrial lumen deeper into the cell, and release it into the cytosol, where less PMCA are located, thereby increasing the global Ca^{2+} concentration.

The full cell 3D model also includes localization and structural determinants of the ER. Since the model predicts that the effect also persists under more physiological conditions, i.e. when SERCAs are functional, we can conclude that the ER is not involved in the control of local and global Ca^{2+} concentrations following T cell activation through the IS. This is also in agreement with experimental evidence [23]. Of course ER-bound STIM 1 or 2 are required to activate Orai channels but once they are activated, mitochondria take over to control the Ca^{2+} signal in T cells. They not only determine local and global Ca^{2+} but they redirect much of the Ca^{2+} away from the SERCAs into the cell center by the same mechanism as they redirect Ca^{2+} away from the PMCA pumps accumulated at the IS. Together with Orai channels, PMCA are also enriched at the IS whereas SERCA is not [23]. It is thus not surprising that in the absence of mitochondria at the IS (e.g. 2 μm away, compare Fig. 4b), the ER does not refill significantly because PMCA export the Ca^{2+} . In this case, Ca^{2+} cycles across the plasma membrane rather than fulfilling its cytosolic functions.

It was shown previously that CRAC channels partially inactivate if mitochondria are not able to accumulate Ca^{2+} [42], however these experiments were carried out under conditions with no IS formation and thus no enrichment of PMCA at certain plasma membrane sites. In case of IS formation the model clearly predicts that a change in CRAC activity is not required to explain the mitochondrial control of local and global Ca^{2+} , only PMCA enrichment at the IS is necessary. Thus in case of IS formation the model reveals a clear hierarchy for the incoming Ca^{2+} . If present at the IS, mitochondria take up the vast majority of Ca^{2+} incoming through CRAC channels,

if not present, PMCA export Ca^{2+} incoming through CRAC channels, and if neither mitochondria are present nor PMCA are enriched at the IS, SERCAs and the ER take up Ca^{2+} , which finally inactivates Orai channels. In conclusion the experimentally described mitochondria, ER, Orai, PMCA and SERCA localization at the IS is well suited to guide Ca^{2+} entering the cell at the IS deeper into the cytosol and to control local Ca^{2+} at the IS. CRAC activity at the IS is not decreased as long as either mitochondria or PMCA or both are enriched at the IS preventing refilling of the ER.

4. Materials and Methods

4.1. 3-dimensional (3D) full cell Ca^{2+} model

Our model for the calcium homeostasis in T-cells consists of several compartments with specific geometry as defined below. The three-dimensional geometry together with explicit incorporation of Ca^{2+} diffusion discriminates our model from other mathematical approaches based on spatially averaged Ca^{2+} concentrations [43]. Ca^{2+} can diffuse within the compartments and exchange Ca^{2+} via channels and pumps: the cell body or cytosol, the mitochondria, and the ER, as sketched in Figs. 4a, 5a, d, and 6a, d. The cell body represents an ideal spherical T-cell with radius $r_{\text{cell}} = 4 \mu\text{m}$, and a spherical nucleus with radius $r_{\text{nuc}} = r_{\text{cell}}/2$. Mitochondrial filaments are assumed to have a rod-like shape with a length of 3.5 μm and a diameter of $d_{\text{M}} = 300 \text{ nm}$, of which 4–10 are arranged in a spindle like geometry as indicated in Fig. 4a. Mitochondrial filaments can take up and release Ca^{2+} over their whole surface, described by a Ca^{2+} current J_{M} to be defined below. Inside mitochondria Ca^{2+} diffuses with a diffusion constant D_{M} .

At the IS, we assume an accumulation of CRAC channels into a cluster of radius $r_{\text{CRAC}} = 0.1 \mu\text{m}$. At a distance of 0.3 μm to this CRAC cluster, a spherical segment of 100 nm width represents an agglomerate of PMCA pumps. In our Base Case scenario this spherical segment contains 50% of all pumps, whereas the other 50% are homogeneously distributed over the whole cell PM (according to fluorescence it is more like 70% at the IS, compare [23]). Inside the cytosol, Ca^{2+} is buffered by a mobile Ca^{2+} buffer b that freely diffuses with constant D_b . The total amount of buffer $[b]_{\text{T}} = [b] + [bc]$ is initially uniform in the cytosol for which we assumed that the binding of Ca^{2+} does not change the diffusion properties of the buffer. We use various geometries for the ER to be defined below. The naturally very thin ER network is modeled as a massive domain and therefore we assume that it is invisible for the cytosolic Ca^{2+} , which means that in the model cytosolic Ca^{2+} freely diffuses through the ER domain.

The spatio-temporal evolution of Ca^{2+} (and buffer) concentrations in the different compartments follows reaction-diffusion equations with sources and sinks as sketched in Fig. 7 and is defined in the following:

$$\frac{\partial c_{\text{cyt}}}{\partial t} = D_{\text{cyt}} \Delta c_{\text{cyt}} - k_1 c_{\text{cyt}} b + k_2 bc$$

$$\frac{\partial b}{\partial t} = D_b \Delta b - k_1 c_{\text{cyt}} b + k_2 bc$$

$$\frac{\partial bc}{\partial t} = D_{bc} \Delta bc + k_1 c_{\text{cyt}} b - k_2 bc$$

$$\frac{\partial c_M}{\partial t} = D_M \Delta c_M$$

$$\frac{\partial c_{\text{ER}}}{\partial t} = D_{\text{ER}} \Delta c_{\text{ER}}$$

The Ca^{2+} currents through the plasma membrane, J_{PM} , and the compartment membranes of the ER, J_{ER} , and the mitochondria, J_{M} , are implemented as flux/boundary conditions on the 2d surfaces separating the corresponding compartments and defined as follows.

The Ca^{2+} exchange across the plasma membrane, J_{PM} , contains two contributions: $J_{\text{PM}} = J_{\text{CRAC}} - J_{\text{PMCA}}$, where J_{CRAC} represents the influx through the CRAC channels and J_{PMCA} represents the export of Ca^{2+} pumped out of the cytosol via the PMCA pumps. J_{CRAC} is only defined on the CRAC cluster surface. The cluster influx is coupled to the Ca^{2+} concentration within the ER (c_{ER}) and at the average calcium concentration ($c_{\text{cyt}}^{(\text{micro})}$) in the micro-domain around the cluster in the following way:

$$J_{\text{CRAC}} = k_{\text{CRAC}} f_1(c_{\text{ER}}) g_{c_{1/2}, \Delta c} \left(\frac{c_{\text{cyt}}^{(\text{micro})}}{c_{\text{cyt}}} \right)$$

where $f_1(x)$ and $g_{c_{1/2}, \Delta c}(x)$ are both smooth sigmoid-shaped functions modeling the CRAC activation by emptied ER and CRAC inhibition by an enhanced Ca^{2+} concentration in the microdomain, respectively. We assume $f_1(x) = 0$ for a full store $x > 500 \mu\text{M}$, $f_1(x) = 1/2$ for $x = 250 \mu\text{M}$ and $f_1(x) = 1$ for an empty store ($x = 0 \mu\text{M}$). The function $g_{c_{1/2}, \Delta c}(x)$ varies smoothly from $g_{c_{1/2}, \Delta c}(x) = 1$ for $x \leq c_{1/2} - \Delta c$ to $g_{c_{1/2}, \Delta c}(x) = 0$ for $x \geq c_{1/2} + \Delta c$.

The plasma membrane Ca^{2+} pump currents at the IS and the plasma membrane is given by

$$J_{\text{PMCA,PM}} = k_{\text{PMCA,IS}} \frac{c_{\text{cyt}}^2}{k_p^2 + c_{\text{cyt}}^2} \quad \text{and} \quad J_{\text{PMCA}} = k_{\text{PMCA,PM}} \frac{c_{\text{cyt}}^2}{k_p^2 + c_{\text{cyt}}^2}$$

where the maximum pump rates $k_{\text{PMCA,IS}}$ and $k_{\text{PMCA,PM}}$ depend on the PMCA accumulation at the IS and on the area ratio of IS and the remaining PM.

The Ca^{2+} exchange across the ER surface, $J_{\text{ER}} = J_{\text{IP}_3} - J_{\text{SERCA}}$, comprises Ca^{2+} release from the ER through the IP_3 receptor channels into the cytosol, J_{IP_3} , and the Ca^{2+} pumped back through the SERCAs from the cytosol into the ER, J_{SERCA} . The first contribution to the current J_{ER} is:

$$J_{\text{IP}_3} = k_{\text{IP}_3} \theta(t_{\text{IP}_3} - t) g_{c_{1/2}, \Delta c}^{\text{IP}_3} \left(c_{\text{cyt}} \right) f_2(c_{\text{ER}})$$

We assume fully activated IP_3 receptor channels during the specified time period t_{IP_3} . For time $t > t_{\text{IP}_3}$ the flux J_{IP_3} is equal to zero; otherwise its release rate depends on c_{cyt} [38] and on c_{ER} through the two sigmoidal-shaped functions $g_{c_{1/2}, \Delta c}^{\text{IP}_3}(x)$ and $f_2(x)$: the first one models the IP_3 channels open probability (which depends on c_{cyt}), the second models the channels inhibition due to

low values of c_{ER} . In particular we set $f_2(x) = 1$ for $x \geq 200 \mu\text{M}$, $f_2(x) = 1/2$ for $x = 100 \mu\text{M}$ and $f_2(x) = 0$ for $x = 0 \mu\text{M}$.

The Ca^{2+} back-flux into the ER caused by the SERCA pumps is assumed to be given by

$$J_{\text{SERCA}} = k_{\text{SERCA}} \frac{c_{\text{cyt}}^2}{c_{\text{cyt}}^2 + k_{\text{ER}}^2}$$

where k_{ER} , as in the previous cases, represents the value of the cytosolic concentration at which the pumps work at the half of their maximal efficiency k_{SERCA} .

The Ca^{2+} current across the mitochondria surface comprises influx through the mitochondrial Ca^{2+} uniporter (MCU) and export by the Na/Ca exchanger. Physiologically, Ca^{2+} uptake through the MCU would depolarise the mitochondria, reducing further influx. We model this effect in a 2nd order Michaelis-Menten form of the inward flux:

$$J_{\text{M}} = k_{\text{inward}} \cdot \frac{c_{\text{cyt}}^2}{c_{\text{cyt}}^2 + k_{\text{m1}}^2} - k_{\text{out}} \cdot \frac{c_{\text{M}}}{c_{\text{M}} + k_{\text{m2}}}$$

To simulate experiments in which the SERCA pumps are blocked by thapsigargin, leading to an emptied ER and fully activated CRAC channels we omit the boundary conditions involving c_{ER} and set

$$J_{\text{CRAC}} = k_{\text{CRAC}} g_{c_{1/2}, \Delta c} \left(\frac{c_{\text{cyt}}^{(\text{micro})}}{c_{\text{cyt}}} \right).$$

To solve our reaction-diffusion equations, we use the package ‘transport of diluted species’ of the finite elements method software ‘Comsol’ (<http://www.comsol.com/>).

4.1.1. Parameters

For the Ca^{2+} diffusion constant in the cytosol we use the estimate of $D_{\text{cyt}} = 200 \mu\text{m}^2/\text{s}$ [44], and set the Ca^{2+} diffusion constant in mitochondria to $D_{\text{M}} = D_{\text{cyt}}$ and in the ER to a smaller value $D_{\text{ER}} = D_{\text{cyt}}/10$. Also the diffusion of mobile Ca^{2+} buffers is usually smaller, with $D_b = D_{bc} = D_{\text{cyt}}/20$ [45]. The reaction rates for Ca^{2+} binding and unbinding k_1 and k_2 and the buffer resting concentration are in good agreement with commonly used modeling parameters [46].

The CRAC channel influx parameter was set to $k_{\text{CRAC}} = 5 \cdot 10^{-5} \text{ mol}/\text{m}^2 \text{ s}$. Since CRAC channels are modeled as an area of size $A_{\text{CRAC}} = 3.1 \cdot 10^{-14} \text{ m}^2$, the total channel capacity is $1.55 \cdot 10^{-17} \text{ mol}/\text{s}$, which is equivalent to $9.3 \cdot 10^5$ particles/s, corresponding to a CRAC cluster of 93 fully activated CRAC channels.

For the PMCA pumps we use globally (i.e. no PMCAs at the IS) $k_{\text{PMCA,global}} = 8 \cdot 10^{-9} \text{ mol}/\text{m}^2 \text{ s}$. With a plasma membrane area of $A_{\text{PM}} = 2 \cdot 10^{-10} \text{ m}^2$ this corresponds to $1.6 \cdot 10^{-18} \text{ mol}/\text{s}$ or 26,000 particles/s. A single PMCA pumps about 10 particles/s, which means that we assume 2600 pumps in total on the PM or 13 pumps/ μm in accordance with values reported in the literature [41]. When in our base case scenario 50% of the PMCA pumps are assumed to be located in a ring of width $0.1 \mu\text{m}$ and radius $0.3 \mu\text{m}$ around the center of the IS this implies $k_{\text{PMCA,IS}} = 3 \cdot 10^{-6} \text{ mol}/\text{m}^2 \text{ s}$ and $k_{\text{PMCA,PM}} = 4 \cdot 10^{-9} \text{ mol}/\text{m}^2 \text{ s}$.

As discussed in Ref. [33], the parameter of the Ca^{2+} flux across mitochondria boundaries are chosen such that total maximum currents through PMCA pumps and across mitochondria boundaries are approximately equal $I_{\text{PMCA}}^{\text{max}}/I_{\text{M}}^{\text{max}} \approx 1$.

The SERCA flux parameter is set to $k_{\text{SERCA}} = 3.5 \cdot 10^{-8} \text{ m}/\text{s}$. Since the ER area is $A_{\text{ER}} = 6 \cdot 10^{-9} \text{ m}^2$ the maximum SERCA pump capacity is $1.3 \cdot 10^6$ particles/s. A single SERCA pumps 5–10 particles/s so that we have ca. 500,000 pumps, which is in agreement with the values used in Refs. [43,47,48]. For the IP_3 channels we assume a maximum flux rate of $k_{\text{IP}_3} = 10 \cdot k_{\text{SERCA}}$.

All parameters for the base case scenario together with the initial conditions for Ca^{2+} concentrations in the different compartments are summarized in Table 1. For the truncated cone geometry

Table 1
Parameters and initial values used for the Base Case scenario in our 3D cell model.

Parameter	Value (unit)	Parameter	Value (unit)
D_{Cyt}	200 ($\mu\text{m}^2 \text{s}^{-1}$)	k_{CRAC}	$5 \cdot 10^{-5}$ (mol/m ² s)
D_M	200 ($\mu\text{m}^2 \text{s}^{-1}$)	$k_{PMCA,IS}$	$3 \cdot 10^{-6}$ (mol/m ² s)
D_b	10 ($\mu\text{m}^2 \text{s}^{-1}$)	$k_{PMCA,PM}$	$4 \cdot 10^{-9}$ (mol/m ² s)
D_{bc}	10 ($\mu\text{m}^2 \text{s}^{-1}$)	k_{SERCA}	$3.5 \cdot 10^{-8}$ (m/s)
D_{ER}	20 ($\mu\text{m}^2 \text{s}^{-1}$)	k_{IP3}	$3.5 \cdot 10^{-7}$ (m/s)
$c_{Cyt}(t=0)$	100 (nM)	k_{inward}	$9 \cdot 10^{-6}$ (mol/m ² s)
$c_M(t=0)$	100 (nM)	k_{out}	$8 \cdot 10^{-6}$ (mol/m ² s)
$c_{ER}(t=0)$	500 (μM)	k_p	300 (nM)
$c_b(t=0)$	10 (μM)	k_{m1}	600 (nM)
$c_{bc}(t=0)$	500 (nM)	k_{m2}	15 (μM)
A_{CRAC}	$3.1 \cdot 10^{-14}$ (m ²)	k_{ER}	300 (nM)
A_{PM}	$2 \cdot 10^{-10}$ (m ²)	$c_{1/2}$	15 (μM)
A_M	$2.44 \cdot 10^{-11}$ (m ²)	Δ_c	1 (μM)
A_{ER}	$5.9 \cdot 10^{-11}$ (m ²)	c_{IP3}^1	600 (nM)
J_{PMleak}	$4.5 \cdot 10^{-10}$ (mol/m ² s)	$\Delta_{IP3}^{1/2}$	200 (nM)
J_{ERleak}	$3.5 \cdot 10^{-9}$ (mol/m ² s)	k_1	100 (m ³ /mol s)
k_2	0.3 s^{-1}		

of the ER we have adapted the parameters for k_{SERCA} , k_{IP3} , and $J_{ER,leak}$ to accommodate for the smaller ER surface A_{ER} in order to maintain the maximum number of Ca^{2+} particles per second into the ER: $A_{ER} = 2.7 \cdot 10^{-9} \text{ m}^2$, $k_{SERCA} = 7.6 \cdot 10^{-8} \text{ m/s}$, $k_{IP3} = 7.6 \cdot 10^{-7} \text{ m/s}$, and $J_{ER,leak} = 7.6 \cdot 10^{-9} \text{ mol/m}^2 \text{ s}$.

4.2. Cell culture

Human Jurkat E6.1 cells were grown in RPMI 1640 medium supplemented with 10% FCS and penicillin-streptomycin and maintained in log-phase. Peripheral blood mononuclear cells (PBMC) were obtained from healthy donors as previously described [49]. CTL stimulated with CD3/CD28 beads were prepared as described before [12]. Raji cells were cultured in RPMI-1640 medium (ThermoFisher Scientific) supplemented with 10% FCS.

4.3. Evanescent-wave imaging

TIRFM experiments were carried out exactly as the ones shown in Fig. 4C, D of our publication by Quintana et al. [23] and are described there. The only difference is that here, the local and global Ca^{2+} concentrations were measured in two different sets of cells and not in the same cells.

The following solutions were used: 155 NaCl, 4.5 KCl, 1 CaCl_2 , 2 MgCl_2 , 10 D-glucose, and 5 Hepes (pH 7.4 with NaOH). CaCl_2 was replaced by 1 mM EGTA for the 0 Ca^{2+} or increased for the 20 mM Ca^{2+} solution. Chemicals not specifically mentioned were from Sigma (highest grade). Fluo-5F (stock 1 mM in DMSO) was from Molecular Probes and anti-human CD3 monoclonal antibodies were from Biozol.

4.4. Plasmids and reagents

All chemicals not specifically mentioned were from Sigma (highest grade). EMTB-3 \times GFP and DsRed2-Mito-7 were purchased from AddGene. MitoTracker Deep Red FM was purchased from Life Technologies.

4.5. Time-lapse imaging

CTL were transfected with EMTB-3 \times GFP alone or with DsRed2-Mito-7. Mitochondria were labeled with MitoTracker Deep Red FM or DsRed2-Mito-7 as indicated in the figure legend. Raji cells were pulsed with SEA (0.1 $\mu\text{g/ml}$)/SEB (0.1 $\mu\text{g/ml}$) at 37°C for 30 min before conjugation with CTL. CTL were settled on poly-L-ornithine coated coverslips, and then target cells were given into the medium.

The translocation of microtubule network (EMTB-3 \times GFP, green channel) and mitochondria (red channel or far-red channel) in CTL was visualized at 37°C using a confocal (Zeiss) equipped with a 63 \times objective (NA 1.4). The step-size of z-stacks is 1 μm . The time interval between each stack is 19.02–21.17 s. For spinning disk confocal microscope CTL were settled on CD3/CD28 antibody-coated coverslips, and the images were acquired at room temperature every 4.66 s with a z-stack step-size of 0.79 μm .

4.6. Extraction of rotation angles from tracking data

From time-lapse imaging obtained with the spinning disk microscope with a time interval of 4.66 s we extracted for each z-stack between 0 s (start of polarization) and 186.4 s (end of polarization) the three-dimensional position coordinates of MTOC, IS, and individual mitochondria (precisely: the center of the light spots indicating their position). The position of the cell center was estimated via a weighted average of the centers of the cross-section of individual planes of the z-stack, where the areas of the cross-sections were used as weight. The cell center was determined for each frame individually.

Since the cell was not stable during the measurement the movement of the cell as a whole had to be subtracted. The cell has three translational and two rotational degrees of freedom. For every z-stack, values of coordinates of the center were subtracted from values of coordinates of mitochondria, MTOC and IS.

Next the position data for all objects in a z-stack were brought into a standard coordinate system by two rotations: In the first one, IS rotates to z axis and MTOC and mitochondria rotate accordingly. In the second rotation, MTOC is moved to x-z plane. The coordinates of mitochondria are transformed by the same manner. IS is always on z axis and MTOC rotates just in x-z plane and the y-axis is the axis of rotation.

We defined the following vectors $\rightarrow MTOC = \rightarrow MT - \rightarrow CT$, $\rightarrow IS = \rightarrow is - \rightarrow CT$, and $\rightarrow mito_i = \rightarrow mt_i - \rightarrow CT_i$, where $\rightarrow MT$, $\rightarrow is$, $\rightarrow CT$ and $\rightarrow mito_i$ are the coordinates of the MTOC, IS, center of the cell and mitochondria, respectively. During the repositioning of the MTOC the angles between the vectors $\rightarrow MTOC$ and $\rightarrow IS$ and between the vectors $\rightarrow mito_i$ and $\rightarrow IS$ change continuously and is recorded between two time frames.

During the rotation of the MTOC in the x-z plane the angle between the vectors $\rightarrow MTOC$ and $\rightarrow IS$ decreases (c.f. the sketch in Fig. 3a) and if the rotation of the whole cytoskeleton drags the mitochondria with it the angles between $\rightarrow mito_i$ and $\rightarrow IS$ have to change according to a rotation around the y-axis. The change of angle between $\rightarrow mito_i$ and $\rightarrow IS$ depends on initial position of mitochondria, or, more concretely, on half-space (left or right) where it is located (c.f. Fig. 3a). In the “right half-space” the angles between $\rightarrow mito_i$ and $\rightarrow IS$ get smaller, as is visible in Fig. 3b. Conversely, the rotation leads to enlargements of angles in “left half-space”. To prove repositioning of mitochondria with microtubules, angles before and after repositioning were measured and results were compared. If the hypothesis of a correlated repositioning of mitochondria and microtubules is true, the angles after repositioning should be smaller at the “right half-space” and lower at the “left half-space”. The histograms in Fig. 3b and c indeed show the expected changes of angles during repositioning and demonstrate the rotation of mitochondria with the MTOC/microtubule part of the cytoskeleton.

Author contributions

M., M.P., K.S. and I.H., H.R. designed and performed all modelling parts. R.Z. performed and analyzed experiments relevant for Figs. 2

and 3. A.Q. and M.P. performed and analyzed experiments shown in Fig. 1. I.M. and R.Z. are responsible for the layout of the figures. H.R. designed the study with contributions from B.Q. and M.H. The manuscript was written by H.R. and M.H. with B.Q. adding parts regarding the experimental data. All authors edited the manuscript and concurred with the submission.

Acknowledgements

Research carried out for this study with human material (leukocyte reduction system chambers from human blood donors) is authorized by the local ethic committee (declaration from 16.4.2015 (84/15; Prof. Dr. Rettig-Stürmer)). We thank Ute Becherer (Saarland University) for help with TIRF microscopy. We thank the Institute for Clinical Hemostaseology and Transfusion Medicine for providing donor blood; Carmen Hässig and Gertrud Schwär for excellent technical help. This project was funded by Sonderforschungsbereich CRC 1027 project A3 (to H.R.) and A2 (to B.Q. and M.H.).

References

- [1] D. Pruyne, A. Legesse-Miller, L. Gao, Y. Dong, A. Bretscher, Mechanisms of polarized growth and organelle segregation in yeast, *Annu. Rev. Cell Dev. Biol.* 20 (2004) 559–591.
- [2] P. van Bergeijk, C.C. Hoogenraad, L.C. Kaptein, Right time, right place: probing the functions of organelle positioning, *Trends Cell Biol.* 26 (2016) 121–134.
- [3] N.B. Martin-Cofreces, F. Baixauli, F. Sanchez-Madrid, Immune synapse: conductor of orchestrated organelle movement, *Trends Cell Biol.* 24 (2014) 61–72.
- [4] G.M. Griffiths, A. Tsun, J.C. Stinchcombe, The immunological synapse: a focal point for endocytosis and exocytosis, *J. Cell Biol.* 189 (2010) 399–406.
- [5] A. Quintana, M. Hoth, Mitochondrial dynamics and their impact on T cell function, *Cell Calcium* 52 (2012) 57–63.
- [6] K.L. Angus, G.M. Griffiths, Cell polarisation and the immunological synapse, *Curr. Opin. Cell Biol.* 25 (2013) 85–91.
- [7] M.L. Dustin, E.O. Long, Cytotoxic immunological synapses, *Immunol. Rev.* 235 (2010) 24–34.
- [8] J.S. Orange, Formation and function of the lytic NK-cell immunological synapse, *Nat. Rev. Immunol.* 8 (2008) 713–725.
- [9] R. Wedlich-Soldner, S. Altschuler, L. Wu, R. Li, Spontaneous cell polarization through actomyosin-based delivery of the Cdc42 GTPase, *Science* 299 (2003) 1231–1235.
- [10] D. Obino, F. Farina, O. Malbec, P.J. Saez, M. Maurin, J. Gaillard, F. Dingli, D. Loew, A. Gautreau, M.I. Yuseff, L. Blanchoin, M. Thery, A.M. Lennon-Dumenil, Actin nucleation at the centrosome controls lymphocyte polarity, *Nat. Commun.* 7 (2016) 10969.
- [11] H.T. Hsu, J.S. Orange, Distinct integrin-dependent signals define requirements for lytic granule convergence and polarization in natural killer cells, *Sci. Signal.* 7 (2014) pe24.
- [12] B. Qu, V. Pattu, C. Junker, E.C. Schwarz, S.S. Bhat, C. Kummerow, M. Marshall, U. Matti, F. Neumann, M. Pfeundschnuh, U. Becherer, H. Rieger, J. Rettig, M. Hoth, Docking of lytic granules at the immunological synapse in human CTL requires Vti1b-dependent pairing with CD3 endosomes, *J. Immunol.* 186 (2011) 6894–6904.
- [13] J.C. Stinchcombe, E. Majorovits, G. Bossi, S. Fuller, G.M. Griffiths, Centrosome polarization delivers secretory granules to the immunological synapse, *Nature* 443 (2006) 462–465.
- [14] A.T. Ritter, Y. Asano, J.C. Stinchcombe, N.M. Dieckmann, B.C. Chen, C. Gawden-Bone, S. van Engelenburg, W. Legant, L. Gao, M.W. Davidson, E. Betzig, J. Lippincott-Schwartz, G.M. Griffiths, Actin depletion initiates events leading to granule secretion at the immunological synapse, *Immunity* 42 (2015) 864–876.
- [15] G. de Saint Basile, G. Menasche, A. Fischer, Molecular mechanisms of biogenesis and exocytosis of cytotoxic granules, *Nat. Rev. Immunol.* 10 (2010) 568–579.
- [16] J.C. Stinchcombe, L.O. Randzavola, K.L. Angus, J.M. Mantell, P. Verkade, G.M. Griffiths, Mother centriole distal appendages mediate centrosome docking at the immunological synapse and reveal mechanistic parallels with ciliogenesis, *Curr. Biol.* 25 (2015) 3239–3244.
- [17] J.C. Stinchcombe, G.M. Griffiths, Communication, the centrosome and the immunological synapse, *Philos. Trans. R. Soc. Lond. B Biol. Sci.* 369 (2014).
- [18] J. Yi, X. Wu, A.H. Chung, J.K. Chen, T.M. Kapoor, J.A. Hammer, Centrosome repositioning in T cells is biphasic and driven by microtubule end-on capture-shrinkage, *J. Cell Biol.* 202 (2013) 779–792.
- [19] A. Kupfer, G. Dennert, Reorientation of the microtubule-organizing center and the Golgi apparatus in cloned cytotoxic lymphocytes triggered by binding to lysable target cells, *J. Immunol.* 133 (1984) 2762–2766.
- [20] A. Kupfer, G. Dennert, S.J. Singer, Polarization of the Golgi apparatus and the microtubule-organizing center within cloned natural killer cells bound to their targets, *Proc. Natl. Acad. Sci. U. S. A.* 80 (1983) 7224–7228.
- [21] F. Baixauli, N.B. Martin-Cofreces, G. Morlino, Y.R. Carrasco, C. Calabia-Linares, E. Veiga, J.M. Serrador, F. Sanchez-Madrid, The mitochondrial fission factor dynamin-related protein 1 modulates T-cell receptor signalling at the immune synapse, *EMBO J.* 30 (2011) 1238–1250.
- [22] G. Morlino, O. Barreiro, F. Baixauli, J. Robles-Valero, J.M. Gonzalez-Granado, R. Villa-Bellosta, J. Cuenca, C.O. Sanchez-Sorzano, E. Veiga, N.B. Martin-Cofreces, F. Sanchez-Madrid, Miro-1 links mitochondria and microtubule Dynein motors to control lymphocyte migration and polarity, *Mol. Cell Biol.* 34 (2014) 1412–1426.
- [23] A. Quintana, M. Pasche, C. Junker, D. Al-Ansary, H. Rieger, C. Kummerow, L. Nunez, C. Villalobos, P. Meraner, U. Becherer, J. Rettig, B.A. Niemeier, M. Hoth, Calcium microdomains at the immunological synapse: how ORAI channels, mitochondria and calcium pumps generate local calcium signals for efficient T-cell activation, *EMBO J.* 30 (2011) 3895–3912.
- [24] A. Quintana, C. Schwindling, A.S. Wenning, U. Becherer, J. Rettig, E.C. Schwarz, M. Hoth, T cell activation requires mitochondrial translocation to the immunological synapse, *Proc. Natl. Acad. Sci. U. S. A.* 104 (2007) 14418–14423.
- [25] C. Schwindling, A. Quintana, E. Krause, M. Hoth, Mitochondria positioning controls local calcium influx in T cells, *J. Immunol.* 184 (2010) 184–190.
- [26] T.A. Lyubchenko, G.A. Wurth, A. Zweifach, Role of calcium influx in cytotoxic T lymphocyte lytic granule exocytosis during target cell killing, *Immunity* 15 (2001) 847–859.
- [27] A.T. Pores-Fernando, A. Zweifach, Calcium influx and signaling in cytotoxic T-lymphocyte lytic granule exocytosis, *Immunol. Rev.* 231 (2009) 160–173.
- [28] A. Maul-Pavicic, S.C. Chiang, A. Rensing-Ehl, B. Jessen, C. Fauriat, S.M. Wood, S. Sjoqvist, M. Hufnagel, I. Schulze, T. Bass, W.W. Schamel, S. Fuchs, H. Pircher, C.A. McCarl, K. Mikoshiba, K. Schwarz, S. Feske, Y.T. Bryceson, S. Ehl, ORAI1-mediated calcium influx is required for human cytotoxic lymphocyte degranulation and target cell lysis, *Proc. Natl. Acad. Sci. U. S. A.* 108 (2011) 3324–3329.
- [29] I. Voskoboinik, M.C. Thia, J. Fletcher, A. Ciccone, K. Browne, M.J. Smyth, J.A. Trapani, Calcium-dependent plasma membrane binding and cell lysis by perforin are mediated through its C2 domain: a critical role for aspartate residues 429, 435, 483, and 485 but not 491, *J. Biol. Chem.* 280 (2005) 8426–8434.
- [30] C. Weidinger, P.J. Shaw, S. Feske, STIM1 and STIM2-mediated Ca²⁺ influx regulates antitumour immunity by CD8⁺ T cells, *EMBO Mol. Med.* 5 (2013) 1311–1321.
- [31] E.C. Schwarz, B. Qu, M. Hoth, Calcium, cancer and killing: the role of calcium in killing cancer cells by cytotoxic T lymphocytes and natural killer cells, *Biochim. Biophys. Acta* 1833 (2013) 1603–1611.
- [32] A. Quintana, E.C. Schwarz, C. Schwindling, P. Lipp, L. Kaestner, M. Hoth, Sustained activity of calcium release-activated calcium channels requires translocation of mitochondria to the plasma membrane, *J. Biol. Chem.* 281 (2006) 40302–40309.
- [33] M. Peglow, B.A. Niemeier, M. Hoth, H. Rieger, Interplay of channels, pumps and organelle location in calcium microdomain formation, *New J. Phys.* 15 (2013).
- [34] X. Liu, D. Weaver, O. Shirihai, G. Hajnoczky, Mitochondrial 'kiss-and-run': interplay between mitochondrial motility and fusion-fission dynamics, *EMBO J.* 28 (2009) 3074–3089.
- [35] M. Yi, D. Weaver, G. Hajnoczky, Control of mitochondrial motility and distribution by the calcium signal: a homeostatic circuit, *J. Cell Biol.* 167 (2004) 661–672.
- [36] M.I. Lioudyno, J.A. Kozak, A. Penna, O. Safrina, S.L. Zhang, D. Sen, J. Roos, K.A. Stauderman, M.D. Cahalan, Orai1 and STIM1 move to the immunological synapse and are up-regulated during T cell activation, *Proc. Natl. Acad. Sci. U. S. A.* 105 (2008) 2011–2016.
- [37] J.W. Putney Jr., A model for receptor-regulated calcium entry, *Cell Calcium* 7 (1986) 1–12.
- [38] G.W. De Young, J. Keizer, A single-pool inositol 1,4,5-trisphosphate-receptor-based model for agonist-stimulated oscillations in Ca²⁺ concentration, *Proc. Natl. Acad. Sci. U. S. A.* 89 (1992) 9895–9899.
- [39] K. Samanta, P. Kar, G.R. Mirams, A.B. Parekh, Ca²⁺ channel re-localization to plasma-membrane microdomains strengthens activation of Ca²⁺-dependent nuclear gene expression, *Cell Rep.* 12 (2015) 203–216.
- [40] M.F. Ritchie, E. Samakaj, J. Soboloff, STIM1 is required for attenuation of PMCA-mediated Ca²⁺ clearance during T-cell activation, *EMBO J.* 31 (2012) 1123–1133.
- [41] D.M. Bautista, M. Hoth, R.S. Lewis, Enhancement of calcium signalling dynamics and stability by delayed modulation of the plasma-membrane calcium-ATPase in human T cells, *J. Physiol.* 541 (2002) 877–894.
- [42] M. Hoth, D.C. Button, R.S. Lewis, Mitochondrial control of calcium-channel gating: a mechanism for sustained signaling and transcriptional activation in T lymphocytes, *Proc. Natl. Acad. Sci. U. S. A.* 97 (2000) 10607–10612.
- [43] C. Schmeitz, E.A. Hernandez-Vargas, R. Flegert, A.H. Guse, M. Meyer-Hermann, A mathematical model of T lymphocyte calcium dynamics derived from single transmembrane protein properties, *Front. Immunol.* 4 (2013) 277.
- [44] N.L. Allbritton, T. Meyer, L. Stryer, Range of messenger action of calcium ion and inositol 1,4,5-trisphosphate, *Science* 258 (1992) 1812–1815.
- [45] Z. Zhou, E. Neher, Mobile and immobile calcium buffers in bovine adrenal chromaffin cells, *J. Physiol.* 469 (1993) 245–273.

- [46] M. Falcke, Reading the patterns in living cells—the physics of Ca²⁺ signaling, *Adv. Phys.* 53 (2004) 255–440.
- [47] S. Means, A.J. Smith, J. Shepherd, J. Shadid, J. Fowler, R.J.H. Wojcikiewicz, T. Mazel, G.D. Smith, B.S. Wilson, Reaction diffusion modeling of calcium dynamics with realistic ER geometry, *Biophys. J.* 91 (2006) 537–557.
- [48] R.K. Dash, F. Qi, D.A. Beard, A biophysically based mathematical model for the kinetics of mitochondrial calcium uniporter, *Biophys. J.* 96 (2009) 1318–1332.
- [49] C. Kummerow, E.C. Schwarz, B. Bufe, F. Zufall, M. Hoth, B. Qu, A simple economic, time-resolved killing assay, *Eur. J. Immunol.* 44 (2014) 1870–1872.

Bibliography: own works

- [Hornak2020] I. Hornak and H. Rieger.
Stochastic Model of T Cell Repolarization during Target Elimination (I).
Biophysical Journal, 118(7), 1733–1748, 2020.
<https://doi.org/10.1016/j.bpj.2020.01.045>.
- [Hornak2022] I. Hornak and H. Rieger.
Stochastic Model of T Cell Repolarization during Target Elimination (II).
Biophysical Journal, 121(7), 1246–1265, 2022.
<https://doi.org/10.1016/j.bpj.2022.02.029>.
- [Hornak2016] I. Maccari, R. Zhao, M. Peglow, K. Schwarz, I. Hornak, M. Pasche, A. Quintana,
M. Hoth, B. Qu, H. Rieger.
Cytoskeleton rotation relocates mitochondria to the immunological synapse and increases
calcium signals.
Cell Calcium, 60,309-321, 2016.
<https://doi.org/10.1016/j.ceca.2016.06.007>.

The scientific code is publicly available on GitHub.

- [Hornak2022B] I. Hornak.
Stochastic model of T Cell repositioning (2022).
GitHub repository: <https://github.com/ihornak>.

Bibliography: references

- [1] Eva Bianconi, Allison Piovesan, Federica Facchin, Alina Beraudi, Raffaella Casadei, Flavia Frabetti, Lorenza Vitale, Maria Chiara Pelleri, Simone Tassani, Francesco Piva, Soledad Perez-Amodio, Pierluigi Strippoli, and Silvia Canaider. An estimation of the number of cells in the human body. *Ann Hum Biol*, 40(6):463–471, December 2013.
- [2] Geoffrey M. Cooper. The Origin and Evolution of Cells. *The Cell: A Molecular Approach. 2nd edition*, 2000.
- [3] Carl R. Woese. On the evolution of cells. *PNAS*, 99(13):8742–8747, June 2002.
- [4] Detlev Arendt. The evolution of cell types in animals: emerging principles from molecular studies. *Nat Rev Genet*, 9(11):868–882, November 2008.
- [5] Jason Yi, Xufeng Wu, Andrew H. Chung, James K. Chen, Tarun M. Kapoor, and John A. Hammer. Centrosome repositioning in T cells is biphasic and driven by microtubule end-on capture-shrinkage. *J Cell Biol*, 202(5):779–792, September 2013.
- [6] B. Geiger, D. Rosen, and G. Berke. Spatial relationships of microtubule-organizing centers and the contact area of cytotoxic T lymphocytes and target cells. *J. Cell Biol.*, 95(1):137–143, October 1982.
- [7] Jane C. Stinchcombe, Endre Majorovits, Giovanna Bossi, Stephen Fuller, and Gillian M. Griffiths. Centrosome polarization delivers secretory granules to the immunological synapse. *Nature*, 443(7110):462–465, September 2006.
- [8] Ilaria Maccari, Renping Zhao, Martin Peglow, Karsten Schwarz, Ivan Hornak, Mathias Pasche, Ariel Quintana, Markus Hoth, Bin Qu, and Heiko Rieger. Cytoskeleton rotation relocates mitochondria to the immunological synapse and increases calcium signals. *Cell Calcium*, 60(5):309–321, 2016.
- [9] Jeffrey R. Kuhn and Martin Poenie. Dynamic Polarization of the Microtubule Cytoskeleton during CTL-Mediated Killing. *Immunity*, 16(1):111–121, January 2002.
- [10] King Lam Hui and Arpita Upadhyaya. Dynamic microtubules regulate cellular contractility during T-cell activation. *Proc Natl Acad Sci USA*, 114(21):E4175–E4183, May 2017.
- [11] Arno Müllbacher, Paul Waring, Ron Tha Hla, Thao Tran, Seow Chin, Thomas Stehle, Crisan Museteanu, and Markus M. Simon. Granzymes are the essential downstream effector molecules for the control of primary virus infections by cytolytic leukocytes. *PNAS*, 96(24):13950–13955, November 1999.
- [12] B. Lowin, M. C. Peitsch, and J. Tschopp. Perforin and granzymes: crucial effector molecules in cytolytic T lymphocyte and natural killer cell-mediated cytotoxicity. *Curr. Top. Microbiol. Immunol.*, 198:1–24, 1995.
- [13] Iliia Voskoboinik, Mark J. Smyth, and Joseph A. Trapani. Perforin-mediated target-cell death and immune homeostasis. *Nat. Rev. Immunol.*, 6(12):940–952, December 2006.
- [14] Harvey Lodish, Arnold Berk, S. Lawrence Zipursky, Paul Matsudaira, David Baltimore, and James Darnell. Overview of Neuron Structure and Function. *Molecular Cell Biology. 4th edition*, 2000.
- [15] Hongkui Zeng and Joshua R. Sanes. Neuronal cell-type classification: challenges, opportunities and the path forward. *Nat Rev Neurosci*, 18(9), September 2017.
- [16] Dmitri B. Chklovskii. Synaptic Connectivity and Neuronal Morphology: Two Sides of the Same Coin. *Neuron*, 43(5):609–617, September 2004.

- [17] Paul Cohen and Bruce M. Spiegelman. Cell biology of fat storage. *Mol Biol Cell*, 27(16):2523–2527, August 2016.
- [18] Paul Cohen and Bruce M. Spiegelman. Brown and Beige Fat: Molecular Parts of a Thermogenic Machine. *Diabetes*, 64(7):2346–2351, July 2015.
- [19] Brenda M. Ogle and Jeffrey L. Platt. The Biology of Cell Fusion: Cells of different types and from different species can fuse, potentially transferring disease, repairing tissues and taking part in development. *American Scientist*, 92(5):420–427, 2004.
- [20] Katrien Vermeulen, Dirk R. Van Bockstaele, and Zwi N. Berneman. The cell cycle: a review of regulation, deregulation and therapeutic targets in cancer. *Cell Prolif*, 36(3):131–149, June 2003.
- [21] Sue Espe. Malacards: The Human Disease Database. *J Med Libr Assoc*, 106(1):140–141, January 2018.
- [22] Athanasia Pavlopoulou, Demetrios A. Spandidos, and Ioannis Michalopoulos. Human cancer databases (Review). *Oncol Rep*, 33(1):3–18, January 2015.
- [23] J. Steven McDougal, Janet K. A. Nicholson, and Alison Mawle. Effects of HIV infection on the immune system. In R. Madhok, C. D. Forbes, and B. L. Evatt, editors, *Blood, Blood Products — and AIDS* —, pages 51–88. 1987. ISBN 978-1-4899-3394-2.
- [24] A. Boasso, G. M. Shearer, and C. Chougnet. Immune dysregulation in human immunodeficiency virus infection: know it, fix it, prevent it? *J Intern Med*, 265(1):78–96, January 2009.
- [25] Sarah Howie, Robert Ramage, and Tim Hewson. Innate Immune System Damage in Human Immunodeficiency Virus Type 1 Infection. *Am J Respir Crit Care Med*, 162:S141–S145, October 2000.
- [26] Gene M. Shearer. HIV-Induced Immunopathogenesis. *Immunity*, 9(5):587–593, November 1998.
- [27] Suk Ran Yoon, Tae-Don Kim, and Inpyo Choi. Understanding of molecular mechanisms in natural killer cell therapy. *Exp Mol Med*, 47(2), February 2015.
- [28] Christoph Wulfig, Bozidar Purtic, Jennifer Klem, and John D. Schatzle. Stepwise cytoskeletal polarization as a series of checkpoints in innate but not adaptive cytolytic killing. *Proc Natl Acad Sci USA*, 100(13):7767–7772, June 2003.
- [29] Bruce Alberts, Alexander Johnson, Julian Lewis, Martin Raff, Keith Roberts, and Peter Walter. Innate Immunity. *Molecular Biology of the Cell. 4th edition*, 2002.
- [30] Eric Vivier and Bernard Malissen. Innate and adaptive immunity: specificities and signaling hierarchies revisited. *Nat Immunol*, 6(1):17–21, January 2005.
- [31] Bruce Alberts, Alexander Johnson, Julian Lewis, Martin Raff, Keith Roberts, and Peter Walter. The Adaptive Immune System. *Molecular Biology of the Cell. 4th edition*, 2002.
- [32] Mihai G. Netea, Andreas Schlitzer, Katarzyna Placek, Leo A. B. Joosten, and Joachim L. Schultze. Innate and Adaptive Immune Memory: an Evolutionary Continuum in the Host’s Response to Pathogens. *Cell Host Microbe*, 25(1):13–26, January 2019.
- [33] Weronika Ratajczak, Paulina Niedźwiedzka-Rystwej, Beata Tokarz-Deptuła, and Wiesław Deptuła. Immunological memory cells. *Cent Eur J Immunol*, 43(2):194–203, 2018.
- [34] Donna L. Farber, Naomi A. Yudanin, and Nicholas P. Restifo. Human memory T cells: generation, compartmentalization and homeostasis. *Nat Rev Immunol*, 14(1):24–35, January 2014.
- [35] Stephen C. Jameson and David Masopust. Understanding subset diversity in T cell memory. *Immunity*, 48(2):214–226, February 2018.
- [36] Nicole C. Smith, Matthew L. Rise, and Sherri L. Christian. A Comparison of the Innate and Adaptive Immune Systems in Cartilaginous Fish, Ray-Finned Fish, and Lobe-Finned Fish. *Frontiers in Immunology*, 10:2292, 2019.

-
- [37] Akiko Iwasaki and Ruslan Medzhitov. Control of adaptive immunity by the innate immune system. *Nature Immunology*, 16(4):343–353, April 2015.
- [38] National Center for Biotechnology Information, U. S. National Library of Medicine 8600 Rockville Pike, Bethesda MD, and 20894 Usa. *The innate and adaptive immune systems*. Institute for Quality and Efficiency in Health Care (IQWiG), July 2020.
- [39] David D. Chaplin. Overview of the Immune Response. *J Allergy Clin Immunol*, 125:S3–23, February 2010.
- [40] Mario Riera Romo, Dayana Pérez-Martínez, and Camila Castillo Ferrer. Innate immunity in vertebrates: an overview. *Immunology*, 148(2):125–139, June 2016.
- [41] Stuart E. Turvey and David H. Broide. Chapter 2: Innate Immunity. *J Allergy Clin Immunol*, 125:S24–S32, February 2010.
- [42] Shizuo Akira, Satoshi Uematsu, and Osamu Takeuchi. Pathogen Recognition and Innate Immunity. *Cell*, 124(4):783–801, February 2006.
- [43] Bruce Alberts, Alexander Johnson, Julian Lewis, Martin Raff, Keith Roberts, and Peter Walter. Pathogens, Infection, and Innate Immunity. *Molecular Biology of the Cell. 4th edition*, 2002.
- [44] Matthew D. Martin and Vladimir P. Badovinac. Defining Memory CD8 T Cell. *Frontiers in Immunology*, 9:2692, 2018.
- [45] Charles A. Janeway Jr, Paul Travers, Mark Walport, Mark J. Shlomchik, Charles A. Janeway Jr, Paul Travers, Mark Walport, and Mark J. Shlomchik. *Immunobiology*. Garland Science, 5th edition, 2001. ISBN 978-0-8153-3642-6.
- [46] R. Luz Elena Cano and H. Damaris E. Lopera. *Introduction to T and B lymphocytes*. El Rosario University Press, July 2013.
- [47] Guillaume Gaud, Renaud Lesourne, and Paul E. Love. Regulatory mechanisms in T cell receptor signalling. *Nat Rev Immunol*, 18(8):485–497, August 2018.
- [48] Juan Carlos Yam-Puc, Lingling Zhang, Yang Zhang, and Kai-Michael Toellner. Role of B-cell receptors for B-cell development and antigen-induced differentiation. *F1000Res*, 7:429, April 2018.
- [49] Jr Charles A Janeway, Paul Travers, Mark Walport, and Mark J. Shlomchik. Generation of lymphocytes in bone marrow and thymus. *Immunobiology: The Immune System in Health and Disease. 5th edition*, 2001.
- [50] Brahma V. Kumar, Thomas Connors, and Donna L. Farber. Human T cell development, localization, and function throughout life. *Immunity*, 48(2):202–213, February 2018.
- [51] C. Nuñez, N. Nishimoto, G. L. Gartland, L. G. Billips, P. D. Burrows, H. Kubagawa, and M. D. Cooper. B cells are generated throughout life in humans. *J Immunol*, 156(2):866–872, January 1996.
- [52] Bruce Alberts, Alexander Johnson, Julian Lewis, Martin Raff, Keith Roberts, and Peter Walter. B Cells and Antibodies. *Molecular Biology of the Cell. 4th edition*, 2002.
- [53] William Hoffman, Fadi G. Lakkis, and Geetha Chalasani. B Cells, Antibodies, and More. *Clin J Am Soc Nephrol*, 11(1):137–154, January 2016.
- [54] Inbal Sela-Culang, Vered Kunik, and Yanay Ofran. The Structural Basis of Antibody-Antigen Recognition. *Frontiers in Immunology*, 4:302, 2013.
- [55] Michele Barry and R. Chris Bleackley. Cytotoxic T lymphocytes: all roads lead to death. *Nat Rev Immunol*, 2(6):401–409, June 2002.
- [56] Jr Charles A Janeway, Paul Travers, Mark Walport, and Mark J. Shlomchik. Macrophage activation by armed CD4 TH1 cells. *Immunobiology: The Immune System in Health and Disease. 5th edition*, 2001.
-

- [57] Bruce Alberts, Alexander Johnson, Julian Lewis, Martin Raff, Keith Roberts, and Peter Walter. Helper T Cells and Lymphocyte Activation. *Molecular Biology of the Cell*. 4th edition, 2002.
- [58] Mads Hald Andersen, David Schrama, Per thor Straten, and Jürgen C. Becker. Cytotoxic T Cells. *Journal of Investigative Dermatology*, 126(1):32–41, January 2006.
- [59] Nu Zhang and Michael J. Bevan. CD8+ T Cells: Foot Soldiers of the Immune System. *Immunity*, 35(2):161–168, August 2011.
- [60] Heesik Yoon, Taeg S. Kim, and Thomas J. Braciale. The Cell Cycle Time of CD8+ T Cells Responding In Vivo Is Controlled by the Type of Antigenic Stimulus. *PLoS One*, 5(11):e15423, November 2010.
- [61] Susan M. Kaech and Rafi Ahmed. Memory CD8+ T cell differentiation: initial antigen encounter triggers a developmental program in naïve cells. *Nat Immunol*, 2(5):415–422, May 2001.
- [62] Jr. Charles A. Janeway, Paul Travers, Mark Walport, and Mark J. Shlomchik. B-cell activation by armed helper T cells. *Immunobiology: The Immune System in Health and Disease*. 5th edition, 2001.
- [63] Rishi Vishal Luckheeram, Rui Zhou, Asha Devi Verma, and Bing Xia. CD4+T Cells: Differentiation and Functions. *Clin Dev Immunol*, 2012:925135, 2012.
- [64] Susan L. Swain, K. Kai McKinstry, and Tara M. Strutt. Expanding roles for CD4+ T cells in immunity to viruses. *Nat Rev Immunol*, 12(2):136–148, February 2012.
- [65] Jorge Luis Galeano Niño, Sophie V Pigeon, Szun S Tay, Feyza Colakoglu, Daryan Kempe, Jack Hywood, Jessica K Mazalo, James Cremasco, Matt A Govendir, Laura F Dagley, Kenneth Hsu, Simone Rizzetto, Jerzy Zieba, Gregory Rice, Victoria Prior, Geraldine M O’Neill, Richard J Williams, David R Nisbet, Belinda Kramer, Andrew I Webb, Fabio Luciani, Mark N Read, and Maté Biro. Cytotoxic T cells swarm by homotypic chemokine signalling. *eLife*, 9:e56554, October 2020.
- [66] Loïc Dupré, Raïssa Houmadi, Catherine Tang, and Javier Rey-Barroso. T Lymphocyte Migration: An Action Movie Starring the Actin and Associated Actors. *Frontiers in Immunology*, 6:586, 2015.
- [67] Cornelis J. M. Melief. “License to Kill” Reflects Joint Action of CD4 and CD8 T Cells. *Clin Cancer Res*, 19(16):4295–4296, August 2013.
- [68] N. Kerkvliet and B. P. Lawrence. 5.05 - Cytotoxic T Cells*. In Charlene A. McQueen, editor, *Comprehensive Toxicology (Second Edition)*, pages 109–132. Elsevier, Oxford, January 2010. ISBN 978-0-08-046884-6.
- [69] Christina M. Trambas and Gillian M. Griffiths. Delivering the kiss of death. *Nat Immunol*, 4(5):399–403, May 2003.
- [70] Eric Vivier, David H. Raulet, Alessandro Moretta, Michael A. Caligiuri, Laurence Zitvogel, Lewis L. Lanier, Wayne M. Yokoyama, and Sophie Ugolini. Innate or Adaptive Immunity? The Example of Natural Killer Cells. *Science*, 331(6013):44–49, January 2011.
- [71] Alex M. Abel, Chao Yang, Monica S. Thakar, and Subramaniam Malarkannan. Natural Killer Cells: Development, Maturation, and Clinical Utilization. *Frontiers in Immunology*, 9, 2018.
- [72] Yili Li and Roy Mariuzza. Structural and Biophysical Insights into the Role of CD4 and CD8 in T Cell Activation. *Frontiers in Immunology*, 4, 2013.
- [73] Andreas Mayer, Yaojun Zhang, Alan S. Perelson, and Ned S. Wingreen. Regulation of T cell expansion by antigen presentation dynamics. *Proceedings of the National Academy of Sciences*, 116(13):5914–5919, March 2019.
- [74] Alex T. Ritter, Yukako Asano, Jane C. Stinchcombe, N. M. G. Dieckmann, Bi-Chang Chen, C. Gawden-Bone, Schuyler van Engelenburg, Wesley Legant, Liang Gao, Michael W. Davidson, Eric Betzig, Jennifer Lippincott-Schwartz, and Gillian M. Griffiths. Actin depletion initiates events leading to granule secretion at the immunological synapse. *Immunity*, 42(5):864–876, May 2015.

-
- [75] Markus G. Rudolph, Robyn L. Stanfield, and Ian A. Wilson. How TCRs bind MHCs, peptides, and coreceptors. *Annu. Rev. Immunol.*, 24:419–466, 2006.
- [76] K. Christopher Garcia. Reconciling views on T cell receptor germline bias for MHC. *Trends Immunol*, 33(9):429–436, September 2012.
- [77] R. M. Zinkernagel and P. C. Doherty. Restriction of in vitro T cell-mediated cytotoxicity in lymphocytic choriomeningitis within a syngeneic or semiallogeneic system. *Nature*, 248(5450):701, April 1974.
- [78] M Attaf, M Legut, D K Cole, and A K Sewell. The T cell antigen receptor: the Swiss army knife of the immune system. *Clin Exp Immunol*, 181(1):1–18, July 2015.
- [79] Kai W Wucherpfennig. T cell receptor crossreactivity as a general property of T cell recognition. *Molecular Immunology*, 40(14):1009–1017, February 2004.
- [80] Bruce P. Babbitt, Paul M. Allen, Gary Matsueda, Edgar Haber, and Emil R. Unanue. Binding of immunogenic peptides to Ia histocompatibility molecules. *Nature*, 317(6035):359, September 1985.
- [81] C. R. Monks, B. A. Freiberg, H. Kupfer, N. Sciaky, and A. Kupfer. Three-dimensional segregation of supramolecular activation clusters in T cells. *Nature*, 395(6697):82–86, September 1998.
- [82] Michael L Dustin, Michael W Olszowy, Amy D Holdorf, Jun Li, Shannon Bromley, Naishadh Desai, Patricia Widder, Frederick Rosenberger, P. Anton van der Merwe, Paul M Allen, and Andrey S Shaw. A Novel Adaptor Protein Orchestrates Receptor Patterning and Cytoskeletal Polarity in T-Cell Contacts. *Cell*, 94(5):667–677, September 1998.
- [83] Michael L. Dustin, Arup K. Chakraborty, and Andrey S. Shaw. Understanding the structure and function of the immunological synapse. *Cold Spring Harb Perspect Biol*, 2(10):a002311, October 2010.
- [84] A Kupfer, D Louvard, and S J Singer. Polarization of the Golgi apparatus and the microtubule-organizing center in cultured fibroblasts at the edge of an experimental wound. *Proc Natl Acad Sci USA*, 79(8):2603–2607, April 1982.
- [85] Morgan Huse, Emily J Quann, and Mark M Davis. Shouts, whispers and the kiss of death: directional secretion in T cells. *Nat Immunol*, 9(10):1105–1111, October 2008.
- [86] William J. Grossman, Paula A. Revell, Zhi Hong Lu, Hillary Johnson, Andrew J. Bredemeyer, and Timothy J. Ley. The orphan granzymes of humans and mice. *Curr. Opin. Immunol.*, 15(5):544–552, October 2003.
- [87] Konrad Krzewski and John E. Coligan. Human NK cell lytic granules and regulation of their exocytosis. *Front Immunol*, 3:335, 2012.
- [88] Peter Groscurth and Luis Filgueira. Killing Mechanisms of Cytotoxic T Lymphocytes. *Physiology*, 13(1):17–21, February 1998.
- [89] Geoffrey M. Cooper. Microtubules. *The Cell: A Molecular Approach. 2nd edition*, 2000.
- [90] Eva Nogales. Structural Insights into Microtubule Function. *Annual Review of Biochemistry*, 69(1):277–302, 2000.
- [91] F. Gittes, B. Mickey, J. Nettleton, and J. Howard. Flexural rigidity of microtubules and actin filaments measured from thermal fluctuations in shape. *The Journal of Cell Biology*, 120(4):923–934, February 1993.
- [92] R. A. Walker, E. T. O’Brien, N. K. Pryer, M. F. Soboeiro, W. A. Voter, H. P. Erickson, and E. D. Salmon. Dynamic instability of individual microtubules analyzed by video light microscopy: rate constants and transition frequencies. *J. Cell Biol.*, 107(4):1437–1448, October 1988.
- [93] Tim Mitchison and Marc Kirschner. Dynamic instability of microtubule growth. *Nature*, 312(5991):237–242, November 1984.
-

- [94] I. A. Vorob'ev and I. S. Grigor'ev. Dynamics and the life cycle of cell microtubules. *Tsitol Genet*, 37(2):22–38, April 2003.
- [95] Tetsuya Horio and Takashi Murata. The role of dynamic instability in microtubule organization. *Front. Plant Sci.*, 5, 2014.
- [96] Gary J. Brouhard. Dynamic instability 30 years later: complexities in microtubule growth and catastrophe. *Mol Biol Cell*, 26(7):1207–1210, April 2015.
- [97] E. M. Mandelkow, E. Mandelkow, and R. A. Milligan. Microtubule dynamics and microtubule caps: a time-resolved cryo-electron microscopy study. *J. Cell Biol.*, 114(5):977–991, September 1991.
- [98] Peter Bieling, Liedewij Laan, Henry Schek, E. Laura Munteanu, Linda Sandblad, Marileen Dogterom, Damian Brunner, and Thomas Surrey. Reconstitution of a microtubule plus-end tracking system in vitro. *Nature*, 450(7172):1100–1105, December 2007.
- [99] Arshad Desai and Timothy J. Mitchison. Microtubule Polymerization Dynamics. *Annual Review of Cell and Developmental Biology*, 13(1):83–117, 1997.
- [100] Jacob W. J. Kerssemakers, E. Laura Munteanu, Liedewij Laan, Tim L. Noetzel, Marcel E. Janson, and Marileen Dogterom. Assembly dynamics of microtubules at molecular resolution. *Nature*, 442(7103):709–712, August 2006.
- [101] Henry T. Schek, Melissa K. Gardner, Jun Cheng, David J. Odde, and Alan J. Hunt. Microtubule assembly dynamics at the nanoscale. *Curr. Biol.*, 17(17):1445–1455, September 2007.
- [102] Melissa K. Gardner, Alan J. Hunt, Holly V. Goodson, and David J. Odde. Microtubule assembly dynamics: new insights at the nanoscale. *Curr Opin Cell Biol*, 20(1):64–70, February 2008.
- [103] Kenneth A. Myers, Kathryn T. Applegate, Gaudenz Danuser, Robert S. Fischer, and Clare M. Waterman. Distinct ECM mechanosensing pathways regulate microtubule dynamics to control endothelial cell branching morphogenesis. *J Cell Biol*, 192(2):321–334, January 2011.
- [104] Benjamin Lacroix, Gaëlle Letort, Laras Pitayu, Jérémy Sallé, Marine Stefanutti, Gilliane Maton, Anne-Marie Ladouceur, Julie C. Canman, Paul S. Maddox, Amy S. Maddox, Nicolas Minc, François Nédélec, and Julien Dumont. Microtubule Dynamics Scale with Cell Size to Set Spindle Length and Assembly Timing. *Dev Cell*, 45(4):496–511.e6, May 2018.
- [105] John Fuesler and Hsin-Jung Li. Dynamic instability — A common denominator in prokaryotic and eukaryotic DNA segregation and cell division. *Cellular and Molecular Biology Letters*, 17(4), January 2012.
- [106] Noa B. Martín-Cófreces, Javier Robles-Valero, J. Román Cabrero, María Mittelbrunn, Mónica Gordón-Alonso, Ching-Hwa Sung, Balbino Alarcón, Jesús Vázquez, and Francisco Sánchez-Madrid. MTOC translocation modulates IS formation and controls sustained T cell signaling. *J. Cell Biol.*, 182(5):951–962, September 2008.
- [107] Tu Nguyen-Ngoc, Katayoun Afshar, and Pierre Gönczy. Coupling of cortical dynein and $G\alpha$ proteins mediates spindle positioning in *Caenorhabditis elegans*. *Nature Cell Biology*, 9(11):1294–1302, November 2007.
- [108] Takamune T. Saito, Daisuke Okuzaki, and Hiroshi Nojima. Mcp5, a meiotic cell cortex protein, is required for nuclear movement mediated by dynein and microtubules in fission yeast. *J Cell Biol*, 173(1):27–33, April 2006.
- [109] Akira Yamashita and Masayuki Yamamoto. Fission Yeast Num1p Is a Cortical Factor Anchoring Dynein and Is Essential for the Horse-Tail Nuclear Movement During Meiotic Prophase. *Genetics*, 173(3):1187–1196, July 2006.
- [110] Vaishnavi Ananthanarayanan, Martin Schattat, Sven K. Vogel, Alexander Krull, Nenad Pavin, and Iva M. Tolić-Nørrelykke. Dynein motion switches from diffusive to directed upon cortical anchoring. *Cell*, 153(7):1526–1536, June 2013.

-
- [111] Ronald D Vale. The Molecular Motor Toolbox for Intracellular Transport. *Cell*, 112(4):467–480, February 2003.
- [112] Naoko Mizuno, Akihiro Narita, Takahide Kon, Kazuo Sutoh, and Masahide Kikkawa. Three-dimensional structure of cytoplasmic dynein bound to microtubules. *PNAS*, 104(52):20832–20837, December 2007.
- [113] Anthony J. Roberts, Takahide Kon, Peter J. Knight, Kazuo Sutoh, and Stan A. Burgess. Functions and mechanics of dynein motor proteins. *Nature Reviews Molecular Cell Biology*, 14(11):713–726, November 2013.
- [114] P. Andre, A. M. Benoliel, C. Capo, C. Foa, M. Buferne, C. Boyer, A. M. Schmitt-Verhulst, and P. Bongrand. Use of conjugates made between a cytolytic T cell clone and target cells to study the redistribution of membrane molecules in cell contact areas. *Journal of Cell Science*, 97(2):335–347, October 1990.
- [115] Joseph Lin, Mark J. Miller, and Andrey S. Shaw. The c-SMAC. *J Cell Biol*, 170(2):177–182, July 2005.
- [116] Kaushik Choudhuri and Michael L Dustin. Signaling microdomains in T cells. *FEBS Lett*, 584(24), December 2010.
- [117] Jane C. Stinchcombe, Giovanna Bossi, Sarah Booth, and Gillian M. Griffiths. The Immunological Synapse of CTL Contains a Secretory Domain and Membrane Bridges. *Immunity*, 15(5):751–761, November 2001.
- [118] Jeffrey Combs, Soo Jin Kim, Sarah Tan, Lee A. Ligon, Erika L. F. Holzbaur, Jeffrey Kuhn, and Martin Poenie. Recruitment of dynein to the Jurkat immunological synapse. *Proc. Natl. Acad. Sci. U.S.A.*, 103(40):14883–14888, October 2006.
- [119] Akiko Hashimoto-Tane, Tadashi Yokosuka, Kumiko Sakata-Sogawa, Machie Sakuma, Chitose Ishihara, Makio Tokunaga, and Takashi Saito. Dynein-Driven Transport of T Cell Receptor Microclusters Regulates Immune Synapse Formation and T Cell Activation. *Immunity*, 34(6):919–931, June 2011.
- [120] Nirdosh Dadwal, Charlie Mix, Annegret Reinhold, Amelie Witte, Christian Freund, Burkhard Schraven, and Stefanie Kliche. The Multiple Roles of the Cytosolic Adapter Proteins ADAP, SKAP1 and SKAP2 for TCR/CD3 -Mediated Signaling Events. *Frontiers in Immunology*, 12, 2021.
- [121] Jane C. Stinchcombe and Gillian M. Griffiths. Communication, the centrosome and the immunological synapse. *Philos Trans R Soc Lond B Biol Sci*, 369(1650), September 2014.
- [122] Liedewij Laan, Nenad Pavin, Julien Husson, Guillaume Romet-Lemonne, Martijn van Duijn, Magdalena Preciado López, Ronald D. Vale, Frank Jülicher, Samara L. Reck-Peterson, and Marileen Dogterom. Cortical dynein controls microtubule dynamics to generate pulling forces that position microtubule asters. *Cell*, 148(3):502–514, February 2012.
- [123] Ariel Quintana, Christian Schwindling, Anna S. Wenning, Ute Becherer, Jens Rettig, Eva C. Schwarz, and Markus Hoth. T cell activation requires mitochondrial translocation to the immunological synapse. *Proc Natl Acad Sci USA*, 104(36):14418–14423, September 2007.
- [124] T. A. Lyubchenko, G. A. Wurth, and A. Zweifach. Role of calcium influx in cytotoxic T lymphocyte lytic granule exocytosis during target cell killing. *Immunity*, 15(5):847–859, November 2001.
- [125] Stephan M Feller. Early beginnings - the emergence of complex signaling systems and cell-to-cell communication. *Cell Commun Signal*, 8:16, July 2010.
- [126] Kristin Wuichet and Igor B. Zhulin. Origins and diversification of a complex signal transduction system in prokaryotes. *Sci Signal*, 3(128):ra50, June 2010.
- [127] Alex L. Sessions, David M. Doughty, Paula V. Welander, Roger E. Summons, and Dianne K. Newman. The Continuing Puzzle of the Great Oxidation Event. *Current Biology*, 19(14):R567–R574, July 2009.
-

- [128] Abderrazak El Albani, Stefan Bengtson, Donald E. Canfield, Andrey Bekker, Roberto Macchiarelli, Arnaud Mazurier, Emma U. Hammarlund, Philippe Boulvais, Jean-Jacques Dupuy, Claude Fontaine, Franz T. Fürsich, François Gauthier-Lafaye, Philippe Janvier, Emmanuelle Javaux, Frantz Ossa Ossa, Anne-Catherine Pierson-Wickmann, Armelle Riboulleau, Paul Sardini, Daniel Vachard, Martin Whitehouse, and Alain Meunier. Large colonial organisms with coordinated growth in oxygenated environments 2.1 Gyr ago. *Nature*, 466(7302):100–104, July 2010.
- [129] Stefan Feske, Heike Wulff, and Edward Y. Skolnik. Ion channels in innate and adaptive immunity. *Annu Rev Immunol*, 33:291–353, 2015.
- [130] Marisa Brini, Tito Cali, Denis Ottolini, and Ernesto Carafoli. Neuronal calcium signaling: function and dysfunction. *Cell Mol Life Sci*, 71(15):2787–2814, August 2014.
- [131] Xiang-Yao Li and Hiroki Toyoda. Role of leak potassium channels in pain signaling. *Brain Res Bull*, 119(Pt A):73–79, October 2015.
- [132] M. Naveen Kumar, Shivaleela Biradar, and R. L. Babu. Chapter 13 - Cell signaling and apoptosis in animals. In Sukanta Mondal and Ram Lakhani Singh, editors, *Advances in Animal Genomics*, pages 199–218. Academic Press, January 2021. ISBN 978-0-12-820595-2.
- [133] Geoffrey M. Cooper. Signaling Molecules and Their Receptors. *The Cell: A Molecular Approach*. 2nd edition, 2000.
- [134] Arathi Nair, Prashant Chauhan, Bhaskar Saha, and Katharina F. Kubatzky. Conceptual Evolution of Cell Signaling. *Int J Mol Sci*, 20(13):3292, July 2019.
- [135] Michal Cifra, Jeremy Z. Fields, and Ashkan Farhadi. Electromagnetic cellular interactions. *Progress in Biophysics and Molecular Biology*, 105(3):223–246, May 2011.
- [136] Ashkan Farhadi. Non-Chemical Distant Cellular Interactions as a potential confounder of cell biology experiments. *Frontiers in Physiology*, 5, 2014.
- [137] Kalliopi-Ioanna Kostaki, Aude Coupel-Ledru, Verity C. Bonnell, Mathilda Gustavsson, Peng Sun, Fiona J. McLaughlin, Donald P. Fraser, Deirdre H. McLachlan, Alistair M. Hetherington, Antony N. Dodd, and Keara A. Franklin. Guard Cells Integrate Light and Temperature Signals to Control Stomatal Aperture1 [OPEN]. *Plant Physiology*, 182(3):1404–1419, March 2020.
- [138] Ben Wang, Chongan Huang, Lijie Chen, Daoliang Xu, Gang Zheng, Yifei Zhou, Xiangyang Wang, and Xiaolei Zhang. The Emerging Roles of the Gaseous Signaling Molecules NO, H₂S, and CO in the Regulation of Stem Cells. *ACS Biomater. Sci. Eng.*, 6(2):798–812, February 2020.
- [139] Eric J. Miller and Sarah L. Lappin. Physiology, Cellular Receptor. In *StatPearls*. StatPearls Publishing, Treasure Island (FL), 2022.
- [140] Carl-Henrik Heldin, Benson Lu, Ron Evans, and J. Silvio Gutkind. Signals and Receptors. *Cold Spring Harb Perspect Biol*, 8(4):a005900, April 2016.
- [141] Ernesto Carafoli. The calcium-signalling saga: tap water and protein crystals. *Nat Rev Mol Cell Biol*, 4(4):326–332, April 2003.
- [142] Martin D. Bootman and Geert Bultynck. Fundamentals of Cellular Calcium Signaling: A Primer. *Cold Spring Harb Perspect Biol*, 12(1):a038802, January 2020.
- [143] Masatsugu Oh-hora and Anjana Rao. Calcium signaling in lymphocytes. *Curr Opin Immunol*, 20(3):250–258, June 2008.
- [144] P. A. Negulescu, T. B. Krasieva, A. Khan, H. H. Kerschbaum, and M. D. Cahalan. Polarity of T cell shape, motility, and sensitivity to antigen. *Immunity*, 4(5):421–430, May 1996.
- [145] Matthew E. Pipkin and Judy Lieberman. Delivering the kiss of death: progress on understanding how perforin works. *Curr Opin Immunol*, 19(3):301–308, June 2007.
- [146] David E. Clapham. Calcium Signaling. *Cell*, 131(6):1047–1058, December 2007.

-
- [147] Michael J. Berridge, Peter Lipp, and Martin D. Bootman. The versatility and universality of calcium signalling. *Nat Rev Mol Cell Biol*, 1(1):11–21, October 2000.
- [148] Marisa Brini and Ernesto Carafoli. Calcium pumps in health and disease. *Physiol Rev*, 89(4):1341–1378, October 2009.
- [149] Jordan Karlstad, Yuyang Sun, and Brij B. Singh. Ca²⁺ Signaling: An Outlook on the Characterization of Ca²⁺ Channels and Their Importance in Cellular Functions. *Adv Exp Med Biol*, 740:143–157, 2012.
- [150] Kelley Fracchia, Christine Pai, and Craig Walsh. Modulation of T Cell Metabolism and Function through Calcium Signaling. *Frontiers in Immunology*, 4, 2013.
- [151] Ernesto Carafoli. Calcium-mediated cellular signals: a story of failures. *Trends Biochem Sci*, 29(7):371–379, July 2004.
- [152] Noah Joseph, Barak Reicher, and Mira Barda-Saad. The calcium feedback loop and T cell activation: How cytoskeleton networks control intracellular calcium flux. *Biochimica et Biophysica Acta (BBA) - Biomembranes*, 1838(2):557–568, February 2014.
- [153] R. S. Lewis. Calcium signaling mechanisms in T lymphocytes. *Annu Rev Immunol*, 19:497–521, 2001.
- [154] M. B. Cannell, H. Cheng, and W. J. Lederer. The Control of Calcium Release in Heart Muscle. *Science*, 268(5213):1045–1049, May 1995.
- [155] William M. Roberts. Spatial calcium buffering in saccular hair cells. *Nature*, 363(6424):74–76, May 1993.
- [156] Martin Peglow, Barbara A. Niemeyer, Markus Hoth, and Heiko Rieger. Interplay of channels, pumps and organelle location in calcium microdomain formation. *New J. Phys.*, 15(5):055022, May 2013.
- [157] Andrea Maul-Pavicic, Samuel C. C. Chiang, Anne Rensing-Ehl, Birthe Jessen, Cyril Fauriat, Stephanie M. Wood, Sebastian Sjöqvist, Markus Hufnagel, Ilka Schulze, Thilo Bass, Wolfgang W. Schamel, Sebastian Fuchs, Hanspeter Pircher, Christie-Ann McCarl, Katsuhiko Mikoshiba, Klaus Schwarz, Stefan Feske, Yanan T. Bryceson, and Stephan Ehl. ORAI1-mediated calcium influx is required for human cytotoxic lymphocyte degranulation and target cell lysis. *Proc Natl Acad Sci USA*, 108(8):3324–3329, February 2011.
- [158] Eva C. Schwarz, Bin Qu, and Markus Hoth. Calcium, cancer and killing: the role of calcium in killing cancer cells by cytotoxic T lymphocytes and natural killer cells. *Biochim Biophys Acta*, 1833(7):1603–1611, July 2013.
- [159] Gerardo R. Corradi, Luciana R. Mazzitelli, Guido D. Petrovich, Felicitas de Tezanos Pinto, Lucia Rochi, and Hugo P. Adamo. Plasma Membrane Ca²⁺ Pump PMCA4z Is More Active Than Splicing Variant PMCA4x. *Frontiers in Cellular Neuroscience*, 15, 2021.
- [160] Ariel Quintana, Mathias Pasche, Christian Junker, Dalia Al-Ansary, Heiko Rieger, Carsten Kummerow, Lucia Nuñez, Carlos Villalobos, Paul Meraner, Ute Becherer, Jens Rettig, Barbara A. Niemeyer, and Markus Hoth. Calcium microdomains at the immunological synapse: how ORAI channels, mitochondria and calcium pumps generate local calcium signals for efficient T-cell activation. *EMBO J*, 30(19):3895–3912, August 2011.
- [161] Michael C. Ashby and Alexei V. Tepikin. ER calcium and the functions of intracellular organelles. *Seminars in Cell & Developmental Biology*, 12(1):11–17, February 2001.
- [162] J. Meldolesi and T. Pozzan. The endoplasmic reticulum Ca²⁺ store: a view from the lumen. *Trends Biochem Sci*, 23(1):10–14, January 1998.
- [163] Elzbieta Kania, Gemma Roest, Tim Vervliet, Jan B. Parys, and Geert Bultynck. IP3 Receptor-Mediated Calcium Signaling and Its Role in Autophagy in Cancer. *Front Oncol*, 7:140, July 2017.
-

- [164] Nagendra Babu Thillaiappan, Pragnya Chakraborty, Gaiti Hasan, and Colin W. Taylor. IP₃ receptors and Ca²⁺ entry. *Biochimica et Biophysica Acta (BBA) - Molecular Cell Research*, 1866(7):1092–1100, July 2019.
- [165] David L. Prole and Colin W. Taylor. Structure and Function of IP₃ Receptors. *Cold Spring Harb Perspect Biol*, 11(4):a035063, April 2019.
- [166] Murali Prakriya and Richard S. Lewis. Store-Operated Calcium Channels. *Physiol Rev*, 95(4):1383–1436, October 2015.
- [167] Andrew N. Stammers, Shanel E. Susser, Naomi C. Hamm, Michael W. Hlynsky, Dustin E. Kimber, D. Scott Kehler, and Todd A. Duhamel. The regulation of sarco(endo)plasmic reticulum calcium-ATPases (SERCA). *Can J Physiol Pharmacol*, 93(10):843–854, October 2015.
- [168] A. Zweifach and R. S. Lewis. Rapid inactivation of depletion-activated calcium current (ICRAC) due to local calcium feedback. *J Gen Physiol*, 105(2):209–226, February 1995.
- [169] Ariel Quintana, Eva C. Schwarz, Christian Schwindling, Peter Lipp, Lars Kaestner, and Markus Hoth. Sustained activity of calcium release-activated calcium channels requires translocation of mitochondria to the plasma membrane. *J Biol Chem*, 281(52):40302–40309, December 2006.
- [170] Juan A. Gilabert and Anant B. Parekh. Respiring mitochondria determine the pattern of activation and inactivation of the store-operated Ca²⁺ current ICRAC. *EMBO J*, 19(23):6401–6407, December 2000.
- [171] Thomas E. Gartner and Arthi Jayaraman. Modeling and Simulations of Polymers: A Roadmap. *Macromolecules*, 52(3):755–786, February 2019.
- [172] Gerald Karp. *Cell and Molecular Biology: Concepts and Experiments*. John Wiley & Sons, October 2009. ISBN 978-0-470-48337-4.
- [173] Bruce Alberts, Alexander Johnson, Julian Lewis, Martin Raff, Keith Roberts, and Peter Walter. *Molecular Biology of the Cell, 5th Edition*. New York, 5th edition edition, November 2007. ISBN 978-0-8153-4105-5.
- [174] Bruce Alberts, Alexander Johnson, Julian Lewis, Martin Raff, Keith Roberts, and Peter Walter. Molecular Motors. *Molecular Biology of the Cell. 4th edition*, 2002.
- [175] T Vellai and G Vida. The origin of eukaryotes: the difference between prokaryotic and eukaryotic cells. *Proc Biol Sci*, 266(1428):1571–1577, August 1999.
- [176] Benjamin M. Skinner and Emma E. P. Johnson. Nuclear morphologies: their diversity and functional relevance. *Chromosoma*, 126(2):195–212, 2017.
- [177] Patries M. Herst, Matthew R. Rowe, Georgia M. Carson, and Michael V. Berridge. Functional Mitochondria in Health and Disease. *Frontiers in Endocrinology*, 8, 2017.
- [178] Dianne S. Schwarz and Michael D. Blower. The endoplasmic reticulum: structure, function and response to cellular signaling. *Cell Mol Life Sci*, 73:79–94, 2016.
- [179] Emily M. Lynes and Thomas Simmen. Urban planning of the endoplasmic reticulum (ER): How diverse mechanisms segregate the many functions of the ER. *Biochimica et Biophysica Acta (BBA) - Molecular Cell Research*, 1813(10):1893–1905, October 2011.
- [180] Yoko Shibata, Gia K. Voeltz, and Tom A. Rapoport. Rough sheets and smooth tubules. *Cell*, 126(3):435–439, August 2006.
- [181] Pramod A. Pullarkat, Pablo A. Fernández, and Albrecht Ott. Rheological properties of the Eukaryotic cell cytoskeleton. *Physics Reports*, 449(1):29–53, September 2007.
- [182] Elisa Sanchez, Xin Liu, and Morgan Huse. Actin clearance promotes polarized dynein accumulation at the immunological synapse. *PLOS ONE*, 14(7):e0210377, March 2019.

-
- [183] Roberto Dominguez and Kenneth C. Holmes. Actin Structure and Function. *Annu Rev Biophys*, 40: 169–186, June 2011.
- [184] Geoffrey M. Cooper. Structure and Organization of Actin Filaments. *The Cell: A Molecular Approach*. 2nd edition, 2000.
- [185] Geoffrey M. Cooper. Intermediate Filaments. *The Cell: A Molecular Approach*. 2nd edition, 2000.
- [186] K. M. Bernot and P. A. Coulombe. Intermediate Filaments. In William J. Lennarz and M. Daniel Lane, editors, *Encyclopedia of Biological Chemistry (Second Edition)*, pages 631–636. Academic Press, Waltham, January 2013. ISBN 978-0-12-378631-9.
- [187] F. Huber, J. Schnauß, S. Rönicke, P. Rauch, K. Müller, C. Fütterer, and J. Käs. Emergent complexity of the cytoskeleton: from single filaments to tissue. *Adv Phys*, 62(1):1–112, January 2013.
- [188] Harvey Lodish, Arnold Berk, S. Lawrence Zipursky, Paul Matsudaira, David Baltimore, and James Darnell. Microtubule Structures. *Molecular Cell Biology*. 4th edition, 2000.
- [189] M. G. L. Van den Heuvel, M. P. de Graaff, and C. Dekker. Microtubule curvatures under perpendicular electric forces reveal a low persistence length. *Proc Natl Acad Sci USA*, 105(23):7941–7946, June 2008.
- [190] Martin Breuss and David A. Keays. Microtubules and Neurodevelopmental Disease: The Movers and the Makers. In Laurent Nguyen and Simon Hippenmeyer, editors, *Cellular and Molecular Control of Neuronal Migration*, volume 800, pages 75–96. Springer Netherlands, Dordrecht, 2014. ISBN 978-94-007-7686-9 978-94-007-7687-6.
- [191] E. De Robertis and C. M. Franchi. The submicroscopic organization of axon material isolated from myelin nerve fibers. *Journal of Experimental Medicine*, 98(3):269–276, September 1953.
- [192] S. L. Palay. Synapses in the central nervous system. *J Biophys Biochem Cytol*, 2(4):193–202, July 1956.
- [193] David B. Slautterback. Cytoplasmic Microtubules : I. Hydra. *Journal of Cell Biology*, 18(2):367–388, August 1963.
- [194] Guy de Thé. Cytoplasmic Microtubules in Different Animal Cells. *Journal of Cell Biology*, 23(2): 265–275, November 1964.
- [195] M. C. Ledbetter and K. R. Porter. A "Microtubule" in Plant Cell Fine Structure. *Journal of Cell Biology*, 19(1):239–250, October 1963.
- [196] William A. Wells. Microtubules get a name. *Journal of Cell Biology*, 168(6):852–853, March 2005.
- [197] M. C. Ledbetter and K. R. Porter. Morphology of Microtubules of Plant Cell. *Science*, 144(3620): 872–874, May 1964.
- [198] Hideo Mohri. Amino-acid Composition of "Tubulin" constituting Microtubules of Sperm Flagella. *Nature*, 217(5133):1053–1054, March 1968.
- [199] M. L. Shelanski and E. W. Taylor. Isolation of a Protein Subunit from Microtubules. *Journal of Cell Biology*, 34(2):549–554, August 1967.
- [200] R. E. Stephens. Thermal fractionation of outer fiber doublet microtubules into A- and B-subfiber components. A- and B-tubulin. *J Mol Biol*, 47(3):353–363, February 1970.
- [201] M. Chalfie and J. N. Thomson. Structural and functional diversity in the neuronal microtubules of *Caenorhabditis elegans*. *J Cell Biol*, 93(1):15–23, April 1982.
- [202] Taviare Hawkins, Matthew Mirigian, M. Selcuk Yasar, and Jennifer L. Ross. Mechanics of microtubules. *J Biomech*, 43(1):23–30, January 2010.
- [203] R. B. Dye, S. P. Fink, and R. C. Williams. Taxol-induced flexibility of microtubules and its reversal by MAP-2 and Tau. *Journal of Biological Chemistry*, 268(10):6847–6850, April 1993.
-

- [204] P. Venier, A. C. Maggs, M. F. Carlier, and D. Pantaloni. Analysis of microtubule rigidity using hydrodynamic flow and thermal fluctuations. *Journal of Biological Chemistry*, 269(18):13353–13360, May 1994.
- [205] J. C. Kurz and R. C. Williams. Microtubule-associated proteins and the flexibility of microtubules. *Biochemistry*, 34(41):13374–13380, October 1995.
- [206] M. Kurachi, M. Hoshi, and H. Tashiro. Buckling of a single microtubule by optical trapping forces: direct measurement of microtubule rigidity. *Cell Motil Cytoskeleton*, 30(3):221–228, 1995.
- [207] H. Felgner, R. Frank, and M. Schliwa. Flexural rigidity of microtubules measured with the use of optical tweezers. *Journal of Cell Science*, 109(2):509–516, February 1996.
- [208] Harald Felgner, Rainer Frank, Jacek Biernat, Eva-Maria Mandelkow, Eckhard Mandelkow, Beat Ludin, Andrew Matus, and Manfred Schliwa. Domains of Neuronal Microtubule-associated Proteins and Flexural Rigidity of Microtubules. *J Cell Biol*, 138(5):1067–1075, September 1997.
- [209] Toru Takasone, Saulius Juodkazis, Yuji Kawagishi, Akira Yamaguchi, Shigeki Matsuo, Hitoshi Sakakibara, Haruto Nakayama, and Hiroaki Misawa. Flexural Rigidity of a Single Microtubule. *Jpn. J. Appl. Phys.*, 41:3015–3019, May 2002.
- [210] Marcel E. Janson and Marileen Dogterom. A Bending Mode Analysis for Growing Microtubules: Evidence for a Velocity-Dependent Rigidity. *Biophysical Journal*, 87(4):2723–2736, October 2004.
- [211] P. J. de Pablo, I. a. T. Schaap, F. C. MacKintosh, and C. F. Schmidt. Deformation and collapse of microtubules on the nanometer scale. *Phys Rev Lett*, 91(9):098101, August 2003.
- [212] Iwan A. T. Schaap, Carolina Carrasco, Pedro J. de Pablo, Frederick C. MacKintosh, and Christoph F. Schmidt. Elastic Response, Buckling, and Instability of Microtubules under Radial Indentation. *Biophysical Journal*, 91(4):1521–1531, August 2006.
- [213] Taviare L. Hawkins, David Sept, Binyam Mogessie, Anne Straube, and Jennifer L. Ross. Mechanical Properties of Doubly Stabilized Microtubule Filaments. *Biophysical Journal*, 104(7):1517, April 2013.
- [214] Kenji Kawaguchi and Atsushi Yamaguchi. Temperature dependence rigidity of non-taxol stabilized single microtubules. *Biochem Biophys Res Commun*, 402(1):66–69, November 2010.
- [215] Lukasz Szatkowski, Dale R. Merz, Nan Jiang, Ifunanya Ejikeme, Liudmila Belonogov, Jennifer L. Ross, and Ruxandra I. Dima. Mechanics of the Microtubule Seam Interface Probed by Molecular Simulations and in Vitro Severing Experiments. *J. Phys. Chem. B*, 123(23):4888–4900, June 2019.
- [216] Robert A Cross. Microtubule lattice plasticity. *Current Opinion in Cell Biology*, 56:88–93, February 2019.
- [217] Hang Zhou, Naoto Isozaki, Kazuya Fujimoto, and Ryuji Yokokawa. Growth rate-dependent flexural rigidity of microtubules influences pattern formation in collective motion. *Journal of Nanobiotechnology*, 19(1):218, July 2021.
- [218] Jinyin Zha, Yuwei Zhang, Kelin Xia, Frauke Gräter, and Fei Xia. Coarse-Grained Simulation of Mechanical Properties of Single Microtubules With Micrometer Length. *Frontiers in Molecular Biosciences*, 7, 2021.
- [219] C. Janke and M. Magiera. The tubulin code and its role in controlling microtubule properties and functions. *Nature Reviews Molecular Cell Biology*, 2020.
- [220] Junko Mizushima-Sugano, Tadakazu Maeda, and Taiko Miki-Noumura. Flexural rigidity of singlet microtubules estimated from statistical analysis of their contour lengths and end-to-end distances. *Biochimica et Biophysica Acta (BBA) - General Subjects*, 755(2):257–262, January 1983.
- [221] Mahito Kikumoto, Masashi Kurachi, Valer Tosa, and Hideo Tashiro. Flexural Rigidity of Individual Microtubules Measured by a Buckling Force with Optical Traps. *Biophys J*, 90(5):1687–1696, March 2006.

-
- [222] Joost van Mameren, Karen C. Vermeulen, Fred Gittes, and Christoph F. Schmidt. Leveraging Single Protein Polymers To Measure Flexural Rigidity. *J. Phys. Chem. B*, 113(12):3837–3844, March 2009.
- [223] M. G. L. van den Heuvel, S. Bolhuis, and C. Dekker. Persistence length measurements from stochastic single-microtubule trajectories. *Nano Lett*, 7(10):3138–3144, October 2007.
- [224] B. Mickey and J. Howard. Rigidity of microtubules is increased by stabilizing agents. *J Cell Biol*, 130(4):909–917, August 1995.
- [225] M. Dogterom and B. Yurke. Measurement of the force-velocity relation for growing microtubules. *Science*, 278(5339):856–860, October 1997.
- [226] Lynne Cassimeris, David Gard, P. T. Tran, and Harold P. Erickson. XMAP215 is a long thin molecule that does not increase microtubule stiffness. *Journal of Cell Science*, 114(16):3025–3033, August 2001.
- [227] Marcel E. Janson and Marileen Dogterom. Scaling of microtubule force-velocity curves obtained at different tubulin concentrations. *Phys Rev Lett*, 92(24):248101, June 2004.
- [228] Clifford P. Brangwynne, Gijsje H. Koenderink, Ed Barry, Zvonimir Dogic, Frederick C. MacKintosh, and David A. Weitz. Bending Dynamics of Fluctuating Biopolymers Probed by Automated High-Resolution Filament Tracking. *Biophys J*, 93(1):346–359, July 2007.
- [229] Kenji Kawaguchi, Shin’ichi Ishiwata, and Toshihide Yamashita. Temperature dependence of the flexural rigidity of single microtubules. *Biochem Biophys Res Commun*, 366(3):637–642, February 2008.
- [230] Francesco Pampaloni, Gianluca Lattanzi, Alexandr Jonáš, Thomas Surrey, Erwin Frey, and Ernst-Ludwig Florin. Thermal fluctuations of grafted microtubules provide evidence of a length-dependent persistence length. *Proceedings of the National Academy of Sciences*, 103(27):10248–10253, July 2006.
- [231] Matthew B. Smith, Hongsheng Li, Tian Shen, Xiaolei Huang, Eddy Yusuf, and Dimitrios Vavylonis. Segmentation and tracking of cytoskeletal filaments using open active contours. *Cytoskeleton (Hoboken)*, 67(11):693–705, November 2010.
- [232] Hideyo Takatsuki, Elina Bengtsson, and Alf Månsson. Persistence length of fascin-cross-linked actin filament bundles in solution and the in vitro motility assay. *Biochimica et Biophysica Acta (BBA) - General Subjects*, 1840(6):1933–1942, June 2014.
- [233] Pattipong Wisanpitayakorn, Keith J. Mickolajczyk, William O. Hancock, Luis Vidali, and Erkan Tüzel. Measurement of the persistence length of cytoskeletal filaments using curvature distributions. *Biophysical Journal*, 121(10):1813–1822, May 2022.
- [234] May Sweet, Samuel Macharia Kang’iri, and Takahiro Nitta. Linking path and filament persistence lengths of microtubules gliding over kinesin. *Sci Rep*, 12(1):3081, February 2022.
- [235] Arif Md. Rashedul Kabir, Tasrina Munmun, Tomohiko Hayashi, Satoshi Yasuda, Atsushi P. Kimura, Masahiro Kinoshita, Takeshi Murata, Kazuki Sada, and Akira Kakugo. Controlling the Rigidity of Kinesin-Propelled Microtubules in an In Vitro Gliding Assay Using the Deep-Sea Osmolyte Trimethylamine N-Oxide. *ACS Omega*, 7(4):3796–3803, February 2022.
- [236] Anja Vinckier, Chantal Dumortier, Yves Engelborghs, and Louis Hellemans. Dynamical and mechanical study of immobilized microtubules with atomic force microscopy. *Journal of Vacuum Science & Technology B: Microelectronics and Nanometer Structures Processing, Measurement, and Phenomena*, 14(2):1427–1431, March 1996.
- [237] A. Kis, S. Kasas, B. Babić, A. J. Kulik, W. Benoît, G. a. D. Briggs, C. Schönenberger, S. Catsicas, and L. Forró. Nanomechanics of microtubules. *Phys Rev Lett*, 89(24):248101, December 2002.
- [238] A. Kis, S. Kasas, A. J. Kulik, S. Catsicas, and L. Forró. Temperature-dependent elasticity of microtubules. *Langmuir*, 24(12):6176–6181, June 2008.
-

- [239] Sandor Kasas, András Kis, Beat Michel Riederer, László Forró, Giovanni Dietler, and Stefan Catsicas. Mechanical Properties of Microtubules Explored Using the Finite Elements Method. *ChemPhysChem*, 5(2):252–257, 2004.
- [240] E. Mandelkow and E. M. Mandelkow. Microtubules and microtubule-associated proteins. *Curr Opin Cell Biol*, 7(1):72–81, February 1995.
- [241] Hugo Bowne-Anderson, Marija Zanic, Monika Kauer, and Jonathon Howard. Microtubule dynamic instability: A new model with coupled GTP hydrolysis and multistep catastrophe. *Bioessays*, 35(5):452–461, May 2013.
- [242] S. Ozon, A. Maucuer, and A. Sobel. The stathmin family – molecular and biological characterization of novel mammalian proteins expressed in the nervous system. *Eur J Biochem*, 248(3):794–806, September 1997.
- [243] Pelin Ayaz, Xuecheng Ye, Patrick Huddleston, Chad A. Brautigam, and Luke M. Rice. A TOG: $\alpha\beta$ -tubulin Complex Structure Reveals Conformation-Based Mechanisms For a Microtubule Polymerase. *Science*, 337(6096):857–860, August 2012.
- [244] Ludovic Pecqueur, Christian Duellberg, Birgit Dreier, Qiyang Jiang, Chunguang Wang, Andreas Plückthun, Thomas Surrey, Benoît Gigant, and Marcel Knossow. A designed ankyrin repeat protein selected to bind to tubulin caps the microtubule plus end. *Proc Natl Acad Sci USA*, 109(30):12011–12016, July 2012.
- [245] W. A. Voter, E. T. O’Brien, and H. P. Erickson. Dilution-induced disassembly of microtubules: relation to dynamic instability and the GTP cap. *Cell Motil Cytoskeleton*, 18(1):55–62, 1991.
- [246] Alexander James Zwetsloot, Gokhan Tut, and Anne Straube. Measuring microtubule dynamics. *Essays Biochem*, 62(6):725–735, October 2018.
- [247] Ariane Dimitrov, Mélanie Quesnoit, Sandrine Moutel, Isabelle Cantaloube, Christian Poüs, and Franck Perez. Detection of GTP-tubulin conformation in vivo reveals a role for GTP remnants in microtubule rescues. *Science*, 322(5906):1353–1356, November 2008.
- [248] Norio Yamashita, Masahiko Morita, Wesley R. Legant, Bi-Chang Chen, Eric Betzig, Hideo Yokota, and Yuko Mimori-Kiyosue. Three-dimensional tracking of plus-tips by lattice light-sheet microscopy permits the quantification of microtubule growth trajectories within the mitotic apparatus. *JBO*, 20(10):101206, November 2015.
- [249] Jennifer S. Tirnauer, Eileen O’Toole, Lisbeth Berrueta, Barbara E. Bierer, and David Pellman. Yeast Bim1p Promotes the G1-specific Dynamics of Microtubules. *J Cell Biol*, 145(5):993–1007, May 1999.
- [250] Yulia A. Komarova, Ivan A. Vorobjev, and Gary G. Borisy. Life cycle of MTs: persistent growth in the cell interior, asymmetric transition frequencies and effects of the cell boundary. *Journal of Cell Science*, 115(17):3527–3539, September 2002.
- [251] Irina B. Alieva, Evgeny A. Zemskov, Igor I. Kireev, Boris A. Gorshkov, Dean A. Wiseman, Stephen M. Black, and Alexander D. Verin. Microtubules Growth Rate Alteration in Human Endothelial Cells, 2010.
- [252] D. Brunner and P. Nurse. CLIP170-like tip1p spatially organizes microtubular dynamics in fission yeast. *Cell*, 102(5):695–704, September 2000.
- [253] Nasser M. Rusan, Carey J. Fagerstrom, Anne-Marie C. Yvon, and Patricia Wadsworth. Cell Cycle-Dependent Changes in Microtubule Dynamics in Living Cells Expressing Green Fluorescent Protein- α Tubulin. *Mol Biol Cell*, 12(4):971–980, April 2001.
- [254] L. Cassimeris, N. K. Pryer, and E. D. Salmon. Real-time observations of microtubule dynamic instability in living cells. *J. Cell Biol.*, 107(6 Pt 1):2223–2231, December 1988.
- [255] Paul J. Sammak and Gary G. Borisy. Direct observation of microtubule dynamics in living cells. *Nature*, 332(6166):724–726, April 1988.

-
- [256] L. D. Belmont, A. A. Hyman, K. E. Sawin, and T. J. Mitchison. Real-time visualization of cell cycle-dependent changes in microtubule dynamics in cytoplasmic extracts. *Cell*, 62(3):579–589, August 1990.
- [257] G. Steinberg, R. Wedlich-Soldner, M. Brill, and I. Schulz. Microtubules in the fungal pathogen *Ustilago maydis* are highly dynamic and determine cell polarity. *Journal of Cell Science*, 114(3):609–622, February 2001.
- [258] A. M. Yvon and P. Wadsworth. Non-centrosomal microtubule formation and measurement of minus end microtubule dynamics in A498 cells. *Journal of Cell Science*, 110(19):2391–2401, October 1997.
- [259] J. L. Carminati and T. Stearns. Microtubules orient the mitotic spindle in yeast through dynein-dependent interactions with the cell cortex. *J. Cell Biol.*, 138(3):629–641, August 1997.
- [260] N. R. Adames and J. A. Cooper. Microtubule interactions with the cell cortex causing nuclear movements in *Saccharomyces cerevisiae*. *J. Cell Biol.*, 149(4):863–874, May 2000.
- [261] D. R. Drummond and R. A. Cross. Dynamics of interphase microtubules in *Schizosaccharomyces pombe*. *Curr. Biol.*, 10(13):766–775, June 2000.
- [262] Daniël Van Damme, Kris Van Poucke, Emmanuel Boutant, Christophe Ritzenthaler, Dirk Inzé, and Danny Geelen. In Vivo Dynamics and Differential Microtubule-Binding Activities of MAP65 Proteins. *Plant Physiol*, 136(4):3956–3967, December 2004.
- [263] Anastasiya Trushko, Erik Schäffer, and Jonathon Howard. The growth speed of microtubules with XMAP215-coated beads coupled to their ends is increased by tensile force. *PNAS*, 110(36):14670–14675, September 2013.
- [264] E Shelden and P Wadsworth. Observation and quantification of individual microtubule behavior in vivo: microtubule dynamics are cell-type specific. *Journal of Cell Biology*, 120(4):935–945, February 1993.
- [265] Dynamic instability of individual microtubules analyzed by video light microscopy: rate constants and transition frequencies. *J Cell Biol*, 107(4):1437–1448, October 1988.
- [266] Colby P. Fees and Jeffrey K. Moore. A unified model for microtubule rescue. *MBoC*, 30(6):753–765, January 2019.
- [267] Christian Tischer, Damian Brunner, and Marileen Dogterom. Force- and kinesin-8-dependent effects in the spatial regulation of fission yeast microtubule dynamics. *Mol Syst Biol*, 5:250, March 2009.
- [268] Laura Schaedel, Sarah Triclin, Denis Chrétien, Ariane Abrieu, Charlotte Aumeier, Jérémie Gaillard, Laurent Blanchoin, Manuel Théry, and Karin John. Lattice defects induce microtubule self-renewal. *Nat. Phys.*, 15(8):830–838, August 2019.
- [269] Yue Ma, Yuxiang Wang, Xuejian Deng, Guanggang Zhou, Sha Khalid, Xiaoliang Sun, Wei Sun, Qiong Zhou, and Guiwu Lu. Dissipative particle dynamics and molecular dynamics simulations on mesoscale structure and proton conduction in a SPEEK/PVDF-g-PSSA membrane. *RSC Adv.*, 7(63):39676–39684, August 2017.
- [270] Theodora Spyriouni and Caroll Vergelati. A Molecular Modeling Study of Binary Blend Compatibility of Polyamide 6 and Poly(vinyl acetate) with Different Degrees of Hydrolysis: An Atomistic and Mesoscopic Approach. *Macromolecules*, 34(15):5306–5316, July 2001.
- [271] Zhonglin Luo, Liling Zhang, and Jianwen Jiang. Atomistic insight into micro-phase separation and gas diffusion in PEO–PBT multiblock copolymers. *Molecular Simulation*, 39(11):902–907, September 2013.
- [272] Chun-Lai Ren, Issei Nakamura, and Zhen-Gang Wang. Effects of Ion-Induced Cross-Linking on the Phase Behavior in Salt-Doped Polymer Blends. *Macromolecules*, 49(1):425–431, January 2016.
- [273] Venkat Ganesan and Arthi Jayaraman. Theory and simulation studies of effective interactions, phase behavior and morphology in polymer nanocomposites. *Soft Matter*, 10(1):13–38, November 2013.
-

- [274] Alexander Kyrychenko, Oleksandr M. Korsun, Iurii I. Gubin, Sergiy M. Kovalenko, and Oleg N. Kalugin. Atomistic Simulations of Coating of Silver Nanoparticles with Poly(vinylpyrrolidone) Oligomers: Effect of Oligomer Chain Length. *J. Phys. Chem. C*, 119(14):7888–7899, April 2015.
- [275] D. Brown, P. Mélé, S. Marceau, and N. D. Albérola. A Molecular Dynamics Study of a Model Nanoparticle Embedded in a Polymer Matrix. *Macromolecules*, 36(4):1395–1406, February 2003.
- [276] Hossein Eslami and Florian Müller-Plathe. Molecular Dynamics Simulation of Sorption of Gases in Polystyrene. *Macromolecules*, 40(17):6413–6421, August 2007.
- [277] Jordan H. Hristov, Stephen J. Paddison, and Reginald Paul. Molecular Modeling of Proton Transport in the Short-Side-Chain Perfluorosulfonic Acid Ionomer. *J. Phys. Chem. B*, 112(10):2937–2949, March 2008.
- [278] Keran Lu, Joseph F. Rudzinski, W. G. Noid, Scott T. Milner, and Janna K. Maranas. Scaling behavior and local structure of ion aggregates in single-ion conductors. *Soft Matter*, 10(7):978–989, January 2014.
- [279] Paul K. Weiner and Peter A. Kollman. AMBER: Assisted model building with energy refinement. A general program for modeling molecules and their interactions. *Journal of Computational Chemistry*, 2(3):287–303, 1981.
- [280] Bernard R. Brooks, Robert E. Bruccoleri, Barry D. Olafson, David J. States, S. Swaminathan, and Martin Karplus. CHARMM: A program for macromolecular energy, minimization, and dynamics calculations. *Journal of Computational Chemistry*, 4(2):187–217, 1983.
- [281] K. M. Liew, Ping Xiang, and L. W. Zhang. Mechanical properties and characteristics of microtubules: A review. *Composite Structures*, 123:98–108, May 2015.
- [282] J. A. Tuszyński, T. Luchko, S. Portet, and J. M. Dixon. Anisotropic elastic properties of microtubules. *Eur Phys J E Soft Matter*, 17(1):29–35, May 2005.
- [283] J. Tuszyński, J. Brown, E. Crawford, E. Carpenter, M. Nip, J. Dixon, and M. Sataric. Molecular dynamics simulations of tubulin structure and calculations of electrostatic properties of microtubules. *Math. Comput. Model.*, 2005.
- [284] David B. Wells and Aleksei Aksimentiev. Mechanical properties of a complete microtubule revealed through molecular dynamics simulation. *Biophys J*, 99(2):629–637, July 2010.
- [285] M. Deriu, S. Enemark, M. Soncini, F. Montevocchi, and A. Redaelli. Tubulin: from atomistic structure to supramolecular mechanical properties. 2007.
- [286] Daniel Havelka, Marco A. Deriu, Michal Cifra, and Ondřej Kučera. Deformation pattern in vibrating microtubule: Structural mechanics study based on an atomistic approach. *Sci Rep*, 7(1):4227, June 2017.
- [287] Dudu Tong and Gregory A. Voth. Microtubule Simulations Provide Insight into the Molecular Mechanism Underlying Dynamic Instability. *Biophys J*, 118(12):2938–2951, June 2020.
- [288] Vagelis A. Harmandaris and Kurt Kremer. Predicting polymer dynamics at multiple length and time scales. *Soft Matter*, 5(20):3920–3926, October 2009.
- [289] José G. Solano Canchaya, Alain Dequidt, Sebastien Garruchet, Benoit Latour, Nicolas Martzel, Julien Devémy, Florent Goujon, Ronald Blaak, Benoit Schnell, Etienne Munch, Nicolas Seeboth, and Patrice Malfreyt. Development of a coarse-grain model for the description of the metal oxide-polymer interface from a bottom-up approach. *J. Chem. Phys.*, 151(6):064703, August 2019.
- [290] Florian Müller-Plathe. Coarse-Graining in Polymer Simulation: From the Atomistic to the Mesoscopic Scale and Back. *ChemPhysChem*, 3(9):754–769, 2002.
- [291] S. Nielsen, C. F. Lopez, G. Srinivas, and M. Klein. TOPICAL REVIEW: Coarse grain models and the computer simulation of soft materials. 2004.

-
- [292] Paul J. Flory. *Statistical mechanics of chain molecules*. Munich ; New York : New York, repr. ed. with corrections edition, 1989. ISBN 978-0-19-520756-9.
- [293] Patrick K. Quoika, Monica L. Fernández-Quintero, Maren Podewitz, Florian Hofer, and Klaus R. Liedl. Implementation of the Freely Jointed Chain Model to Assess Kinetics and Thermodynamics of Thermosensitive Coil–Globule Transition by Markov States. *J. Phys. Chem. B*, 125(18):4898–4909, May 2021.
- [294] Jörg Baschnagel, Hendrik Meyer, Joachim Wittmer, Igor Kulić, Hervé Mohrbach, Falko Ziebert, Gi-Moon Nam, Nam-Kyung Lee, and Albert Johner. Semiflexible Chains at Surfaces: Worm-Like Chains and beyond. *Polymers*, 8(8):286, August 2016.
- [295] John F. Marko and Eric D. Siggia. Stretching DNA. *Macromolecules*, 28(26):8759–8770, December 1995.
- [296] Ruizheng Hou, Nan Wang, Weizhu Bao, and Zhisong Wang. Polymer-Based Accurate Positioning: An Exact Worm-like-Chain Study. *ACS Omega*, 3(10):14318–14326, October 2018.
- [297] S. W. Fetsko and P. T. Cummings. Brownian dynamics simulation of bead–spring chain models for dilute polymer solutions in elongational flow. *Journal of Rheology*, 39(2):285–299, March 1995.
- [298] Patrick T. Underhill and Patrick S. Doyle. On the coarse-graining of polymers into bead-spring chains. *Journal of Non-Newtonian Fluid Mechanics*, 122(1-3):3–31, September 2004.
- [299] J. M. Wiest and R. I. Tanner. Rheology of Bead-NonLinear Spring Chain Macromolecules. *Journal of Rheology*, 33(2):281–316, February 1989.
- [300] Chih-Chen Hsieh, Semant Jain, and Ronald G. Larson. Brownian dynamics simulations with stiff finitely extensible nonlinear elastic-Fraenkel springs as approximations to rods in bead-rod models. *J. Chem. Phys.*, 124(4):044911, January 2006.
- [301] J. Kierfeld, O. Niamploy, V. Sa-yakanit, and R. Lipowsky. Stretching of semiflexible polymers with elastic bonds. *Eur Phys J E Soft Matter*, 14(1):17–34, May 2004.
- [302] Ruxandra I. Dima and Harshad Joshi. Probing the origin of tubulin rigidity with molecular simulations. *Proceedings of the National Academy of Sciences*, 105(41):15743–15748, October 2008.
- [303] Marco A. Deriu, Monica Soncini, Mario Orsi, Mishal Patel, Jonathan W. Essex, Franco M. Monteverchi, and Alberto Redaelli. Anisotropic Elastic Network Modeling of Entire Microtubules. *Biophys J*, 99(7):2190–2199, October 2010.
- [304] Kelly E. Theisen, Neha J. Desai, Allison M. Volski, and Ruxandra I. Dima. Mechanics of severing for large microtubule complexes revealed by coarse-grained simulations. *J. Chem. Phys.*, 139(12):121926, September 2013.
- [305] Carole Lazarus, Mohammad Soheilypour, and Mohammad R.K. Mofrad. Torsional Behavior of Axonal Microtubule Bundles. *Biophys J*, 109(2):231–239, July 2015.
- [306] Mohammad Soheilypour, Mohaddeseh Peyro, Stephen J. Peter, and Mohammad R.K. Mofrad. Buckling Behavior of Individual and Bundled Microtubules. *Biophys J*, 108(7):1718–1726, April 2015.
- [307] Mark J. Stevens. The long persistence length of model tubules. *J. Chem. Phys.*, 147(4):044902, July 2017.
- [308] Xiang-Ying Ji and Xi-Qiao Feng. Coarse-grained mechanochemical model for simulating the dynamic behavior of microtubules. *Phys. Rev. E*, 84(3):031933, September 2011.
- [309] Xiang-Ying Ji and Xi-Qiao Feng. Mechanochemical modeling of dynamic microtubule growth involving sheet-to-tube transition. *PLoS One*, 6(12):e29049, 2011.
- [310] Olga Kononova, Yaroslav Kholodov, Kelly E. Theisen, Kenneth A. Marx, Ruxandra I. Dima, Fazly I. Ataullakhanov, Ekaterina L. Grishchuk, and Valeri Barsegov. Tubulin Bond Energies and Microtubule Biomechanics Determined from Nanoindentation in Silico. *J. Am. Chem. Soc.*, 136(49):17036–17045, December 2014.
-

- [311] James F. Dama, Anton V. Sinitskiy, Martin McCullagh, Jonathan Weare, Benoît Roux, Aaron R. Dinner, and Gregory A. Voth. The Theory of Ultra-Coarse-Graining. 1. General Principles. *J. Chem. Theory Comput.*, 9(5):2466–2480, May 2013.
- [312] Aram Davtyan, James F. Dama, Anton V. Sinitskiy, and Gregory A. Voth. The Theory of Ultra-Coarse-Graining. 2. Numerical Implementation. *J. Chem. Theory Comput.*, 10(12):5265–5275, December 2014.
- [313] Harshwardhan H. Katkar, Aram Davtyan, Aleksander E.P. Durumeric, Glen M. Hocky, Anthony C. Schramm, Enrique M. De La Cruz, and Gregory A. Voth. Insights into the Cooperative Nature of ATP Hydrolysis in Actin Filaments. *Biophys J*, 115(8):1589–1602, October 2018.
- [314] Yuwei Zhang, Zexing Cao, John Zenghui Zhang, and Fei Xia. Double-Well Ultra-Coarse-Grained Model to Describe Protein Conformational Transitions. *J. Chem. Theory Comput.*, 16(10):6678–6689, October 2020.
- [315] Masao Doi, S. F. Edwards, and Samuel Frederick Edwards. *The Theory of Polymer Dynamics*. Clarendon Press, 1988. ISBN 978-0-19-852033-7.
- [316] Michael P. Allen and Dominic J. Tildesley. *Computer Simulation of Liquids: Second Edition*. Oxford University Press, Oxford, 2 edition, 2017. ISBN 978-0-19-880319-5.
- [317] D. C. Rapaport. *The Art of Molecular Dynamics Simulation*. Cambridge University Press, Cambridge, 2 edition, 2004. ISBN 978-0-521-82568-9.
- [318] Daan Frenkel and B. Smit. *Understanding Molecular Simulation: From Algorithms to Applications*. Academic Press, San Diego, 2nd edition edition, October 2001. ISBN 978-0-12-267351-1.
- [319] Carlo Vanderzande. *Lattice Models of Polymers*. Cambridge Lecture Notes in Physics. Cambridge University Press, Cambridge, 1998. ISBN 978-0-521-55993-5.
- [320] Sharon C. Glotzer and Wolfgang Paul. Molecular and Mesoscale Simulation Methods for Polymer Materials. *Annual Review of Materials Research*, 32(1):401–436, 2002.
- [321] R. B. Bird, R. C. Armstrong, and O. Hassager. Dynamics of polymeric liquids. Vol. 1, 2nd Ed. : Fluid mechanics. January 1987.
- [322] J. Castillo-Tejas, O. Castrejón-González, S. Carro, V. González-Coronel, J. F. J. Alvarado, and O. Manero. Associative polymers. Part III: Shear rheology from molecular dynamics. *Colloids and Surfaces A: Physicochemical and Engineering Aspects*, C(491):37–49, 2016.
- [323] P. J. Daivis, M. L. Matin, and B. D. Todd. Nonlinear shear and elongational rheology of model polymer melts by non-equilibrium molecular dynamics. *Journal of Non-Newtonian Fluid Mechanics*, 111(1):1–18, March 2003.
- [324] In-Chul Yeh, Jan W. Andzelm, and Gregory C. Rutledge. Mechanical and Structural Characterization of Semicrystalline Polyethylene under Tensile Deformation by Molecular Dynamics Simulations. *Macromolecules*, 48(12):4228–4239, June 2015.
- [325] R.B. Bird and A.J. Giacomin. Polymer Fluid Dynamics: Continuum and Molecular Approaches. *Annual Review of Chemical and Biomolecular Engineering*, 7(1):479–507, 2016.
- [326] Malgorzata Kloc, Jacek Z. Kubiak, Xian C. Li, and Rafik M. Ghobrial. The newly found functions of MTOC in immunological response. *J Leukoc Biol*, 95(3):417–430, March 2014.
- [327] Ariana D. Sanchez and Jessica L. Feldman. Microtubule-organizing centers: from the centrosome to non-centrosomal sites. *Curr Opin Cell Biol*, 44:93–101, February 2017.
- [328] Heide Schatten. The mammalian centrosome and its functional significance. *Histochem Cell Biol*, 129(6):667–686, June 2008.
- [329] Christian Arquint, Anna-Maria Gabryjonczyk, and Erich A. Nigg. Centrosomes as signalling centres. *Philos Trans R Soc Lond B Biol Sci*, 369(1650):20130464, September 2014.

-
- [330] Paul Guichard, Virginie Hachet, Norbert Majubu, Aitana Neves, Davide Demurtas, Natacha Olieric, Isabelle Fluckiger, Akinori Yamada, Kumiko Kihara, Yuichiro Nishida, Shigeharu Moriya, Michel O. Steinmetz, Yuichi Hongoh, and Pierre Gönczy. Native architecture of the centriole proximal region reveals features underlying its 9-fold radial symmetry. *Curr. Biol.*, 23(17):1620–1628, September 2013.
- [331] Tetsuo Kobayashi and Brian D. Dynlacht. Regulating the transition from centriole to basal body. *J Cell Biol*, 193(3):435–444, May 2011.
- [332] Juliette Azimzadeh and Michel Bornens. Structure and duplication of the centrosome. *Journal of Cell Science*, 120(13):2139–2142, July 2007.
- [333] Nathalie Delgehyr, James Sillibourne, and Michel Bornens. Microtubule nucleation and anchoring at the centrosome are independent processes linked by ninein function. *Journal of Cell Science*, 118(8):1565–1575, April 2005.
- [334] Kim Baumann. Order in the pericentriolar material. *Nat Rev Mol Cell Biol*, 13(12):749–749, December 2012.
- [335] Katharina F. Sonnen, Lothar Schermelleh, Heinrich Leonhardt, and Erich A. Nigg. 3D-structured illumination microscopy provides novel insight into architecture of human centrosomes. *Biology Open*, 1(10):965–976, August 2012.
- [336] V. Mennella, B. Keszthelyi, K. L. McDonald, B. Chhun, F. Kan, G. C. Rogers, B. Huang, and D. A. Agard. Subdiffraction-resolution fluorescence microscopy reveals a domain of the centrosome critical for pericentriolar material organization. *Nat Cell Biol*, 14(11):1159–1168, November 2012.
- [337] Marisa M. L. Tillery, Caitlyn Blake-Hedges, Yiming Zheng, Rebecca A. Buchwalter, and Timothy L. Megraw. Centrosomal and Non-Centrosomal Microtubule-Organizing Centers (MTOCs) in *Drosophila melanogaster*. *Cells*, 7(9):121, August 2018.
- [338] M. Moritz, M. B. Braunfeld, V. Guénebaut, J. Heuser, and D. A. Agard. Structure of the gamma-tubulin ring complex: a template for microtubule nucleation. *Nat. Cell Biol.*, 2(6):365–370, June 2000.
- [339] Michel Bornens. Centrosome composition and microtubule anchoring mechanisms. *Curr Opin Cell Biol*, 14(1):25–34, February 2002.
- [340] Stephen Doxsey, Dannel McCollum, and William Theurkauf. Centrosomes in cellular regulation. *Annu Rev Cell Dev Biol*, 21:411–434, 2005.
- [341] Roop Mallik and Steven P. Gross. Molecular Motors: Strategies to Get Along. *Current Biology*, 14(22):R971–R982, November 2004.
- [342] Ronald D. Vale and Ronald A. Milligan. The Way Things Move: Looking Under the Hood of Molecular Motor Proteins. *Science*, 288(5463):88–95, April 2000.
- [343] Manfred Schliwa and Günther Woehlke. Molecular motors. *Nature*, 422(6933):759–765, April 2003.
- [344] Andrew P. Carter. Crystal clear insights into how the dynein motor moves. *Journal of Cell Science*, 126(3):705–713, February 2013.
- [345] Lynne Coluccio, editor. *Myosins: A Superfamily of Molecular Motors*. Advances in Experimental Medicine and Biology. Springer International Publishing, 2 edition, 2020. ISBN 978-3-030-38061-8.
- [346] Arnau Sebé-Pedrós, Xavier Grau-Bové, Thomas A. Richards, and Iñaki Ruiz-Trillo. Evolution and Classification of Myosins, a Paneukaryotic Whole-Genome Approach. *Genome Biol Evol*, 6(2):290–305, January 2014.
- [347] S. M. Heissler and J. R. Sellers. Myosins. In Ralph A. Bradshaw and Philip D. Stahl, editors, *Encyclopedia of Cell Biology*, pages 597–607. Academic Press, Waltham, January 2016. ISBN 978-0-12-394796-3.
-

- [348] Mira Krendel and Mark S. Mooseker. Myosins: Tails (and Heads) of Functional Diversity. *Physiology*, 20(4):239–251, August 2005.
- [349] Alexander Marx, Andreas Hoenger, and Eckhard Mandelkow. Structures of Kinesin Motor Proteins. *Cell Motil Cytoskeleton*, 66(11):958–966, November 2009.
- [350] Krishanu Ray. How kinesins walk, assemble and transport: A birds-eye-view of some unresolved questions. *Physica A: Statistical Mechanics and its Applications*, 372(1):52–64, December 2006.
- [351] Carolyn J. Lawrence, R. Kelly Dawe, Karen R. Christie, Don W. Cleveland, Scott C. Dawson, Sharyn A. Endow, Lawrence S. B. Goldstein, Holly V. Goodson, Nobutaka Hirokawa, Jonathon Howard, Russell L. Malmberg, J. Richard McIntosh, Harukata Miki, Timothy J. Mitchison, Yasushi Okada, Anireddy S. N. Reddy, William M. Saxton, Manfred Schliwa, Jonathan M. Scholey, Ronald D. Vale, Claire E. Walczak, and Linda Wordeman. A standardized kinesin nomenclature. *J Cell Biol*, 167(1):19–22, October 2004.
- [352] Wei Hua, Edgar C. Young, Margaret L. Fleming, and Jeff Gelles. Coupling of kinesin steps to ATP hydrolysis. *Nature*, 388(6640):390–393, July 1997.
- [353] G. Woehlke and M. Schliwa. Walking on two heads: the many talents of kinesin. *Nat Rev Mol Cell Biol*, 1(1):50–58, October 2000.
- [354] Iftikhar Ali and Wei-Cai Yang. The functions of kinesin and kinesin-related proteins in eukaryotes. *Cell Adh Migr*, 14(1):139–152.
- [355] Stan A. Burgess, Matt L. Walker, Hitoshi Sakakibara, Peter J. Knight, and Kazuhiro Oiwa. Dynein structure and power stroke. *Nature*, 421(6924):715–718, February 2003.
- [356] K. Kevin Pfister. Dynein. In William J. Lennarz and M. Daniel Lane, editors, *Encyclopedia of Biological Chemistry*, pages 827–831. Elsevier, New York, January 2004. ISBN 978-0-12-443710-4.
- [357] Peter Höök and Richard B. Vallee. The dynein family at a glance. *Journal of Cell Science*, 119(21):4369–4371, November 2006.
- [358] Stephen M. King. Axonemal Dynein Arms. *Cold Spring Harb Perspect Biol*, 8(11), November 2016.
- [359] I. R. Gibbons. Dynein family of motor proteins: present status and future questions. *Cell Motil Cytoskeleton*, 32(2):136–144, 1995.
- [360] Travis Walton, Hao Wu, and Alan Brown. Structure of a microtubule-bound axonemal dynein. *Nature Communications*, 12(1):477, January 2021.
- [361] Somdatta Karak, Julie S. Jacobs, Maike Kittelmann, Christian Spalthoff, Radoslaw Katana, Elena Sivan-Loukianova, Michael A. Schon, Maurice J. Kernan, Daniel F. Eberl, and Martin C. Göpfert. Diverse Roles of Axonemal Dyneins in *Drosophila* Auditory Neuron Function and Mechanical Amplification in Hearing. *Scientific Reports*, 5(1):17085, November 2015.
- [362] Richard B. Vallee, John C. Williams, Dileep Varma, and Lora E. Barnhart. Dynein: An ancient motor protein involved in multiple modes of transport. *J Neurobiol*, 58(2):189–200, February 2004.
- [363] K. Kevin Pfister. Distinct Functional Roles of Cytoplasmic Dynein Defined by the Intermediate Chain Isoforms. *Exp Cell Res*, 334(1):54–60, May 2015.
- [364] Meng-meng Fu and Erika L. F. Holzbaur. Integrated regulation of motor-driven organelle transport by scaffolding proteins. *Trends Cell Biol*, 24(10):564–574, October 2014.
- [365] Victoria J. Allan, Heather M. Thompson, and Mark A. McNiven. Motoring around the Golgi. *Nat Cell Biol*, 4(10):E236–242, October 2002.
- [366] C. Roghi and V. J. Allan. Dynamic association of cytoplasmic dynein heavy chain 1a with the Golgi apparatus and intermediate compartment. *J Cell Sci*, 112 (Pt 24):4673–4685, December 1999.

- [367] David J. Sharp, Gregory C. Rogers, and Jonathan M. Scholey. Cytoplasmic dynein is required for poleward chromosome movement during mitosis in *Drosophila* embryos. *Nature Cell Biology*, 2(12):922–930, December 2000.
- [368] Clare M. Waterman-Storer, Sher B. Karki, Sergei A. Kuznetsov, Joel S. Tabb, Dieter G. Weiss, George M. Langford, and Erika L. F. Holzbaur. The interaction between cytoplasmic dynein and dynactin is required for fast axonal transport. *PNAS*, 94(22):12180–12185, October 1997.
- [369] Majid Hafezparast, Rainer Klocke, Christiana Ruhrberg, Andreas Marquardt, Azlina Ahmad-Annuar, Samantha Bowen, Giovanna Lalli, Abi S. Witherden, Holger Hummerich, Sharon Nicholson, P. Jeffrey Morgan, Ravi Oozageer, John V. Priestley, Sharon Averill, Von R. King, Simon Ball, Jo Peters, Takashi Toda, Ayumu Yamamoto, Yasushi Hiraoka, Martin Augustin, Dirk Korthaus, Sigrid Wattler, Philipp Wabnitz, Carmen Dickneite, Stefan Lampel, Florian Boehme, Gisela Peraus, Andreas Popp, Martina Rudelius, Juergen Schlegel, Helmut Fuchs, Martin Hrabe de Angelis, Giampietro Schiavo, David T. Shima, Andreas P. Russ, Gabriele Stumm, Joanne E. Martin, and Elizabeth M. C. Fisher. Mutations in dynein link motor neuron degeneration to defects in retrograde transport. *Science*, 300(5620):808–812, May 2003.
- [370] N. Hirokawa, R. Sato-Yoshitake, T. Yoshida, and T. Kawashima. Brain dynein (MAP1C) localizes on both anterogradely and retrogradely transported membranous organelles in vivo. *J Cell Biol*, 111(3):1027–1037, September 1990.
- [371] Marvin E Tanenbaum, Anna Akhmanova, and René H Medema. Bi-directional transport of the nucleus by dynein and kinesin-1. *Commun Integr Biol*, 4(1):21–25, 2011.
- [372] S. M. King. AAA domains and organization of the dynein motor unit. *J Cell Sci*, 113 (Pt 14):2521–2526, July 2000.
- [373] A. F. Neuwald, L. Aravind, J. L. Spouge, and E. V. Koonin. AAA+: A class of chaperone-like ATPases associated with the assembly, operation, and disassembly of protein complexes. *Genome Res*, 9(1):27–43, January 1999.
- [374] Anthony J. Roberts, Bara Malkova, Matt L. Walker, Hitoshi Sakakibara, Naoki Numata, Takahide Kon, Reiko Ohkura, Thomas A. Edwards, Peter J. Knight, Kazuo Sutoh, Kazuhiro Oiwa, and Stan A. Burgess. ATP-Driven Remodeling of the Linker Domain in the Dynein Motor. *Structure*, 20(10):1670–1680, October 2012.
- [375] Frank B. Cleary, Mark A. Dewitt, Thomas Bilyard, Zaw Min Htet, Vladislav Belyy, Danna D. Chan, Amy Y. Chang, and Ahmet Yildiz. Tension on the linker gates the ATP-dependent release of dynein from microtubules. *Nature Communications*, 5(1):4587, August 2014.
- [376] Anthony J. Roberts, Naoki Numata, Matt L. Walker, Yusuke S. Kato, Bara Malkova, Takahide Kon, Reiko Ohkura, Fumio Arisaka, Peter J. Knight, Kazuo Sutoh, and Stan A. Burgess. AAA+ Ring and Linker Swing Mechanism in the Dynein Motor. *Cell*, 136(3):485–495, February 2009.
- [377] I. R. Gibbons, Joan E. Garbarino, Carol E. Tan, Samara L. Reck-Peterson, Ronald D. Vale, and Andrew P. Carter. The affinity of the dynein microtubule-binding domain is modulated by the conformation of its coiled-coil stalk. *J Biol Chem*, 280(25):23960–23965, June 2005.
- [378] Melissa A. Gee, John E. Heuser, and Richard B. Vallee. An extended microtubule-binding structure within the dynein motor domain. *Nature*, 390(6660):636–639, December 1997.
- [379] Takahide Kon, Masaya Nishiura, Reiko Ohkura, Yoko Y. Toyoshima, and Kazuo Sutoh. Distinct Functions of Nucleotide-Binding/Hydrolysis Sites in the Four AAA Modules of Cytoplasmic Dynein. *Biochemistry*, 43(35):11266–11274, September 2004.
- [380] Michael P. Koonce. Identification of a Microtubule-binding Domain in a Cytoplasmic Dynein Heavy Chain*. *Journal of Biological Chemistry*, 272(32):19714–19718, August 1997.
- [381] Takahide Kon, Toshifumi Mogami, Reiko Ohkura, Masaya Nishiura, and Kazuo Sutoh. ATP hydrolysis cycle-dependent tail motions in cytoplasmic dynein. *Nat Struct Mol Biol*, 12(6):513–519, June 2005.

- [382] Stephen J. King and Trina A. Schroer. Dynactin increases the processivity of the cytoplasmic dynein motor. *Nat Cell Biol*, 2(1):20–24, January 2000.
- [383] R. A Cross. Molecular Motors: Dynein’s Gearbox. *Current Biology*, 14(9):R355–R356, May 2004.
- [384] Arne Gennerich, Andrew P. Carter, Samara L. Reck-Peterson, and Ronald D. Vale. Force-Induced Bidirectional Stepping of Cytoplasmic Dynein. *Cell*, 131(5):952–965, November 2007.
- [385] Shiori Toba, Tomonobu M. Watanabe, Lisa Yamaguchi-Okimoto, Yoko Yano Toyoshima, and Hideo Higuchi. Overlapping hand-over-hand mechanism of single molecular motility of cytoplasmic dynein. *PNAS*, 103(15):5741–5745, April 2006.
- [386] Roop Mallik, Dmitri Petrov, S. A. Lex, S. J. King, and S. P. Gross. Building complexity: an in vitro study of cytoplasmic dynein with in vivo implications. *Curr. Biol.*, 15(23):2075–2085, December 2005.
- [387] Roop Mallik, Brian C. Carter, Stephanie A. Lex, Stephen J. King, and Steven P. Gross. Cytoplasmic dynein functions as a gear in response to load. *Nature*, 427(6975):649–652, February 2004.
- [388] Samara L. Reck-Peterson, Ahmet Yildiz, Andrew P. Carter, Arne Gennerich, Nan Zhang, and Ronald D. Vale. Single-Molecule Analysis of Dynein Processivity and Stepping Behavior. *Cell*, 126(2):335–348, July 2006.
- [389] Masaya Nishiura, Takahide Kon, Katsuyuki Shiroguchi, Reiko Ohkura, Tomohiro Shima, Yoko Y. Toyoshima, and Kazuo Sutoh. A single-headed recombinant fragment of Dictyostelium cytoplasmic dynein can drive the robust sliding of microtubules. *J. Biol. Chem.*, 279(22):22799–22802, May 2004.
- [390] Takayuki Torisawa, Muneyoshi Ichikawa, Akane Furuta, Kei Saito, Kazuhiro Oiwa, Hiroaki Kojima, Yoko Y. Toyoshima, and Ken’ya Furuta. Autoinhibition and cooperative activation mechanisms of cytoplasmic dynein. *Nature Cell Biology*, 16(11):1118–1124, November 2014.
- [391] Carol Cho, Samara L. Reck-Peterson, and Ronald D. Vale. Regulatory ATPase sites of cytoplasmic dynein affect processivity and force generation. *J. Biol. Chem.*, 283(38):25839–25845, September 2008.
- [392] Melanie J. I. Müller, Stefan Klumpp, and Reinhard Lipowsky. Tug-of-war as a cooperative mechanism for bidirectional cargo transport by molecular motors. *Proc. Natl. Acad. Sci. U.S.A.*, 105(12):4609–4614, March 2008.
- [393] Junya Ikuta, Nagendra K. Kamisetty, Hirofumi Shintaku, Hidetoshi Kotera, Takahide Kon, and Ryuji Yokokawa. Tug-of-war of microtubule filaments at the boundary of a kinesin- and dynein-patterned surface. *Scientific Reports*, 4:5281, June 2014.
- [394] Reinier Cárdenas, Javier Martínez-Seoane, and Carlos Amero. Combining Experimental Data and Computational Methods for the Non-Computer Specialist. *Molecules*, 25(20):4783, October 2020.
- [395] Mi Zhou, Qing Li, and Renxiao Wang. Current Experimental Methods for Characterizing Protein–Protein Interactions. *ChemMedChem*, 11(8):738–756, April 2016.
- [396] Enrique M. De La Cruz, Amber L. Wells, Steven S. Rosenfeld, E. Michael Ostap, and H. Lee Sweeney. The kinetic mechanism of myosin V. *Proceedings of the National Academy of Sciences*, 96(24):13726–13731, November 1999.
- [397] Y. Z. Ma and E. W. Taylor. Mechanism of microtubule kinesin ATPase. *Biochemistry*, 34(40):13242–13251, October 1995.
- [398] Jared C. Cochran, Christopher A. Sontag, Zoltan Maliga, Tarun M. Kapoor, John J. Correia, and Susan P. Gilbert. Mechanistic Analysis of the Mitotic Kinesin Eg5. *J Biol Chem*, 279(37):38861–38870, September 2004.
- [399] Enrique M. De La Cruz and E. Michael Ostap. Relating biochemistry and function in the myosin superfamily. *Curr Opin Cell Biol*, 16(1):61–67, February 2004.

-
- [400] Anatoly B. Kolomeisky. Motor Proteins and Molecular Motors: How to Operate Machines at Nanoscale. *J Phys Condens Matter*, 25(46):10.1088/0953-8984/25/46/463101, November 2013.
- [401] Sarah Rice, Abel W. Lin, Daniel Safer, Cynthia L. Hart, Nariman Naber, Bridget O. Carragher, Shane M. Cain, Elena Pechatnikova, Elizabeth M. Wilson-Kubalek, Michael Whittaker, Edward Pate, Roger Cooke, Edwin W. Taylor, Ronald A. Milligan, and Ronald D. Vale. A structural change in the kinesin motor protein that drives motility. *Nature*, 402(6763):778–784, December 1999.
- [402] H. Lee Sweeney and Anne Houdusse. Structural and functional insights into the Myosin motor mechanism. *Annu Rev Biophys*, 39:539–557, 2010.
- [403] Zachary Abraham, Emma Hawley, Daniel Hayosh, Victoria A. Webster-Wood, and Ozan Akkus. Kinesin and Dynein Mechanics: Measurement Methods and Research Applications. *J Biomech Eng*, 140(2):0208051–02080511, February 2018.
- [404] David Dulin, Jan Lipfert, M. Charl Moolman, and Nynke H. Dekker. Studying genomic processes at the single-molecule level: introducing the tools and applications. *Nat Rev Genet*, 14(1):9–22, January 2013.
- [405] Kurt Thorn. A quick guide to light microscopy in cell biology. *Mol Biol Cell*, 27(2):219–222, January 2016.
- [406] Carlos J. Bustamante, Yann R. Chemla, Shixin Liu, and Michelle D. Wang. Optical tweezers in single-molecule biophysics. *Nat Rev Methods Primers*, 1(1):1–29, March 2021.
- [407] Claudia Veigel and Christoph F. Schmidt. Moving into the cell: single-molecule studies of molecular motors in complex environments. *Nat Rev Mol Cell Biol*, 12(3):163–176, March 2011.
- [408] William J. Greenleaf, Michael T. Woodside, and Steven M. Block. High-resolution, single-molecule measurements of biomolecular motion. *Annu Rev Biophys Biomol Struct*, 36:171–190, 2007.
- [409] E. D. Salmon. VE-DIC light microscopy and the discovery of kinesin. *Trends Cell Biol*, 5(4):154–158, April 1995.
- [410] Sharron X H Lin and Christine A Collins. Immunolocalization of cytoplasmic dynein to lysosomes in cultured cells. page 14, 1992.
- [411] Jennifer L. Ross, Karen Wallace, Henry Shuman, Yale E. Goldman, and Erika L. F. Holzbaur. Processive bidirectional motion of dynein–dynactin complexes in vitro. *Nat Cell Biol*, 8(6):562–570, June 2006.
- [412] Winfield S. Sale, Laura A. Fox, and Elizabeth F. Smith. Chapter 6 Assays of Axonemal Dynein-Driven Motility. In Jonathan M. Scholey, editor, *Methods in Cell Biology*, volume 39 of *Motility Assays for Motor Proteins*, pages 89–104. Academic Press, January 1993.
- [413] Osamu Kutomi, Manabu Hori, Masaki Ishida, Takashi Tominaga, Hiroyuki Kamachi, France Koll, Jean Cohen, Norico Yamada, and Munenori Noguchi. Outer Dynein Arm Light Chain 1 Is Essential for Controlling the Ciliary Response to Cyclic AMP in *Paramecium tetraurelia*. *Eukaryot Cell*, 11(5):645–653, May 2012.
- [414] Mitchell W. Ross, David J. Mitchell, John C. Cain, Kiev R. Blasier, and K. Kevin Pfister. Live cell imaging of cytoplasmic dynein movement in transfected embryonic rat neurons. *Methods Cell Biol*, 131:253–267, 2016.
- [415] Bo Huang, Mark Bates, and Xiaowei Zhuang. Super-resolution fluorescence microscopy. *Annu Rev Biochem*, 78:993–1016, 2009.
- [416] Derek Toomre and Joerg Bewersdorf. A new wave of cellular imaging. *Annu Rev Cell Dev Biol*, 26:285–314, 2010.
- [417] Leonhard Möckl and W. E. Moerner. Super-resolution Microscopy with Single Molecules in Biology and Beyond—Essentials, Current Trends, and Future Challenges. *J. Am. Chem. Soc.*, 142(42):17828–17844, October 2020.
-

- [418] Bo Huang, Mark Bates, and Xiaowei Zhuang. Super resolution fluorescence microscopy. *Annu Rev Biochem*, 78:993–1016, 2009.
- [419] Lothar Schermelleh, Rainer Heintzmann, and Heinrich Leonhardt. A guide to super-resolution fluorescence microscopy. *J Cell Biol*, 190(2):165–175, July 2010.
- [420] S. W. Hell and J. Wichmann. Breaking the diffraction resolution limit by stimulated emission: stimulated-emission-depletion fluorescence microscopy. *Opt Lett*, 19(11):780–782, June 1994.
- [421] Stephanie L. Silva-Del Toro and Lee-Ann H. Allen. Microtubules and Dynein Regulate Human Neutrophil Nuclear Volume and Hypersegmentation During *H. pylori* Infection. *Frontiers in Immunology*, 12, 2021.
- [422] Ahmet Yildiz, Michio Tomishige, Ronald D. Vale, and Paul R. Selvin. Kinesin walks hand-over-hand. *Science*, 303(5658):676–678, January 2004.
- [423] G. I. Mashanov and J. E. Molloy. Automatic Detection of Single Fluorophores in Live Cells. *Biophys J*, 92(6):2199–2211, March 2007.
- [424] Francesca Cella Zanacchi, Carlo Manzo, Raffaella Magrassi, Nathan D. Derr, and Melike Lakadamyali. Quantifying Protein Copy Number in Super Resolution Using an Imaging-Invariant Calibration. *Biophys J*, 116(11):2195–2203, June 2019.
- [425] Bason E. Clancy, William M. Behnke-Parks, Johan O. L. Andreasson, Steven S. Rosenfeld, and Steven M. Block. A universal pathway for kinesin stepping. *Nat Struct Mol Biol*, 18(9):1020–1027, August 2011.
- [426] Anita Jannasch, Volker Bormuth, Marko Storch, Jonathon Howard, and Erik Schäffer. Kinesin-8 Is a Low-Force Motor Protein with a Weakly Bound Slip State. *Biophys J*, 104(11):2456–2464, June 2013.
- [427] Jeffrey R. Moffitt, Yann R. Chemla, Steven B. Smith, and Carlos Bustamante. Recent Advances in Optical Tweezers. *Annual Review of Biochemistry*, 77(1):205–228, 2008.
- [428] Christina Leidel, Rafael A. Longoria, Francisco Marquez Gutierrez, and George T. Shubeita. Measuring Molecular Motor Forces In Vivo: Implications for Tug-of-War Models of Bidirectional Transport. *Biophysical Journal*, 103(3):492–500, August 2012.
- [429] Benjamin H. Blehm, Trina A. Schroer, Kathleen M. Trybus, Yann R. Chemla, and Paul R. Selvin. In vivo optical trapping indicates kinesin’s stall force is reduced by dynein during intracellular transport. *Proceedings of the National Academy of Sciences*, 110(9):3381–3386, February 2013.
- [430] Paulomi Sanghavi, Pankaj Kumar, Ankit Roy, M. S. Madhusudhan, and Roop Mallik. On and off controls within dynein–dynactin on native cargoes. *Proceedings of the National Academy of Sciences*, 118(23):e2103383118, June 2021.
- [431] Yoshimi Kinoshita, Taketoshi Kambara, Kaori Nishikawa, Motoshi Kaya, and Hideo Higuchi. Step Sizes and Rate Constants of Single-headed Cytoplasmic Dynein Measured with Optical Tweezers. *Sci Rep*, 8(1):16333, November 2018.
- [432] Rupa Sarkar and Valentin V. Rybenkov. A Guide to Magnetic Tweezers and Their Applications. *Frontiers in Physics*, 4, 2016.
- [433] Charlie Gosse and Vincent Croquette. Magnetic tweezers: micromanipulation and force measurement at the molecular level. *Biophys J*, 82(6):3314–3329, June 2002.
- [434] G. Charvin, D. Bensimon, and V. Croquette. Single-molecule study of DNA unlinking by eukaryotic and prokaryotic type-II topoisomerases. *Proc Natl Acad Sci USA*, 100(17):9820–9825, August 2003.
- [435] Omar A Saleh, Corine Péral, François-Xavier Barre, and Jean-François Allemand. Fast, DNA-sequence independent translocation by FtsK in a single-molecule experiment. *EMBO J*, 23(12):2430–2439, June 2004.

-
- [436] Todd L. Fallesen, Jed C. Macosko, and G. Holzwarth. Force-velocity relationship for multiple kinesin motors pulling a magnetic bead. *Eur Biophys J*, 40(9):1071–1079, September 2011.
- [437] S. C. Kuo, J. Gelles, E. Steuer, and M. P. Sheetz. A model for kinesin movement from nanometer-level movements of kinesin and cytoplasmic dynein and force measurements. *J Cell Sci Suppl*, 14:135–138, 1991.
- [438] K Hall, D Cole, Y Yeh, and R J Baskin. Kinesin force generation measured using a centrifuge microscope sperm-gliding motility assay. *Biophys J*, 71(6):3467–3476, December 1996.
- [439] Carlos Garzon-Coral, Horatiu A. Fantana, and Jonathon Howard. A force-generating machinery maintains the spindle at the cell center during mitosis. *Science*, 352(6289):1124–1127, May 2016.
- [440] Jing Xie, Javad Najafi, Rémi Le Borgne, Jean-Marc Verbavatz, Catherine Durieu, Jeremy Sallé, and Nicolas Minc. Contribution of cytoplasm viscoelastic properties to mitotic spindle positioning. *Proceedings of the National Academy of Sciences*, 119(8):e2115593119, February 2022.
- [441] G. Binnig, C. F. Quate, and Ch. Gerber. Atomic Force Microscope. *Phys. Rev. Lett.*, 56(9):930–933, March 1986.
- [442] Francesco Simone Ruggeri, Tomas Šneideris, Michele Vendruscolo, and Tuomas P. J. Knowles. Atomic force microscopy for single molecule characterisation of protein aggregation. *Archives of Biochemistry and Biophysics*, 664:134–148, March 2019.
- [443] Nader Jalili and Karthik Laxminarayana. A review of atomic force microscopy imaging systems: application to molecular metrology and biological sciences. *Mechatronics*, 14(8):907–945, October 2004.
- [444] Iwan A. T. Schaap, Bernd Hoffmann, Carolina Carrasco, Rudolf Merkel, and Christoph F. Schmidt. Tau protein binding forms a 1 nm thick layer along protofilaments without affecting the radial elasticity of microtubules. *J Struct Biol*, 158(3):282–292, June 2007.
- [445] Iwan A. T. Schaap, Pedro J. de Pablo, and Christoph F. Schmidt. Resolving the molecular structure of microtubules under physiological conditions with scanning force microscopy. *Eur Biophys J*, 33(5):462–467, August 2004.
- [446] Schaap, I.A.T., Carrasco, C., Harder, S., Hoffmann, B., de Pablo, P.J., Schmidt, C., and Physics of Living Systems. Cytoskeletal filaments and their associated proteins studied with atomic force microscopy. *Unknown journal*, page 309A, 2007.
- [447] Hayato Yamashita, Noriyuki Kodera, Atsushi Miyagi, Takayuki Uchihashi, Daisuke Yamamoto, and Toshio Ando. Tip-sample distance control using photothermal actuation of a small cantilever for high-speed atomic force microscopy. *Review of Scientific Instruments*, 78(8):083702, August 2007.
- [448] Noriyuki Kodera, Daisuke Yamamoto, Ryoki Ishikawa, and Toshio Ando. Video imaging of walking myosin V by high-speed atomic force microscopy. *Nature*, 468(7320):72–76, November 2010.
- [449] Oliver I. Wagner, Jennifer Ascaño, Mariko Tokito, Jean-Francois Leterrier, Paul A. Janmey, and Erika L. F. Holzbaur. The Interaction of Neurofilaments with the Microtubule Motor Cytoplasmic Dynein. *Mol Biol Cell*, 15(11):5092–5100, November 2004.
- [450] Toru Niina, Yasuhiro Matsunaga, and Shoji Takada. Rigid-body fitting to atomic force microscopy images for inferring probe shape and biomolecular structure. *PLOS Computational Biology*, 17(7):e1009215, 2021.
- [451] Sithara S. Wijeratne, Michelle F. Marchan, Jason S. Tresback, and Radhika Subramanian. Atomic force microscopy reveals distinct protofilament-scale structural dynamics in depolymerizing microtubule arrays. *Proceedings of the National Academy of Sciences*, 119(5):e2115708119, February 2022.
- [452] Hiroshi Imai, Tomohiro Shima, Kazuo Sutoh, Matthew L. Walker, Peter J. Knight, Takahide Kon, and Stan A. Burgess. Direct observation shows superposition and large scale flexibility within cytoplasmic dynein motors moving along microtubules. *Nature Communications*, 6(1):1–11, September 2015.
-

- [453] Eva Nogales. The development of cryo-EM into a mainstream structural biology technique. *Nat Methods*, 13(1):24–27, January 2016.
- [454] Dmitry Lyumkis. Challenges and opportunities in cryo-EM single-particle analysis. *J Biol Chem*, 294(13):5181–5197, March 2019.
- [455] Jacques Dubochet. On the Development of Electron Cryo-Microscopy (Nobel Lecture). *Angew Chem Int Ed Engl*, 57(34):10842–10846, August 2018.
- [456] Richard Henderson. From Electron Crystallography to Single Particle CryoEM (Nobel Lecture). *Angew Chem Int Ed Engl*, 57(34):10804–10825, August 2018.
- [457] Joachim Frank. Single-Particle Reconstruction of Biological Molecules-Story in a Sample (Nobel Lecture). *Angew Chem Int Ed Engl*, 57(34):10826–10841, August 2018.
- [458] Sinan Can, Samuel Lacey, Mert Gur, Andrew P. Carter, and Ahmet Yildiz. Directionality of dynein is controlled by the angle and length of its stalk. *Nature*, 566(7744):407–410, February 2019.
- [459] In-Gyun Lee, Mara A. Olenick, Malgorzata Boczkowska, Clara Franzini-Armstrong, Erika L. F. Holzbaur, and Roberto Dominguez. A conserved interaction of the dynein light intermediate chain with dynein-dynactin effectors necessary for processivity. *Nat Commun*, 9(1):986, March 2018.
- [460] Hiroyasu Itoh, Akira Takahashi, Kengo Adachi, Hiroyuki Noji, Ryohei Yasuda, Masasuke Yoshida, and Kazuhiko Kinosita. Mechanically driven ATP synthesis by F1-ATPase. *Nature*, 427(6973):465–468, January 2004.
- [461] C. Bustamante, D. Keller, and G. Oster. The physics of molecular motors. *Acc Chem Res*, 34(6):412–420, June 2001.
- [462] Debashish Chowdhury. Stochastic mechano-chemical kinetics of molecular motors: A multidisciplinary enterprise from a physicist’s perspective. *Physics Reports*, 529(1):1–197, August 2013.
- [463] Frank Jülicher, Armand Ajdari, and Jacques Prost. Modeling molecular motors. *Rev. Mod. Phys.*, 69(4):1269–1282, October 1997.
- [464] A. W. C. Lau, D. Lacoste, and K. Mallick. Nonequilibrium fluctuations and mechanochemical couplings of a molecular motor. *Phys Rev Lett*, 99(15):158102, October 2007.
- [465] Anatoly B. Kolomeisky and Michael E. Fisher. Molecular Motors: A Theorist’s Perspective. *Annual Review of Physical Chemistry*, 58(1):675–695, 2007.
- [466] Evgeny B. Stukalin, Hubert Phillips, and Anatoly B. Kolomeisky. Coupling of two motor proteins: a new motor can move faster. *Phys Rev Lett*, 94(23):238101, June 2005.
- [467] Young C. Kim and Michael E. Fisher. Vectorial loading of processive motor proteins: implementing a landscape picture. *J Phys Condens Matter*, 17(47):S3821–3838, November 2005.
- [468] Denis Tsygankov, Adrian W.R. Serohijos, Nikolay V. Dokholyan, and Timothy C. Elston. A Physical Model Reveals the Mechanochemistry Responsible for Dynein’s Processive Motion. *Biophys J*, 101(1):144–150, July 2011.
- [469] Ganhui Lan and Sean X. Sun. Flexible Light-Chain and Helical Structure of F-Actin Explain the Movement and Step Size of Myosin-VI. *Biophys J*, 91(11):4002–4013, December 2006.
- [470] Ganhui Lan and Sean X. Sun. Mechanochemical models of processive molecular motors. *Molecular Physics*, 110(9-10):1017–1034, May 2012.
- [471] Peter Ashwin, Congping Lin, and Gero Steinberg. Queueing induced by bidirectional motor motion near the end of a microtubule. *Phys Rev E Stat Nonlin Soft Matter Phys*, 82(5 Pt 1):051907, November 2010.
- [472] D A Smith and R M Simmons. Models of motor-assisted transport of intracellular particles. *Biophys J*, 80(1):45–68, January 2001.

-
- [473] L. Trott, M. Hafezparast, and A. Madzvamuse. A mathematical understanding of how cytoplasmic dynein walks on microtubules. *R Soc Open Sci*, 5(8):171568, August 2018.
- [474] Andreja Šarlah and Andrej Vilfan. The Winch Model Can Explain both Coordinated and Uncoordinated Stepping of Cytoplasmic Dynein. *Biophys J*, 107(3):662–671, August 2014.
- [475] Sutapa Mukherji. Model for the unidirectional motion of a dynein molecule. *Phys Rev E Stat Nonlin Soft Matter Phys*, 77(5 Pt 1):051916, May 2008.
- [476] Denis Tsygankov, Adrian W. R. Serohijos, Nikolay V. Dokholyan, and Timothy C. Elston. Kinetic models for the coordinated stepping of cytoplasmic dynein. *J Chem Phys*, 130(2):025101, January 2009.
- [477] Yisong Y Wan. Multi-tasking of helper T cells. *Immunology*, 130(2):166–171, June 2010.
- [478] Kenneth M. Murphy and Steven L. Reiner. The lineage decisions of helper T cells. *Nat Rev Immunol*, 2(12):933–944, December 2002.
- [479] Bruce Walker and Andrew McMichael. The T-Cell Response to HIV. *Cold Spring Harb Perspect Med*, 2(11):a007054, November 2012.
- [480] Xiaoliang Zhu and Jinfang Zhu. CD4 T Helper Cell Subsets and Related Human Immunological Disorders. *Int J Mol Sci*, 21(21):8011, October 2020.
- [481] Dario A. A. Vignali, Lauren W. Collison, and Creg J. Workman. How regulatory T cells work. *Nat Rev Immunol*, 8(7):523–532, July 2008.
- [482] Ekaterina A. Ivanova and Alexander N. Orekhov. T Helper Lymphocyte Subsets and Plasticity in Autoimmunity and Cancer: An Overview. *Biomed Res Int*, 2015:327470, 2015.
- [483] Lan Wu and Luc Van Kaer. Natural killer T cells in health and disease. *Front Biosci (Schol Ed)*, 3:236–251, January 2011.
- [484] Dale I. Godfrey, H. Robson MacDonald, Mitchell Kronenberg, Mark J. Smyth, and Luc Van Kaer. NKT cells: what’s in a name? *Nat Rev Immunol*, 4(3):231–237, March 2004.
- [485] Luc Van Kaer. NKT cells: T lymphocytes with innate effector functions. *Current Opinion in Immunology*, 19(3):354–364, June 2007.
- [486] Leonid S. Metelitsa, Olga V. Naidenko, Anita Kant, Hong-Wei Wu, Matthew J. Loza, Bice Perussia, Mitchell Kronenberg, and Robert C. Seeger. Human NKT Cells Mediate Antitumor Cytotoxicity Directly by Recognizing Target Cell CD1d with Bound Ligand or Indirectly by Producing IL-2 to Activate NK Cells. *The Journal of Immunology*, 167(6):3114–3122, September 2001.
- [487] Dale I. Godfrey, Sanda Stankovic, and Alan G. Baxter. Raising the NKT cell family. *Nat Immunol*, 11(3):197–206, March 2010.
- [488] Jennifer L. Matsuda, Thierry Mallevaey, James Scott-Browne, and Laurent Gapin. CD1d-restricted iNKT cells, the “Swiss-Army knife” of the immune system. *Curr Opin Immunol*, 20(3):358–368, June 2008.
- [489] Yingyu Qin, Sejin Oh, Sojung Lim, Jung Hoon Shin, Min Sang Yoon, and Se-Ho Park. Invariant NKT cells facilitate cytotoxic T-cell activation via direct recognition of CD1d on T cells. *Exp Mol Med*, 51(10):1–9, October 2019.
- [490] S. Middendorp and E. E. S. Nieuwenhuis. NKT cells in mucosal immunity. *Mucosal Immunol*, 2(5):393–402, September 2009.
- [491] Catherine M. Crosby and Mitchell Kronenberg. Tissue-specific functions of invariant natural killer T cells. *Nat Rev Immunol*, 18(9):559–574, September 2018.
- [492] Emmanuel Tupin, Yuki Kinjo, and Mitchell Kronenberg. The unique role of natural killer T cells in the response to microorganisms. *Nat Rev Microbiol*, 5(6):405–417, June 2007.
-

- [493] L. Gabriel Curtis, Wu Lan, V. Parekh Vrajesh, and Van Kaer Luc. Invariant Natural Killer T Cell-Based Therapy of Autoimmune Diseases. *Current Immunology Reviews (Discontinued)*, 6(2):88–101, May 2010.
- [494] Daniëlle Krijgsman, Marianne Hokland, and Peter J. K. Kuppen. The Role of Natural Killer T Cells in Cancer—A Phenotypical and Functional Approach. *Front Immunol*, 9:367, February 2018.
- [495] Yueh-hsiu Chien, Christina Meyer, and Marc Bonneville. $\gamma\delta$ T cells: first line of defense and beyond. *Annu Rev Immunol*, 32:121–155, 2014.
- [496] Timothy J. Allison and David N. Garboczi. Structure of $\gamma\delta$ T cell receptors and their recognition of non-peptide antigens. *Molecular Immunology*, 38(14):1051–1061, May 2002.
- [497] Julie C. Ribot, Noëlla Lopes, and Bruno Silva-Santos. $\gamma\delta$ T cells in tissue physiology and surveillance. *Nat Rev Immunol*, 21(4):221–232, April 2021.
- [498] Min Cheng and Shilian Hu. Lung-resident $\gamma\delta$ T cells and their roles in lung diseases. *Immunology*, 151(4):375–384, August 2017.
- [499] Ryunosuke Muro, Hiroshi Takayanagi, and Takeshi Nitta. T cell receptor signaling for $\gamma\delta$ T cell development. *Inflammation and Regeneration*, 39(1):6, March 2019.
- [500] David Vermijlen, Deborah Gatti, Ariadni Kouzeli, Teja Rus, and Matthias Eberl. $\gamma\delta$ T cell responses: How many ligands will it take till we know? *Semin Cell Dev Biol*, 84:75–86, December 2018.
- [501] Pierre Vantourout and Adrian Hayday. Six-of-the-best: unique contributions of $\gamma\delta$ T cells to immunology. *Nat Rev Immunol*, 13(2):88–100, February 2013.
- [502] Marc Bonneville, Rebecca L. O’Brien, and Willi K. Born. $\gamma\delta$ T cell effector functions: a blend of innate programming and acquired plasticity. *Nat Rev Immunol*, 10(7):467–478, July 2010.
- [503] Gang Qin, Huawei Mao, Jian Zheng, Sin Fun Sia, Yinping Liu, Ping-Lung Chan, Kwok-Tai Lam, J. S. Malik Peiris, Yu-Lung Lau, and Wenwei Tu. Phosphoantigen-expanded human gammadelta T cells display potent cytotoxicity against monocyte-derived macrophages infected with human and avian influenza viruses. *J Infect Dis*, 200(6):858–865, September 2009.
- [504] Myriam Lawand, Julie Déchanet-Merville, and Marie-Caroline Dieu-Nosjean. Key Features of Gamma-Delta T-Cell Subsets in Human Diseases and Their Immunotherapeutic Implications. *Front Immunol*, 8:761, June 2017.
- [505] Katrien Deroost and Jean Langhorne. Gamma/Delta T Cells and Their Role in Protection Against Malaria. *Frontiers in Immunology*, 9:2973, 2018.
- [506] Yijing Zhao, Chao Niu, and Jiuwei Cui. Gamma-delta ($\gamma\delta$) T cells: friend or foe in cancer development? *Journal of Translational Medicine*, 16(1):3, January 2018.
- [507] Mahboubeh Yazdanifar, Giulia Barbarito, Alice Bertaina, and Irma Airoidi. $\gamma\delta$ T Cells: The Ideal Tool for Cancer Immunotherapy. *Cells*, 9(5):1305, May 2020.
- [508] Bruce Alberts, Alexander Johnson, Julian Lewis, Martin Raff, Keith Roberts, and Peter Walter. T Cells and MHC Proteins. *Molecular Biology of the Cell. 4th edition*, 2002.
- [509] J. P. Lévesque, I. G. Winkler, S. R. Larsen, and J. E. J. Rasko. Mobilization of Bone Marrow-Derived Progenitors. In Katalin Kauser and Andreas-Michael Zeiher, editors, *Bone Marrow-Derived Progenitors*, Handbook of Experimental Pharmacology, pages 3–36. Springer, Berlin, Heidelberg, 2007. ISBN 978-3-540-68976-8.
- [510] Nadia Kurd and Ellen A. Robey. T cell selection in the thymus: a spatial and temporal perspective. *Immunol Rev*, 271(1):114–126, May 2016.
- [511] Chapter 9 - T Cell Development, Activation and Effector Functions. In Tak W. Mak, Mary E. Saunders, and Bradley D. Jett, editors, *Primer to the Immune Response (Second Edition)*, pages 197–226. Academic Cell, January 2014. ISBN 978-0-12-385245-8.

-
- [512] L. E. Samelson and R. D. Klausner. The T-cell antigen receptor. Structure and mechanism of activation. *Ann N Y Acad Sci*, 540:1–3, 1988.
- [513] Jr Charles A Janeway, Paul Travers, Mark Walport, and Mark J. Shlomchik. Antigen recognition by T cells. *Immunobiology: The Immune System in Health and Disease. 5th edition*, 2001.
- [514] Alexander M. Mørch, Štefan Bálint, Ana Mafalda Santos, Simon J. Davis, and Michael L. Dustin. Coreceptors and TCR Signaling – the Strong and the Weak of It. *Frontiers in Cell and Developmental Biology*, 8, 2020.
- [515] David F. Tough and Jonathan Sprent. Life span of naive and memory t cells. *STEM CELLS*, 13(3): 242–249, 1995.
- [516] Theo van den Broek, José A. M. Borghans, and Femke van Wijk. The full spectrum of human naive T cells. *Nat Rev Immunol*, 18(6):363–373, June 2018.
- [517] Ineke den Braber, Tendai Mugwagwa, Nienke Vriskoop, Liset Westera, Ramona Mögling, Anne Bregje de Boer, Neeltje Willems, Elise H. R. Schrijver, Gerrit Spierenburg, Koos Gaiser, Erik Mul, Sigrid A. Otto, An F. C. Ruiter, Mariette T. Ackermans, Frank Miedema, José A. M. Borghans, Rob J. de Boer, and Kiki Tesselaar. Maintenance of Peripheral Naive T Cells Is Sustained by Thymus Output in Mice but Not Humans. *Immunity*, 36(2):288–297, February 2012.
- [518] Jeong-Ryul Hwang, Yeongseon Byeon, Donghwan Kim, and Sung-Gyoo Park. Recent insights of T cell receptor-mediated signaling pathways for T cell activation and development. *Exp Mol Med*, 52(5):750–761, May 2020.
- [519] Nathan D. Pennock, Jason T. White, Eric W. Cross, Elizabeth E. Cheney, Beth A. Tamburini, and Ross M. Kedl. T cell responses: naïve to memory and everything in between. *Adv Physiol Educ*, 37(4):273–283, December 2013.
- [520] Jennifer E. Smith-Garvin, Gary A. Koretzky, and Martha S. Jordan. T Cell Activation. *Annu Rev Immunol*, 27:591–619, 2009.
- [521] Thiago A. Patente, Mariana P. Pinho, Aline A. Oliveira, Gabriela C. M. Evangelista, Patrícia C. Bergami-Santos, and José A. M. Barbuto. Human Dendritic Cells: Their Heterogeneity and Clinical Application Potential in Cancer Immunotherapy. *Frontiers in Immunology*, 9, 2019.
- [522] G. M. Griffiths. Protein sorting and secretion during CTL killing. *Semin. Immunol.*, 9(2):109–115, April 1997.
- [523] Susan M. Kaech, E. John Wherry, and Rafi Ahmed. Effector and memory T-cell differentiation: implications for vaccine development. *Nat Rev Immunol*, 2(4):251–262, April 2002.
- [524] Linda Wooldridge, Julia Ekeruche-Makinde, Hugo A. van den Berg, Anna Skowera, John J. Miles, Mai Ping Tan, Garry Dolton, Mathew Clement, Sian Llewellyn-Lacey, David A. Price, Mark Peakman, and Andrew K. Sewell. A Single Autoimmune T Cell Receptor Recognizes More Than a Million Different Peptides. *J Biol Chem*, 287(2):1168–1177, January 2012.
- [525] Markus G. Rudolph and Ian A. Wilson. The specificity of TCR/pMHC interaction. *Curr Opin Immunol*, 14(1):52–65, February 2002.
- [526] T. P. Arstila, A. Casrouge, V. Baron, J. Even, J. Kanellopoulos, and P. Kourilsky. A direct estimate of the human alphabeta T cell receptor diversity. *Science*, 286(5441):958–961, October 1999.
- [527] Jr Charles A Janeway, Paul Travers, Mark Walport, and Mark J. Shlomchik. The major histocompatibility complex and its functions. *Immunobiology: The Immune System in Health and Disease. 5th edition*, 2001.
- [528] Marek Wieczorek, Esam T. Abualrous, Jana Sticht, Miguel Álvaro Benito, Sebastian Stolzenberg, Frank Noé, and Christian Freund. Major Histocompatibility Complex (MHC) Class I and MHC Class II Proteins: Conformational Plasticity in Antigen Presentation. *Frontiers in Immunology*, 8, 2017.
-

- [529] Jacques Neefjes, Marlieke L. M. Jongsma, Petra Paul, and Oddmund Bakke. Towards a systems understanding of MHC class I and MHC class II antigen presentation. *Nat Rev Immunol*, 11(12): 823–836, November 2011.
- [530] Thomas Peacock and Benny Chain. Information-Driven Docking for TCR-pMHC Complex Prediction. *Frontiers in Immunology*, 12, 2021.
- [531] Michael L. Dustin. The immunological synapse. *Cancer Immunol Res*, 2(11):1023–1033, November 2014.
- [532] M. L. Dustin, S. K. Bromley, Z. Kan, D. A. Peterson, and E. R. Unanue. Antigen receptor engagement delivers a stop signal to migrating T lymphocytes. *Proc Natl Acad Sci USA*, 94(8):3909–3913, April 1997.
- [533] Kinjal Shah, Amr Al-Haidari, Jianmin Sun, and Julhash U. Kazi. T cell receptor (TCR) signaling in health and disease. *Sig Transduct Target Ther*, 6(1):1–26, December 2021.
- [534] Alex T. Ritter, Karen L. Angus, and Gillian M. Griffiths. The role of the cytoskeleton at the immunological synapse. *Immunol Rev*, 256(1):107–117, November 2013.
- [535] C. Wülfing and M. M. Davis. A receptor/cytoskeletal movement triggered by costimulation during T cell activation. *Science*, 282(5397):2266–2269, December 1998.
- [536] A. Grakoui, S. K. Bromley, C. Sumen, M. M. Davis, A. S. Shaw, P. M. Allen, and M. L. Dustin. The immunological synapse: a molecular machine controlling T cell activation. *Science*, 285(5425): 221–227, July 1999.
- [537] Benjamin A. Freiberg, Hannah Kupfer, William Maslanik, Joe Delli, John Kappler, Dennis M. Zaller, and Abraham Kupfer. Staging and resetting T cell activation in SMACs. *Nat Immunol*, 3(10):911–917, October 2002.
- [538] Emily J. Quann, Ernesto Merino, Toshiaki Furuta, and Morgan Huse. Localized diacylglycerol drives the polarization of the microtubule-organizing center in T cells. *Nat. Immunol.*, 10(6):627–635, June 2009.
- [539] Xin Liu, Tarun M. Kapoor, James K. Chen, and Morgan Huse. Diacylglycerol promotes centrosome polarization in T cells via reciprocal localization of dynein and myosin II. *Proc Natl Acad Sci USA*, 110(29):11976–11981, July 2013.
- [540] Benjamin Geiger, Dalia Rosen, and d Gideon Berke. Spatial relationships of microtubule-organizing centers and the contact area of cytotoxic T lymphocytes and target cells. *J Cell Biol*, 95(1):137–143, October 1982.
- [541] A Kupfer, G Dennert, and S J Singer. Polarization of the Golgi apparatus and the microtubule-organizing center within cloned natural killer cells bound to their targets. *Proc Natl Acad Sci USA*, 80(23):7224–7228, December 1983.
- [542] Stefanie Redemann, Jacques Pecreaux, Nathan W. Goehring, Khaled Khairy, Ernst H. K. Stelzer, Anthony A. Hyman, and Jonathon Howard. Membrane Invaginations Reveal Cortical Sites that Pull on Mitotic Spindles in One-Cell *C. elegans* Embryos. *PLOS ONE*, 5(8):e12301, August 2010.
- [543] Peter Jan Hooikaas, Hugo GJ Damstra, Oane J Gros, Wilhelmina E van Riel, Maud Martin, Yesper TH Smits, Jorg van Loosdregt, Lukas C Kapitein, Florian Berger, and Anna Akhmanova. Kinesin-4 KIF21B limits microtubule growth to allow rapid centrosome polarization in T cells. *eLife*, 9:e62876, December 2020.
- [544] Chiara Cassioli and Cosima T. Baldari. Lymphocyte Polarization During Immune Synapse Assembly: Centrosomal Actin Joins the Game. *Front Immunol*, 13:830835, 2022.
- [545] Aglaja Kopf and Eva Kiermaier. Dynamic Microtubule Arrays in Leukocytes and Their Role in Cell Migration and Immune Synapse Formation. *Frontiers in Cell and Developmental Biology*, 9, 2021.

-
- [546] Mun Ju Kim and Ivan V. Maly. Deterministic Mechanical Model of T-Killer Cell Polarization Reproduces the Wandering of Aim between Simultaneously Engaged Targets. *PLOS Computational Biology*, 5(1):e1000260, September 2009.
- [547] Oane J. Gros, Hugo G. J. Damstra, Lukas C. Kapitein, Anna Akhmanova, and Florian Berger. Dynein self-organizes while translocating the centrosome in T-cells. *MBoC*, 32(9):855–868, April 2021.
- [548] Meng Sun and Muhammad H. Zaman. Modeling, signaling and cytoskeleton dynamics: integrated modeling-experimental frameworks in cell migration. *WIREs Systems Biology and Medicine*, 9(1):e1365, 2017.
- [549] Vijay Rajagopal, William R. Holmes, and Peter Vee Sin Lee. Computational modeling of single-cell mechanics and cytoskeletal mechanobiology. *WIREs Systems Biology and Medicine*, 10(2):e1407, 2018.
- [550] Ting-Jung Chen, Chia-Ching Wu, and Fong-Chin Su. Mechanical models of the cellular cytoskeletal network for the analysis of intracellular mechanical properties and force distributions: A review. *Medical Engineering & Physics*, 34(10):1375–1386, December 2012.
- [551] Francois Nedelec and Dietrich Foethke. Collective Langevin dynamics of flexible cytoskeletal fibers. *New J. Phys.*, 9(11):427–427, November 2007.
- [552] Jonathan J Ward, Hélio Roque, Claude Antony, and François Nédélec. Mechanical design principles of a mitotic spindle. *eLife*, 3:e03398, December 2014.
- [553] Johanna Roostalu, Jamie Rickman, Claire Thomas, François Nédélec, and Thomas Surrey. Determinants of Polar versus Nematic Organization in Networks of Dynamic Microtubules and Mitotic Motors. *Cell*, 175(3):796–808.e14, October 2018.
- [554] Anna Kabanova, Vanessa Zurli, and Cosima Tatiana Baldari. Signals Controlling Lytic Granule Polarization at the Cytotoxic Immune Synapse. *Frontiers in Immunology*, 9, 2018.
- [555] J. C. Stinchcombe, G. Bossi, S. Booth, and G. M. Griffiths. The immunological synapse of CTL contains a secretory domain and membrane bridges. *Immunity*, 15(5):751–761, November 2001.
- [556] J. C. Stinchcombe, D. C. Barral, E. H. Mules, S. Booth, A. N. Hume, L. M. Machesky, M. C. Seabra, and G. M. Griffiths. Rab27a is required for regulated secretion in cytotoxic T lymphocytes. *J. Cell Biol.*, 152(4):825–834, February 2001.
- [557] Jr Charles A Janeway, Paul Travers, Mark Walport, and Mark J. Shlomchik. T cell-mediated cytotoxicity. *Immunobiology: The Immune System in Health and Disease. 5th edition*, 2001.
- [558] J. K. Burkhardt, S. Hester, C. K. Lapham, and Y. Argon. The lytic granules of natural killer cells are dual-function organelles combining secretory and pre-lysosomal compartments. *J Cell Biol*, 111 (6 Pt 1):2327–2340, December 1990.
- [559] Yovan Sanchez-Ruiz, Salvatore Valitutti, and Loic Dupre. Stepwise Maturation of Lytic Granules during Differentiation and Activation of Human CD8+ T Lymphocytes. *PLOS ONE*, 6(11):e27057, 2011.
- [560] M. Lettau, D. Kabelitz, and O. Janssen. Lysosome-Related Effector Vesicles in T Lymphocytes and NK Cells. *Scand J Immunol*, 82(3):235–243, September 2015.
- [561] J. W. Shiver, L. Su, and P. A. Henkart. Cytotoxicity with target DNA breakdown by rat basophilic leukemia cells expressing both cytolysin and granzyme A. *Cell*, 71(2):315–322, October 1992.
- [562] Jamie A. Lopez, Olivia Susanto, Misty R. Jenkins, Natalya Lukyanova, Vivien R. Sutton, Ruby H. P. Law, Angus Johnston, Catherina H. Bird, Phillip I. Bird, James C. Whisstock, Joseph A. Trapani, Helen R. Saibil, and Iliia Voskoboinik. Perforin forms transient pores on the target cell plasma membrane to facilitate rapid access of granzymes during killer cell attack. *Blood*, 121(14):2659–2668, April 2013.
-

- [563] Dipanjan Chowdhury and Judy Lieberman. Death by a thousand cuts: granzyme pathways of programmed cell death. *Annu Rev Immunol*, 26:389–420, 2008.
- [564] Pierre Golstein and Gillian M. Griffiths. An early history of T cell-mediated cytotoxicity. *Nat. Rev. Immunol.*, 18(8):527–535, 2018.
- [565] T. L. Rothstein, M. Mage, G. Jones, and L. L. McHugh. Cytotoxic T lymphocyte sequential killing of immobilized allogeneic tumor target cells measured by time-lapse microcinematography. *J Immunol*, 121(5):1652–1656, November 1978.
- [566] D. Zagury, Jacky Bernard, Noelle Thierness, M. Feldman, and G. Berke. Isolation and characterization of individual functionally reactive cytotoxic T lymphocytes: conjugation, killing and recycling at the single cell level. *European Journal of Immunology*, 5(12):818–822, 1975.
- [567] M. Poenie, R. Y. Tsien, and A. M. Schmitt-Verhulst. Sequential activation and lethal hit measured by $[Ca^{2+}]_i$ in individual cytolytic T cells and targets. *EMBO J*, 6(8):2223–2232, August 1987.
- [568] Mark T. Esser, Rocio D. Marchese, Lisa S. Kierstead, Lynda G. Tussey, Fubao Wang, Narendra Chirmule, and Michael W. Washabaugh. Memory T cells and vaccines. *Vaccine*, 21(5-6):419–430, January 2003.
- [569] Anna-Karin E. Palm and Carole Henry. Remembrance of Things Past: Long-Term B Cell Memory After Infection and Vaccination. *Frontiers in Immunology*, 10, 2019.
- [570] Federica Sallusto, Jens Geginat, and Antonio Lanzavecchia. Central memory and effector memory T cell subsets: function, generation, and maintenance. *Annu Rev Immunol*, 22:745–763, 2004.
- [571] A. Lanzavecchia and F. Sallusto. Dynamics of T lymphocyte responses: intermediates, effectors, and memory cells. *Science*, 290(5489):92–97, October 2000.
- [572] Arne Knörck, Gertrud Schäfer, Dalia Alansary, Josephine Richter, Lorenz Thurner, Markus Hoth, and Eva C. Schwarz. Cytotoxic Efficiency of Human CD8+ T Cell Memory Subtypes. *Frontiers in Immunology*, 13, 2022.
- [573] Jörg J. Goronzy and Cornelia M. Weyand. Successful and Maladaptive T Cell Aging. *Immunity*, 46(3):364–378, March 2017.
- [574] Pasquine Saule, Jacques Trauet, Virginie Dutriez, Véronique Lekeux, Jean-Paul Dessaint, and Myriam Labalette. Accumulation of memory T cells from childhood to old age: central and effector memory cells in CD4(+) versus effector memory and terminally differentiated memory cells in CD8(+) compartment. *Mech Ageing Dev*, 127(3):274–281, March 2006.
- [575] Marta Czesnikiewicz-Guzik, Won-Woo Lee, Dapeng Cui, Yuko Hiruma, David L. Lamar, Zhi-Zhang Yang, Joseph G. Ouslander, Cornelia M. Weyand, and Jörg J. Goronzy. T cell subset-specific susceptibility to aging. *Clin Immunol*, 127(1):107–118, April 2008.
- [576] M. K. Hellerstein. Measurement of T-cell kinetics: recent methodologic advances. *Immunol Today*, 20(10):438–441, October 1999.
- [577] Derek C. Macallan, Diana Wallace, Yan Zhang, Catherine de Lara, Andrew T. Worth, Hala Ghattas, George E. Griffin, Peter C.L. Beverley, and David F. Tough. Rapid Turnover of Effector–Memory CD4+ T Cells in Healthy Humans. *J Exp Med*, 200(2):255–260, July 2004.
- [578] D. C. Douek, R. D. McFarland, P. H. Keiser, E. A. Gage, J. M. Massey, B. F. Haynes, M. A. Polis, A. T. Haase, M. B. Feinberg, J. L. Sullivan, B. D. Jamieson, J. A. Zack, L. J. Picker, and R. A. Koup. Changes in thymic function with age and during the treatment of HIV infection. *Nature*, 396(6712):690–695, December 1998.
- [579] Jörg J. Goronzy, Won-Woo Lee, and Cornelia M. Weyand. Aging and T-cell diversity. *Exp Gerontol*, 42(5):400–406, May 2007.

-
- [580] Frances T. Hakim, Sarfraz A. Memon, Rosemarie Cepeda, Elizabeth C. Jones, Catherine K. Chow, Claude Kasten-Sportes, Jeanne Odom, Barbara A. Vance, Barbara L. Christensen, Crystal L. Mackall, and Ronald E. Gress. Age-dependent incidence, time course, and consequences of thymic renewal in adults. *J Clin Invest*, 115(4):930–939, April 2005.
- [581] Keith Naylor, Guangjin Li, Abbe N. Vallejo, Won-Woo Lee, Kerstin Koetz, Ewa Bryl, Jacek Witkowski, James Fulbright, Cornelia M. Weyand, and Jörg J. Goronzy. The influence of age on T cell generation and TCR diversity. *J Immunol*, 174(11):7446–7452, June 2005.
- [582] Daniela Weiskopf, Birgit Weinberger, and Beatrix Grubeck-Loebenstein. The aging of the immune system. *Transpl Int*, 22(11):1041–1050, November 2009.
- [583] Jean-Baptiste Manneville and Sandrine Etienne-Manneville. Positioning centrosomes and spindle poles: looking at the periphery to find the centre. *Biol Cell*, 98(9):557–565, September 2006.
- [584] Julien Elric and Sandrine Etienne-Manneville. Centrosome positioning in polarized cells: common themes and variations. *Exp Cell Res*, 328(2):240–248, November 2014.
- [585] Snezhana Oliferenko, Ting Gang Chew, and Mohan K. Balasubramanian. Positioning cytokinesis. *Genes Dev*, 23(6):660–674, March 2009.
- [586] Elizabeth S. Fleming, Mark Zajac, Darcy M. Moschenross, David C. Montrose, Daniel W. Rosenberg, Ann E. Cowan, and Jennifer S. Tirnauer. Planar Spindle Orientation and Asymmetric Cytokinesis in the Mouse Small Intestine. *J Histochem Cytochem*, 55(11):1173–1180, November 2007.
- [587] Luis Alberto Baena-López, Antonio Baonza, and Antonio García-Bellido. The orientation of cell divisions determines the shape of Drosophila organs. *Curr Biol*, 15(18):1640–1644, September 2005.
- [588] Nicholas D. Poulson and Terry Lechler. Robust control of mitotic spindle orientation in the developing epidermis. *J Cell Biol*, 191(5):915–922, November 2010.
- [589] Terry Lechler and Elaine Fuchs. Asymmetric cell divisions promote stratification and differentiation of mammalian skin. *Nature*, 437(7056):275–280, September 2005.
- [590] Gregg G. Gundersen and Howard J. Worman. Nuclear positioning. *Cell*, 152(6):1376–1389, March 2013.
- [591] Jessica L. Feldman and James R. Priess. A role for the centrosome and PAR-3 in the hand-off of MTOC function during epithelial polarization. *Curr Biol*, 22(7):575–582, April 2012.
- [592] U Euteneuer and M Schliwa. Mechanism of centrosome positioning during the wound response in BSC-1 cells. *Journal of Cell Biology*, 116(5):1157–1166, March 1992.
- [593] Andrew D. Doyle, Francis W. Wang, Kazue Matsumoto, and Kenneth M. Yamada. One-dimensional topography underlies three-dimensional fibrillar cell migration. *J Cell Biol*, 184(4):481–490, February 2009.
- [594] Edgar R. Gomes, Shantanu Jani, and Gregg G. Gundersen. Nuclear Movement Regulated by Cdc42, MRCK, Myosin, and Actin Flow Establishes MTOC Polarization in Migrating Cells. *Cell*, 121(3):451–463, May 2005.
- [595] S. Etienne-Manneville and A. Hall. Integrin-mediated activation of Cdc42 controls cell polarity in migrating astrocytes through PKCzeta. *Cell*, 106(4):489–498, August 2001.
- [596] E. L. Holzbaur and R. B. Vallee. DYNEINS: molecular structure and cellular function. *Annu Rev Cell Biol*, 10:339–372, 1994.
- [597] Y. Y. Li, E. Yeh, T. Hays, and K. Bloom. Disruption of mitotic spindle orientation in a yeast dynein mutant. *Proc Natl Acad Sci USA*, 90(21):10096–10100, November 1993.
- [598] Christopher B. O’Connell and Yu-li Wang. Mammalian Spindle Orientation and Position Respond to Changes in Cell Shape in a Dynein-dependent Fashion. *Mol Biol Cell*, 11(5):1765–1774, May 2000.
-

- [599] Lea Stevermann and Dimitris Liakopoulos. Molecular mechanisms in spindle positioning: structures and new concepts. *Current Opinion in Cell Biology*, 24(6):816–824, December 2012.
- [600] Stephan W. Grill, Karsten Kruse, and Frank Jülicher. Theory of Mitotic Spindle Oscillations. *Phys. Rev. Lett.*, 94(10):108104, March 2005.
- [601] Cleopatra Kozlowski, Martin Srayko, and Francois Nedelec. Cortical microtubule contacts position the spindle in *C. elegans* embryos. *Cell*, 129(3):499–510, May 2007.
- [602] Stephan W. Grill and Anthony A. Hyman. Spindle positioning by cortical pulling forces. *Dev Cell*, 8(4):461–465, April 2005.
- [603] Karsten Kruse and Frank Jülicher. Oscillations in cell biology. *Curr Opin Cell Biol*, 17(1):20–26, February 2005.
- [604] Kelly Colombo, Stephan W. Grill, Randall J. Kimple, Francis S. Willard, David P. Siderovski, and Pierre Gönczy. Translation of polarity cues into asymmetric spindle positioning in *Caenorhabditis elegans* embryos. *Science*, 300(5627):1957–1961, June 2003.
- [605] Stephan W. Grill, Jonathon Howard, Erik Schäffer, Ernst H. K. Stelzer, and Anthony A. Hyman. The Distribution of Active Force Generators Controls Mitotic Spindle Position. *Science*, 301(5632):518–521, July 2003.
- [606] Stephan W. Grill, Pierre Gönczy, Ernst H. K. Stelzer, and Anthony A. Hyman. Polarity controls forces governing asymmetric spindle positioning in the *Caenorhabditis elegans* embryo. *Nature*, 409(6820):630–633, February 2001.
- [607] Karsten H. Siller and Chris Q. Doe. Spindle orientation during asymmetric cell division. *Nat Cell Biol*, 11(4):365–374, April 2009.
- [608] Claudia Couwenbergs, Jean-Claude Labbé, Morgan Goulding, Thomas Marty, Bruce Bowerman, and Monica Gotta. Heterotrimeric G protein signaling functions with dynein to promote spindle positioning in *C. elegans*. *Journal of Cell Biology*, 179(1):15–22, October 2007.
- [609] Jacques Pécereaux, Jens-Christian Röper, Karsten Kruse, Frank Jülicher, Anthony A. Hyman, Stephan W. Grill, and Jonathon Howard. Spindle oscillations during asymmetric cell division require a threshold number of active cortical force generators. *Curr Biol*, 16(21):2111–2122, November 2006.
- [610] Hai-Yin Wu, Ehssan Nazockdast, Michael J. Shelley, and Daniel J. Needleman. Forces positioning the mitotic spindle: Theories, and now experiments. *BioEssays*, 39(2):1600212, 2017.
- [611] J. Howard. Elastic and damping forces generated by confined arrays of dynamic microtubules. *Phys. Biol.*, 3(1):54–66, February 2006.
- [612] Jacques Pécereaux, Stefanie Redemann, Zahraa Alayan, Benjamin Mercat, Sylvain Pastezeur, Carlos Garzon-Coral, Anthony A. Hyman, and Jonathon Howard. The Mitotic Spindle in the One-Cell *C. elegans* Embryo Is Positioned with High Precision and Stability. *Biophys J*, 111(8):1773–1784, October 2016.
- [613] Sven K. Vogel, Nenad Pavin, Nicola Maghelli, Frank Jülicher, and Iva M. Tolić-Nørrelykke. Self-Organization of Dynein Motors Generates Meiotic Nuclear Oscillations. *PLoS Biology*, 7(4):e1000087, April 2009.
- [614] D. Q. Ding, Y. Chikashige, T. Haraguchi, and Y. Hiraoka. Oscillatory nuclear movement in fission yeast meiotic prophase is driven by astral microtubules, as revealed by continuous observation of chromosomes and microtubules in living cells. *J Cell Sci*, 111 (Pt 6):701–712, March 1998.
- [615] A. Yamamoto, R. R. West, J. R. McIntosh, and Y. Hiraoka. A cytoplasmic dynein heavy chain is required for oscillatory nuclear movement of meiotic prophase and efficient meiotic recombination in fission yeast. *J Cell Biol*, 145(6):1233–1249, June 1999.

-
- [616] C. P. Broedersz and F. C. MacKintosh. Modeling semiflexible polymer networks. *Rev. Mod. Phys.*, 86(3):995–1036, July 2014.
- [617] Ursula W. Goodenough, Brian Gebhart, Valerie Mermall, David R. Mitchell, and John E. Heuser. High-pressure liquid chromatography fractionation of *Chlamydomonas* dynein extracts and characterization of inner-arm dynein subunits. *Journal of Molecular Biology*, 194(3):481–494, April 1987.
- [618] Ursula Goodenough and John Heuser. Structural comparison of purified dynein proteins with in situ dynein arms. *Journal of Molecular Biology*, 180(4):1083–1118, December 1984.
- [619] Helgo Schmidt, Emma S. Gleave, and Andrew P. Carter. Insights into dynein motor domain function from a 3.3 Å crystal structure. *Nat Struct Mol Biol*, 19(5):492–S1, March 2012.
- [620] Narutoshi Kamiya, Tadaaki Mashimo, Yu Takano, Takahide Kon, Genji Kurisu, and Haruki Nakamura. Elastic properties of dynein motor domain obtained from all-atom molecular dynamics simulations. *Protein Eng Des Sel*, 29(8):317–325, August 2016.
- [621] Charles B. Lindemann and Alan J. Hunt. Does axonemal dynein push, pull, or oscillate? *Cell Motil. Cytoskeleton*, 56(4):237–244, December 2003.
- [622] Hitoshi Sakakibara, Hiroaki Kojima, Yukako Sakai, Eisaku Katayama, and Kazuhiro Oiwa. Inner-arm dynein c of *Chlamydomonas* flagella is a single-headed processive motor. *Nature*, 400(6744):586–590, August 1999.
- [623] Hitoshi Sakakibara and Kazuhiro Oiwa. Molecular organization and force-generating mechanism of dynein. *The FEBS Journal*, 278(17):2964–2979, 2011.
- [624] Comert Kural, Hwajin Kim, Sheyum Syed, Gohta Goshima, Vladimir I. Gelfand, and Paul R. Selvin. Kinesin and dynein move a peroxisome in vivo: a tug-of-war or coordinated movement? *Science*, 308(5727):1469–1472, June 2005.
- [625] Kenji Kikushima, Toshiki Yagi, and Ritsu Kamiya. Slow ADP-dependent acceleration of microtubule translocation produced by an axonemal dynein. *FEBS Letters*, 563(1-3):119–122, 2004.
- [626] Wilhelm J. Walter, Bernhard Brenner, and Walter Steffen. Cytoplasmic dynein is not a conventional processive motor. *J. Struct. Biol.*, 170(2):266–269, May 2010.
- [627] Vladislav Belyy, Max A. Schlager, Helen Foster, Armando E. Reimer, Andrew P. Carter, and Ahmet Yildiz. The mammalian dynein-dynactin complex is a strong opponent to kinesin in a tug-of-war competition. *Nat. Cell Biol.*, 18(9):1018–1024, 2016.
- [628] Ambarish Kunwar, Suvranta K. Tripathy, Jing Xu, Michelle K. Mattson, Preetha Anand, Roby Sigua, Michael Vershinin, Richard J. McKenney, Clare C. Yu, Alexander Mogilner, and Steven P. Gross. Mechanical stochastic tug-of-war models cannot explain bidirectional lipid-droplet transport. *Proc. Natl. Acad. Sci. U.S.A.*, 108(47):18960–18965, November 2011.
- [629] Alberto Montesi, David C. Morse, and Matteo Pasquali. Brownian dynamics algorithm for bead-rod semiflexible chain with anisotropic friction. *J. Chem. Phys.*, 122(8):084903, February 2005.
- [630] Yanping Huang, Darrell D. Norton, Patricia Precht, Jennifer L. Martindale, Janis K. Burkhardt, and Ronald L. Wange. Deficiency of ADAP/Fyb/SLAP-130 destabilizes SKAP55 in Jurkat T cells. *J. Biol. Chem.*, 280(25):23576–23583, June 2005.
- [631] A. Kupfer and G. Dennert. Reorientation of the microtubule-organizing center and the Golgi apparatus in cloned cytotoxic lymphocytes triggered by binding to lysable target cells. *J. Immunol.*, 133(5):2762–2766, November 1984.
- [632] A Kupfer, S L Swain, C A Janeway, and S J Singer. The specific direct interaction of helper T cells and antigen-presenting B cells. *Proc Natl Acad Sci USA*, 83(16):6080–6083, August 1986.
- [633] Pinar S. Gurel, Anna L. Hatch, and Henry N. Higgs. Connecting the Cytoskeleton to the Endoplasmic Reticulum and Golgi. *Current Biology*, 24(14):R660–R672, July 2014.
-

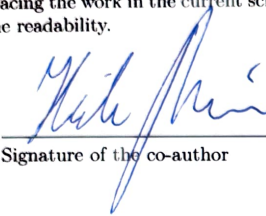
- [634] C. Lee and L. B. Chen. Dynamic behavior of endoplasmic reticulum in living cells. *Cell*, 54(1):37–46, July 1988.
- [635] C. M. Waterman-Storer and E. D. Salmon. Endoplasmic reticulum membrane tubules are distributed by microtubules in living cells using three distinct mechanisms. *Curr. Biol.*, 8(14):798–806, July 1998.
- [636] Krysten J. Palmer, Peter Watson, and David J. Stephens. The role of microtubules in transport between the endoplasmic reticulum and Golgi apparatus in mammalian cells. *Biochem. Soc. Symp.*, (72):1–13, 2005.
- [637] J. W. Putney. A model for receptor-regulated calcium entry. *Cell Calcium*, 7(1):1–12, February 1986.
- [638] M. Hoth, D. C. Button, and R. S. Lewis. Mitochondrial control of calcium-channel gating: a mechanism for sustained signaling and transcriptional activation in T lymphocytes. *Proc Natl Acad Sci USA*, 97(19):10607–10612, September 2000.

Appendix A.

Demarcation from the work of the co-authors

Demarcation from the work of the co-authors

The author of this thesis, Ivan Hornak, designed the research and developed the scientific goals and questions that were answered in [Hornak2020;Hornak2022] in a collaborative effort with the second author of the publication, Heiko Rieger. The author developed and implemented the models, designed and performed the simulations and analyzed the results. For the publications, the author prepared the results and the figures, designed the visualizations of the simulations presented in the manuscripts and supplementary materials and wrote the drafts of the manuscripts. Heiko Rieger supervised the work giving inspiration and direction through discussions. Heiko Rieger also helped to write the introductions and parts of discussions placing the work in the current scientific context. Moreover, he rewrote parts of the manuscripts to increase the readability.



Signature of the co-author

[Hornak2020] I. Hornak and H. Rieger.
Stochastic Model of T Cell Repolarization during Target Elimination I.
Biophysical Journal, 118, 1733–1748, 2020.

[Hornak2022] I. Hornak and H. Rieger.
Stochastic Model of T Cell Repolarization during Target Elimination II.
Biophysical Journal, 118, 1733–1748, 2020.

Faculty of Natural Sciences and Technology

Cumulative thesis: Demarcation from the work of the co-authors

Computational study of T cell repolarization during target elimination

Cytoskeleton rotation relocates mitochondria to the immunological synapse and increases calcium signals

Authors: Ilaria Maccari, Renping Zhao, Martin Peglow, Karsten Schwarz, Ivan Hornak, Mathias Pasche, Ariel Quintana, Markus Hoth, Bin Qu, Heiko Rieger

Journal: Cell Calcium

Volume: 60

Pages: 309--321

Publisher: Elsevier

Year: 2016

Statement of the contributions of the co-authors

IH developed and implemented a geometric model to analyze the data of Fig.2 and produced Fig. 3.

M. Pas. and AQ performed the Calcium measurements for the data shown in Fig. 1.

IM, M. Peg. and KS implemented and analyzed the mathematical Calcium reaction-diffusion model for the Calcium data of Fig. 1 and produced the results shown in Figs. 4-7.

RZ performed the microscopy experiments for the data shown in Fig. 2

BQ and MH designed and advised the experimental work

HR designed and advised the theoretical work

Signature of the PhD candidate



Signature of the supervisor



Appendix B.

Permissions to reprint articles

The articles were used in the thesis in agreement with the permissions of Elsevier stated at <https://www.elsevier.com/about/policies/copyright/permissions>.

According to the permission guidelines:

- Authors can include their articles in full or in part in a thesis or dissertation for non-commercial purposes.
- As an Elsevier journal author, you have the right to include the article in a thesis or dissertation (provided that this is not to be published commercially) whether in full or in part, subject to proper acknowledgment; see the Copyright page for more information. No written permission from Elsevier is necessary.
- This right extends to the posting of your thesis to your university's repository provided that if you include the published journal article, it is embedded in your thesis and not separately downloadable.

The permission to reuse the articles were confirmed by a senior copyrights coordinator in an email conversation.

Appendix C.

Permission to reprint figures

C.1. Permission to reprint Figure 1.1

The Figure was taken from a free PMC article [74] <https://pubmed.ncbi.nlm.nih.gov/25992860/>.

C.2. Permission to reprint Figures 1.2, 1.4 and 1.6

The Figures was reprinted from [5]. This article is distributed under the terms of an Attribution-Noncommercial-Share Alike-No Mirror Sites license for the first six months after the publication date (see <http://www.rupress.org/terms>). After six months it is available under a Creative Commons License (Attribution-Noncommercial-Share Alike 3.0 Unported license, as described at <http://creativecommons.org/licenses/by-nc-sa/3.0/>). <http://creativecommons.org/licenses/by-nc-sa/3.0/>, <http://jcb.rupress.org/content/202/5/779>.

C.3. Permission to reprint Figure 1.5

The Figures was reprinted from open access [156]. It was adjusted in the following way: from the three sketches of the cell I have removed the middle one labeled "Activation without Polarization". Usage and adjustment was done with the Creative Common license Attribution-NonCommercial-ShareAlike 3.0 Unported (CC BY-NC-SA 3.0) <https://creativecommons.org/licenses/by-nc-sa/3.0/>, <https://doi.org/10.1088/1367-2630/15/5/055022>.

C.4. Permission to reprint Figure 2.1

This file is licensed under the Creative Commons Attribution-Share Alike 3.0 Unported license <https://creativecommons.org/licenses/by-sa/3.0/deed.en>, [https://commons.wikimedia.org/wiki/File:EukaryoticCell\(animal\).jpg](https://commons.wikimedia.org/wiki/File:EukaryoticCell(animal).jpg)

C.5. Permission to reprint Figure 2.2b

This file has been identified as being free of known restrictions under copyright law, including all related and neighboring rights <https://creativecommons.org/publicdomain/mark/1.0/deed.en>, <https://en.wikipedia.org/wiki/Cytoskeleton#/media/File:FluorescentCells.jpg>

C.6. Permission to reprint Figure 2.3

This royalty-free image was purchased from <https://www.vectorstock.com/>.

C.7. Permission to reprint Figure 2.4

This file is licensed under the Creative Commons Attribution-Share Alike 4.0 International license <https://creativecommons.org/licenses/by-sa/4.0/deed.en>, https://commons.wikimedia.org/wiki/File:Microtubule_structure.png.

C.8. Permission to reprint Figure 2.5

The Figures was reprinted from the Free PMC article [201]. The copyright can be found here <https://pubmed.ncbi.nlm.nih.gov/7068753/>.

C.9. Permission to reprint Figure 2.6

Re-use of this Figure is permitted in accordance with the Creative Commons Deed, Attribution 2.5, which does not permit commercial exploitation <https://creativecommons.org/licenses/by/2.5/>, https://www.researchgate.net/publication/236084130_Microtubule_dynamic_instability_A_new_model_with_coupled_GTP_hydrolysis_and_multistep_catastrophe/figures?lo=1.

C.10. Permission to reprint Figure 2.7

This article is distributed under the terms of an Attribution–Noncommercial–Share Alike–No Mirror Sites license for the first six months after the publication date (see <http://www.rupress.org/terms>). After six months it is available under a Creative Commons License (Attribution–Noncommercial–Share Alike 4.0 Unported license, as described at <http://creativecommons.org/licenses/by-nc-sa/4.0/>), <https://www.ncbi.nlm.nih.gov/pmc/articles/PMC2289108/>.

C.11. Permission to reprint Figure 2.10

This file is licensed under the Creative Commons Attribution 3.0 Unported license <https://creativecommons.org/licenses/by/3.0/deed.en>, [https://commons.wikimedia.org/wiki/File:Centrosome_\(borderless_version\)-en.svg](https://commons.wikimedia.org/wiki/File:Centrosome_(borderless_version)-en.svg).

C.12. Permission to reprint Figure 2.13

The Figures was reprinted from the Open Access article [452]. This work is licensed under a Creative Commons Attribution 4.0 International License. The images or other third party material in this article are included in the article's Creative Commons license, unless indicated otherwise in the credit line; if the material is not included under the Creative Commons license, users will need to obtain permission from the license holder to reproduce the material. To view a copy of this license, visit <https://creativecommons.org/licenses/by/4.0/>. The copyright can be found here <https://www.nature.com/articles/ncomms9179>.

C.13. Permission to reprint Figure 2.16

The Figure was taken from [534]. [534] is a free PMC article <https://pubmed.ncbi.nlm.nih.gov/24117816/>.

C.14. Permission to reprint Figure 2.17

The Figure was taken from [74]. [74] is a free PMC article <https://pubmed.ncbi.nlm.nih.gov/25992860/>.

C.15. Permission to reprint Figure 2.20

The Figures was reprinted from the open access article [546]. The copyright can be found here <https://journals.plos.org/ploscompbiol/article?id=10.1371/journal.pcbi.1000260>. Content from this work may be used under the terms of the Creative Commons Attribution-NonCommercial-ShareAlike 3.0 licence. Any further distribution of this work must maintain attribution to the author(s) and the title of the work, journal citation and DOI. <https://creativecommons.org/licenses/by-nc-sa/3.0/>.

C.16. Permission to reprint Figure 2.21

The Figures was reprinted from [547]. This article is distributed by The American Society for Cell Biology under license from the author(s). Two months after publication it is available to the public under an Attribution–Noncommercial–Share Alike 3.0 Unported Creative Commons License. <https://www.molbiolcell.org/doi/10.1091/mbc.E20-10-0668>, <http://creativecommons.org/licenses/by-nc-sa/3.0>.

C.17. Permission to reprint Figure 2.22

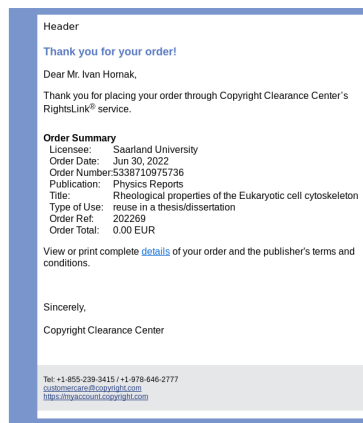
The Figure was taken from [534]. [534] is a free PMC article <https://pubmed.ncbi.nlm.nih.gov/24117816/>.

C.18. Permission to reprint Figure 4.3

The Figures was reprinted from open access [156] in agreement with the Creative Commons license Attribution-NonCommercial-ShareAlike 3.0 Unported (CC BY-NC-SA 3.0) <https://creativecommons.org/licenses/by-nc-sa/3.0/>, <https://doi.org/10.1088/1367-2630/15/5/055022>.

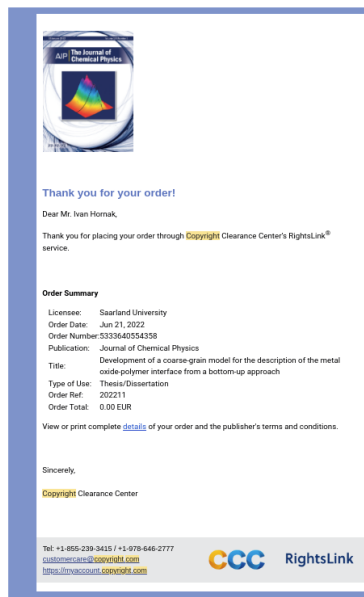
C.19. Permission to reprint Figure 2.2a

The Figures was reprinted from [181] with the following permission cleared via Copyright Clearance center <https://www.copyright.com/>.



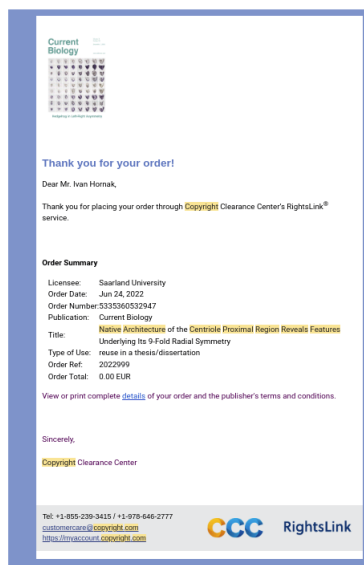
C.20. Permission to reprint Figure 2.8

The Figures was reprinted from [289] with the following permission cleared via Copyright Clearance center <https://www.copyright.com/>.



C.21. Permission to reprint Figure 2.11

The Figures was reprinted from [330] with the the following permission cleared via Copyright Clearance center <https://www.copyright.com/>



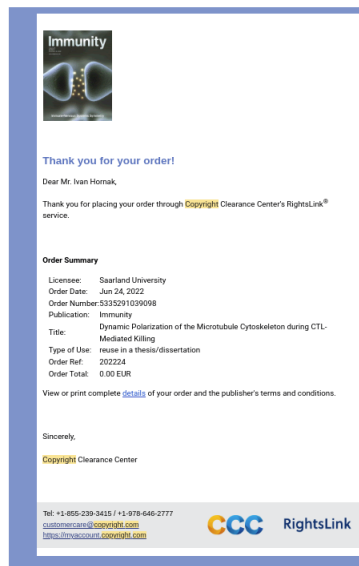
C.22. Permission to reprint Figure 2.12

The Figures was reprinted from [344] with the following permission cleared via Copyright Clearance center <https://www.copyright.com/>.

Journal of Cell Science		0.00 EUR	
Article	Crystal clear insights into how the cytoskeleton works	Publisher Terms and Conditions	
ISSN	1471-0547	Journal Title	Journal of Cell Science
Type of Use	Reproduction	Author	COMPANY OF BIOLOGISTS LTD.
		Publisher	ingenta.com
LINKED CONTENT			
Publication Title	Journal of Cell Science	Publication Type	Journal
Article Title	Crystal clear insights into how the cytoskeleton works	Start Page	755
Author/Editor	Company of Biologists	End Page	774
Date	2022/06	Issue	143
Language	English	Volumes	128
Country	United Kingdom	URL	https://doi.org/10.1242/jcs.25410
Rights Holder	Company of Biologists Ltd.		
REQUEST DETAILS			
Product Type	Image/Photo/Illustration	Distribution	Workbooks
Number of Images / Photos / Illustrations	1	Transmission	Original language of publication
Reproduction Method Applied	Print, Electronic	Copies for the Publisher?	No
Who will reproduce the content?	Academic Institution	Material being reprinted?	No
Source of Use	Use of material from previous editions	Intentional professional use?	No
Literature Used Quantity	Up to 4%	Country	USA
Right Requirement	Other product		
NEW WORK DETAILS			
Title	Computational study of cell coordination during morpho-education	Institution Name	Saarland University
Instructor Name	Ivan Horak	Deposit and expiration date	2022-11-01
ADDITIONAL DETAILS			
Order reference number	20224	The reporting person / organization to appear on the invoice	Ivan Horak
REVISE CONTENT DETAILS			
Title description or numeric label of the part(s) used	Figure 1.C	Title of the article/ chapter the part(s) is from	Crystal clear insights into how the cytoskeleton works
Author of part(s)	Company of Biologists	Author of part(s)	Company of Biologists
Volume of journal or magazine	128	Issue of publication or article from a book	143
Page or page range of part(s)	755-774	Publication date of part(s)	2022/06/01

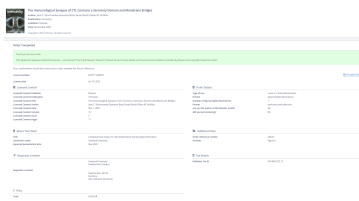
C.23. Permission to reprint Figure 2.19

The Figures was reprinted from [9] with the the following permission cleared via Copyright Clearance center <https://www.copyright.com/>,



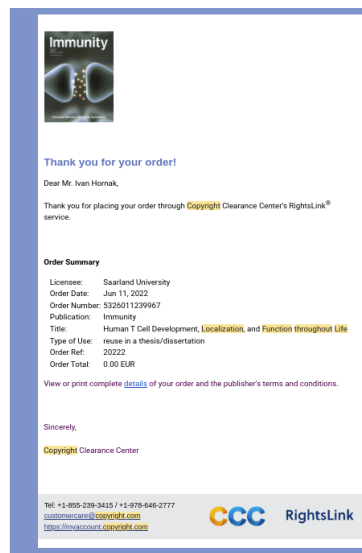
C.24. Permission to reprint Figure 2.23

The Figures was reprinted from [555] with the following permission cleared via Copyright Clearance center <https://www.copyright.com/>.



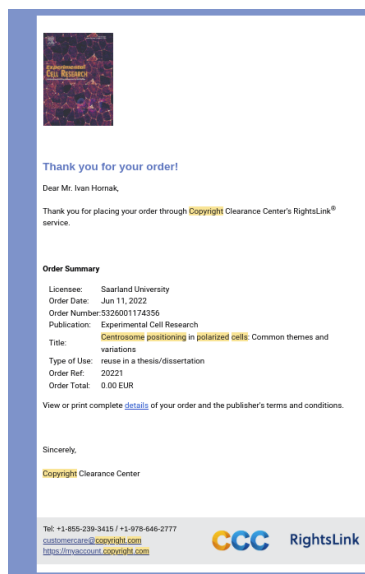
C.25. Permission to reprint Figure 2.24

The Figures was reprinted from [50] with the following permission cleared via Copyright Clearance center <https://www.copyright.com/>.



C.26. Permission to reprint Figure 2.25

The Figures was reprinted from [584] with the following permission cleared via Copyright Clearance center <https://www.copyright.com/>.



Appendix D.

Requirements for the cumulative dissertation

Vorläufiger Leitfaden und vorläufige Vorgaben für die Erstellung, Einreichung und Veröffentlichung von kumulativen Dissertationsschriften

Beschluss des Promotionsausschusses vom 06.12.2018

Allgemeine Festlegungen

Für Doktorandinnen und Doktoranden der Naturwissenschaftlich-Technischen Fakultät besteht die Möglichkeit, ihre Doktorarbeit in Form einer kumulativen Dissertationsschrift einzureichen, falls die wesentlichen Ergebnisse bereits in einschlägigen wissenschaftlichen Zeitschriften publiziert worden sind.

Die kumulative Dissertation muss eine ausführliche Darstellung des wissenschaftlichen Kontextes (state of the art) zu Beginn der eigenen Forschung enthalten sowie eine angemessene Würdigung der für die Ergebnisse der Arbeit relevanten Literatur. Weiterhin muss eine Diskussion der erzielten Ergebnisse der gesamten Arbeit gegeben werden. Der innere Zusammenhang und der eigene Anteil an den verwendeten wissenschaftlichen Arbeiten sind in einer erweiterten Zusammenfassung darzulegen.

Das Vorliegen einer kumulativen Dissertation muss im Antrag auf Eröffnung des Promotionsverfahrens angezeigt werden.

Auf die Einreichung einer kumulativen Dissertationsschrift besteht kein Anspruch. In jedem Fall bedarf die Einreichung in kumulierter Form des Einverständnisses der Betreuerin/ des Betreuers. Im Sinne der Transparenz und klaren Absprachen wird die Übereinkunft am besten bereits in der Betreuungsvereinbarung formuliert.

Anforderungen an die einzubindenden Publikationen

- Als Dissertationen können auch mehrere wissenschaftliche Arbeiten anerkannt werden, wenn sie in einem inneren Zusammenhang stehen und in ihrer Gesamtheit den Anforderungen nach §4 Abs. 1 der Promotionsordnung (selbständig erarbeiteter Beitrag zur wissenschaftlichen Forschung; einem Fachgebiet der Fakultät zugehörig) entsprechen. Der innere Zusammenhang und der eigene Anteil an den Arbeiten sind in einer erweiterten Zusammenfassung darzulegen.
- Grundlage müssen sein: insgesamt mindestens drei Originalpublikationen, die nach dem peer-reviewed-Verfahren begutachtet wurden, davon mindestens zwei in Erstautorenschaft. Die dritte Publikation kann auch eine Patentschrift sein.
- Übersichtsartikel zählen nicht als Originalpublikation.
- Der Anteil und die Tätigkeit der Mitautoren/innen muss genau beschrieben werden und diese Beschreibung muss in die Arbeit eingebunden werden. Weiterhin muss dem Promotionsbüro eine entsprechende Beschreibung mit Unterschriften von allen anderen Mitautoren/innen für die Akten übergeben werden.
- Von den Journalen endgültig angenommene Publikationen sind im Hinblick auf kumulative Dissertationsschriften an der Fakultät als äquivalent zu veröffentlichten Originalarbeiten zu behandeln. Dies ist jedoch daran geknüpft, dass bei Eröffnung des Promotionsverfahrens (=Abgabe der Arbeit) der „Letter of acceptance“ für den bzw. die noch nicht veröffentlichten Publikation/en beigelegt wird.

Im Rahmen von kumulativen Dissertationsschriften ist eine Arbeit in geteilter Erstautorenschaft grundsätzlich zulässig und wird als eine der zwei mindestens notwendigen Veröffentlichungen als Erstautor/in anerkannt. Bei mehr als einer geteilten Erstautorenschaft ist die Arbeit zusammen mit dem Antrag auf Eröffnung des Promotionsverfahrens dem Promotionsausschuss vorzulegen, der auf Basis der Unterlagen (sowie ggf. unter Hinzuziehung von Experten/innen) jeweils eine Einzelfallentscheidung trifft.

Abgabe der Dissertationsschrift bei Eröffnung des Promotionsverfahrens:

Zur Begutachtung Ihrer Dissertationsschrift muss diese den kompletten Abdruck aller Artikel/ Originalarbeiten enthalten. Da es sich hierbei um eine Prüfungsleistung handelt, die zudem nicht öffentlich gemacht wird, verletzen Sie damit keine Verlagsrechte.

Veröffentlichung der kumulativen Dissertationsschrift:

Gemäß §13 der Promotionsordnung müssen die Bewerberinnen/ Bewerber zur Veröffentlichung der Dissertationsschrift sowohl gedruckte Pflichtexemplare abgeben als auch der Universität das Recht einräumen, die Dissertation in Datennetzen zu vervielfältigen und öffentlich wiederzugeben. Dies beinhaltet die Unterzeichnung eines Veröffentlichungsvertrages.

Bei kumulativen Dissertationen müssen Sie sich daher **rechtzeitig vorab** bei den jeweiligen Verlagen zumindest die **Publikationsrechte für die Verwendung in Ihrer Dissertationsschrift** (inklusive der Online-Version) sichern!!

Wie gehen Sie da vor?

- Kümmern Sie sich um die Klärung dieser Frage **sehr frühzeitig**, auch wenn Sie noch nicht sicher sind, ob Sie kumulativ promovieren werden.
- Schreiben Sie die Verlage an, dass Sie die Publikationsrechte für die Verwendung in Ihrer Dissertationsschrift behalten möchten.
- Einige Verlage haben dazu auf ihren Internetseiten ihre „Policy“ veröffentlicht, die sie sich für Ihren Fall bestätigen lassen sollten.
- Prüfen Sie vor Einreichung Ihres Artikels über die Sherpa-Romeo-Datenbank, <http://www.sherpa.ac.uk/romeo/index.php>, ob der Verlag eine Verwertung in der Dissertation zulässt. Wenn nein, schreiben Sie den Verlag dennoch an, ob es in Ihrem Fall zur Veröffentlichung Ihrer Dissertationsschrift möglich ist.

Wenn Sie die Rechte zur Verwendung der Originalpublikationen in Ihrer Dissertationsschrift erhalten, dürfen und müssen Sie diese sowohl in die gedruckten Pflichtexemplare als auch in die finale elektronische Version einbinden. In der Regel entspricht dann also das Pflichtexemplar dem zur Eröffnung des Promotionsverfahrens eingereichten Exemplar.

Es kann sein, dass die Verlage bestimmte Bedingungen vorgeben, z.B.

- Abweichende Seitenzählung
- Änderung des Layouts (insb. Herausnahme des Verlagslogos)
- Ergänzung eines deutlichen Links auf die Publikation des Verlags (z.B. DOI...).
- Einhaltung von Sperrfristen

In einigen Fällen würden die abgegebenen Pflichtexemplare von der zur Eröffnung des Promotionsverfahrens abgegebenen Version abweichen, so dass diese Änderungen oder eine verzögerte Veröffentlichung der Dissertation vorab schriftlich vom Vorsitzenden des Promotionsausschusses genehmigt werden müssen.

Sollten Sie trotz größter Bemühungen **keine** Genehmigung zur Einbindung der Veröffentlichung/en in Ihre Dissertationsschrift erhalten, müssen Sie für Ihren individuellen Fall schriftlich eine Ausnahmegenehmigung des Vorsitzenden des Promotionsausschusses beantragen, dahingehend, dass die copyright-geschützten Originalpublikationen in den Pflichtexemplaren entfernt werden und anstelle dessen lediglich der DOI und bibliographische Daten, die das Auffinden der Publikation ermöglichen (z.B. Autoren, Titel, Journal, Volume, Issue, Seiten) aufgeführt werden.¹

ACHTUNG:

Mit Verabschiedung einer überarbeiteten Promotionsordnung, spätestens aber ab dem 01.01.2020 gilt:

Sollten Sie keine Genehmigung zur Einbindung der Veröffentlichung in Ihre Dissertationsschrift erhalten, ist eine kumulative Dissertationsschrift mit dieser Publikation **ausgeschlossen**. Die Dissertationsschrift muss stets den **gesamten Text** der Arbeiten einbinden.

¹ Sollten die Verlage Ihnen nicht das Recht einräumen, Ihre Artikel als Teil Ihrer Dissertationsschrift zu veröffentlichen, können Sie auch nicht die Manuskriptform der Artikel nutzen, da die Rechte an dieser inhaltsgleichen Version ebenfalls an die Verlage übertragen sind.

Appendix E.

Curriculum vitae

Ivan Horňák

Ph.D. Candidate

 23. February 1988

 Plechamr 430, Bechyně, CZ

 +4915204566421

 hornak.ivn@gmail.com

[Github:/ihornak](#)

Skills

Programming languages

C/C++, Matlab: advanced

Python: intermediate

MCNP: intermediate

Webpages

Drupal: expert

HTML, CSS: advanced

Languages

English: expert

German: intermediate

Czech: native speaker

French: fluent(not active)

Other Skills

Modeling: expert

Monte Carlo: expert

Numerics: advanced

Statistics: advanced

POV-Ray: advanced

Linux: advanced

Latex: expert

3D graphics: intermediate

Work related interests

Modeling, Monte Carlo Methods

Simulation, Traffic

Work Experience

3.2015-
present

Ph.D. in Theoretical Biophysics
Saarland University
Faculty of Natural Sciences and Technology

Work group of Heiko Rieger, Prof. Dr. Dr. h.c.
Created stochastic models of the T Cell repolarization

- Modeled cytoskeleton and motor proteins
- Coarse-grained models of polymers
- Dynamics of rigid structures
- Applied Monte Carlo and Molecular dynamics methods
- Segmentation of complex geometries
- Constrained inertialess dynamics
- Parallel and distributed computing
- Data analysis in Python and Matlab
- Visualization of simulations in POV-Ray
- Created web pages for scientific conferences

9.2013-
2.2015

Institute of Information Theory and Automation
Czech Academy of Science, Prague

Created macroscopic models for the prediction of traffic flow

- Applied the Cell Transmission Model for numerical simulations
- Regression analysis, control theory, traffic flow theory
- Gathering and processing data from measurement stations

2002-
2008

Guide (Summer job)
Tourist Information Center, Bechyně

Guided tours in English, French, and Czech

Education

1.2016 -
present

Ph.D. in Theoretical Biophysics
Saarland University
Faculty of Natural Sciences and Technology

- Researched calcium diffusion, cellular mechanics, and the adaptive immune system responses

09.2013 -
06.2015

Study of software engineering
Czech Technical University
Faculty of Nuclear Science and Physical Engineering

- Monte Carlo simulations of statistical gases, Metropolis algorithm
- Random number generators testing by statistical simulations
- Tutor of Monte Carlo methods
- Linear regression

09.2007 -
06.2013

Master in Nuclear Engineering
Czech Technical University
Faculty of Nuclear Science and Physical Engineering

- Participated in DIRAC experiment in CERN
- Personal dosimetry, medical applications of ionizing radiation
- Simulations of ionizing radiations in MCNP
- Nuclear physics and engineering, numerical mathematics
- Nuclear medicine

09.2001 -
03.2007

High School
"Gymnasium" of Pierre de Coubertin, Tábor
Courses in French predominantly by native speakers

Ivan Horňák



Plechamr 430, Bechyně, CZ



+4915204566421



hornak.ivn@gmail.com

Created webpages

- SFB1027: <https://www.sfb1027.uni-saarland.de/>
- Cell Physics 2021: <http://www.cell-physics.uni-saarland.de/> (2019, 2016, 2015)
- AG Rieger: <https://www.rieger.uni-saarland.de/>

Acknowledgments

I would like to thank my supervisor Professor Heiko Rieger for giving me the opportunity to work on this important topic and for his support. I benefited strongly from his expertise and advises. He allowed his employees a great independence when working on their research topics and was always open to questions and discussions.

I am grateful to Dr. Bin Qu and Dr. Renping Zhao for helping me to understand intracellular processes including CTL polarization. Thanks to them I also gained an insight into experimental methods which is priceless for someone who focuses mainly on theory.

I would like to express my gratitude to my colleagues Michael Welter and Thierry Fredrich who helped me in the world of computing. Their advises had a profound impact on my work and made my progress faster. Being the masters of visualization, they also showed me how to display complex biophysical processes, which is invaluable when presenting the results to interdisciplinary audience.

I would like to thank Barbara Schmidt, Benjamin Bogner, Anil Kumar Dasanna and Adam Wysocki for providing valuable advice when I was writing my thesis.

I would like to thank my friends and colleagues Benjamin Blaß, Shauri Chakraborty, Swarnajit Chatterjee, Marwa Hijazi, Matthieu Mangeat, Hugues Meyer, Zeinab Sadjadi, Karsten Schwarz, Johannes Sicks, Christian Thome and Andre Winter for inspiring advises, friendly support and nice chats over a cup of coffee.

This work would not be possible without the financial support of Deutsche Forschungsgemeinschaft (DFG) within the Collaborative Research Center SFB 1027.

In particular, I would like to thank my family. I am especially grateful to my wife Andrea for her continuous support and to my daughter Sára for giving me energy. Finally, I am grateful to my mother, my mother-in-law, and my grandmother who did not hesitate to travel over seven hundred kilometers to babysit my daughter when the kindergartens were closed in the crazy year 2020.

